LBL-16679
UC-94cd

Lawrence Berkeley Laboratory
UNIVERSITY OF CALIFORNIA

APPLIED SCIENCE DIVISION

RECEIVED
LAWRENCE
BERKELEY LABORATORY
JAN 17 1984
LIBRARY AND
DOCUMENTS SECTION

OXYGEN ELECTRODES FOR ENERGY CONVERSION AND STORAGE - Final Report

L. Gestaut

September 1983

TWO-WEEK LOAN COPY

This is a Library Circulating Copy which may be borrowed for two weeks. For a personal retention copy, call Tech. Info. Division, Ext. 6782.

APPLIED SCIENCE DIVISION

Prepared for the U.S. Department of Energy under Contract DE-AC03-76SF00098

LBL-16679

DISCLAIMER

This document was prepared as an account of work sponsored by the United States Government. While this document is believed to contain correct information, neither the United States Government nor any agency thereof, nor the Regents of the University of California, nor any of their employees, makes any warranty, express or implied, or assumes any legal responsibility for the accuracy, completeness, or usefulness of any information, apparatus, product, or process disclosed, or represents that its use would not infringe privately owned rights. Reference herein to any specific commercial product, process, or service by its trade name, trademark, manufacturer, or otherwise, does not necessarily constitute or imply its endorsement, recommendation, or favoring by the United States Government or any agency thereof, or the Regents of the University of California. The views and opinions of authors expressed herein do not necessarily state or reflect those of the United States Government or any agency thereof or the Regents of the University of California.

LBL-16679

OXYGEN ELECTRODES FOR ENERGY CONVERSION AND STORAGE*

Final Report

September 1983

Lawrence Gestaut
Eltech Systems, Inc.
(subsidiary of Diamond Shamrock Corp.)
470 Center St.
Chardon, Ohio 44024

submitted to:

Technology Base Research Project
Lawrence Berkeley Laboratory
University of California, Berkeley
#1 Cyclotron Road
Berkeley, California 94720

---

* This work was supported by the Assistant Secretary for Conservation and Renewable Energy, Office of Energy Systems Research, Energy Storage Division of the U.S. Department of Energy, under Contract No. DE-AC03-76SF00098 and DE-AC02-77ET25502.

TABLE OF CONTENTS

		Page
1.0	Summary of the Four Year Report	1
2.0	Introduction	2
3.0	Summary of Research During the Past Three Years: 1 October 1977 to 30 September 1980	4
4.0	Summary of Research During the Fourth Year for the period 1 October 1980 to 30 September 1981	8
5.0	Research During the Year: 1 October 1980 to 30 September 1981	16
5.1	Research at C.W.R.U.	16
5.1.1	Oxygen Reduction on Gold in Alkaline Solution in the Presence of Bismuth Ions	16
5.1.2	Oxygen Reduction on Gold in Alkaline Solution in the Presence of Thallium Ions	56
5.1.3	Oxygen Reduction on Ag Electrodes Modified by Ad-atoms Pd and Pt	94
5.1.4	Oxygen Reduction and Evolution on Intermetallic Compounds Based on Ni with Group IVB, VB and VIB Transition Metals	113
5.1.5	Intrinsic Voltammetric Studies of the Adsorbed and Solution Phase Macrocyclics on Gold Electrodes	145
5.1.6	The UV-Visible Absorption and Voltammetry Measurements of Macrocyclics	170
5.1.7	Resonant Raman Spectra of Aqueous Solution of Cobalt and Iron Tetra-Sulfonated Phthalocyanines	204
5.1.8	Thin Layer Cell for UV and Visible Spectrochemical Studies	213
5.1.8.(a)	Thin Layer Spectro-electrochemistry of Binuclear Cobalt (II) and Nickel (II) taph Macrocyclic Complexes	226
5.1.8.(b)	Preliminary Report on Electrocatalytic Properties of the Fe (II) and Fe (III) Complexes of 'dhph'	240
5.1.9	The Effect of Impurity on Surface Raman Spectra of Pyridine on Ag Electrode	246
5.1.10	Investigation of UPD and Bulk Deposition of Metals Using Surface-enhanced Raman on Ag Electrode	251
5.1.11	In situ and Ex situ Mossbauer Spectroscopy Studies of Iron Phthalocyanine Adsorbed on High Surface Area Carbon	259
5.1.12	Determination of the Equilibrium Constant for Superoxide Dismutation	294
5.1.13	Comments on the Van Der Brink, Barendrecht and Visscher Method to Evaluate Rate Constants for Hydrogen Peroxide Decomposition at Rotating Disk Electrodes	313
5.1.14	Gas-fed Porous Electrodes	320

TABLE OF CONTENTS

		Page
6.0	The Fabrication and Evaluation of High Current Density Air Cathodes at Diamond Shamrock	347
6.1	Introduction	347
6.2	Carbon Modifications	347
6.2.1	Experimental	347
6.2.2	Untreated Carbons	348
6.2.3	RB Carbon	351
6.2.3.1	Carbon Powder Studies	351
6.2.3.2	Electrode Studies	351
6.2.4	Shawinigan Black Powder Studies	353
6.2.4.1	Carbon Powder Studies	353
6.2.4.2	Electrode Studies	355
6.2.4.3	Evaluation	358
6.2.5	XC-72R Carbon	359
6.2.5.1	Carbon Powder Studies	361
6.2.5.2	Electrode Studies	361
6.2.6	Ketjenblack Carbon	364
6.2.6.1	Catalyzed Unmodified Carbon Powder Studies	364
6.2.6.2	Catalyzed Modified Ketjenblack Carbon Powder Studies	367
6.2.6.3	Modified Ketjenblack Electrode Study	368
6.2.7	Discussion	370
6.3	Commercial Prototype Electrolyzer Scale-Up	371
6.4	Conclusions	384
6.5	References	385
7.0	Appendix	386
7.1	Publications Under D.O.E. Project	386
7.2	Ph.D. Thesis Under D.O.E. Project	387

1.0 SUMMARY OF THE FOUR-YEAR REPORT

In October, 1977, a four-year project was initiated by the Diamond Shamrock Corporation (DSC) and Case Western Reserve University (CWRU) on the development of high performance oxygen electrodes for a spectrum of applications including industrial electrolysis, metal-air batteries, and fuel cells. The project was sponsored by the U.S. Department of Energy with DSC as the prime contractor and CWRU as the sub-contractor.

The research at CWRU emphasizes the development of more effective electrocatalysts for O_2 reduction and optimization of electrode structures (particularly O_2 cathodes) for utilizing these catalysts. The research approach involved the development of a predictive base through the understanding of the relation of the pathways and kinetics of the electrode reactions to the surface electronic and morphological properties of the electrocatalysts. The DSC group has been concerned principally with the evaluation of catalysts recommended by CWRU as well as by their own staff and the fabrication of electrode structures for these evaluations. A specific objective of the portion of the work in cooperation with DSC has been the achievement of high performance O_2 cathodes now used in the generation of chlorine and caustic. This one application offers the promise of saving many hundreds of millions of dollars of electric power per year for the United States.

CWRU has examined over 100 catalyst systems with the choice influenced on the basis of the anticipated interaction of O_2 with their surface. Many have shown considerable activity in alkaline and a few in acid electrolytes. Particularly exciting are the transition metal macrocyclic complexes and some partially pyrolyzed transition metal macrocycles. High catalytic activity is also obtained with pyrochlores, some spinels and perovskites and some of the carbons (RB carbon of Pittsburgh Carbon Company). Mechanistic studies have identified pathways relying much on kinetic data obtained with a modification of the rotating ring-disk technique developed at Case involving the highly dispersed catalyst on a carbon/graphite support in alkaline electrolytes. Other fundamental developments have included:

1.1 direct detection and quantitative rate measurements in the generation of the superoxide radical ion at electrochemical interfaces using electron spin resonance techniques;

1.2 proof that the O_2 reduction proceeds on certain transition metal macrocycles via an overall 4-electron reduction to OH^- in alkaline solutions with high intrinsic catalytic activity;

1.3 studies on electrosorbed transition metal macrocyclics on carbon and graphite at monolayer levels to provide insight into the factors which control the activity of such adsorbed species;

1.4 synthesis of new binuclear cobalt (II) macrocyclic catalysts $(Co_2taph)^{4+}$ which catalyze the overall reduction of O_2 to OH^- rather than just to the peroxide;

1.5 the role of carbon and graphite surfaces as catalysts for O_2 reduction in alkaline electrolytes as well as supports for dispersed catalysts;

1.6 showing that the UPD layer on Pt and Au can have a pronounced effect in promoting O_2 reduction in alkaline solutions with also the ability to offset the inhibiting effects of various impurities;

1.7 Raman and specular reflectance studies of transition metal macrocyclics adsorbed on electrode surfaces including the detection of the O_2 adduct;

1.8 a better understanding of the effects of the electric field at the interface on the bonding of adsorbed species to the surface through the use of surface enhanced Raman spectroscopy and theoretical calculations based on molecular orbital theory;

1.9 the use of in situ Raman spectroscopy to demonstrate the photo-electrochemical generation of AgO out of Ag_2O on silver in alkaline electrolytes;

1.10 the in situ use of the Mossbauer spectroscopic studies of iron phthalocyanines adsorbed on high surface area carbons to demonstrate the various physical states of the complex in gas-fed porous electrodes in alkaline solutions at relatively high loadings;

1.11 demonstrating the enhancement of O_2 reduction on gold through the addition of trifluoromethane sulfonic acid to concentrated KOH or NaOH solutions, through increased solubility of O_2;

1.12 the understanding of the kinetics of peroxide decomposition on spinels, perovskites, mixed metal oxides and carbons with measurement of rate constants;

1.13 preparation of highly dispersed platinum catalysts on carbon supports by electrocrystallization techniques.

2.0 INTRODUCTION

Electrochemistry is one of the technologies which can make important contributions toward solving energy problems. A significant portion ($\sim$8%) of this nation's electrical power is consumed for industrial electrolytic processes, most of which are carried out with relatively low energy efficiency. Improvements in the efficiencies of these processes will result in substantial power savings. Further, electrochemical energy conversion and storage systems using various fuel cells, batteries, and electrolysis cells offer substantial promise for stationary and vehicle applications.

A key component in the optimization of these energy-important electrochemical systems is the oxygen electrode, both as an O_2 consuming cathode and O_2 generating anode. In practice, the O_2 reduction reactions and the corresponding reverse anodic reactions are very irreversible at low and moderate temperatures and the operating potentials deviate very substantially from the thermodynamic values. Further problems associated with the air-consuming O_2 cathode in fuel cell and metal-air battery applications are limited life (ranging from a few weeks to 5 years) and relatively high cost, particularly if platinum is used as the catalyst at substantial loadings.

Of the various large scale applications envisioned for O_2 electrodes, the most promising in the short term is the use of air-consuming O_2 cathodes in the chlor-alkli industry. The replacement of the presently used H_2 evolving cathodes in chlorine cells with air-consuming cathodes is expected to save $\sim$1.0 V per cell and is very attractive when the H_2 gas is not being used for chemical synthesis. If adopted for a substantial fraction of the chlor-alkali industry nationally, the annual electricity savings would amount to several hundred million dollars. The development of this O_2 electrode technology in the United States is also attractive because of the highly competitive position it would give us internationally in both chlorine-caustic manufacture and the supplying of equipment for such manufacture.

A specific performance target for air cathodes for the chlor-alkali cell application is a O_2 cathode capable of operation on CO_2-free air at a current density of 300 mA/cm2 and voltage of $\geq$0.8 V vs. RHE in approximately 10M NaOH at 85°C with a life expectancy of $\geq$ 10,000 hours.

In October, 1977, a four-year project was initiated by the Diamond Shamrock Corporation (DSC) and Case Western Reserve University (CWRU) on the development of high performance oxygen electrodes for a spectrum of applications including industrial electrolysis, metal-air batteries and fuel cells. The project was sponsored by the U.S. Department of Energy with DSC as the prime contractor and CWRU as the sub-contractor.

The research at CWRU emphasized the development of more effective electrocatalysts for both O_2 reduction and electrogeneration and the development of more effective electrode structures (particularly for O_2 cathodes) for utilizing these catalysts. It also included the development of a predictive base to guide the search for the new catalyst systems. The DSC group was concerned principally with the evaluation of catalysts recommended by CWRU as well as by their own staff and the fabrication of electrode structures for these evaluations.

3.0. SUMMARY OF RESEARCH DURING THE PAST THREE YEARS: 1 October 1977 to 30 September, 1980

3.1 CWRU

3.1.1 Catalyst Systems:

Catalysts which have been examined at CWRU included the following:

3.1.1.1 Metal Catalysts:

Pt, Au, Pd and Ag
Alloys involving these metals
Intermetallics (Ni, Pt and Pd)

3.1.1.2 Underpotential deposited metals.

3.1.1.3 Oxide Catalysts:

Spinels
Perovskites
Mixed oxides of Mn
Pyrochlores

3.1.1.4 Transition Metal Macrocyclics.

3.1.1.5 Various Carbons.

3.1.2 Gas-fed Electrodes

This included the development of more effective electrode structures for utilizing these catalysts. In most instances these catalysts have been prepared at CWRU in low and high surface area forms. In addition to the examination of O_2 reduction kinetics on these surfaces, they have been characterized with such techniques as ESCA, x-ray diffraction, scanning and transmission electron microscopy, BET, Raman and reflectance spectroscopy, as well as various electrical methods. In most instances the kinetics of H_2O_2 reduction and decomposition have also been determined. The research studies have been carried out with the O_2 supplied to the electrode through the electrolyte phase and the more applied work carried out with gas-fed electrodes. The basic research has included the examinatin of the O_2 reduction kinetics with the rotating ring-disk electrode technique which permitted the determination of the amount of H_2O_2 generated as well as the examination of the O_2 reduction kinetics. A modified form of the rotating ring-disk electrode technique has also been developed and used to examine the high area electrocatalysts.

3.1.3 Accomplishments

Some of the accomplishments of the past three years in the development of high performance O_2 cathodes included the following:

A. Catalyst Systems

1. Transition metal macrocyclic catalysts prepared by CWRU exhibited activity comparable to or better than that of highly dispersed platinum at reasonable loadings in alkaline electrolytes such as involved in the chlor-alkali application in the gas-fed carbon O_2 cathodes. The cobalt tetramethoxyphenylporphyrin was found to be particularly effective. This catalyst maintained its high performance throughout approximately 500 hrs. in the life tests carried out at DSC, but thereafter declined a few millivolts per day. The 500 hrs. of high performance before a drop-off in performance, however, is quite adequate for a metal-air cell such as the aluminum-air cell in vehicle applications.

2. Highly dispersed platinum catalysts were prepared by CWRU on carbon supports by electrocrystallization techniques and also by chemical reduction methods. Gas-fed high area electrodes using these catalysts exhibited low polarization even with low loadings (< 0.5 mg/cm^2).

3. Both CWRU and DSC developed high performance gas-fed O_2 test cathodes.

4. It was found that a working (kneading) of the carbon-Teflon mixtures at room temperature resulted in electrodes which were physically more durable and possessed superior mass transport properties. Also matrixing of materials with Teflonated Shawinigan black was found a successful technique if a high degree of material working is involved.

5. DSC developed electrode fabrication techiques and in cell electrode test facilities for the chlor-alkali appplications.

Some of the important findings of a more fundamental nature included the following:

6. Studies on electrosorbed transition metal macrocyclics on carbon and graphite at monolayer levels provided insight into the factors which control the activity of such adsorbed species.

7. Using optical reflectance spectroscopy, the CWRU group were successful in detecting the O_2 adduct for the first time with the adsorbed iron and cobalt tetrasulfonated phthalocyanines on such electrode surfaces as graphite, gold and platinum.

8. Underpotential deposited metals, such as lead and copper on gold, were found to be effective catalysts for the overall 4-electron reduction on gold in alkaline electrolytes.

9. The nickel-cobalt spinels were found to be highly effective catalysts for peroxide decomposition in NaOH. Some of the mixed oxides of manganese afforded even higher activity for peroxide decomposition.

A. Catalyst Systems (contd.)

10. Electrocrystallization techniques were developed for forming platinum crystallites of controlled size on carbon and graphite substrates. Transmission electron microscopy has identified platelet structures exposing principally the (111) surface which had greater stability than would have otherwise been expected.

11. Oxygen reduction to hydrogen peroxide proceeded readily on most carbon and graphite surfaces with a high exchange current density in alkaline electrolytes. However, the further reduction of the peroxide to hydroxide was found to be very irreversible.

12. The presence of traces of Tl in the electrolyte improved the O_2 reduction on Au to a greater extent than Pb. These ions do not only enhance the O_2 reduction on Pt in NaOH solutions, but also offset the inhibitive effect of some ions such as Cd and alkaline earth cations.

13. For most applications carbon and graphite (porous and nonporous) electrodes have been used as support for dispersed catalysts. Carbon and graphite, however, are in themselves catalytically active for O_2 reduction in alkaline solutions. An understanding of the mechanism of O_2 reduction on these electrodes is of considerable importance, not only from a fundamental viewpoint but in view of the possible relatively inexpensive applications of carbon supported dispersed catalysts. The O_2 reduction on glassy carbon in various concentrated NaOH solutions follows the 2e reduction pathway to H_2O_2 quantitatively. However, in the case of Pt dispersed on carbon, it is the $4e^-$ reduction pathway to OH^-. The ratio of $4e^-$ to $2e^-$ reduction is increased by increasing the Pt loading on carbon.

14. Perovskites $LaCoO_3$ and $LaCoO_3$ doped with Sr were prepared by the freeze-dry method and characterized by BET, x-ray diffraction, ESCA measurements, the heterogeneous rate constant for H_2O_2 decomposition, voltammetry and rotating ring-disk measurements for O_2 reduction. It is found that catalyst surface area is not changed much by doping with Sr. In the case of $LaCoO_3$, increasing the thermal treatment temperature considerably reduced the surface area, although this occurs to a lesser extent with $La_{0.5}Sr_{0.5}CoO_3$. Oxygen is reduced on Shawinigan black almost quantitatively to H_2O_2 but with 50% $La_{0.5}Sr_{0.5}CoO_3$ on Shawinigan black, O_2 reduction follows the parallel mechanisms.

15. It is demonstrated that <u>in situ</u> Raman spectroscopy is capable of monitoring the photo-electrochemical generation of AgO out of Ag_2O. Due to the molecular selectivity of Raman spectroscopy, it was possible to show that two electrochemical processes, formation of Ag(I) and Ag(II) species, contribute to the photo current during illumination of the Ag_2O layer. It is shown that the intensity of the Raman bands is directly related to the amount of charge transferred during the electrochemical activation of the silver. The frequencies of several vibrational bands of pyridine, pyrazine, p-nitrosodimethlaniline and

A. Catalyst Systems (contd.)

cyanide adsorbed on a silver electrode have been investigated as a function of the electrode potential using in situ Raman spectroscopy. The frequencies of all bands investigated were found to decrease linearly with cathodic potential. The potential dependece of the C-N- and Ag-C stretching frequencies for cyanide adsorbed on a silver electrode has also been determined using in situ Raman spectroscopy. Model calculations for the force constants of CN^- adsorbed on Ag_4 clusters using an atom superposition and electron delocalization quantum mechanical procedures reveal the same result and indicate that adsorption takes place on one-fold sites.

16. In order to understand the factors controlling the catalytic activity of transition metal macrocyclics for the $2e^-$ and $4e^-$ reduction of O_2 and stability of the adsorbed layer, intrinsic voltammetric studies of the adsorbed and solution phase macrocyclics and solution phase ultraviolet visible absorption measurements have been carried out. Binuclear cobalt(II) macrocyclic catalyst ($Co_2taph(NO_3)_4$), in which two Co(II) ions are separated by approximately 4Å, has been synthesized in the laboratory. The results indicate two pathways for O_2 reduction: $2e^-$ reduction to yield H_2O_2 as well as $4e^-$ reduction to yield H_2O in the presence of the adsorbed macrocyclic on pyrolytic graphite electrodes.

B. Gas-Fed Electrodes:

The CWRU electrode fabrication technique has undergone evolution and refinemet since it was first conceived. In the present technique, the carbon is wetted by agitation using the Genie vortex and the slurry is transferred to a beaker and placed in the cavity of an ultrasonic cleaner. A diluted suspension ($\sim$ 50 mg/ml) of T30B Teflon emulsion is further diluted 10:1 with water. This very dilute suspension is added slowly to the agitated carbon slurry. The slurry is then filtered onto a Nucleopore filter (1 μpore size). The filtered mixture is placed on a Teflon or aluminum sheet and worked with a spatula for several minutes. If a fine carbon is used and the Teflon content is too high (such as 45-50%), the material requires several minutes of kneading at a temperature of 50°C to 70°C (on a steam bath). With working, the mixture becomes quite rubbery and can be pressed into a somewhat flexible electrode. The material is then placed in the pressing die and shaped (using hand pressure) in order to make a reasonably uniform disk and to squeeze out much of the water. The disk is heated in flowing N_2 or He for 2 to 4 hours at a temperature of 250°C to 280°C. This heating thoroughly dries it and also sublimes out much Triton X-100 surfactant (Teflon stabilizer) which has adsorbed on the carbon. The dried disk is pressed in the die at 1 to 2 tons per square inch pressure. A nickel screen is placed on top of the disk and it is pressed again at 6 tons per square inch pressure. The pressing time is 2 to 3 minutes. The disk is removed from the die and then placed in again screen side down. A circular piece of porous Teflon paper is placed on top of the disk and pressed at about 500 lb/in^2.

It should be noted here that the use of ultrasonic agitation in the Teflonation and the extensive kneading of the Teflonated carbon generally produces electrodes which press nicely and are more durable, but the mass transport properties are usually poorer. Depending upon the type of carbon and the extent of working, the amount of Teflon can also make a significant difference. Larger amounts of Teflon stabilize the electrode for long life, but the electrical conductivity, wettability and porosity are affected.

Gas-fed porous electrodes for O_2 reduction can be made from several different catalyzed carbons, but the best ones are: (1) pyrolyzed porphyrins on RB carbon, or (2) very finely divided Pt on RB carbon. RB carbon is specified here because it results in electrodes which work well and generally have good mass transport properties. The long-term failure of RB based electrodes operating in 9M NaOH at 85°C is due to oxidation of the carbon, but this can be minimixed by employing the proper fabrication techniques. Research at Diamond Shamrock indicates that matrixing with Shawinigan black slows down the RB oxidation.

Electrodes fabricated from fine carbons suffer from physical inflexibility and poorer mass transport compared to those made from RB carbon, especially when air is used for the O_2 source.

Some unpyrolyzed macrocyclics (phthalocyanines in particular) have characteristics which make them good catalysts but most of them degenerate and lose activity in hot concentrated caustic in the presence of O_2 and carbon.

Addition of a second metal to a good Pt catalyzed carbon generally decreases the catalytic activity of the platinum.

Spinels and perovskites are reputed to be good peroxide eliminators, but they are generally coarse and possess low surface area. Deposition of fine particles of either upon a carbon is tricky and time-consuming. Also electrodes containing these compounds yield electrode structures which have poor mass transport. Mixing with carbon(s) and Teflonating was tried and a matrixing with Teflonated Shawinigan black was also tried. None of the electrodes made in this manner did well at high current densities.

4.0 SUMMARY OF RESEARCH DURING THE FOURTH YEAR: 1 October 1980 to 30 September 1981

This annual report covers the fourth year, extending from 1 Ocotober 1980 to 30 September 1981 of the four-year project sponsored by the U.S. Department of Energy with Diamond Shamrock Corporation as the prime contractor and Case Western Reserve University as the sub-contractor. The main objective of the project has been to develop high performance oxygen electrodes for a spectrum of applications including industrial electrolysis, metal-air batteries and fuel cells.

The research at CWRU emphasizes the development of more effective electrocatalysts for O_2 reduction and also more effective electrode structures (particularly for O_2 cathodes) for utilizing these catalysts. The approach used by the CWRU group involves the development of a predictive base to guide the search for the new catalyst systems. The DSC group is concerned principally with the evaluation of catalysts developed and recommended by CWRU as well as by their own staff and the fabrication of the electrode structures for these evaluations.

The specific research during the year 1980-81 at CWRU has included the following:

4.1 CWRU

4.1.1 Underpotential Deposited Species

The UPD of bismuth on gold was studied using cyclic voltammetry and the disk-ring method. The effect of bismuth on the O_2 reduction was examined in the following systems:

I) Gold electrode immersed in a solution containing Bi(III).
II) Gold electrode exposed to a Bi(III)-containing solution and then immersed in a Bi(III)-free solution.

In both cases an enhancement of the O_2 reduction with respect to pure gold in a pure electrolyte was observed. For System II the enhancement effect was observed mainly in the kinetic region.

Two distinct classes of results were obtained for System II even in experiments where an effort was made to have all the conditions the same. This diversity probably reflects two different states for the Bi on or in the surface after the Bi preadsorption. In one set of results the analysis of the disk-ring data showed that a series mechanism is operative on this modified surface. Some experiments, however, yielded I_D/I_R ratios which were essentially independent of rotation rate. This behavior can be explained either in terms of a parallel mechanism with HO_2^- not further reduced or decomposed or a slow desorption-adsorption of HO_2^-.

Hydrogen peroxide oxidation and reduction were studied for System I. The reduction of hydrogen peroxide was significantly enhanced with respect to pure gold. A slight depression of the currents for HO_2^- oxidation was observed in the presence of Bi(III) and the reaction order was found to be 1, in contrast to the value of $\sim$0.5 found in the absence of Bi(III).

The combined reduction of HO_2^- and O_2 was examined for both System I and System II. For System I at the same peroxide-O_2 concentrations, the combined reduction currents were much higher than for pure Au. This is explained by the catalytic effect of the Bi(III) on the peroxide reduction process. (The results are given in Section 5.1.1.)

The UPD of thallium has been studied using cyclic voltammetry and the disk-ring method. The addition of Tl(I) to 1M NaOH causes a marked increase in the current for O_2 reduction on Au, although the half-wave potential is not appreciably shifted with respect to the clean Au. An overall exchange of $4e^-$ per O_2 reaching the electrode surface was calculated form the $1/i$ vs. $1/f^{1/2}$ plot for the data with Tl(I) present.

Disk-ring data for O_2 reduction on Au with Tl(I) present should be interpreted with caution since the oxidation of Tl(I) to Tl(III) can interfere at the ring, and the oxidation of hydrogen peroxide is strongly kinetically controlled. Another possible source of error is represented by the small value of the ring currents: a small error in reading these currents can cause a large scatter in the $I_d/I_r \times N$ vs. $1/f^{1/2}$ plots. Consequently qualitative efforts to interpret the disk-ring data in the work with Tl(I) have been limited to situations where the Tl(I) concentration is very low compared to the oxygen concentration. Within the experimental limitations the O_2 reduction on Au with Tl(I) proceeds via a series mechanism as for the clean Au.

Studies with HO_2^- added to the electrolyte showed that Tl(I) has a large catalytic effect on the HO_2^- reduction but an inhibitive effect on the HO_2^- oxidation. (The results are given in Section 5.1.2.)

The Ag electrode has reasonable catalytic activity for O_2 reduction and evolution reactions. In order to enhance the catalytic activity of Ag electrodes, the effect of adatoms such as Pd and Pt in mono- or submono-layers on Ag, as well as the influence of some metal ions such as Tl and Pb, for O_2 reduction have been investigated. Pt and Pd adatoms on Ag surfaces enhance the catalytic activity of the Ag electrode. Tl has a negative effect for oxygen reduction on Pd, in contrast to Pt. However, Pt adatoms codeposited with Pd on Ag are more sensitive to the effect of Tl ions in increasing the catalytic activity for O_2 reduction, but the negative effect of Tl ions is obtained in concentrations greater than 10^{-5} M. Similar results are obtained with Pb ions. (The results are given in Section 5.1.3).

4.1.2 Oxygen Reduction on Carbon

This work gives the study of O_2 reduction on various carbon surfaces in alkaline electrolytes. The work has involved both smooth carbons (e.g. pyrolytic graphite, glassy carbon) and various commercially available high area carbons. The latter has been discussed principally in this report.

Oxygen reduction has been carried out with the rotating ring-disk electrode technique with various carbon powders attached to the disk in a thin layer using Teflon as the binder. The layer is prepared by mixing the carbon particles with a Teflon suspension (du Pont T30B, containing Triton X-100 as the surfactant) and then applying a thin layer ($\sim$10 mm thick) to an ordinary pyrolytic graphite disk (superficial area = 0.20 cm^2). Various catalysts have also been

incorporated in the carbon layer. Oxygen is transported to the outer electrode disk surface through the solution phase with the O_2 then transported within the porous layer through the highly efficient gas capillary wick structure provided by the Teflon. At infinite rotation rate, however, a diffusional O_2 contribution within the porous electrode will persist since the rotation has no direct effect on transport within the electrode. Hydrogen peroxide generated within the porous layer diffuses out of the layer through the electrolyte phase and then is monitored on the gold ring in terms of the anodic limiting current for hydrogen peroxide oxidation. The peroxide transport within the electrolyte phase in the porous layer is usually not as effective as the O_2 transport within the gas-filled wicks. This must be taken into account in interpreting the ring-disk data.

For Ketjenblack thin porous coated (TPc) electrodes in 1M NaOH at a sweep rate of 10 mV/s, it is shown that cathodic and anodic peaks are associated with the reduction of O_2 principally to HO_2^- and the corresponding reverse oxidation process respectively. The peroxide oxidized to O_2 in the anodic peak is formed principally during the cathodic peak. At potentials cathodic to the O_2/HO_2^- peak, the O_2 is still reduced mostly to peroxide with the current under diffusion control in the Nernst layer adjacent to the electrode. Much of the current is probably carried through the outside surface of the TPc electrode. With a catalyst such as Pt (5% by wt.) in Ketjenblack, the anodic peak is no longer present since the platinum catalyzed the 4-electron reduction as well as catalyzed the reduction and decomposition of any peroxide that was produced.

The steady state behavior of the TPc disk-gold ring system showed that the intercept values for $(I_D/I_R)N$ vs. $1/\omega^{1/2}$ plots are greater than unity and somewhat potential dependent, but there is no significant slope. This is most likely the result of the difficulty of transporting peroxide out of the pore structure. The long residence time of the peroxide within the electrode then provides a better opportunity for the peroxide to undergo electrochemical or heterogeneous catalytic decomposition. With a high ash carbon such as the RB carbon of Pittsburgh Active Carbon Co., the $(I_D/I_R)N$ values are much higher but the slopes of the plots vs. $1/\omega^{1/2}$ are essentially zero. At lower polarizations, much of the peroxide is probably reduced or decomposed in the TPc, but at higher polarizations the O_2 reduction is mostly on the outer surface and peroxide escapes into the bulk electrolyte more readily.

The results for various carbons are discussed in relation to the properties of the carbon. The quantitative aspects of the method are also reviewed. (The results are given in Ph.D thesis to be submitted soon).

4.1.3 Nickel Intermetallics: O_2 Generation and Reduction

Pure Ni has reasonable catalytic activity for O_2 generation and reduction. In order to see if the catalytic activity could be increased by combining nickel with transition metals, sixteen intermetallic compounds based on Ni in combination with Mo, V, Zr, Hf,

Ti and Nb were prepared. Most of them were confirmed by x-ray diffraction. Background electrochemical data obtained for the pure metals in 1 M NaOH showed that Zr, Ti and Nb passivate while Mo and V do not.

Voltammetry for most of the compounds was similar to that for Ni except that compounds in the Ni-Mo and Ni-V systems showed an extra anodic peak due to Mo or V dissolution. At potentials between -0.7 and -0.4 V anodic films were formed which inhibited O_2 reduction. NiZr, NiHf and NiTi gave small voltammetric peaks, possibly due to resistive anodic film formation. These three compounds illustrate the overall trend of increasing overpotentials for both O_2 reduction and generation with increasing content of the second metal.

Exceptions to this trend were the Ni-Mo and Ni-V systems, in which increasing Mo or V content was accompanied by slightly lowered evolution overpotentials, due partly to increased surface area. (The results are given in Section 5.1.4).

4.1.4 Transition Metal Macrocyclics

In order to understand the factors controlling the catalytic activity of transition metal macrocyclics for the $2e^-$ and $4e^-$ reduction of O_2 and stability of the adsorbed layer, intrinsic voltammetric studies of the adsorbed and solution phase macrocyclics as well as solution phase UV-visible absorption measurements have been carried out. Cobalt tetrasulfonated phthalocyanine (CoTSPc) and iron tetrasulfonated phthalocyanine (FeTSPc) were synthesized in the laboratory for these studies.

Intrinsic voltammetry of the adsorbed and solution phase macrocyclics has been carried out in 0.1 M NaOH and 0.05 M H_2SO_4 using gold disk electrodes. The effect of concentration of the macrocyclic, sweep rate, stirring of the solution and window opening has been studied to determine the nature of the peaks. In general it is seen that with 10^{-5} M phthalocyanines in solution, only the redox properties of the surface phase species are exhibited. When the concentration is increased to 10^{-3} M, new peaks are obtained which are stirring sensitive and not given by the preadsorbed electrode from the same solution when dipped in the electrolyte alone. These peaks correspond to the redox process of the solution phase species. Based on the voltammetry of the free base H_2TSPc in 0.1 M NaOH and 0.05 M H_2SO_4, an attempt has been made to characterize these peaks. (The results are given in section 5.1.5.)

Cyclic voltammetry measurements of metal-free, Fe(III), Co(II) and Cu(II) tetrasulfonated phthalocyanies and Fe and Co phthalocyanines were done on OPG disk electrodes as a function of pH. It was found that all observed voltammetry peaks showed pH dependence with a slope of 59 mV/pH but not in the whole pH region. Some of the peaks show such a dependence only in acid and some of them only in alkaline regions. All voltammetry peaks are due to surface redox processes except a couple of peaks in the case of H_2TSPc and Cu(II)TSPc, which involve solution phase species.

The influence of oxygen was also examined. It was found that only in the case of Co compounds oxygen influences the most anodic voltammetry peak by changing its anodic-cathodic intensity ratio but not its position. These changes in the anodic region are due to the oxidation of H_2O_2 generated during oxygen reduction in the more cathodic potential range. This was confirmed by an experiment under nitrogen atmosphere with H_2O_2 in solution.

These macrocyclics behave differently except in pH dependence, so that a common conclusion cannot be drawn. (The results are given in Section 5.1.6).

Aqueous solutions of metal-free, Fe(III) and Co(II) tetrasulfonated phthalocyanines were studied by absorption spectroscopy in the UV-visible regions. The absorption spectra were analyzed as a function of phthalocyanine concentration, pH, temperature, presence of foreign ions and some organic solvents, time and exposure to O_2, He and in some cases H_2. It was found that absorption bands did not obey the Lambert-Beer law when the concentration was altered from 10^{-6} to 10^{-3} M. This is explained by the monomer/dimer equilibrium which depends on the total macrocyclic concentration. This equilibrium is shifted towards the dimer side if the total concentration increases and particularly if the ionic strength of solutions increases. However, the opposite trend was observed in the presence of organic solvents such as pyridine, methanol and ethanol. The pH did not show significant influence on Co(II) and Fe(III) TSPc spectra, whereas quite different spectra of H_2TSPc were obtained in acid and alkaline solutions. The influence of oxygen was found only in alkaline and acid solutions of Co(II)-TSPc. when these oxygenated solutions were resaturated with He, only a partial reversibility was found. In regard to the stability of phthalocyanines, it was found that only pure water and neutral salt solutions were fairly stable, whereas in alkaline and acid solutions the decomposition occurred with time. At elevated temperature (70°C) all processes were speeded up. (The results are given in Section 5.1.6).

Tetrasulfonated cobalt and iron phthalocyanines (Co-TSPc and Fe-TSPc) have been studied by Raman spectroscopy in aqueous solutions at various pH. Raman spectra were recorded between 200-1700 cm^{-1} by the polarized and the depolarized light scattered from phthalocyanines in acidic, neutral and alkaline solution phases with the objective of providing more definitive data in order to obtain an understanding of molecular behavior of these molecules, which are increasingly being used and studied as catalyzers in electrochemical aqueous system. (The results are given in Section 5.1.7).

In order to understand the redox properties of (Co(II)taph$(NO_3)_4$) thin layer spectroelectrochemical studies have been carried out in DMF medium using gold mini-grid electrodes. The spectral and redox properties of the Co(II) macrocyclic have been compared with the Ni(II) analog. The electrochemical behavior of the Co(II) and Ni(II) macrocyclics are found to be similar in the anodic region (0 to +1.0 V) which corresponds to the redox behavior of the ring. However, some differences appear in the cathodic region (0 to -1.4 V) which may be due to the involvement of the metal centers.

A binuclear iron(III) complex of 1,4-dihydrazinophthalazine (dhph) has been synthesized in the laboratory and found to catalyze the reduction of H_2O_2 to OH^- in alkaline solution efficiently. Oxygen reduction on a pyrolytic graphite electrode in the presence of the adsorbed complex follows a series mechanism. The graphite probably reduces the O_2 to H_2O_2 which in turn is reduced to OH^- by the complex, in contrast to the analogous Co(II) complex which follows a parallel mechanism and Ni(II) complex which shows no catalytic activity for O_2 reduction. (The results are given in Section 5.1.8).

4.1.5 Fundamental Exploratory Research

4.1.5.1 The Effect of Impurities on Raman Spectra of Pyridine on Silver Electrodes

In-situ Raman spectra of pyridine on Ag in 0.1 M KCl solution prepared in distilled water and pyrolyzed water were taken. Potassium chloride obtained from JMC Puratronic and Fisher Scientific Company (certified A.C.S. grade) was used. It is shown that the hysteresis in intensities of Raman spectra of pyridine, when sweeping potentials in cathodic and anodic directions, can be used as a measure of impurity in a solution. The peak at 10,025 cm^{-1} is shown to be due to AgCl, which was formed during the oxidation-reduction cycle and this peak is more pronounced when the electrode is subjected to progressive roughening. (The results are given in Section 5.1.9).

4.1.5.2 Investigation of UPD and Bulk Deposition of Metals Using Surface- Enhanced Raman Spectra on Ag Electrode

In-situ Raman spectra of pyridine on Ag electrodes were taken in 0.1 M KCl solutions containing cations such as Cd^{++}, Tl^+ and Pb^{++} while simultaneously recording the voltammetry. Cd^{++} ions do not change the Raman frequency shift but decrease Raman intensities at -0.8 V becuse of bulk deposition. In the case of Tl^+ ions, Raman Signals are shifted to smaller values and are explained in terms of electrical field changes in the double layer. A change in intensity after the addition of Tl^+ ions is due to the adsorption of Tl^+ ions on the Ag electrode. Pb^{++} ions do not change Raman peak positions, but the signal disappears completely when the concentration of Pb^{++} ions exceeds 8.4×10^{-5} M. This is explained by the fact that a deposit of Pb is formed on the Ag surface at this concentration and no surface-enhanced Raman effect is observed on Pb. (The results are given in Section 5.1.10).

4.1.5.3 In-situ and Ex-situ Mossbauer Spectroscopic Studies of Iron Phthalocyanine Adsorbed on High Surface Area Carbons

The physical state of monomeric iron phthalocyanine adsorbed on high surface area carbons has been investigated by using ex situ and in situ Mossbauer spectroscopy. Ex situ measurements have indicated that at relatively high loadings, (> 15%) the spectrum is characterized by two doublets (δ_1 0.39 $\pm$ 0.01 $mm.s^{-1}$ (vs. α-Fe), Δ_1 2.60 $\pm$ 0.01 mm/s; δ_2 0.35 $\pm$ 0.02 mm/s (vs. α-Fe), Δ_2 0.95 $\pm$ 0.06 mm/s).

The parameters corresponding to doublet 1 compare favorably with bulk FePc probably present in the form of small crystallites dispersed in the support matrix. At low loadings ($\sim$3.5%) only doublet 2 attributed to FePc chemically bound to the carbon surface was observed. The relative fraction of these two iron species has also been shown to be sensitive to the specific method of preparation of the sample.

In-situ Mossbauer experiments have indicated that the quadrupole splitting decreases about 15-20% upon immersion of the electrode in an alkaline solution, corroborating earlier results obtained by this group. Further evidence concerning the formation of an octahedral complex with OH^- bound in an axial position was obtained by in situ measurements at pH 0. In this case the magnitude of the quadrupole splitting was larger than that obtained in basic solution.

Conventional oxygen reducton polarization curves with fuel cell type electrodes prepared from Mossbauer characterized 15% w/w FePc on XC-72 carbon (Cabot Corp.) have indicated that the crystalline material plays an important role in the overall electrocatalytic process. A thorough discussion of these results as well as a critical review of earlier work have been included. (The results are given in Section 5.1.11).

4.1.5.4 Determination of the Equilibrium Constant for Superoxide Dismutation

By combining polarographic and electron spin resonance (ESR) techniques, the equilibrium constant for $O_2^{\cdot-}$ dismutation $[2O_2^{\cdot-} + H_2O \rightleftharpoons HO_2^- + O_2 + OH^-]$ was determined to be 3.2 ($\pm$ 0.3) x 10^7 in alkaline solutions ranging from 2 to 6 M at 20 $\pm$ 2°C. From this constant and the standard potential for the O_2/HO_2^- couple available in the literature (-0.064 V vs. SHE), the standard potential for the $O_2/O_2^{\cdot-}$ couple was calculated to be -0.286 V vs. SHE at $\sim$ 25°C. (The results are given in Section 5.1.12).

4.1.6 Gas fed Electrodes

The best polarization data were obtained for platiunum catalyzed RV carbon and porphyrin (CoTMPP or CoOEP) catalyzed RB carbon. Other carbons show good activity with these catalysts but mass transport, especially with air, is poorer. Other macrocyclics besides the porphyrins have been tried but either the activity or stability is inferior. Platinum catalyzed carbons are, in general, quite good but the finely deposited Prototec and Stonehart varieties are the best. Depositions on carbon of second metals with platinum have been done but these generally show less activity than platinum alone. The best RB carbon electrodes perform very well at high current densities even when no other catalyst is present. Since potentials are poorer (more cathodic) than the catalyzed ones at low current densities, then this high current density behavior indicates that mass transport processes are probably the limiting factors at very high current densities.

Tests of electrodes made from various spinels and perovskites show promising catalytic activity but the electrical conductivity and mass transport are poor. A lead-doped perovskite shows some promise and a doped lead ruthenate exhibits very high cathodic activity. Samples of clamshell type cobalt phthalocyanines (dimer and polymer) were deposited on RB carbon and electrodes have been made from them. The polarization curves are disappointing because of the low catalytic activity exhibited by the electrodes.

Many of the various catalyzed carbons which were made at CWRU were given to Diamond Shamrock for fabriction into electrodes. Samples of these electrodes were tested here. The polarization measurements are qualitatively indicative of the same catalytic activity and performance as the ones made at CWRU but the mass transport and durability characteristics are generally superior. (The results are given in Section 5.1.14).

5.0 RESEARCH DURING THE YEAR 1 OCTOBER, 1980 TO 30 SEPTEMBER, 1981

5.1 CWRU

5.1.1 OXYGEN REDUCTION ON GOLD IN ALKALINE SOLUTION IN THE PRESENCE OF BISMUTH IONS

R. Amadelli and E. Yeager

INTRODUCTION

Oxygen reduction on noble metal electrodes in the presence of foreign metal ions has been extensively investigated, especially in recent years in view of a renewed interest in this reaction for application purposes. The study of O_2 reduction in the presence of foreign ions is interesting in many aspects. These ions can be originally present in the electrolyte and in some instances can be difficult to eliminate by standard purification procedures such as pre-electrolysis (e.g. earth alkali metal ions in caustic solutions). It is, therefore, of interest to investigate what their effect on O_2 reduction is.

Metal ions introduced into the electrolyte may be specifically adsorbed onto the electrode and change its catalytic activity. This can be increased or decreased depending on the mechanism and particularly the role of adsorbed intermediates in the O_2 reduction. It has been shown, in fact, that some metal ion species have an inhibitive effect while others enhance the catalytic activity of a platinum electrode. The positive effect of the latter ionic species is also observed in the presence of the first (1). Some of these metal ions can be underpotential depositied (UPD) on the substrate (see, e.g., 2). In this chapter, the reduction of O_2 is examined on gold in 1M NaOH in the presence of bismuth ions.

The O_2 reduction on Au is known to proceed via $2e^-$ to form hydrogen peroxide (3). The use of a gold electrode for the study of the effect of foreign metal ions has the advantage that the surface is free of phase oxides in the range where these ions adsorb onto the surface and O_2 is reduced. In alkaline solutions, however, OH^- adsorption occurs at much more cathodic potentials than in acid electrolytes and is present at significant surface coverages at potentials of interest for the O_2 reduction. The charge associated with the OH adsorption corresponds to $\sim$0.35 electrons per surface gold atom at the end limit of the relatively flat plateau in the voltammetry curve (see curve 1 in Fig. 1) just before the peak in the anodic sweep at 0.3 V. This can be interpreted as corresponding either to 35% of a monolayer of discharged "OH" or to a monolayer of OH^{x-} ($0 > x > 1$) and with an electrosorption valency of 0.35 (4).

Oxygen reduction on gold in 1M $HClO_4$ was found to be markedly enhanced in the presence of bismuth by Adzic et al. (5). We undertook a similar study in 1M NaOH in view of the interest of the oxygen cathode for the chlor-alkali industry. While this manuscript was in preparation, an investigation of the O_2 reduction on Au in 1M NaOH was also published by Adzic et al. (6).

EXPERIMENTAL

The reduction of O_2 has been examined on smooth Au in 1M NaOH (Baker, low in carbonates). The preparation and purification of the solution, including pre-electrolysis, have been carried out as described in Chapter II. The Au electrode (99.999%) was polished with alumina powder (Buehler Ltd., 0.3 and 0.05 μm), washed in an ultrasound cleaner in triple distilled water and soaked in 1M NaOH for 1 or 2 hrs. The pre-treatment of the disk-ring electrode was carried out in the test solution and consisted of cycling it a few times (less than 10) between -0.7 and 0.4 V* at 50 mV/s. Excursions to potentials more positive than 0.1 V were limited to a few sweeps to minimize possible gold dissolution and roughening of the electrode. In the presence of bismuth, substantial hysteresis was observed when the polarization curves were recorded in the reverse direction, as is to be expected due to adsorption-desorption of the Bi(III). Negligible hysteresis was found in the absence of Bi(III).

A stock solution (10^{-3}M in bismuth) was prepared by dissolving Bi_2O_3 in 10^{-3} M $HClO_4$ (Baker, Ultrex). This was necessary because the solubility of Bi_2O_3 in NaOH is low [0.012 g/l (7)] and concentrated stock solutions of exact molarity could not be prepared in caustic. Since the amount of stock Bi(III) solution which was added to the test 1M NaOH solution did not exceed 0.5 ml, this did not cause any appreciable variation of the pH. Separate experiments have shown no

---

*All potentials are given vs. $Hg/HgO,OH^-$ with the activity of the OH^- the same as in the test solution. The potential of this electrode is 0.098 V vs. nhe at pH = 14.

influence of the ClO_4^- ions on O_2 reduction in alkaline solution. The Bi(III) solution was added with the electrode at open circuit. During O_2 reduction in the presence of Bi(III), the potential was never swept more negative than -0.55 V to avoid bulk deposition.

Stock solutions of H_2O_2 were prepared from unstabilized hydrogen peroxide (FMC, 90%).

The measuring equipment was described in a previous chapter. The rotating gold ring-gold disk electrode was fabricated at Case Western Reserve University. The disk area was 0.2 cm^2 and the collection efficiency 0.4. For some experiments, a commercial electrode from Pine Instruments was also used. The potential of the ring during the O_2 reduction studies was set at a value of 0.15 V in the limiting current range for H_2O_2 oxidation. When the gold ring is held at this potential for a significant time (> 10 min), an anodic film is believed to build up on the electrode and may result in the current no longer corresponding to the diffusion limiting value. To avoid this problem, the ring potential was stepped to -0.6 V for a few seconds before the recording of each polarization curve. For the studies with Bi(III) present, such a cathodic pretreatment could not be used becuse of the bulk deposition of Bi. A deposit forms at such cathodic potentials and is not removed when the electrode is returned to more anodic potentials. Consequently the best compromise procedure for the disk-ring studies with Bi(III) was to allow the gold ring to sit at open circuit for a few seconds before the O_2 polarization measurements. Separate studies with peroxide added to the electrolyte have indicated this treatment to help to restore the gold surface to a condition where the activity for peroxide oxidation is higher.

RESULTS AND DISCUSSION

A. Cyclic Voltammetry

Cyclic voltammetry curves obtained for Au in argon saturated 1M NaOH with increasing concentrations of added Bi(III) are shown in Fig. 1. For the lower Bi(III) concentration of $\sim 10^{-6}$M (curve 2), the cathodic peak potential is separated by $\sim$ 20 mV from the corresponding anodic peak. Increasing the concentration (3 in Fig. 1) to 5 x 10^{-6}M results in a broadening of the peak and in a shift of the cathodic peak potential in the cathodic direction by $\sim$ 40 mV. A closer examination reveals that this actually represents a double peak. This is clearly shown in Fig. 2. A doublet in the anodic peak was also observed by McIntyre and Peck (8) for the system Bi(III)/Au to pH = 8. This behavior may indicate an adsorption on more than one site or the adsorpition of more than one species. On increasing the concentration to 1.4 x 10^{-5} M (curve 4 in Fig. 1), the cathodic peak potential moves to the cathodic direction. No further shift was observed for higher concentrations. The total shift in potential with respect to the peak at lower concentration was $\sim$ 55 mV. The anodic stripping peak at -0.26 V does not shift appreciably with concentration. As mentioned above, another anodic peak appears at -0.28 V when the concentration of Bi(III) is $\sim$ 5 x 10^{-6}M. At a concentration of 1.4 x 10^{-5} M,

only a broader peak at -0.28 V is present, slightly decreased in height. At this concentration, a new sharp peak appears at ∿-0.43 V which is separated from the complementary anodic peak by ∿30 mV. This peak can be attributed to a phase transition on the surface, although the consensus on the interpretation of anologous peaks for other UPD systems is not unanimous (9,10). As observed in similar cases (11,12), a marked depression of the gold oxide formation is observed in the presence of Bi(III). A broad shoulder is observed around 0.4 V. This could be due to the formation of Bi_4O_7 according to

$$2Bi_2O_3 + H_2O = Bi_4O_7 + 2H^+ + 2e \qquad (1)$$

for which Pourbaix (13) gives

$$E = 1.338 - 0.059\ pH \qquad (2)$$

On the $Hg/HgO,OH^-$ scale, at pH = 14, the potential of reaction (1) is 0.4126 V. It is also likely that the shoulder corresponds to the formation of mixed bismuth and gold oxides. The reduction of the oxides gives rise to two broad cathodic peaks at ∿0.35 V and ∿0.17 V respectively. The first may correspond to the reduction of bismuth oxides, while the second appears to be attributable to gold oxide reduction. No apparent dependence on stirring was observed in the potential range from 0.0 V to 0.6 V.

While it is clear that bismuth is underpotential deposited on Au, the detailed interpretation of all the peaks in the voltammogram is complicated by many factors. In the first place, bismuth oxides can be formed at quite negative potentials (13). Generally, the UPD layers or submonolayers posses a more noble character than the corresponding bulk phase (2). However, it is by no means certain that this would prevent the formation of bismuth oxides, given the strong tendency of this element to oxidize in the range where the underpotential deposition occurs. Gold itself is covered by a submonolayer of partially discharged "OH" species in this potential region (4,14). It seems possible that the deposited Bi species may be present on the surface in some hydroxylated form, also because of a strong interaction with OH groups on the surface.

A further complication for the interpretation of the results is represented by the fact that the nature of the Bi(III) species in alkaline solution is not known (15). The solubility product of $Bi(OH)_3$ is estimated to be 10^{-36} (25) and hence Bi(III) cannot be present as a simple aquo ion. It is likely that the soluble species is $Bi(OH)_4^-$ (16); i.e.,

$$Bi_2O_3 + 3H_2O + 2OH^- \rightleftharpoons 2Bi(OH)_4^- \qquad (3)$$

Schumb and Rittner (16) proposed BiO_2^- as the soluble species formed when Bi_2O_3 is dissolved in NaOH. They reported an equilibrium constant of 5.2×10^{-6} for the process

$$2NaOH + Bi_2O_3 = 2NaBiO_2 + H_2O \qquad (4)$$

Charlot, on the other hand, considers the formation of BiO_2^- only in hot concentrated caustic (18). The possibility that suspensions of Bi_2O_3 are formed cannot be ruled out, especially at higher concentrations.

The dependence on stirring at low and high Bi(III) concentrations is shown in Fig. 3. At the lowqer concentrations (10^{-6} to 10^{-5}M) the dependence on stirring is significant. The solution agitation increases the Bi(III) concentration at the surface. None of the peaks shows appreciable stirring dependence for concentrations of added Bi(III) > 10^{-5} M. The peak current varied linearly with scan rate (from 5 mV to 150 mV/s), while the peak potential remained essentially invaried. This behavior is characteristic of surface controlled reactions (19).

To gain some further insight into the UPD of bismuth, the phenomenon was studied with a disk-ring electrode in an argon saturated solution. A disk-ring study of the UPD of bismuth in $HClO_4$ was carried out earlier by Cadle and Bruckenstein (20). In such studies, great care must be exercised not to confuse iR coupling effects between the ring and disk currents with time effects associated with oxidized or reduced species reaching the ring. The former usually appear as derivatives of the disk current and can only be partially compensated through the use of iR drop compensation-correction circuits. In the present work the ohmic losses in the electrolyte were very small because of the concentrated electrolyte. As a further check, some measurements were also made with two double potentiostats with special iR compensation-correction. This two-potentiostat set-up had been optimized to minimize coupling effects between disk and ring. The results were essentially the same (the ohmic drop correction was $\sim$ 0.1 mV) as those obtained with the Pine dual potentiostat for which the results are herein reported.

Fig. 4 shows the disk current - disk potential and the corresponding ring current - disk potential curves obtained in the present work in 1M NaOH. The curves shown were recorded in the cathodic direction for two different concentrations of Bi(III). The electrode was rotated at 2500 rpm and the ring was potentiostatted at -0.9 V where the Bi(III) bulk deposition was convective-diffusion controlled (Fig. 5). For the lower concentration (curves A, A' in Fig. 4), it is seen that the ring current begins to shield at a disk potential of -0.27 V, indicating the deposition of Bi(III) at the disk. For the higher concentration (curves B,B'), the ring current increased, reaching a maximum at -0.34 V before decreasing to its shielded value. This phenomenon is also clear in Fig. 6, which shows the disk-ring currents for both the cathodic and the anodic scans. The increase in ring current indicates that some soluble species are formed at the disk. This would seem improbable since the phenomenon occurring at the disk is a deposition. However, extensive literature data indicate that the discharge-ionization of bismuth takes place in successive stages (21-25). Delimarskii et al. (24) reported the following scheme for Bi(III) reduction in molten sodium hydroxide:

1) $Bi(III) + 2e^-$ $\rightleftharpoons$ $Bi\ (I)$

2) $Bi(I) + Bi(III)$ $\rightleftharpoons$ $2Bi(II)$
(reaction in the layer near the electrode)

3) $Bi(II) + 2e^-$ $\rightleftharpoons$ Bi

The scheme was postulated by the above authors on the basis of chronopotentiograms which showed two waves. The number of electrons participating in each stage was found to be the same. A typical scheme proposed in concentrated acid solution is the following (22):

1) $Bi(III) + e^-$ $\rightleftharpoons$ $Bi(II)$

2) $Bi(II) + e^-$ $\rightleftharpoons$ $Bi(I)$

3) $Bi(I) + e^-$ $\rightleftharpoons$ Bi

Apart from the details of the mechanism, it seems likely that intermediate products are formed. These may have a certain stability and be desorbed, so that they, or the products of their possible dismutation in the layer near the electrode, would be collected at the ring causing the observed increase in current at -0.34V.

In a subsequent experiment (Fig. 7), the disk was potentiostatted at different potentials for the same length of time (90 s). The deposit was then stripped and the collection of the species produced was monitored by the ring, which was potentiostatted, as above, at -0.9V. Peak A increased with holding time and corresponds to the stripping of the bulk deposit. Peak B, attributable to a phase transition on the surface, reached its maximum height for a holding time of 30 s. Holding the disk at -0.4 V yielded a double peak (D and E). Peak E decreased progressively with holding at potentials more negative than -0.4 V. The small peak F became more pronounced, and shifted to the cathodic direction when the disk was held at potentials more negative than -0.7 V. Since this peak is sensitive to the cathodic holding potential, it appears to involve the oxidation of bismuth in the electrode phase. The process associated with peak F is probably the formation of an oxide layer since the ring did not detect any further production of a solution phase bismuth. This electrode phase bismuth may have been metal deposited on the Au in sufficient quantity that residual Bi metal is still available after the processes associated with the more cathodic peaks (e.g. C, D, E). Alternatively, the Bi may have penetrated into the gold surface through grain boundary diffusion during the holding at the more cathodic potentials.

It is interesting to note that peaks C, C' (Fig. 7) appear in the same potential range as peaks B, B' in Fig. 5-2. They may represent related processes, occurring during the stripping and the deposition of Bi(III) respectively. Peaks B, B' (Fig. 4) have been attributed to a multi-step deposition of Bi(III), as mentioned above. By analogy, peaks C, C' in Fig. 5-7 may be attributable to a multi-step ionization of the Bi(0) deposit. A possible first step in this ionization is the formation of BiOH, as proposed by Williams and Wright (15) for the

oxidation of a Bi electrode in an alkaline solution. This point will be further discussed later.

Except for peak A, the charge derived from the areas under the ring curves did not exceed 40% of the disk charge, and the collection was as low as 10% when the disk was held at -0.35 V (Fig. 7). This is also illustrated in Fig. 8 in which the disk current has been reconstructed by dividing the corresponding ring currents by the collection efficiency.

The plot of $\Delta I_R = (I_{R_L} - (I_{R_{sh}})$ vs. concentration of Bi(III) in solution and of steady-state values of I_{D_L} vs. concentration yielded straight lines with slopes m_1 and m_2 respectively. Here, I_{R_L} is the ring limiting current when there is no disk process and $I_{R_{sh}}$ is the shielded ring current, i.e. when the disk process is at the limiting current. The experimental value of the collection efficiency was calculated from the ratio of m_1/m_2 (26). Its value was 0.18, compared to the theoretical one of 0.1829.

Because of the incomplete stripping of the bismuth from the surface, the electrosorption valency could not be derived with the method of Bruckenstein et al. (27). Bismuth was not stripped even at high anodic potentials. This is seen in Fig. 9. In this experiment, the gold electrode was withdrawn under potential control (at -0.8 V) from a solution containing 10^{-5} M Bi(III) and introduced into a bismuth-free 1M NaOH solution. The electrode was then scanned from -0.8 V to 0.6 V at 100 mV/s. Bismuth was lost into the solution. However, after 5 min scanning, some bismuth still remained on the surface and its quantity (as indicated by the peak areas) did not decrease even after prolonged scanning (curve 2 in Fig. 9). The electrode was then potentiostatted at -1.0V for 30, 60 ad 120 s. The stripping of a bulk deposit was observed at $\sim$ -0.78 V and the UPD peak around -0.3 V increased in height. The interesting point is that the corresponding cathodic peak also increased with holding, despite the fact that the scan reached fairly anodic potentials before being reversed. It is evident, therefore, that bismuth, once deposited on the gold electrode, is very tenacious and the surface never becomes completely free of it. This conclusion is in agrement with McIntyre and Peck (8).

B. Bulk Deposition and Behavior of Deposits Formed from Concentrated Bi(III) Solutions

A polarization curve for bulk deposition of Bi(III), obtained point by point, is given in Fig. 5. In the experiment of Fig. 10 the bulk deposition was studied by scanning the potential and using a relatively high concetation of Bi(III). During the sweep in the cathodic direction the cathodic current corresponds to the steady state convective-diffusion controlled value only at potentials more negative than -0.7 V. A large peak is observed at $\sim$ 0.63 V which is slightly rotation rate dependent and only appears at higher concentrations of Bi(III), i.e. $\sim 10^{-4}$ M. It may correspond to the deposition of Bi species having a valency < 3. For the scan in the anodic direction a

current plateau is obtained from -1.0 to -0.6 V. The plot I_D, in the limiting current region (e.g. -0.8 V), vs. $f^{1/2}$ gives a straight line with a zero intercept. This means that the deposition is mass-transport controlled. As a check, the concentration of Bi(III) was estimated from the slope of the plot of I_D vs. $f^{1/2}$ On the assumption that the diffusion coefficient is $\sim 10^{-6}$ cm^2/s and that the process involves $3e^-$, the estimated concentration was 2×10^{-4}M. This value compares fortuitously well with the concentration of Bi(III) added to the solution (2×10^{-4}M). This favorable comparison should not be overinterpretd, but implies that the diffusing species is in solution rather than in a colloid or large polymeric form.

Fig. 11 illustrates the ring current of a shielding experiment in which the deposition of Bi(III) was examined on a gold disk in a solution containing $\sim 1.5 \times 10^{-5}$M Bi(III). The ring was potentiostatted at a potential at which bulk Bi(III) deposition occurs (-0.9 V). The polarization curve was obtained point by point scanning at the rate of 20 mV/s between points, and waiting at least 15 s before recording each point. The experimental points were recorded proceeding in the cathodic direction. The relatively large current observed between a and b decreases to the open-circuit disk value (i.e., the ring current when the disk is not connected) within 5 to 10 s. This indicates that Bi species are produced at the disk since the current is higher than that observed for the disk at open circuit. This phenomenon has already been discussed above (see Fig. 2). From points c to g the current decreases below the open disk value but increases again to the latter value within 5 s when the potential scan is interrupted. It is not very clear which species is deposited. One possibility would be the reduction of Bi(III) to species having an oxidation state lower than 3. The deposition of Bi(III) to Bi(0) under mass-transport control occurs at -0.6 V.

It was felt appropriate to study also the stripping of a thick bismuth deposit and to compare the potentiodynamic curves obtained with those obtained for mono- or submonolayers. Fig. 12 shows the cyclic voltammetry curves for an ordinary pyrolytic graphite electrode onto which Bi(III) was deposited for different lengths of time. The cyclic voltammetry profile has some similarity to that of a bulk Bi electrode in alkaline solutions (34). This figure indicates the formation of oxides at potentials of -0.5 V and higher. It is clear, therefore, that especially at relatively high concentrations of Bi(III) in solution (near to or higher than 10^{-5}M) the bismuth species adsorbed on a gold surface may be present in an oxidized form at potentials more anodic than -0.3 V. This is further illustrated in Fig. 13. In this case, a gold disk electrode was potentiostatted for 30, 60 and 90 s at -0.55 V in a solution containing 2×10^{-5}M Bi(III). An isopotential point in the stripping curves is observed at -0.24 V. This isopotential point was not observed at the ring when this was used to monitor the stripping at the disk. The ring did not detect any significant change in Bi(III) solution phase concentration in the vicinity of either peak C or D (see also Fig. 7). Thus the processes responsible for peaks C and D (Fig. 13) did not involve a solution phase species and

must be surface reactions. The holding time at the cathodic potential limit influenced the coverage of the species associated with peaks D and C. The isopotential point can be explained if the peaks are irreversible (no back reactions) and the sum of the surface concentrations of the species controlling the rates for peaks C and D add up to a constant independent of the holding time. A theoretical treatment of isopotential points has been reported by Untereker and Bruckenstein (35).

The following specific processes can be proposed to explain peaks A to D in Fig. 13 (see also Fig. 7):

$$Bi(0) \longrightarrow Bi[III(1 - \lambda)] + 3\lambda e^-$$

where λ is the partial charge transfer coefficient of Lounz (see Chapter II) and Bi(0) is either metallic bismuth on the Au surface or bismuth intergranularly penetrated below the surface. The $Bi[III(1 - \lambda)]$ can be either a UPD species with significant metallic character or, more likely, still retaining ionic character perhaps in the form of a complex with OH^-, i.e., of the form $[Bi(III)(OH)_x(OH_2)_y]^{3-}$. This complex species may then undergo a transformation into an oxide as the potential is made more positive. This transformation may take place already after peak C in Fig. 13.

For the voltammetry curve in Fig. 14, the electrode was introduced under potential control at 0.0 V into a solution containing 6×10^{-6}M Bi(III), and the potential window was progressively opened in the cathodic direction. Peak I appears at a potential of -0.29 V. The peak potential of peak II, in the anodic direction, is -0.25 V. This anodic peak increases to its maximum height when the cathodic potential limit is -0.4 V. The amount of charge under the curve in region III (from -0.2 V to 0.0 V) increases as the potential scan limit is made progressively more cathodic. It is likely that this is due to the formation of bismuth oxides (see also Fig. 12). It is also apparent that some of the species oxidized at III are reduced, upon reversing the scan, at $\sim$ -0.3 V as indicated by the increase of the height of peak I. However, the charge under peaks II and III is much larger than that under peak I alone. Therefore the reduction of the species formed curing the anodic sweep must continue past peak I in the cathodic sweep. This reduction does not appear to be complete even when the potential has become sufficiently cathodic for the bulk deposition of Bi(III) to occur.

C. Oxygen Reduction on Au in 1M NaOH Containing Bi(III)

Fig. 15 shows the disk-ring polarization curves for O_2 reduction on Au in 1M NaOH containing 4×10^{-6}M Bi(III). In contrast to what was reported by Adzic *et al.* (6) at comparable concentration, no ihibition was found in the kinetic controlled region, when the polarization curves are compared to those obtained on pure gold. The hysteresis was negligible for Au and for Au/Bi_{ad} in the kinetic controlled region from 0.0 to $\sim$ -0.25 V. At potentials more negative than -0.25 V the hysteresis becomes quite significant in the

presence of Bi(III). This occurs by reason of the adsorption of Bi(III) which changes the state of the surface.

The ring currents of Fig. 15 in the disk potential region from 0.0 to -0.3 V are higher than those reported by Adzic et al. (6). We have found that lower ring currents were observed when the ring potential was set more anodic than 0.2 V. Adzic et al. used 0.3 V for the ring potential. Most likely this arises because of a deactivation of the ring due to the formation of a thicker oxide layer. In the present work, the ring potential was held at 0.15 V to avoid the formation of a thick layer of oxides and the consequent deactivation of the ring electrode.

Fig. 16 shows a comparison of the disk-ring polarization curves for O_2 reduction in the absence and in the presence of increasing Bi(III) concentrations. We found the catalytic activity to increase for increasing concentrations of Bi(III) from 10^{-6}M to 10^{-5}M. For Bi(III) concentrations of 10^{-5}M and higher, the observed enhancement of the activity was less than for lower Bi(III) concentrations, but always higher than for pure Au.

For a first order kinetic with respect to dissolved molecular oxygen, the Levich treatment gives

$$\frac{1}{i} = \frac{1}{i_k} + \frac{1}{B\sqrt{f}} \qquad (5)$$

where i_k is the current with pure kinetic control, f is the rotation rate (rotations per minute) and

$$B = 0.62nFD^{2/3}\nu^{-} 116C_o \qquad (6)$$

Here, n is the number of electrons per O_2 molecules passing through the Nernst diffusion layer, D is the diffusion coefficient of O_2, ν is the kinematic viscosity and C_o is the bulk concentration of O_2. The plot of $1/i$ vs. $1/f^{1/2}$ at different potentials should yield straight lines with slopes equal to $1/B$. These plots are shown in Fig. 17 for the O_2 reduction on Au in the absence and in the presence of Bi(III). The plot for Au at -0.5 V has a zero intercept, indicating pure mass-transport control at this potential. The intercepts are also very close to zero with Bi(III) present at voltages from -0.25 to -0.4 V, indicating mass-transport control, now even at less cathodic potentials (e.g., -0.25 V). The current is entirely O_2 reduction: the contribution from deposition of Bi(III) at 4×10^{-6}M is negligible. The value of the constant B derived from the slope of the straight lines in Fig. 17 was 8.8×10^{-3} mA/(rpm)$^{1/2}$ for pure Au. This value agrees very well with the calculated one of 8.6×10^{-3}, using the data of Gubbins et al. (28) for the solubility and diffusion coefficient of O_2 in 1M KOH, assuming a 2-electron process. The B value obtained in the presence of 4×10^{-6}M Bi(III) was approximately 16×10^{-3} mA/(rpm)$^{1/2}$ at potentials from -0.15 V to -0.4 V. This value

corresponds to $\sim$ 3.7 electrons per O_2 reaching the electrode surface, which indicates that OH^- is the principal product.

Within the precision of the data, the intercept with Bi(III) present at -0.45 V and -0.5 V is actually negative. Negative intercepts have also been obtained for the reduction of HO_2^- on Au in the presence of Pb(II). Possible explanations will be discussed in a later chapter.

The disk-ring data (Fig. 15) were analyzed using the diagnostic criterion of Wroblowa et al. (29). The ring polarization curves showed some background current (see Fig. 15) which was subtracted from the observed ring currents prior to making disk-ring calculations. This background ring current was negligible in the experiments without bismuth addition in the electrolyte. This suggests, therefore, that the background current is due to an anodic process involving the metal species added to the electrolyte, i.e., Bi(III) oxidation. The background current of $\sim$ 15 μA seems reasonable taking into account the Bi(III) concentration in the electrolyte (4×10^{-6}M).

The ratio of the disk to ring current multiplied by the collection efficiency was plotted against the reciprocal of the square root of the rotation rate, for different disk potentials. These plots are shown in Fig. 18. The polarization curves were recorded in the direction of increasing (more anodic) potentials and in Fig. 5-19 for the cathodic direction. The plots yielded straight lines with potential dependent slopes and a common intercept of 1 in the potential region from -0.1 to -0.25 V in Fig. 18 and -0.125 to -0.5 V in Fig. 19. In terms of the Wroblowa et al. analysis, a common intercept of 1 for the $(I_D/I_R) \times N$ vs. $1/f^{1/2}$ plots is predicted when $k_1 = 0$ and $(2k_3 + k_4/k_5)$ is negligible with respect to 1 (see Chapter I). At potentials more negative than -0.225 V with scanning in the anodic direction the intercepts as well as the slopes become potential dependent (Fig. 18). Since this was not observed when scanning in the cathodic direction, this marked change in the $(I_D/I_R) \times N$ vs. $1/f^{1/2}$ plot in Fig. 5-18 may be associated with some type of hysteresis effect in the number of electrons at some cathodic potential where the electrode surface is not at steady state. In the absence of Bi(III), Au does not show such hysteresis.

The interpretation of the above results is therefore complicated by the fact that, for concentrations less than 10^{-5}M of added Bi(III), the quantity of bismuth on the surface depends on the agitation of the solution (see Fig. 3).

A Tafel plot (corrected for mass-transport) obtained for the reduction of O_2 in the presence of Bi(III) is reported in Fig. 20. The Tafel slope obtained for Au in the absence of Bi(III) was -120 mV/dec. In contrast to Adzic et al. (6) who reported a Tafel slope of -120mV/dec both in the presence and in the absence of Bi(III), the plot of Fig. 20 reveals a more complicated situation. The validity of this plot for mechanistic considerations will be discussed in a later chapter. The region of lower overpotentials should be interpreted with caution, particularly in view of the fact that the curves did not

approach the zero current asymptotically but yielded a small residual positive current of ∿5 μA.

D. O_2 Reduction on Au Electrodes Pre-exposed to Bismuth

In a separate series of experiments, a gold electrode was scanned from -0.55 V to +0.1 V about 10 times in 7 x 10-6M Bi(III) in 1M NaOH, held at -0.55 V in this solution for 20 s, removed in air and then immersed in a Bi(III)-free 1M NaOH saturated with O_2. Polarization curves for O_2 reduction were then recorded point by point (Fig. 21). The data of Fig. 21 show that the effect of the bismuth on O_2 reduction still persists. The plot of $1/i$ vs $1/f^{1/2}$ yielded straight lines approximately parallel to each other between -0.1 V to -0.2 V (Fig. 22). The B value in this potential range is $\sim 11 \times 10^{-3}$ mA/(rpm)$^{1/2}$, corresponding to ∿2.6 e^-. At more negative potentials, the slope of the plots increases slightly, indicating a decrease in the number of electrons. Thus at -0.5 V the B value is 9.8×10^{-3} mA/(rpm)$^{1/2}$.

The I_D/I_R vs. $1/f^{1/2}$ plot, constructed from the disk and ring polarization curves, yielded straight lines with both the intercepts and the slopes potential dependent (Fig. 23). For this case, the analysis by Wroblowa et al. predicts a relationship between the slopes (S) and the intercepts (J) of the form:

$$J = 1 + 2\frac{k_1}{k_2} + \frac{zS}{k_6} \qquad (7)$$

The slope vs. intercept plot for the data of Fig. 23 is shown in Fig. 24. The new intercept J' is very close to 1, indicating $k_1/k_2 \ll 1$ and hence only the series process is operative.

A Tafel plot obtained point by point for the O_2 reduction under these conditions is shown in Fig. 25. The plot shows two limited linear regions of slopes -42 mV/dec and -142 mV/dec, in each case only over a part of a decade. The higher value is the more reproducible and compares well also with the value of -150 mV/dec obtained at the more negative potentials in experiments with Bi(III) present in the solution (Fig. 20).

In a separate set of experiments (Fig. 26) with scanning at 10 mV/s, under what was believed to be identical conditions, the analysis of the data yields $(I_D/I_r) \times N$ vs. $1/f^{1/2}$ plots (Fig. 27) which are straight lines with potential dependent intercepts and zero, or almost zero, slopes. The different behavior observed in Figs. (23) and (27) is probably due to a difference in the state of the Bi on or in the surface of the gold. This different behavior persisted even after sweeping the potential several times in both directions.

The data of Figs. 21 to 25 will be referred to as data of type I for pre-adsorbed Bi on Au and that of Figs. 26 to 3- as type II. The type II behavior in Fig. 27 indicates one of two situations:

1. The O_2 reduction proceeds via the parallel mechanism involving $4e^-$ to OH^- and $2e^-$ to HO_2^- but not by further reduction of HO_2^- to OH^-; or

2. The desorption of HO_2^- from the electrode surface is very slow (small k_5 and k_6 of the Wroblowa et al. analysis).

It is not possible to distinguish between the two alternatives with the Wroblowa et al. analysis, and hence to reach any conclusion as to whether k_1 is negligible or not. The experimental data were also analyzed according to the procedure indicated by Bagotskii et al. (30). Considering that the adsorption-desorption of O_2 and HO_2^- are at equilibrium, the following equation can be derived:

$$\left(\frac{I_A^\circ - I_D}{}\right) \times N = 1 + 2\left(\frac{Z_A}{Z_B}\right)\frac{k_2' + k_3 + k_4}{k_2} + \frac{2Z_A}{k_2} \qquad (8)$$

In eq. (8), $Z_A = 0.62D^{2/3}\nu^{1/6}$ and $I_A^\circ = 4FZ_A f^{1/2}CO_2$ is the convective-diffusion limiting current for the $4e^-$ process. The term Z_B is a parameter analogous to Z_A but referred to H_2O_2. According to eq. (8), k_2 can be calculated from the slope of the plot $(I_A^\circ - I_D/I_R) \times N$ vs. $f^{1/2}$. These plots are shown in Fig. 28. The potential dependence of the slopes is not surprising since they depend on $1/k_2$, which is potential dependent. In Table 1 are reported the values of k_2 calculated from Fig. 28.

TABLE 1

Potential Dependent Values of k_2 and k_1 for O_2 Reduction on Au with Pre-adsorbed Bi: Data Set II Obtained from Fig. 27.

E(V)	$k_1 \times 10^2$ (cm/s)	$k_2 \times 10^2$ (cm/s)
-0.1	1.132	0.234
-0.125	1.27	0.326
-0.15	1.653	0.507
-0.175	2.295	0.76
-0.2	3.1	1.05
-0.225	3.76	1.28

The values of k_1 listed in this table were obtained from the intercepts in Fig. 27 (i.e., $1 + 2k_1/k_2$). The intercept in Fig. 28 is close to 1, indicating that $(k_2' + k_3 + k_4)$ is negligible with respect to k_2.

The values of log k_1 and log k_2 were plotted vs. the potential (Fig. 29). The slope of the log k_2 vs. E plot is -158 mV/dec. This value is not unexpected since Tafel slopes, of the overall current, between -40 mV/dec and -150 mV/dec were obtained for the O_2 reduction on this modified surface. However, the slope of log k_1 vs. E was -205 mV/dec. The plot of Fig. 28 is of course based on the assumption that the adsorption-desorption of hydrogen peroxide is essentially at equilibrium.

Bagotskii et al. (31) have also proposed an analysis which takes into account the possibility of slow adsorption-desorption not only of HO_2^- but also of O_2. Because of the serveral constants which cannot be determined independently, this analysis does not allow one to establish unambiguously if k_1 is significant or negligible.

It remains to be explained how experiments which were carried out in a similar fashion (see Figs. 21 and 26) can give such different results (see Figs. 23 and 24). Voltammograms which were taken at the end of these experiments showed some quantitative difference (Fig. 30). The show that it is difficult to control the quantity of bismuth remaining on the surface after the electrode has been removed from a Bi(III) containing solution and immersed into a Bi(III)-free solution. The question whether these differences alone are sufficient to explain the differences in the analysis of the O_2 reduction data, cannot be answered with the data obtained here. This point needs further investigation.

The state of activity of the ring during the O_2 reduction in the presence of metal ions represents a problem as far as the reproducibility of the data is concerned. Even when the O_2 reduction was investigated in a Bi(III)-free solution, on an electrode which had been pre-exposed to Bi(III), the ring could not be pre-treated by cathodic pulses because of bismuth deposition. In fact, some bismuth is desorbed into the solution during the first few scans (see Fig. 9) and might be deposited on the ring during a cathodic pre-treatment. It should be noted, in this respect, that a cathodic pre-treatment of the ring was necessary to obtain reproducible results on pure gold. Otherwise, progressive anodic film formation interfered with the measurement of the diffusion limiting current for perioxide oxidation. Experimental work in the subsequent section shows that the actual current for peroxide oxidation is lower than the expected limiting value by 10%-20%, depending on the rotation rate, when Bi(III) is present in the solution. A plot of I_D/I_R vs. $1/f^{1/2}$ was constructed from the data of Fig. 15 using values of the ring current approximately corrected for the mentioned decrease in the current for peroxide oxidation. This plot is shown in Fig. 31. It is seen that, even with this correction, the O_2 reduction on Au with Bi(III) in the solution still occurs predominantly via a series mechanism.

E. Hydrogen Peroxide Oxidation and Reduction in Argon Saturated Solutions

In order to gain more insight into the mechanism of O_2 reduction, the oxidation and reduction of hydrogen peroxide were studied in the absence and in the presence of Bi(III) (Fig. 32). The solutions were saturated with argon in an attempt to depress the O_2 concentration to a low value and thus minimize any reduction current associated with O_2. On the other hand, O_2 is generated during the oxidation of peroxide on the electrode surface and also during the heterogeneous and homogeneous decomposition of HO_2^-. The extent to which this O_2 modifies the observed polarization curves for the peroxide oxidation and reduction currents is not fully clear, but probably was quite small, particularly for the oxidation curves.

Fig. 32 shows the polarization curves for the oxidation of hydrogen peroxide on Au in an argon-saturated 1M NaOH containing Bi(III) solution. A polarization curve obtained in the absence of Bi(III) is included in Fig. 32 for comparison. It is seen that Bi(III) has an inhibitive effect on the H_2O_2 oxidation. Such an inhibitive effect was also observed with Pb(II) and especially with Tl(I) (see later chapters).

The reaction order for peroxide oxidation on Au was found to be 0.5 with respect to H_2O_2 (3). This was confirmed in the present work (see Chapter IV). However, the reaction order derived from the log i vs. log $(i_L - i/i_L)$ plots (32) was found to be 1 when Bi(III) was present in the solution (Fig. 33).

With the dismutation reaction as the second step in the mechanism proposed by Zurilla et al. (3) for O_2 reduction on gold, the reverse oxidation process would be explained to be 1/2 order in O_2 as well as 1/2 order in HO_2^-. These authors had difficulty in verifying the 1/2 order dependence on O_2 because of a lack of adequate control of O_2 concentration in the presence of the peroxide. In an O_2 free solution, the concentration of O_2 at the disk surface during the peroxide oxidation might be proportional to the peroxide concentration at the surface and thus the two half-power dependencies on O_2 and HO_2^- concentrations might appear equivalent to a first order dependence in HO_2^-, not considering directly the O_2 concentration at the disk. Saturating the solution with O_2 did modify the polarization curves in Fig. 32 at potentials cathodic to 0.0V but this would be expected because of the back reaction.

Experiments on hydrogen peroxide reduction on pure Au were discussed in Chapter IV. The results showed some irreproducibility and a large dependence on the pre-treatment of the electrode.

In the presence of Bi(III), the reduction currents increased substantially with respect to pure Au and the half-wave potentials shifted to more positive values (Fig. 34). The marked time dependence of the currents observed with pure Au was not observed in the presence of Bi after stopping the potential scan at a given voltage for from a few seconds to a few minutes. The rotation rate dependence also becomes

more pronounced with Bi present at potentials between -0.1 V to -0.3 V.

While the voltammetry curves after repeated sweeping indicate very little current associated with the deposition of Bi at potentials >-0.1 V, nonetheless the Bi addition still produces a substantial increment in the peroxide reduction current at such potentials (see also Fig. 1).

More striking is the pronounced effect of Bi(III) on HO_2^- oxidation even at potentials where the Bi is not expected to be in UPD form on the surface (Fig. 32), but rather an adsorbed complex ion as discussed earlier in this chapter.

The cyclic voltammetry and disk-ring experiments discussed above showed that gold never becomes completely free of Bi(III) once this species has been deposited onto the surface. Bismuth is then most likely present on the surface even before the underpotential deposited region in the cycling voltammogram. A transformation of the Bi(III) species into a less catalytically active form could cause the sharp decrease in current observed at potentials negative to $\sim$-0.26 V (Fig. 34). The B value derived from the slopes of the 1/i vs. $1/f^{1/2}$ plots (Fig. 35) was 13.3×10^{-3} mA/(rpm)$^{1/2}$. This value is in good agreement with the B value of 13.15×10^{-3} and 13.5×10^{-3} for the oxidation of hydrogen peroxide on gold in the presence and in the absence of Bi(III) respectively. The first value was derived from the slopes of 1/i vs. $1/f^{1/2}$ shown in Fig. 36. The first order dependence of the HO_2^- reduction current was confirmed with plots of log i vs. log (i_L-i), which yielded a slope of 1.0 $\pm$ 0.05.

F. Combined O_2 and HO_2^- Reduction on a Bi-Pretreated Au Electrode and on Au Electrodes with Bi(III) in Solution

Fig. 37 shows a comparison of polarization curves for the reduction of both O_2 and HO_2^- on Au, both with and without Bi pre-adsorption. For curve 2 in Fig. 37 the gold electrode was scanned in a solution containing 8×10^{-6}M Bi(III), held in this solution at -0.55 V for 15 s and then introduced into a Bi(III)-free solution saturated with O_2 to which hydrogen peroxide was subsequently added. It was calculated from cyclic voltammetry that, in this case, the quantity of Bi(III) on the surface is about 10-15% of a monolayer (see also Fig. 9, curve 2, and Fig. 30). This calculation assumed that the Bi(III) is discharged to Bi(0) with the charge for a monolayer that given by Cadle and Bruckenstein for the Bi UPD in $HClO_4$ (20) on polycrystalline Au.

For the case of curve 2 in Fig. 38, the currents are slightly higher than for pure gold (curve 1 in Fig. 37) only at potentials less negative than -0.2 V. The 1/i vs. $1/f^{1/2}$ plots (Fig. 38) yielded B values which were dependent on the potential. At -0.1 V the B value was 2.6×10^{-3} mA/(rpm)$^{1/2}$ and decreased with increasing negative potentials, reaching a value of 9.6×10^{-3} mA/(rpm)$^{1/2}$ at -0.5 V. The latter is only slightly larger than the calculated value of 8.6×10^{-3} for O_2 reaction only in an O_2 saturated solution, and is far less than expected for the diffusion controlled reduction of

HO_2^- at a concentration of 3×10^{-3}M HO_2^-. Thus, at potentials of $\sim$ -0.1 V with Bi preadsorbed on Au, the reduction current is predominantly associated with the peroxide in an O_2 saturated solution containing 3×10^{-3}M HO_2^-, while at potentials of $\sim$ -0.5 V, in the same solution, the reduction current is predominantly that for O_2 reduction to peroxide.

When O_2 and HO_2^- reduction was studied in 8×10^{-6}M Bi(III), with HO_2^- as well as O_2 present in the solution (curve 3 in Fig. 38), the plot of 1/i vs. $1/f^{1/2}$ (Fig. 39) yielded straight lines which were approximately parallel to each other over a wide range of potentials (up to -0.4 V), in contrast to the behavior in Fig. 38). The B value calculated from the plots in Fig. 39 was 2.8×10^{-3} $mA/(rpm)^{1/2}$. This suggests that the peroxide elimination reaction contributes significantly to the observed overall current. With Bi(III) added to the solution, the bismuth surface coverage increases and this may be responsible for the increased decomposition of peroxide at relatively more cathodic potentials than for the case of curve 2 in Fig. 38. Alternatively, the Bi pre-adsorbed may be in the form of a surface alloy, while with Bi(III) in solution, an adsorbed layer of Bi, perhaps as a complex ion, is formed.

REFERENCES

1. R. Amadelli, J. A. Molla and E. Yeager, J. Elecronal. Chem. 126, 265 (1981).

2. D. M. Kolb, M. Przasnyski and H. Gerischer, J. Electronal. Chem., 54, 25 (1974).

3. R. W. Zurilla, R. K. Sen and E. Yeager, J. Electrochem. Soc., 125, 1103 (1978).

4. H. Angerstein-Kozlowska, B. E. Conway and J. Mozota, J. Electroanal. Chem., 100, 417 (1979).

5. R. R. Adzic and A. R. Despic, Z. Phys. Chem. N.F., 98, 95 (1975).

6. R. R. Adzic, N. M. Markovic and A. V. Tripkovic, Bull. Soc. Chimique Beograd, 45, 399 (1980).

7. W. F. Linke, Solubilities, Inorganic and Metal Organic Compounds, Vol. 1, Van Nostrand, Princeton, NJ 1958.

8. J.D.E. McIntyre and W. F. Peck, J. Electrochem. Soc., 123, 1800 (1976).

9. A. Bewick, J. Jovicevic and B. Thomas, Symposia of the Faraday Soc., Vol. 12 (1977), p. 24.

10. W. J. Lorenz, E. Schmidt, G. Staikov and H. Bozt, ibid., p. 14.

11. R. Amadelli, J. Molla, P. Bindra and E. Yeager, J. Electrochem. Soc., 128, 2727 (1981).

12. R. R. Adzic, A. V. Tripkovic and N. M. Markovic, J. Electroanal. Chem., 114, 37 (1980).

13. M. Pourbaix, Atlas of Electrochemical Equilibria in Aqueous Solutions, Natl. Assoc. Corrosion Engineers, Houston (1974).

14. R. Cordova O., M. E. Martins and A. J. Arvia, Electrochim. Acta, 25, 453 (1980).

15. D. E. Williams and G. A. Wright, Electrochim. Acta, 22, 505 (1977).

16. Stability Constants, Suppl. No. 1, Special Publ. 17, The Chemical Soc., London, 1971.

17. W. C. Schumb and E. S. Pittner, J. Amer. Chem. Soc., 65, 1055 (1943).

18. G. Charot, Théorie et méthode nouvelles d'analyse qualitative, 3rd ed., Manon, Paris 1949.

19. S. Srinivasan and E. Gileadi, Electrochim. Acta, 11, 321 (1966).

20. L. H. Cadle and S. Bruckenstein, J. Electrochem. Soc., 119, 1166 (1972).

21. V. V. Gorodetskii and V. V. Losev, Elektrokhimiya, 3, 1192 (1967).

22. V. V. Gorodetskii, L. I. Federtsov and V. V. Loesev, Elektrokhimiya, 4, 967 (1969).

23. V. V. Gorodetskii, A. G. Alemina and V. V. Losev, Elektrokhimiya, 5, 227 (1969).

24. Yu. K. Delimorakii, O. G. Zarubitskii and V. G. Budnik, Elektrokhimiya, 6, 1635 (1970).

25. P. K. Wrona and Z. Galus, Electrochim. Acta, 25, 419 (1980).

26. S. Bruckenstein and P. R. Gilford, Anal. Chem., 51, 250 (1979).

27. T. M. Riedhammer, L. S. Helnicki and S. Bruckenstein, Z. Phys. Chem. N.F., 111, 177 (1978).

28. K. E. Gubbins and R. D. Walker, J. Electrochem. Soc., 112, 469 (1965).

29. H. Wroblowa, Y. C. Pan and B. Razumney, J. Electroanal. Chem. 69, 195 (1976).

30. V. S. Bagotskii, M. R. Tarasevich and V. Yu. Filinovskii, Elektrokhimiya, 5, 1218 (1969).

31. V. S. Bagotskii, M. R. Tarasevich and V. Yu. Filinovskii, Elektrokhimiha, 8, 84 (1972).

32. L. Müller and H. Prühmke, Elektrokhimiya, 8, 1359 (1972).

33. P. L. Hagans, Thesis, Case Western Reserve University, 1979.

34. D. E. Williams and G. A. Wright, Electrochim. Acta, 21, 1009 (1976).

35. D. F. Untereker and S. Bruckenstein, Anal. Chem., 44, 1009 (1972).

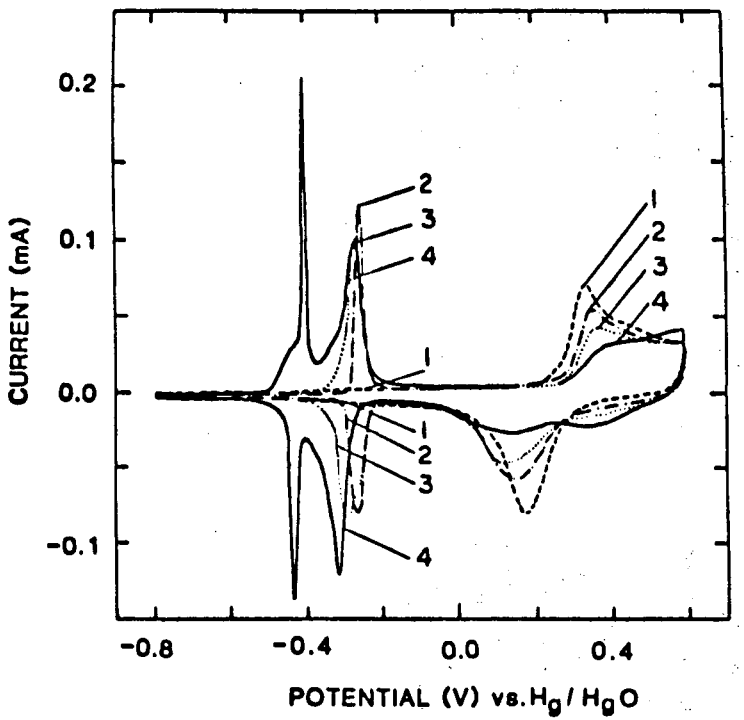


Fig. 5.1.1.1. Cyclic voltammetry curves for Au in N_2 saturated 1M NaOH in the absence and in the presence of increasing amounts of added Bi(III): 1) Au, 2) 1.9×10^{-6}M, 3) 4×10^{-6}M, 4) 2.5×10^{-5}M. Scan rate: 50 mV/s. Electrode area: 2.5 cm^2.

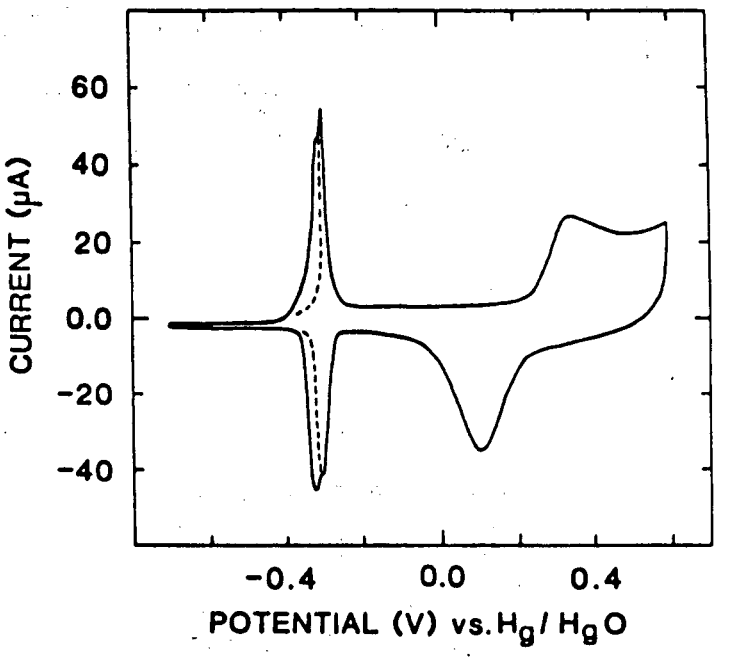


Fig. 5.1.1.2. Cyclic voltammetry curve for Au in N_2 saturated 1M NaOH containing 4×10^{-6}M Bi(III). Scan rate: 20 mV/s. Electrode area: 0.458 cm^2. Dashed line: approximate deconvolution of the peaks.

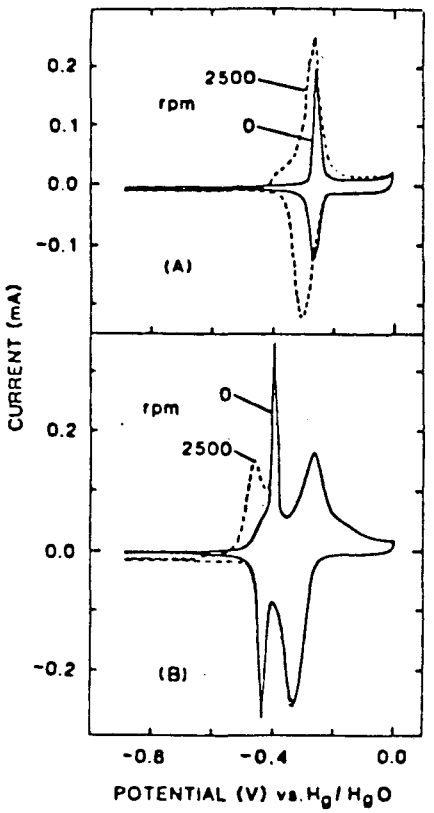


Fig. 5.1.1.3. Effect of the rotation of the electrode on the voltammetry curves for Au in Ar saturated 1M NaOH in the presence of: A) $2x10^{-6}$M Bi(III), B) $1.4x10^{-5}$M Bi(III). Electrode area : 0.458 cm^2. Scan rate: 100 mV/s.

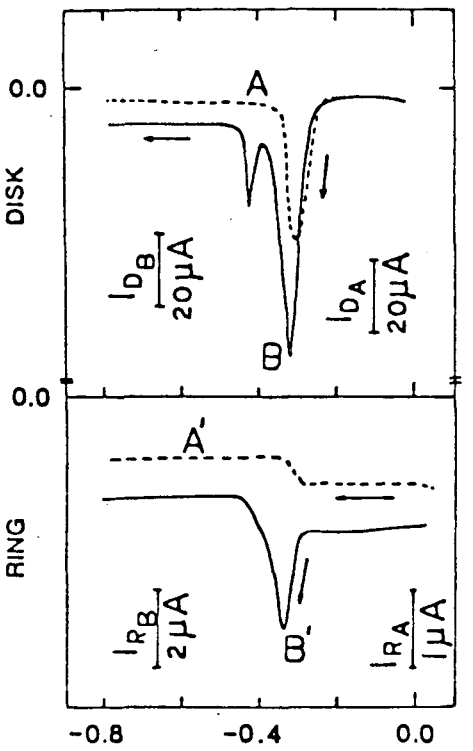


Fig. 5.1.1.4. Disk-ring potentiodynamic curves for Au in 1M NaOH saturated with Ar and containing : A) $2x10^{-6}$M Bi(III) B) $7x10^{-6}$M Bi(III). Electrode area: 0.458 cm^2. Rotation rate: 2500 rpm. Scan rate: 15 mV/s. N=0.18. Cathodic scan shown.

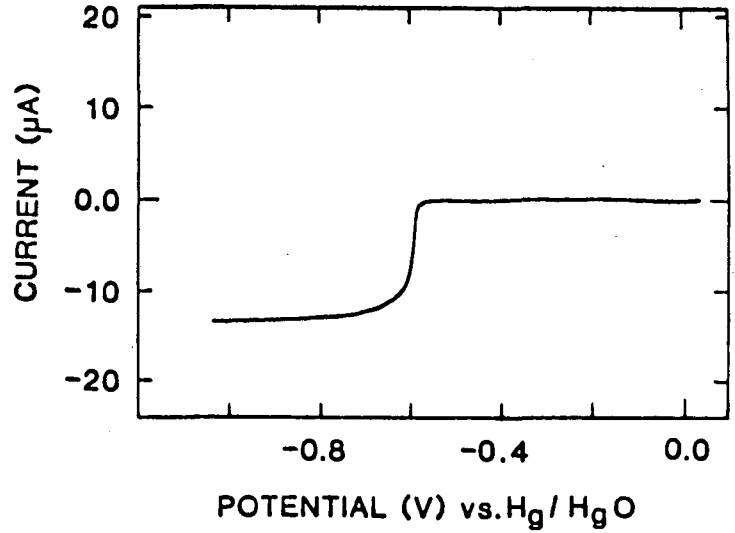


Fig. 5.1.1.5. Steady-state polarization curve for Bi(III) bulk deposition on Au in Ar saturated 1M NaOH containing 1.4 x 10^{-5}M Bi(III). Electrode area:0.458 cm^2. Rotation rate: 2500 rpm.

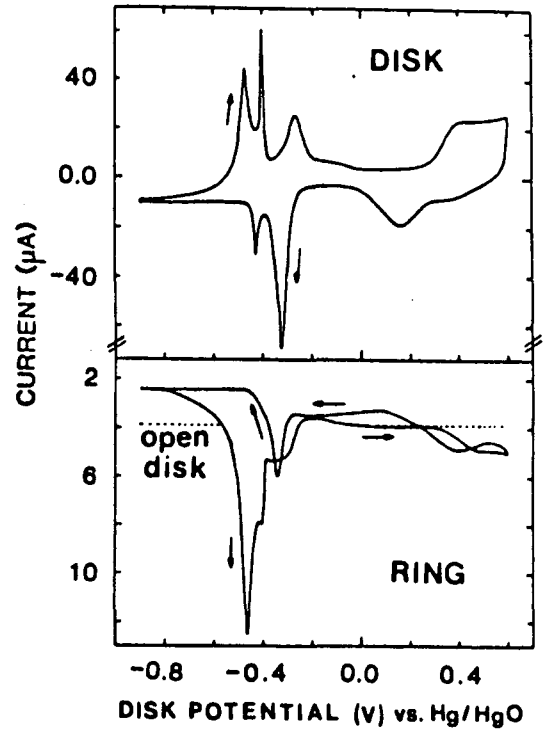


Fig. 5.1.1.6. Disk-ring potentiodynamic curves for Au in Ar saturated 1M NaOH containing $7x10^{-6}$ M Bi(III). Scan Rate: 20 mV/s. Electrode area:0.458 cm^2. Rotation rate: 2500 rpm.Ring potential:-0.9V. N=0.18.

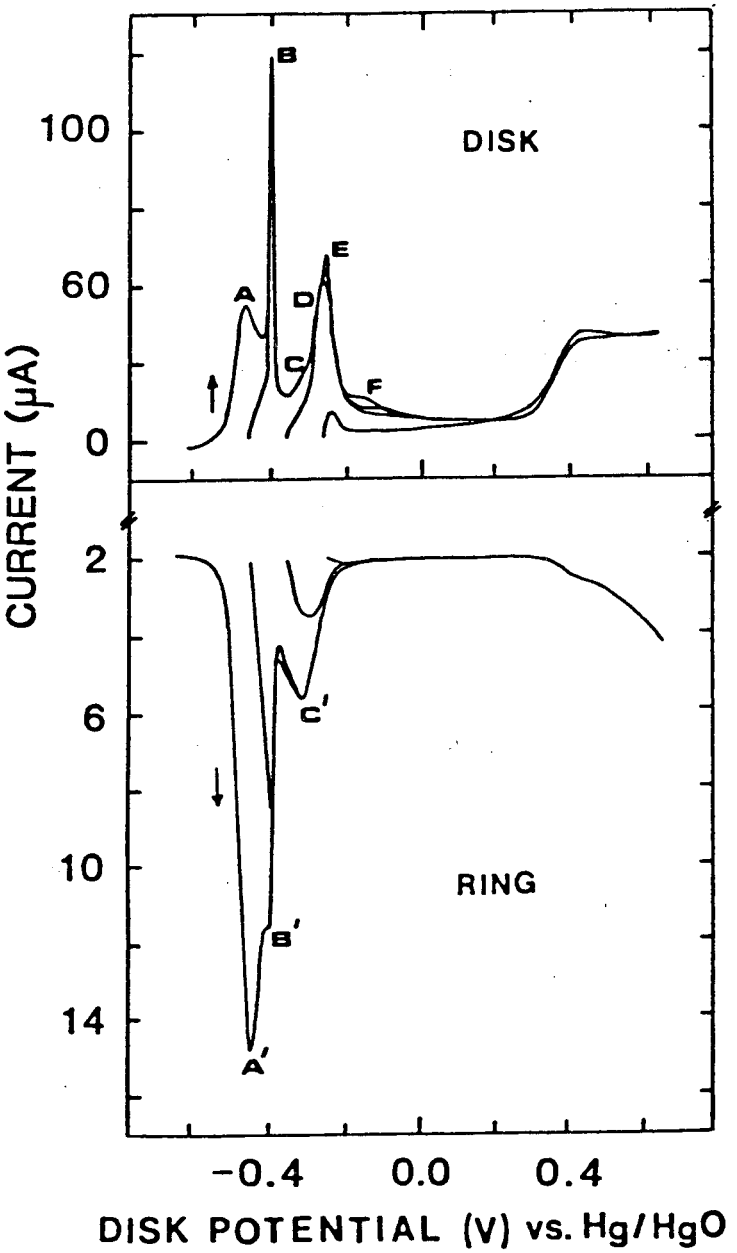


Fig. 5.1.1.7. Disk-ring potentiodynamic curves for Au in Ar saturated 1M NaOH containing 4×10^{-6} M Bi(III). Electrode held at various potentials for 90s and the sweep in the anodic direction recorded at 50 mV/s. Rotation rate: 2500 rpm. Electrode area: 0.458 cm^2. Ring potential: -0.9V. N= 0.18.

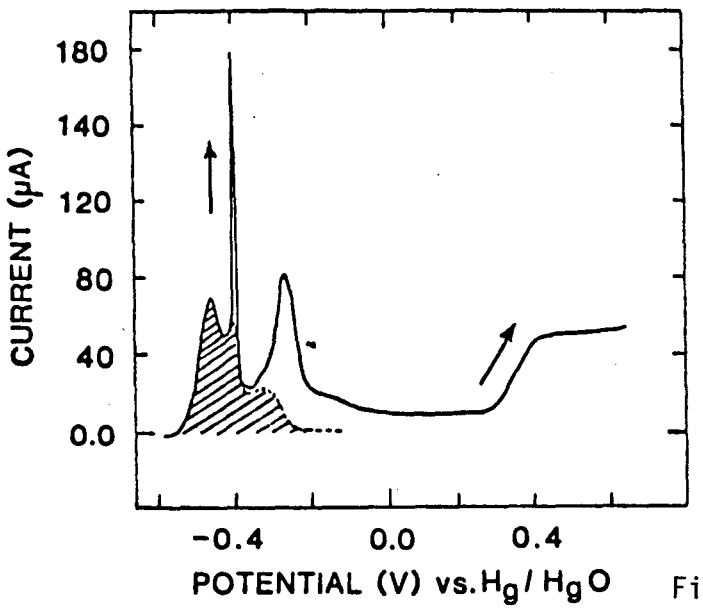


Fig. 5.1.1.8. Reconstruction of the disk current by dividing the observed ring currents by the collection efficiency (shaded area). Data from Fig.5-7.

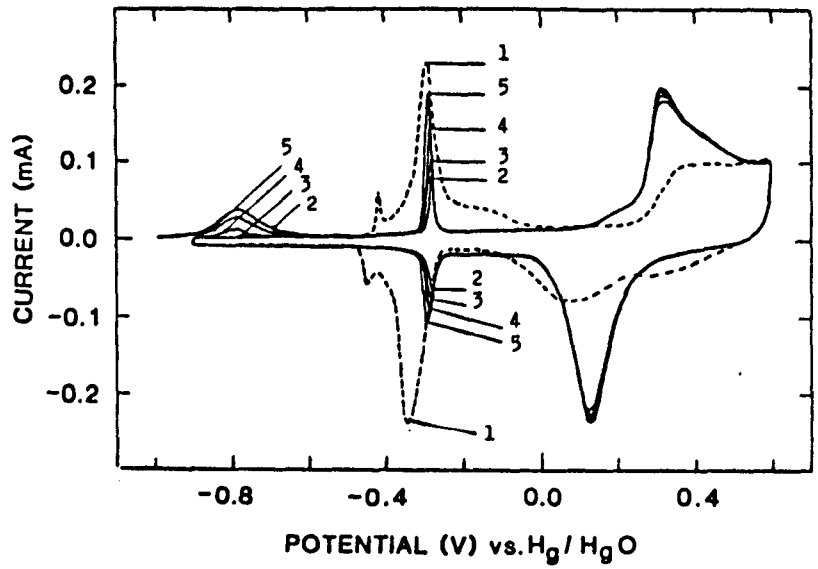


Fig. 5.1.1.9. Cyclic voltammetry curves for Au in Ar saturated 1M NaOH in the presence of Bi(III): 1) electrode withdrawn under potentiostatic control at -0.8V and introduced into a Bi(III) free solution, 2) after 5 min. scanning in the new solution, 3),4),5) after potentiostating the electrode at -1V for 30,60 and 120s respectively(see text). Electrode area:0.458 cm^2. Scan rate: 100 mV/s.

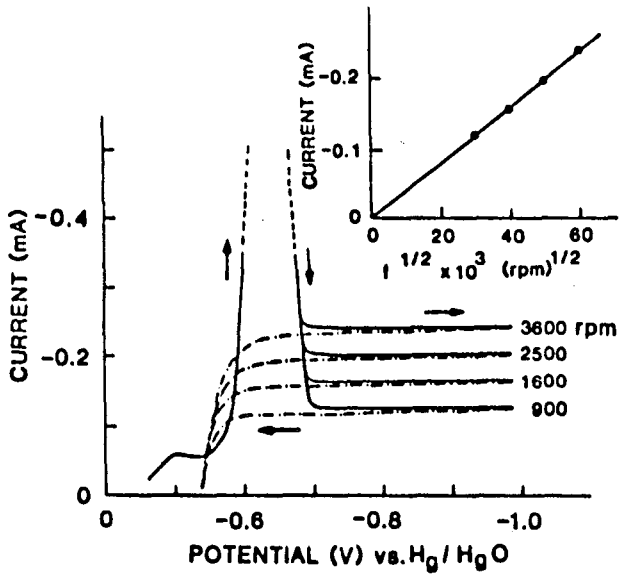


Fig. 5.1.1.10. Polarization curves for bulk deposition of Bi(III) on Au in Ar saturated 1M NaOH containing 2×10^{-4} M Bi(III). Scan rate: 20 mV/s. Electrode area: 0.458 cm^2. Insert: i vs. $1/f^{1/2}$ plot in the limiting current region.

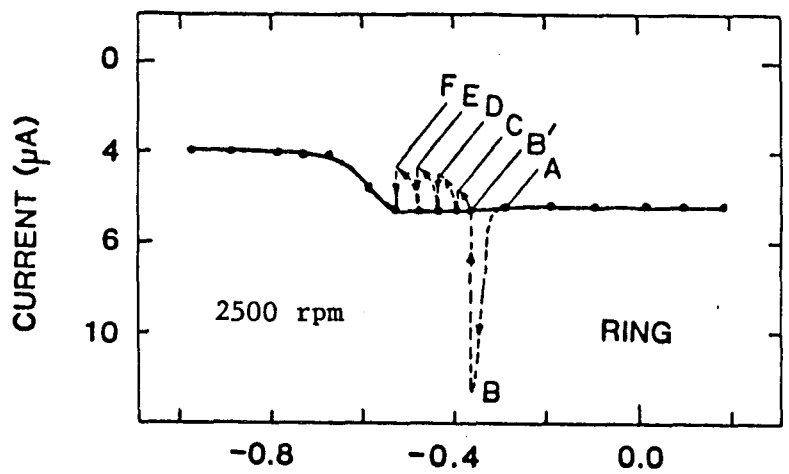


Fig. 5.1.1.11. Ring curve of a disk-ring experiment for the bulk deposition of Bi(III) from a Ar saturated 1M NaOH containing 1.5×10^{-5} M Bi(III). Disk area : 0.458 cm^2. N=0.18. Ring potential:-0.9V. The points indicate the potential at which the current was recorded. Electrode scanned between points at 20 mV/s.

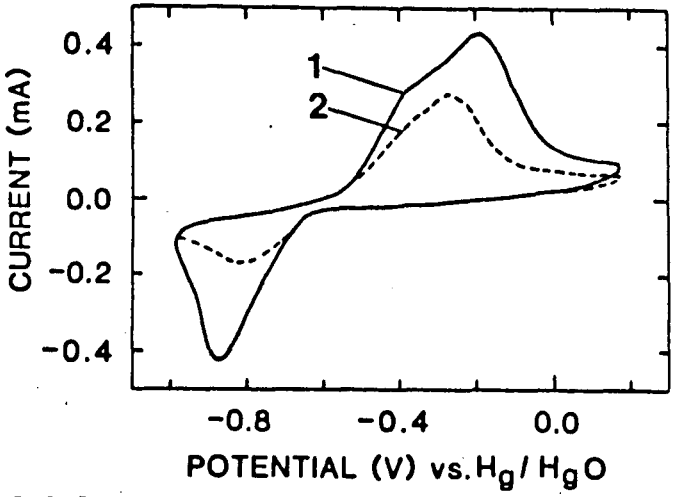


Fig. 5.1.1.12. Cyclic voltammetry curves for an ordinary pyrolytic graphite electrode onto which Bi(III) was deposited for 1) 20s, 2) 60s at -1V from a Ar saturated 1M NaOH containing 2x 10^{-4}M Bi(III).Potential sweep recorded first in the anodic direction at 100 mV/s. Electrode geometric area: 0.2 cm^2.

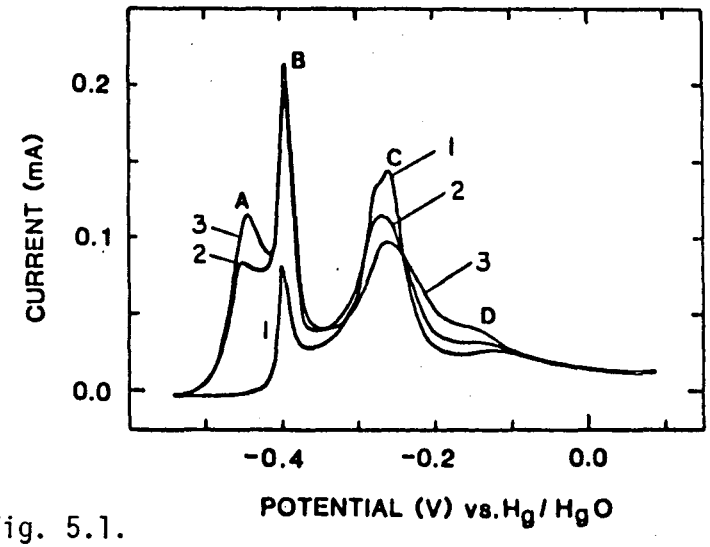


Fig. 5.1.1.13. Potentiodynamic curves for Au held for: 1) 30s, 2) 60s, 3) 180s, at -0.55V in Ar saturated 1M NaOH containing 2.5 x 10^{-3}M Bi(III). Scan rate: 100 mV/s. Electrode area:0.458 cm^2.

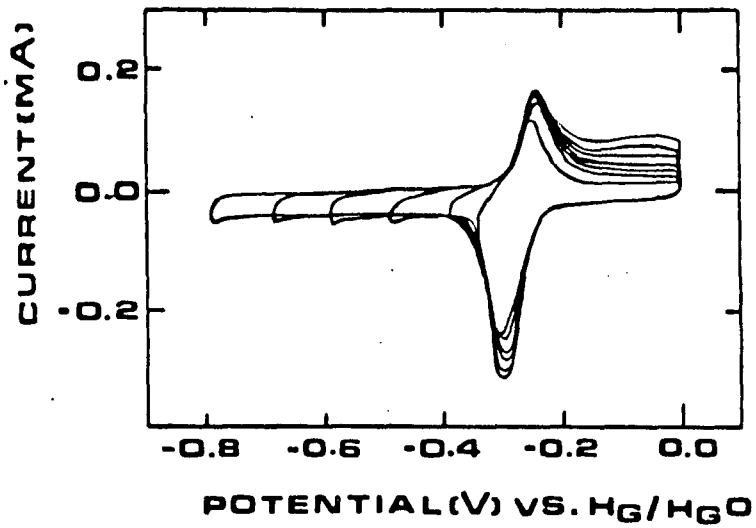


Fig. 5.1.1.14. Cyclic voltammetry curves for Au in Ar saturated 1M NaOH containing 6×10^{-6} M Bi(III). Electrode introduced into the solution under potentiostatic control at 0.0V. Potential window opened in the cathodic direction. Scan rate:50 mV/s. Electrode area: 2 cm^2.

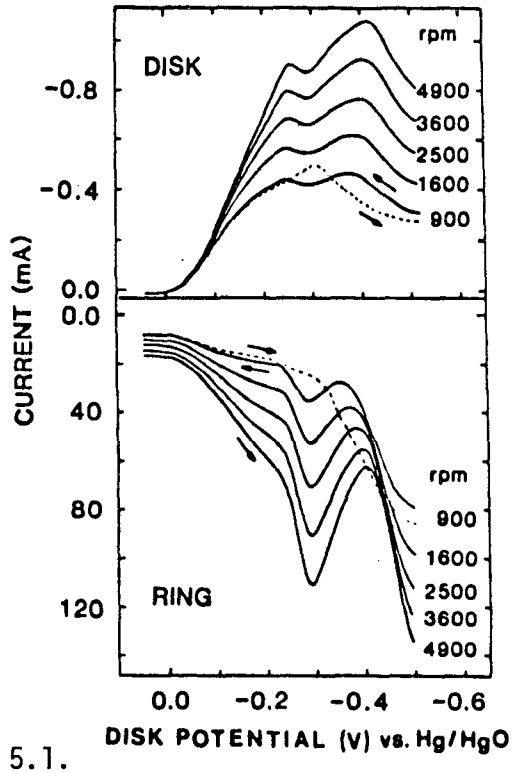


Fig. 5.1.1.15. Disk-ring polarization curves for O_2 reduction on Au in 1M NaOH containing 4×10^{-6} M Bi(III). Scan rate: 10 mV/s. Ring potential: 0.15 V. Electrode area:0.2 cm^2.

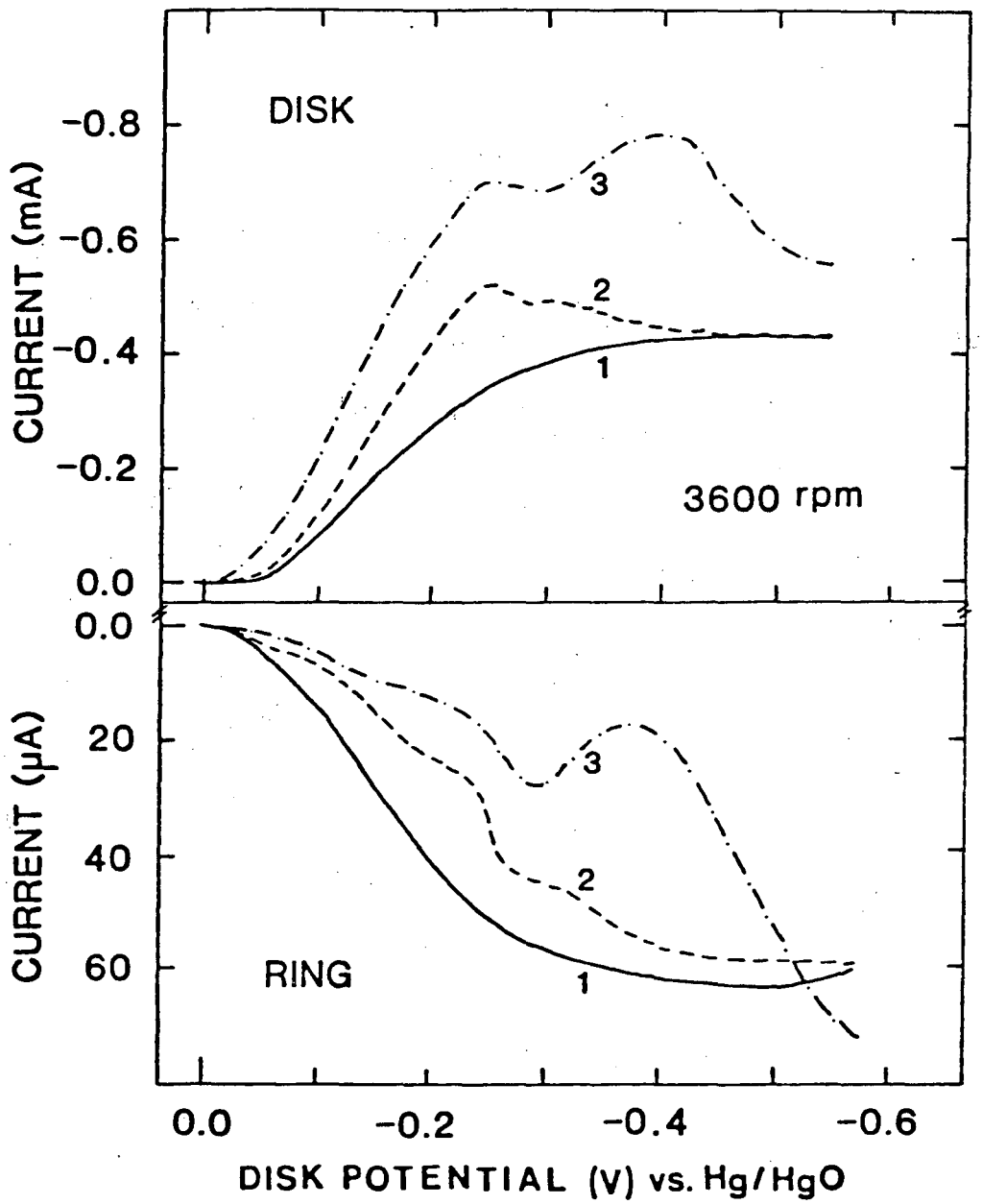


Fig. 5.1.1.16. Disk-ring polarization curves at a fixed electrode rotation rate for the reduction of O_2 on Au in 1M NaOH in the absence (1) and in the presence of 1.5×10^{-6}M (2) and 4×10^{-6}M (3) Bi(III). Rotation rate: 10 mV/s. Electrode area: 0.2 cm^2.

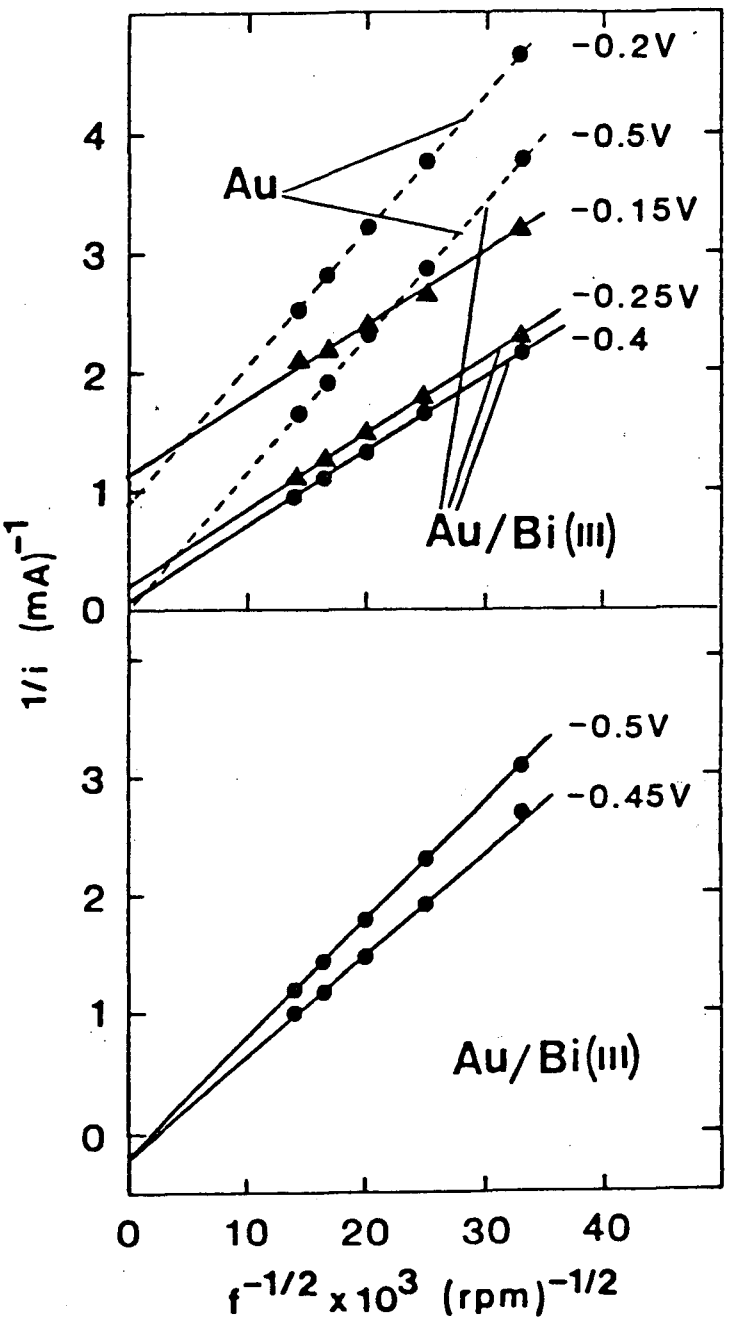


Fig. 5.1.1.17. Plots of 1/i vs. $1/f^{1/2}$ at various potentials for the reduction of O_2 on Au in the absence (dashed lines) and in the presence of Bi(III) (solid lines). Data for the Au/Bi_{ad} system taken from Fig.5-15.

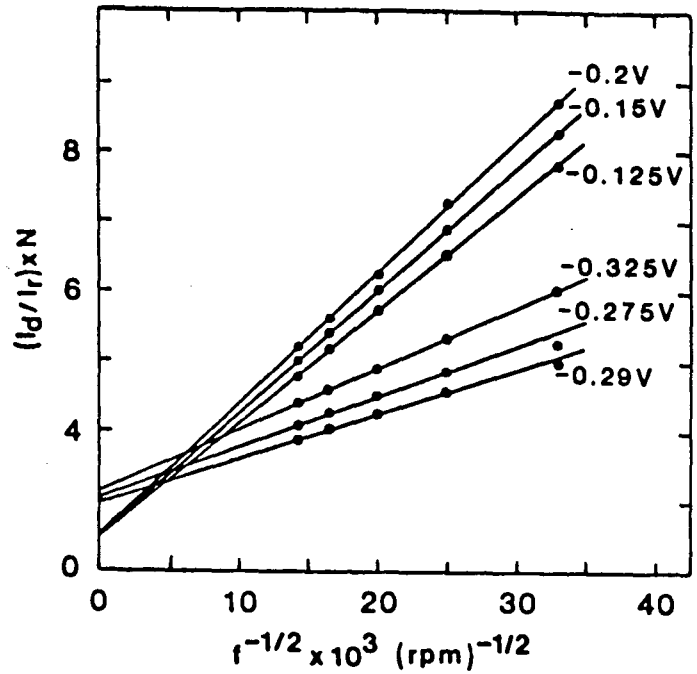


Fig. 5.1.1.18. Plot of I_d/I_r xN vs. $1/f^{1/2}$ constructed from the data of Fig.5-15 for the sweep in the anodic direction with 4×10^{-6} M Bi(III) in 1M NaOH.

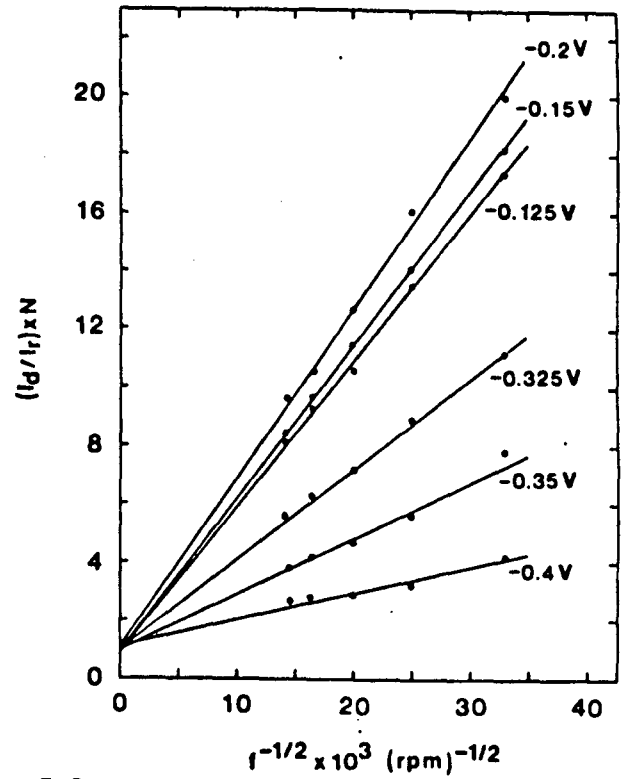


Fig. 5.1.1.19. Plot of I_d/I_r x N vs. $1/f^{1/2}$ constructed from the data of Fig.5-15 for the sweep in the cathodic direction with 4×10^{-6} M Bi(III) in 1M NaOH.

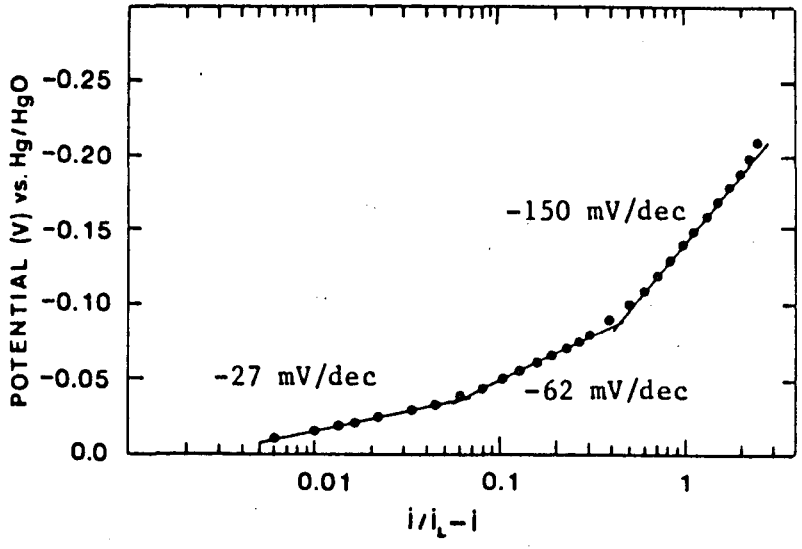


Fig. 5.1.1.20. Tafel plot of $i/(i_L-i)$ vs.E for O_2 reduction on Au in the presence of Bi(III). Data taken from Fig.5-15.

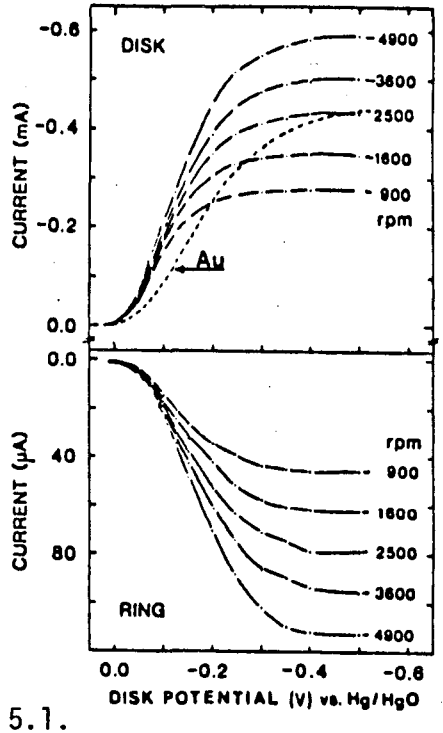


Fig. 5.1.1.21. Disk ring polarization curves obtained point by point for the O_2 reduction on Au pre-exposed to Bi(III), in 1M NaOH (see text). Disk polarization curve on clean Au shown for comparison. Electrode area: 0.2 cm^2.

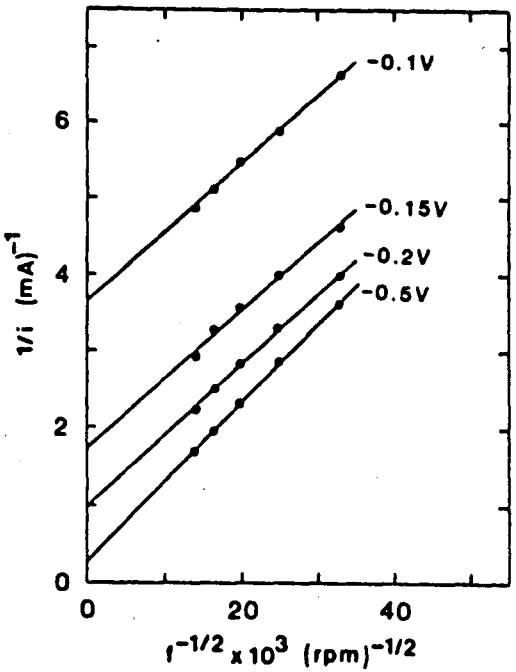


Fig. 5.1.1.22. Plot of 1/i vs. $1/f^{1/2}$ at various potentials constructed from the data of Fig.5-21.

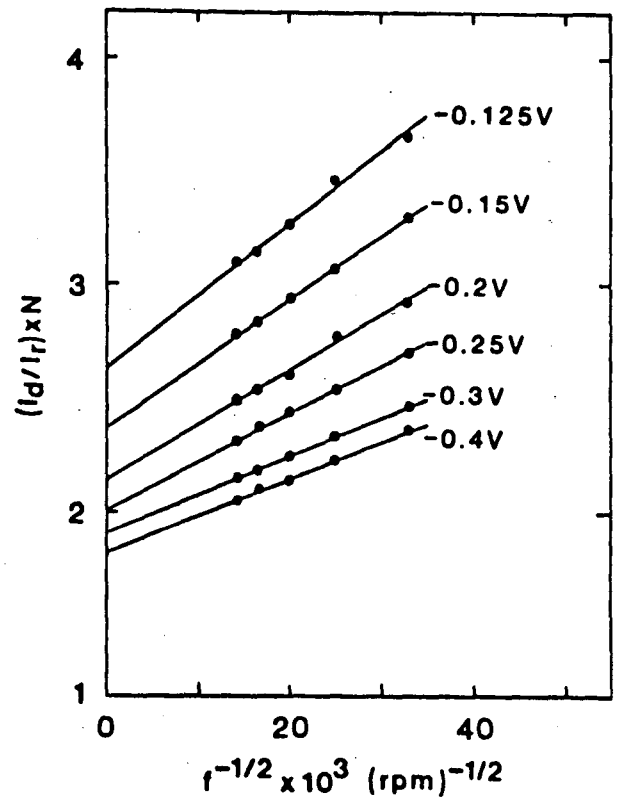


Fig. 5.1.1.23. Plot of $I_d/I_r \times N$ vs. $1/f^{1/2}$ constructed from the data of Fig.5-21.

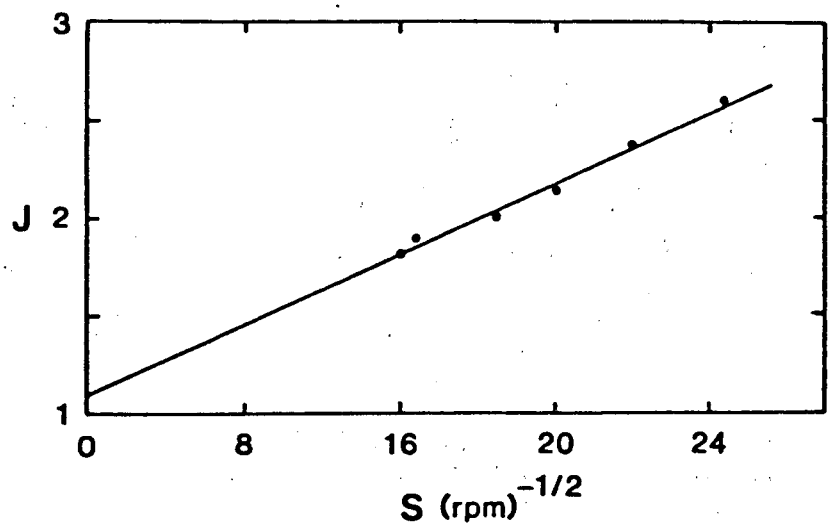


Fig. 5.1.1.24. Plot of the intercept vs. slope constructed from the data of Fig.5-23.

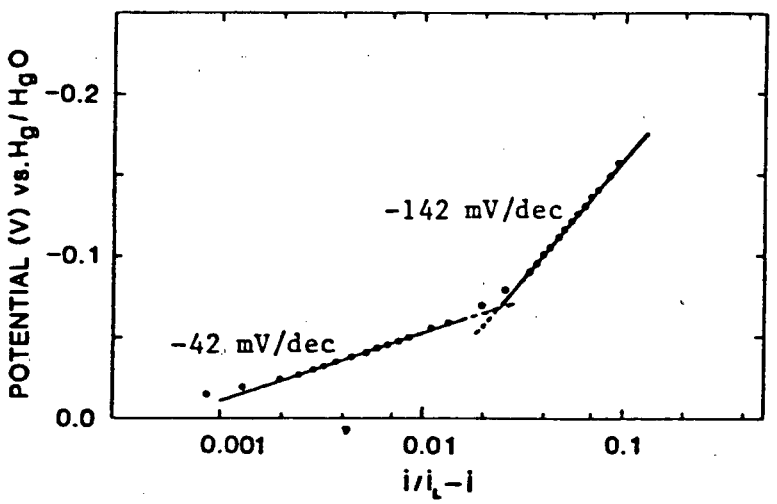


Fig. 5.1.1.25. Tafel plot of $i/(i_L-i)$ vs. E for O_2 reduction on Au pre-exposed to Bi(III). Data taken from Fig.5-21

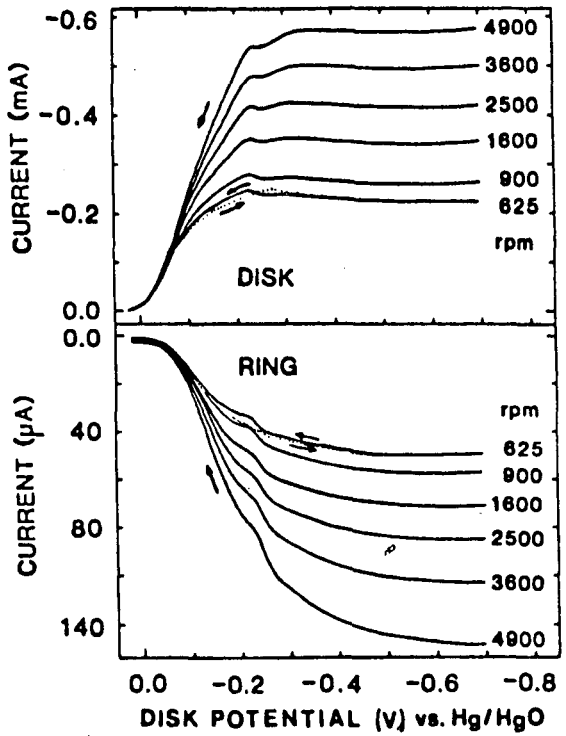


Fig. 5.1.1.26. Disk-ring polarization curves for O_2 reduction on Au pre-exposed to Bi(III) in 1M NaOH (see text). Scan rate: 10 mV/s. Electrode area: 0.2 cm^2.

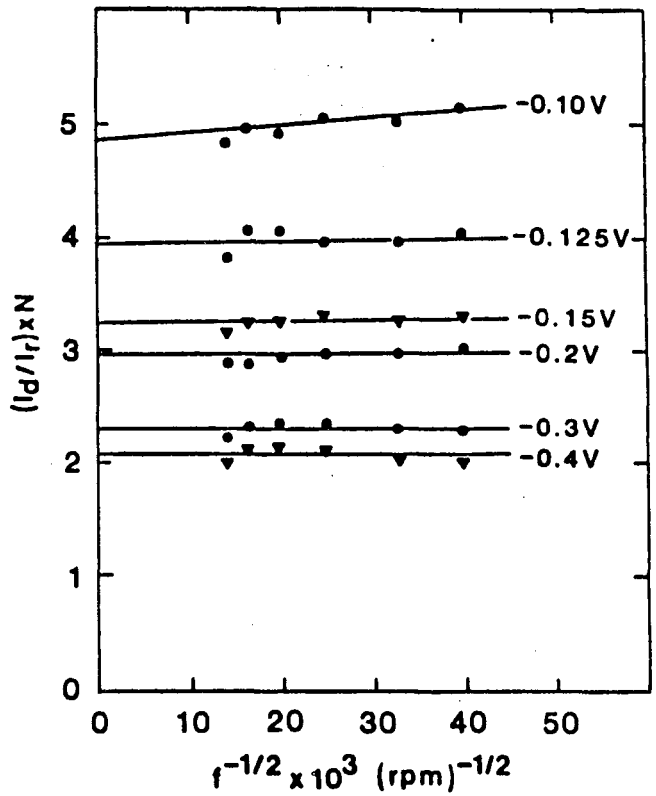


Fig. 5.1.1.27. Plots Of $(I_D/I_R)xN$ vs. $1/f^{1/2}$ constructed from the data of Fig. 5-26.

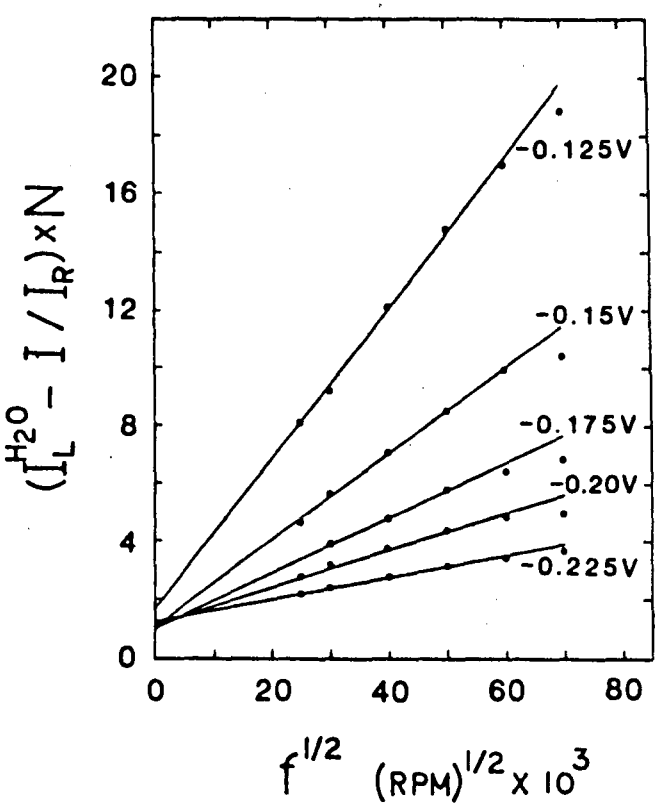


Fig. 5.1.1.28. Plots of $(I_A^o - I_R/N)/I_R/N$ vs. $1/f^{1/2}$ constructed from the data of Fig.5-26.

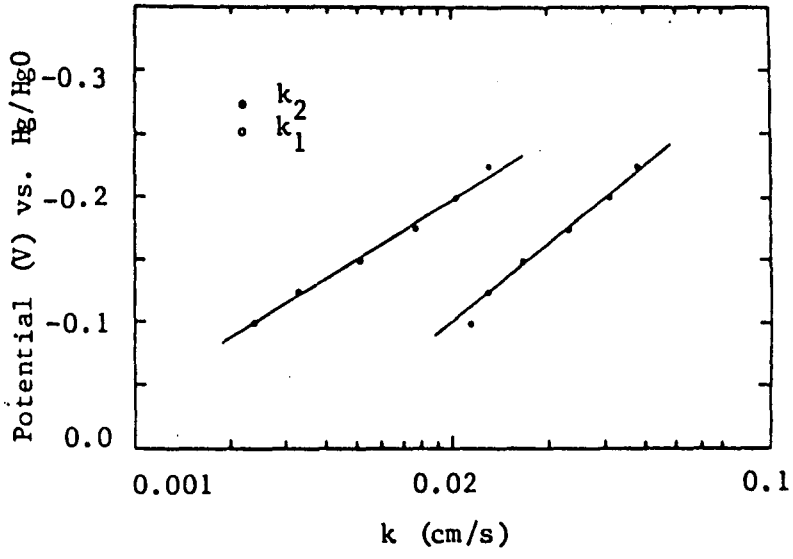


Fig. 5.1.1.29. Potential dependence of the heterogeneous constants for $4e^-$ reduction (k_1) and for $2e^-$ reduction (k_2) of O_2 on Au pre-exposed to Bi(III) in 1M NaOH.

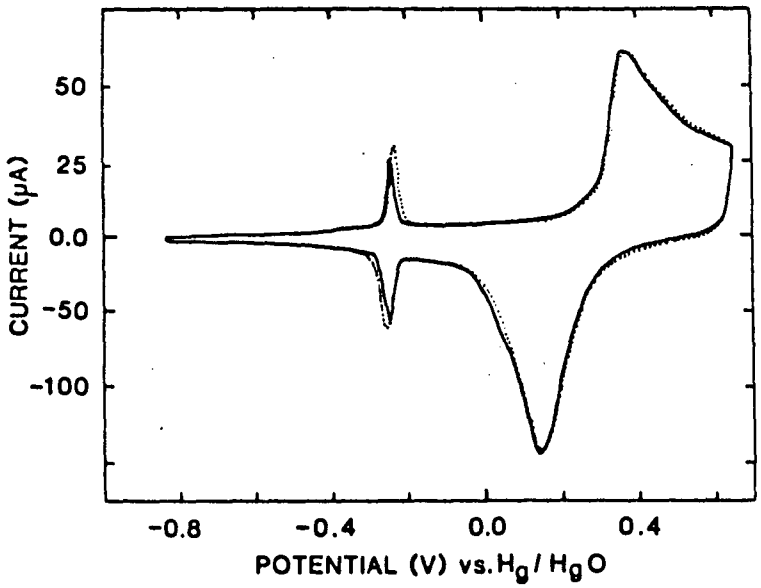


Fig. 5.1.1.30. Cyclic voltammetry curves for Au pre-exposed to Bi(III) (see text) taken at the end of the O_2 reduction experiments of Fig.5-21 (dotted line) and Fig.5-26 (continuous line) with the solution saturated with Ar. Scan rate : 100 mV/s. Electrode area: 0.2 cm^2.

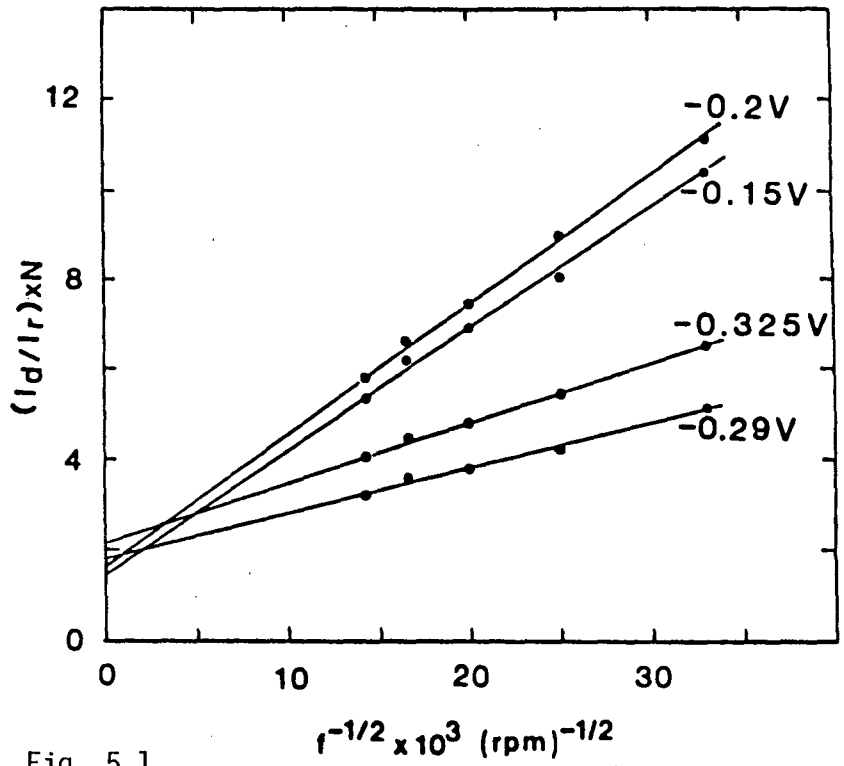


Fig. 5.1.1.31. Plots of $(I_D/I_R)xN$ vs. $1/f^{1/2}$ constructed from the data of Fig.5-15 (anodic scan). Ring current corrected by taking into account the percent deviation from the limiting current value in the oxidation of peroxide with Bi(III) added to the electrolyte.

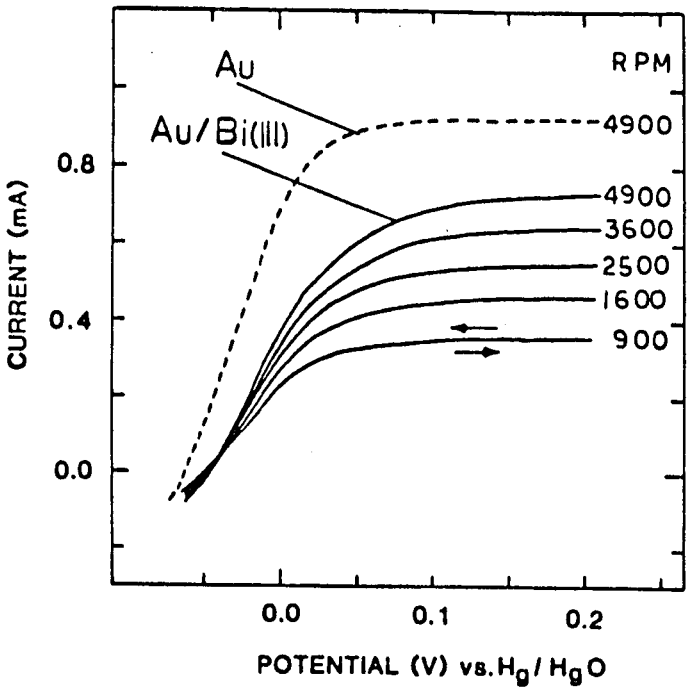


Fig. 5.1.1.32. Polarization curves for HO_2^- oxidation on Au in 1M NaOH in the absence (at 4900 rpm) and in the presence of 1.9×10^{-3} M Bi(III). HO_2^- concentration: 2.8×10^{-3} M. Scan rate: 10 mV/s. Electrode area: 0.2 cm^2.

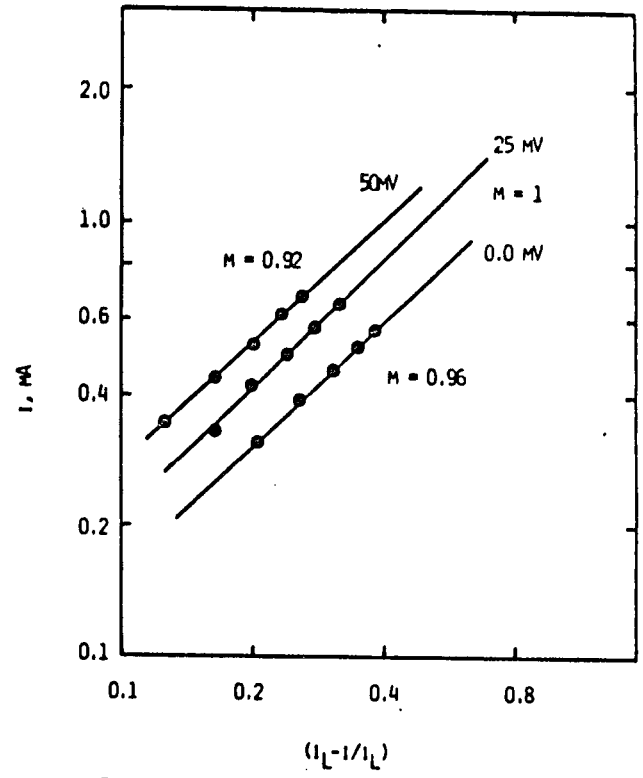


Fig. 5.1.1.33. Reaction order plot for the oxidation of HO_2^- on Au in 1M NaOH in the presence of Bi(III) constructed from the data of Fig. 5-32.

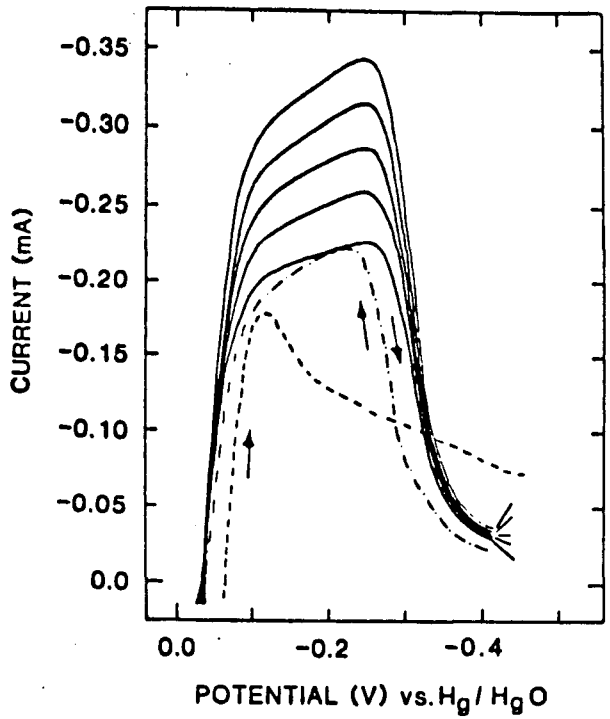


Fig. 5.1.1.34. Hydrogen peroxide reduction on Au in 1M NaOH in the absence (dashed line) and in the presence of 1.9×10^{-6} M Bi(III). HO_2^- concentration: 2.8×10^{-3} M. Scan rate: 20 mV/s. Electrode area: 0.2 cm^2.

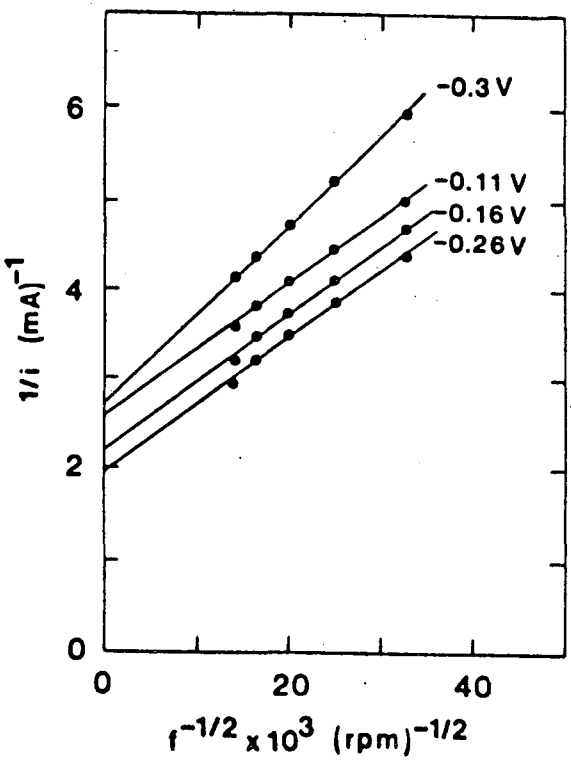


Fig. 5.1.1.35. Plots of $1/i$ vs. $1/f^{1/2}$ for HO_2^- reduction on Au in 1M NaOH containing Bi(III). Data taken from Fig. 5-34.

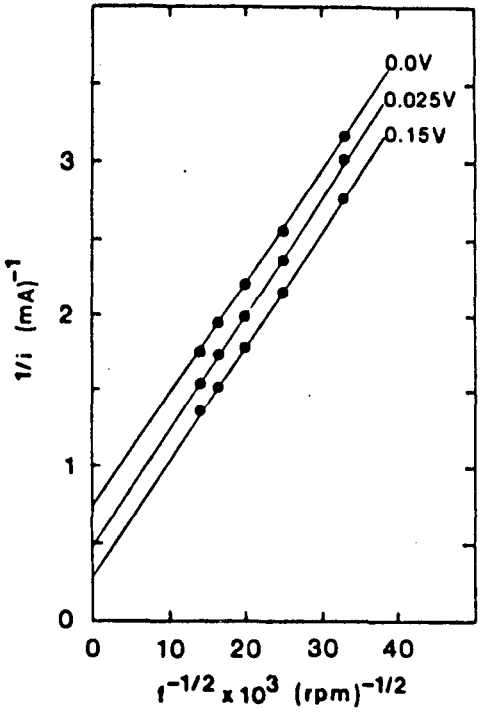


Fig. 5.1.1.36. Plots of 1/i vs. $1/f^{1/2}$ for HO_2^- oxidation on Au in 1M NaOH containing Bi(III). Data taken from Fig. 5-32.

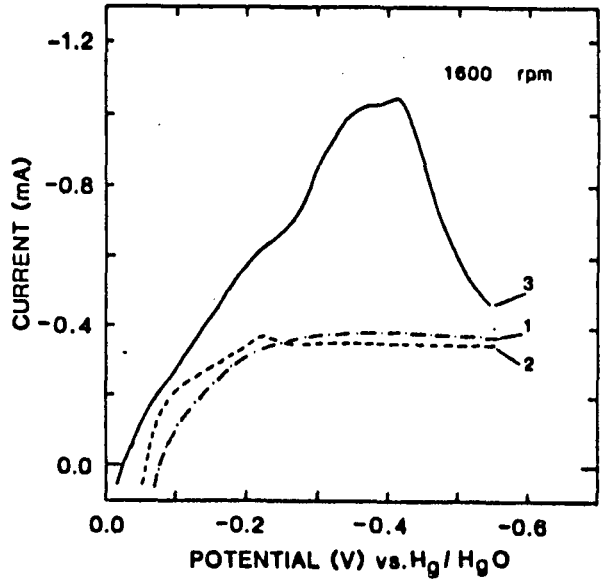


Fig. 5.1.1.37. Polarization curves for the combined reduction of O_2 and HO_2^- in 1M NaOH on: 1.clean Au; 2.Au pre-exposed to Bi(III) (see text); 3. Au with Bi(III) in the solution (6.6×10^{-6} M). Scan rate:10 mV/s. Electrode area:0.2 cm^2. Hydrogen peroxide concentration: 3.5×10^{-3} M.

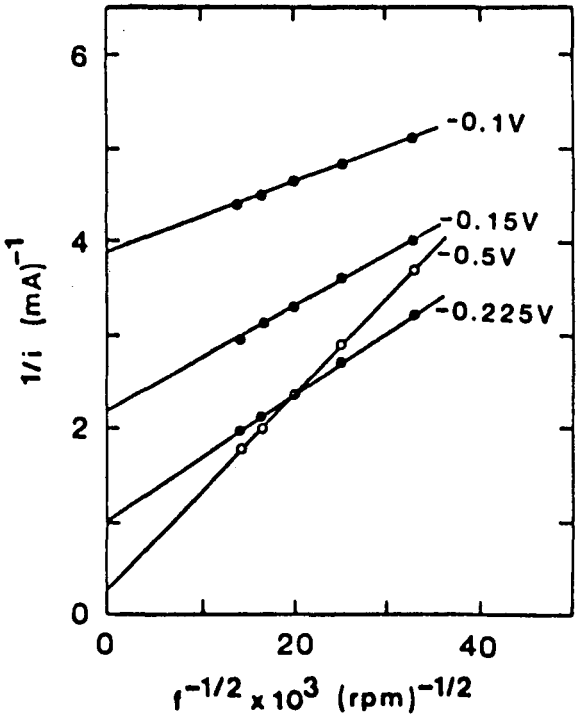


Fig. 5.1.1.38. Plots of 1/i vs. $1/f^{1/2}$ for the combined reduction of O_2 and HO_2^- on Au pre-exposed to Bi(III). Data corresponding to Fig.5-37, curve 2.

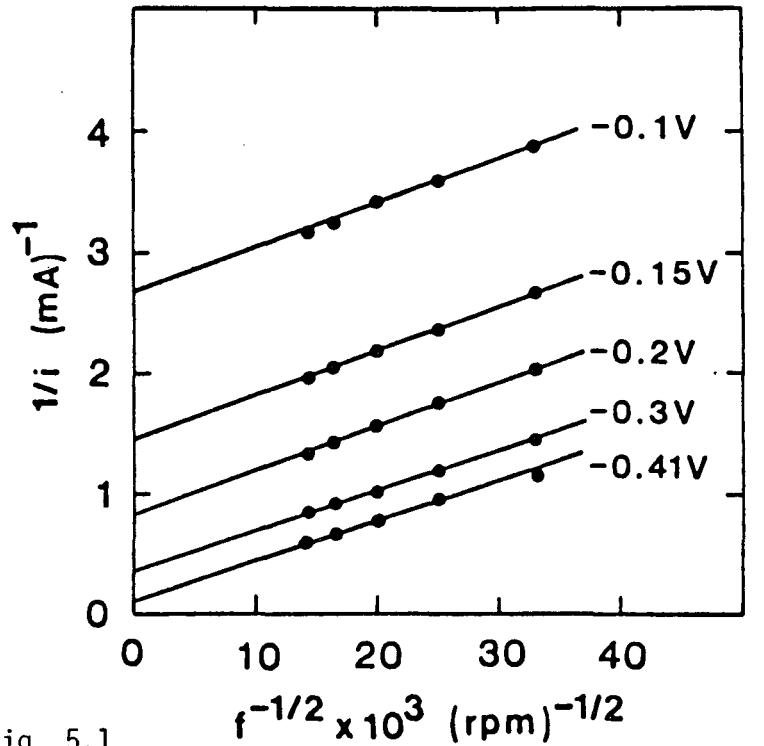


Fig. 5.1. 1.39. Plots of 1/i vs. $1/f^{1/2}$ for the combined reduction of O_2 and HO_2^- on Au in 1M NaOH containing 6.6×10^{-6}M Bi(III) Hydrogen peroxide concentration: 4×10^{-3}M. Data corresponding to Fig.5-37, curve 3.

5.1.2 OXYGEN REDUCTION ON Au IN ALKALINE SOLUTION IN THE PRESENCE OF THALLIUM IONS

R. Amadelli and E. Yeager

INTRODUCTION

The adsorption of thallium on noble metal electrodes has been investigated by several authors. In many of the studies the substrate used was silver both in polycrystalline (e.g. 1,2) and single crystal form (3-5). Other electrode substrates used include gold (5,6), platinum (7,8) and copper (6). The deposition of thallium on these substrates occurs at underpotentials.

Vicente and Bruckenstein (9) studied the underpotential deposition of thallium on gold in KCl and $HClO_4$ with a rotating disk-ring electrode. These authors found that a monolayer of Tl(0) was stripped at three different potentials in KCl and that the stripping of the adsorbed Tl was not complete in KCl. From comparison of the data in KCl and $HClO_4$, the above authors concluded that the chloride ions enhance the specific adsorption of Tl(I).

McIntyre and Peck (10) have found that the deposition as well as the anodic dissolution of Au is enhanced by Tl(I) ions in buffered phosphate (pH = 8.8). Their conclusion is in agreement with earlier data of Cathro and Koch (11). The increased anodic dissolution of Au was explained by the inhibition by Tl(I) of the formation of a passivating oxide layer. The absorbed Tl may not be present in metallic form at the more anodic potentials involved in the Au dissolution experiments and rather may be present in somewhat ionic form.

In recent years, the influence of Tl(I)-UPD on various electrochemical reactions has been examined. Thallium adsorbates on Ag single-crystals have been found to inhibit H^+ reduction (12) and O_2 reduction (13) in acid solutions. A slight enhancement of the O_2 reduction on polycrystalline Au in $HClO_4$ has been reported by Adzic and Despic (14). In contrast to the results in the acid solution, McIntyre and Peck (15) and Yeager *et al.* (16) reported a large enhancement effect on O_2 reduction on Au in alkaline solutions. The present work aims at a deeper understanding of the increased activity for O_2 reduction on the Tl-modified Au surface in the caustic electrolyte.

The results presented in this chapter indicate that the adsorption of thallium at potentials anodic to the bulk deposition potential cannot be explained as simple underpotential deposition of a metal-like species on the electrode surface from a bulk solution phase. Rather, the results suggest first at relatively anodic potentials a coadsorption of a Tl(I) species and OH^-, perhaps in the form of TlOH with conversion of this species to (Tl)ads of more metal-like character, at somewhat more cathodic potential, corresponding to the more conventional UPD layer.

The (TlOH)ads is in equilibrium with the species in the solution phase. In the more anodic potential range $Tl(OH)_3$ can be formed from (TlOH)ads and from Tl(I) in the solution phase. Difficulties in the detailed interpretation of the fine structure revealed by the potentiodynamic curves are discussed.

EXPERIMENTAL

The preparation of the solutions and the measuring equipment have been described in Chapter III. Thallium was added to the solution as $TlNO_3$. Separate experiments were carried out to test the effect of NO_3^- ions on oxygen reduction and on the cyclic voltammetry curves by adding $NaNO_3$ to the caustic electrolyte. No appreciable influence was observed even at concentrations of NO_3^- as high as 10^{-3}M.

The rotating gold disk-gold ring electrode assembly used for the kinetic studies was fabricated at Case Western Reserve University. The disk-ring shielding experiments have been carried out using a commercial electrode from the Pine Instruments Co. The characteristics of these electrodes were given in Chapter III. The choice of the ring electrode potential during the O_2 reductive studies is discussed later in this chapter. All potentials are given vs. $Hg/HgO,OH^-$.

RESULTS AND DISCUSSION

A. Cyclic Voltammetry

Cyclic voltammetry curves for the Au in 1M NaoH in the presence of increasing amounts of Tl(1) are shown in Fig. 1. For the lower concentration (2.5×10^{-6}M), a rather broad peak appears at $\sim$-0.2V in the cathodic sweep. Its width at half-height is $\sim$ 180 mV. The separation between the anodic and the cathodic peaks (a, a' in Fig. 1) is $\sim$40 mV and independent of sweep rate over the range 5 to 150 mV/s. These peaks are due to adsorbed Tl(I) species.

An increase in Tl(I) concentration to e.g., 2.2×10^{-5}M (dashed line in Fig. 1), reveals much more fine structure. Peaks A and A' increase in height and are shifted in the cathodic direction by $\sim$20 mV with respect to the cathodic peak at the lower concentration (Fig. 1). Peaks A and A' now occur at approximately the same potential for sweep rates from 5 to 150 mV/s. The shoulders B, B' and the small peak, C, C' are not exactly reproducible between separate experiments. For the same concentration of added Tl(I), they are more pronounced on bright foil electrodes which have undergone a cleaning treatment in, for example, a mixture of 1:1 concentrated HNO_3 and H_2SO_4 but not mechanically polished. These peaks (B, B', C, C') are pronounced on mechanically polished electrode (cleaned in 1M NaOH with ultrasound agitation) only at concentrations of $\sim 10^{-4}$M as compared to 10^{-5}M, for a scan rate of 50 mV/s. Bewick and Thomas (3) also observed more fine structure for the UPD of thallium on chemically polished polycrystalline silver than on mechanically polished silver. It is likely that peaks C, C' and the shoulders B, B' are due to adsorption on different sites with different crystallographic orientations or to some rearrangement of the adsorbate on these sites.

The peak potential for peak A in Fig. 1 did not depend on the scan rate while the peak current varied linearly with scan rate. The dependence of peaks A, B, C on the solution agitation was influenced by the anodic limit. If the potential was not swept to values more positive than 0.05V, none of the above mentioned peaks showed appreciable dependence on the solution agitation. For potential limits more anodic than 0.05V the agitation dependence is discussed later.

The formation of gold anodic film is substantially modified by Tl(I) (Fig. 1). This modification results from the formation of thallium oxides or gold and thallium mixed oxides. Thallium oxide formation can occur both by oxidation of TlOH deposited on the surface at more negative potentials or directly from Tl(I) in solution. The assignment of all the peaks in the anodic region (b, c, F, G in Fig. 1) is therefore complicated by the occurrence of reactions involving both species on the surface and in the solution phase. The potentials for the formation of thallium oxides and the relative reactions are the following (17):

$$Tl^+ + 3H_2O = Tl_2O_3 + 6H^+ + 4e^- \qquad (1)$$

$$E_o = 1.189 - 0.0887\ pH - 0.0295\ lg(Tl^+) \qquad (1a)*$$

$$E_o = 1.329 - 0.0887\ pH - 0.0295\ lg(Tl^+) \qquad (1b)$$

$$Tl_2O + 2H_2O = Tl_2O_3 + 4H^+ + 4e^- \qquad (2)$$

$$E_o = 0.778 - 0.0591\ pH \qquad (2a)$$

$$E_o = 0.905 - 0.0591\ pH \qquad (2b)$$

For concentrations of 2×10^{-5}M Tl(I) (Fig. 1) and pH = 14, the values of E_o derived from the above equations are reported in the following Table:

TABLE 1

Equalibrium potentials for the formation of thallium oxides for a Tl(I) concentration of 2×10^{-5}M and pH = 14

Reaction	E_o(V) vs Hg/HgO
1a	-0.0134
1b	0.1266
2a	-0.147
2b	-0.02

*(a) and (b) refer to the hydrated and anhydrous oxides respectively, i.e., $Tl(OH)_3$, Tl_2O_3, TlOH and Tl_2O.

For the formation of TlOH according to:

$$Tl + OH^- = TlOH + e^- \qquad (3)$$

E_o is given by (0.485 - 0.0591). At pH = 14, a value of -0.44 V is obtained on the Hg/HgO scale.

The peaks in the anodic region are not readily assigned from the E_o values reported in Table 6-1. Peak F in Fig. 6-1 can probably be assigned to the formation and reduction respectively of $Tl(OH)_3$ present on the surface. The other peaks (G, H) may correspond to the transformatoin of the $Tl(OH)_3$ on the surface, e.g. to Tl_2O_3, and/or to the formation of gold and thallium mixed oxides as will be discussed later.

The anodic region of the gold voltammogram is already modified by thallium even without exposing the electrode to negative potentials where Tl is adsorbed or bulk deposition occurs (Fig. 2). For the experiment illustrated by Fig. 2a, the electrode was introduced into the solution under potential control at 0.0 V. Subsequent scans in the anodic direction were then recorded (1-3 in Fig. 2a). Peak I at $\sim$0.25 V, which is stirring sensitive, corresponds most probably to the formation of $Tl(OH)_3$ from Tl(I) in the solution phase. Thallic oxide may remain on the surface because of its low solubility product (17) and cause an inhibition of the gold oxide formation. When the cathodic window is opened (Fig. 2b), thallium is underpotential deposited at $\sim$-0.2 V (peak III). Peak I at $\sim$ 0.25 V also increases, probably because the Tl-UPD on the Au surface is oxidized to $Tl(OH)_3$.

The behavior of the cathodic opening curves in Fig. 3 may be due to a reconstruction of the surface (see peaks G and A) or more likely to the reduction of thallic oxide formed in appreciable amount during the scanning in the anodic region. Figure 3 also shows that the height of peak F is dependent on the cathodic limit. This peak, which appears when the concentration of added Tl(I) is close to, or higher than 10^{-5} M is not dependent on the solution agitation (see also Fig. 5). It is most likely due to a surface oxidation of TlOH to $Tl(OH)_3$. The anodic opening curves for a relatively high concentration of Tl(I) (Fig. 4) show a main oxide reduction peak L at -0.04 V. This peak can be attributed to the reduction of thallic oxide (or hydroxide) formed both by oxidation of Tl(I) on the surface (see also Figs. 3 and 5, peak F) and of Tl(I) in the solution phase. The small peak I in Fig. 4 may be due to gold oxide reduction, assuming that the gold oxide and the thallium oxide are in separate phases. The peaks in the anodic region of the voltammograms will be further discussed later.

Figure 5 shows a marked dependence of the current on the electrode rotation at potentials more anodic than 0.2 V during the anodic sweep due to oxidation of the solution phase Tl(I). The height of the reduction peaks G', L also increase when the electrode is rotated. They correspond to the reduction of Tl(III) as an oxide or hydroxide produced at the more anodic potentials. The large increase in the height of the reduction peaks with rotation (Fig. 5) is probably due to the fact that a larger amount of Tl(I) is transported to the electrode and oxidized to Tl(I). In fact, when the scan was stopped at peaks L and G' the current decreased to the residual value within a few seconds even at 400 rpm.

In a separate experiment (Fig. 6), the electrode was potentiostated at different potentials for at least 30s at zero rotation rate. At a fixed potential the rotation rate was then increased from zero to 2500 rpm and the points recorded. Anodic and cathodic waves were obtained (Fig. 6) which correspond to the oxidation of Tl(I) to Tl(III) and to the bulk deposition of Tl(I) respectively. The height of the anodic wave is less than twice that of the cathodic wave, as would be expected for a 2 electrons vs a 1 electron process. Deviations from the proportionality between diffusion current and concentration were observed by Delahay and Stiehl (18) who studied the oxidation of Tl(I) on Pt. Kolthoff and Jordan (19), however, reported a difference of less than 2% in the proportionality between the anodic diffusion currents and the concentration of Tl(I). These authors pointed out the extreme sensitivity of the reaction to the pre-treatment of the electrode. They used electrodes which were strongly oxidized in 10M HNO_3 before the experiment. Guidelli *et al.* (20) also reported that the rate of the process $Tl(III) + 2e^- \rightleftharpoons Tl(I)$ on Pt is greater on an oxidized surface. The curve in Fig. 6 of the present work was actually recorded in the anodic direction, starting with a reduced electrode. This may be one of the reasons for the observed deviation of the anodic wave from perfect reversibility. A comparison of Figs. 5 and 6 seems to indicate that the oxidation to Tl(III) of the Tl(I) specifically adsorbed on the surface may be superimposed on the oxidation of Tl(I) in the bulk solution phase. In fact, in Fig. 5 the oxidation wave is shifted to more positive potentials than in the experiment of Fig. 6, which was carried out at quasi steady-state.

The mechanism of the redox reactions of Tl(I)/Tl(III) have been studied by several authors (e.g. 20-23) and it is generally accepted that the Tl(I) oxidation to Tl(III) and the reverse reaction proceed stepwise through a mechanism involving Tl(II) as an intermediate.

The purpose of the experiment reported in Fig. 6 was to define the potential regions in which Tl(I) bulk deposition and its oxidation to Tl(III) occur, rather than to attempt a kinetic analysis of these reactions. With regard to the last point, especially as to the formation of Tl(II), James (22) pointed out that the mechanism of the Tl(I)/Tl(III) reaction cannot be satisfactorily proven by conventional electrochemical kinetic methods.

B. pH Dependence of the Tl-UPD Peak

Cyclic voltammetry curves obtained for different pH's of the Tl(I) containing soution are reported in Fig. 7. The pH was varied by adding the required amount of 1M $HClO_4$ to a 0.1M NaOH solution which was 1M in $NaClO_4$ to maintain the ionic strength constant. The

variation of the OH^- concentration of the electrolyte causes a marked change of the shape of the whole voltammograms and not only of the UPD peak region. The principal UPD peak is considerably broadened and decreased in height as the pH is decreased. Lowering the OH^- concentration also causes a shift of the peak potential in the anodic direction. For pH's in the neutral and acid range, no pH dependence was observed.

A plot of the cathodic peak potential vs pH is reported in Fig. 8. The slope of the straight line in the alkaline pH range varied from -57 to -63 mV/pH unit. The observed pH dependence may be explained by the following process:

$$TlOH + e^- \rightleftharpoons Tl(ads) + OH^- \qquad (4)$$

This implies that the underpotential deposited thallium is actually present on the surface initially as TlOH. This can be formed by the interaction of adsorbed thallium with adsorbed OH groups or by direct coadsorption of Tl(I) and OH^-. The behavior of the UPD peak in Fig. 7 is that expected for the adsorption of metal ions in the presence of strongly adsorbing anions (24). In this case, in fact, the UPD peaks increase in height when the anion concentration is increased, and the peak potential is displaced in the cathodic direction. According to Gerischer et al. (24), the shift of the peak potential is caused by a variation of the potential of zero charge due to the anion adsorption.

C. Disk-Ring Studies in N_2 Saturated Solution Containing Tl(I)

The adsorption of thallium on Au was also examined potentiodynamically using a rotating disk-ring electrode. The ring was potentiostated at -0.95 V where the bulk deposition of Tl(I) is convective-diffusion controlled (Fig. 6). When the disk electrode is not connected (open disk), the ring current is given by (25):

$$i_{R_L}^{o} = \beta^{2/3} i_{D_L} \qquad (5)$$

β is a constant which depends on the geometry of the electrode. For the electrode used in this experiment β was 0.207. In Fig. 9, the ring current increases relative to $i_{R_L}^{o}$ as the disk potential is swept from $\sim$-0.8 V to $\sim$ 0.3 V. This indicates that thallium species stripped at the disk are collected by the ring. As the disk is swept anodically from -0.3 V to -0.03 V the ring current decreases below $i_{R_L}^{o}$, indicating the consumption of Tl(I) at the disk. It is

difficult to say which thallium species is deposited in this potential region. The formation of $Tl(OH)_3$ from Tl(I) in the solution phase is expected to occur only at -0.003 V, for the concentration of Tl(I) employed. On the other hand, the oxidation, on the surface, of TlOH to $Tl(OH)_3$ is not expected to produce any variation in the ring current because $Tl(OH)_3$ is rather insoluble (17). It is not possible at this point to offer any conclusive explanation of this decrease in ring current. Some possibilities are:

1. An oxidation of Tl(I) to Tl(III) occurring at potentials more cathodic than expected on the basis of the Nernst potential because of surface involvement. The deposition of $Tl(OH)_3$ from Tl(I) at potentials less positive than the equilibrium potential for the reaction $Tl(I) + 3OH^- \rightarrow Tl(OH)_3 + 2e^-$ has been discussed by Brainina et al. (26).

2. Tl(I) may be oxidized to Tl(II) to form a surface species of the type $Au(0)_xTl(II)$ which may then undergo dismutation on the surface to give Tl(I) and Tl(II). Tl(II) has been often suggested as an intermediate in oxidation-reduction reactions involving Tl(I) and Tl(III) and evidence of its formation has been reported in several cases. It is not possible, however, to provide any evidence of its formation in the present case.

3. A likely explanation for the mentioned ring current decrease is that it is due to the influence of traces of dissolved oxygen, remaining in the electrolyte despite considerable effort to eliminate it completely. Oxygen, or the product of its reduction HO_2^- may oxidize Tl(I) to Tl(III). Since very low ring currents are involved, the method would be very sensitive to relatively low amounts of dissolved O_2, i.e., 1 atm or less.

When the potential is made more positive (i.e. $\sim$ -0.04 V), the ring current becomes equal to $i_{R_L}^o$ and no process occurs at the disk. Thallium is then consumed at the disk from $\sim$0.0 to 0.6 V. This process is probably due to the oxidation of the solution phase Tl(I) to Tl(III) some of which may remain on the electrode surface as $Tl(OH)_3$ or Tl_2O_3.

For the scan in the cathodic direction, the disk peak I does not give rise to any ring current and is probably attributable to gold oxide reduction or to a mixed Au and Tl oxide reduction. Both the reduction process corresponding to peaks L and G at the disk produce soluble species which are detected by the ring (peaks G' and L'). These processes can be identified as corresponding to the reduction of thallic species in the form of an oxide and/or hydroxide on the surface. The ring current decreases below $i_{R_L}^o$ at $\sim$-0.3 V and a full shielding

is observed at potentials more negative than -0.8 V (Fig. 9). It is noteworthy that the occurrence of peak A at the disk, attributable to the adsorbed thallium, does not cause the ring current to decrease below the $i_{R_L}^{o}$ value. This point will be discussed below.

In a subsequent experiment (Fig. 10) the Tl(I) was monitored with the ring at +0.3 V at which potential Tl(I) is oxidized to Tl(III) yielding $Tl(OH)_3$ and/or Tl_2O_3 on the electrode surface. The experiment was carried out by progressively opening the anodic window from -0.02 to 0.6 V. For curve 1 the ring current lies below the limiting ring current (disk at open circuit), as the disk potential is swept cathodically from -0.02 to -0.2 V. At $\sim$-0.3 V the ring current reaches the open-disk value $i_{R_L}^{o}$ indicating no net consumption or release of Tl(I) in either the anodic or cathodic sweep. For more cathodic potentials, the ring is shielded again by the disk. Curve 2 shows no disk process from $\sim$0.0 to -0.2 V. In fact, the ring current increases from its shielded value and at 0.0 V reaches its unshielded value $i_{R_L}^{o}$. The ring remains unshielded up to $\sim$ -0.2 V when the current decreases again. The subsequent opening curves (3 to 8) show that soluble species are formed during the reduction process at the disk from +0.05 V to $\sim$-0.25 V and are collected by the ring. The first observation is, therefore, that the deposition process observed for curve 1 is completely obsecured or even suppressed when the potential limit is made more anodic than 0.0 V. Peaks A, G, I and L have been observed also in the experiments reported above. As the disk potential is made progressively more anodic, the height of peak L increases up to +0.4 V (curve 6 in Fig. 10). It then decreases first slightly (curve 7) and then markedly when the anodic limit is +0.6 V. Curves 7 and 8 also show the appearance of two other peaks (I and G) at $\sim$+0.12 V and $\sim$ -0.16 V, respectively. This situation is exactly reflected by the ring. Peaks L and G have been assigned above to the reduction of Tl (III) oxides. Probably peak L corresponds to the reduction of $Tl(OH)_3$ to TlOH while peak G may be due to the reduction of Tl_2O_3 formed at the more anodic potentials. The formation of Tl_2O_3 reduces the amount of Tl(III) with hydrated form on the surface and this may be one explanation for the decrease in peak L which accompanies all increases in peak G. Peak I can be tentatively assigned to the reduction of gold oxides or mixed gold and thallium oxides, as it was mentioned above.

In contrast to the behavior in Fig. 9, the ring current is remarkably constant for disk potentials above 0.1 V with no hysteresis. In this experiment, it appears that the ring properly monitors only Tl(I) and that its oxidation on the disk was under pure convective-diffusion control. The corresponding disk current for Tl(I) oxidation under pure convective-diffusion control, as calculated semiquantitatively from the ring shielding, is shown by the dotted curve in Fig. 9. The excess disk current then must involve surface oxidation most likely of gold to form $Au(OH)_3$ and possible the oxidation of residual $Tl(OH)_x$ onthe surface to form $Tl(OH)_3/Tl_2O_3$.

A simple explanation for the increased current on the ring, when held at -0.85 V (Fig. 9), at disk potentials >0.1 V is that a second species other than Tl^+ was reaching the ring and undergoes reduction. A good condidate is Au in soluble form. Alternatively, it is possible that some Tl(III) is produced in the solution phase during the oxidation of Tl(I), despite the extraordinarily low solubility of Tl(III) in the 1M NaOH electrolyte. Supersaturation may occur and a relatively long period be required for the precipitation process.

The experiment illustrated in Fig. 11 was carried out using a low concentration of Tl(I) and potentiostating the disk at various potentials for a fixed length of time (60s). Only peaks D and C are detected at the ring. The stripping of the underpotential deposit at the disk, from $\sim$-0.4 to 0.0 V, does not produce any ring current. This is clearly illustrated in Fig. 12 where the disk current has been reconstructed by dividing the ring current by the collection efficiency. The low ring current observed during the occurrence of peaks B and A at the disk can be explained by a very slow dissolution of the deposit at the ring. As mentioned above, the thallium species are coadsorbed together with OH^- leading to the formation of TlOH on the Au surface. The detection of a ring current thus depends on the extent that the TlOH-like adsorbate dissolves into the solution phase. This explanation seems to be in part corroborated by the fact that for lower scan rates (20 mV/s) and higher rotation rates (4900 rpm) than in Figs. 11 and 12, a slightly larger ring current is observed ($\sim$ 5% more than in Fig. 12, at -0.2 V). Even by slowing the scan rate, the ring current at the potential where peaks A and E occur at the disk (Fig. 11) remains negligible. Therefore, the dissolution of (TlOH)ads into the solution must be a slow process.

It is opportune to summarize at this point the results of the potentiodynamic studies reported above. The authors propose that peaks A and A' (see e.g. Fig. 1) are due to the following process:

$$(TlOH)ads + e^- \rightarrow Tl(UPD) + OH^- \qquad (6)$$

where Tl(UPD) may be essentially in a zero valent state. Evidence to support this involves:

1. Lack of stirring sensitivity over the Tl(I) concentraton range examined (2×10^{-6}M to 5×10^{-5}M) for sweep rates of 5 to 150 mV/s.

2. Peak potentials independent of sweep rate for the same range of concentrations and sweep rates.

3. A pH dependence of the peak potential of $\sim$ 0.06 V/pH unit in the correct direction for reaction 6, over the pH range 10 to 13.

4. Peak A and A'; (see e.g. Fig. 1) are complementary.

5. The peak heights are linearly dependent on the sweep rate.

The adsorption of TlOH would in turn occur from the soluble species

$$Tl(1) + OH^- \rightleftharpoons Tl(OH)ads \qquad (7)$$

where the adsorption isotherm, whatever it may be, will lead to a dependence of Tl(OH)ads coverage on the solution concentration of Tl(I). The adsorption process 6-7 does not involve any formal charge transfer through the external circuit and hence will at the most be only a minor peak or perturbation in the voltammetry curve.

Peaks B and B' (see Fig. 1) may be explained as corresponding to adsorption on sites having different crystallographic orientation. Peaks C and C' are sharp and narrow. Such sharp peaks have been observed with transitions in UPD layers such as order-disorder and even phase transitions involving condensation into patches. Such a transition is the likely explanation for peaks C and C'.

D. O_2 Reduction on Au in 1M NaOH Containing Tl(I)

Figure 13 shows a comparison of the disk and ring polarization curves for O_2 reduction on Au obtained in the absence and in the presence of 6.6×10^{-6} M Tl(I). In agreement with McIntyre and Peak (15) it is seen that the half-wave potential is not appreciably shifted with respect to the pure Au. At potentials more negative than -0.1 V, however, the current with Tl(I) rises steeply and at -0.2 V it reaches a value which is approximately two-fold that observed for Au in the absence of Tl(I). This value does not increase further for higher concentrations of added Tl(I). The ring current is almost completely suppressed in the potential range from 0.0 to -0.3 V. Starting at $\sim$-0.4 V it increases rapidly and approaches the value obtained in the absence of Tl(I) at $\sim$-0.6 V. The background ring current is quite significant and can be attributed to the oxidation of Tl(I) to Tl(III) since its magnitude is dependent on the concentration of Tl(I). The background obtained in the absence of Tl(I) was negligible. The ring currents were corrected for the background for the analysis of the disk-ring data.

Plots of $1/i$ vs $1/f^{1/2}$ for the reduction of O_2 in the presence of Tl(I) are shown in Figs. 14 and 15. Straight lines are obtained which are parallel to each other over the potential range from $\sim$-0.15 to -0.3 V. This indicates that the O_2 reduction follows first order kinetics. At more cathodic potentials, the intercept approaches zero indicating that O_2 reduction becomes essentially mass-transport controlled. Figure 6-15b shows a comparison of the plots in the presence and in the absence of Tl(I). In the latter case the B value is 8.8×10^{-3} mA/(rpm)$^{1/2}$ which is in agreement with the one calculated from the data of Gubbins et al. (27) of 8.6×10^{-3} mA/(rpm)$^{1/2}$ for a two electron process. In the presence of Tl(I) the B value is 17×10^{-3} mA/(rpm)$^{1/2}$ at potentials from -0.15 to -0.3 V, which represents an almost two fold increase with respect to the one obtained with no Tl(I) present. This implies an overall exchange of $4e^-$ per O_2 molecule reaching the electrode surface. For potentials more negative than -0.3 V the B value decreases at first slightly and then more markedly. Its value is 16×10^{-3} mA/(rpm)$^{1/2}$ at -0.4 V and 13.15×10^{-3} mA/(rpm)$^{1/2}$ at -0.6 V (Fig. 15b).

A Tafel plot of E vs $\log(i/i_L - i)$ has been constructed for two different rotation rates (Fig. 16). The plot yields straight lines with slopes of -55 mV/dec which were independent of rotation rate.

Figure 17 shows a very expanded polarization curve for O_2 reduction in the absence and in the presence of Tl(I) added to the electrolyte. In agreement with the data of Fig. 13, the current with Tl(I) present rises steeply at $\sim$ -0.1 V. It is, however, only slightly higher than for pure gold at less cathodic potentials.

When the Tafel plot was constructed from the data of Fig. 17, two linear regions were obtained (Fig. 18). The one at the lower overpotentials extends over less than one decade and has a slope of -115 mV/dec while the second linear region, extending approximately over one and a half decade has a slope of -55 mV/dec, as for Fig. 16. The region of higher TAfel slope at lower polarization did not show up in Fig. 16 because of the lack of sufficient data points at low current densities.

The value of -55 mV/dec was obtained in most of the experiments. Values of -50 and -40 mV/dec were, however, also obtained. These variations were observed even in successive series of polarization measurements scanning in the positive potential direction with the same electrode in the same solution. The Tafel slopes tended to increase numerically from values of $\sim$-40 to -55 mV/dec but no higher. The slopes did not change, however, with rotation rate or Tl(I) concentration over the range examined (4×10^{-6} to 25×10^{-5} M). This behavior suggests surface aging effects which are probably potential dependent. Surfaces with UPD layers are known to undergo structural changes particularly at more negative potentials (see e.g. 28).

In Figure 18 the Tafel plot for pur Au in the absence of Tl(I) is reported for comparison. In this case deviations from Tafel linearity are observed starting at $\sim$-0.07 V and more positive potentials. These deviations are explained by the back reaction of O_2 reduction, i.e., HO_2^- to O_2. With Tl(I) present, the reduction proceeds all the way to OH^- and the back reaction does not become significant in the range for which polarization data can be obtained.

The similarity of the slopes (-115 mV/dec vs - 121 mV/dec) suggests that the rate controlling steps both with and without Tl(I) present are the same and most likely the first electron transfer. By probably coincidence the -115 mV/dec region of the curve for the Tl(I) containing solution is nearly co-linear with that for pure gold at higher polarizations. Actually with the same initial kinetic controlling step, the current i for Au with Tl(I) present would be expected to be $\sim$ 2 fold higher than without Tl(I) after correction for the mass-transport since O_2 reduction is to principally HO_2^- with Au in the absence of Tl(I) and to OH^- with Tl(I).

In the region of the -115 mV/dec Tafel slope with Tl(I) in solution, the coverage with UPD Tl is low according to the earlier discussion of the voltammetry curve (see also insert in Fig. 18). In this region, however, there may be still significant coverage with a species such as TlOH and this promotes the peroxide elimination reaction. At potentials when the Tafel slope is -55 mV/dec, the coverage with UPD Tl appears to become significant and to increase substantially with potential in the cathodic direction. It appears that, UPD Tl catalyzes the O_2 reduction quite substantially. The low Tafel slope is probably the combined result of changes in the potential energy barrier height and changes in the site (UPD) concentration with potential. For example, for a first electron transfer step rate controlling of the type:

$$O_2 + Tl_{UPD} + e^- \rightarrow Tl_{UPD} \text{ — } O_2^- \qquad (8)$$

$$i = FKC_{O_2} \theta \exp - \frac{\alpha F}{RT} \phi \qquad (9)$$

where θ is the fraction of the gold surface covered by Tl_{UPD} which are available for interaction with O_2. For $\theta \ll 1$ (Langmuirian region):

$$\theta = Ka_{Tl} + \exp - \frac{\gamma F}{RT} \phi \qquad (10)$$

where k is a constant and γ is the electrosorption valence. Combining eqs. -9 and -10:

$$i = FkC_{O_2} K \exp - \left(\frac{\gamma+\alpha}{RT}\right) \phi \qquad (11)$$

or

$$i = i_o \exp - \left(\frac{\gamma+\alpha}{RT}\right) \eta \qquad (12)$$

If $\alpha = 1/2$ and $\gamma = 1$ this equation predicts a Tafel slope of -40 mV/dec at 25°C. Either deviations from Langmuirian behavior or an electrosorption valence γ less than unity can result in higher slopes. For example $\gamma = 0.6$ would yield, with a Langmuir adsorption isotherm, a Tafel slope of -55 mV/dec. The state of Tl in a UPD layer on the surface can influence the electrosorption valence. Changes in the state of the Tl-UPD layer are a possible source of the small variations of the Tafel slope in successive voltage sweeps. A further discussion of the Tafel slopes will appear in a later chapter in the framework of the discussion of the O_2 reduction mechanism on UPD layers.

E. Analysis of the Disk-Ring Data

In the early work by the author (16), carried out in this laboratory, results of a disk-ring analysis of O_2 reduction in the presence of Tl(I) were reported which showed that the O_2 reduction proceeded via a parallel mechanism with $K_1/K_2 = 0.4$. The analysis was carried out, however, only at rather negative potentials in the diffuse limiting region since in the kinetic region the ring currents were quite small and difficult to measure (see Fig. 13). The data obtained in this way provide only limited information for kinetic studies. In the more recent work the disk-ring analysis was attempted by recording the polarization curves point by point and using a much lower concentration of Tl(I) in the solution (Fig. 20). One should always be aware, however, of the severe complications in the interpretation of disk-ring data for the reduction of O_2 with ions as Tl(I) or Tl(III) present in the solution. These complications for the present course involve mainly:

1. Relatively high background ring currents (as compared to the total observed currents) are involved due to the couple Tl(I)/Tl(III) at the ring. Further, HO_2^- can both oxidize Tl(I) to Tl(III) and also reduce Tl(III) to Tl(I). Thus

$$HO_2^- + H_2O + Tl(I) \rightarrow 3OH^- + Tl(III) \quad (13)$$

and

$$HO_2^- + OH^- + Tl(III) \rightarrow O_2 + H_2O + Tl(I) \quad (14)$$

It is not clear whether these reactions proceed sufficiently rapidly to consume any significant amount of the peroxide during the transport of peroxide from the disk to the ring. It is difficult to establish the rates of these reactions without a detailed study. Consequently qualitative efforts to interpret the disk-ring data in the work with Tl(I) have been limited to situations where the Tl(I) concentration is very low compared to the oxygen concentration. Under such conditions, the peroxide generated should be large compared to the amount concerned in either of the above reactions unless the peroxide yield is very low. If the kinetics are sufficiently fast for these two reactions, they together are equivalent to the Tl catalyzed homogeneous decomposition of HO_2^-, therefore, even if Tl(I) and Tl(III) are low in concentration, they can perturb the disk-ring analysis since the Wroblowa *et al.* (29) scheme does not take into account homogeneous decomposition.

Doronin and Shirokova (30) have examined the reaction of HO_2^- with Tl(I) in NaOH solutions. They attempted to monitor the formatin of O_2 with Tl(I) present in the range of 1.7×10^{-5} to 5.0×10^{-4} M and HO_2^- in the range of 6.5×10^{-3} to 7.9×10^{-2} M. Using an electrochemical O_2 analyzer involving a Pt electrode coated with a polyethylene film (with a sensitivity of 10^{-6} M O_2) they were unable to detect the Tl(I) catalyzed peroxide decomposition. This indicates that in alkaline solutions the Tl catalyzed homogeneous decomposition to form O_2 is relatively slow. On the other hand, the studies of these workers with Tl and HO_2^- in alkaline solution using amalgamated silver disk electrodes lead them to postulate the following reactions:

$$Tl(I) + HO_2^- + H_2O \rightarrow Tl(III) + 3OH^- \quad (15)$$

$$nTl(III) + mHO_2^- \rightleftharpoons [Tl_n(HO_2)_m]^{(3n-m)+} \quad (16)$$

where the Tl(III) complex is then reduced according to:

$$[Tln(HO_2)_m]^{(3n-m)+} + Me^- \rightarrow nTl(II) + mHO_2^- \quad (17)$$

$$[Tln(HO_2)_m]^{(3n-m)+} + 2ne^- \rightarrow nTl(I) + mHO_2^- \quad (18)$$

The divalent thallium then undergoes disproportionation:

$$2Tl(II) \rightleftharpoons Tl(I) + Tl(III) \quad (19)$$

reduction

$$Tl(II) + e \rightarrow Tl(I) \quad (20)$$

or oxidation to Tl(III) in the solution by HO_2^-

$$2nTl(II) + (2m + 1)HO_2^- + H_2O \rightarrow 2[Tl_n(HO_2^-)_m]^{(3n-M)+} + 3OH^- \quad (21)$$

There is some evidence that the Tl(III) complexes with HO_2^- render Tl(III) soluble in NaOH where otherwise $Tl(OH)_3$ would precepitate because of the very low solubility of Tl(III) in alkaline solutions. According to Doronin and Shirokova, it is also possible that reactions similar to 15 and 16 may form a complex compound of Tl(II) with HO_2^-.

2. The ring cannot be pre-treated by cathodic pulses because Tl(I) would be plated on the ring. These cathodic pulses are necessary ordinarily to avoid the progresive formation of a thick oxide layer which would inhibit the oxidtion of HO_2^-. In the presence of Tl(I) in solution, the gold oxide formation is modified and the

inhibition of the peroxide oxidation becomes an even more serious problem, as will be discussed.

The ring potential for the disk-ring studies has to be carefully selected so as to minimize the interference of the thallium reactions. In the present work a potential of 0.1 V was chosen. This potential corresponds to the maximum current observed for the oxidation of hydrogen peroxide when this was added to the solution. The choice of the ring potentials was also based on the disk-ring experiments carried out under conditions similar to those for O_2 reduction in the presence of Tl(I) except that the solution was saturated with nitrogen (Fig. 19). These experiments were carried out using different ring potentials and different anodic limits of the disk potential. It is seen that either a too high anodic disk potential (Fig. 19a) or a too anodic ring potential (Fig. 19c) cause the appearance of a ring current which is high enough to seriously disturb those observed during O_2 reduction studies. Therefore the compromise situation in Fig. 19b was adopted for O_2 reduction experiments.

With these considerations in mind, the disk-ring data of Fig. 20 have been analyzed using the diagnostic criterion of Wroblowa *et al.* (29). The plots of $(I_d/I) \times N$ vs $1/f^{1/2}$ are given in Fig. 21. Both the intercepts and the slopes of these plots are pure Au which have a common intercept of 1. In terms of the Wroblowa *et al.* analysis, the slopes (J) and the intercepts (S) are relabeled by the following equation:

$$J = 1 + 2\frac{k_1}{k_2} + \frac{ZS}{k_6} \qquad (22)$$

The plot of J vs S predicts an intercept ≥ 1 depending on whether $k_1 = 0$ (series process) or $k_1 \neq 0$ (parallel process). The intercept observed in the plot of J vs S reported in Fig. 22 is actually negative. This may be due to the large scatter of the points. The scatter is not unexpected considering that the ring currents are much smaller than the disk currents. Within the experimental error, and in the framework of the limitations given above, the reduction of O_2 on Au in the presence of Tl(I) can be considered to proceed via a series mechanism, as for Au in the absence of Tl(I).

F. HO_2^- Oxidation and Reduction in N_2 Saturated 1M NaOH

Figure 23 shows a comparison of polarization curves for HO_2^- oxidation and reduction obtained in the presence and in the absence of Tl(I). For the case with thallium present, the polarization curves are shown in more detail in Figs. 24 and 28 for the oxidation and reduction of HO_2^- respectively. The potential of zero current of the anodic-cathodic wave with thallium presnet is $\sim$ 0.1 V more anodic than for gold in the pure electrolyte (Fig. 23).

The oxidation of HO_2^- is strongly inhibited in the presence of thallium. This inhibition may be caused by the modification of the Au surface as a consequence of the formation of a thallic oxide layer (see above votammograms), and/or due to the impossibility of pre-treating the electrode by cathodic pulses. This cathodic pre-treatment was necessary in order to achieve a limiting current for the HO_2^- oxidation on Au.

A reaction order plot is shown in Fig. 25. The plot could be constructed in a narrow range of potentials only. The value of the reaction order at 0.09 V and 0.1 V is $\sim$1, while values larger than 1 were obtained for less positive potentials. These large values presumably reflect complication due to the back reactions. The reaction order obtained in the absence of Tl(I) was $\sim$0.5.

A plot of $1/i$ vs $1/f^{1/2}$ (Fig. 26) was constructed from the polarization curves presented in Fig. 24. This plot shows that the B value, and hence the number of electrons, varies with potential, as seen in the following Table.

TABLE II

B values as a function of potential for the oxidation of HO_2^- in the presence of Tl(I)

E(V)	B mA/(rpm)$^{1/2}$ x 10^3
0.05	6
0.06	7.4
0.075	11.05
0.125	16.5

The value of 0.125 V, which is the maximum value observed, is only slightly lower than the observed one of 16.85 mA/(rpm)$^{1/2}$ for the oxidation of HO_2^- on clean Au, indicating two electrons per O_2 molecule. The intercepts of the plots of Fig. 26 are greater than zero at all potentials, indicating that the oxidation of HO_2^- never becomes completely mass-transport controlled.

The construction of Tafel plots for the HO_2^- oxidation in the presence of Tl(I) presents some difficulty. The plot of E vs $i/(i_L-i)$ is not correct since the cathodic current is not negligible. A plot can be constructed using the equation for pure concentration overpotential

$$\eta_c = -\frac{2.3RT}{nF} \log \left[\frac{I_D + i}{I_d - i} \cdot \frac{I_d}{I_D}\right] \qquad (23)$$

which applies when the transport of the reactant to the electrode surface and the removal of the reaction products away from it are diffusion controlled. I_D and I_d are the cathodic and anodic limiting currents respectively and i is the observed current, negative for a cathodic process and positive for an anodic one. If the oxidation of HO_2^- according to the overall reaction

$$HO_2^- + OH^- = O_2 + H_2O + 2e^- \qquad (24)$$

is diffusion controlled, the plot of E vs $\log[I_D + i/I_d - i]$ should give a slope of 30 mV. The value of the slope observed in the present work was actually -100 mV/dec, indicating that the oxidation of HO_2^- in the presence of Tl(I) is not mass-transport controlled and the plots according to equation 24 cannot be used for mechanistic considerations.

The oxidation of Tl(I) to Tl(III) in the range of potentials where HO_2^- oxidation occurs (see Fig. 6) represents an additional problem in the interpretation of the results. The formation of a thallic hydroxide layer causes a change in the nature of the electrode surface. This new surface may be less active for the electrochemical decomposition of HO_2^-. In principle, however, the Tl(III) species promote a chemical oxidation of HO_2^- according to

$$Tl(III) + HO_2^- \rightarrow Tl(I) + 1/2\ O_2 + OH^- \qquad (25)$$

The Tl(III) then might be regenerated electrochemically yielding overall 2 electrons per peroxide converted to O_2. At these positive potentials, the O_2 will not be reduced back to peroxide.

In contrast to the oxidation process, the reduction of HO_2^- is greatly enhanced when Tl(I) is added to the electrolyte (Figs. 23, 27). The hysteresis in the current-potential curves is small at potentials anodic to $\sim$0.3 V. For potentials more negative than this, it becomes larger the larger is the cathodic limit of the potential sweep.

A plot of $1/i$ vs $1/f^{1/2}$ derived from the polarization data of Fig. 27 is presented in Fig. 28. The straight lines obtained at potentials from -0.05 V to -0.2 V are approximately parallel and the intercept becomes zero at -0.2 V indicating that the HO_2^- reduction becomes pure mass-transport controlled. The B value derived from the slope of these plots is 16.9×10^{-3}(mA)/(rpm)$^{1/2}$ obtained for the oxidation of HO_2^- in the absence of Tl(I). The reduction of HO_2^- on clean Au is difficult to study as discussed in Chapter IV.

The plot of Fig. 29 confirms that the reaction order with respect to HO_2^- is 1 for the reduction process. The value of 2 obtained at -0.01 V is most likely due to the superimposition of the back reaction.

REFERENCES

1. E. Schmidt and H. Gygax, J. Electroanal. Chem., 12, 300 (1966).

2. E. Schmidt and H. Gygax, Helv. Chem. Acta., 48, 1584 (1965).

3. A. Bewick and B. Thomas, J. Electroanal. Chem., 65, 911 (1975).

4. H. Siegenthaler, K. Jüttner, E. Schmidt and W.J. Lorenz, Electrochim. Acta, 23, 1009 (1978).

5. W.J. Lorenz, J. Mountzis and E. Schmidt, J. Electroanal. Chem. 33, 121 (1971).

6. E. Schmidt and H.R. Gygax, J. Electroanal. Chem., 12, 300 (1966).

7. B.J. Bowles, Electrochim. Acta, 10, 717, 731 (1965).

8. R.R. Adzic, D.N. Simic, A.R. Despic and D.M. Drazic, J. Electroanal. Chem., 65, 587 (1975).

9. V.A. Vicente and S. Bruckenstein, J. Electroanal. Chem. 82, 187 (1977).

10. J.D.E. McIntyre and W.F. Peck, J. Electrochem. Soc., 123, 1800 (1976).

11. K.J. Cathro and D.F.A. Kodi, J. Electrochem. Soc., 111, 1416 (1964).

12. A.M. Abd El Halim, K. Juttner and W.J. Lorenz, J. Electroanal. Chem., 106, 193 (1980).

13. A. Zvetanova and K. Jüttner, J. Electroanal. Chem., 119, 149 (1981).

14. R.R. Adzic and A.R. Despic, Z. Phys. Chem. N.F., 98, 95 (1975).

15. J.D.E. McIntyre and W.F. Peck, Proceedings of the 3rd Symposium on Electrode Porcesses, The Electrochem. Soc., Inc., (1979).

16. R. Amadelli, J. Molla, P. Bindra and E. Yeager, J. Electrochem. Soc., 128, 2706 (1981).

17. M. Pourbaix, Atlas of Electrochemical Equilibria in Aqueous Solutions, Natl. Assoc. Corrosion Engineers, Houston (1974).

18. P. Delahay and G.L. Stiehl, J. Am. Chem. Soc., 73, 1655 (1951).

19. I.M. Kolthoff and J. Jordan, J. Am. Chem. Soc., 74, 382 (1952).

20. R. Guidelli, G. Pezzatini and M.L. Foresti, J. Phys. Chem., 76, 976 (1972).

REFERENCES

21. H.A. Caltherino and J. Jordan, Talanta, 11, 159 (1964).

22. S. D. James, Electrochim. Acta, 12, 939 (1967).

23. J. Ulstrup, Electrochim. Acta, 13, 535 (1968).

24. D.M. Kolb, M. Przasnyski and H. Gerischer, J. Electroanal. Chem., 54, 25 (1974).

25. W.J. Albery and M.I. Hitchman, Ring-disc Electrodes, Clarendon Press, Oxford, 1971.

26. Kh.Z. Brainina, N.K. Kiva and V.B. Belyavskaya, Elektrokhimiya, 1, 311 (1965).

27. K.E. Gubbins and R.D. Walker, J. Electrochem. Soc., 112, 469 (1965).

28. P.L. Hagans, Thesis, case Western Reserve University, 1979.

29. H.S. Wroblowa, Y.D. Pan and G. Razumney, J. Electroanal. Chem., 60, 195 (1976).

30. A.N. Doronin and V.I. Shirokova, Elektrokhimiya, 13, 1147 (1977).

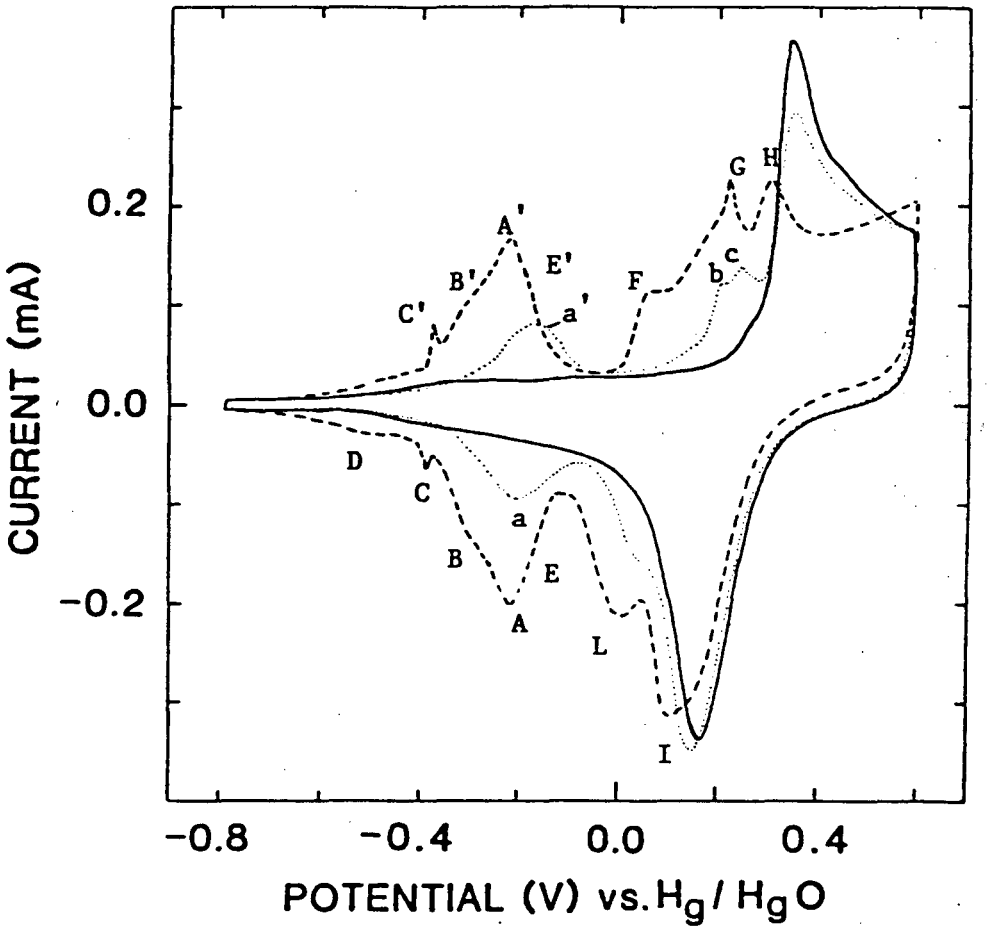


Fig. 5.1.2.1. Cyclic voltammetry curves for Au in N_2 saturated 1M (solid line) and with increasing amounts of Tl^{+}(I): 2.5×10^{-6}M (dotted line), 2.2×10^{-5}M (dashed line). Scan rate: 50 mV/s. Electrode area: 2 cm^2.

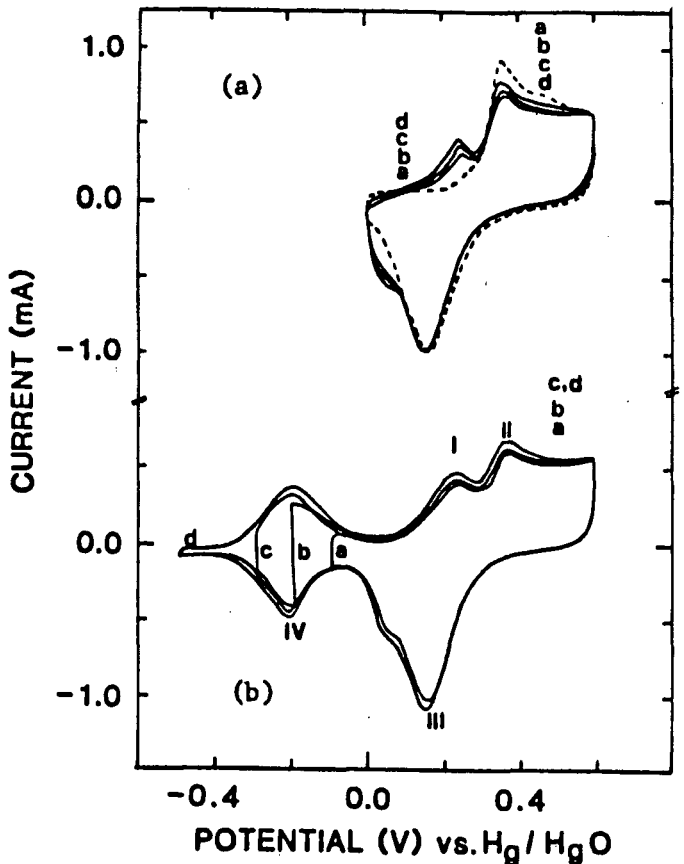


Fig. 5.1.2.2. Cyclic voltammetry curves for Au in N_2 saturated 1M NaOH in the presence of 1.6×10^{-6} M Tl(I): a) Electrode introduced at 0.0 V and anodic scan recorded, b) Progressive cathodic opening. Scan rate: 50 mV/s. Electrode area: 4.5 cm^2.

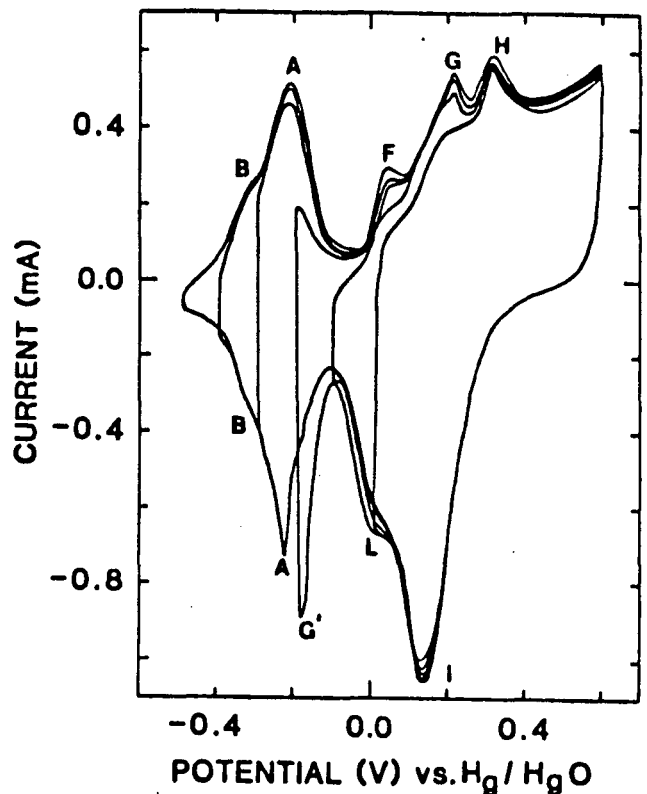


Fig. 5.1.2.3. Cyclic voltammetry curves for Au in N_2 saturated 1M NaOH containing 2×10^{-5} M Tl(I). Cathodic opening curves. Scan rate: 50 mV/s. Electrode area: 4.5 cm^2.

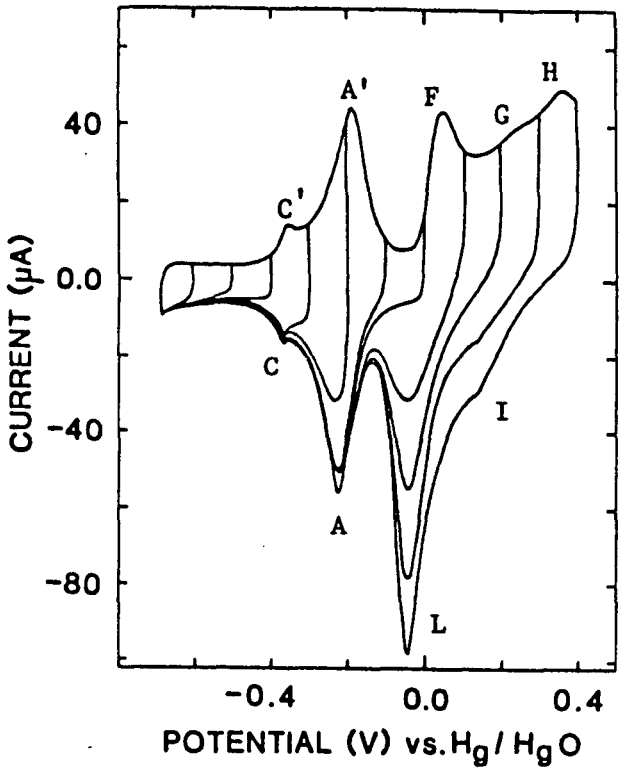


Fig. 5.1.2.4. Cyclic voltammetry curves for Au in N_2 saturated 1M NaOH containing 1 x 10^{-4}M Tl(I). Anodic opening curves. Scan rate: 100 mV/s. Electrode area: 0.2 cm^2.

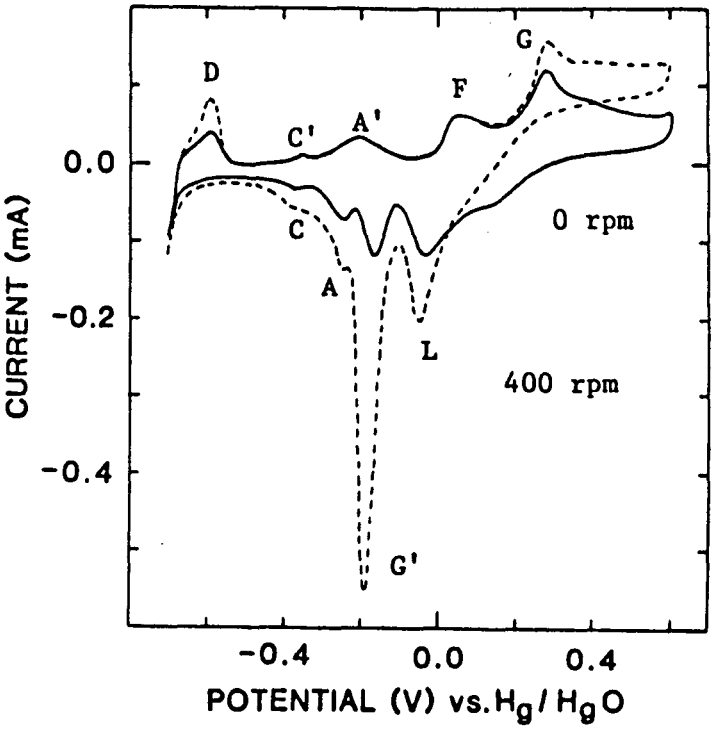


Fig. 5.1.2.5. Cyclic voltammetry curves for Au in N_2 satureated 1M NaOH in the presence of 4x10^{-4}M Tl(I). Scan rate: 100 mV/s. Electrode area: 0.2 cm^2.

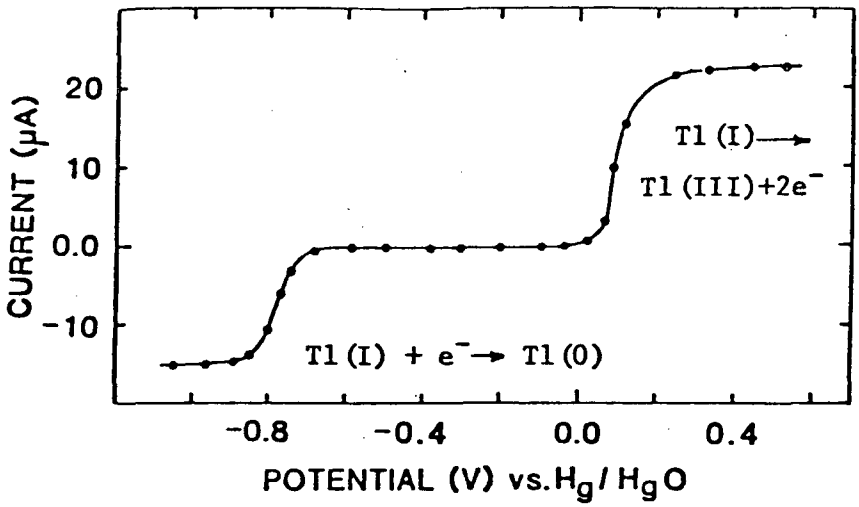


Fig. 5.1.2.6. Quasi steady-state polarization curve for the reduction and oxidation of Tl(I) on Au in 1M NaOH. The potential was scanned between the chosen points with the electrode at 0 rpm. The potential sweep was interrupted and the rotation rate was simultaneously changed to 2500 rpm. Tl(I) concentration: 1.7×10^{-5} M. Electrode area: 0.458 cm^2.

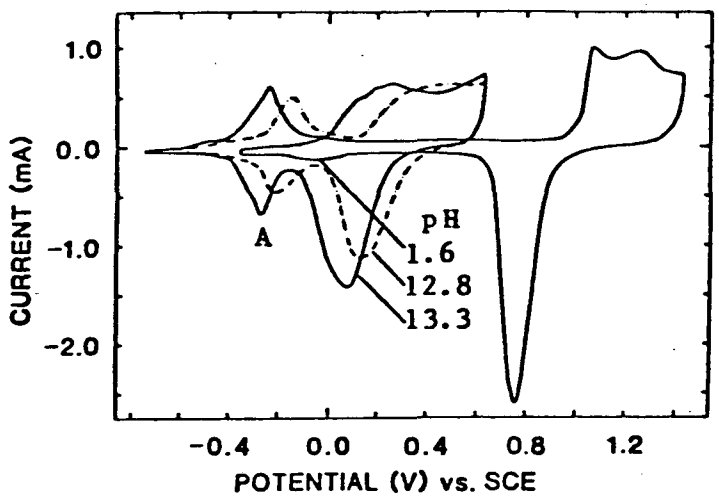


Fig. 5.1.2.7. Cyclic voltammetry curves for Au in solutions of different pH containing 1.7×10^{-5} M Tl(I). Scan rate: 50 mV/s. Electrode area: 10 cm^2. Ionic strength of the solution:1, established with $NaClO_4$.

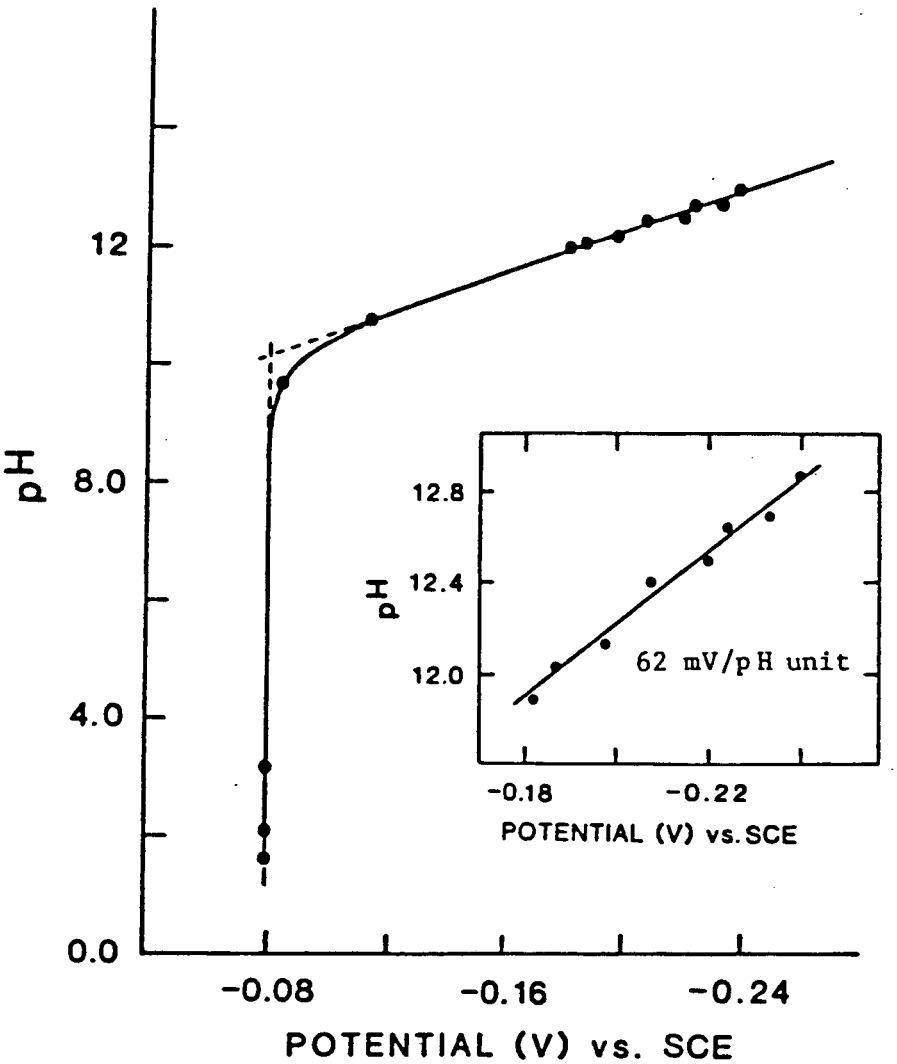


Fig. 5.1.2.8. pH dependence for peak A in Fig. -7.

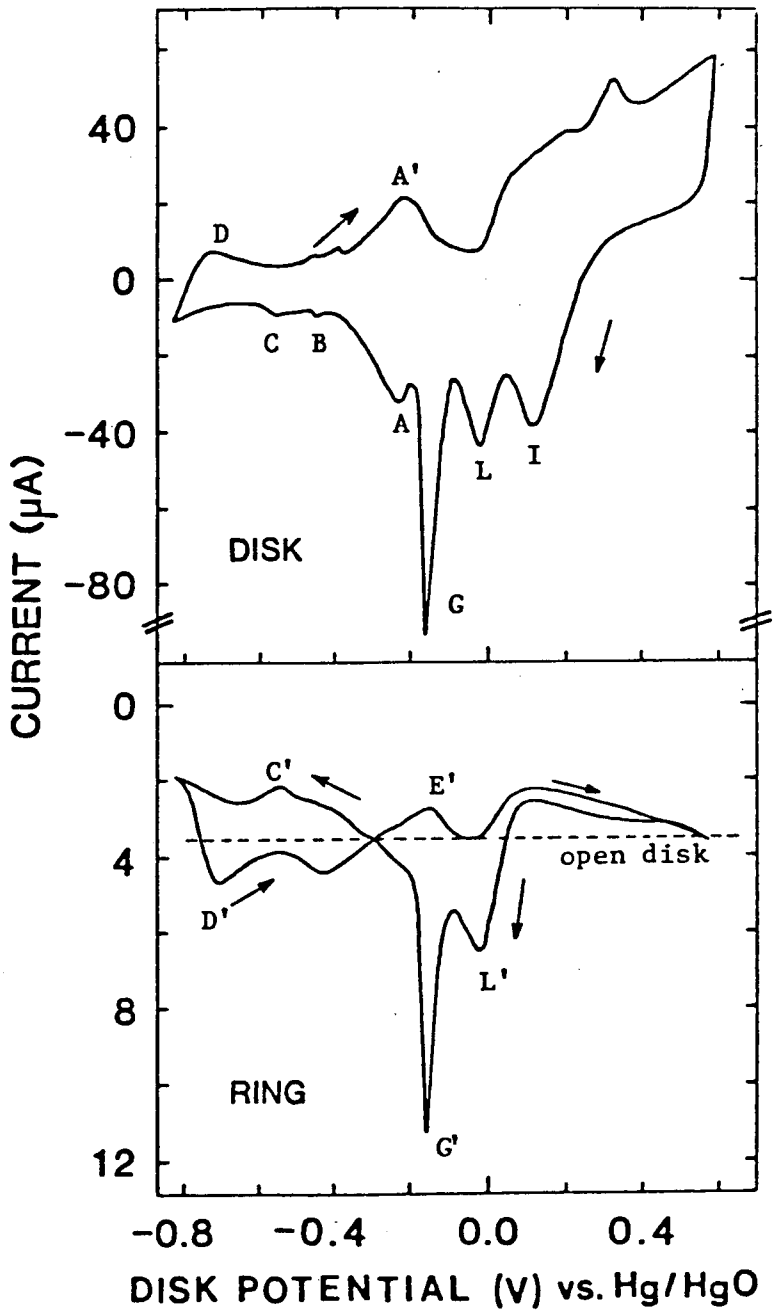


Fig. 5.1.2.9. Disk-ring potentiodynamic curves for Au in N_2 saturated 1M NaOH containing 9×10^{-6} M Tl(I). Scan rate: 50 mV/s. Rotation rate: 2500 rpm. Electrode area: 0.458 cm^2. Ring potential: -0.95 V. N= 0.18.

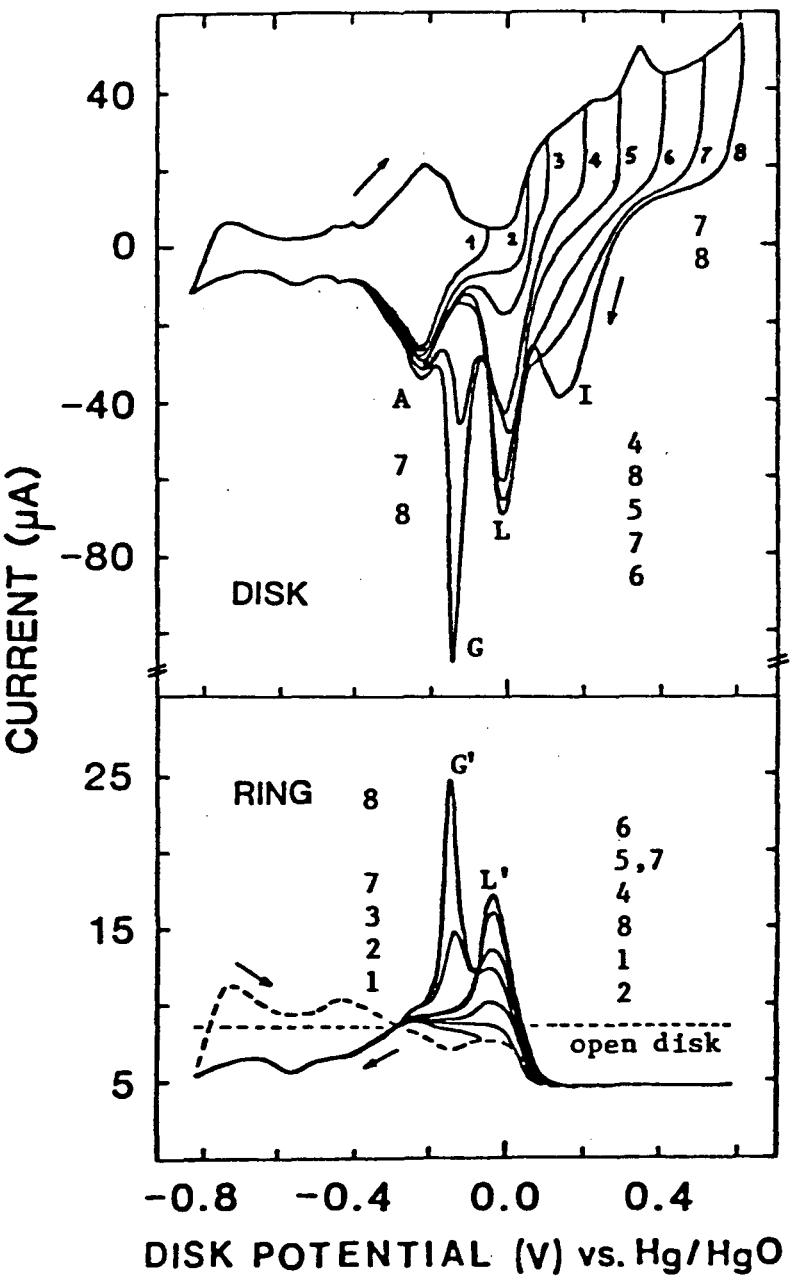


Fig. 5.1.2.10. Disk-ring potentiodynamic curves in N_2 saturated 1M NaOH containing 9×10^{-6} M Tl(I). Scan rate: 50 mV/s. Rotation rate: 2500 rpm. Electrode area: 0.458 cm^2. Ring potential: 0.3 V. N= 0.18.

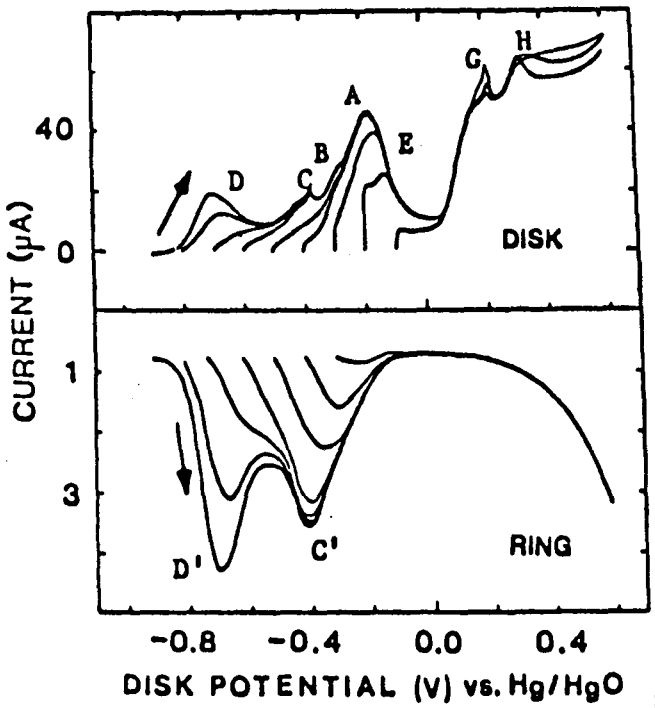


Fig. 5.1.2.11 Disk-ring potentiodynamic curves for Au in N_2 saturated 1M NaOH containing 3.8×10^{-6}M Tl(I). Electrode held at various potentials for 60s and the sweep in the anodic direction recorded at 100 mV/s. Electrode area: 0.458 cm^2. Rotation rate: 2500 rpm. Ring potential: -0.95 V. N = 0.18.

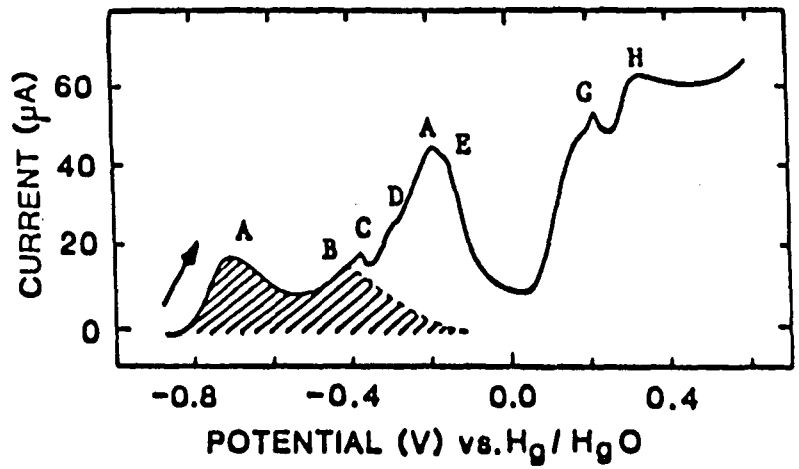


Fig.5.1.2.12. Reconstruction of the disk curve by dividing the ring current by the collection efficiency (shaded area delimited by the dashed line). Data from Fig.6-11.

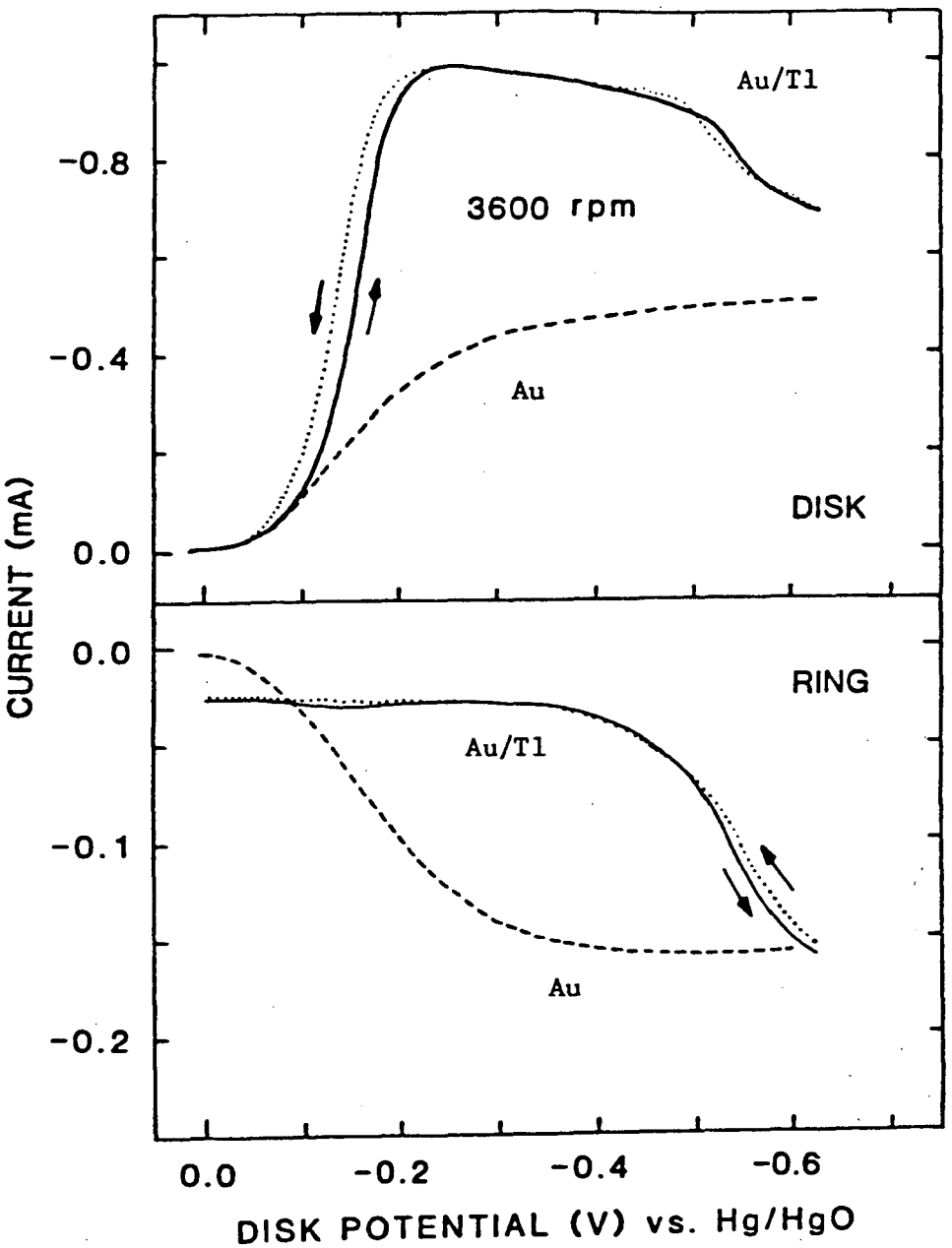


Fig. 5.1.2.13. Comparison of the disk-ring polarization curves for O_2 reduction on Au in 1M NaOH in the absence (dashed line) and in the presence of 6.6×10^{-6} M Tl(I) (solid line). Scan rate: 10 mV/s. Disk area: 0.2 cm^2.

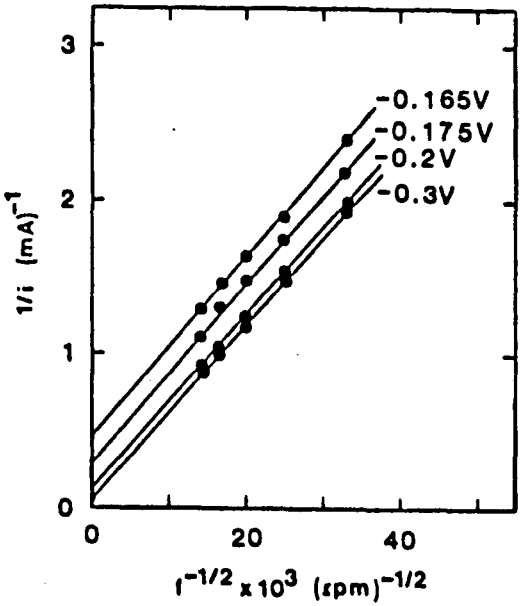


Fig. 5.1.2.14. Plots of $1/i$ vs. $1/f^{1/2}$ for the reduction of O_2 on Au in the presence of Tl(I). Data taken from Fig.6-13 and other similar curves at different rotation rates.

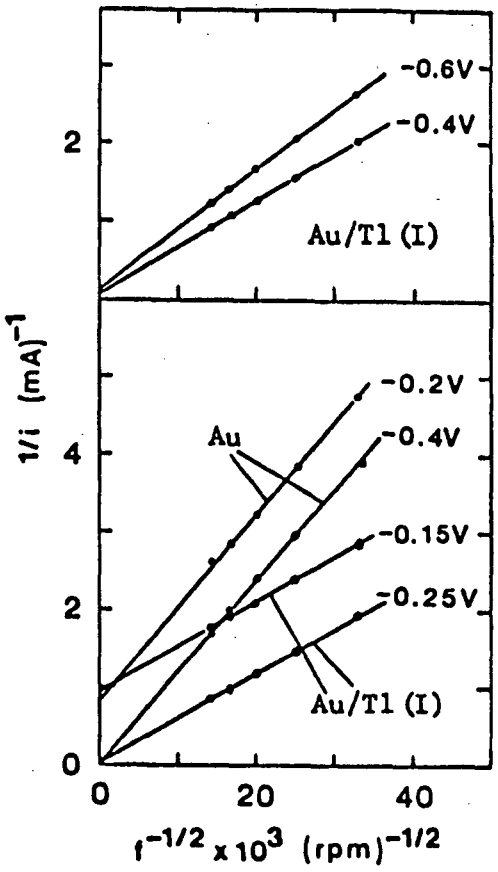


Fig. 5.1.2.15. a):Same as for Fig.6-14 but at more negative potentials. b): Comparison of the plots in the absence and in the presence of 6.6×10^{-6} M Tl(I).

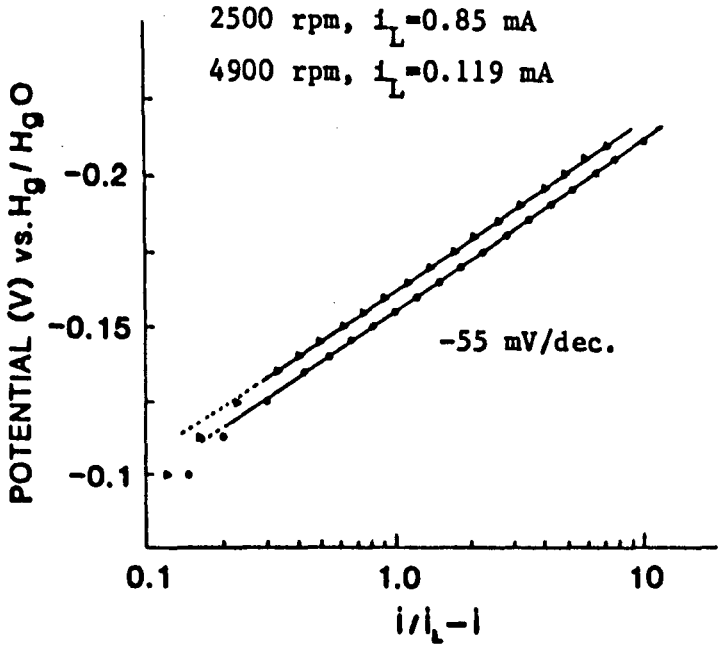


Fig. 5.1.2.16. Tafel plots for O_2 reduction on Au in 1M NaOH containing 1.5×10^{-5}M Tl(I). Scan rate: 10 mV/s. Electrode area:0.2 cm^2.

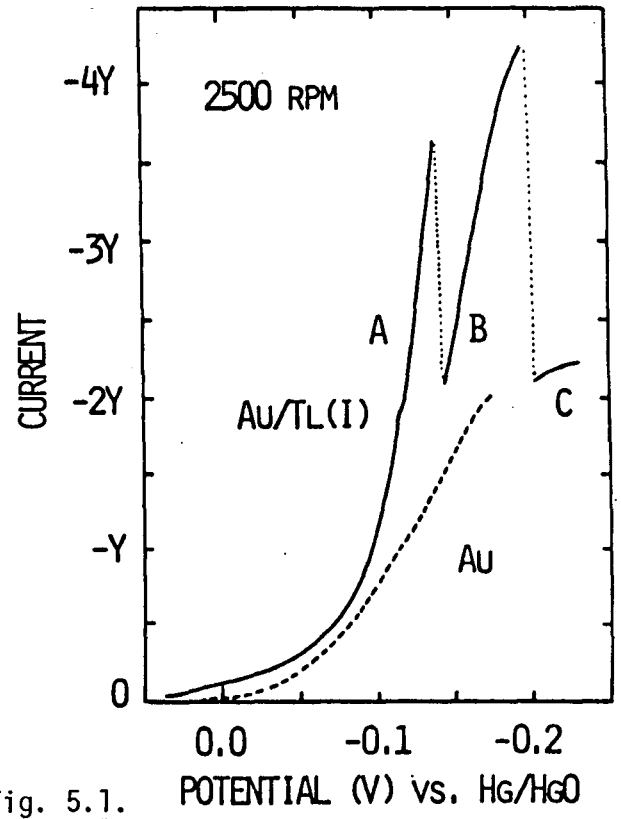


Fig. 5.1. 2.17. Polarization curve for O_2 re-reduction on Au in 1M NaOH in in the absence (dashed line, Y=25 uA) and in the presence of 10^{-5}M Tl(I) (solid line). Scan rate: 10 mV/s. Electrode area:0.2 cm^2. Curve A:Y=100 µA; Curve B: Y=200 µA; Curve C: Y= 400 µA.

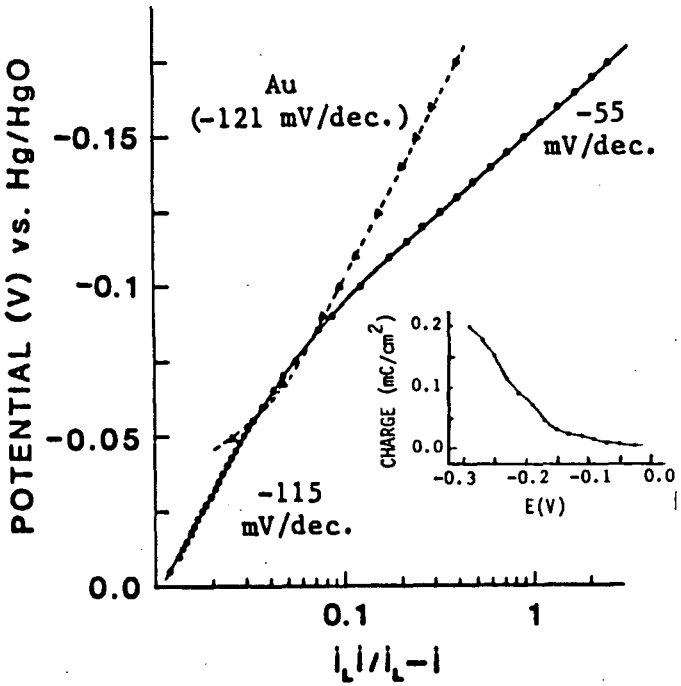


Fig. 5.1.2.18. Tafel plots of $i_L i/i_L - i$ for O_2 reduction on Au and Au/Tl(I). Plot for Au/Tl(I) constructed from the data of Fig.6-17. Insert: Charge vs. potential curve constructed from a voltammetry curve for Au in 1M NaOH with 10^{-5}M Tl(I): anodic direction considered.

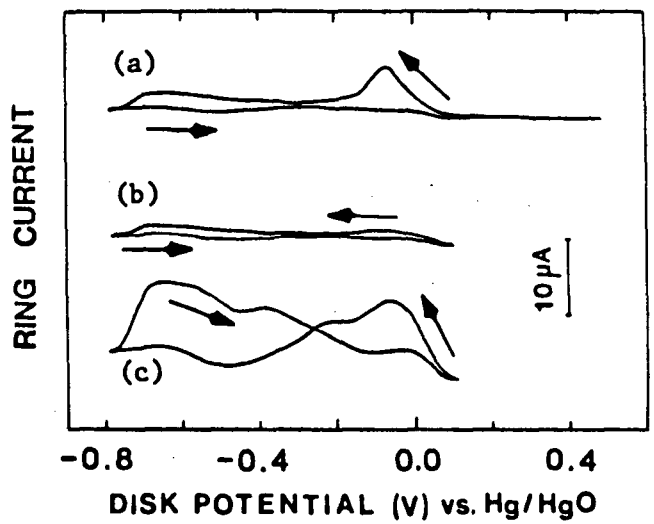


Fig. 5.1.2.19. Ring curves of a disk-ring experiment for Au in N_2 saturated 1M NaOH containing 1.3×10^{-5}M Tl(I) showing the effect of the ring potential and the anodic disk potential limit. a) Ring at 0.1 V, disk anodic limit: 0.5 V; b) Ring at 0.1 V, disk anodic limit: 0.1 V; c) Ring at 0.3 V, disk anodic limit: 0.1 V. Scan rate: 100 mV/s. Disk area: 0.2 cm^2. N=0.38. Rotation rate: 2500 rpm.

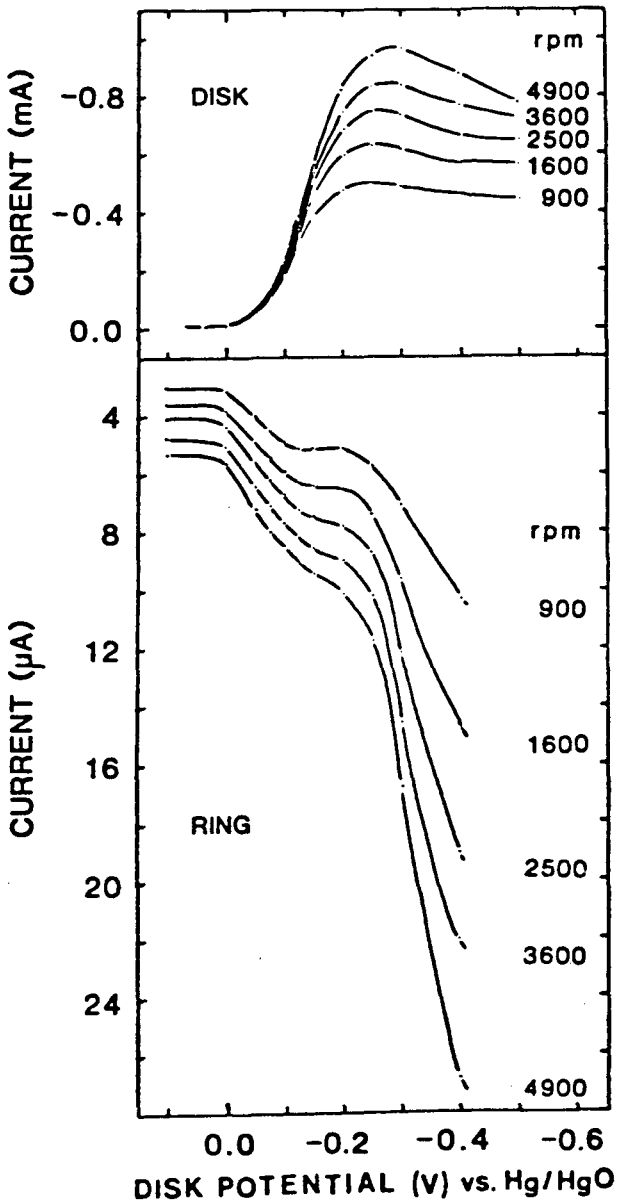


Fig. 5.1.2.20. Steady-state polarization curves for O_2 reduction on Au in 1M NaOH containing 1.2×10^{-6} M Tl(I). Electrode area: 0.2 cm^2.

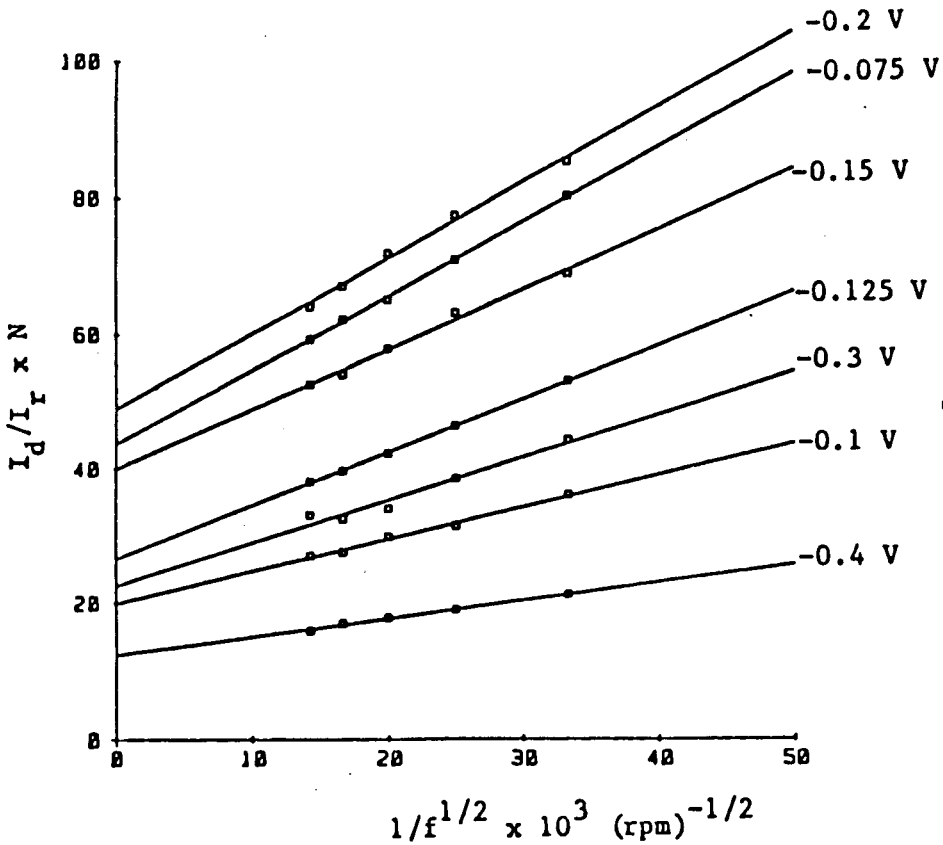


Fig. 5.1.2.21. Plot of I_d/I_r x N vs. $1/f^{1/2}$ constructed from the data of Fig.6-20.

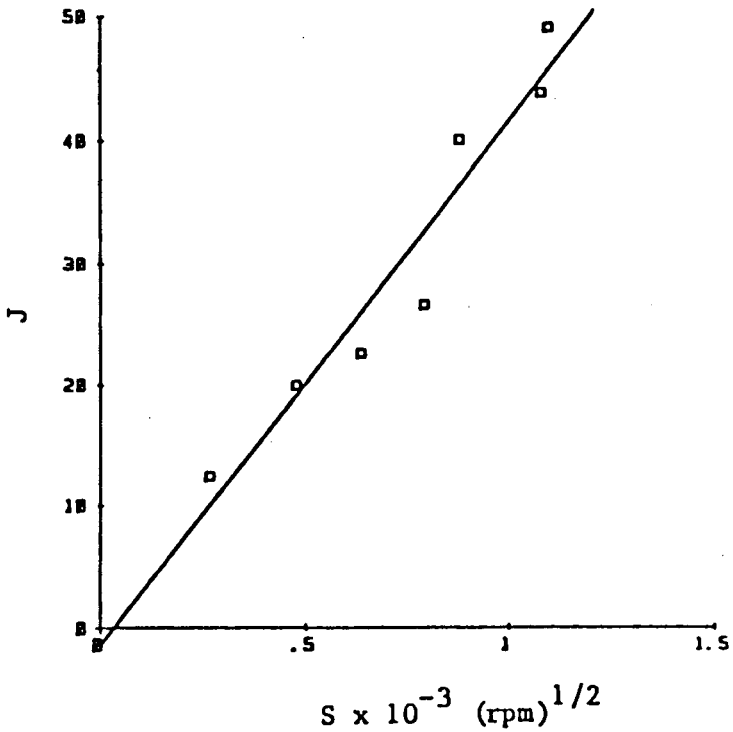


Fig. 5.1.2.22. Plot of the intercept vs. the slope constructed from the data of Fig.6-21.

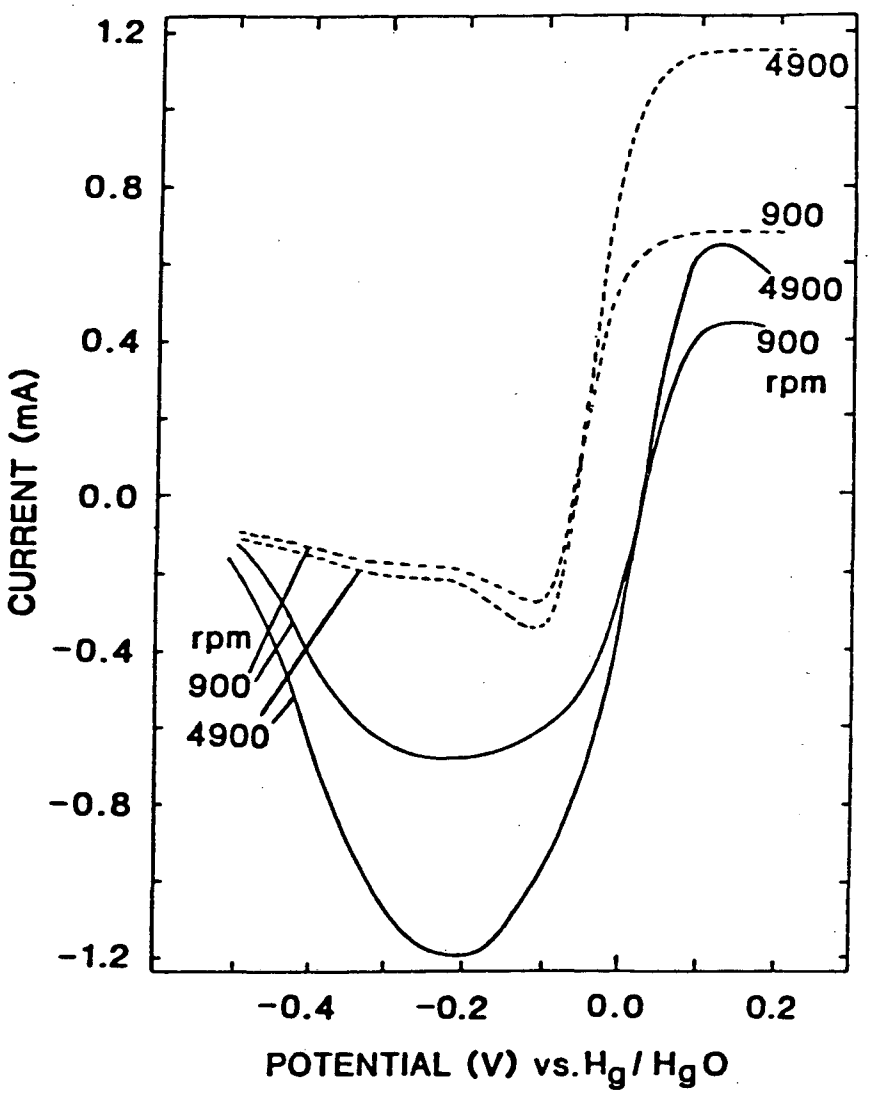


Fig. 5.1.2.23. Polarization curves for the oxidation and reduction of Hydrogen peroxide on Au in N_2 saturated 1M NaOH in the absence (dashed lines) and in the presence of 8×10^{-6} M Tl (I). Hydrogen peroxide concentration: 3.2×10^{-3} M. Scan rate: 20 mV/s. Electrode area: 0.2 cm^2.

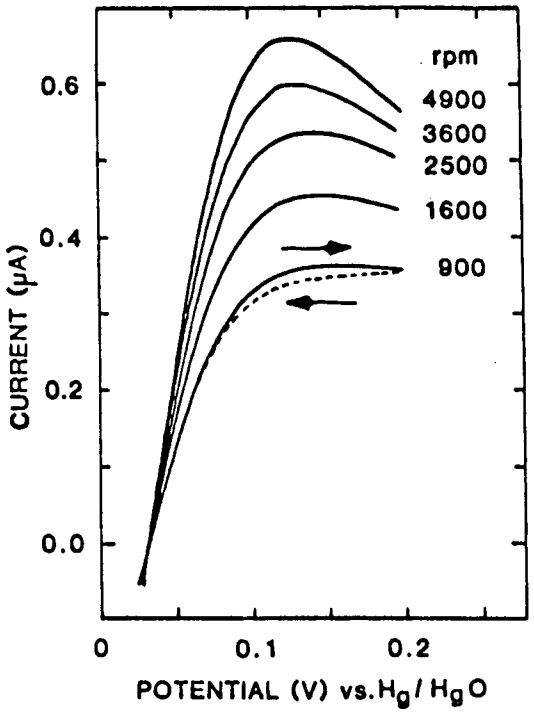


Fig. 5.1.2.24. Polarization curves for HO_2^- oxidation on Au in N_2 saturated 1M NaOH containing 8×10^{-6}M Tl(I). Hydrogen peroxide concentration: 3.2×10^{-3}M. Scan rate: 15 mV/s. Electrode area: 0.2 cm^2.

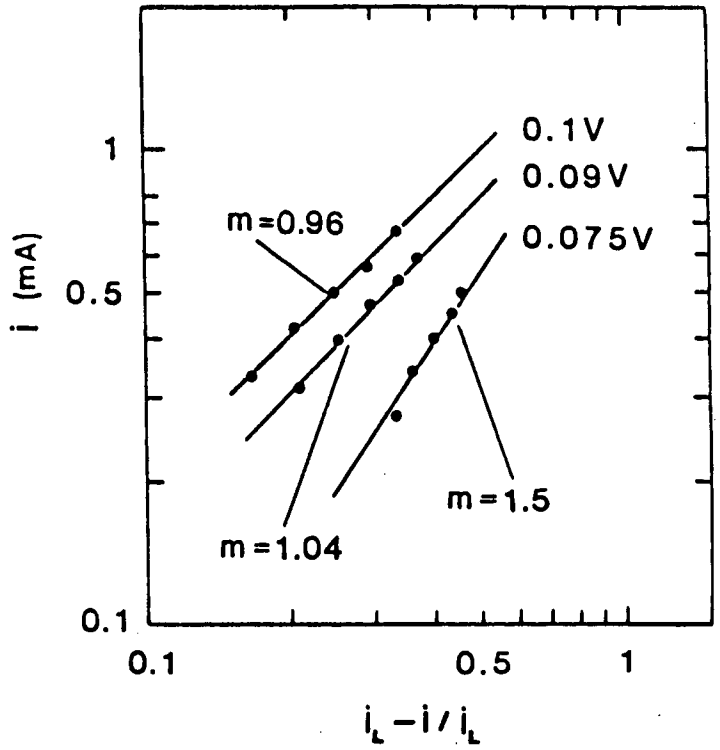


Fig. 5.1.2.25. Reaction order plot for HO_2^- oxidation on Au in N_2 saturated 1M NaOH containing Tl(I) and HO_2^-. Data taken from Fig. 6-24.

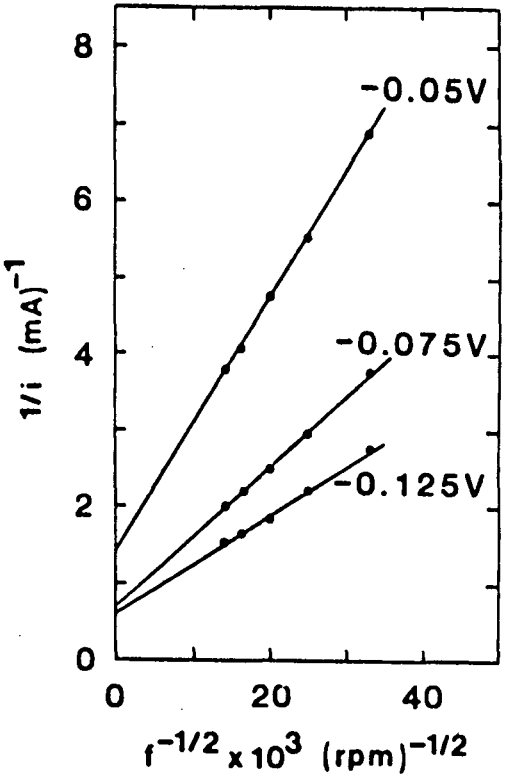


Fig. 5.1.2.26. Plots of 1/i vs. $1/f^{1/2}$ for hydrogen peroxide oxidation on Au. Data taken from Fig. 6-23.

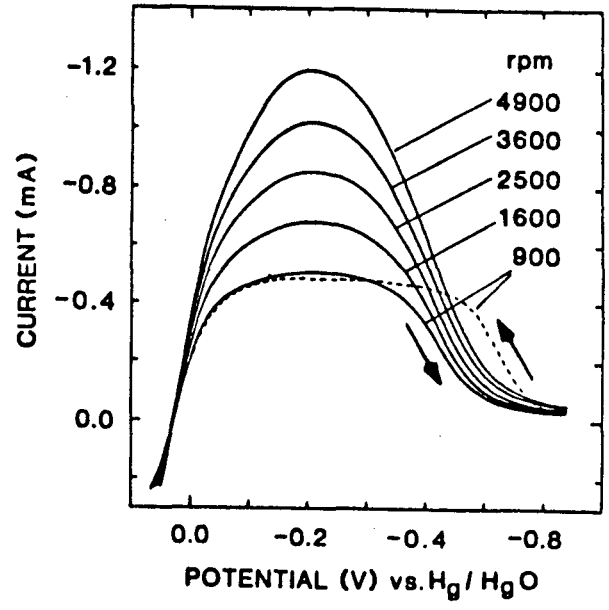


Fig. 5.1.2.27. Polarization curves for HO_2^- reduction on Au in N_2 saturated 1M NaOH containing 8×10^{-6} M Tl(I). Hydrogen peroxide concentration: 3.2×10^{-3} M. Scan rate: 15 mV/s. Electrode area: 0.2 cm^2.

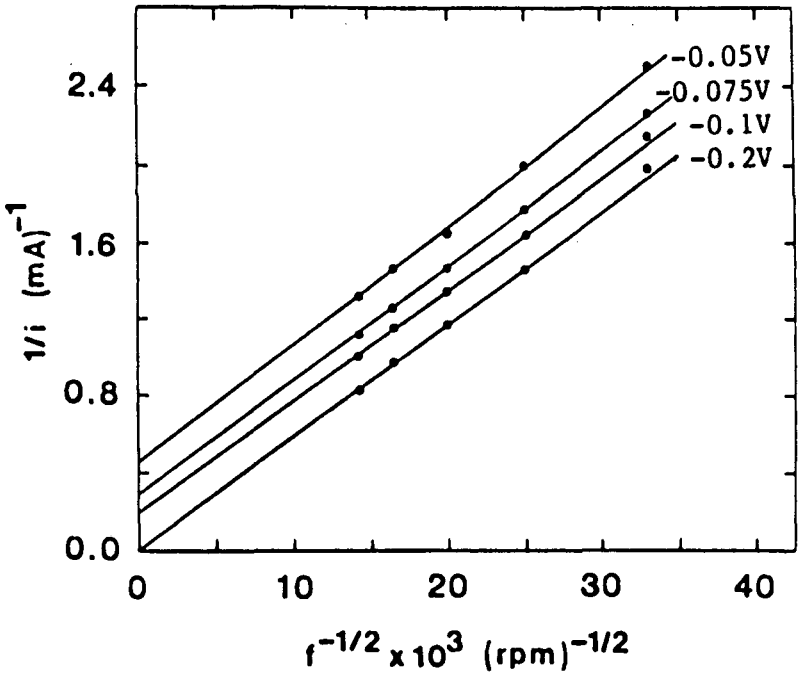


Fig. 5.1.2.28. Plots of $1/i$ vs. $1/f^{1/2}$ for hydrogen peroxide reduction on Au in N_2 saturated 1M NaOH in the presence Tl(I) . Data taken from Fig.6-27.

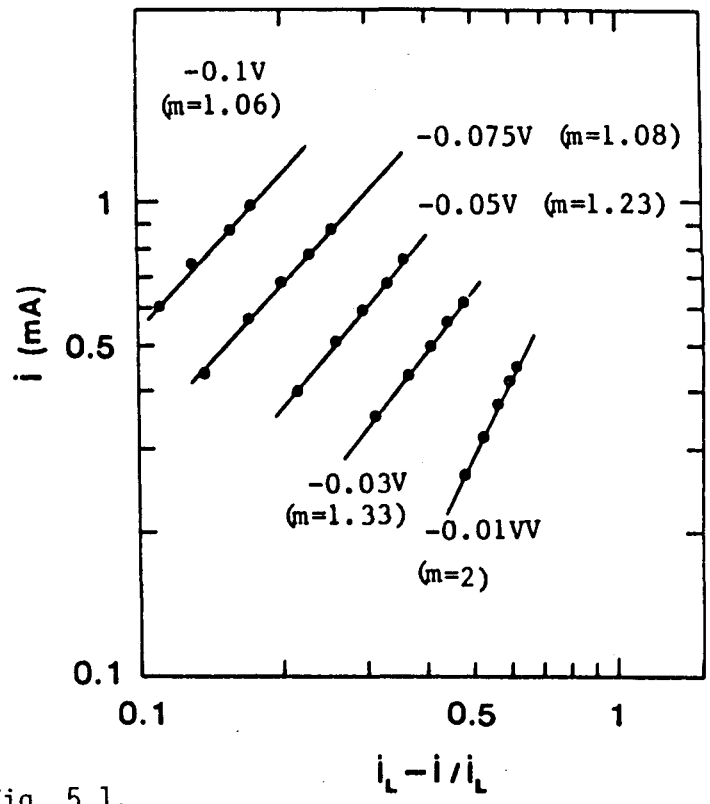


Fig. 5.1. 2.29. Reaction order plot for hydrogen peroxide reduction on Au in N_2 saturated 1M NaOH containing Tl(I). Data taken from Fig.6-28.

5.1.3 OXYGEN REDUCTION ON AG ELECTRODES MODIFIED BY AD-ATOMS PD AND PT

B. C. Wang

INTRODUCTION

Ag is widely used as electrocatalyst in oxygen reduction and evolution and has reasonable catalytic activity. The question is whether it is possible to modify Ag electrode surface to enhance its catalytic activity. As some authors point out, a complete monolayer of platinum atoms or palladium atoms deposited on gold electrodes make it as active as a platinum electrode or a palladium electrode itself for hydrogen evolution [1]. The same effect was obtained for HCOOH oxidation [2] and it was shown that Bi ad-atoms enhance the activity of Au electrodes to the same extent as they do to a platinum electrode for the oxidation. On the other hand, palladium electrodes show even more high catalytic activity for oxygen reduction than Pt [3]. It is interesting from fundamental and practical points of view to increase catalytic properties of Ag electrodes by forming mono- or submonolayers of Pd or Pt ad-atoms on Ag electrodes. The present study is intended to investigate the oxygen reduction on Ag, modified by ad-atoms Pd, Pt and the influence of some metal ions like Tl, Pb, Cd on oxygen reduction by rotating disk electrode technique and voltammetry. ESCA and SEM were useful to identify the surface change of Ag electrodes with the addition of Pd, Tl, Pb and other ions.

EXPERIMENTAL

All measurements were carried out in 1.0 M NaOH at 25°C. Solutions were prepared from stock solution (50% NaOH, Baker Analyzed Reagents, low in carbonate) as reported elsewhere [4]. Pyrolyzed water was used in preparing the solutions. Ag and Pd smooth electrodes were polished in a polishing cloth using 0.05μ alpha aluminum powder (Buehler). Solutions were pre-electrolyzed using gold (8 cm^2) as a cathode and H_2-fed palladium anode (thin-wall tube). The pre-electrolysis was carried out for at least 12 h in 60-70 cm^3 of solution agitated by purified N_2 bubbling through the solution. The potential of the Au pre-electrolysis cathode was set to -1.1 V. All potentials are given with reference to Hg/HgO.

Ag and Pd electrodes were pretreated in the test solution by cycling it several times between -0.7 and 0.0 V at 50 mv/s until the voltammetry curves reproduced on repeated cycles. Then the solution was saturated with O_2. The polarization curves were recorded with voltage scanning (10 mv/s) in most cases from cathodic to anodic direction. For the measurements in the presence of foreign metal ions (Pd, Tl, Pb, Cd), the procedure was similar.

In the ESCA measurements, the samples were fixed to a sample mount with scotch tape and irradiated with Mg Kα rays ($h\nu$ = 1253.6 eV) at 10^{-7} Torr of the vacuum in a Varian IEE-15 ESCA instrument. The value of 284.4 eV for the carbon 1s peak was used as a calibration

standard for the identification of the energies of other peaks in the ESCA spectrum.

Microscopy was carried out using a Cambridge Model 5410 Scanning Electron Microscope operated by the Case Laboratories for Materials Characterization. A 20-Kv electrobeam was used and the tilt angle was 30° from normal. All of the microscopy presented here was done on samples which were sputter-deposited with carbon.

RESULTS AND DISCUSSIONS

Fig. 1 shows the polarization curve for oxygen reduction on Ag electrodes in 1 M NaOH solution, saturated with O_2. The half-wave potential is about -0.2 V. The calculation, made by Levich plot, gives the number of electrons as 3.6 transferred in oxygen reduction. Adding Pd in the form $PdNO_3$ in concentration range of 2×10^{-6} M to 5×10^{-5} M the oxygen reduction halfwave potential is shifted to the more anodic side. The diffusion current of oxygen reduction is increased to some extent too as it is shown in Fig. 2. In order to determine Ag surface change with addition of Pd, the voltammetry curve of Ag, modified by Pd, was taken in 1M NaOH solution saturated with N_2. For comparison the voltammogram of pure Ag electrode is included in Fig. 3 too.

From Fig. 3 it can be seen that in anodic sweeping direction, I peak ($Ag \longrightarrow Ag_2O$) is increased due to PdO formation (see the voltammogram of pure Pd in Fig. 4), and II peak ($Ag_2O \longrightarrow AgO$) is shifted to more anodic potential in the presence of Pd. In cathodic sweeping direction, AgO is reduced to Ag_2O at more cathodic potentials. The oxidation-reduction couple $Ag^{2+} \longrightarrow Ag^{+}$ becomes more irreversible in the presence of Pd. The reduction potential of Ag_2O to Ag is moved to more cathodic potential too. A more characteristic new reduction peak was obtained (at potential about -0.3 V). From Fig. 4 it is evident that this peak is associated with reduction of PdO to Pd. It is likely that Pd is deposited on Ag in the form of small particles and does not form complete monolayer or coating of Pd. For confirming this postulate ESCA spectra of Ag electrode with Pd ad-atoms were taken and are presented in Fig. 5. The curve I is pure Ag ESCA spectrum. The curve II shows ESCA spectra of Ag with Pd ad-atom deposited in concentration 10^{-5} M Pd on Ag. The height of the Ag peak in the latter case is decreased, but doesn't disappear. The peak position is not changed too. This means that on the Ag surface layers of Pd, ad-atoms are separated in the form of islands. SES photographic pictures indicate that in the case of Ag with Pd ad-atoms, a more rough and heterogeneous surface is obtained and this can explain the high catalytic activity of Ag with Pd ad-atoms.

Fig. 6 and Fig. 7 show the polarization curves for oxygen reduction on Ag with Pd ad-atoms and pure Pd. They have similar shape and the same behavior. From this it can be concluded that Pd ad-atoms deposited on Ag substrates have the same catalytic properties for oxygen reduction as bulk Pd.

INFLUENCE OF Tl, Pb, Cd IONS ON OXYGEN REDUCTION ON Pd.

Fig. 8 shows the polarization curves for oxygen reduction on Pd with the addition of Tl ions from 2×10^{-6} M to 10^{-4}M. Contrary to Pt [5], addition of Tl ions to 1 M NaOH solution supresses the oxygen reduction appreciably. The voltammogram of Pd electrode in the presence of Tl ions is presented in Fig. 9. The reduction peak is shifted to a more anodic potential in comparison with pure Pd. This, perhaps, is due to alloy formation of Pd with Tl. Probably this alloy is not active for H_2O_2 decomposition, hence oxygen reduction is inhibited. The same effect was obtained in the cases of Pb and Cd. Fig. 10 and Fig. 11 show the polarization behavior of oxygen reduction and the voltammogram of Pd in the presence of Pb respectively. The Pb ion slows down the oxygen reduction but to a lesser extent than Tl. An interesting feature in Fig. 10 is that, after addition of Pb ion in concentration 10^{-3} M, the oxygen evolution over-voltage is decreased by 200 mV. Further work is needed to explain this positive effect of Pb ion on oxygen evolution. Fig. 12 shows the effect of Cd^{++} on oxygen reduction on Pd. Cd ion inhibits oxygen reduction to a lesser extent than Pb.

INFLUENCE OF Tl, Pb IONS ON OXYGEN REDUCTION ON Ag ELECTRODE MODIFIED BY Pd AND Pt AD-ATOMS

Fig. 13 shows the influence of Tl ions on oxygen reduction on Ag modified by Pd ad-atoms. When Ag electrode is modified by Pd, oxygen reduction is enhanced, but Tl ions inhibit oxygen reduction as it was obtained on Pd. A separaste experiment shows that Tl ion has no effect on oxygen reduction on Ag electrode.

Fig. 14 shows the effect of Pb ions on oxygen reduction on Ag electrodes modified by Pt ad-atoms. In case of Pt the oxygen reduction is not enhanced so muchas in the case of Pd, but Pb ions shift the oxygen reduction potential to the anodic side appreciably. The enhanced effect of Pb ions on oxygen reduction on Pt electrodes was reported elsewhere [5]. This indicates again that Pt ad-atoms on Ag electrodes have the same catalytic properties as bulk Pt metal. As it was mentioned earlier, Tl and Pb ions have different effects on Pt and Pd. It is interesting to know how Tl and Pd ions affect oxygen reduction on Ag electrode modified by ad-atoms of Pd and Pt. Fig. 15 shows this effect when Ag electrode is modified by Pd and Pt in 1 M NaOH containing H_2PtCl_6 and $Pt(NO_3)_2$. Fig. 16 shows oxygen reduction on Ag modified first by Pd and then by Pt. Fig. 17 shows oxygen reduction on Ag modified first by Pt and then by Pd. All these figures show that Tl ions are more sensitive to Pt ad-atoms, co-deposited with Pd on Ag electrodes and enhance catalytic activity for oxygen reduction. Only when Tl ion concentration exceeds 10^{-5}M, negative effect of Tl ions for oxygen reduction is obtained.

CONCLUSIONS

1. Ad-atoms of Pt and Pd on Ag surfaces enhance catalytic activity of Ag electrode for oxygen reduction.

2. Tl and Pb have the negative effect for oxygen reduction on Pd contrary to Pt electrodes.

3. Pt ad-atoms co-deposited with Pd on Ag are more sensitive to the effect of Tl ions, but the negative effect of Tl is obtained only in concentration greater than 10^{-5} M for Pd co-deposited with Pt.

4. Ag electrode modified by Pt and Pd in the presence of Pb, Tl ions show the stable short-term performance for oxygen reduction.

References

1. N. Furuya and S. Motoo, J. Electroanal. Chem. 88, 151 (1978).

2. Samoshi Motoo and Masahiro Watanabe, J. Electroanal. Chem. 18, 203 (1979).

3. V.V. Sokol', E.I. Krushchera and V.A. Dagaeve, Elektrochimiya, Vol 11, 1332 (1965).

4. R. Zurilla, R.K. Sen and E. Yeager, J. Electrochem. Soc. 125, 1103 (1978).

5. R. Amadelli, J. Molla and E. Yeager, submitted to J. Electroanal. Chem.

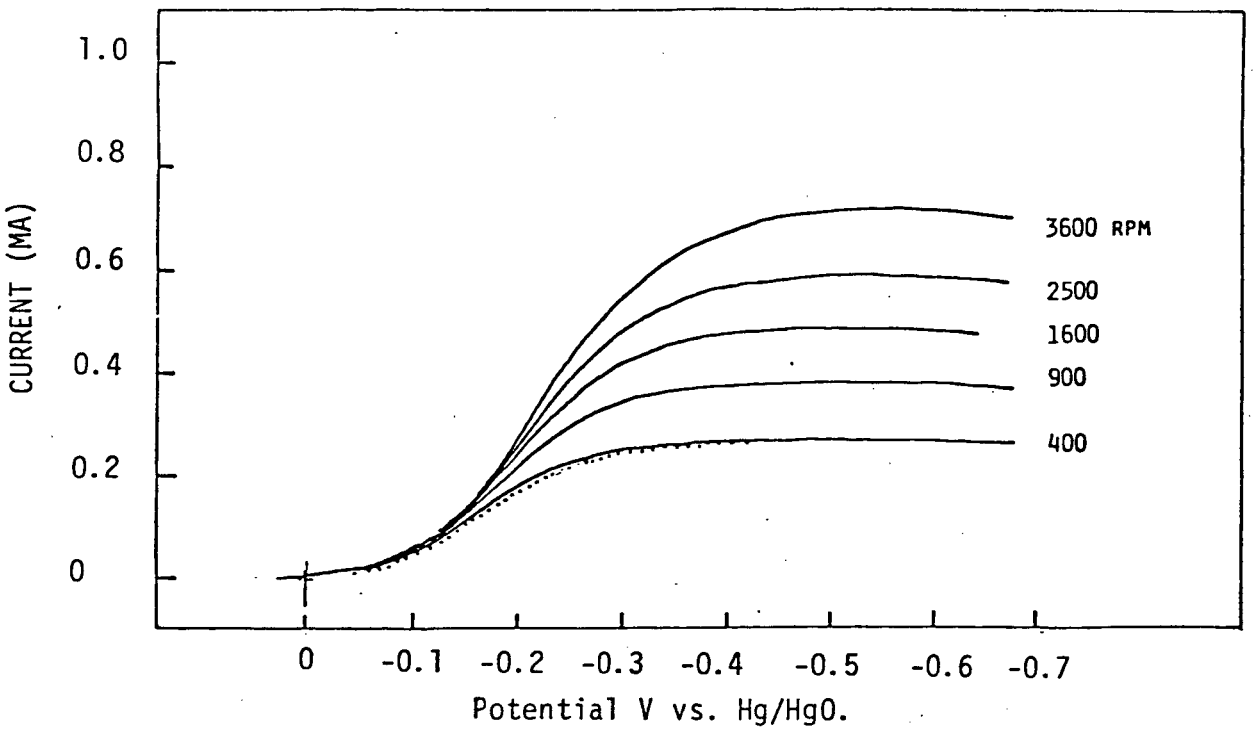


Fig. 5.1.3.1. Polarization curves of oxygen reduction on Ag in IM NaOH solution. Apparent area of disc-electrode: 0.2 cm^2. Data obtained by sweeping in cathodic direction with rate of 10 mv/s.

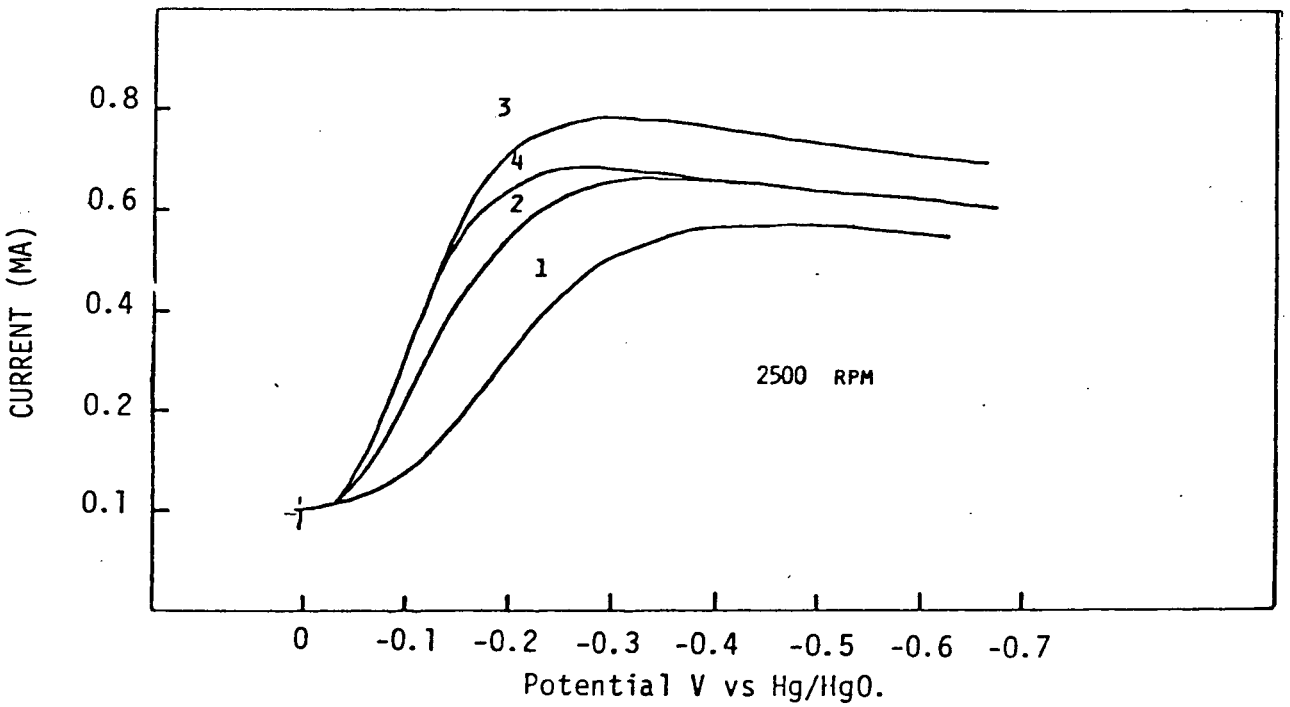


Fig. 5.1.3.2. Polarization curves of oxygen reduction on Ag with different amounts of $Pd(NO_3)$ added in IM NaOH solution. Area of electrode: 0.2 cm^2; 1. No Pd., 2. 2 x 10^{-6}m., 3. 4 x 10^{-6}m, 4. 5 x 10^{-5}m Pd.

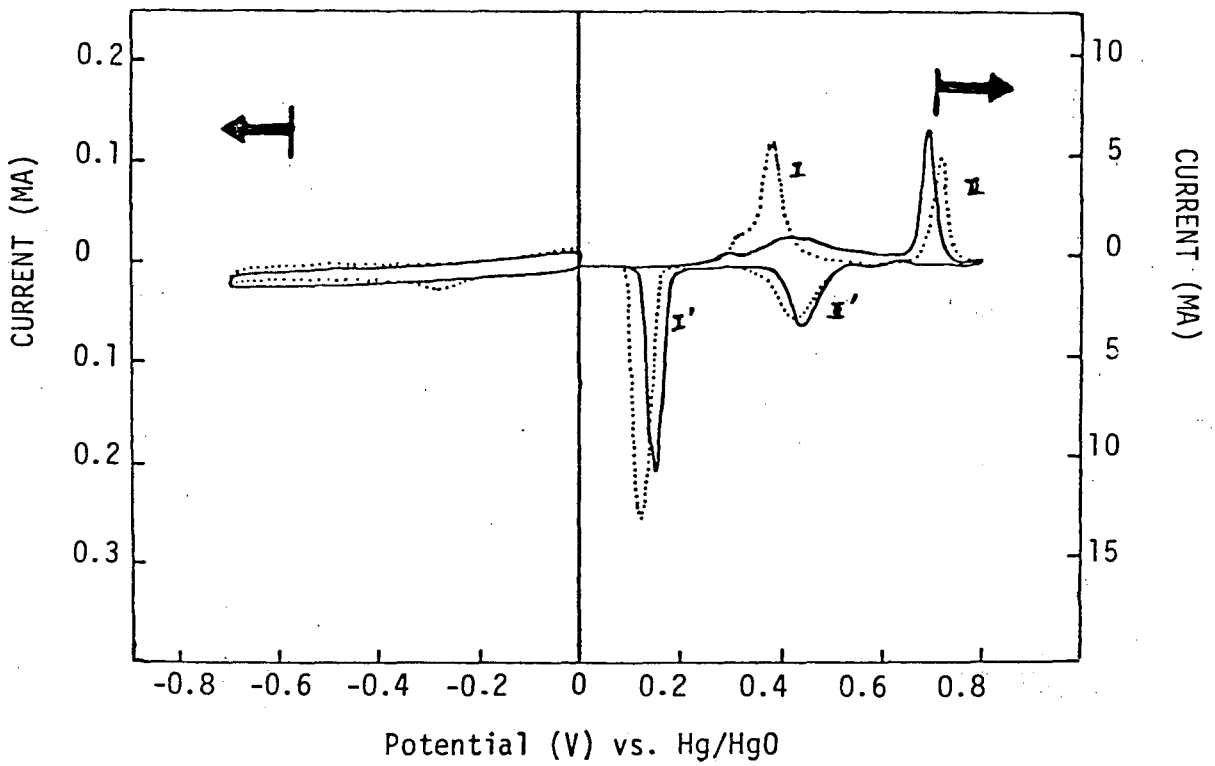


Fig. 5.1.3.3. Cyclic voltammogram obtained on Ag (solid line); and Ag with 2×10^{-6}m $PdNO_3$ in IM NaOH solution saturated with N_2 (dotted line); Sweep rate: 50 mv/s. Rotation rate 2500 RPM. Electrode area: 0.5 cm^2.

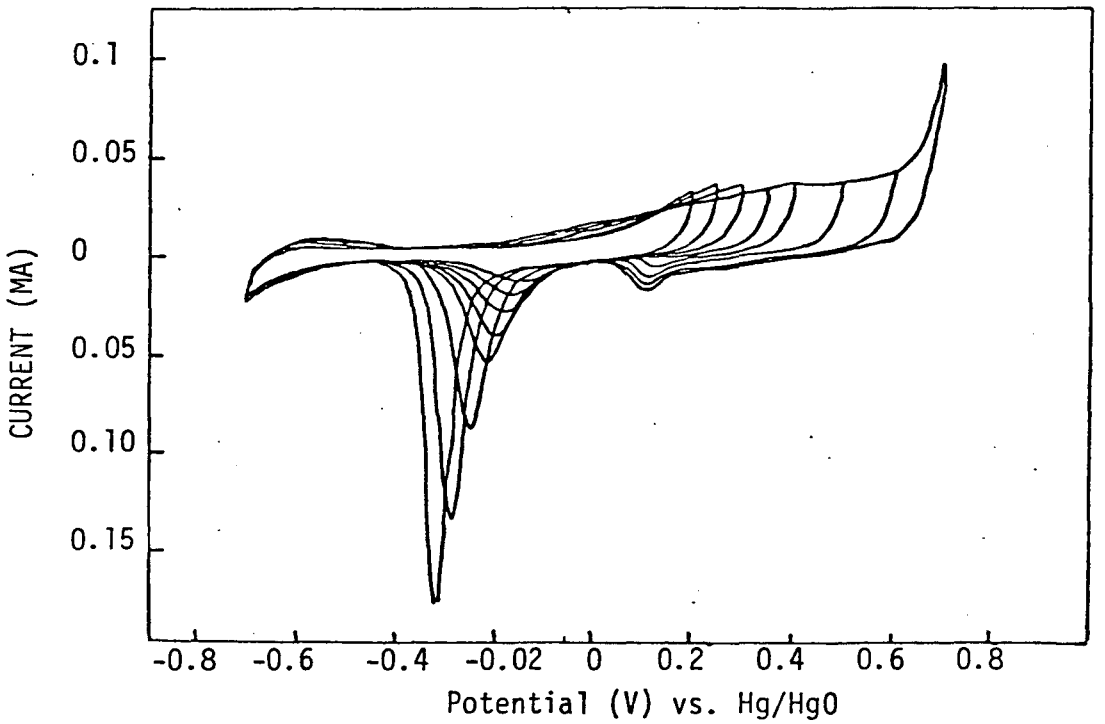


Fig. 5.1.3.4. Cyclic voltammogram obtained on Pd in 1m NaOH solution saturated with N_2. Sweep Rate: 50 mv/s. Rotation Rate: 2500 RPM. Electrode Area: 0.2 cm^2.

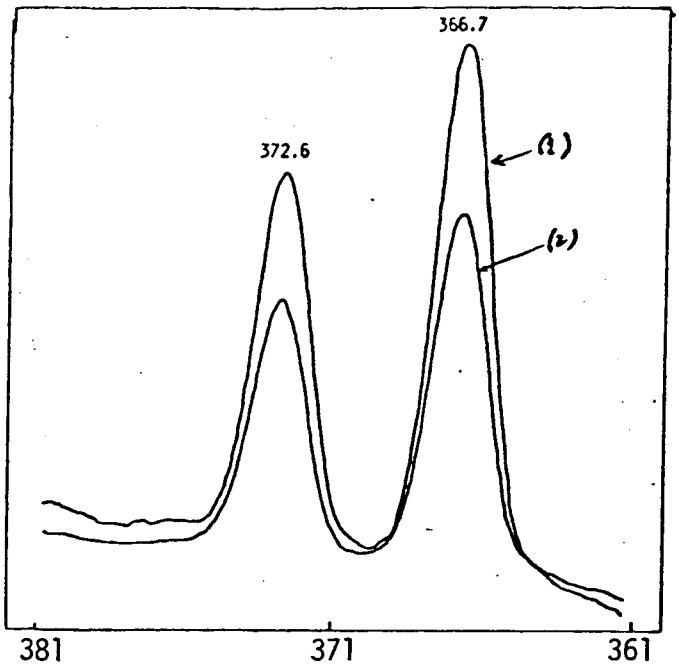


Fig. 5.1.3.5. ESCA spectra showing Ag for pure Ag [1] and Ag [2] with Pd alloying.

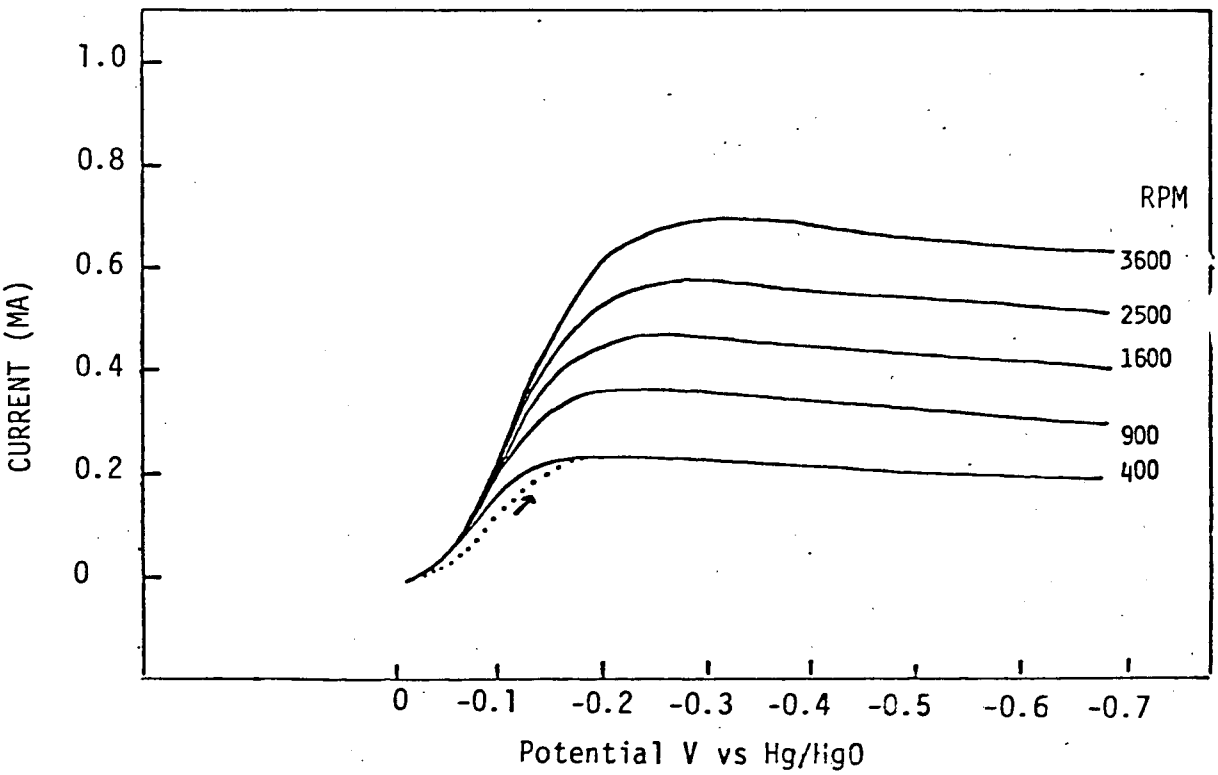


Fig. 5.1.3.6. Polarization curves of oxygen reduction on Ag with addition of 10^{-5}m $Pd(NO_3)$ area of electrode: 0.2 cm^2.

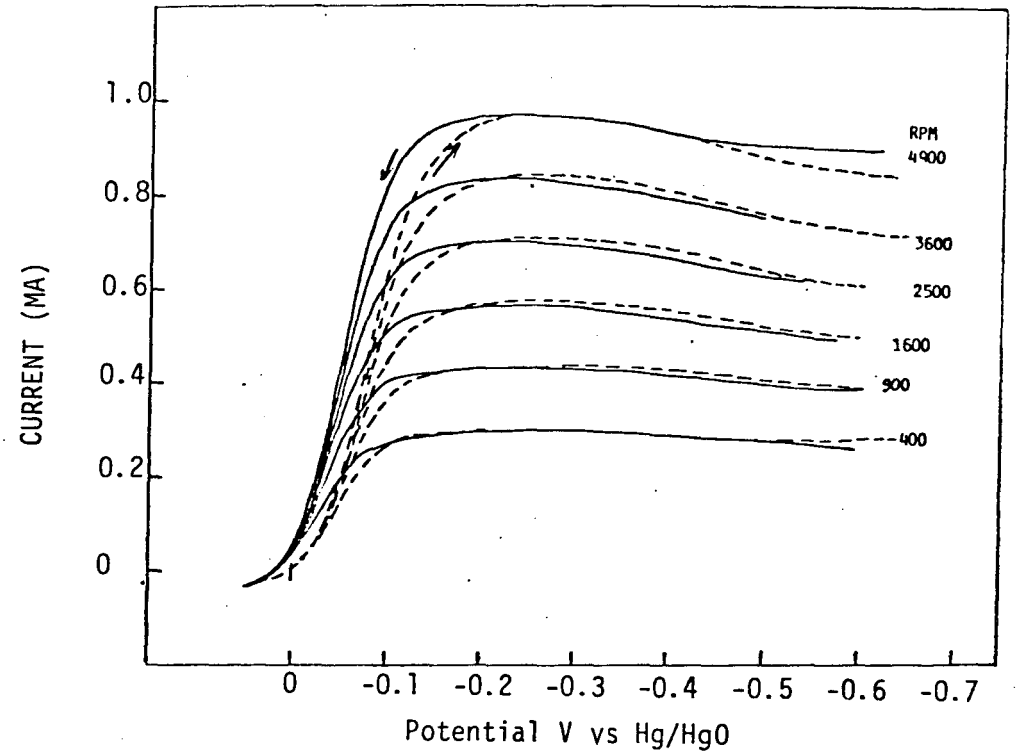


Fig. 5.1.3.7. Polarization curves of oxygen reduction on Pd in 1 M NaOH solution. Area of electrode: 0.2 cm^2. Potential sweep rate 20 mv/s.

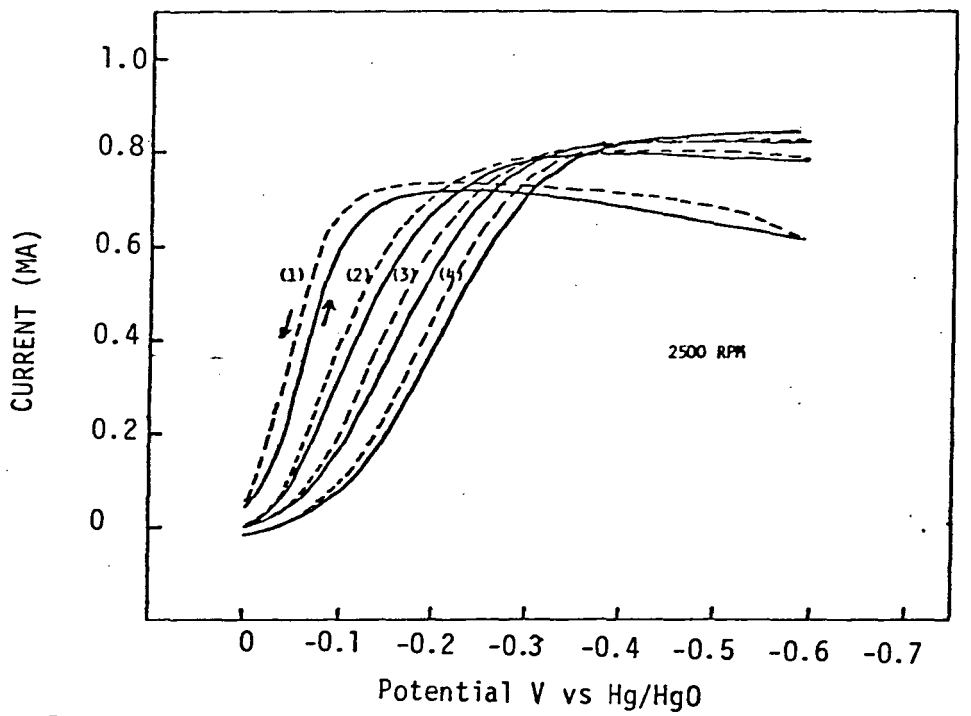


Fig. 5.1.3.8. Polarization curves of oxygen reduction on Pd in 1 M NaOH solution with addition of different amounts of $Tl(NO_3)$. (1) 1 M NaOH; (2) 1 M NaOH + 2 x 10^{-6} m; (3) 1 M NaOH + 10^{-5}m; (4) 1 M NaOH + 10^{-4}m Tl^+.

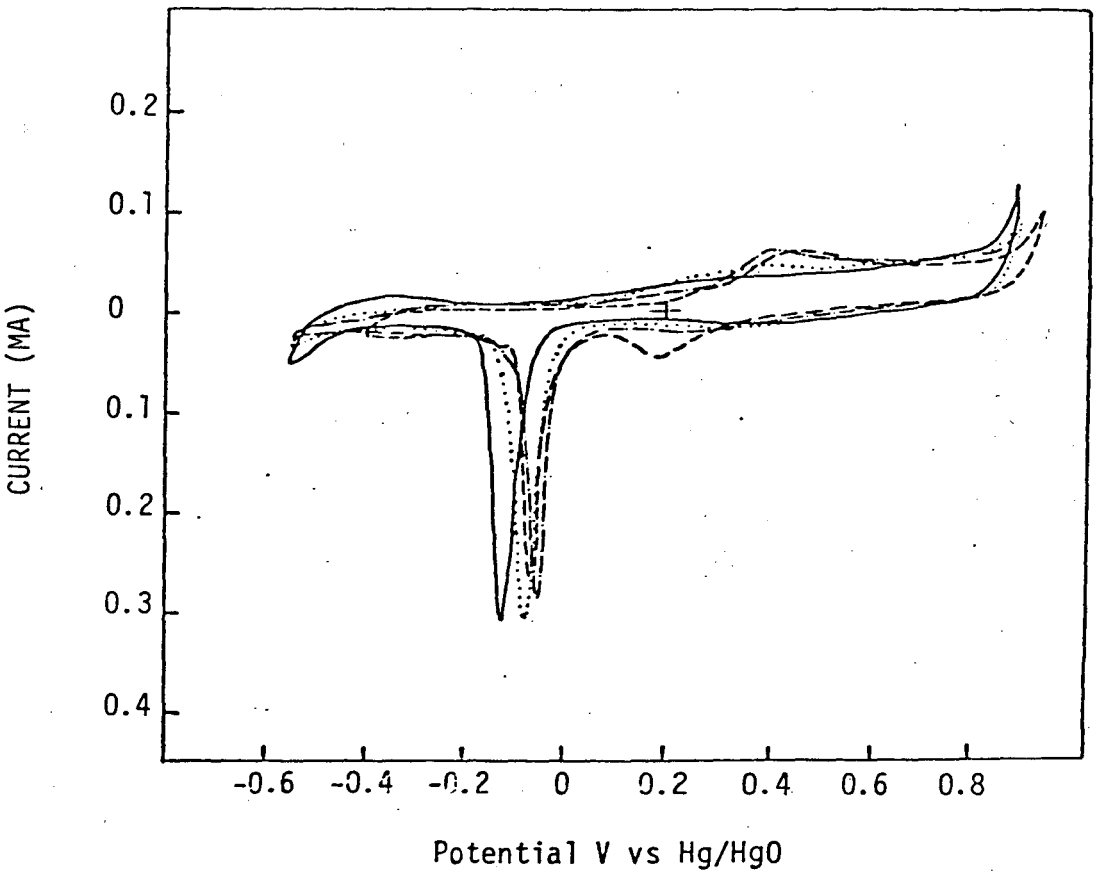


Fig. 5.1.3.9. Cyclic voltammograms obtained on Pd in IM NaOH solution containing different amounts of $TlNO_3$; .... 10^{-6}m, ---- 2×10^{-6}m, -.-.- 10^{-5}m, —— NO Tl^+; sweep rate: 50 Mv/s, rotation rate: 2500 RPM, electrode area: 0.2 cm^2.

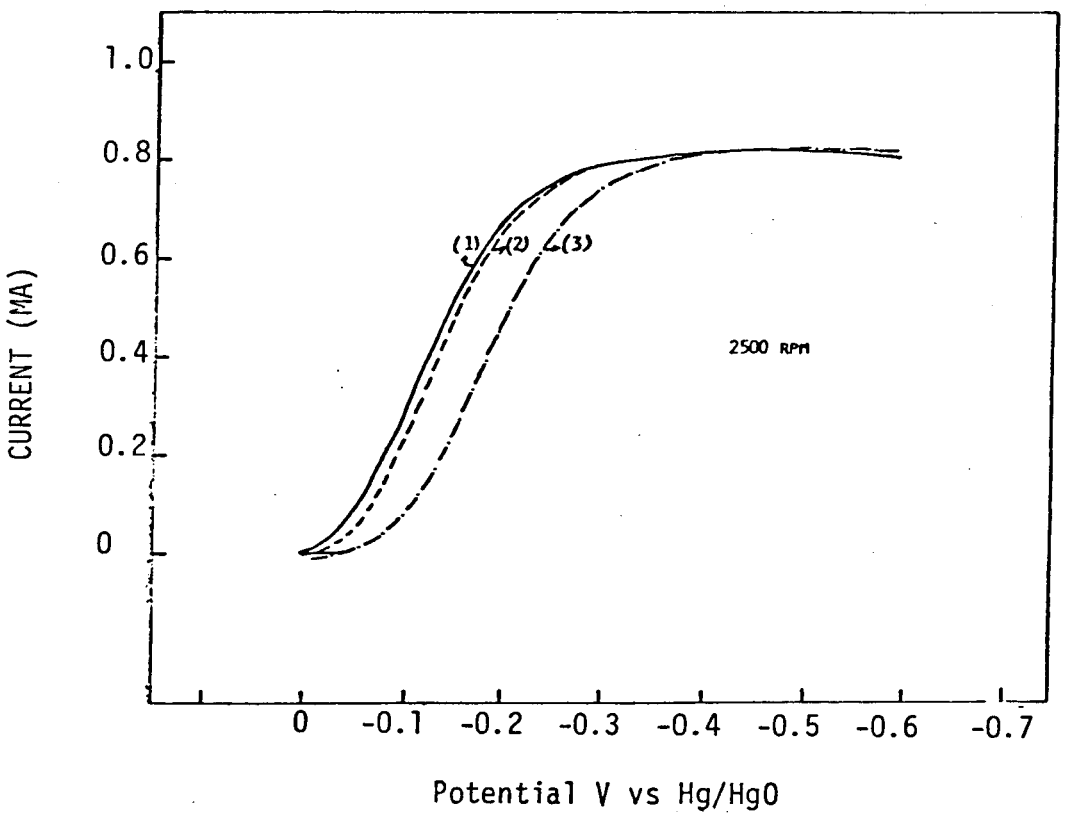


Fig. 5.1.3.10. Polarization curves of oxygen reduction on Pd in 1M NaOH solution with addition of different amounts of $Pb(No_3)_2$; (1) Pd; (2) 2×10^{-6}m and 10^{-5}m ; (3) 10^{-3}m and 10^{-2}m Pb^{+2}.

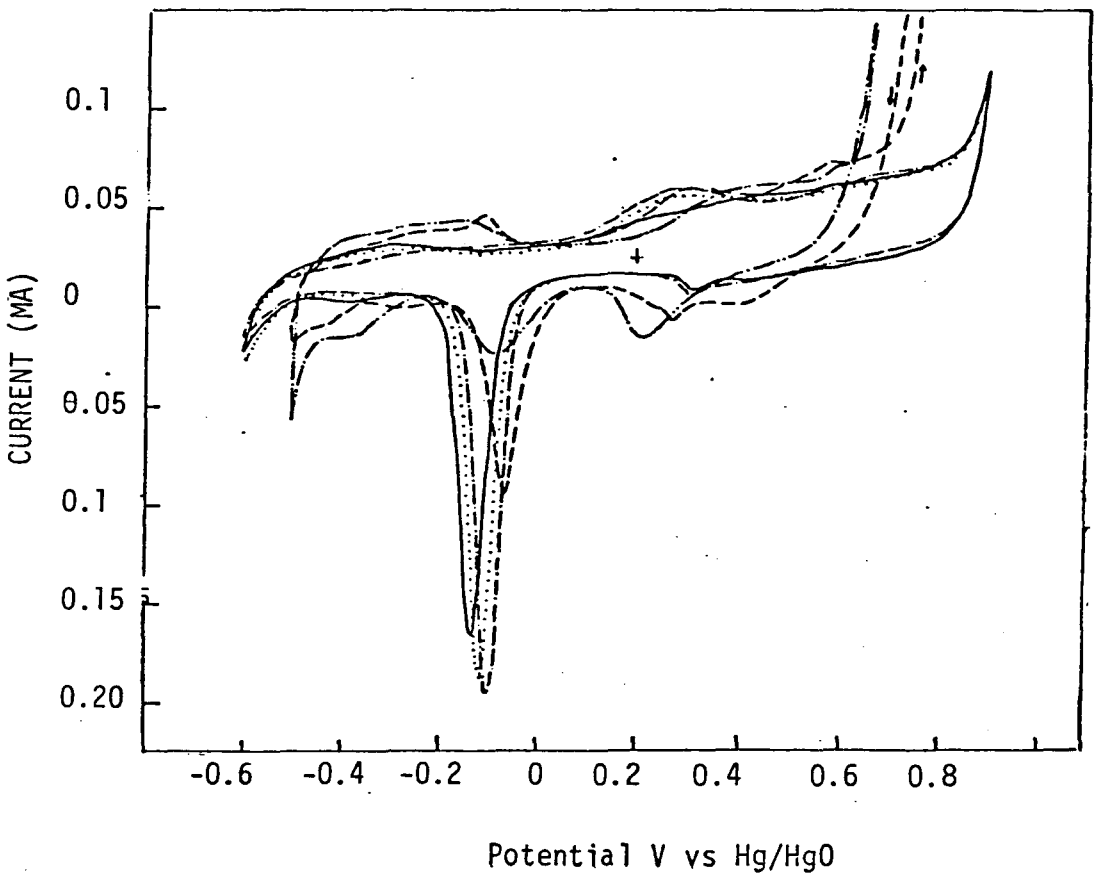


Fig. 5.1.3.11. Cyclic voltammograms obtained on Pd in 1M NaOH solution containing different amounts of $Pb(NO_3)_2$; .... 2×10^{-6}, —·—·— 10^{-5}m, ---- 10^{-4}m, —·—·— 10^{-3}m. —— no Pb^{++}. Sweep Rate: 50 mv/s. Rotation rate: 2500 RPM. Electrode area: 0.2 cm^2.

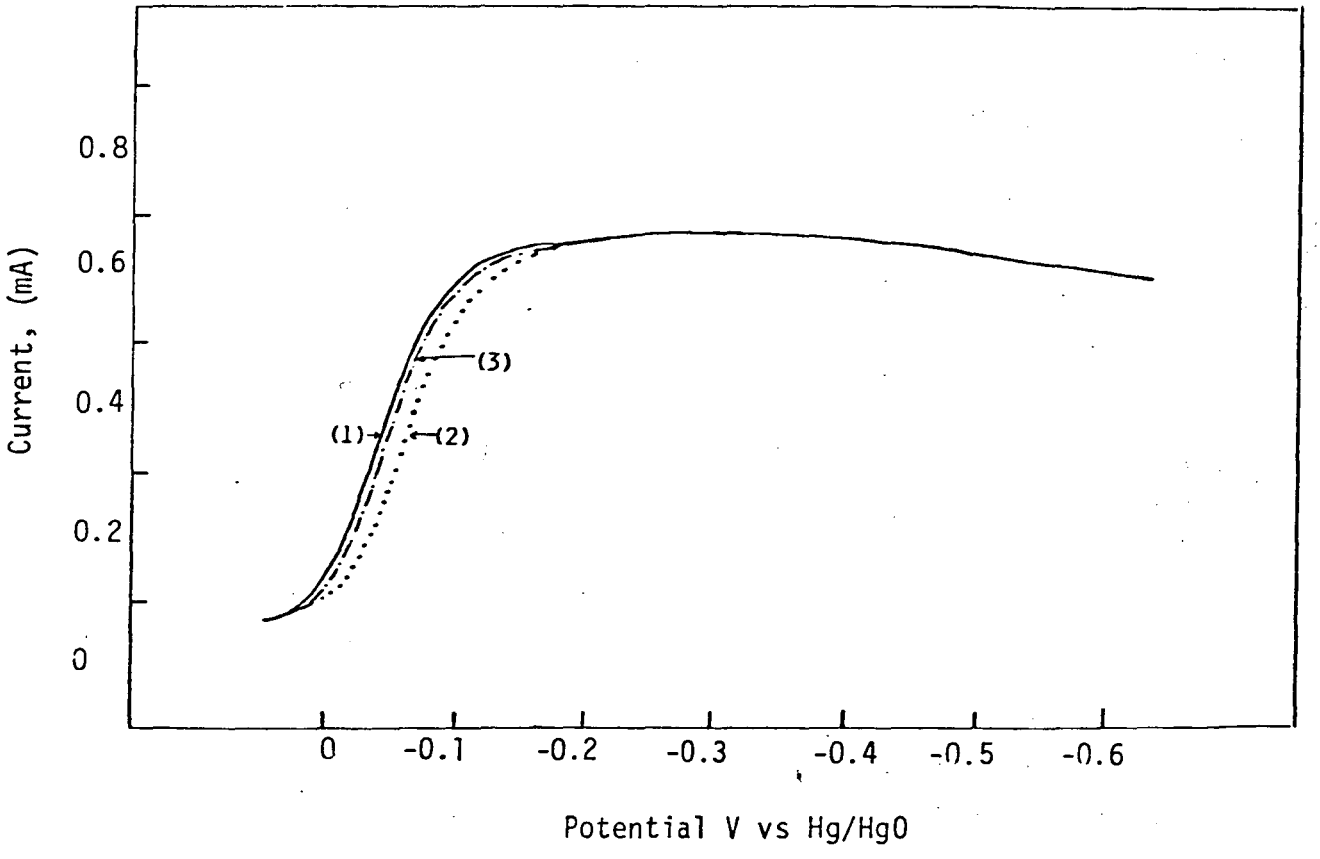


Fig. 5.1.3.12. Polarization curves of oxygen reduction on Pd in IM NaOH (1), IM NaOH + 6 x 10^{-6}m $CdSO_4$; (2), IM NaOH + 3 x 10^{-5}m $CdSO_4$; (3), Potential sweep rate = 20 mv/s; rotation rate = 1600 RPM; area of the electrode = 0.5 cm^2.

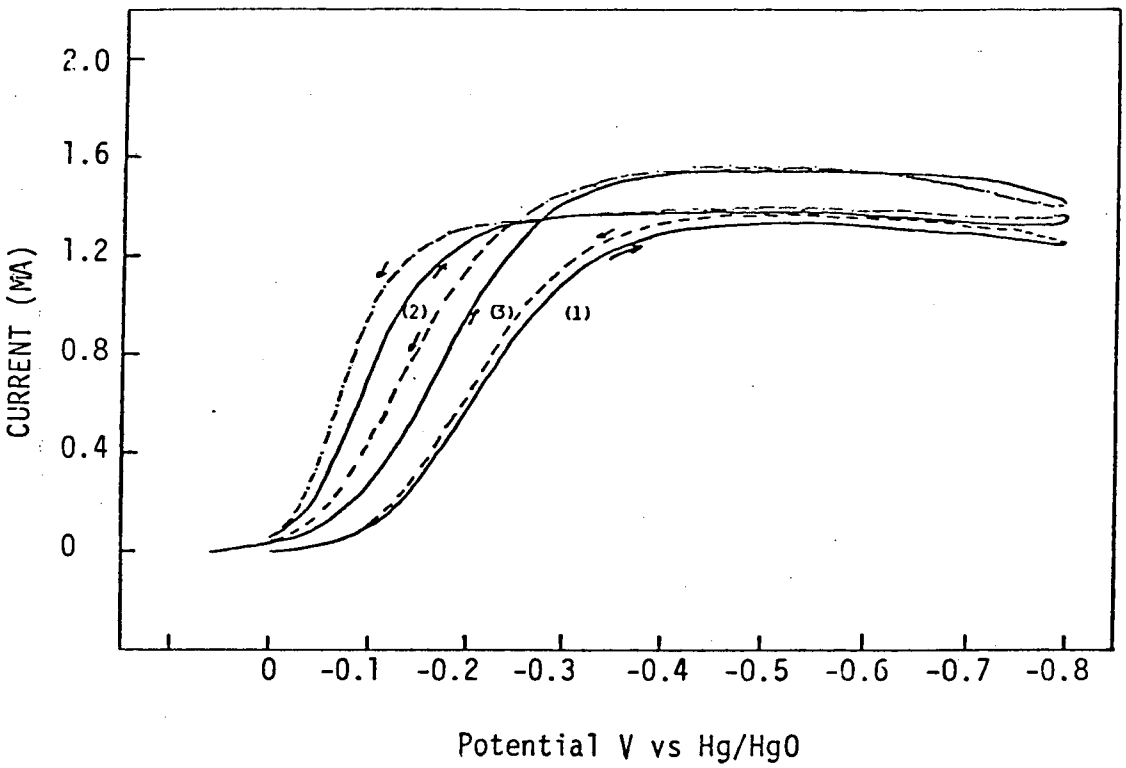


Fig. 5.1.3.13. Polarization curves of oxygen reduction on Ag in IM NaOH solution (1), in IM NaOH solution + 2 x 10^{-6}m $Pd(NO_3)$; (2), and IM NaOH solution + 2 x 10^{-6}m $Pd(NO_3)$ + 3 x 10^{-6}m $Tl(NO_3)$; (3), potential sweeping rate 20 mv/s. Rotation rate 1600 RPM. Area of electrode = 0.5 cm^2.

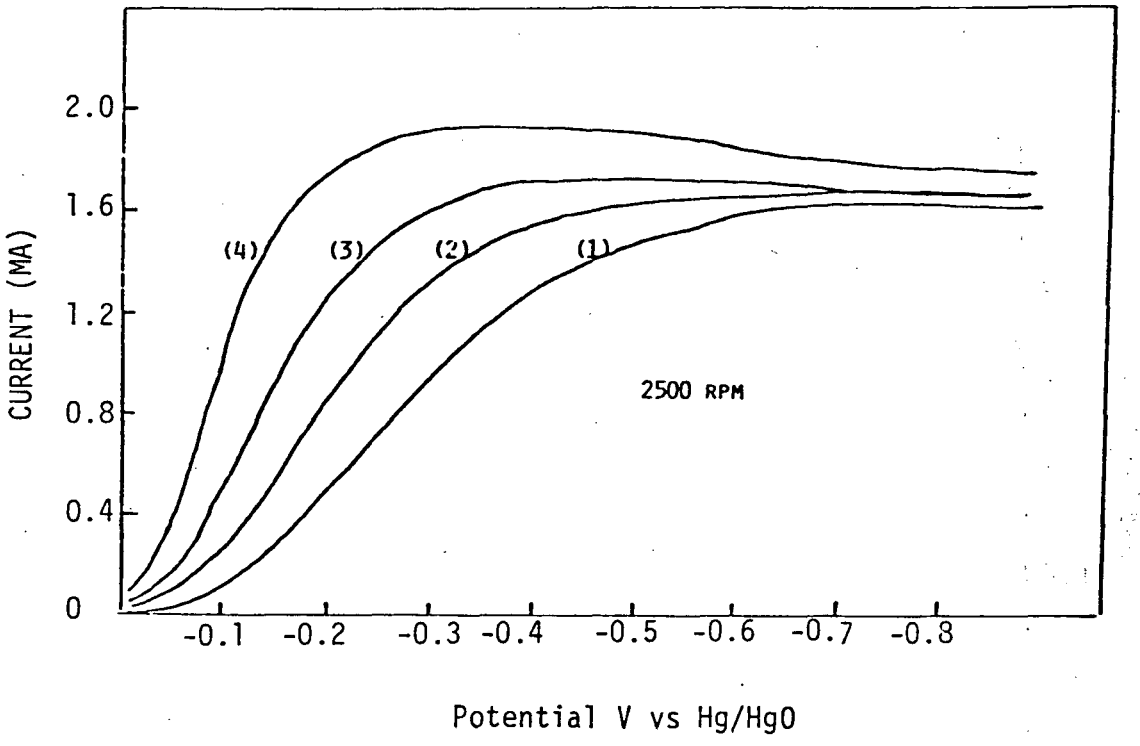


Fig. 5.1.3.14. Polarization curves of oxygen reduction on Ag in IM NaOH (1), IM NaOH + 10^{-6} m H_2PtCl_6; (2), IM NaOH + 10^{-6}m H_2PtCl_6 + 10^{-6} m $Pb(NO_2)_2$; (3), IM NaOH + 10^{-6}m H_2PtCl_6 + 2 x 10^{-6} m $Pb(NO_3)_2$; (4), potential sweeping rate - 10 mv/s. Area of electrode = 0.5 cm^2.

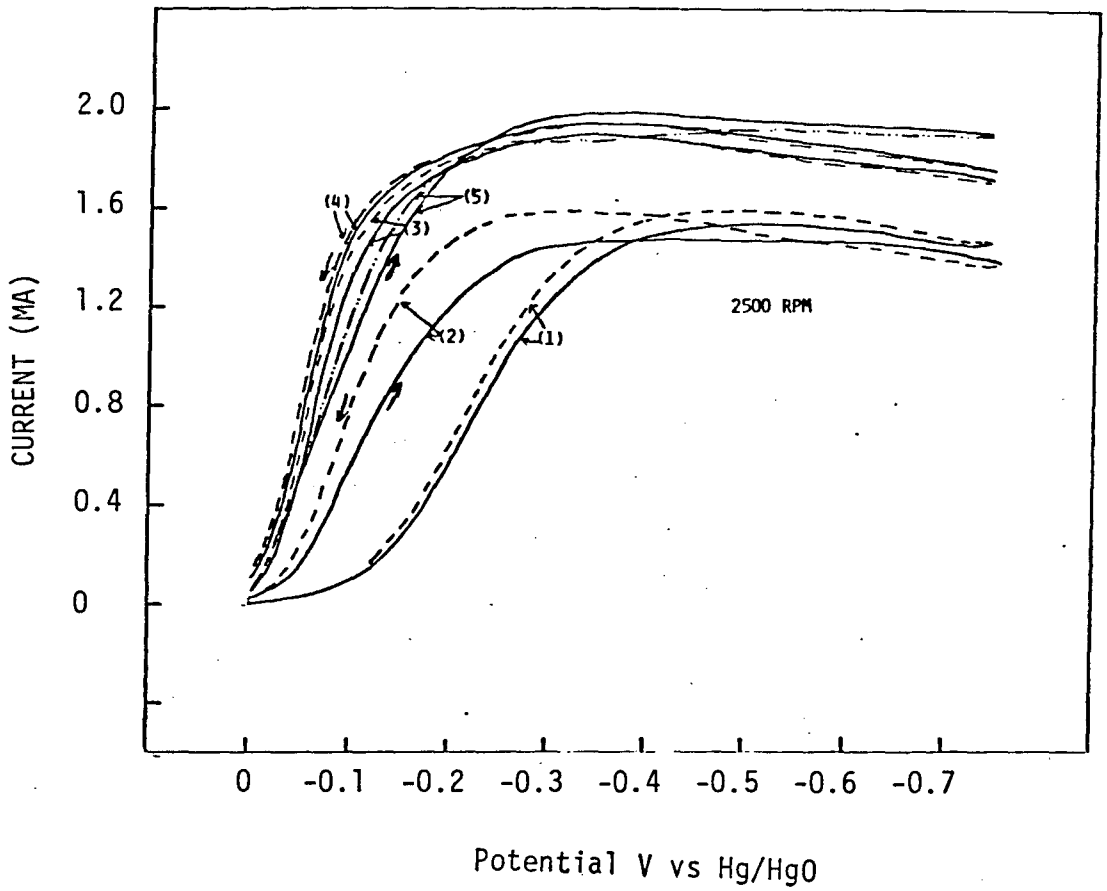


Fig. 5.1.3.15. Polarization curves of oxygen reduction on Ag in IM NaOH solution (1), IM NaOH solution + 1.5×10^{-5} m H_2PtCl_6 + 5×10^{-7} m $Pd(NO_3)$; (2), IM NaOH solution + $1.5\ 10^{-5}$ m H_2PtCl_6 + 5×10^{-7} m $Pd(NO_3)$ + 10^{-6} m $Tl(NO_3)$; (3), IM NaOH solution + 1.5×10^{-5} m H_2PtCl_6 + 5×10^{-7}m $Pd(NO_3)$ + 2×10^{-6} m $Tl(NO_3)$; (4), IM NaOH solution + 1.5×10^{-5} m H_2PtCl_6 + 5×10^{-7} m $Pd(NO_3)$ + 1×10^{-5} m $Tl(NO_3)$; (5), potential sweep rate = 20 mv/s.

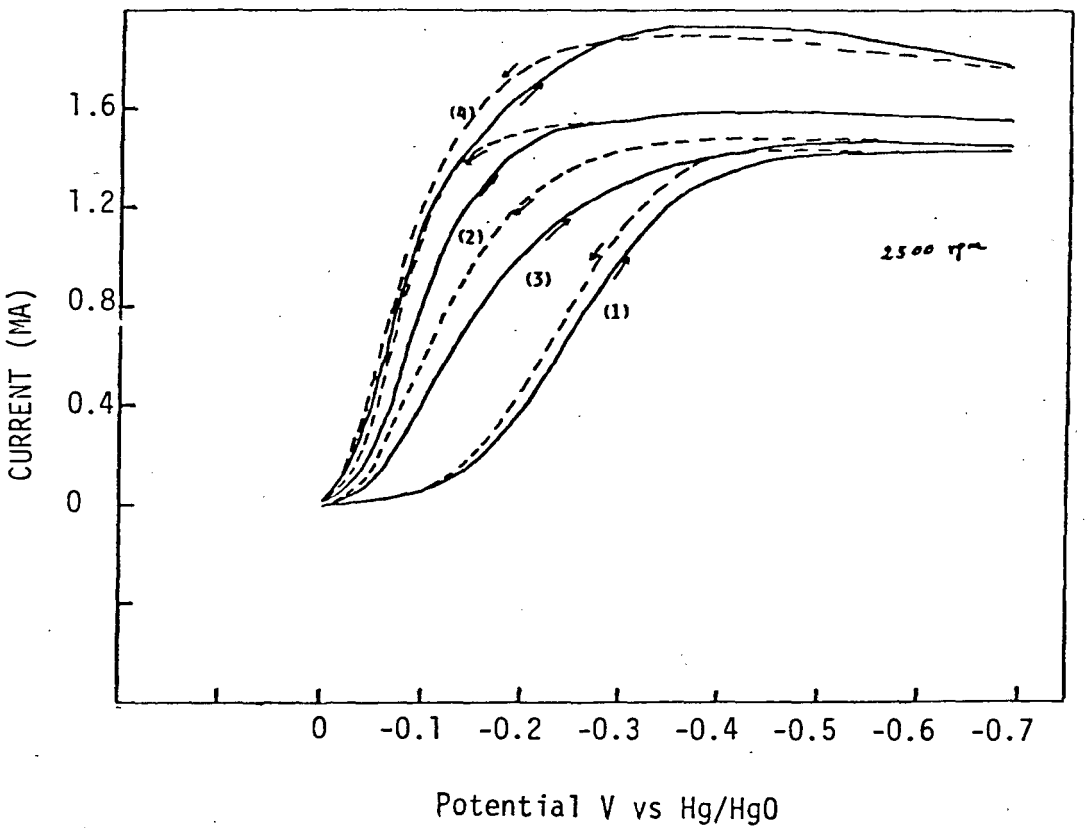


Fig. 5.1.3.16. Polarization curves of oxygen reduction on Ag in IM NaOH solution (1), IM NaOH solution + 10^{-6} m $Pd(NO_3)$; (2), IM NaOH solution + 10^{-6} m $Pd(NO_3)$ + 3 x 10^{-5} m H_2PtCl_6; (3), IM NaOH solution + 10^{-6} m $Pd(NO_3)$ + 3 x 10^{-5} m H_2PtCl_6 + 10^{-6} m $Tl(NO_3)$ or 3 x 10^{-6} m $Tl(NO_3)$.

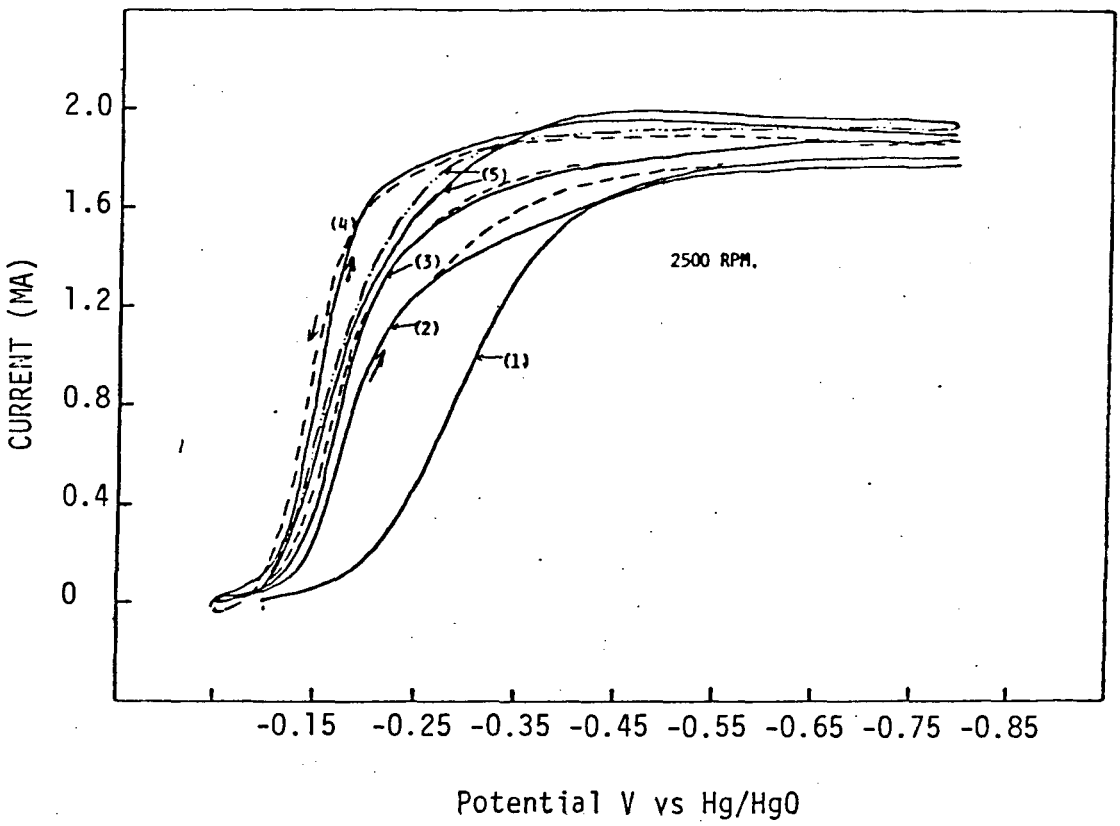


Fig. 5.1.3.17. Polarization curves of oxygen reduction on Ag in IM NaOH solution (1), IM NaOH solution + 3×10^{-5} m H_2PtCl_6; (2), IM NaOH solution + 3×10^{-5} m H_2PtCl_6 + 2×10^{-6} m $Pd(NO_3)$; (3), IM NaOH solution + 3×10^{-5} m H_2PtCl_6 + 2×10^{-6} m $Pd(NO_3)$ + 2×10^{-6} m $Tl(NO_3)$; (4) and IM NaOH solution + 3×10^{-5} m H_2PtCl_6 + 2×10^{-6} m $Pd(NO_3)$ + 4×10^{-6} m $Tl(NO_3)$ or 10^{-5}m $Tl(NO_3)$ or 2×10^{-5} m $Tl(NO_3)$; (5), area of electrode = 0.5 cm^2, potential sweeping rate - 20 mv/s.

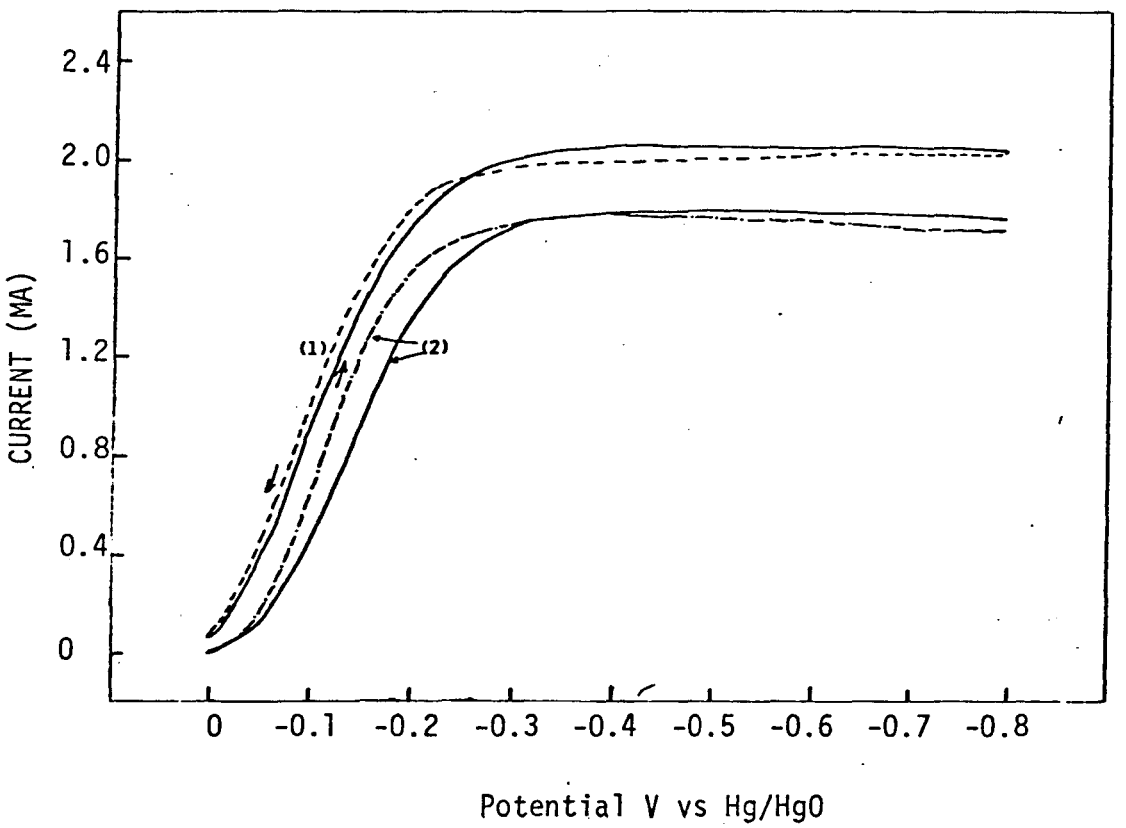


Fig. 5.1.3.18. Polarization curves of oxygen reduction on Ag in IM NaOH solution + 3 x 10^{-5} m H_2PtCl_6 + 10^{-4} m $Tl(NO_3)$ (1), and after 22 hours keeping in water and in new NaOH test solution (2). Potential sweep rate = 20 mv/s; rotation rate = 2500 RPM; electrode area = 0.5 cm^2.

5.1.4 OXYGEN REDUCTION AND EVOLUTION ON INTERMETALLIC COMPOUNDS BASED ON Ni WITH GROUP IV, VB AND VIB TRANSITION METALS

Z.-y. Jiang, D. Tryk, E. Yeager

INTRODUCTION

The oxygen electrode has much significance in electrochemistry not only in theory by also in practice, e.g. metal-air batteries and water electrolysis. Several intermetallic compounds have been investigated as catalysts for oxygen electrodes in the past. The activity for oxygen reduction on $ZrPt_4$ and VPt_3 supported on carbon is better than on pure platinum supported on carbon (1). Oxygen evolution on Ni_3Ti is slightly better than on pure nickel at 80°C in 30% NaOH (2).

This chapter will discuss some electrochemical properties especially oxygen reduction and evolution on intermetallic compounds based on Ni with the transition metals Mo, V, Zr, Hf, Ti and Nb. Data were obtained in the form of oxygen reduction potential sweep curves, oxygen evolution polarization curves and voltammetry curves using rotating disk electrodes fabricated from these compounds. These data will be compared to those obtained for pure nickel.

BACKGROUND

Bagotzky and coworkers have investigated oxygen reduction on the nickel RDE and RRDE (3,4). They found that the oxide film on nickel inhibits both oxygen and hydrogen peroxide reduction. Several workers have performed sweep voltammetry on nickel electrodes and discussed the change of the surface oxide layer in alkali solution (5-10). When the potential is swept in the positive direction, nickel is oxidized to $Ni(OH)_2$ and then to NiOOH at high potentials in alkaline solution. Others have studied oxygen evolution on nickel and discussed the mechanism of this process (11-13). Paeolog et al. (14) studied anodic passivation on Ni, Ti and Ni-Ti alloys and found that the main potential drop under conditions of anodic polarization on Ti is concentrated in the oxide film, and that on oxidized nickel it is in the Helmholtz layer.

EXPERIMENTAL PROCEDURE

Pure Ni, Mo, V, Zr, Ti, Nb rods were obtained from Alfa/Ventron (Danvers, MA). Intermetallic compounds were made in an arc furnace using the pure metal powders. Nickel powder was obtained from Atomergic Chemicals (Plainview, NY). Other metal powders were from Alfa/Ventron. The purities of these rods and powders were (%):

	Ni	Mo	V	Zr	Ti	Nb	Hf
Rod	99.998	99.9	99.5	99.2	99.96	99.98	-
Powder	99.999	99.7	99.9	99.9	99.9	99.99	99.3

The purities of O_2 and Ar were 99.998% respectively.

The intermetallic compounds were analyzed using X-ray diffraction on a GE XRD-5 diffractometer and the patterns were compared with literature data (15). The electrochemical cell was fabricated from Teflon. The reference electrode used was Hg/HgO in 1M NaOH. All potentials in this paper are referenced to this electrode. The counter electrode was platinum. The working electrode was a rotating disk with 0.2 cm^2 surface. 1M NaOH was prepared using "Baker Analyzed" reagent grade NaOH (Baker Chemical Company, Phillipsburg, NJ) and distilled water. In some cases preelectrolysis was carried out in a Teflon cell with Pt cathode nd Pd-H_2 anode. The electrode treatment was as follows. Electrodes were mechanically polished using Buehler Ltd. (Evanston, IL) special emery grinding paper (00 and 0000 grit) and then 1.0μ , 0.3μ aplha alumina and 0.05μ AB gamma alumina. After washing, the electrodes were cleaned ultrasonically. Finally the electrodes were put into the cell under potential control.

Before doing voltammetry the potential was kept at -1.1V for 10 minutes in Ar-saturated 1M NaOH. The sweep range was between H_2 evolution and O_2 evolution, from -1.1V to +0.64V. The rotation rate was 3000 rpm. The potential sweep rate was 100 mv/s. For oxygen reduction the potential was initially kept at -1.1V for 20 minutes in O_2-saturated 1M NaOH. Then the potential was swept in the positive direction until the current became zero and then reversed. The sweep rate was 5 mv/s with a rotation rate of 3000 rpm. Oxygen evolution curves were obtained in O_2-saturated solution. At first the potential was kept at -1.1V for 2 minutes and then at +0.4V for 4 minutes, after which the oxygen evolution polarization curve was measured. Here the potential sweep rate was 1 mv/s with a rotation rate of 4000 rpm. At high currents IR drop was compensated. All of the experiments were performed at room temperature, 20 $\pm$ 2°C.

For several of the pure metals the experimental conditions were modified slightly, as will be noted later.

RESULTS AND DISCUSSION

Pure Metals.

Intermetallic compounds discussed in this chapter consisted of Ni with Mo, V, Zr, Ti, Hf or Ni. Initially the electrochemical properties of these metals were studied using linear sweep voltammetry.

Fig. 1 shows voltammetry for Ni in Ar-saturated 1M NaOH solution. Before sweeping, the potential was kept at -1.1V for 10 minutes. In the first cycle there are three peaks. The first peak, at -0.6V, corresponds to the oxidation of Ni to $Ni(OH)_2$. The second peak, at +0.6V, corresponds to the oxidation of $Ni(OH)_2$ to NiOOH and the third (cathodic) peak at +0.43V, is the reverse of the second peak. The first peak does not reappear in the second sweep because the $Ni(OH)_2$ does not reduce to Ni completely during the first cycle. The increase in current of the second and third peaks probably indiates a modification of the surface.

Fig. 2 shows oxygen reduction curves at a Ni RDE at various rotation speeds. Initially the potential was kept at -1.1V for 45 minutes and then the polarization curves were recorded in an anodic sweep. Each curve exhibits a current drop starting around -0.8 to -0.7V, which corresponds to peak 1 in Fig. 3. This indicates that the $Ni(OH)_2$ layer inhibits oxygen reduction. If the kinetics are first order with respect to dissolved O_2, the current is related (16) to rotation rate w by the equation.

$$\frac{1}{i} = \frac{1}{(i_l)_k} + \frac{1}{B\sqrt{w}} \qquad (1)$$

where $(i_l)_k$ is the kinetic limiting current for O_2 reduction. Fig. 3 shows plots of i^{-1} vs. $w^{-1/2}$ obtained from data in Fig. 2 in the form of paralleled straight lines. The slope of these lines is 11.6 mA^{-1} $rpm^{1/2}$. B equals 0.086 mA $rpm^{-1/2}$, corresponding to a 4-electron reduction. If the data of Davis et al. (17) are used, the equation

$$i_d = 0.621\ nFCw^{1/2}\nu^{-1/6}D^{2/3} \qquad (2)$$

yields a value of 4.16 electrons. Here it must be pointed out that the data from (17) were obtained using 1M KOH solution.

At low current density, the Tafel slope for the oxygen evolution polarization curve is 0.045V $decade^{-1}$ while at high current density an uncompensated IR drop presumably contributes to some curvature (Fig. 4).

A potential sweep curve for oxygen reduction is seen in Fig. 5. When the current became zero, the current was reversed. There is a large hysteresis indicating that the oxide film is hard to reduce and inhibits oxygen reduction.

Ni-Mo system.

Three intermetallic compunds, Ni_4Mo, Ni_3Mo and NiMo were prepared. Figs. 6-8 show their voltammetry. The slope of the voltammetric curve for Ni_4Mo is very similar to that for Ni. Again there are three main peaks, two anodic and one cathodic. The small shoulder at +0.35V has been described in the literature also on pure nickel after many cycles (7). A peak for molybdenum dissolution is not evident in this figure, but the magnitudes of the second and third peaks are greaer than for nickel. In the case of Ni_3Mo the second and third peaks also became large. The reason for the anodic current increase near potential -0.1V in the first cycle is the dissolution of molybdenum. Because of the dissolutiuon of Mo at the surface, the real electrode area became larger, so that the magnitudes of the nickel peaks are also greater than for pure nickel.

For NiMo the molybdenum dissolution peak also became large. After these experiments a fine black powder-like surface was observed. Using X-ray diffraction data from Ref. 15 Ni_4Mo, Ni_3Mo have been confirmed, but a standard X-ray pattern for NiMo could not be found.

Large hysteresis was found in oxygen reduction potential sweep curves for Ni-Mo intermetallic compounds (Fig. 9). The half-wave potentials obtained for positive-going oxygen reduction curves for NiMo intermetallic compounds are more negative than that obtained with pure Ni.

Oxygen evolution polarization curves for Ni_4Mo and Ni_3Mo are similar to that of nickel (Fig. 10). For Ni_3Mo the potentials are lower by about 5mV than for nickel at the same current density. The polarization curve for NiMo is much lower than for nickel, but NiMo is corroded over this potential range.

Ni-V system

Voltammetry curves for Ni_8V, Ni_3V and Ni_2V show a behavior similar to those for the Ni-Mo system (Figs. 11,12). The greater the concentration of vanadium, the higher the vanadium dissolution peak, but this effect was not as pronounced as in the Ni-Mo system. After the electrochemical experiments, the surface of the electrode remained bright. Both oxygen reduction and evolution curves are very similar to those for nickel (Fig. 13). For this and the rest of the binary systems, the oxygen evolution curves were virtually parallel to that for Ni and thus will not be shown. For the purposes of comparison, polarization potentials are given in Table I.

Ni-Zr system

Four Ni-Zr intermetallic compounds have been tested. The voltammetry curves for Ni_3Zr are quite similar to those for nickel (Fig. 14). Both Ni_7Zr_2 and Ni_3Zr have similar voltammetry curves (Figs. 15, 16). The $Ni(OH)_2/NiOOH$ peaks are large. The voltammetric peaks for NiZr are smaller than those for nickel (Fig. 17) probably due to a zirconium oxide covered electrode surface. Fig. 18 shows oxygen reduction curves for Ni-Zr intermetallic compounds. Oxygen evolution curves for all of the Ni-Zr intermetallic compounds are similar with potentials slightly more positive than for nickel.

Ni-Hf system

The voltammetry curves and oxygen reduction curves for NiHf, Ni_3Hf, and Ni_7Hf_2 are similar to those for the Ni-Zr system (Figs. 19,20). The oxygen evolution curves showed that as the concentration of hafnium increases the anodic polarization also increases. Although voltammetry was not done on pure Hf, it is believed to also passivate.

Ni-Ti system.

Voltammetry curves are shown in Fig. 21. The behavior of Ni_3Ti and NiTi is similar to that of the Ni-Hf system (Fig. 22).

Ni-Nb system.

Only one sample was tested in this system. The voltammetry and O_2 reduction behavior for Ni_3Nb was similar to that for nickel (Figs. 23,24), but the oxygen evolution behavior was poorer than for nickel.

Table I contains a summary of the data. In this table are listed the following oxygen reduction parameters. I_d is the half wave current obtained in a positive-going sweep, and $E_{1/2_{1+}}$ is the corresponding half wave potential. $E_{1/2_{1-}}$ was obtained in a negative going sweep. Due to difficulty in obtaining the true limiting current, the potential was taken assuming the same limiting current as in the positive going sweep. The potential separation between $E_{1/2_{1+}}$ and $E_{1/2_{1-}}$, ΔE, indicates the degree of hysteresis. For oxygen evolution, Table I lists the potentials at a current density of 2 mA/cm^2 and the Tafel slopes over the current range from 0.5 to 5 mA/cm^2.

Table I. Polarization data for the oxygen electrode reactions on Ni-based intermetallic compounds using rotating disk electrodes in 1M NaOH at ~25°C.

Electrodes	Oxygen Reduction				Oxygen Evolution	
	$I_{d'_2}$ mA/cm^2	$E_{1/2_1+}$, v*	$E_{1/2_1-}$, v	ΔE, v	E_{ev}, V at i=2mA/cm^2	Tafel slope, V/decade
Ni	4.7	-0.52	-0.98	0.46	0.644	0.045
Ni_4Mo	4.55	-0.54	-1.04	0.50	0.644	0.50
Ni_3Mo	4.7	-0.57	-1.00	0.43	0.638	0.05
NiMo	4.55	-0.62	-1.00	0.38	--	--
Ni_8V	4.8	-0.55	-0.95	0.405	0.65	0.059
Ni_3V	4.7	-0.56	-0.99	0.43	0.645	0.048
Ni_2V	4.6	-0.56	-0.96	0.395	0.642	0.050
Ni_5Zr	4.4	-0.64	-0.86	0.215	0.65	0.051
Ni_7Zr_2	4.0	-0.58	-0.97	0.395	0.65	0.055
Ni_3Zr	4.1	-0.62	-0.90	0.285	0.65	0.052
NiZr	3.9	-0.62	-0.91	0.285	0.655	0.054
Ni_7Hf_2	4.45	-0.62	-0.90	0.285	0.647	0.053
Ni_3Hf	4.2	-0.57	-0.97	0.40	0.652	0.065
NiHf	3.9	-0.63	-0.99	0.36	0.658	0.050
Ni_3Ti	4.1	-0.55	-0.95	0.395	0.663	0.065
NiTi	4.1	-0.57	-0.94	0.375	0.677	0.070
Ni_3Nb	4.2	-0.56	-0.97	0.41	0.667	0.052

*Potentials are referred to Hg/HgO, OH^-.

References

1. Philip N. Ross, Jr., "Oxygen Reduction on Supported Pt Alloys and Intermetallic compounds in Phosphoric Acid," final report for Contract RP P00-5, Lawrence Berkeley Laboratory, University of California, Berkeley, CA, March 1980.

2. P. W. T. Lu and S. Srinivasan, J. Electrochem. Soc., 125, 265 (1978).

3. N. A. Shumilova and V. S. Bagotzky, Electrochim. Acta, 13, 283 (1968).

4. V. S. Bagotsky, N. A. Shumilova, G. P. Smoilov and F. I. Khrushcheva, Electrochim. Acta, 17, 1635 (1972).

5. J. L. Weininger and M. W. Breiter, J. Electrochem. Soc., 110, 484 (1963).

6. J. L. Weininger and M. W. Breiter, J. Electrochem. Soc., 111, 707 (1964).

7. R. S. Schrebler Guzman, J. R. Vilche and A. J. Arvia, Corros. Sci. Vol. 18 765 (1978).

8. R. S. Schrebler Guzman, J. R. Vilche and A. J. Arvia, J. Electrochem. Soc., 125, 1578 (1978).

9. H. Gomez Meier, J. R. Vilche and A. J. Arvia, J. Appl. Electrochem., 10, 611 (1980).

10. J. F. Wolf, L.-S. R. Yeh and A. Damjanovic, Electrochim. Acta, 26, 409 (1981).

11. M. H. Miles, G. Kissel, P.W.T. Lu and S. Srinivasan, J. Electrochem. Soc., 123, 332 (1976).

12. P.W.T. Lu and S. Srinivasan, J. Electrochem. Soc., 125, 1416 (1978).

13. G. Bronoel and J. Reby, Electrochim. Acta, 25, 973 (1980).

14. E. N. Paleolog, A. Z. Fedolova, O. G. Derjagina and N. D. Tomashov, J. Electrochem. Soc., 125, 1410 (1978).

15. Powder Diffraction File, International Center for Diffraction Data, American Society for Testing and Materials, Philadelphia, PA.

16. V. G. Levich, "Physiocochemical Hydrodynamics" Prentice-Hall International, Inc., Englewood Cliffs, NJ (1962).

17. R. E. Davis, G. L. Horvath and C. W. Tobias, Electrochim. Acta, 12, 287 (1967).

References

18. L. D. Burke and O. J. Murphy, J. Electroanal. Chem., 109, 373 (1980).

19. W. G. Maffatt, "The Handbook of Binary Phase Diagrams," 1978, General Electric Co., Schenectady, NY, 1978.

20. F. A. Shunk, "Constitution of Binary Alloys", McGraw-Hill, 1969.

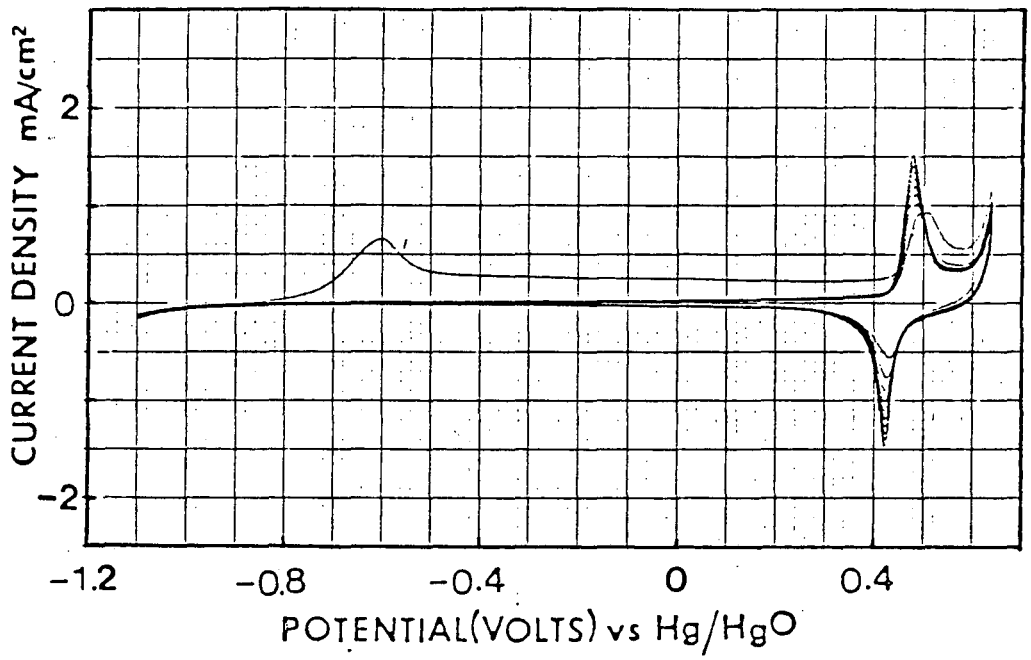


Fig. 5.1.4.1. Voltammetry curves for Ni in Ar-saturated 1 M NaOH. Rotation rate 3000 rpm. Potential sweep rate 100 mv/s

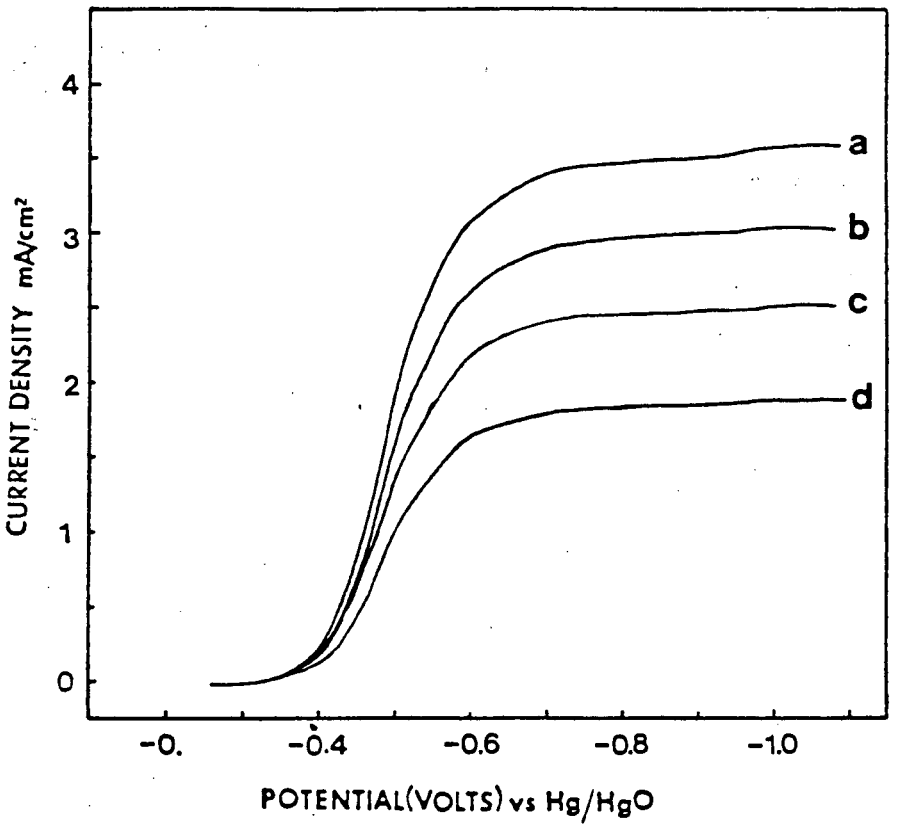


Fig. 5.1.4.2. Oxygen reduction on Ni in O_2-saturated 1 M NaOH. Potential sweep rate 5 mv s^{-1}. Rotation rates are: curve a-2000 rpm, b-1400 rpm, c-900 rpm, d-500 rpm.

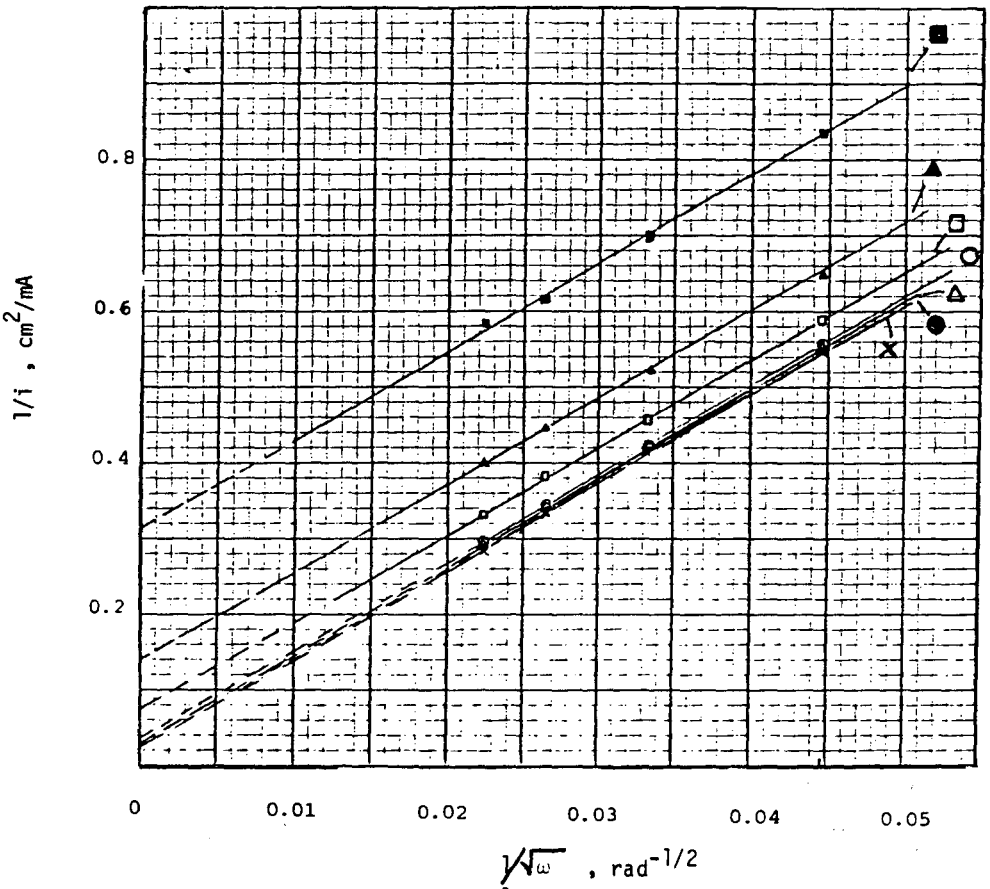


Fig. 5.1.6.3. Plots of $\frac{1}{i}$ and $\frac{1}{\sqrt{\omega}}$ for a Ni rotating disk electrode. Data are from Fig. 2. Potentials are:

x	-1.1 v	●	-0.9 v
△	-0.8 v	○	-0.7 v
□	-0.6 v	▲	-0.55 v
■	-0.5 v		

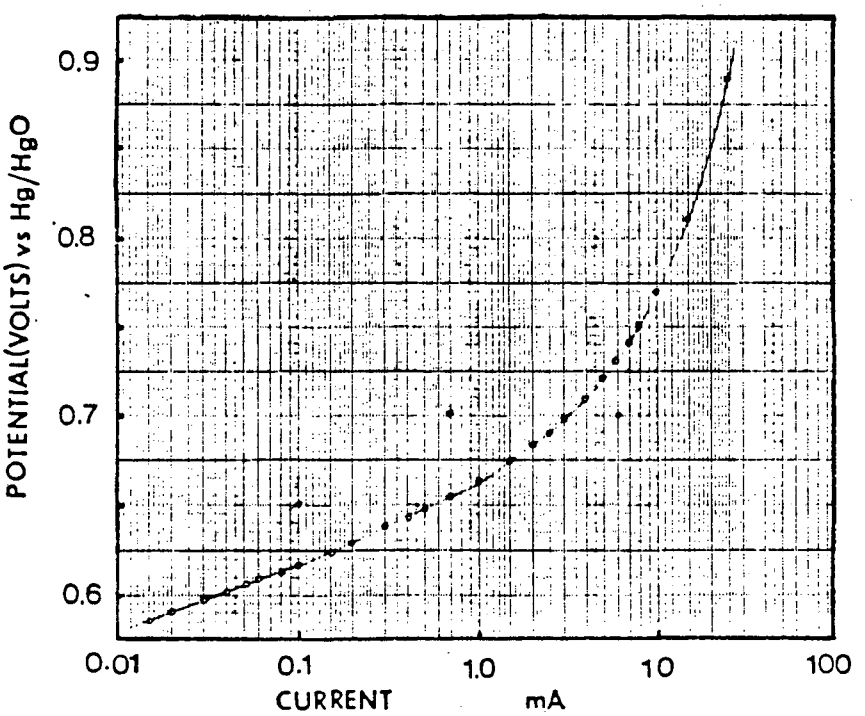


Fig. 5.1.4.4 Oxygen evolution on Ni in O_2-saturated 1 M NaOH. Rotation rate 4000 rpm. Potential sweep rate 1 mv/s. Electrode area 0.2 cm^2.

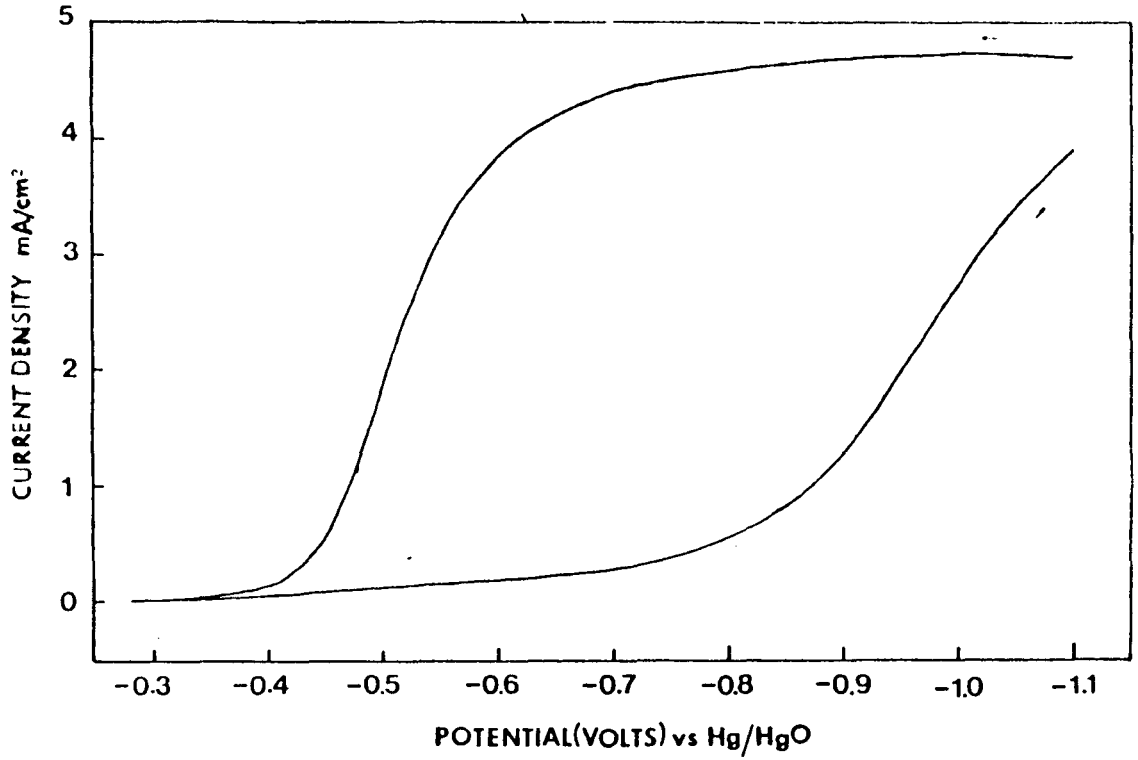


Fig. 5.1.4.5. Oxygen reduction on Ni in O_2-saturated 1 M NaOH. Rotation rate 3000 rpm. Potential sweep rate 5 mv/s.

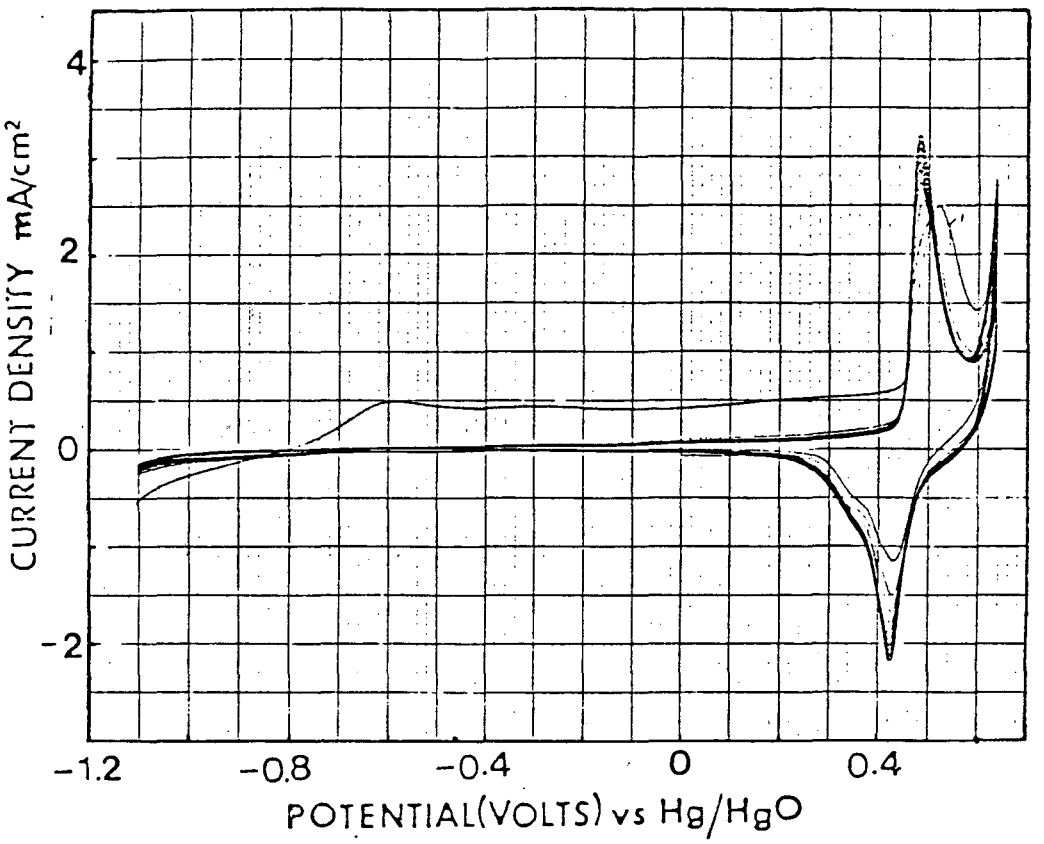


Fig. 5.1.4.6. Voltammetry curves for Ni_4Mo in Ar-saturated 1 M NaOH. Rotation rate 3000 rpm. Potential sweep rate 100 mv/s.

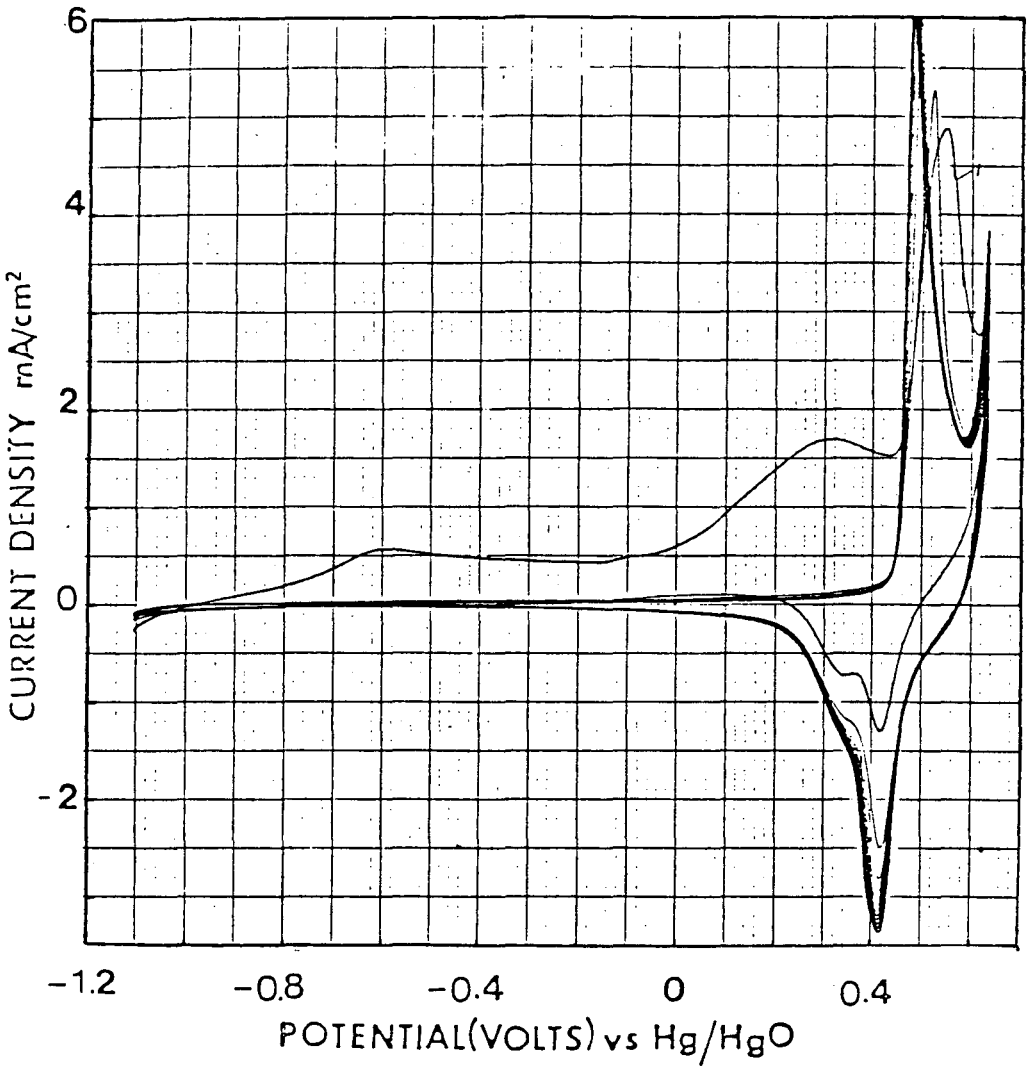


Fig. 5.1.4.7. Voltammetry curves for Ni_3Mo in Ar-saturated 1 M NaOH. Rotation rate 3000 rpm. Potential sweep rate 100 mv/s.

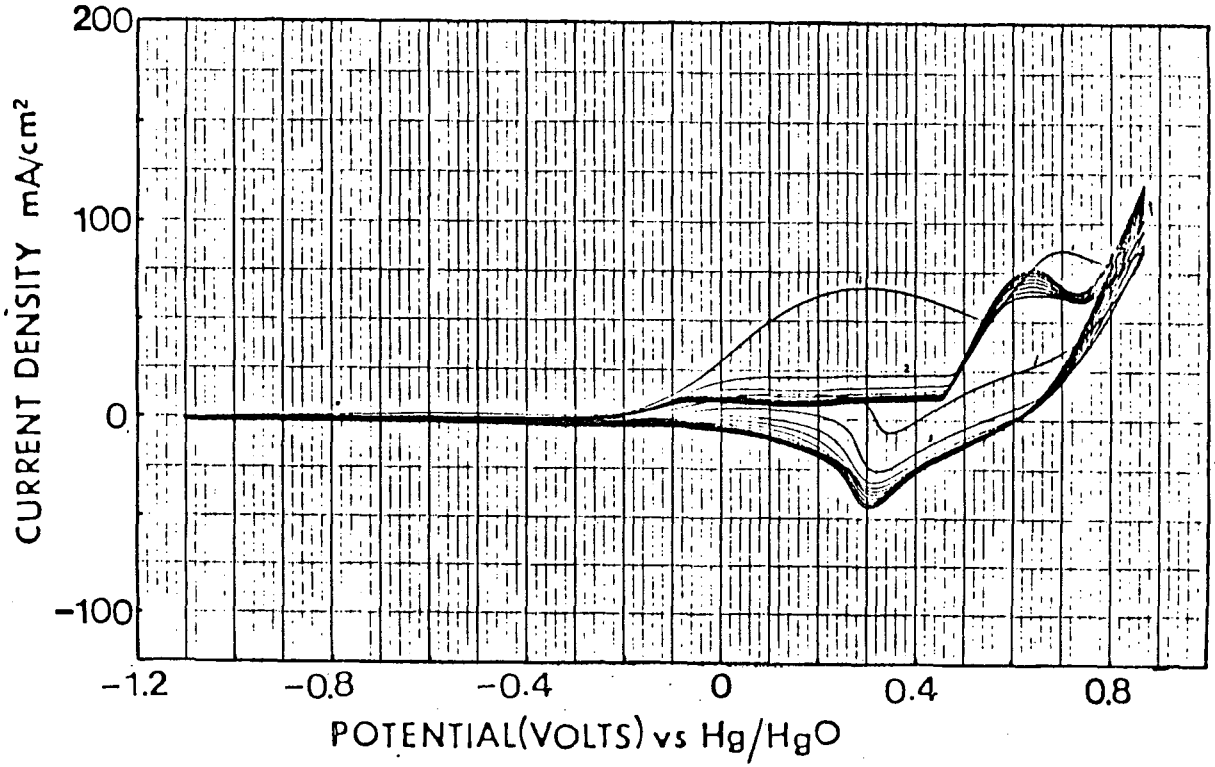


Fig. 5.1.4.8. Voltammetry curves for NiMo in Ar-saturated 1 M NaOH. Rotation rate 3000 rpm. Potential sweep rate 100 mv/s.

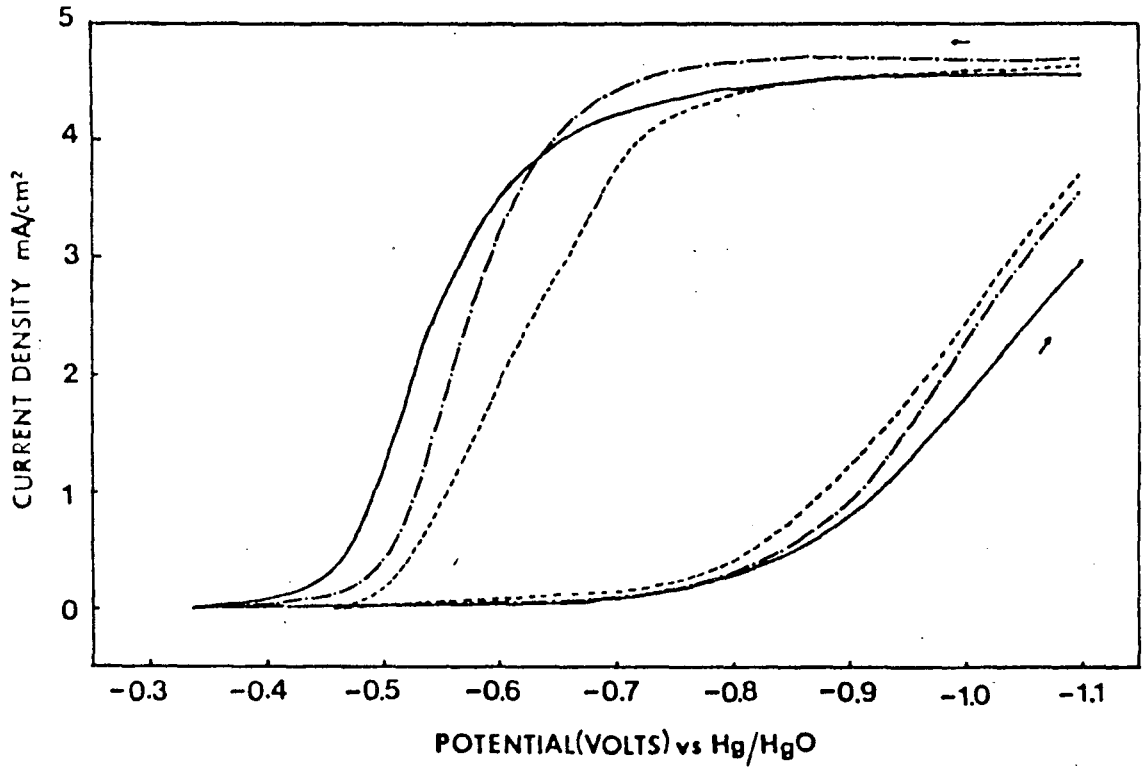


Fig. 5.1.4.9. Oxygen reduction on Ni - Mo intermetallic compounds in O_2-saturated 1 M NaOH. Rotation rate 3000 rpm. Potential sweep rate 5 mv/s.
——— Ni_4Mo ; —·—·— Ni_3Mo ; ------- NiMo

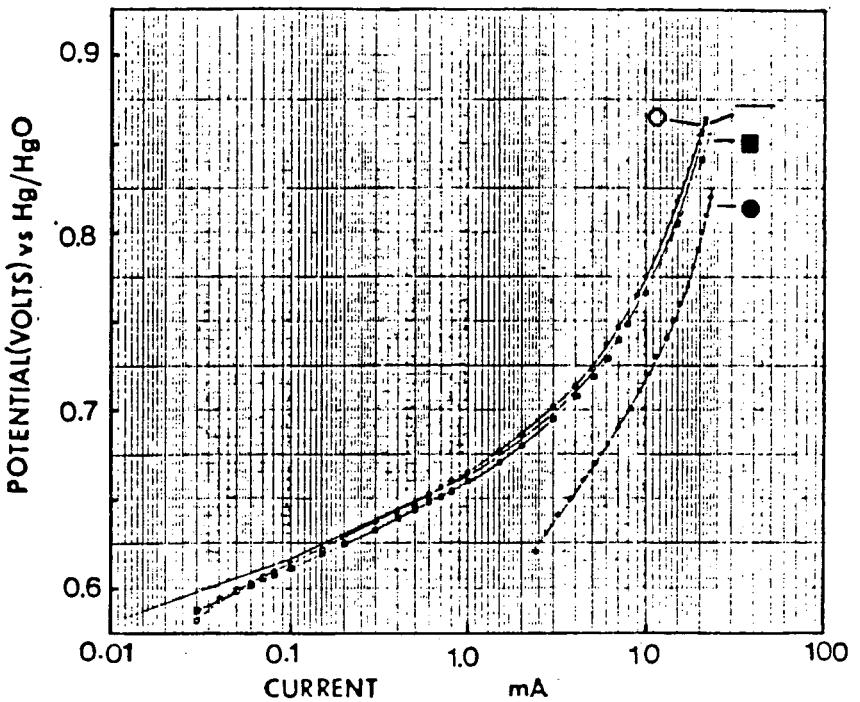


Fig. 5.1.4.10. Oxygen evolution on Ni - Mo intermetallic compounds in O_2-saturated 1 M NaOH. Rotation rate 4000 rpm. Potential sweep rate 1 mv/s. Electrode area 0.2 cm^2

curves are:

Ni_4Mo ; Ni_3Mo

NiMo ; Ni

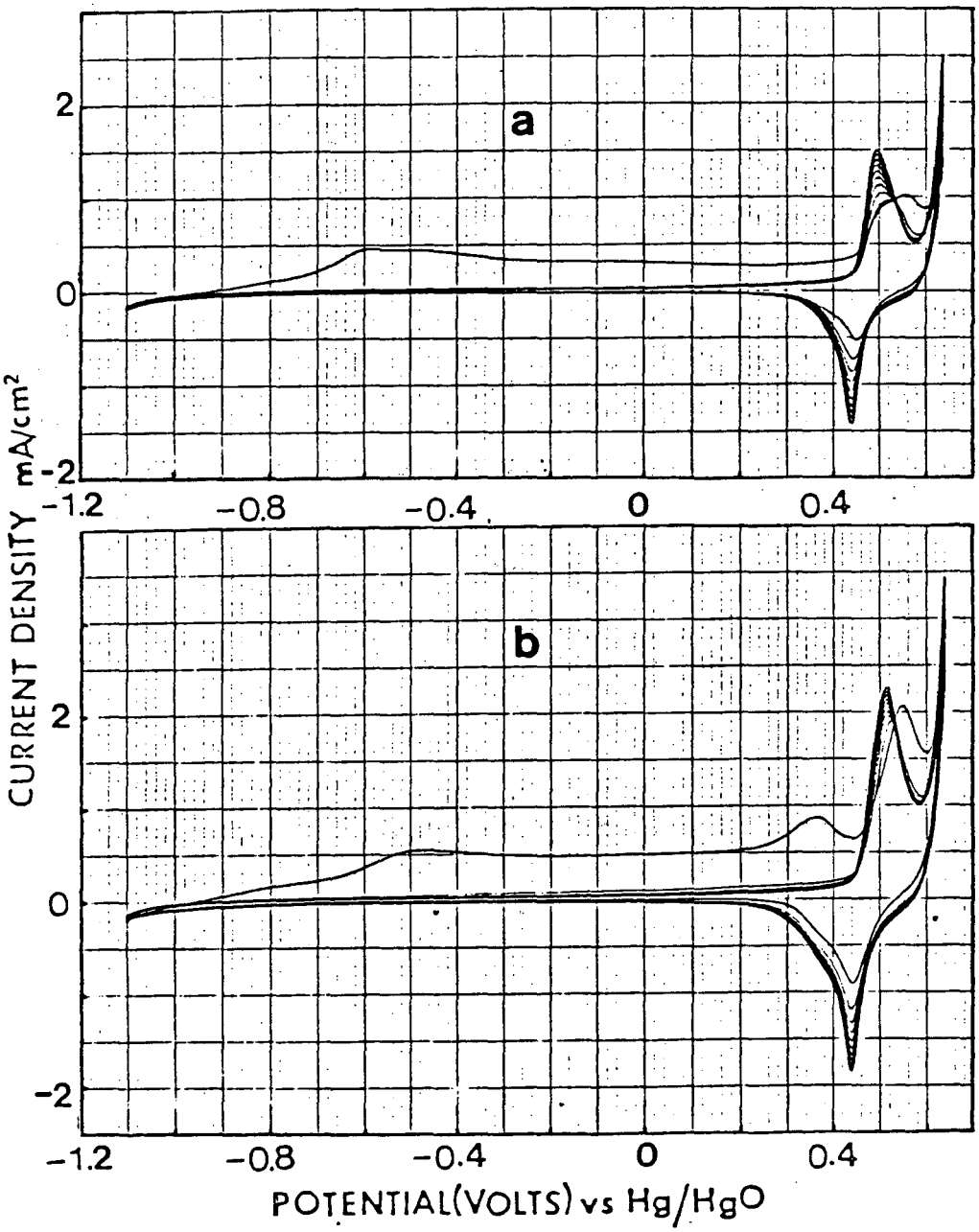


Fig. 5.1.4.11. Voltammetry curves, a - Ni_8V, b - Ni_3V, in Ar-saturated 1 M NaOH. Rotation rate 3000 rpm. Potential sweep rate 100 mV/s.

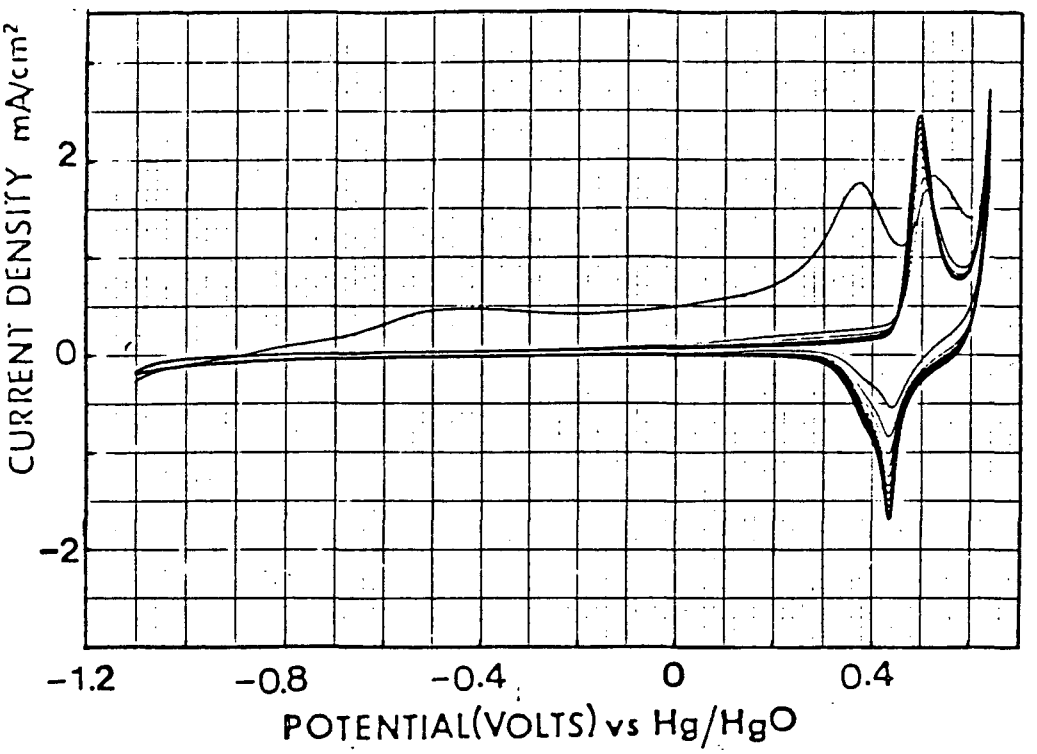


Fig. 5.1.4.12. . Voltammetry curves for Ni_2V in Ar-saturated 1 M NaOH. Rotation rate 3000 rpm. Potential sweep rate 100 mV/s.

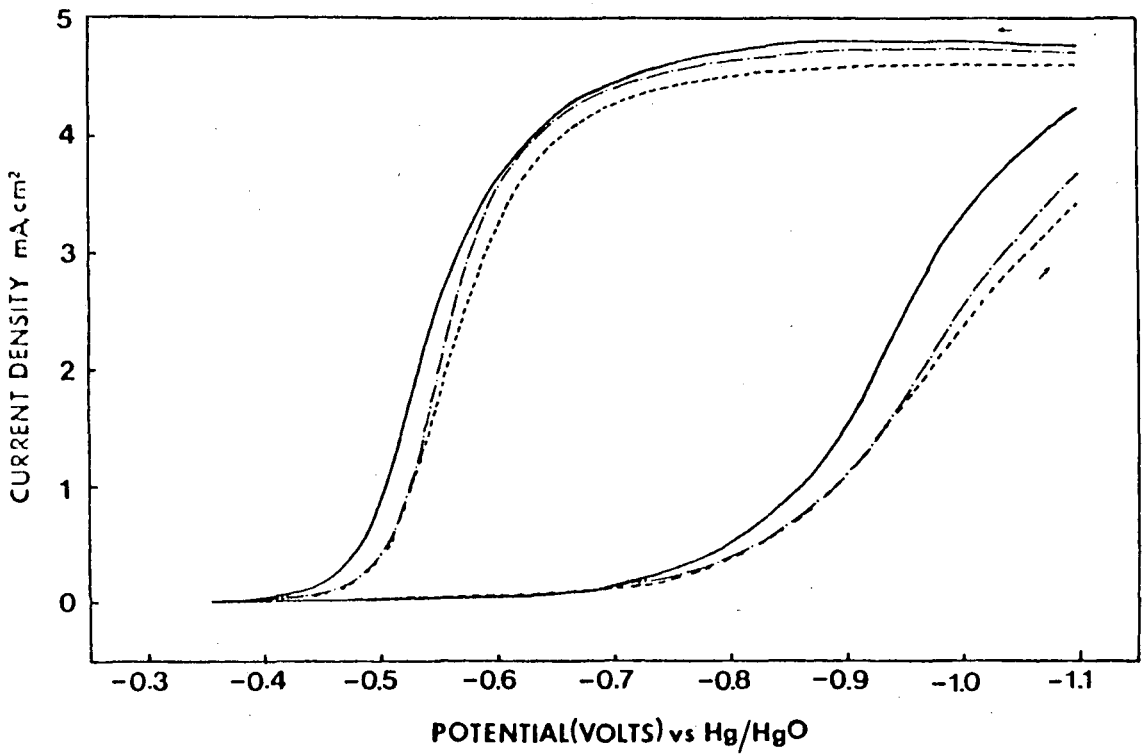


Fig. 5.1.4.13. Oxygen reduction on Ni - V intermetallic compounds in O_2-saturated 1 M NaOH. Rotation rate 3000 rpm. Potential sweep rate 5 mV/s.

——— Ni_8V ; — - — - — Ni_3V ; ------ Ni_2V

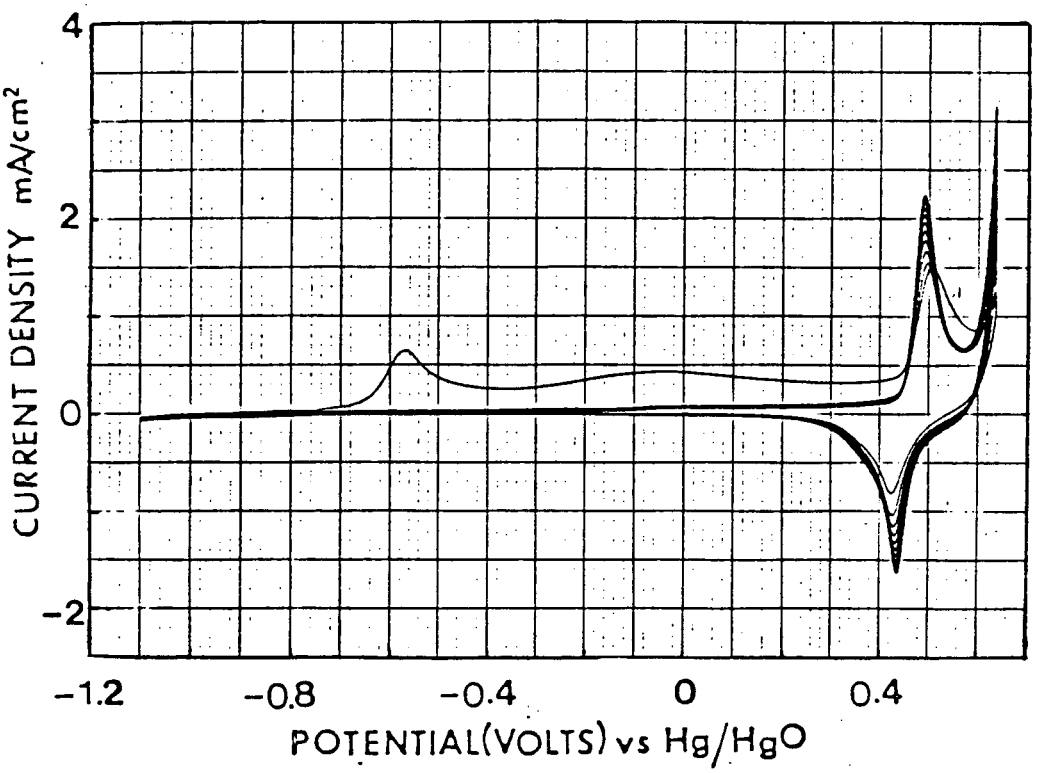


Fig. 5.1.4.14. Voltammetry curves for Ni_5Zr in Ar-saturated 1 M NaOH. Rotation rate 3000 rpm. Potential sweep rate 100 mV/s.

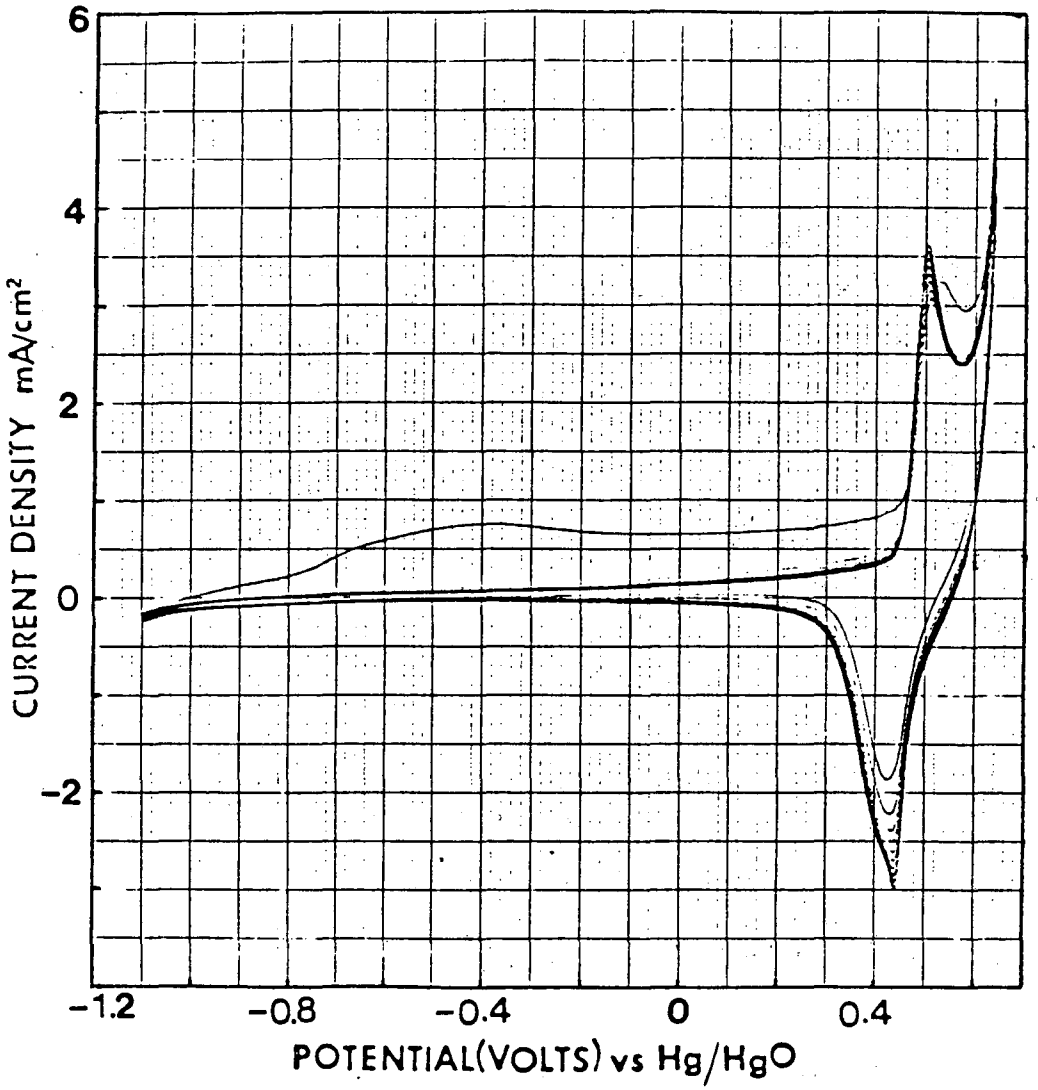


Fig. 5.1.4.15. Voltammetry curves for Ni_7Zr_2 in Ar-saturated 1 M NaOH. Rotation rate 3000 rpm. Potential sweep rate 100 mV/s.

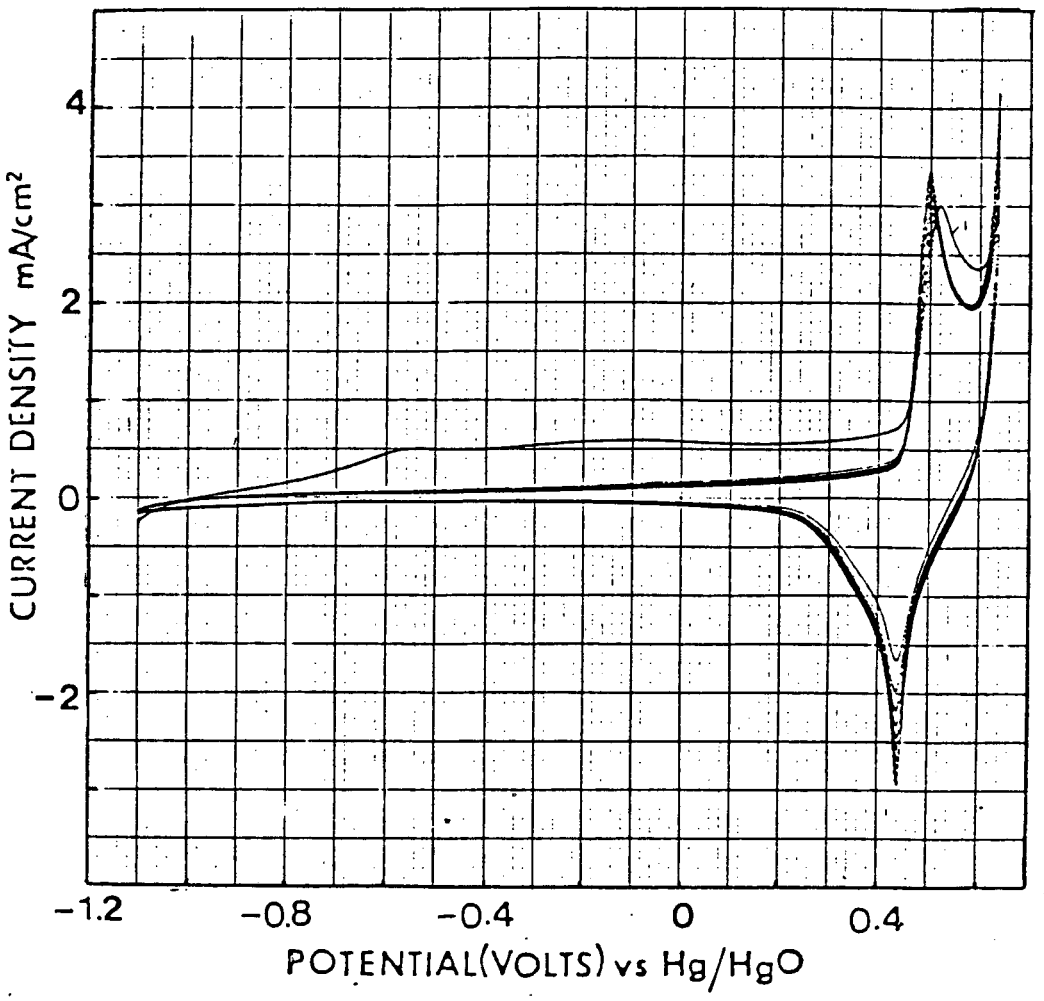


Fig. 5.1.4.16. Voltammetry curves for Ni_3Zr in Ar-saturated 1 M NaOH. Rotation rate 3000 rpm. Potential sweep rate 100 mV/s.

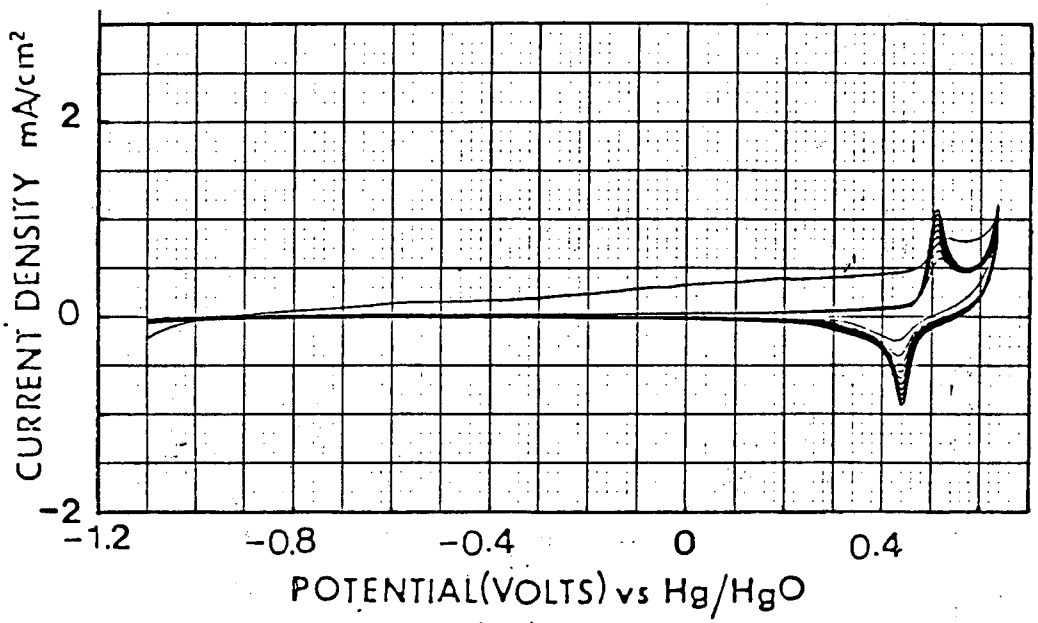


Fig. 5.1.4.17. Voltammetry curves for NiZr in Ar-saturated 1 M NaOH. Rotation rate 3000 rpm. Potential sweep rate 100 mV/s.

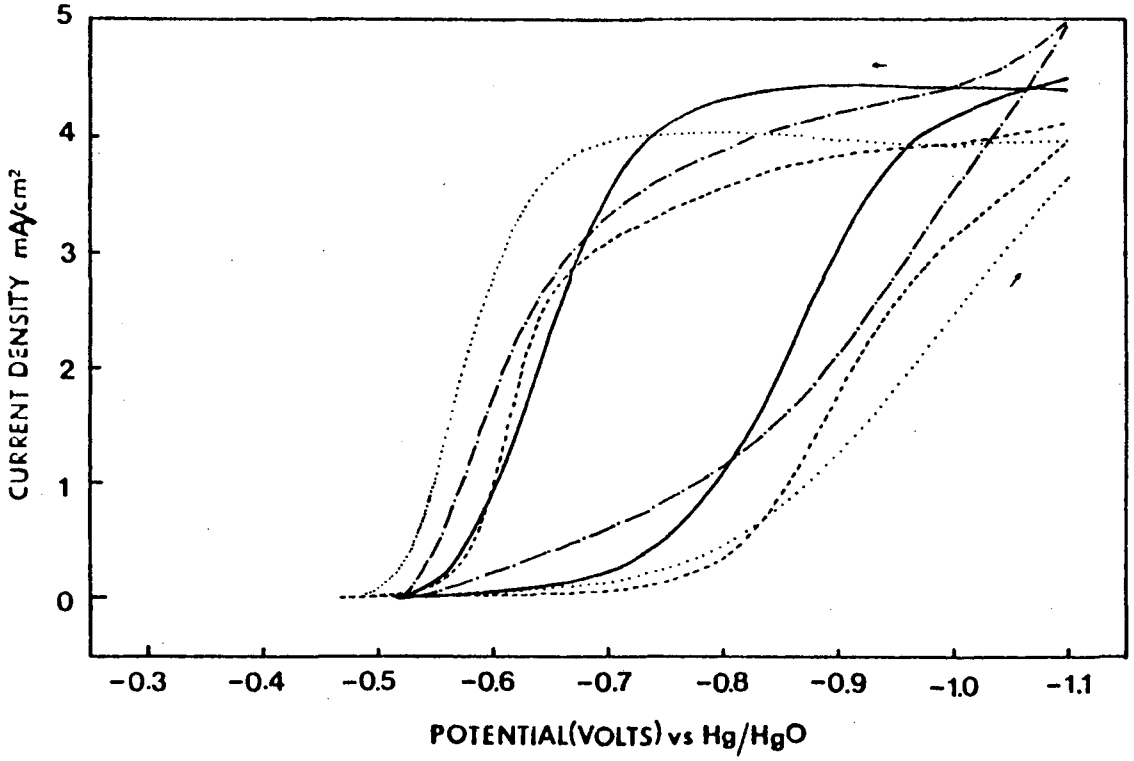


Fig. 5.1.4.18. Oxygen reduction on Ni - Zr intermetallic compounds in O_2-saturated 1 M NaOH. Rotation rate 3000 rpm. Potential sweep rate 5 mV/s.

——— Ni_5Zr ; —•—•— Ni_3Zr ; ..... Ni_7Zr_2 ; - - - - - - NiZr.

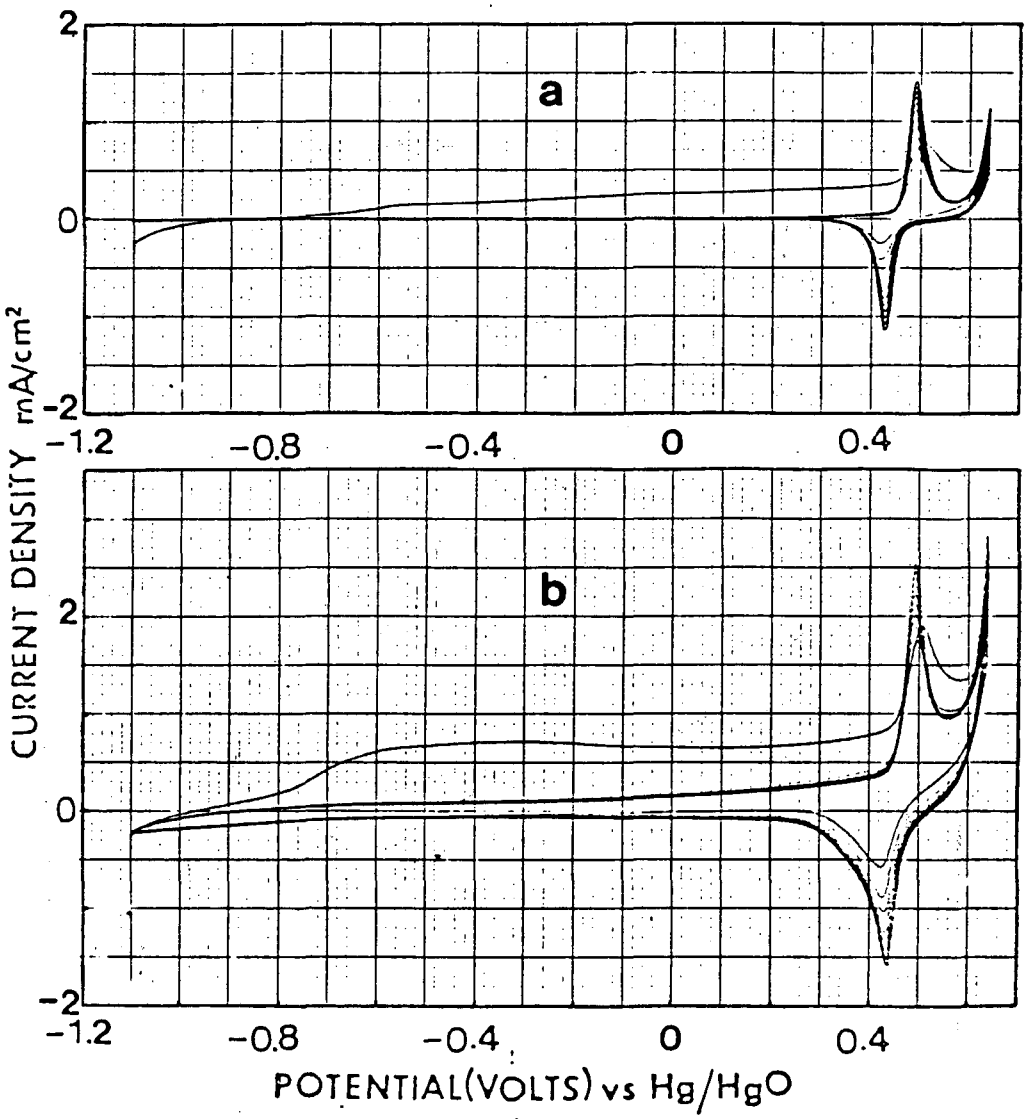


Fig. 5.1.4.19. Voltammetry curves, a - NiHf, b - Ni_3Hf, in Ar-saturated 1 M NaOH. Rotation rate 3000 rpm. Potential sweep rate 100 mV/s.

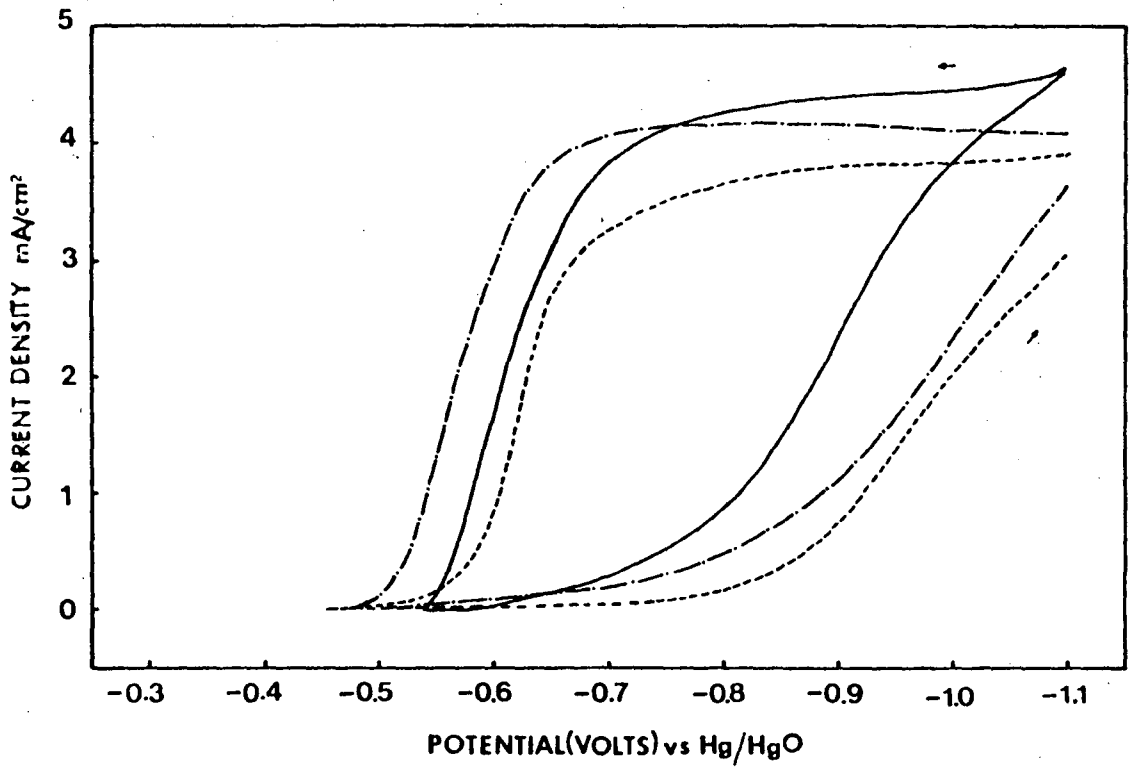


Fig. 5.1.4.20. Oxygen reduction on Ni - Hf intermetallic compounds in O_2-saturated 1 M NaOH. Rotation rate 3000 rpm. Potential sweep rate 5 mV/s.

——— Ni_7Hg_2 ; —·—·— Ni_3Hg ; - - - - - - NiHg

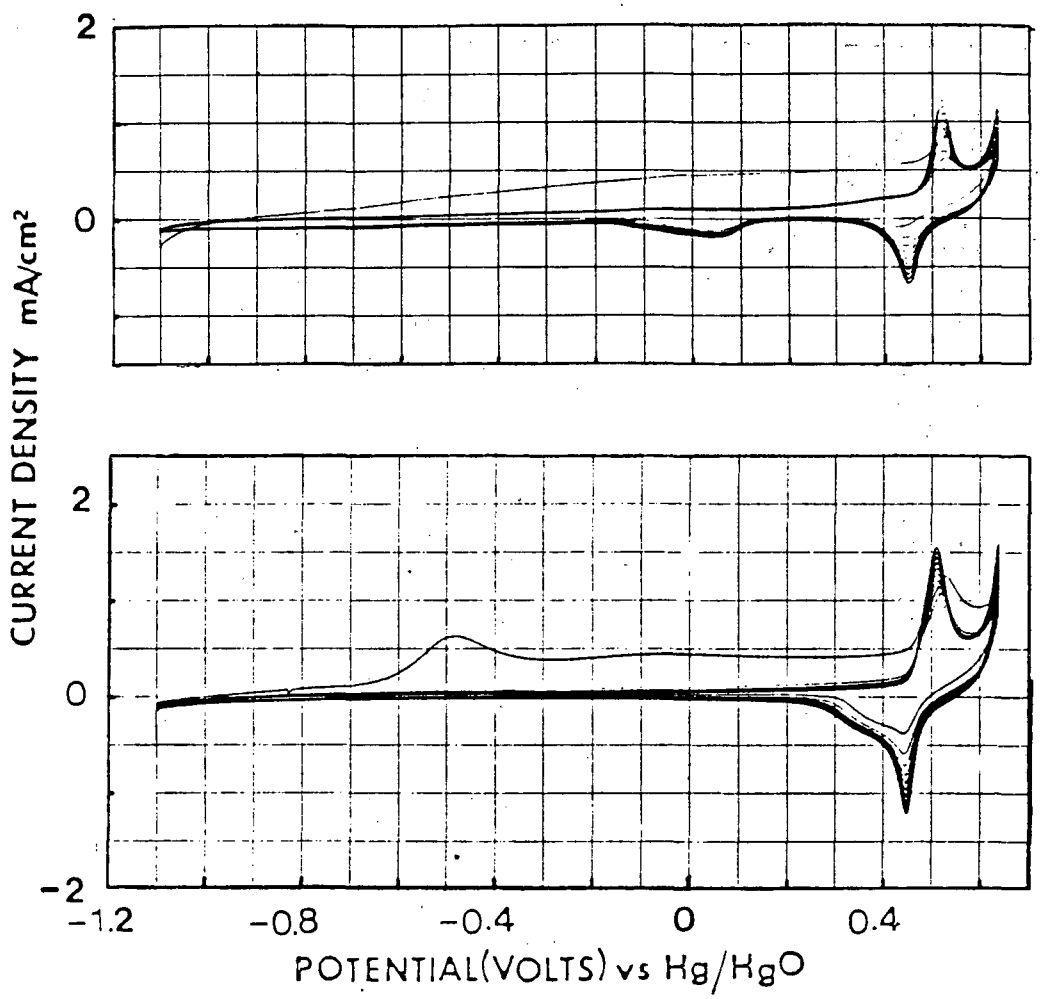


Fig. 5.1.4.21. Voltammetry curves for Ni - Ti intermetallic compounds in Ar-saturated a - NiTi, b - Ni_3Ti. Rotation rate 3000 rpm. Potential sweep rate 100 mV/s.

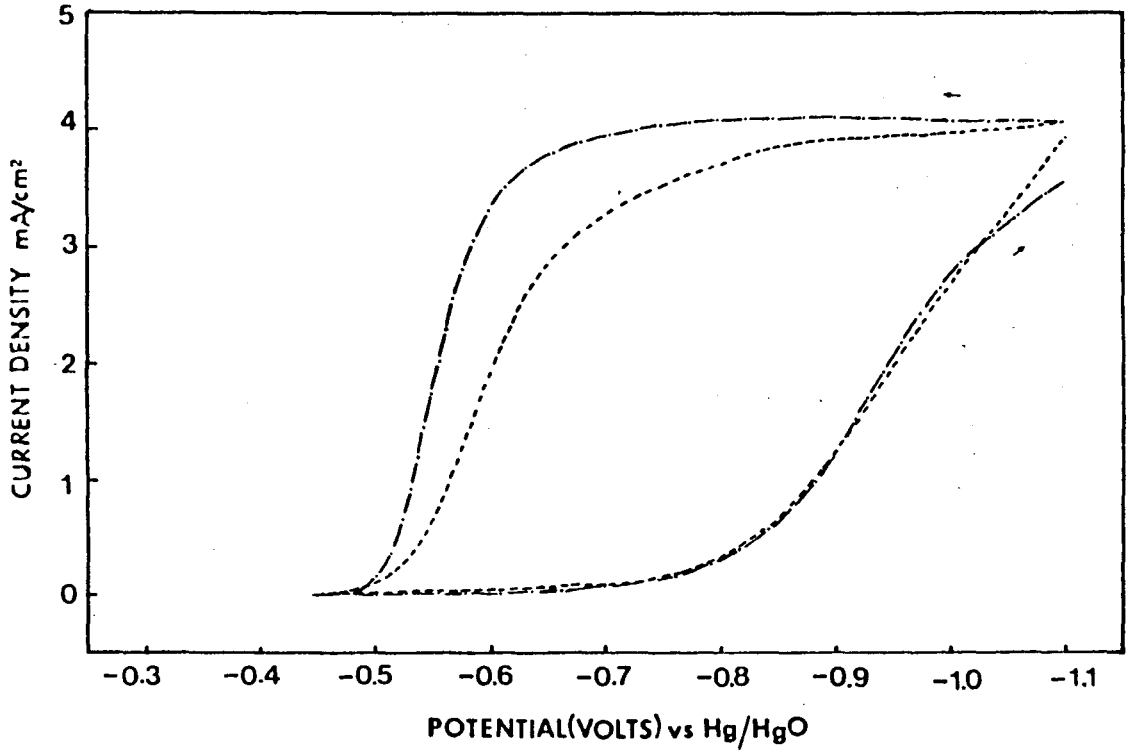


Fig. 5.1.4.22. Oxygen reduction on Ni - Ti intermetallic compounds in O_2-saturated 1 M NaOH. Rotation rate 3000 rpm. Potential sweep rate 5 mV/s.

—— • —— • —— Ni_3Ti ; - - - - - - - - NiTi

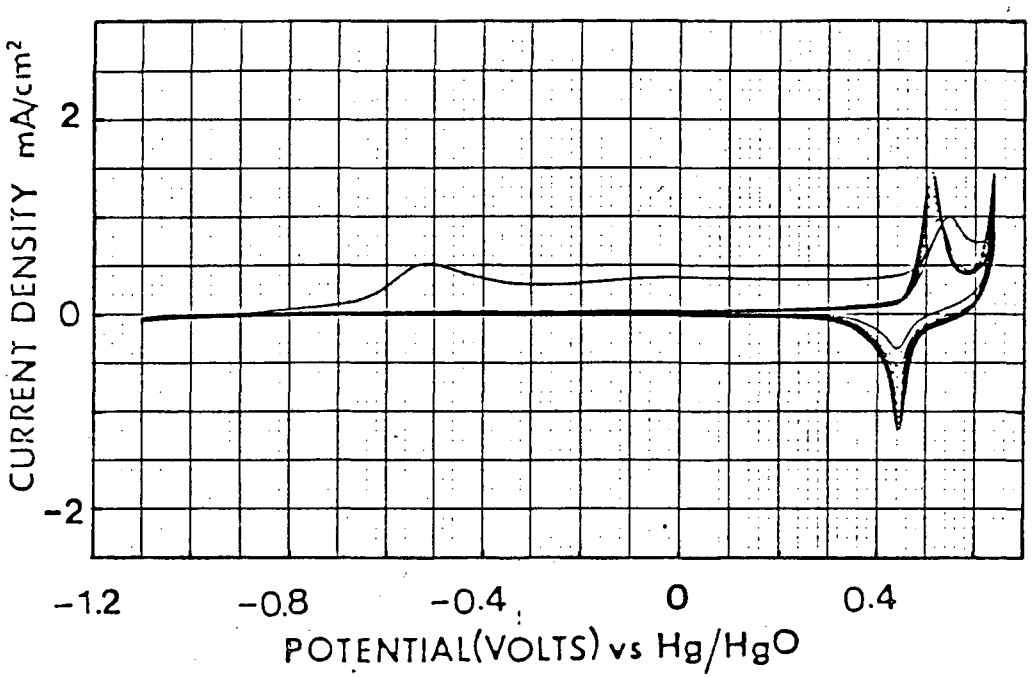


Fig. 5.1.4.23. Voltammetry curves for Ni_3Nb in Ar-saturated 1 M NaOH. Rotation rate 3000 rpm. Potential sweep rate 100 mV/s.

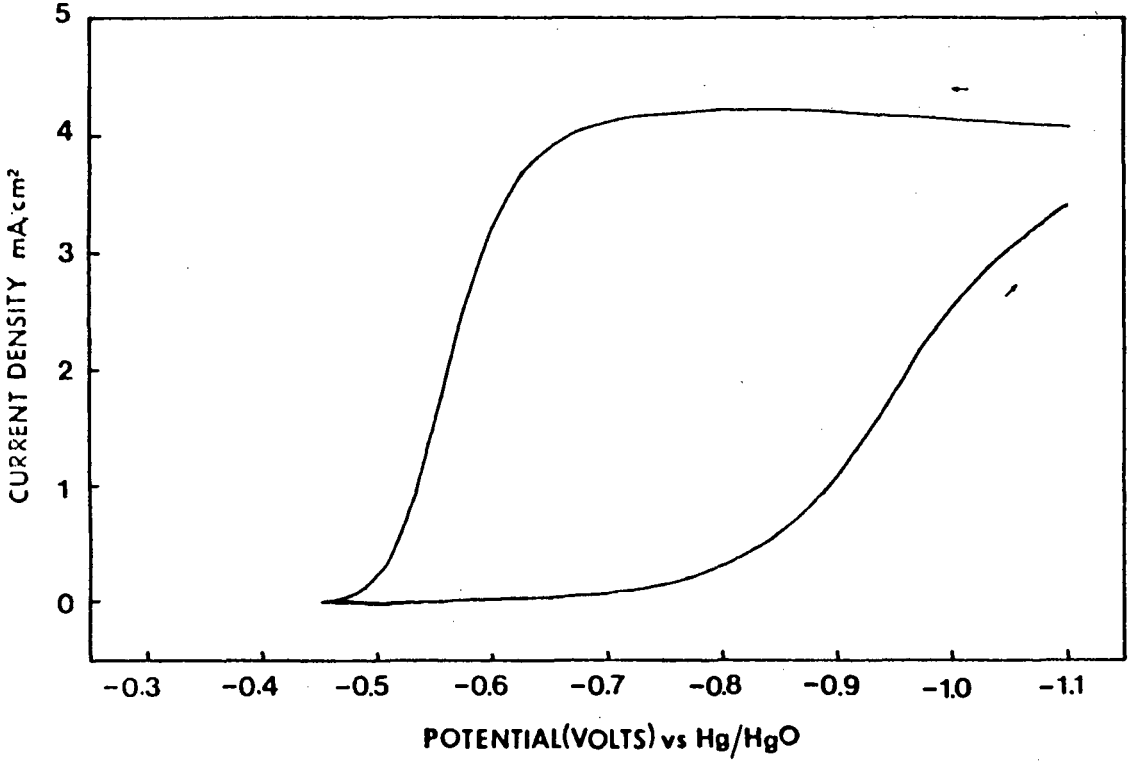


Fig. 5.1.4.24. Oxygen reduction on Ni_3Nb in O_2-saturated 1 M NaOH. Rotation rate 3000 rpm. Potential sweep rate 5 mV/s.

5.1.5 INTRINSIC VOLTAMMETRIC STUDIES OF THE ADSORBED AND SOLUTION PHASE MACROCYCLICS ON GOLD ELECTRODES

S. L. Gupta

In the previous studies at Case, the aqueous soluble tetrasulfonated metal phthalocyanimes (M.TSPc) have been prepared and studied in the acid and alkaline electrolytes. The complexes have been found to absorb strongly at monolayer levels on metals such as gold, platinum and graphite, including the basal plane of stress annealed pyrolytic graphite (1,2,3). These transition metal complexes have high activity for O_2 reduction, usually to peroxide state, but in the instance of the Fe-TSPc to water or OH^- (i.e., the overall 4e reduction). The redox properties of these complexes appear to be of considerable importance to the reduction mechanisms (4-6). Because of the high O_2 catalytic activity of the adsorbed Co-TSPc and Fe-TSPc, special emphasis has been placed on these electrocatalysts in the present cyclic voltammetric studies with a view to differenciate between the redox properties of the adsorbed and solution phase species using gold electrode.

EXPERIMENTAL

Cobalt-tetra sulfonated phthalocyanine (Co-TSPc) and iron-tetrasulfophthalocyanine (Fe-TSPc) were prepared and purified according to the method of Weber and Busch (7), whereas metal-free tetrasulfonated phthalocyanine (H_2TSPc) was obtained by the procedure described by Linstead and Weiss (8). Absorption and Raman spectra of these samples compared very well with the literature data (9,10). Gold disk (area = 0.196 cm^2) embedded in Teflon rod, was used as working electrode and polished before every experiment (3). Saturated calomel electrode (SCE) with a salt bridge was used as the reference electrode and gold foil as the counter electrode. 0.05M H_2SO_4 (Baker Ultrex) and 0.1M NaOH (J.T. Baker) were used as electrolytes in triply distilled water. Cyclic voltammetry has been used to investigate the intrinsic redox properties of the adsorbed and solution phase species of the metal chelates.

RESULTS

1. Fe-TSPc in 0.1M NaOH

Figure 1 shows the cyclic voltammograms for different concentrations of Fe-TSPc in 0.1M NaOH. There seems to be a tendency for the cathodic peaks to develop with increase in concentration of Fe-TSPc and with 10^{-3}M Fe-TSPc two cathodic peaks (-0.83V and 1.05V) are obtained. However, the corresponding anodic peaks are not good. These peaks are very sensitive to the stirring of the solution (Fig. 2). The cathodic peak potentials shift to more cathodic values with increase in sweeprate and the peak currents are proportional to the square root of the scan rate (Fig. 3). There is practically no effect of extending the anodic voltage limit on these peaks. The preadsorbed

electrode from 10^{-3}M Fe-TSPc in 0.1M NaOH when dipped in 0.1M NaOH alone shows no peaks. These results indicate that these peaks with 10^{-3}M FeTSPc in solution correspond to the redox properties of the solution phase species. Figure 4 gives the voltammogram of 5 x 10^{-4}M H_2TSPc in 0.1M NaOH which shows two cathodic peaks at about the same potentials. This suggests that the peaks obtained with 10^{-3}M FeTSPc in 0.1M NaOH correspond to the solution phase redox properties of the ligand. It may be noted that the gold electrode does not show any peak for the pre-adsorbed species. This may be either due to the absence of adsorbed layer or to the high background current associated with the gold electrode.

2. Fe-TSPc in 0.05M H_2SO_4

Figure 5 gives the voltmmograms of 10^{-3}M Fe-TSPc in 0.05M H_2SO_4 at various scan rates. It can be seen that a very sharp anodic and cathodic peak appear at + 0.5V and $_$ 0.4V respectively. Anodic peak potential becomes more anodic and cathodic peak potential more cathodic with increase of scan rate. Figure 6 shows that peak currents (ip) vs. (scan rate) $^{1/2}$ relation is linear. Further this peak is very sensitive to the stirring of the solution showing the redox properties of the solution phase species. By extending the cathodic voltage limit there appear two small anodic peaks at about -0.16V and -0.3V respectively (Fig. 7). The peak potentials of these peaks are almost independent of scan rate. The preadsorbed electrode from 10^{-3}M Fe-TSPc in 0.05M H_2SO_4 when dipped in 0.05M H_2SO_4 alone shows a small anodic peak at about -0.16V (Fig. 8). This indicates that this peak corresponds to the redox process of the adsorbed species which is supported by the ip vs scan rate curve which is linear (Fig. 6). This peak at -0.16V is also obtained with 10^{-5}M Fe-TSPc in 0.05M H_2SO_4. Extending the anodic potential limit has no effect on these peaks. Figures 9 and 10 give the voltammograms of 5 x 10^{-4}M H_2TSPc in 0.05M H_2SO_4 and for the preadsorbed electrode from the same solution dipped in 0.05M H_2SO_4 alone respectively. This suggests that the peak at about -0.16V with Fe-TSPc in 0.05M H_2SO_4 as well as for the preadsorbed electrode from the same solution corresponds to the surface phase redox process of the ligand. The well defined sharp peak at about +0.5V with Fe^{+3}/Fe^{+2} couple in solution as indicated by the same studies with OPG electrode (10). However, the peak at -0.3V needs more study for its identification.

3. Co-TSPc in 0.1M NaOH

Figure 11 gives the cyclic voltammograms of 10^{-3}M Co-TSPc in 0.1M NaOH at different sweeprates. It shows a sharp anodic and less sharp cathodic peak at -0.85 and -0.9V respectively with 50 mV/s. The peak currents are proportional to the scan rate. This peak is sensitive to the stirring of the solution. Extending the anodic voltage limit gives another anodic peak at +0.14V which is stirring insensitive (Fig. 12). The preadsorbed electrode from the same solution when dipped in 0.1M NaOH alone gives two peaks at -0.85V and +0.14V respectively at 50

mV/s. (Fig. 13). The peak currents for both these peaks show linear relation with scan rate (Fig. 14). This indicates that both the peaks correspond to the redox process of the adsorbed species. The fact that the peak at -0.85V with CoTSPc in solution is stirring dependent and is also given by the preadsorbed electrode suggests it to be a mixed peak. This mixed peak corresponds to the solution as well as surface phase redox process of the ligand as H_2TSPc also gives a peak at about the same potential in solution. The peak at +0.14V needs more study for its identification.

4. Co-TSPc in 0.05M H_2SO_4

10^{-5} Co-TSPc in 0.05M H_2SO_4 gives a small anodic peak at about -0.17V particularly at higher scan rates (Fig. 15). This peak is not sensitive to the stirring of the solution and is also obtained with the preadsorbed electrode from the same solution at the same potential showing thereby the redox process of the adsorbed species. 10^{-4} Co-TSPc in 0.05M H_2SO_4 gives another small peak at +0.94V in addition to the peak at -0.17V (Fig. 16). This peak is quite sensitive to stirring the solution. The peak currents at -0.17V are proportional to the scan rate whereas peak currents at +0.94V are proportional to the square root of the scan rate (Fig. 17). The preadsorbed electrode from the same solution when dipped in 0.05M H_2SO_4 alone gives only one peak at -0.17V. These results further confirm that the peak at -0.17V relates to the redox process of the adsorbed species. The peak at +0.94V corresponds to the solution phase process.

With 10^{-3}M Co-TSPc in 0.05M H_2SO_4 we get another peak at +0.8V along with peaks at +0.94V and -0.17V (Fig. 18). The peaks at +0.8V and +0.94V are very sensitive to the stirring of the solution. The peak potential of the peak at +0.8V is very much scan rate dependent whereas the peak potential of peaks at +0.94V and -0.17V are almost scan rate independent. The peak current at -0.17V vs scan rate again follows a linear relation whereas the peak currents for the other two peaks vs. $(\text{scan rate})^{1/2}$ give linear relation (Figs. 19,20). The preadsorbed electrode from the solution when dipped in 0.05M H_2SO_4 alone gives the peak at -0.18V only (Fig. 21). These results again confirm that the peak at -0.18V is due to the redox process of the adsorbed species whereas the peaks at +0.80V and +0.94V correspond to the process of the solution phase species. It appears that the peaks at -0.17V and +0.94V give the redox process of the ligand as 5×10^{-4}M H_2TSPc also gives peaks at about the same potentials in 0.05M H_2SO_4 whereas the peak at +0.8V perhaps corresponds to the solution phase redox process of the $Co^{(II)}/Co^{(III)}$ couple.

References

1. R. K. Sen, J. Jagal and E. Yeager, Inorg. Chem. 16, 3379 (1977).
2. J. Jagal, R.K. Sen and E. Yeager, J. Electroanal. Chem. 83, 207 (1977).
3. J. Jagal, Ph.D. Thesis, Chemistry Department, CWRU (1978).
4. J.P. Randin, Electrochim. Acta 19, 83 (1976).
5. J. Manessen and A. Bar-Ilan, J. Catalysis 17, 85 (1970).
6. F. Beck, J. Appl. Electrochem. 7, 239 (1977).
7. J. Weber and D.N. Busch, Inorg. Chem. 4, 469 (1965).
8. R.P. Linstead and F.T. Weiss, J. Chem. Soc. 2975 (1950).
9. J. Veprek-Siska, E. Schwestnerova and D.M. Wagnerova, Chima 26, 756 (1972).
10. R. Kotz and E. Yeager, J. Electroanal. Chem. 113, 113 (1980).
11. S.L. Gupta, D.O.E. Annual Report, CWRU, 163 (1979-80).

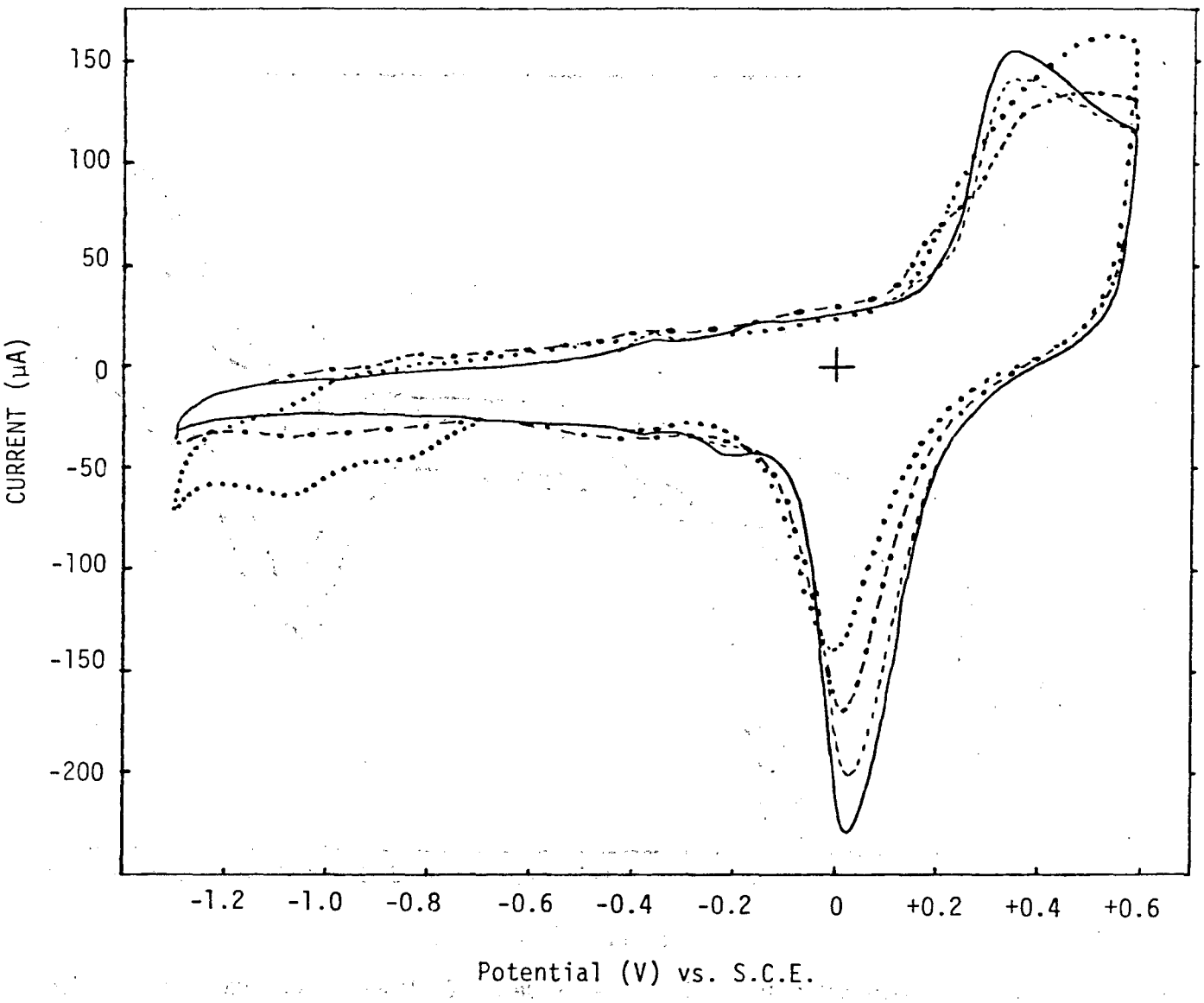


Fig. 5.1.5.1 Voltammograms on Au disk electrode in 0.1M NaOH (N_2 satd.) containing different concentrations of Fe-TSPc. Electrode area = 0.196cm^2, Scan rate = 200mv/s. (——) 0.1M NaOH, (----) 10^{-5}M Fe-TSPc (•-•-•) 10^{-4}M Fe-TSPc, (•••) 10^{-3}M Fe-TSPc.

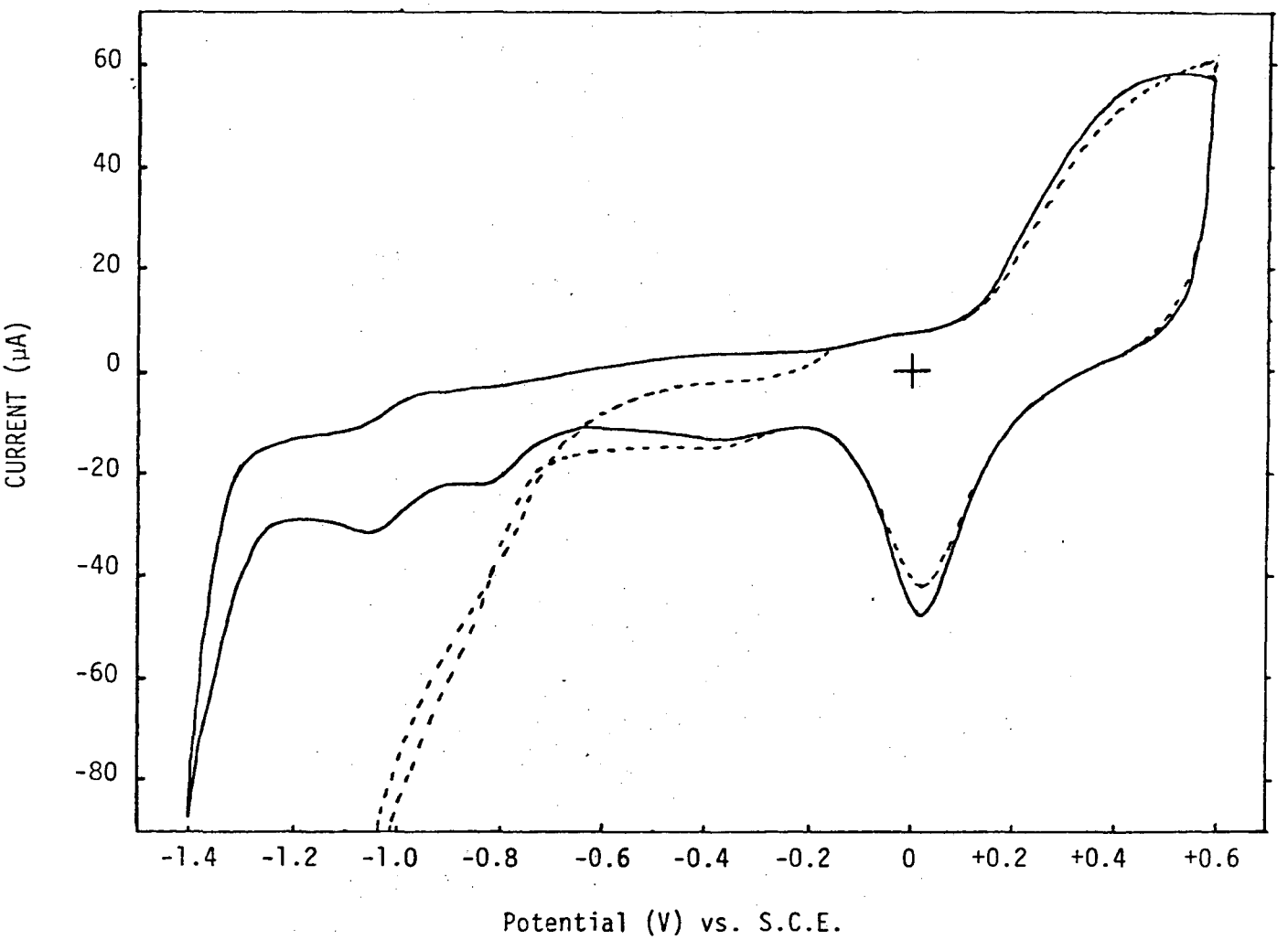


Fig. 5.1.5.2 Voltammograms on Au disk electrode in 0.1M NaOH (N_2 satd.) containing 10^{-3}M Fe-TSPc. Solid line - without rotation; dashed line - with rotation. Scan rate = 50mv/s.

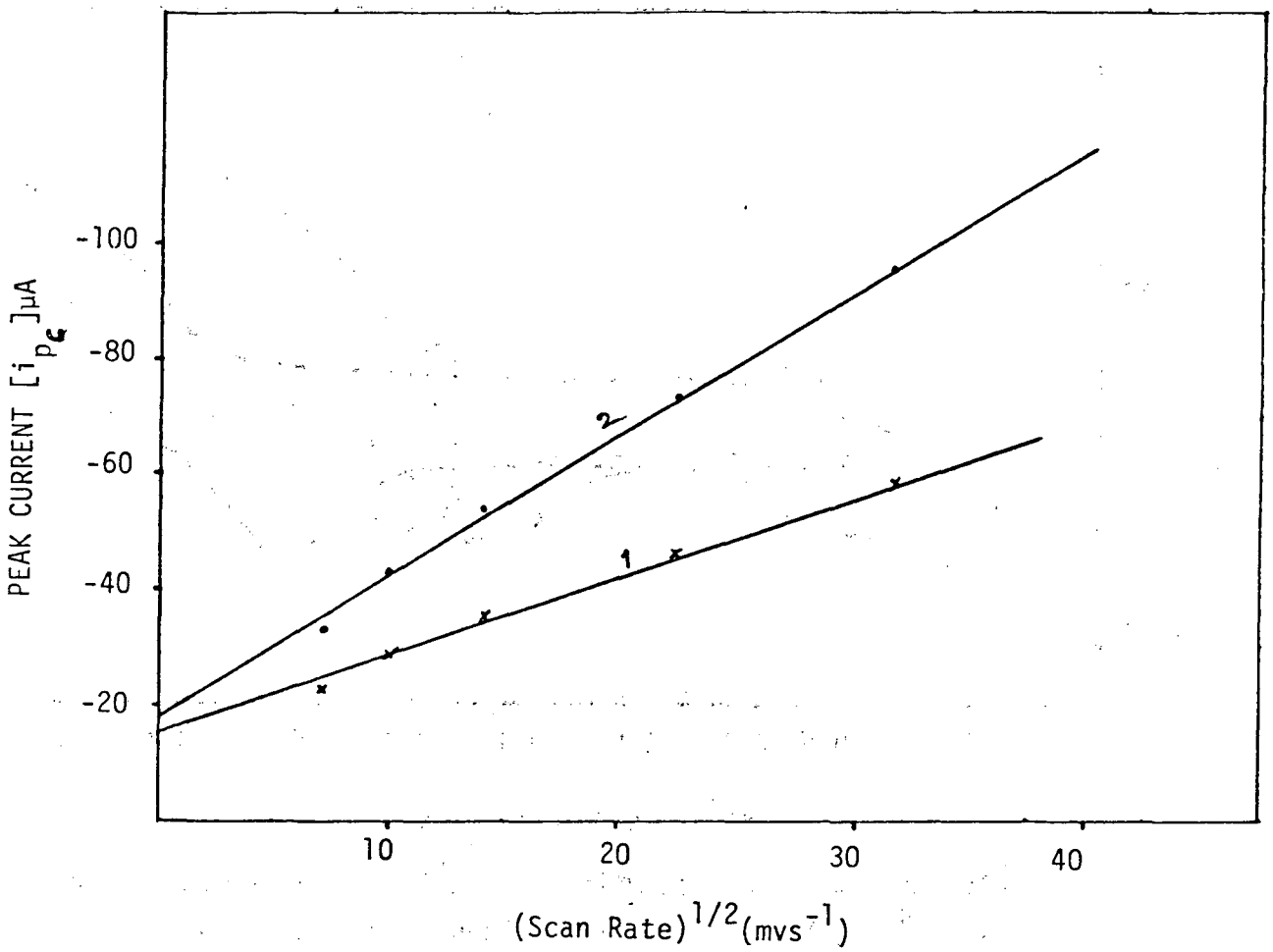


Fig. 5.1.5.3 Scan rate dependence of the cathodic peaks on Au electrode. 10^{-3}M Fe-TSPc in 0.1M NaOH (N_2 satd.). 1 - peak at 0.83V; 2 - peak at -1.05V.

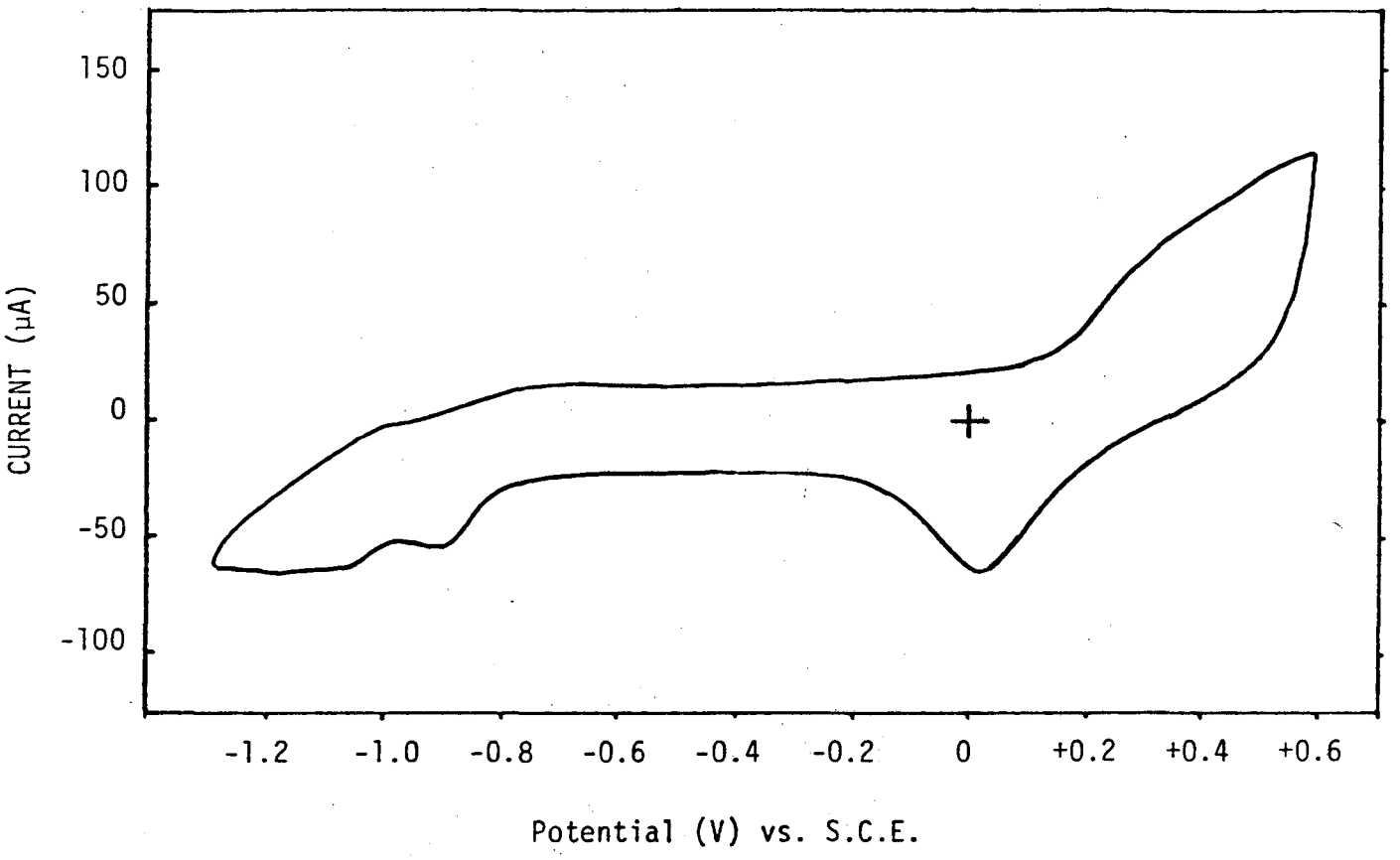


Fig. 5.1.5.4 Voltammogram on Au disk electrode in 0.1M NaOH (N_2 satd.) containing 5×10^{-4}M H_2-TSPc in solution. Scan rate = 200 mv/s.

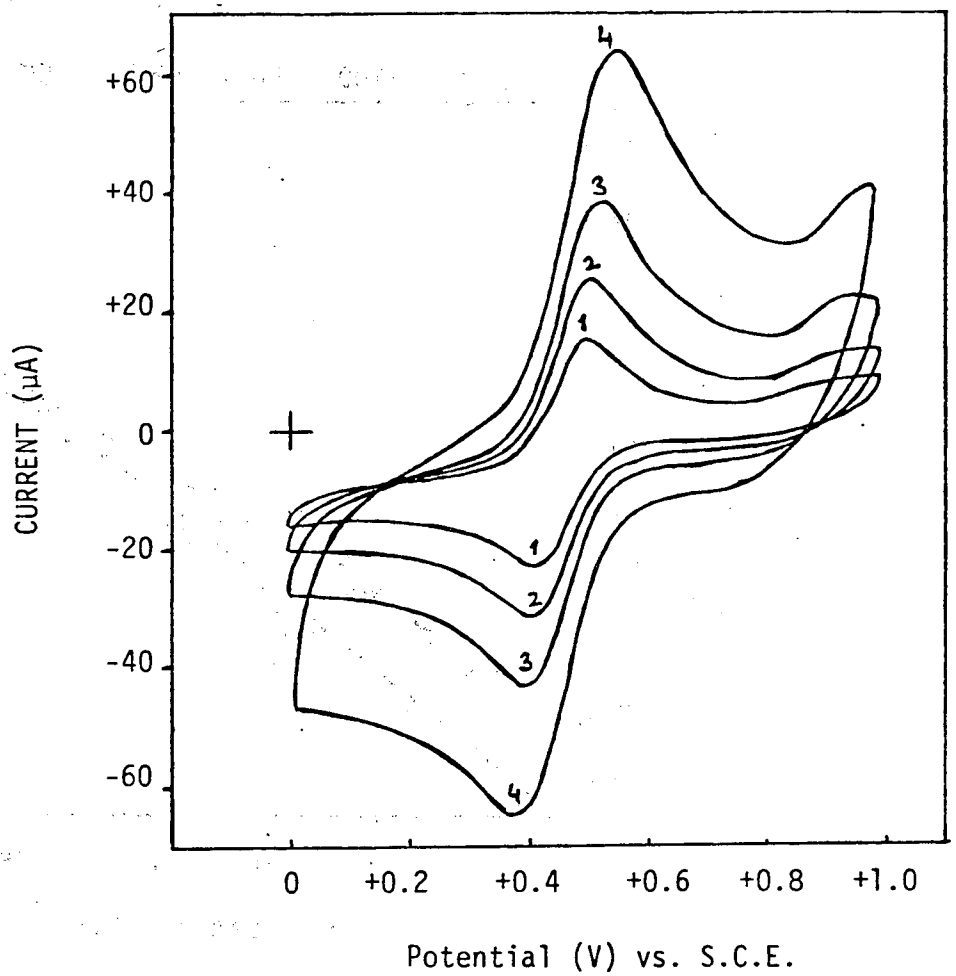


Fig. 5.1.5.5 Voltammograms at different scan rates on Au disk electrode in 0.05M H_2SO_4 (N_2 satd.) containing 10^{-3}M Fe-TSPc. 1 - 50mv/s; 2 - 100mv/s; 3 - 200mv/s; 4 - 500mv/s.

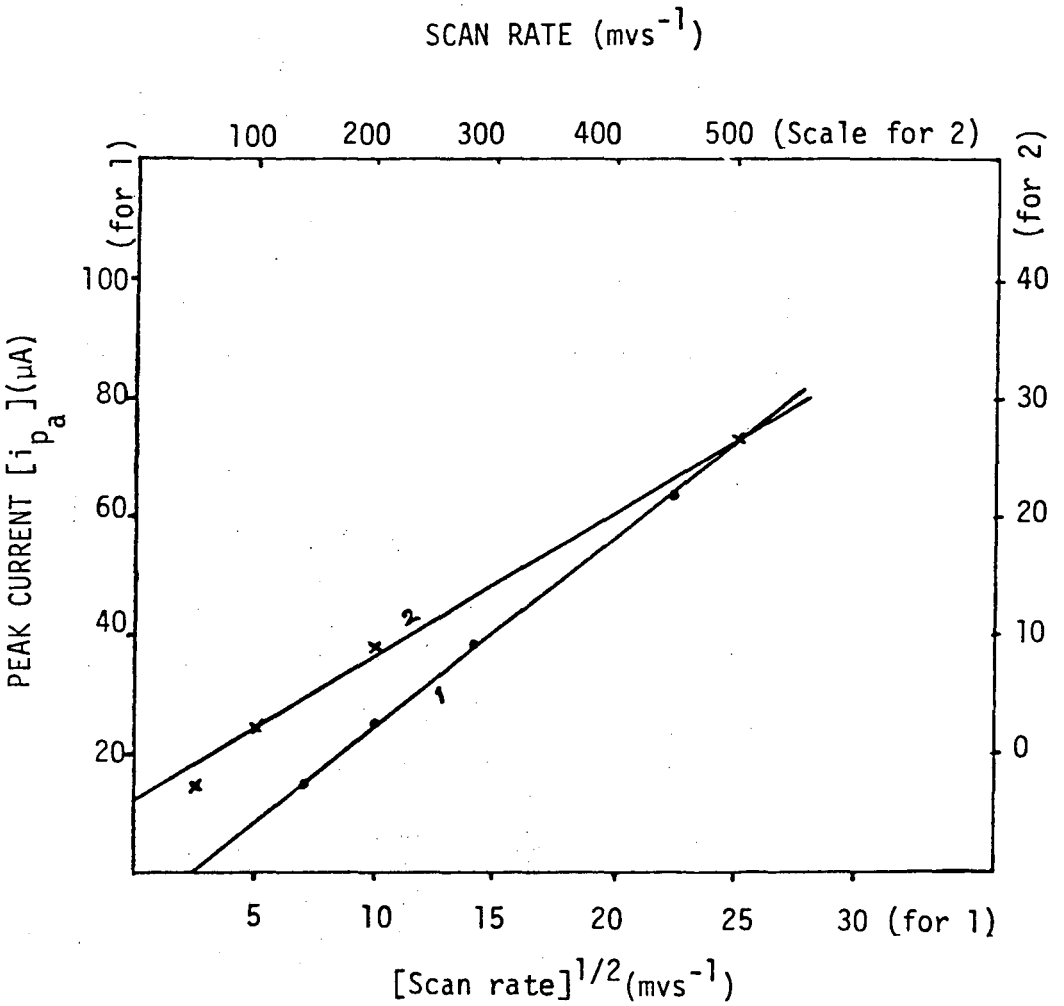


Fig. 5.1.5.6. Scan rate dependence of the anodic peaks; 10^{-3}M Fe-TSPc in 0.05M H_2SO_4 (N_2 satd.). Au disk electrode. 1 - anodic peak at +0.5V; 2 - anodic peak at -0.16V.

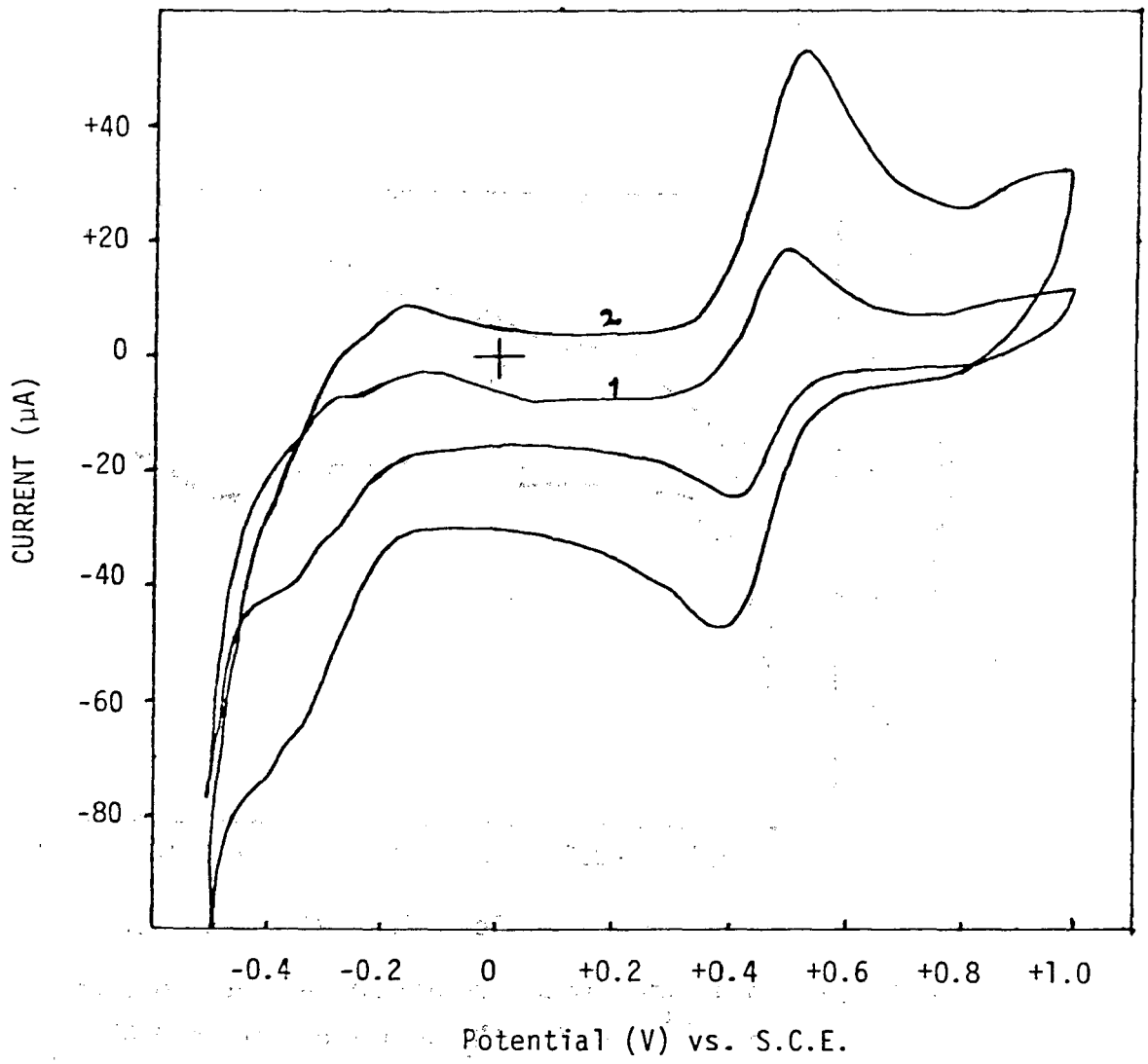


Fig. 5.1.5.7 Effect of extending the cathodic voltage limit. 10^{-3}M Fe-TSPc in 0.05M H_2SO_4 (N_2 satd.). Au electrode. 1 - 50mv/s; 2 - 200mv/s.

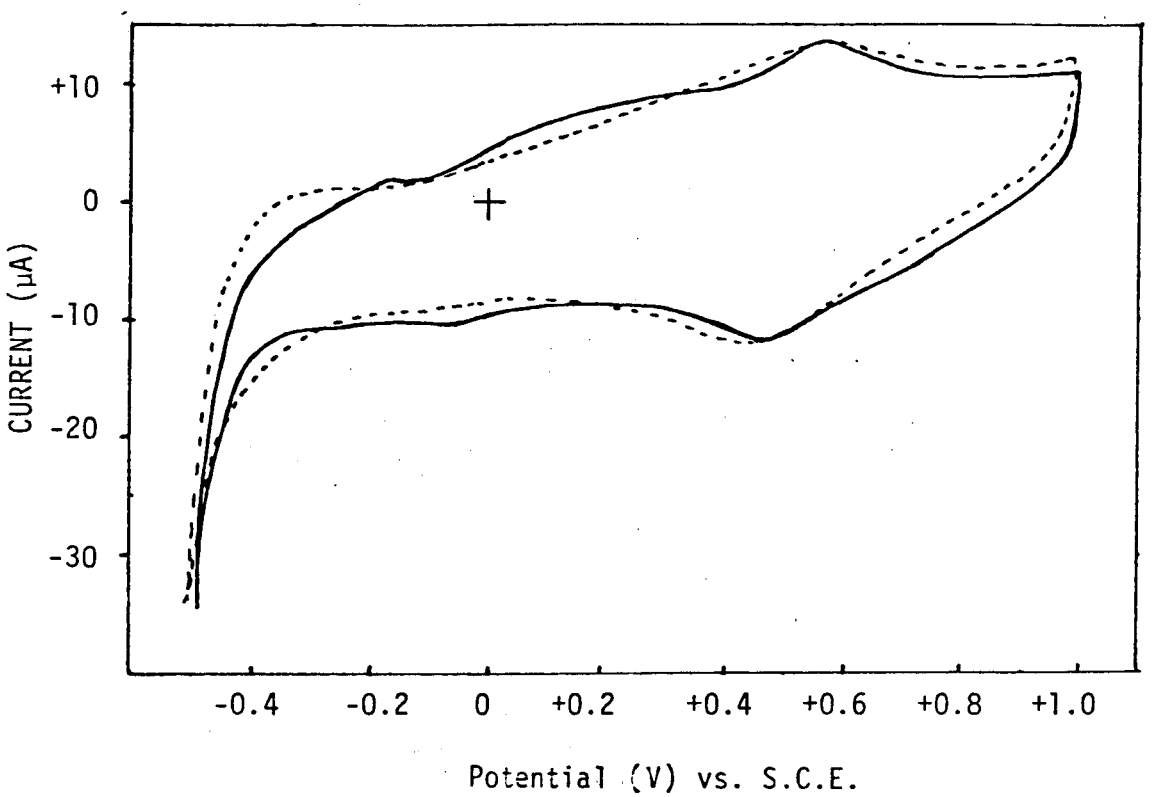


Fig. 5.1.5.8 Voltammogram of preadsorbed Au electrode from 0.05M H_2SO_4 + 10^{-3}M Fe-TSPc (N_2 satd.) dipped in 0.05M H_2SO_4 (N_2 satd.) Polished electrode dipped in 0.05M H_2SO_4 (N_2 satd.) - dashed line. Scan rate = 200mv/s.

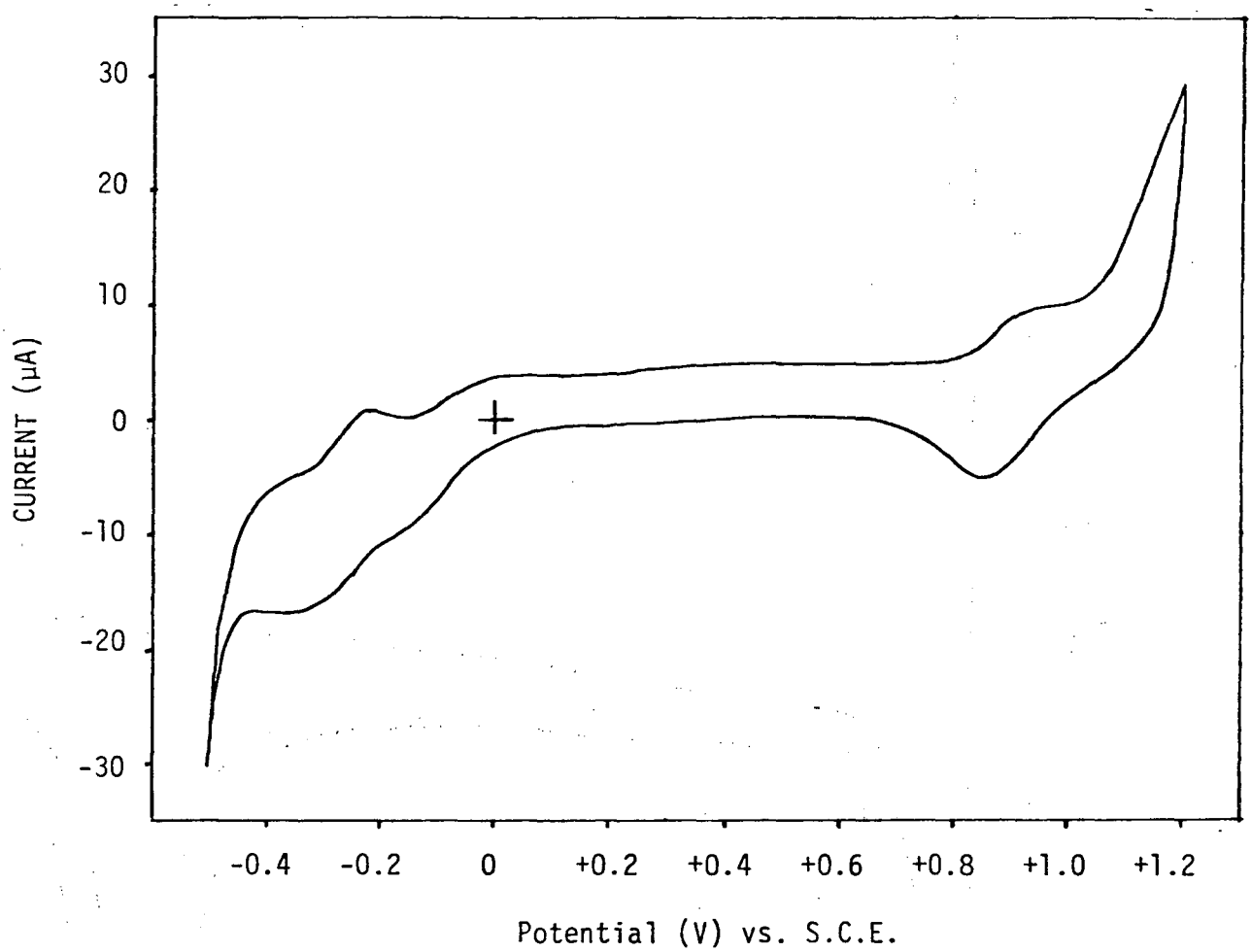


Fig. 5.1.5.9 Voltammogram on Au disk electrode in 0.05M H_2SO_4 (N_2 satd.) containing 5 x 10^{-4}M H_2-TSPc. Scan rate = 50mv/s.

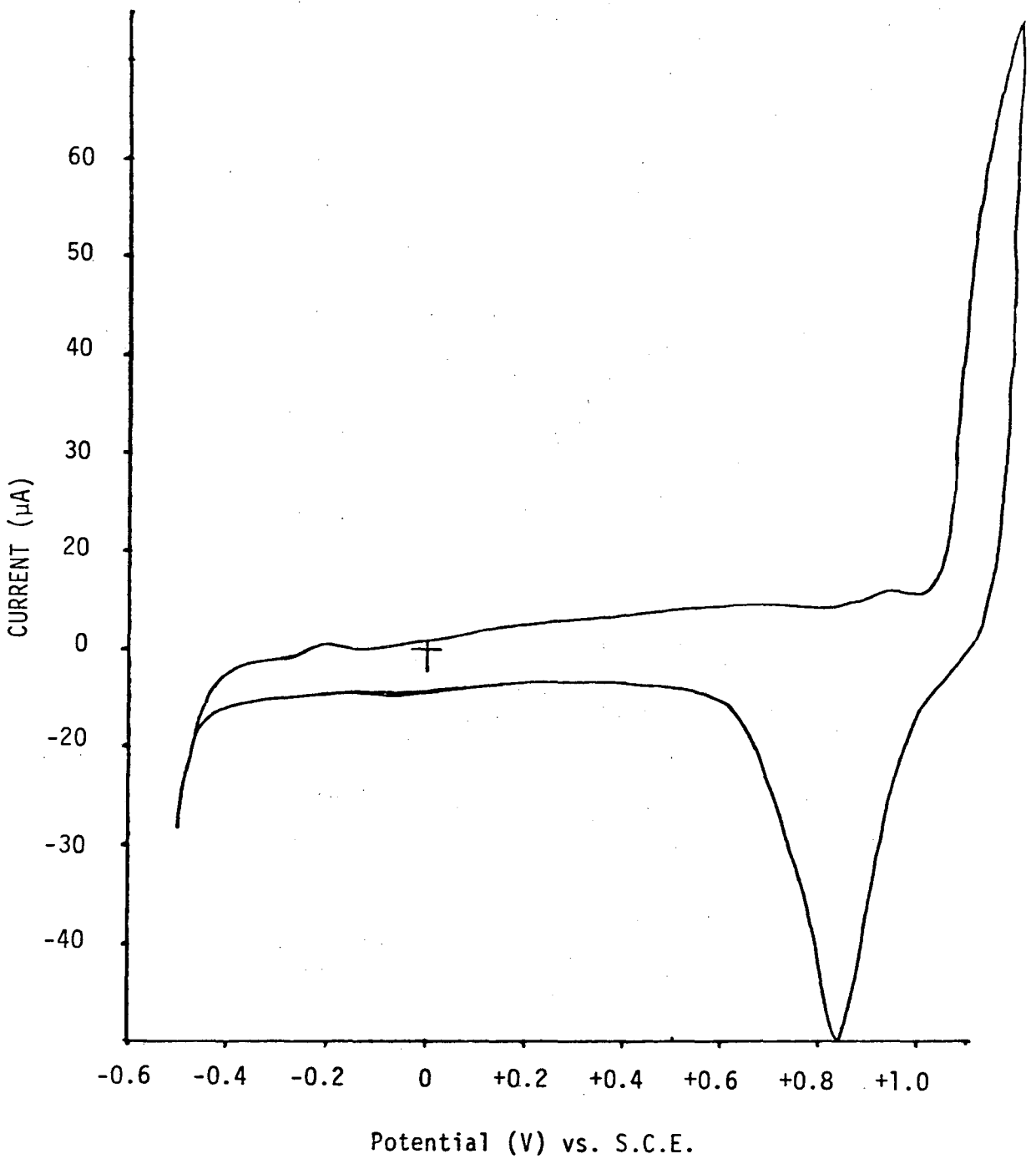


Fig. 5.1.5.10 Voltammogram of preadsorbed Au disk electrode from 0.05M H_2SO_4 + 5 x 10^{-4}M H_2-TSPc (N_2 satd.) dipped in 0.05M H_2SO_4 (N_2 satd.). Scan rate = 200 mv/s.

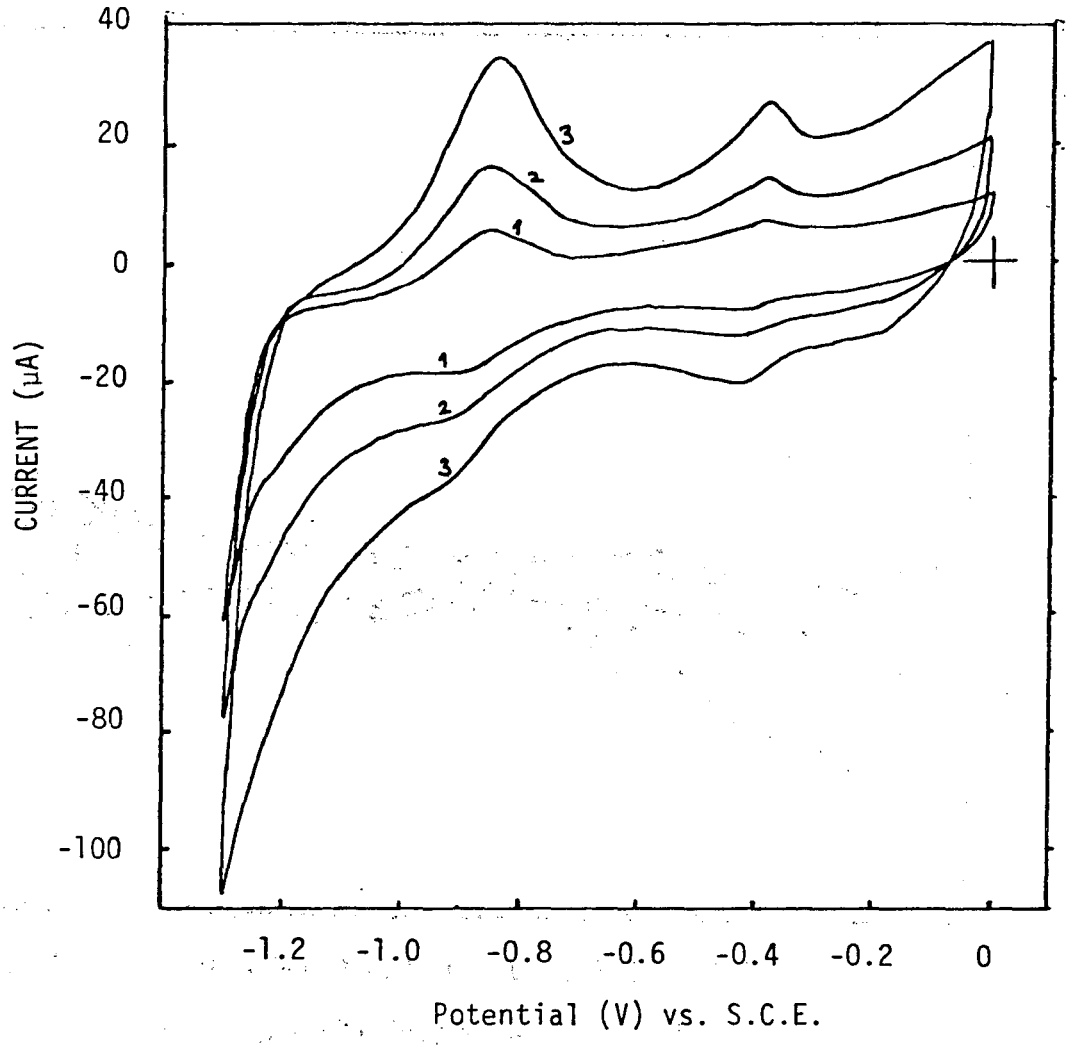


Fig. 5.1.5.11 Voltammograms at different scan rates on Au disk electrode in 0.1M NaOH (N_2 satd.) containing 10^{-3}M Co-TSPc. 1 - 50mv/s; 2 - 100vm/s; 3 - 200mv/s.

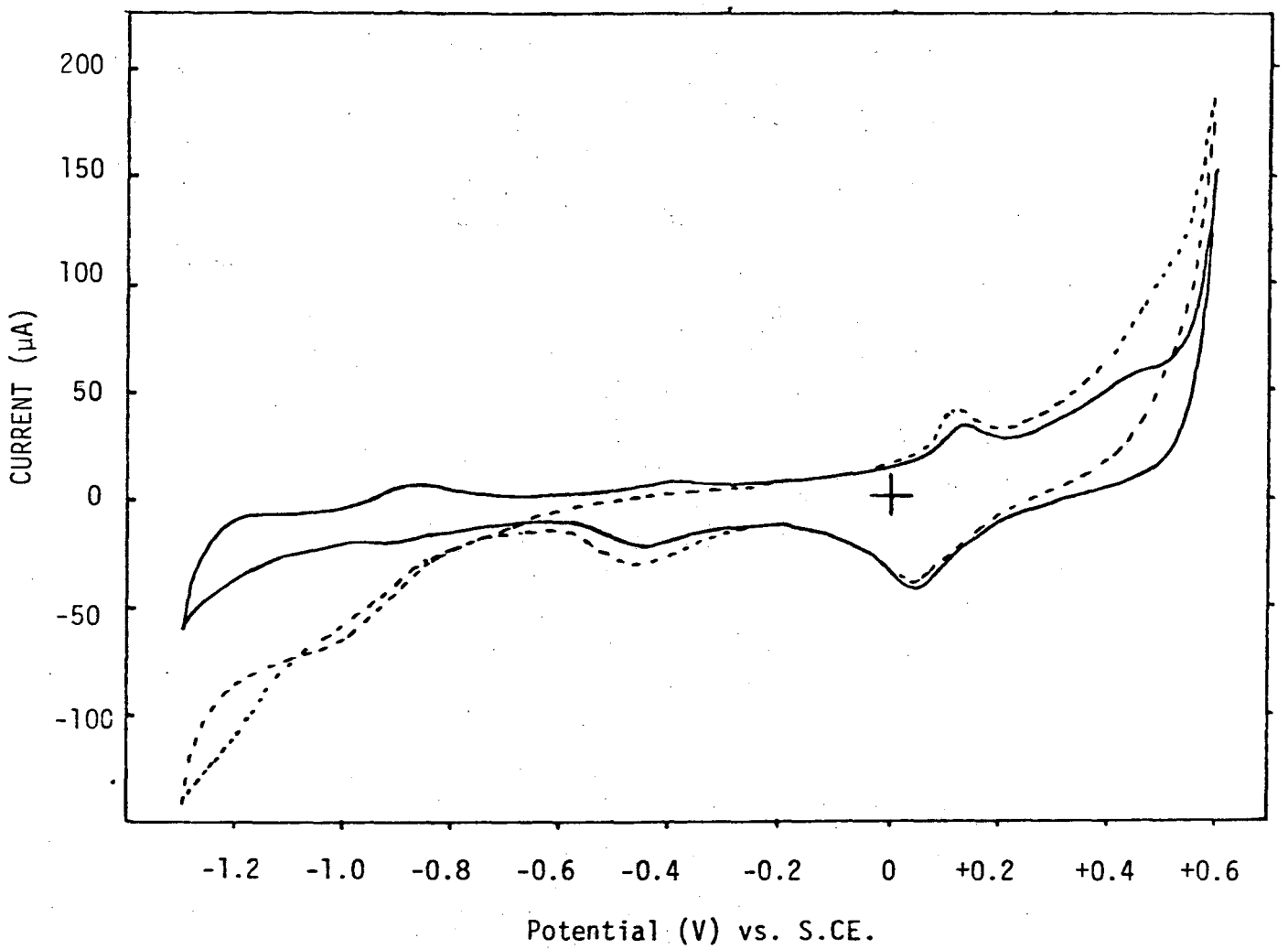


Fig. 5.1.5.12 Effect of extending the anodic voltage limit. 10^{-3}M Co-TSPc in 0.1M NaOH (N_2 satd.). Scan rate = 50mv/s. Au electrode. Solid line - without rotation; dashed line - with rotation.

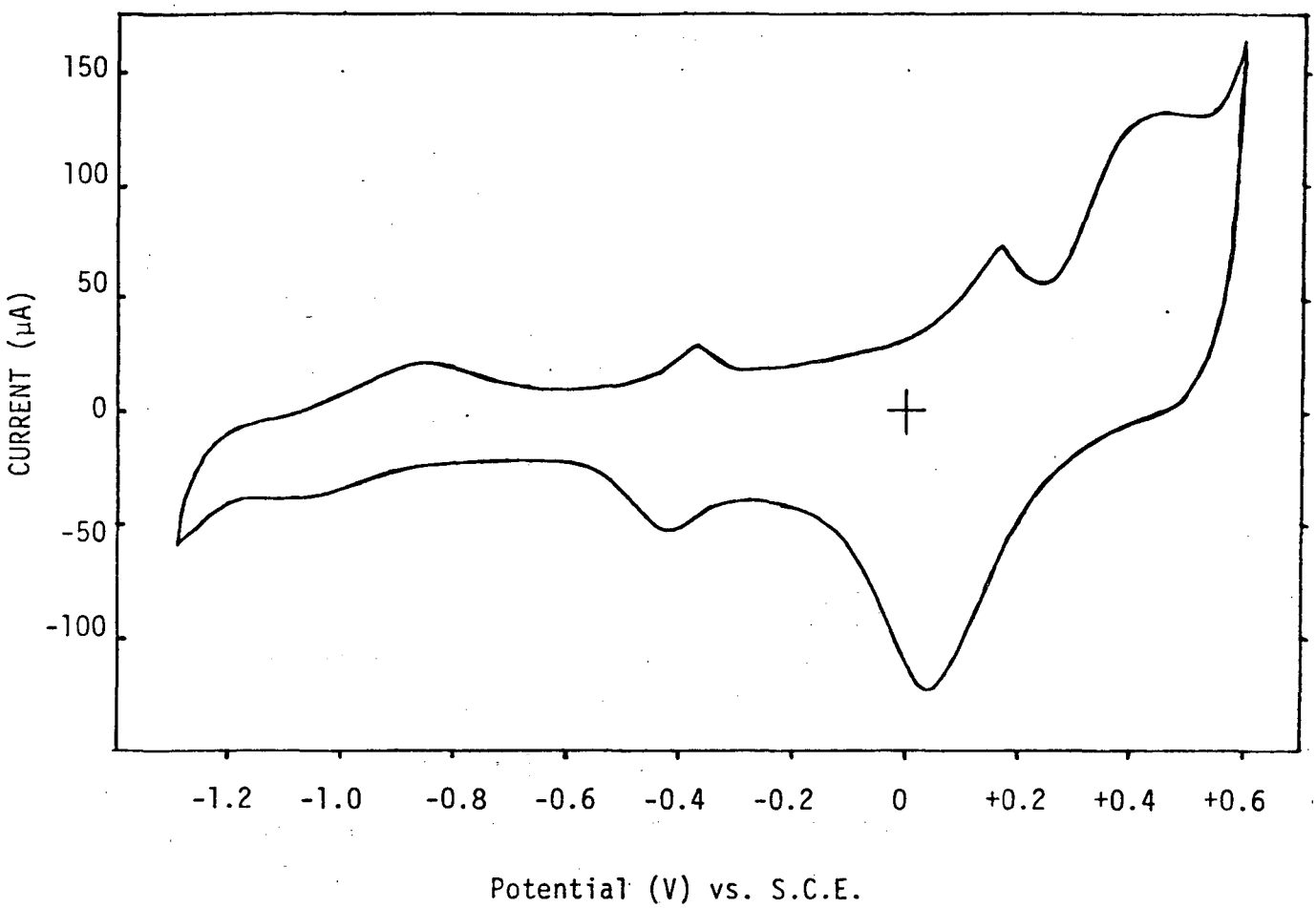


Fig. 5.1.5.13 Voltammogram of preadsorbed Au electrode from 0.1M NaOH + 10^{-3}M Co-TSPc (N_2 satd.) dipped in 0.1M NaOH (N_2 satd.). Scan rate = 200mv/s.

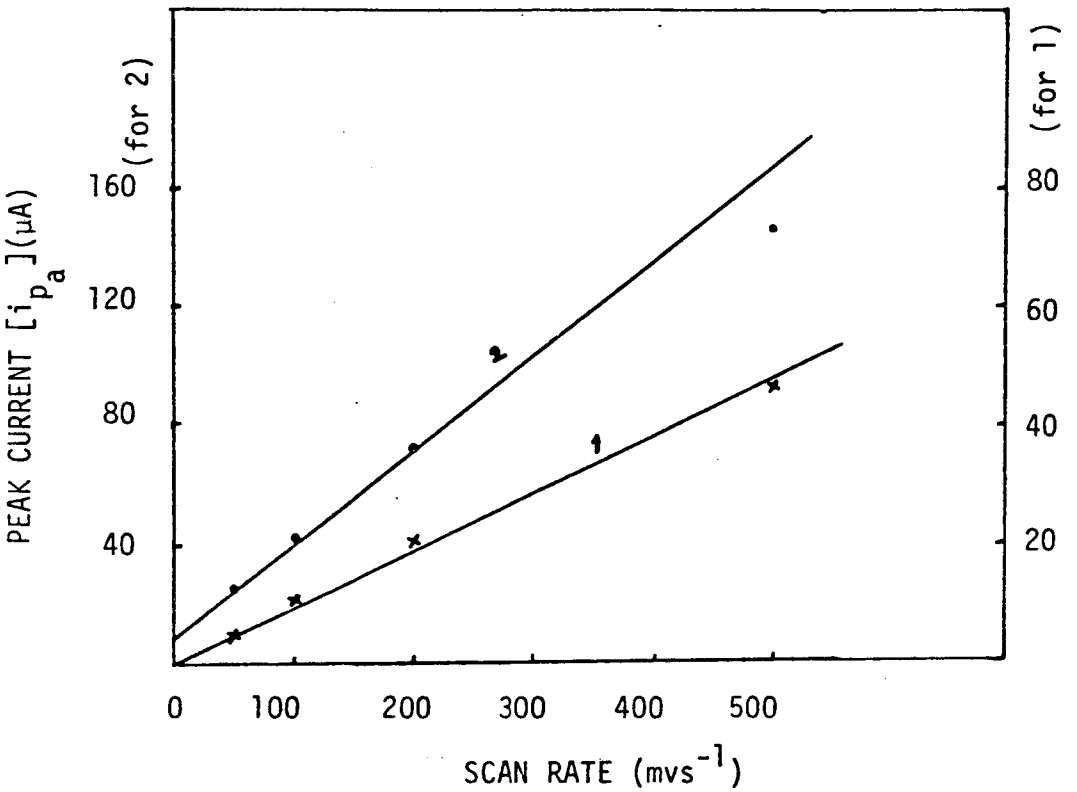


Fig. 5.1.5.14 Scan rate dependence of the anodic peaks on Au electrode. Preadsorbed electrode from 0.1M NaOH + 10^{-3}M Co-TSPc (N_2 satd.). 1 - anodic peak at -0.85V; 2 - anodic peak at +0.14V.

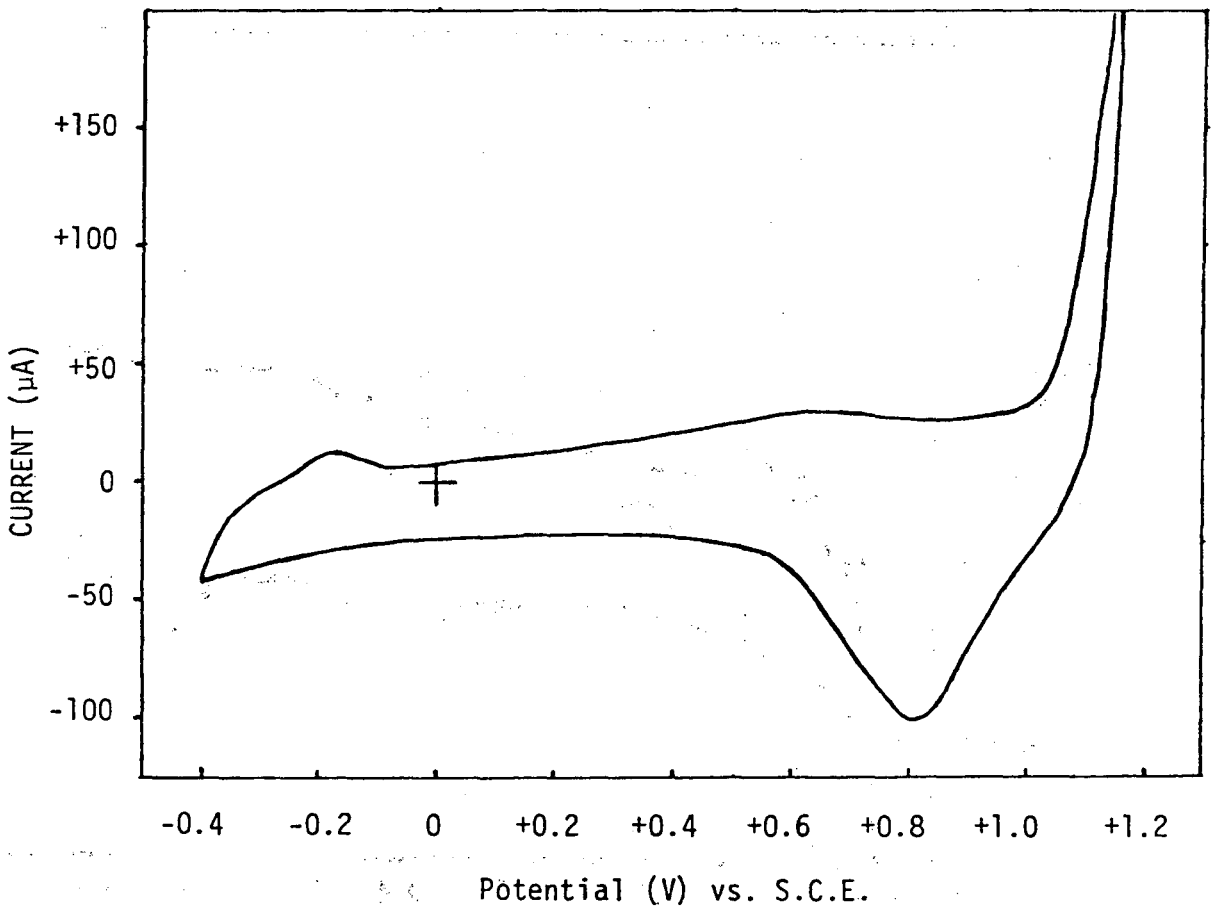


Fig. 5.1.5.15 Voltammogram on Au disk electrode in 0.05M H_2SO_4 (N_2 satd.) containing 10^{-5}M Co-TSPc. Scan rate = 500mv/s.

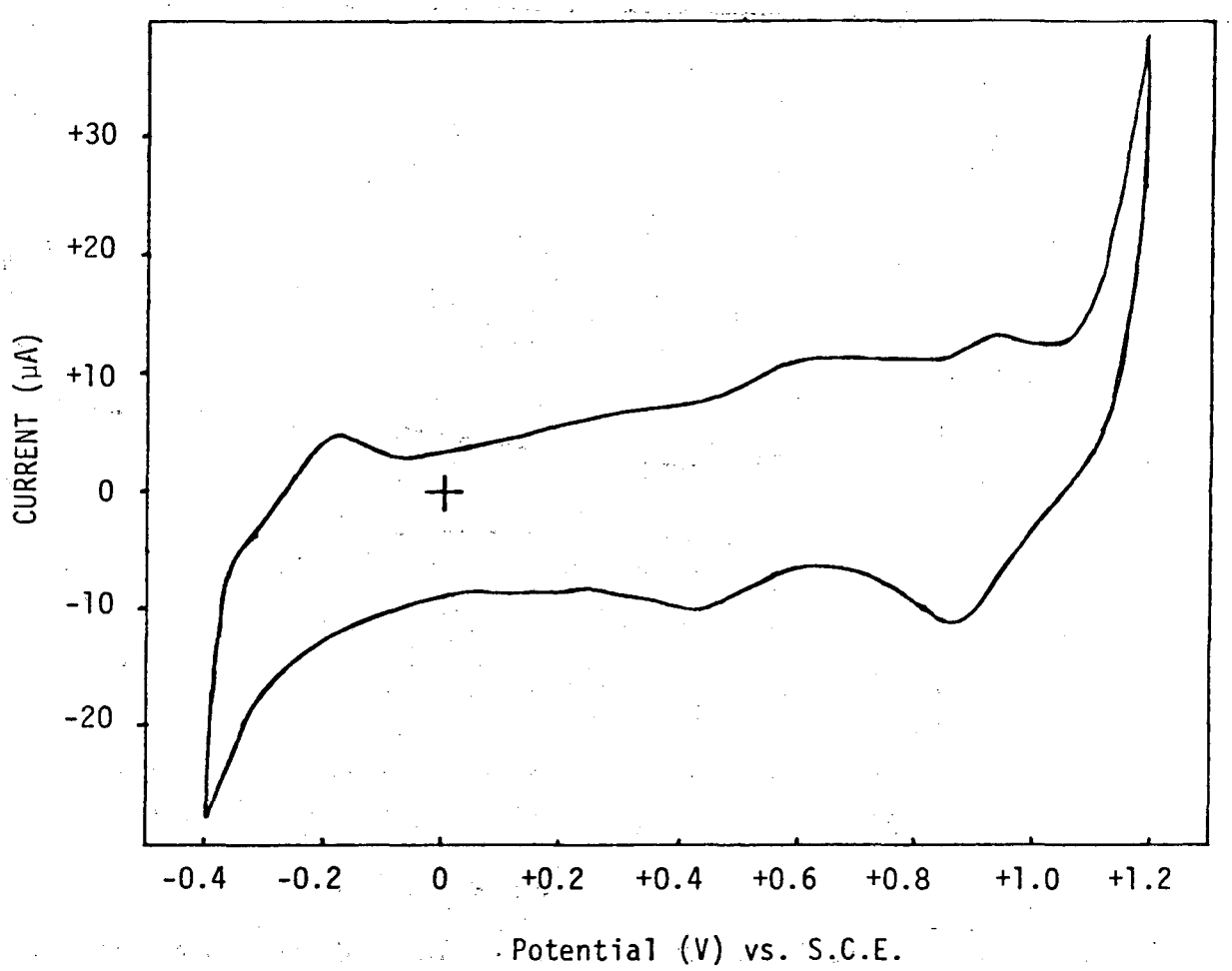


Fig. 5.1.5.16 Voltammogram on Au disk electrode in 0.05M H_2SO_4 (N_2 satd.) containing 10^{-4}M Co-TSPc. Scan rate = 200mv/s.

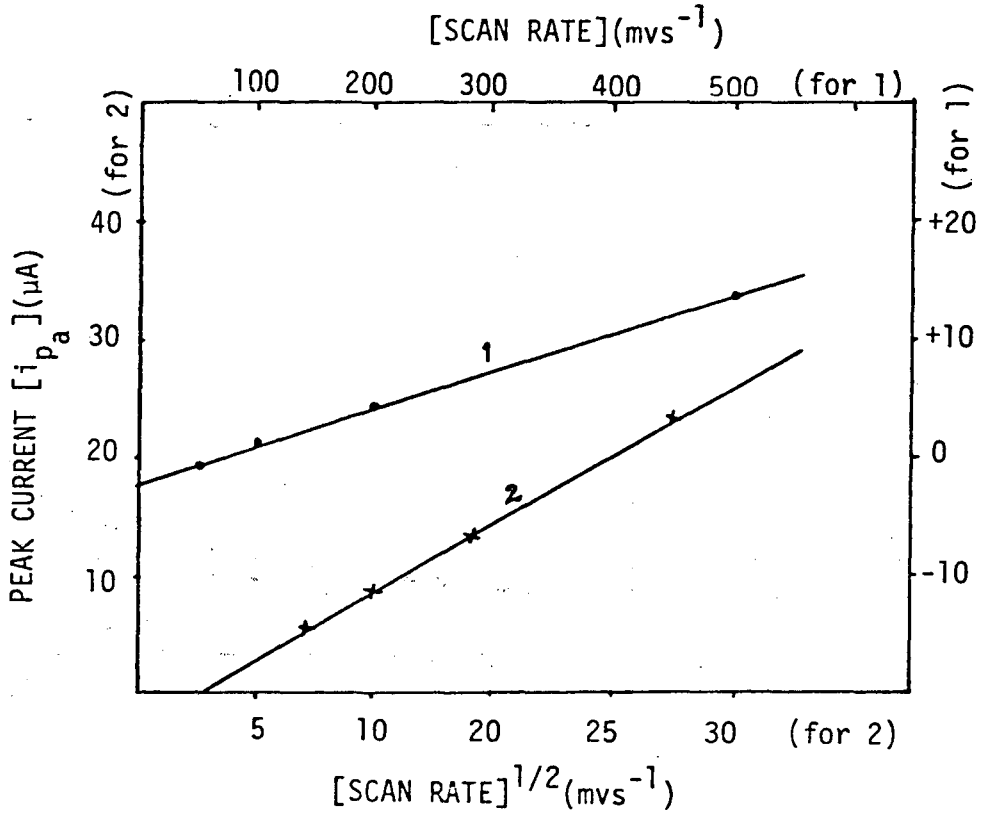


Fig. 5.1.5.17 Scan rate dependence of the anodic peaks on Au electrode. 10^{-4}M Co-TSPc in 0.05M H_2SO_4 (N_2 satd.). 1 - peak at -0.17V; 2 - peak at +0.94V.

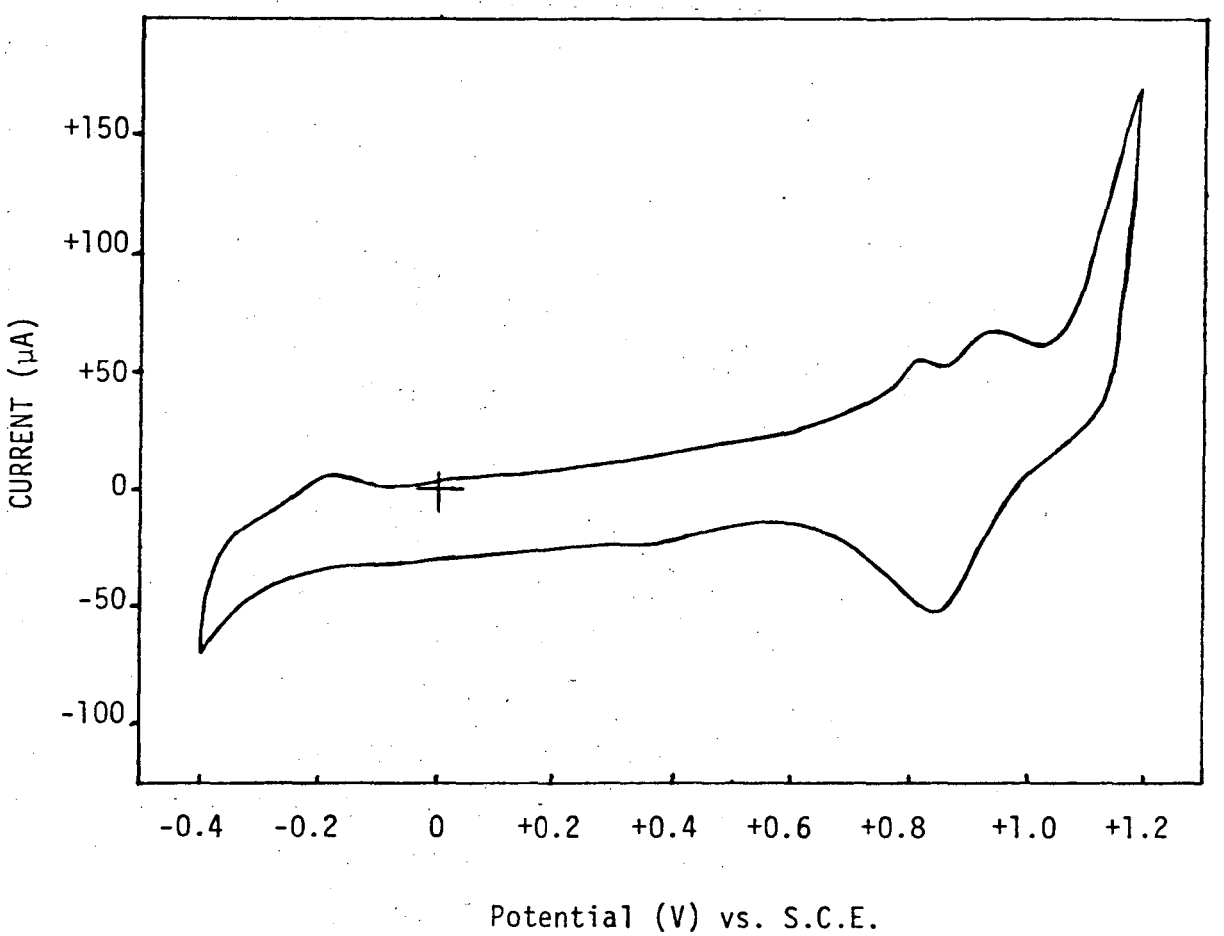


Fig. 5.1.5.18 Voltammogram on Au disk electrode in 0.05M H_2SO_4 (N_2 satd.) containing 10^{-3}M Co-TSPc. Scan rate = 200mv/s.

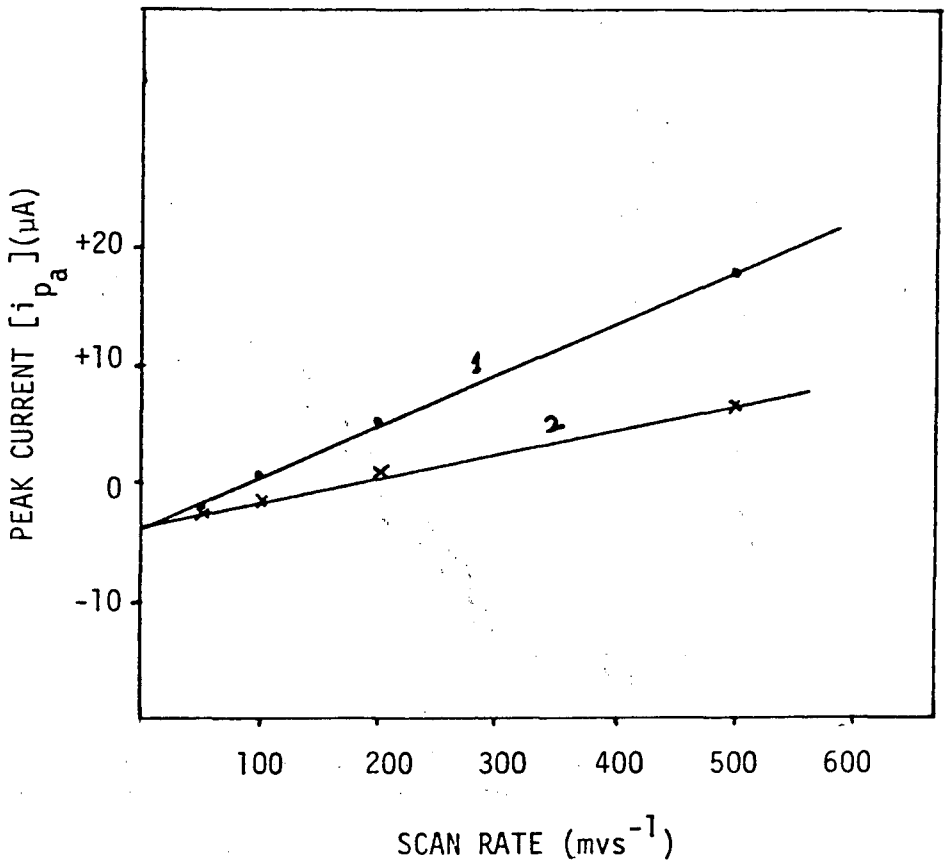


Fig. 5.1.5.19 Scan rate dependence of the anodic peak at -0.17V. 10^{-3}M Co-TSPc in 0.05M H_2SO_4 (N_2 satd.). Au electrode. 1 - in solution; 2 - at the surface.

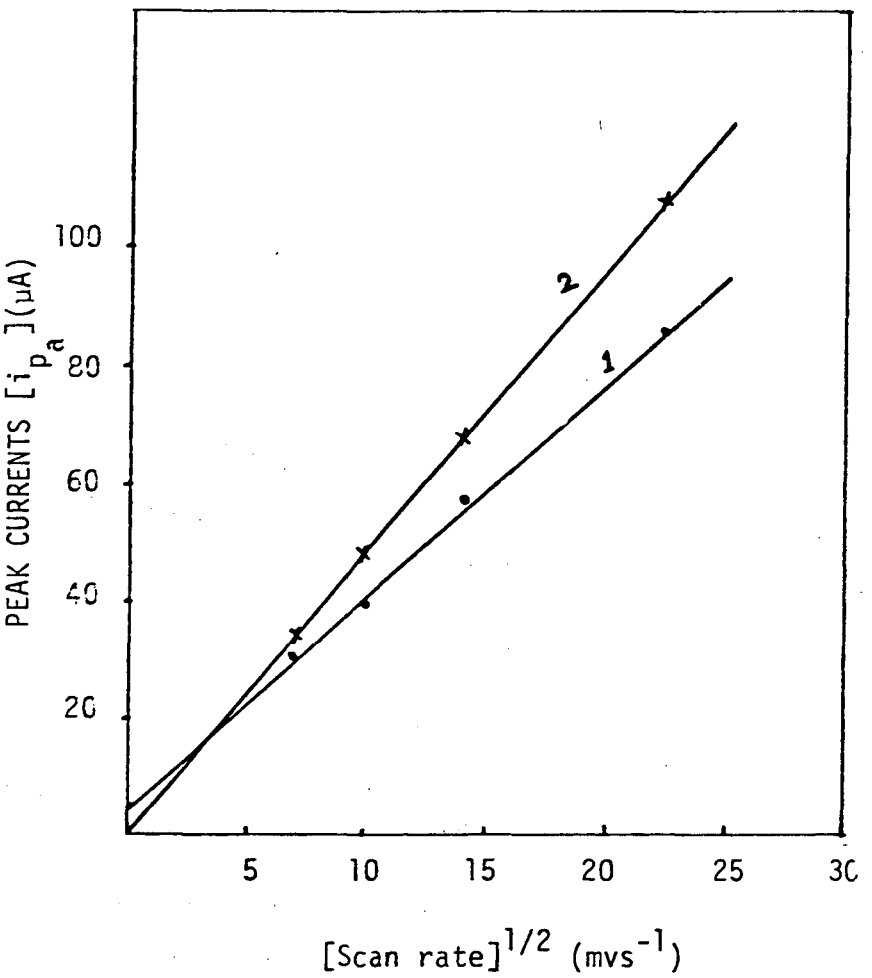


Fig. 5.1.5.20 Scan rate dependence of the anodic peaks on Au electrode. 10^{-3}M Co-TSPc in 0.05M H_2SO_4 (N_2 satd.). 1 - peak at +0.08V; 2 - peak at +0.94V.

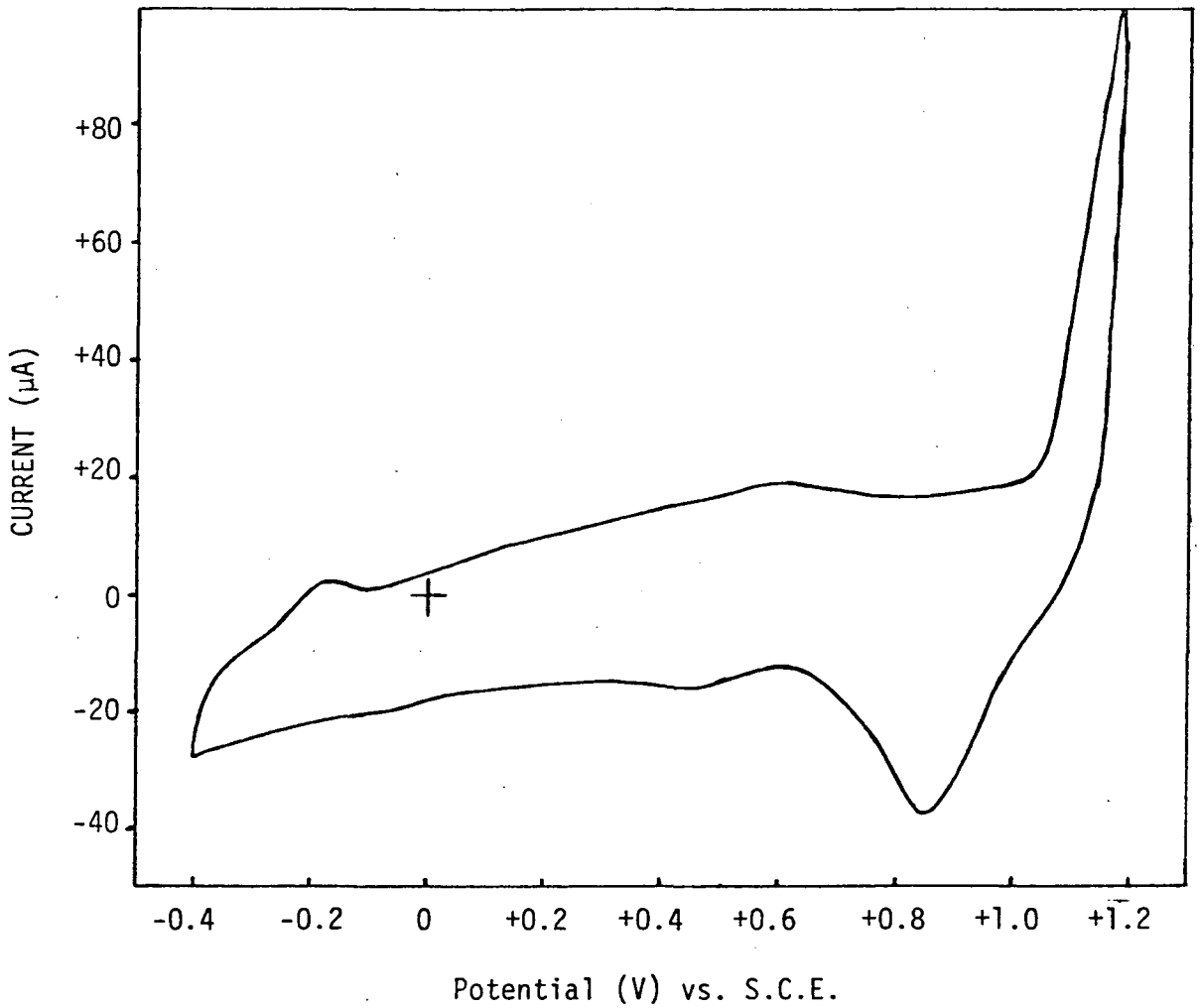


Fig. 5.1.5.21 Voltammogram of preadsorbed Au electrode from 0.05M H_2SO_4 + 10^{-3}M Co-TSPc (N_2 satd.) dipped in 0.05M H_2SO_4(N_2 satd.). Scan rate = 200mv/s.

5.1.6 THE UV-VISIBLE ABSORPTION AND VOLTAMMETRY MEASUREMENTS OF MACROCYCLICS

S. Zecevic

OBJECTIVES

The UV-visible absorption measurements of tetrasulphonated phthalocyanines Co(II)TSPc, Fe(III)TSPc and H_2TSPc have been undertaken with the aim of getting new information about the chemistry of these compounds in solution phase. These results as well as the voltammetry measurement results will be the starting base in dealing with the uv-visible specular reflectance spectroscopy and also with Raman Spectroscopy, which should give us new information about the nature of the interaction between the electrode surface and these macrocyclics.

THE UV-VISIBLE ABSORPTION MEASUREMENTS

BACKGROUND

Amongst many papers which have dealt with the optical properties of phthalocyanines in solution phase, two questions have arisen as very intriguing: The question of an oxygen adduct with macrocyclics and the question concerning the macrocyclics aggregation i.e. the existance of monomer, dimer or perhaps higher forms of these compounds. For the time being, there is no unique answer to these questions. Different authors have investigated under different experimental conditions and mainly pure water solutions (without any additions) were studied. In the case of CoTSPc, alkaline solutions were also examined, but practically nothing was done in acid media. Yet, the investigated macrocyclics concentration were relatively low and in a very narrow range 10^{-6}-10^{-5}M.

The present study has been undertaken with the aim of clarifying the behavior of Co(II)TSPc, Fe(III)TSPc and H_2TSPc in acid, alkaline and neutral salt solutions as well as in pure water solutions without any additions, in a much larger concentration range from 5×10^{-7} to 10^{-3}M.

EXPERIMENTAL

Metal-tetrasulfonated phthalocyanines have been synthesized and purified according to the method of Weber and Busch (1), whereas metal-free tetrasulfonated phthalocyanine was obtained by a direct sulfonation of H_2Pc (Kodak) by the procedure described by Linsted and Weiss (2).

Four different types of water were used: common distilled, deionized, ultra pure (reverse osmosis) and pyrolytic water. The following concentrations of the macrocyclics were studied: 5×10^{-7}, 10^{-6}, 10^{-5}, 10^{-4} and 10^{-3}M in the case of Co(II)TSPc and 2×10^{-6}, 2×10^{-5}, 2×10^{-4} and 2×10^{-3}M in the case of Fe(III)TSPc and H_2TSPc with and without an addition of

0.05M H_2SO_4 (Ultrex), 0.1M NaOH (special low carbonate pellets NaOH-J. T. Baker) or 0.05M Na_2SO_4 (AR grade-Fisher).

Solutions were prepared in the air atmosphere and then the saturation with different purified gases was done. In the case of Co(II)TSPc, purified He and O_2 were used, and in the case of Fe(III)TSPc H_2, N_2 and O_2 were used. The saturations were carried out at room temperature as well as elevated temperature (70°C), but, absorption spectra were recorded always at room temperature. In experiments where the aging effect was studied, prepared solutions were left in closed glass vials (without any treatment) at room temperature and at 70°C, and absorption spectra were recorded during that time (up to one month). The influence of H_2O_2 and several organic solvents was also examined (methanol, ethanol, ethyl glycol and pyridine).

Absorption spectra were recorded by spectrophotometer (Carry 14) in cells of 100, 10, 1 and 0.1mm optical path length for different concentrations of the order of 10^{-6}, 10^{-5}, 10^{-4} and 10^{-3}M respectively.

RESULTS AND DISCUSSION

1.1 Absorption spectra and aging effect

1.1a. Absorption spectra of Co(II)TSPc

The uv-visible absorption spectra of Co(II)TSPc in water solutions without any additions show two areas of interest, the 600-700 nm region and 200-400 nm region. However, it is very difficult to say precise wave length positions of absorption peaks because they depend on concentration (Figs. 1 and 2). Nevertheless, in the visible region two absorption peaks can be recognized. Their relative heights depend on concentration and time, that means this behavior does not obey the Lamber-Beer Law. Furthermore, this means that not only one but at least two different forms of CoTSPc are present in solution. Acccording to the literature the higher wave length peak is attributed to the monomer form and the lower wave length peak is attributed to the dimer form of CoTSPc and it is shifted toward dimer form as the total concentration increases.

It should be noted that the height of the monomer peak, at very low concentrations, decreases during time (Fig. 9), but this does not mean that a degradation of CoTSPc occurs. In consideration of the fact that at the same time the dimmer peak increases and the shape of the spectrum in the uv-region tends to one of higher concentration, we believe that the dimerization process occurs. It is interesting, for example, to note that the spectrum for 10^{-6}M CoTSPc concentration becomes after 32 days practically the same as the spectrum of the fresh 10^{-5}M solution. Similar changes were observed with 5 x 10^{-7}M solution.

Absorption spectra of CoTSPc in acid and alkaline solutions are, at first glance, very similar to those in pure water solutions (Figs. 3-6). However, the changes during time are quite opposite to those in pure water solutions. In the uv-region the spectrum of the more concentrated solutions, during time, gradually takes the shape of those of lower concentration solutions. In the visible region the dimer peak (626 nm) decreases during time, whereas the peak at 668 nm, whose position is very stable and independent of concentration, at first increases, and then decreases (Figs. 8, 10 and 11), when the absorption at the whole region (200-750 nm) decreases too. Hence, it seems that during time, at first a transformation of CoTSPc occurs and then a degradation process takes place.

It should be noted that these changes are more rapid in alkaline than in acid solutions.

1.1b. Absorption spectra of Fe(III)TSPc

Absorption spectra of Fe(III)TSPc water solutions look simpler than those of Co(II)TSPc, particularly in the uv-region (Fig. 19). Both the uv and visible region contain one peak and one shoulder. In terms of the monomer/dimer equilibrium, the shorter wave length peak in the visible region is attributed to the dimer form of FeTSPc and the shoulder is attributed to the monomer form.

In regard to the stability of Fe(III)TSPc solutions, it was found that only pure water solutions and solutions which contain a neutral salt (0.05M Na_2SO_4) were stable during time. However, a gradual decrease of absorption in the whole region during time, was found in acid and particularly in alkaline solution. Contrary to the CoTSPc acid and alkaline solution, this decrease of absorption starts immediately after the solution preparation. This aging effect was very pronounced at elevated temperature (70°C) and it was observed even in neutral salt and pure water solutions.

1.1c. Absorption spectra of H_2TSPc

Absorption spectra of H_2TSPc are rather different from those of Co(II)TSPc and FE(III)TSPc. First of all, the visible region contains more than two peaks, and on the other hand, pH effect is tremendous: The "acid" spectrum is quite different from the spectrum of alkaline solutions (Fig. 20). Nevertheless, there are some indications that the monomer-dimer equilibrium exists here too, that will be shown later.

1.2 The Influence of Oxygen

1.2a. Co(II)TSPc solutions

What is the main cause for the time change of spectra? In the case of pure water solutions it seems that the dimerization of the CoTSPc monomer is responsible for these changes, because, there is no indication that a degradation occurs, and on the other hand the spectra of very low concentrated solutions during time take the shape

of those of more concentrated solutions. Yet, these later are quite stable during time.

However, the changes in acid and alkaline solutions are attributed to the reaction of CoTSPc with molecular O_2 which is present in solution. This assumption was confirmed by independent experiments in which the acid, alkaline, water solutions of neutral salt Na_2SO_4 and pure water solutions were saturated with O_2 during a long period of time (several days). During saturation the monomer peak (662 nm) disappears, the 668 nm peak appears (the oxygen adduct peak (3-5)) and gradually increases, while the dimer peak (626 nm) gradually decreases and finally disappears. It should be noted that this behavior is observed only in acid and alkaline solutions but not in neutral Na_2SO_4 or pure water solutions. These later solutions were unaffected by O_2 and during a longer saturation with O_2 the same changes occured as during time in closed vials. Furthermore, the changes in Na_2SO_4 solution were almost identical to those in pure water solutions and when experiments were carried out at 70°C all changes were more rapid and more pronounced (Fig. 13).

So, it can be concluded that the oxygen adduct of Co(II)TSPc is formed only in acid and alkaline media but due to its relatively low stability, a slow irreversible degradation of this species takes place.

These results are in disagreement with findings of Wagner et al. (3) who reported that after acidifying the oxygenated alkaline solution, the oxygen adduct peak immediately disappears and after a repeated alkalization this peak reappears, that should mean that the oxygen adduct is formed only in alkaline solutions. These authors claim that the oxygen adduct is formed only at pH higher than 12. We have also done similar experiments: the oxygenated alkaline solution of 10^{-5}M Co(II)TSPc was undertaken to the successive acidifying alkalization cycles and absorption spectra were recorded. However, the oxygen adduct peak (668 nm) was always present. The only difference between acid and alkaline solutions was with respect to the height of this peak being higher in alkaline solutions.

Finally, it should be added that the rate of the oxygen adduct formation is much higher in alkaline than in acid solutions (more than 10 times) (Figs. 10, 11, 12).

1.2b. Fe(III)TSPc solutions

Although the nature of the time changes of Fe(III)TSPc spectra is different from those of CO(II)TSPc, in order to see whether an oxygen adduct formation in Fe(III)TSPc solutions takes place, the influence of O_2, H_2 and N_2 was studied. Water solutions of 2 x 10^{-5}M Fe(III)TSPc in neutral, acid and alkaline media, at room and elevated temperature (70°C) were saturated with these gases for more than 10 days. However, contrary to the case of Co(II)TSPc, there was no peak sensitive to the presence of any of the used gases. This means that Fe(III)TSPc does not form an oxygen adduct. The situation in the literature with respect to this question is not quite clear

because some authors (12) claim that only Fe(II)TSPc forms an oxygen adduct, and some others (4) claim that even Fe(III)TSPc can do it. However, it seems that these later authors were not quite sure which form of FeTSPc they used.

We tried to reduce Fe(III)TSPc in solution phase by bubbling H_2 at 70°C and also by an electrochemical reduction using Au electrode. However, there was no success.

1.2c. H_2TSPc solutions

Having in mind that H_2TSPc is not a catalyst for oxygen reduction reaction, we did not investigate the influence of O_2 in this case. At this moment, it should be noted that Cu(II)TSPc also does not form an oxygen adduct (10), although it shows oxygen reduction catalysis.

1.3 The release of O_2 from the oxygen adduct

With respect to this question we have also found a disagreement with literature data (3-5). Our results have shown that this process is possible even at room temperature by bubbling He, but after rather long period of time (more than 10 days) and without full reversibility. The oxygen adduct peak could be considerably depresed but the height of the dimer peak is not changed. This process and also the formation of the oxygen adduct are much faster at elevated temperature (70°C), but at the same time a considerable degradation of the macrocyclic was found (Fig. 15).

Finally, this oxygenation-deoxygenation cycle can be repeated a few times but without full reversibility, just due to the irreversible degradation of the macrocyclic.

1.4 The effect of impurities and foreign substances

1.4a. The effect of foreign substances

In view of the dimer-monomer equilibrium it is important to point out that this equilibrium is greatly influenced by foreign ions present in solution. The equilibrium is shifted toward dimer form as the concentration of foreign ions increases. In the case of Co(II)TSPc solutions this influence can be observed even at very low concentration of Na_2SO_4 such as 10^{-7}M (Fig. 17). The similar effect of Na_2SO_4 was observed also in the case of Fe(III)TSPc and H_2TSPc too (Fig. 21).

1.4b. The effect of different types of distilled water

It should be noted that even distilled water can show a significant influence on the absorption spectra of Co(II)TSPc solutions. In solutions prepared with common distilled and deionized water, the monomer peak is considerably depressed and the rate of the oxygen adduct formation is lower.

It is very surprising, however, that the pyrolytic water has shown almost the same results as obtained with a common distilled water.

This water effect was found with Fe(III)TSPc solutions too, but in this case it could be observed at the dimer peak rather than at the monomer peak. It should be noted that this water effect was less pronounced wlhen the macrocyclics concentration was higher and at concentration of 10^{-3}M it disappeared. However, there was no effect of water in the case of H_2TSPc.

1.4c. The influence of some organic solvents

The monomer peak of Fe(III)TSPc solutions is at about 668 nm, that is very close to the main peak of Fe(II)TSPc at 670 nm (12). In order to eliminate the doubt that the monomer peak is in fact Fe(II)TSPc peak, we investigated the influence of some organic solvents such as methanol, ethanol, ethylglycol and pyridine. It is known that some of these solvents favor the monomer peak in the case of Co(II)TSPc and Cu(II)TSPc (14). Our experiments have shown the same results. In the presence of these solvents, the monomer peak is considerably increased and the dimer peak is decreased. This effect was more pronounced when the organic solvent concentration was higher. The similar effect was observed with H_2TSPc solution in the presence of ethanol in agreement with the literature data (6).

1.4d. The influence of H_2O_2

H_2O_2 has shown different influence on the absorption spectra of Co(II)TSPc and Fe(III)TSPc solutions at different pH.

Fe(III)TSPc - After an addition of H_2O_2 in Fe(III)TSPc solution (10^{-5}M concentration of H_2O_2 as that of Fe(III)TSPc), in the whole region of the spectrum, absorption was gradually decreasing during time in all cases except in acid solution (Fig. 22). Namely, after a very sharp decrease of absorption immediately after H_2O_2 has been added, a gradual increase of absorption occured during time, but absorption never reached the value observed before the H_2O_2 addition.

Co(II)TSPc - In pure water solution a considerable decrease of the monomer peak ws found after H_2O_2 has been added and this decrease continued during a few days (Fig. 23). In the presence of Na_2SO_4, very small absorption decrease was observed at dimer peak, whereas in acid solution a significant increase of the 668 nm peak and decrease of the dimer peak were observed. In fact, the same changes were found as during saturation of this solution with O_2. This means that H_2O_2 increased the rate of the oxygen adduct formation. In alkaline solution, however, it seems that H_2O_2 has speeded up the rate of the oxygen adduct decomposition.

REFERENCES

1. J. H. Weber and D. H. Busch, Inorg. Chem. 4, 469 (1965).

2. R. P. Linstead and F. T. Weiss, J. Chem. Soc., 2975 (1950).

3. D. M. Wagnerova, E. Schwertnerowa and J. Veprek-Siska, J. Coll. Czechoslov. Chem. Commun., 39, 1980 (1974).

4. J. Veprek-Siska, E. Schwertnerova and D. M. Wagnerova, Chimia, 26 25 (1972).

5. L. C. Gruen and R. J. Blagrove, Aust. J. Chem., 26, 319 (1973).

6. K. Bernauer and S. Falab, Helvetica Chim. Acta, 44 1287 (1961).

7. J. H. Weber and D. H. Busch, Inorg. Chem., 4, 472 (1965).

8. Z. A. Schelly, R. D. Farina, and E. M. Eyring, J. Phys. Chem., 74, 619 (1970).

9. Z. A. Schelly, D. J. Harward, P. Hemmes and E. M. Eyring, J. Phys. Chem., 74, 3040 (1970).

10. R. J. Blagrove and L. C. Gruen, Aust. J. Chem., 25, 2553 (1970).

11. K. Fenkart and C. H. Brubeker, J. Inorg. Nucl. Chem., 30, 324 (1968).

12. D. Vonderschmitt, K. Bernauer, and S. Fallab, Helv. Chim. Acta, 48, 951 (1965).

13. B. Z. Nikolic, R. R. Adzic, and E. b. Yeager, J. Electroanal. Chem., 103, 281 (1979).

14. H. Sigel, P. Waldmeir, and Prijsb, Inorg. Nucl. Chem. Lett., 7, 161 (1971).

2. VOLTAMMETRY MEASUREMENTS

EXPERIMENTAL

All investigations were done on OPG disk electrode in N_2 atmosphere. The starting electrolyte was 0.05M Na_2SO_4. After saturating this solution with N_2 (30 minutes) 1 ml of 10^{-3}M tetrasulfonated phthalocyanine water solution was added into 100 ml of electrolyte and 10^{-5}M solution was obtained. After voltammetry measurements had been done pH of the solution was measured by using a pH-meter. In order to get appropriate pH value of the electrolyte, a small amount (1 ml) of concentrated H_2SO_4 or NaOH was added, then voltammetry was done, pH was measured and so on. In this way solutions of pH 1.3 to 12.8 were examined. Some of these experiments were repeated in borate buffer (pH 8,7) also.

The following macrocyclics were studied: Fe(III)TSPc, Co(II)TSPc, Cu(II)TSPc, H_2TSPc, CoPc. These two latter were dissolved in pyridine. In this case pre-adsorption was done by putting a drop of pyridine solution onto the electrode surface and then, washing with pyridine, ethanol and finally with distilled water. The influence of O_2 and H_2O_2 on voltammetry peaks was also studied.

RESULTS AND DISCUSSION

The main attention in this work was directed toward the pH dependence of voltammetry peaks. This dependence of voltammetry peaks for the system Fe(III)TSPc/OPG was already known, and in this work such dependence was also found at several other systems. Furthermore, two quite new peaks were found: one at very anodic potentials just before the oxygen evolution starts and the other at cathodic side close to the hydrogen evolution. Both peaks are very well pronounced and show the same pH dependence with a slope of 59 mV/pH. As a matter of fact almost all observed peaks with all studied phthalocyanines show the same slope. However, in some cases (FeTSPc and CoTSPc) some of the peaks show such dependece only in acid or only in alkaline region (Fig. 30-34). Almost in all cases observed peaks are due to the redox process of the adsorbed species (the peak currents are directly proportional to the scan rate, the peak separation is very small and there is no stirring effect). However, in the case of Cu(II)TSPc and H_2TSPc there are some peaks which are stirring dependent and with anodic or cathodic part only (Fig. 33 and 34).

In all investigated complexes, very anodic potentials (more anodic than the most anodic peak) and also very cathodic potentials (more cathodic than the most cathodic peak) give rise to the destruction of the adsorbed species. Furthermore, the cathodic and anodic limits exert an influence on the shape of voltammogram but in some cases the influence is tremendous (some of the peaks disappear completely) and in some cases this influence is negligible.

The most stable voltammograms are those of Fe(III)TSPc, Co(II)TSPc and CoPc. It is to be noted that FePc(Kodak) did not show any voltammetry peak. In connection with the adsorption of all of tetrasulfonated phthalocyanines, one experimental fact should be pointed out. In order to get adsorbed layers of these complexes, it is not enough to immerse the electrode into the phthalocyanines solution only, but a rather long potential cycling is needed. This problem was not studied in detail but one can say that at least half an hour of cycling is needed to get a good adsorption. In addition, it was observed that this process was speeded up when the rate of cycling was higher but not higher than 20 V s^{-1}. After such a treatment, voltammogram with preadsorbed Fe(III)TSPc was exactly the same as when Fe(III)TSPc was present in electrolyte (Fig. 25).

In order to get some more information about the origins of the voltammetry peaks, the influence of O_2 and H_2O_2 was examined. Results have shown that only one peak is influenced by the H_2O_2 generated or added in electrolyte. This is the most positive peak which is shifted in the direction of anodic current when H_2O_2 was present in the electrolyte, but the peak potential is not changed. This shift toward higher anodic current is attributed to the appearance of anodic oxidation of H_2O_2, which takes place at potentials close to the potential of this peak. It should be noted, however, that this effect of H_2O_2 was observed only in the case of Co complexes in both acid and alkaline regions.

A small H_2O_2 oxidation peak was found in the case of Fe(III)TSPc in alkaline solution too, but the most anodic voltammetric peak of Fe(III)TSPc was not influenced.

In connection with these experiments, one interesting phenomenon, observed in the case of Co(II)TSPc, should be pointed out. Namely at lower scan rates there is no H_2O_2 oxidation peak in the forward scan direction whereas a huge peak appeared in the reverse direction (Fig. 36). This effect is more pronounced when the scan rate is lower and electrode rotation rate is higher. However, it is important to note, that this effect exists only if the cathodic limit is more negative than the potential of the peak denoted as 2. Yet, this phenomenon has been observed only at pH>7.

Amongst all voltammetry peaks, it is obvious that some of them are associated with redox processes of ligand and some of them are probably associated with redox processes of the central metal atom. However, it is surprising that more of the peaks have the same behavior in all the investigated cases.

In earlier investigations, it has been shown that peak #4 in the case of Co(II)TSPc acidic solutions represents the 1-electron surface redox process, and this peak was attributed to the oxidation of Co(II) to Co(III) i.e.

$$[Co(II)TSPc]_{ads} \rightleftharpoons [Co(III)TSPc]^{+}_{ads} + e \qquad (a)$$

However, as one can see in Fig. 31 this peak is also present in alkaline solutions, but, its potential is pH dependent. It is not quite clear what type of process is involvedin this case, but, if reaction (a) is valid and having in mind the fact that macrocyclic complexes of transition metals in the oxidation state III undergo hydrolysis in water solutions (11, 14) one can suppose the following redox reaction:

$$S\text{-}Co(II)TSP.OH_2 + OH^- \rightleftharpoons S - Co(III)TSP.OH + H_2O + e \quad (b)$$

where S represents the graphite substrate . The potential of the Co(III)/Co(II) redox couple according to reaction (b) should shift with pH by -59 mV/pH which is experimentally found. The same peak #4 and the same pH dependence has been also found in the case of CoPc pre-adsorbed from pyridine solution (Fig. 27 and 32).

The similar explanation can be applied for peak #3 in the case of FeTSPc, i.e.

$$S\text{-}Fe(II)TSP.OH_2 + OH^- \rightleftharpoons S - Fe(III)TSP.OH + H_2O + e \quad (c)$$

It should be pointed out that there is a great similarity between FeTSPc and CoTSPc with respect to the peaks designated as #1 and #2. The peak #1 can probably be attributed to the hydrogen adsorption-desorption process while it is not clear what type of process is associated with peak #2. It is particularly interesting to note a quite opposite pH dependence behavior of this peak with respect to that of peak #3 in the case of FeTSPc and peak #4 in the case of CoTSPc and CoPc. Although without a strong evidence, peak #2 can be attributed to metal reduction to valency state I in alkaline solution, and to a ligand reduction associated with its protonation in acidic media. The similar behavior was found in the case of H_2TSPc and CuTSPc in acidic solution but not in alkaline one. Yet, the hydrogen adsorption-desorption peak was also found in the case of CuTSPc in both acidic and alkaline solutions.

In the case of Fe(III)TSPc, the peak #4 is of the same area as that of peak #2. Hence, this is a 1-electron transfer process and, yet, the pH-dependence is observed in the same region as for peak #3. The only difference is that peak #4 disappears at pH $< \sim 3$ while peak #3 becomes independent of pH at pH $< \sim 3$. One can suppose that this peak is due to the Fe(III)/Fe(IV) redox couple. It should be added that the similar peak was found in the case of H_2TSPc and CuTSPc. However, in the case of CuTSPc, that peak has been observed in acidic solutions only, whereas in the case of H_2TSPc the change in the pH dependence slope is observed at pH ~ 6. Therefore it is likely that these peaks are due to the redox process of ligand.

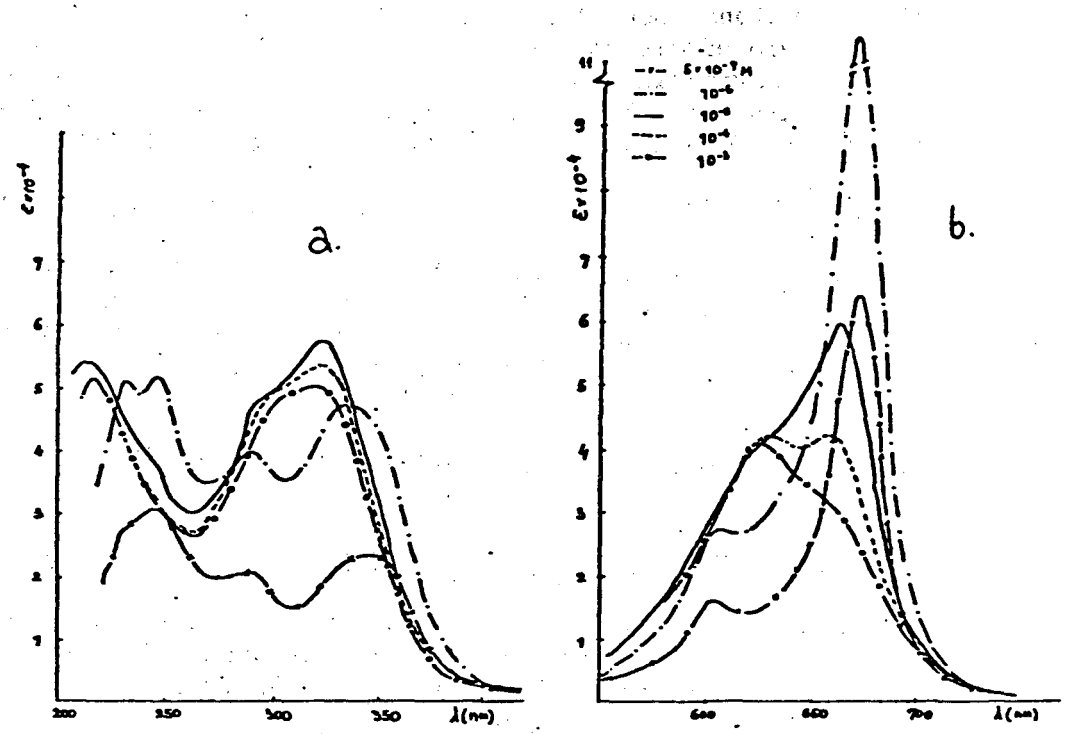


Fig. 5.1.6.1. Absorption spectra of $CoTSP_c$ in water as a function of concentration.- 90 minutes after preparing soluitons;a)UV region b) visible region.

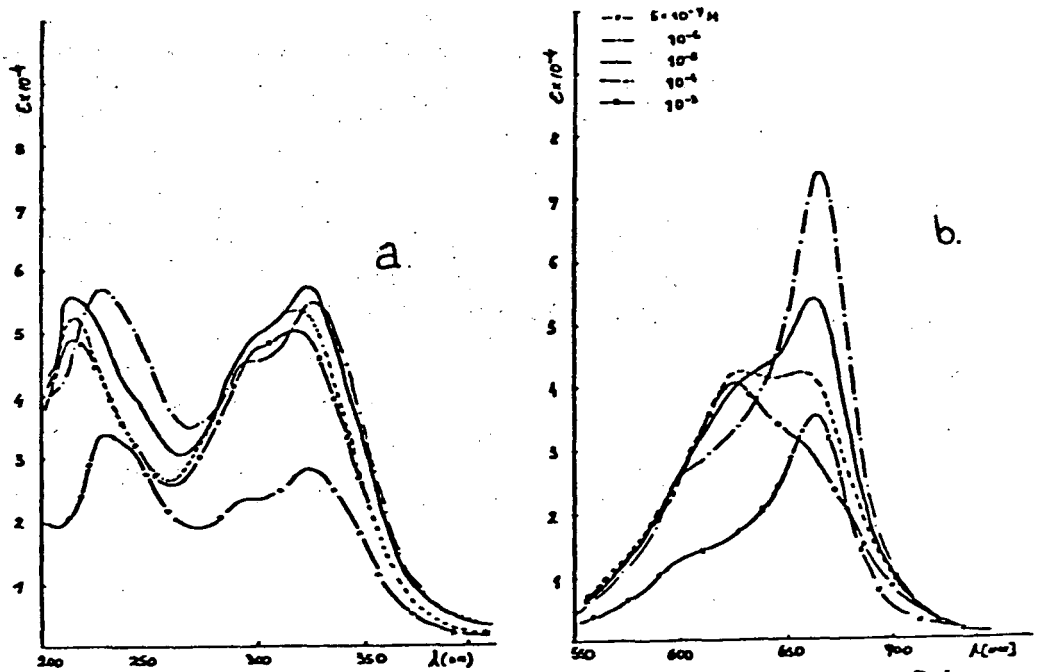


Fig. 5.1.6.2. Absorption spectra of $CoTSP_c$ in water as a function of concentration.- 18 days after preparing solutions;a) UV region b) visible region

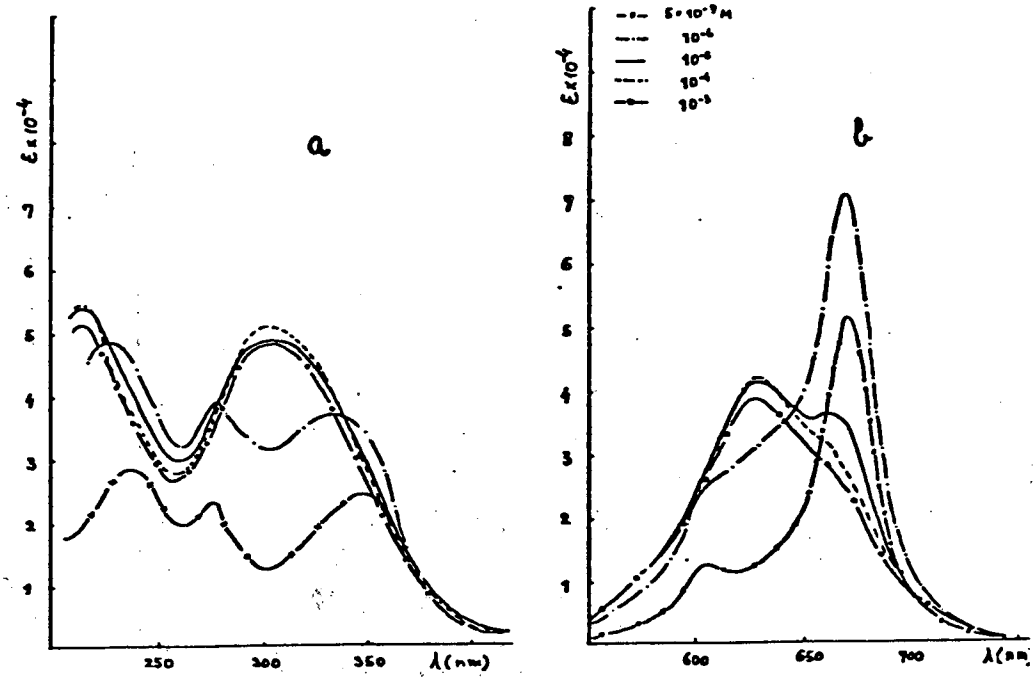


Fig. 5.1.6.3. Absorption spectra of $CoTSP_c$ in 0.05M H_2SO_4 as a function of concentration - 90 minutes after preparaing solutions; a)UV region b) visible region.

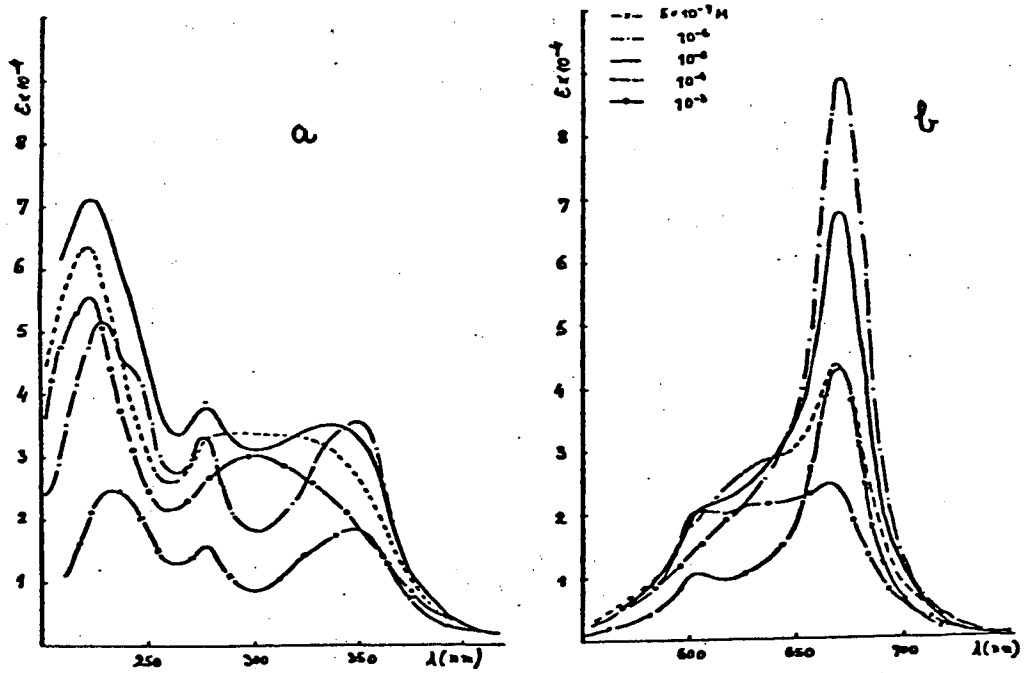


Fig. 5.1.6.4. Absorption spectra of $CoTSP_c$ in 0.05 M H_2SO_4 as a function of concentration - 18 days after preparing solutions; a)UV region b) visible region.

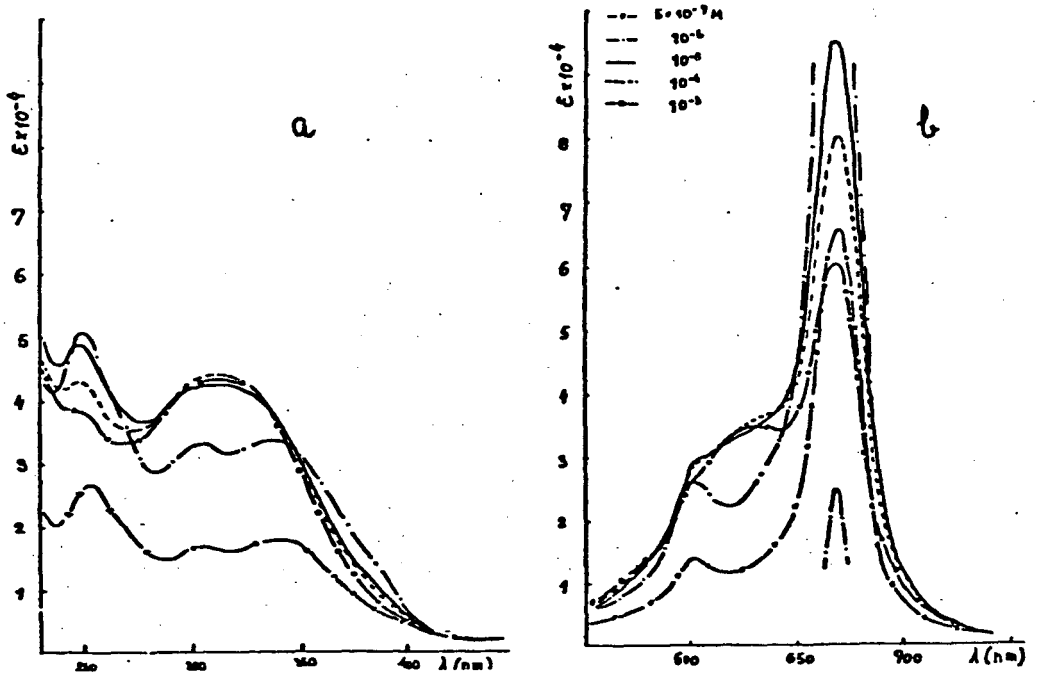


Fig. 5.1.6.5. Absorption spectra of $CoTSP_c$ in 0.1 M NaOH as a function of concentration - 90 minutes after preparing solutions; a) UV region b) visible region.

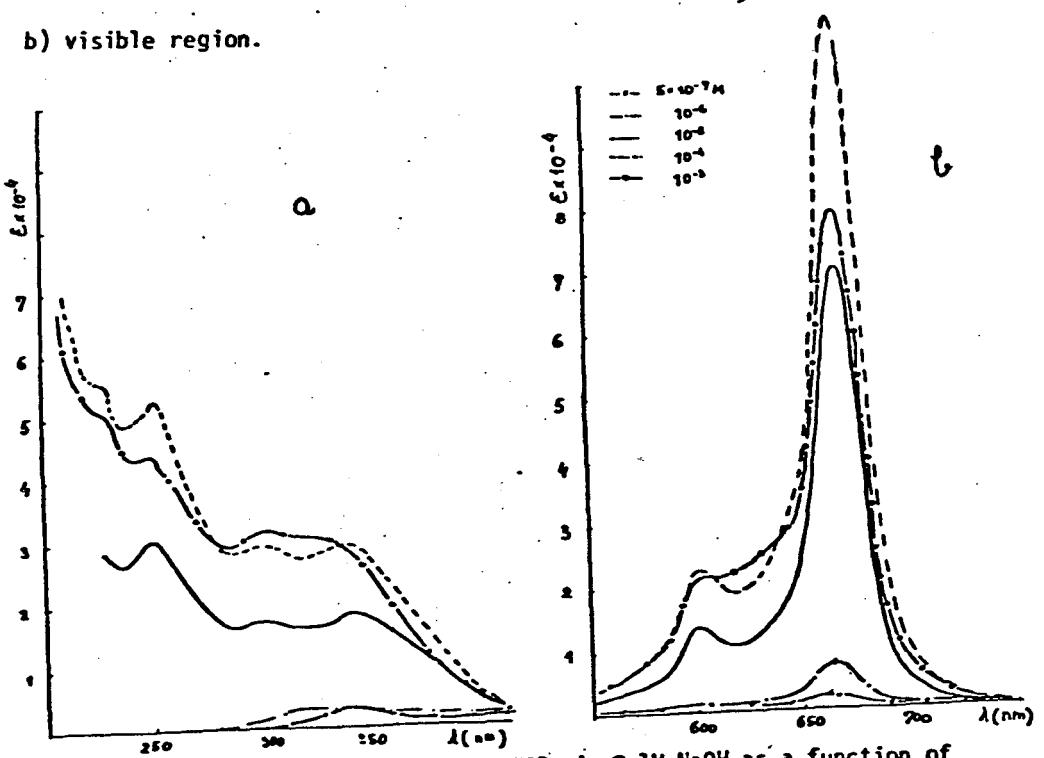


Fig. 5.1.6.6. Abosrption spectra of $CoTSP_c$ in 0.1M NaOH as a function of concentration - 10 days after preparing solutions; a) UV region b) visible region.

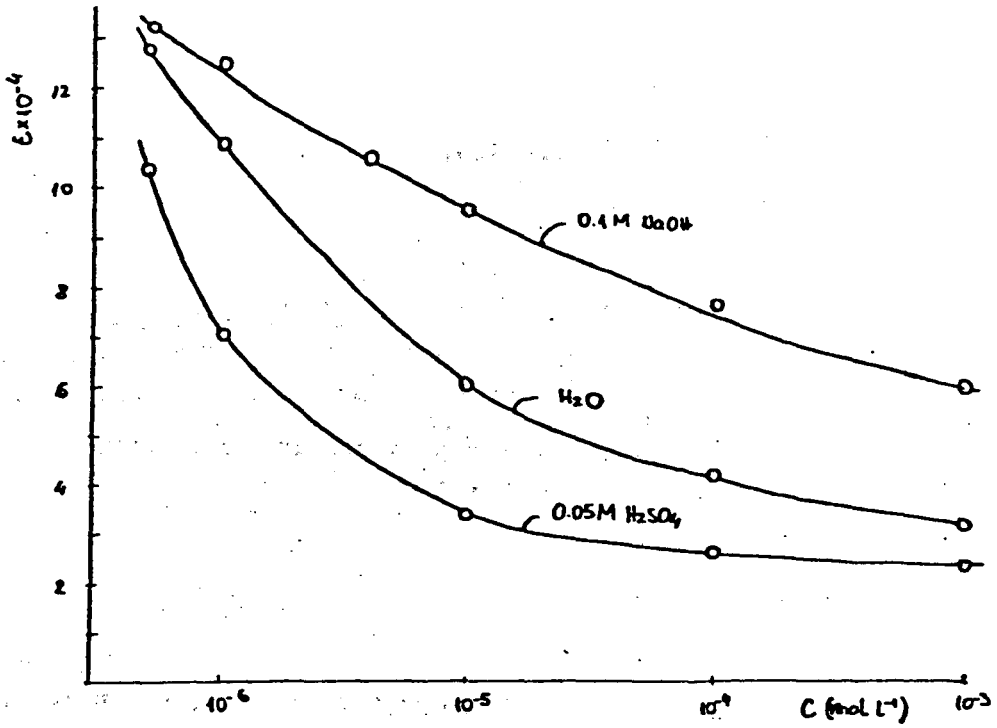


Fig. 5.1.6.7. The height of the main absorption peak of $CoTSP_c$ in water (662nm), acid (668 nm) and alkaline (668nm) solution as a function of concentration of $COTSP_c$ - 90 minutes after preparing solutions.

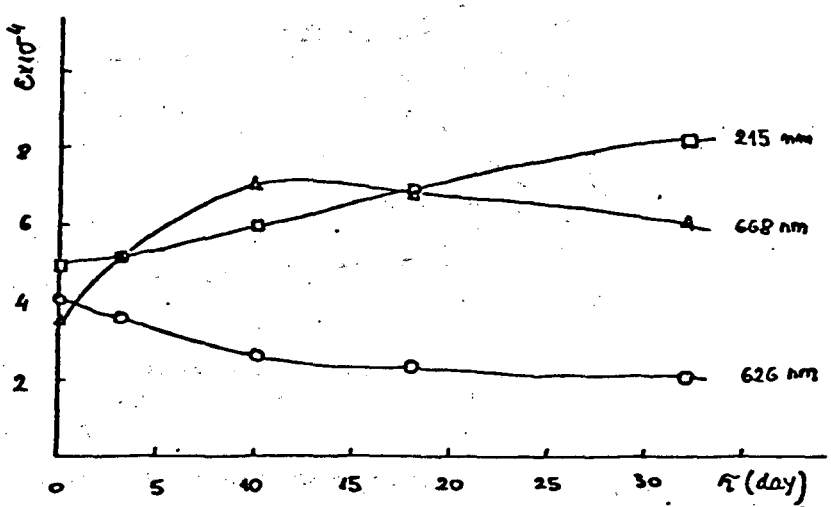


Fig. 5.1.6.8. The change of absorption peak height during time, 10^{-5} M $CoTSP_c$ + 0.05M H_2SO_4.

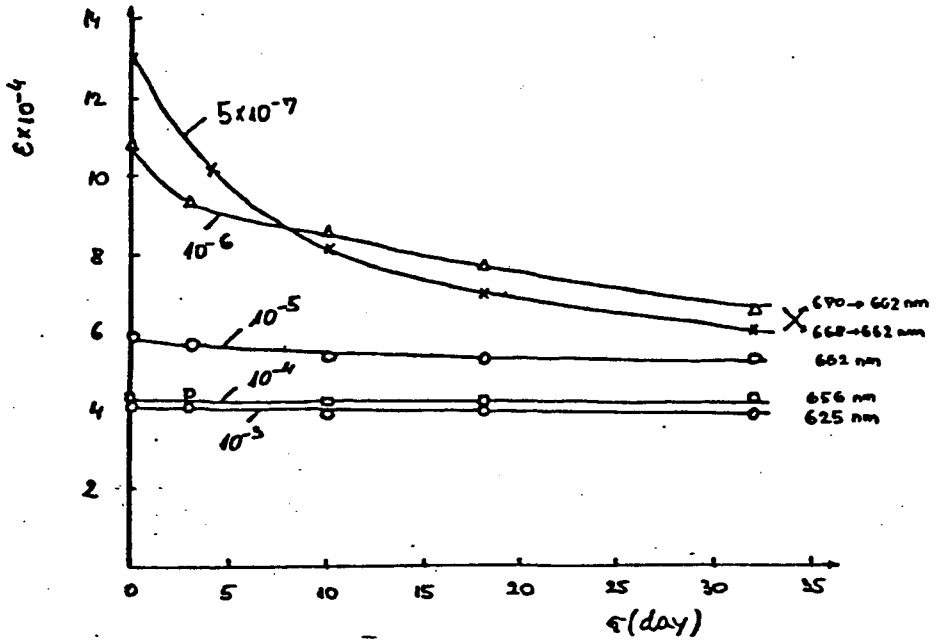


Fig. 5.1.6.9. The change of absorption peaks heights during time for different $CoTSP_c$ concentrations in water (peak wave lengths are showen in the diagram).

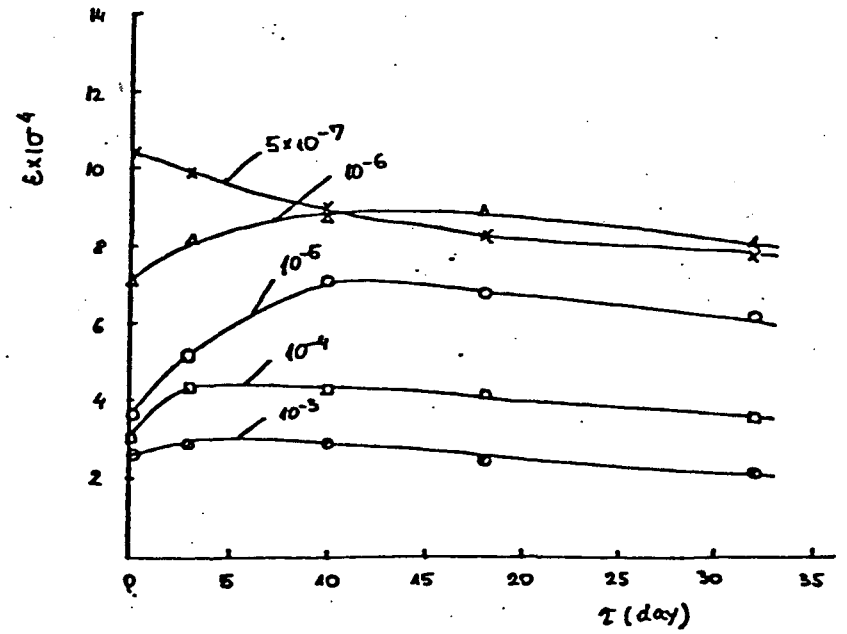


Fig. 5.1.6.10. The height of the 668 nm absorption peak during time for different $CoTSP_c$ concentrations in 0.05M H_2SO_4.

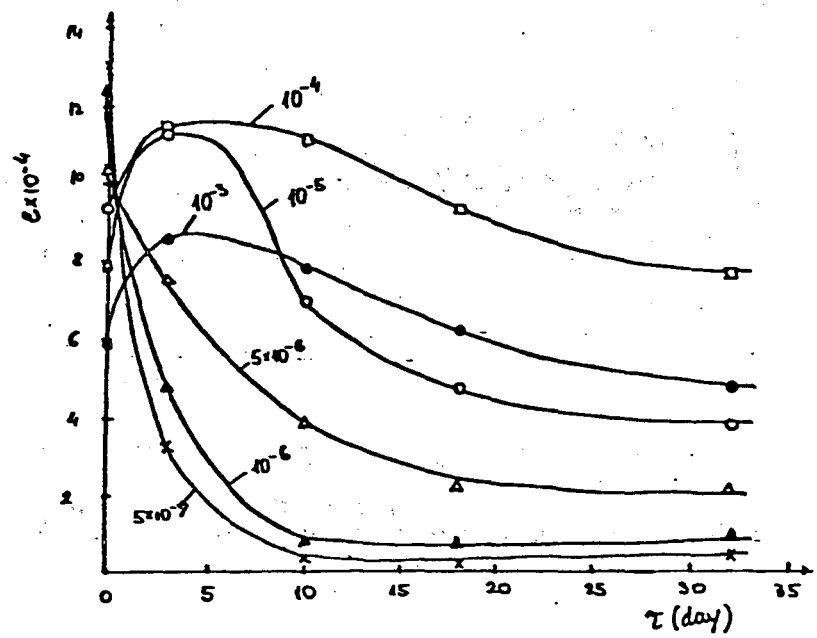


Fig. 5.1.6.11. The height of the 668 nm absorption peak during time for different $CoTSP_c$ concentrations in 0.1 M NaOH.

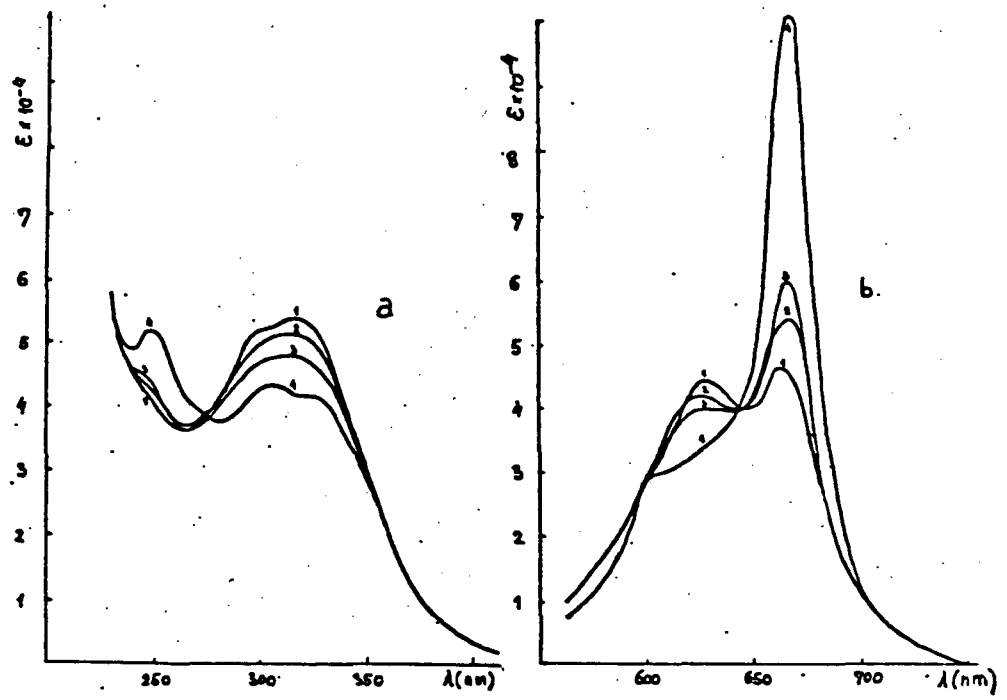


Fig. 5.1.6.12. Absorption spectra of 10^{-5}M CoTSPc in 0.1M NaOH during time; a) UV region b) visible region 1-immediately after alkalization, 2-after 5 min, 3-after 17 min and 4-after 90 min.

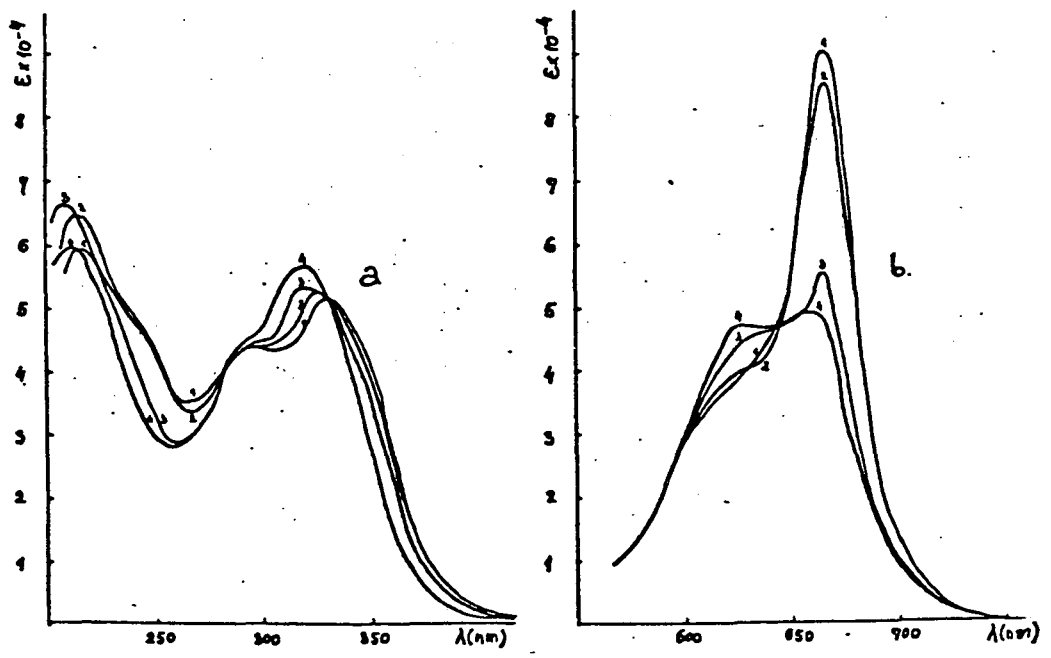


Fig. 5.1.6.13. Absorption spectra of 10^{-5}M CoTSPc in water during time at 70°C; a) UV region b) visible region; 1-fresh solution, 2-after 2 h, 3-after 1 day, 4-after 2 days.

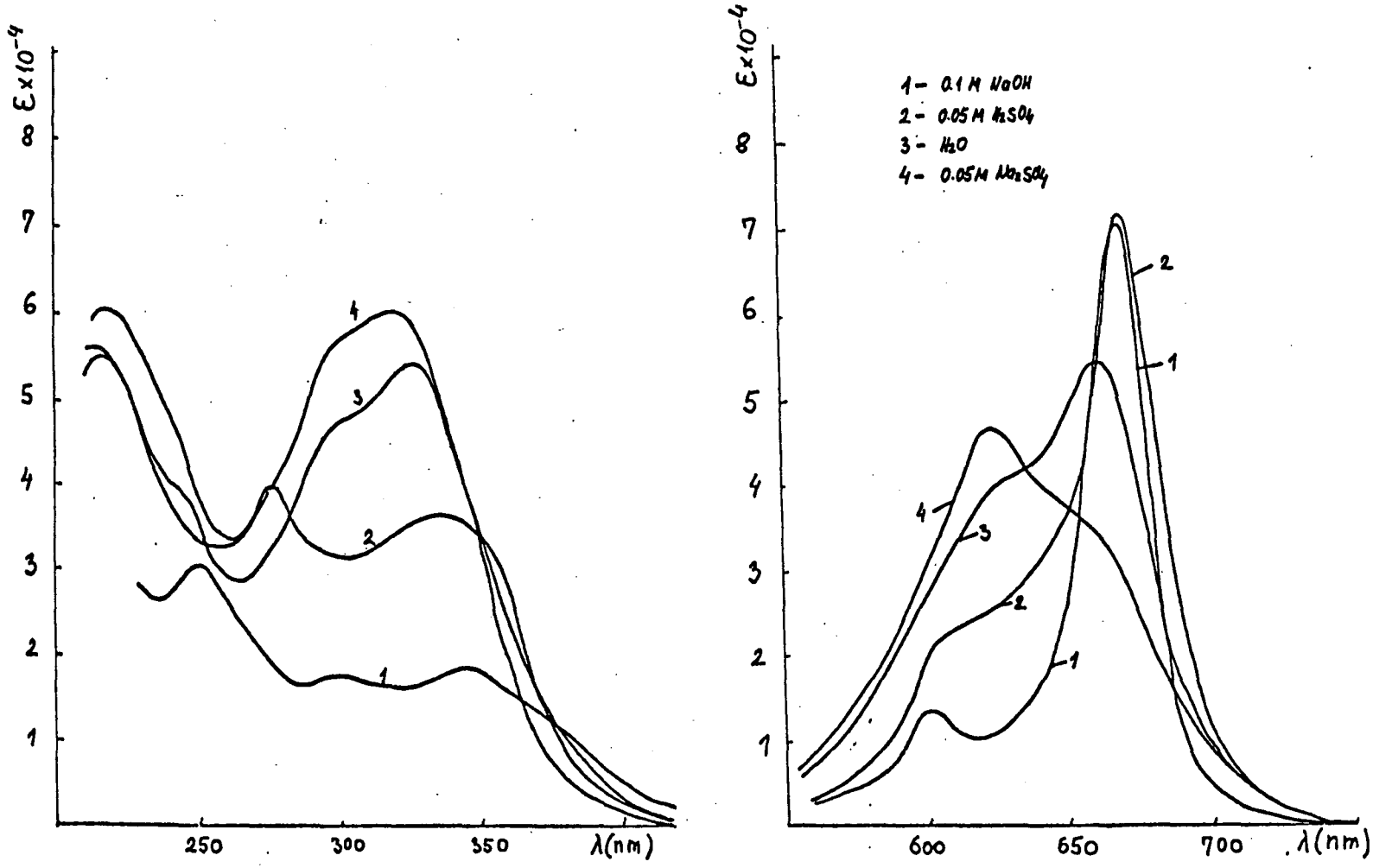


Fig. 5.1.6.14. Absorption spectra of 10^{-5}M $CoTSP_c$ solution in water, acid, alkaline and neutral solution -10 days after preparing solutions.

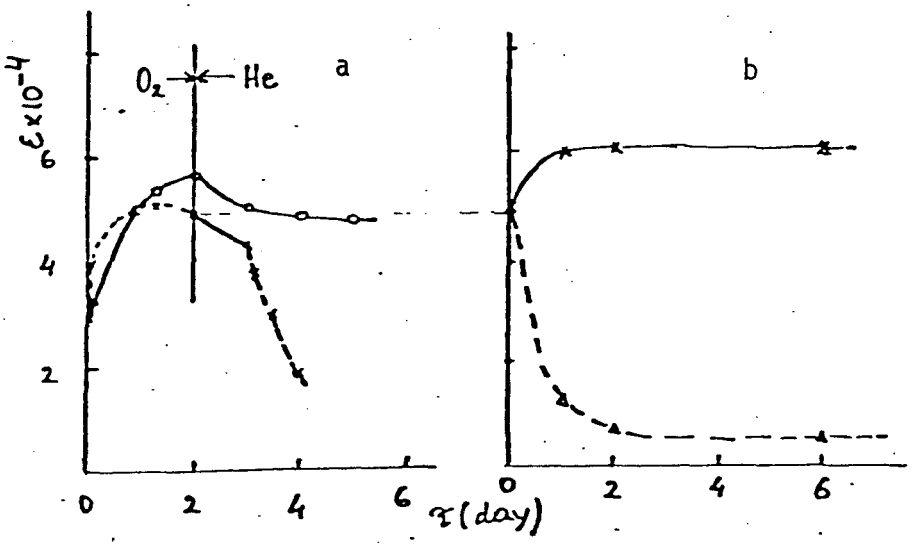


Fig. 5.1.6.15. The height of the oxygen adduct peak during saturation; 10^{-5}M $CoTSP_c$ + 0.05M H_2SO_4 solution with oxygen and helium (a) and during standing of oxygenated solution at room temperature and at 70°C (b) - solid lines - room temperature, dotted lines +70°C).

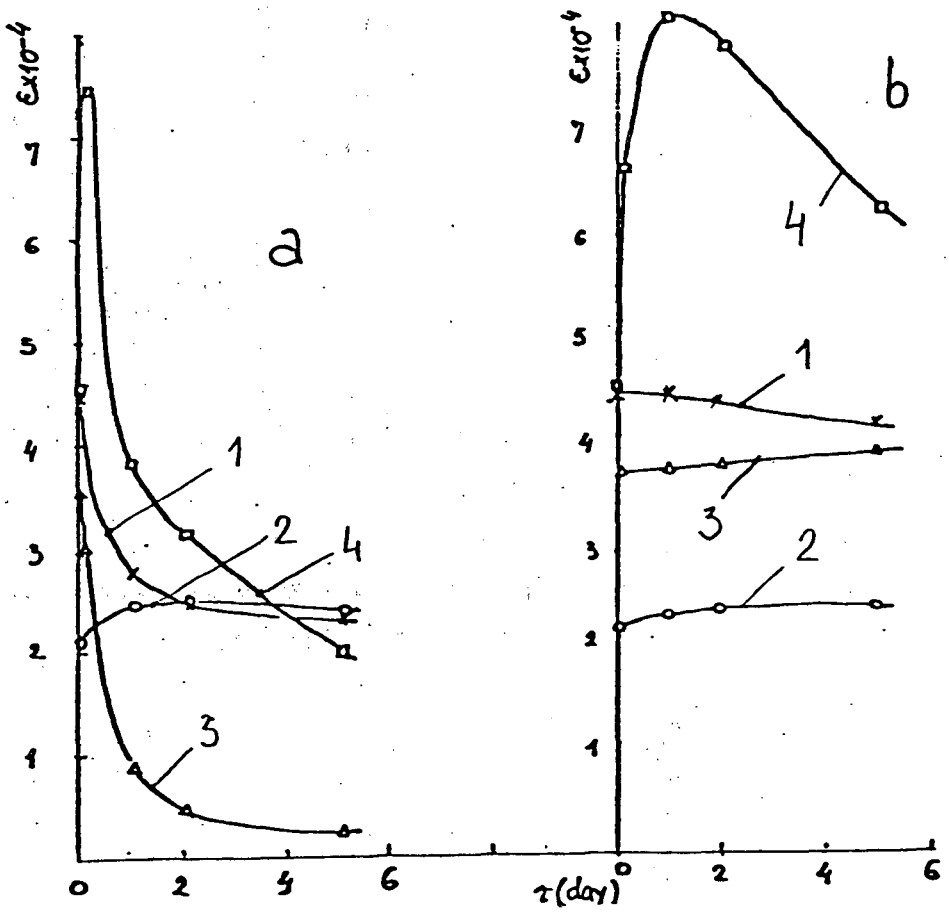


Fig. 5.1.6.16. The heights of the main absorption peaks in the visible region of 10^{-5}M CoTSPc solution in 1) pure water, 2) 0.05M Na_2SO_4, 3) 0.05M H_2SO_4, 4) 0.1M NaOH at a) 70°C and b) 25°C.

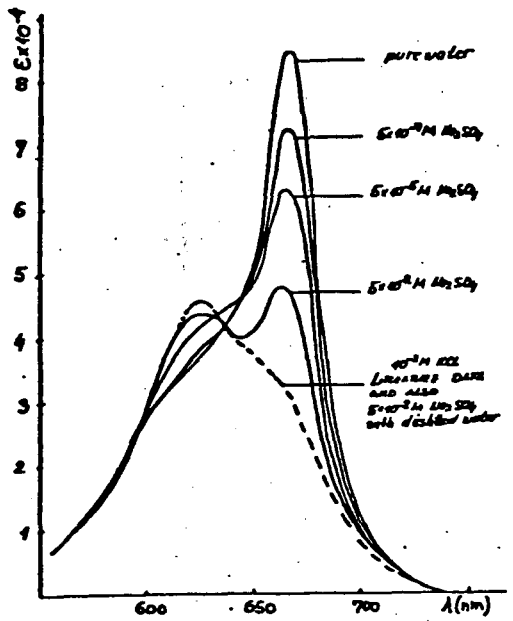


Fig. 5.1.6.17. Absorption spectra of 10^{-5}M $CuTSP_c$ water solution with different concentration of Na_2SO_4 in it.

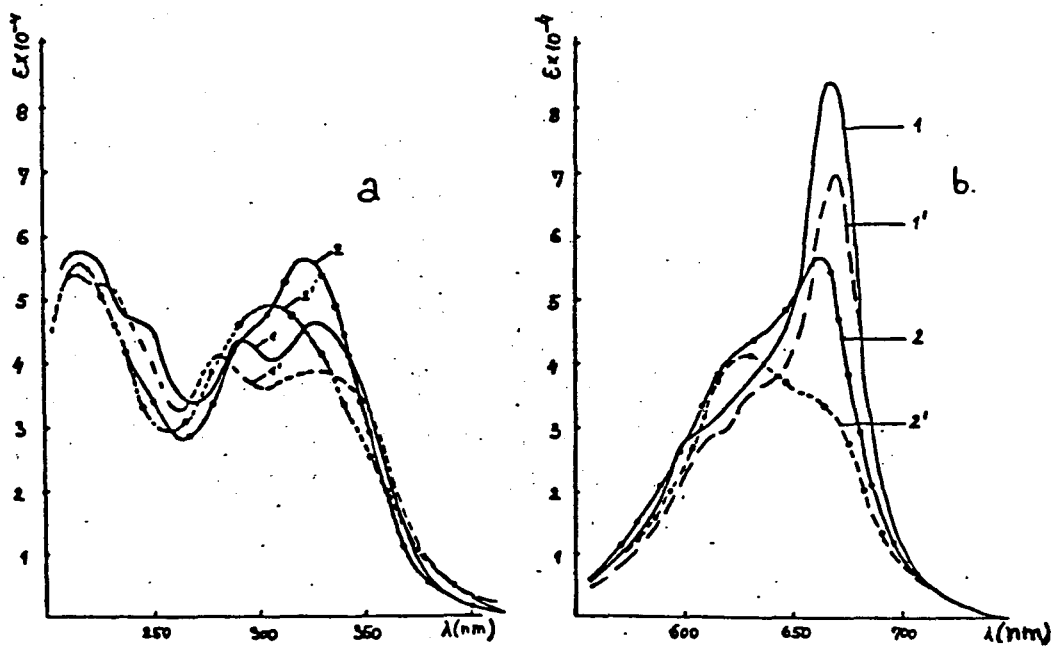


Fig. 5.1.6.18. Absorption spectra of 10^{-5}M CoTSPc water solutions prepared with common distilled and very pure water; a) UV region b) visible region; 1- pure water, 1'- 0.05M H_2SO_4 in pure water, 2- distilled water, 2'- 0.05M H_2SO_4 in distilled water.

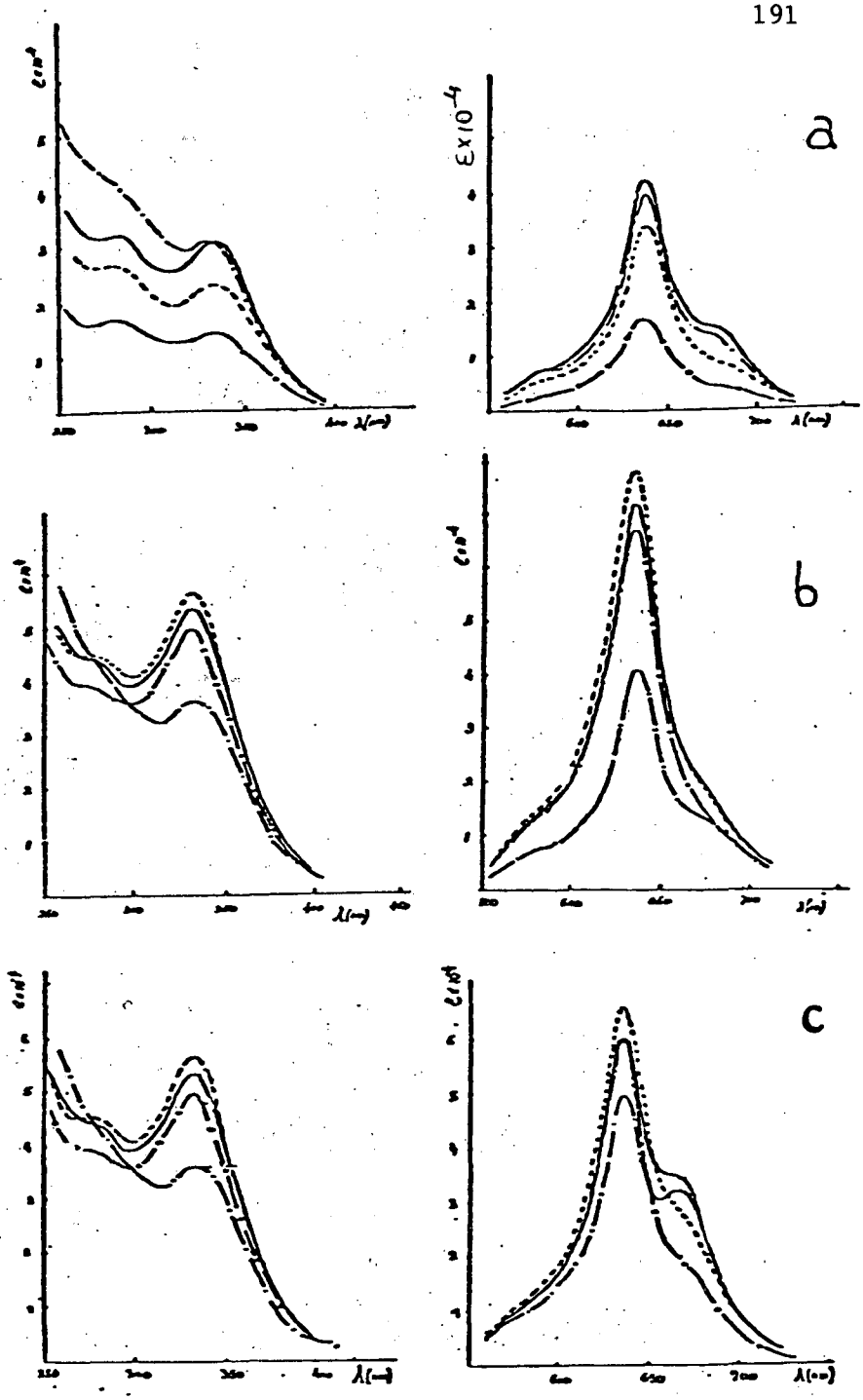


Fig. 5.1.6.19. Absorption spectra of Fe(III)TSPC solutions as a function of concentration in a) 0.05M H_2SO_4, b) pure water, c) 0.1M NaOH; -.- $2x10^{-6}$M, —— $2x10^{-5}$M, --- $2x10^{-4}$M, -•- $2x10^{-3}$M.

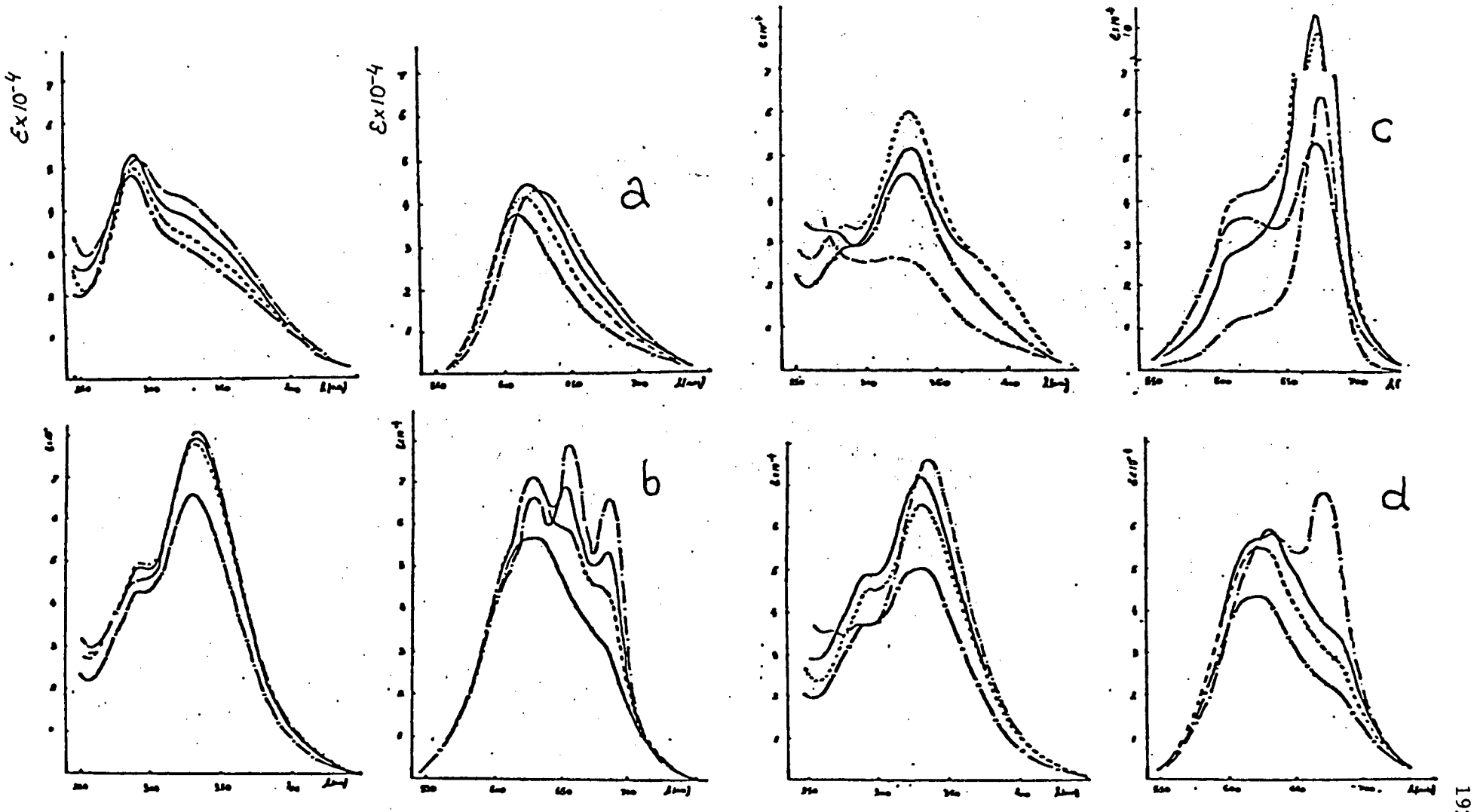


Fig. 5.1.6.20. Absorption spectra of H_2TSPc solutions as a function of concentration; -.- $2x10^{-6}M$, — $2x10^{-5}M$, --- $2x10^{-4}M$, -•- $2x10^{-3}M$; in a) 0.05M H_2SO_4, b) pure water, c) 0.1M NaOH, d) 0.05M Na_2SO_4

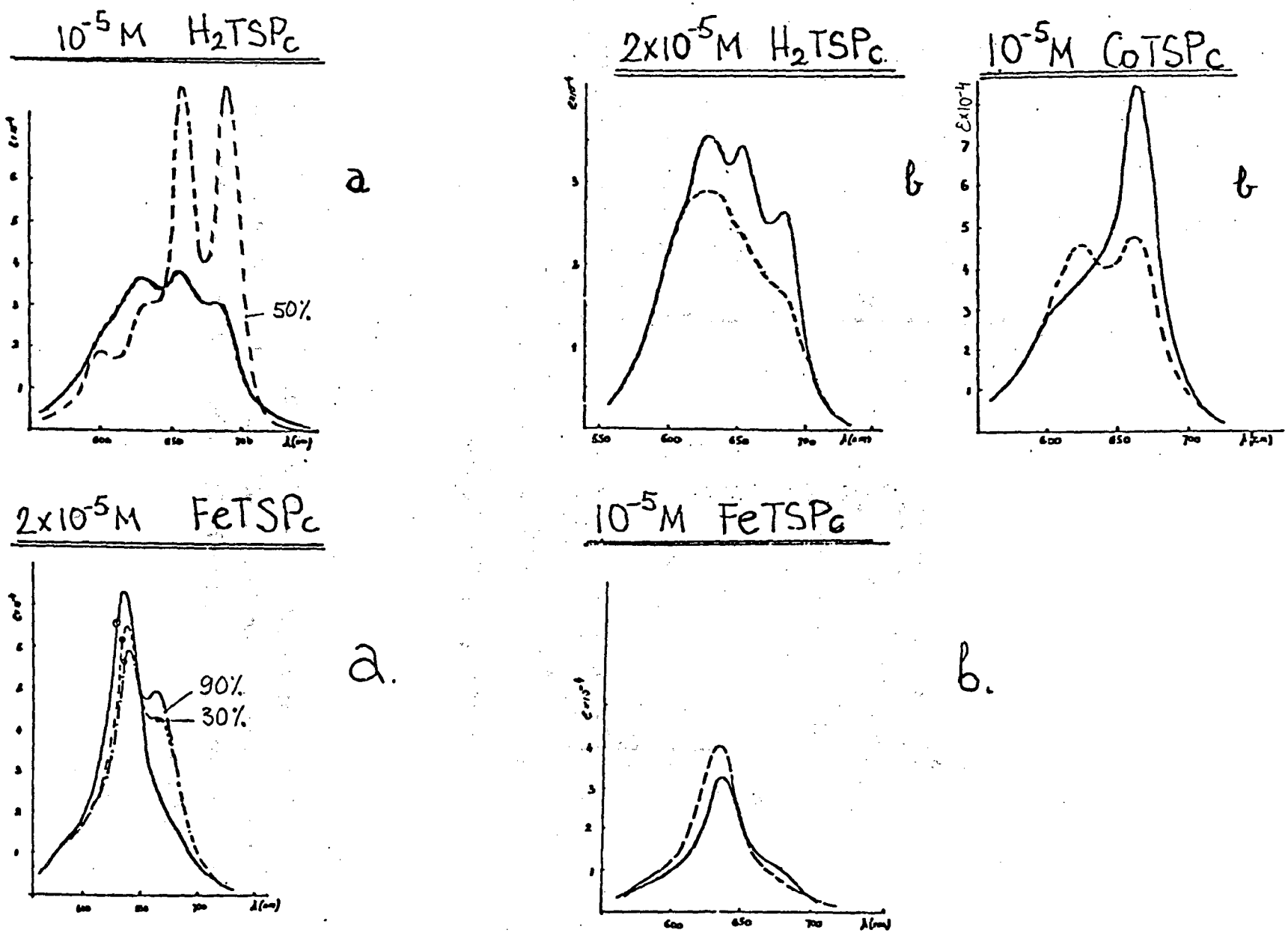


Fig. 5.1.6.21. Absorption spectra of tetrasulfonatedphthalocyanines in the presence of a) ethanol and b) 0.05M Na_2SO_4 (solid lines-pure water solutions, dashed lines-in the presence of ethanol or Na_2SO_4)

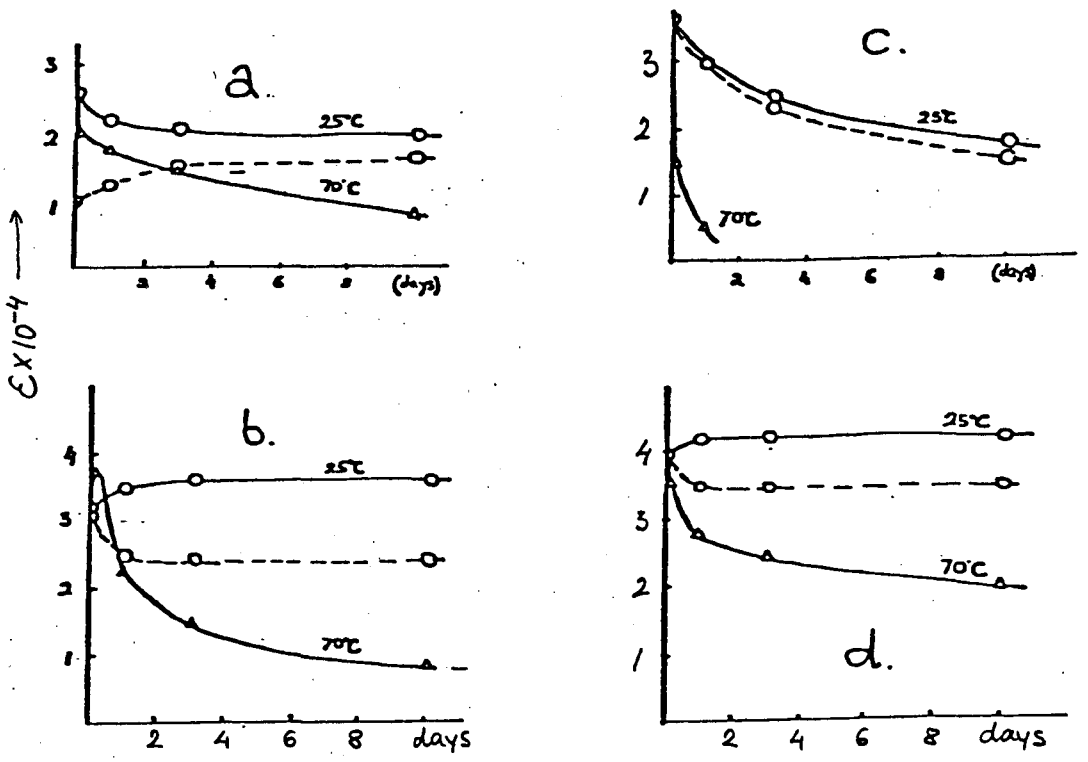


Fig. 5.1.6.22. The height of the 635 nm absorption peak of $2x10^{-5}$M Fe(III)TSPc solutions during time in a) 0.05M H_2SO_4, b) pure water, c) 0.1M NaOH and d) 0.05M Na_2SO_4 , at 25°C and 70°C; dashed lines - in the presence of 10^{-5}M H_2O_2 at 25°C.

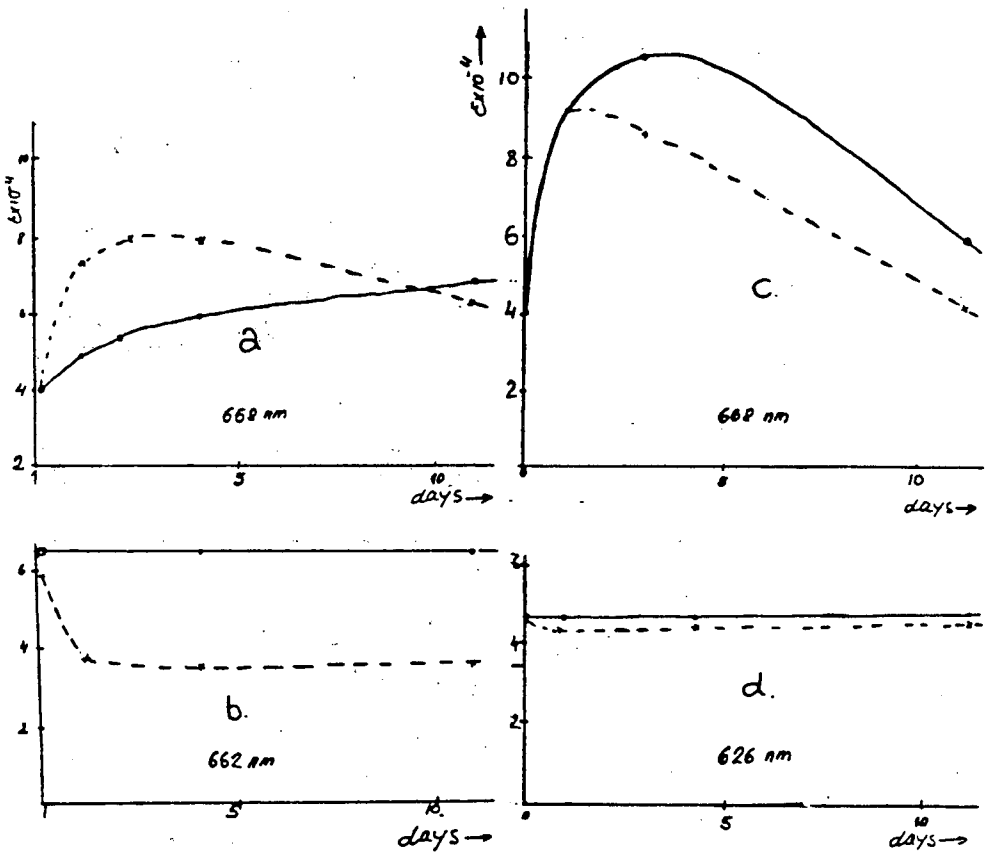


Fig. 5.1.6.23. The heights of the main absorption peaks (indicated in the figure) of 10^{-5}M CoTSPc solutions during time in a) 0.05M H_2SO_4, b) pure water, c) 0.1M NaOH and d) 0.05M Na_2SO_4; dashed lines-in the presence of 10^{-5}M H_2O_2 at 25°C.

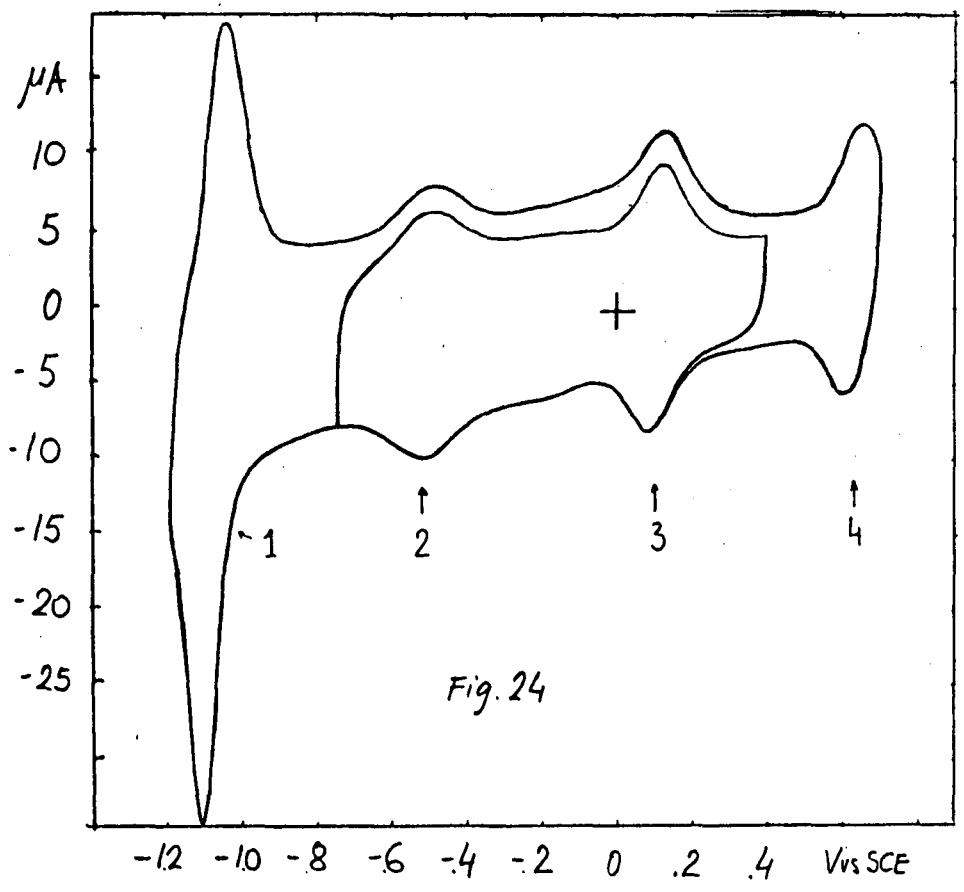


Fig. 24

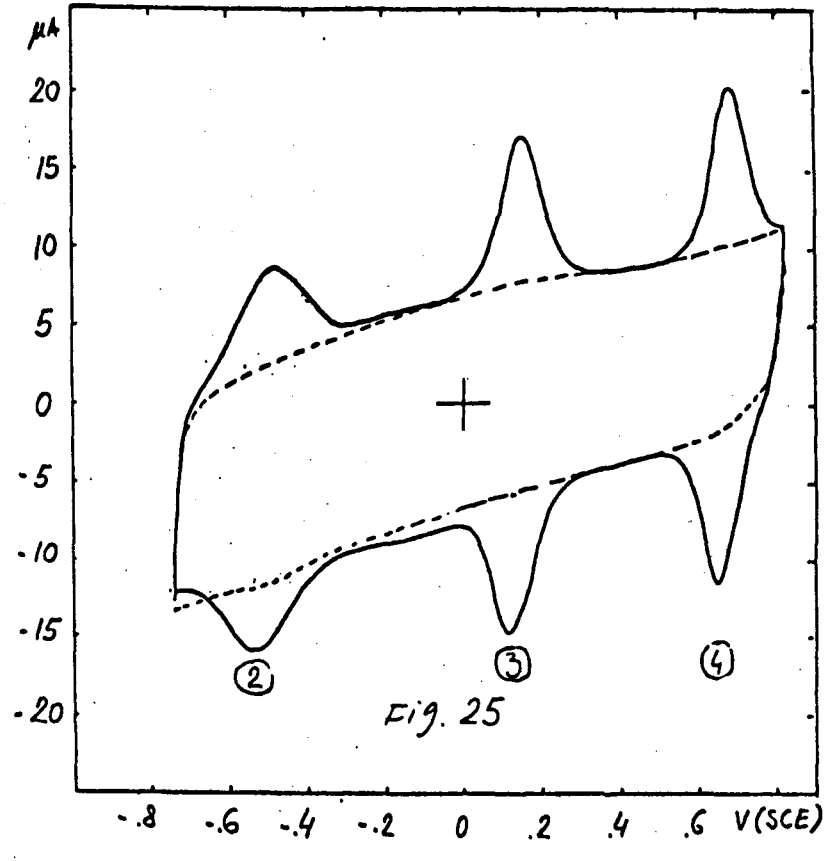
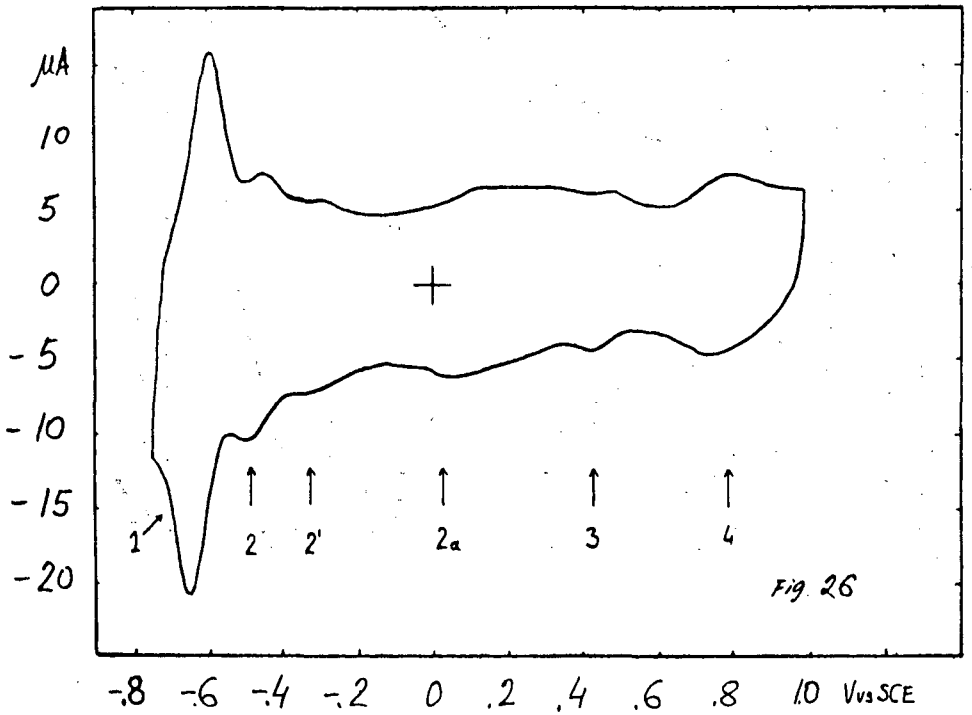


Fig. 25

Fig. 5.1.6.24. Voltammograms of 10^{-5}M Fe(III)TSPc on OPG at pH 9.5; scan rate 500mV/s, t=25°C, under N_2

Fig. 5.1.6.25. Voltammograms of pre-adsorbed Fe(III)TSPc on OPG in borate buffer solution pH 8.7; dashed line - blank OPG; scan rate 500mV/s, t=25°C, under N_2



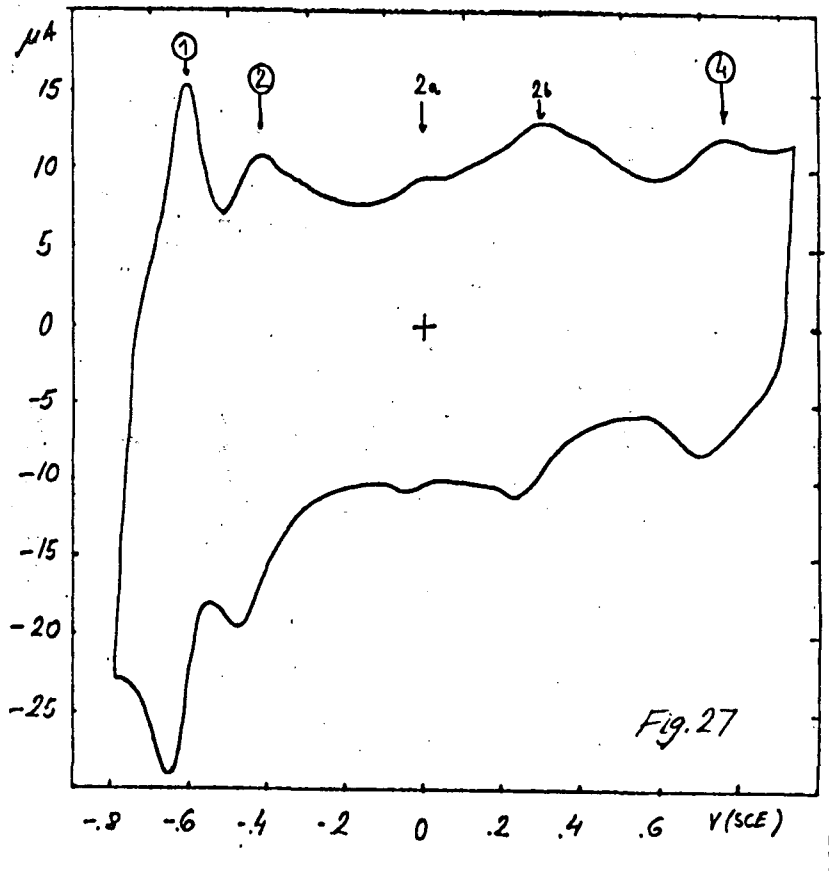


Fig. 5.1.6.26. Voltammogram of 10^{-5}M Co(II)TSPc on OPG in acid solution pH 3.5; scan rate 500mV/s, t=25°C.

Fig. 5.1.6.27. Voltammogram of pre-adsorbed CoPc on OPG in acid solution pH 2.4; scan rate 500mV/s, t=25°C, under N_2

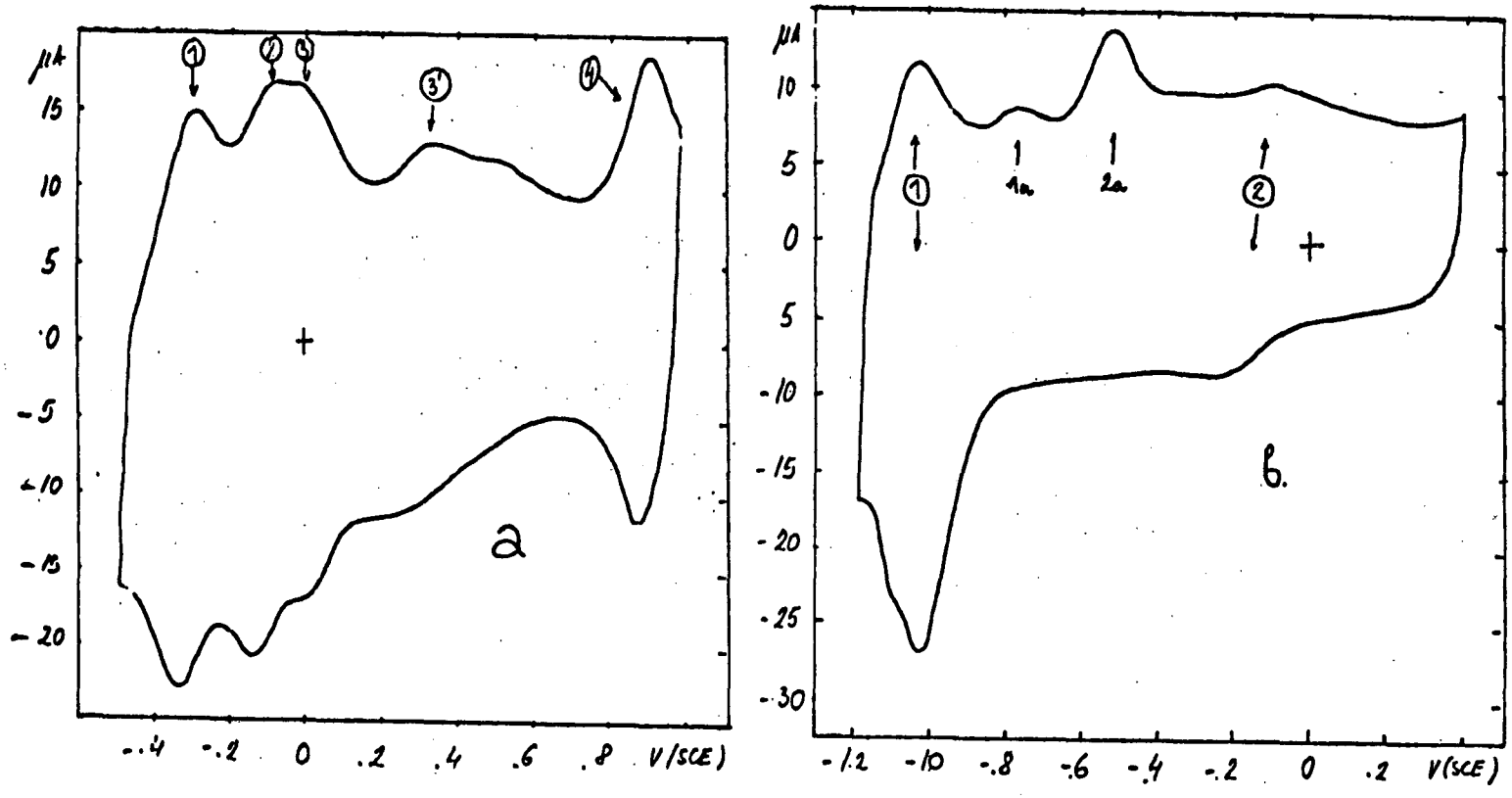


Fig. 5.1.6.28. Voltamograms of 10^{-5}M Cu(II)TSPc on OPG in a) acidic pH 1.8 and b) alkaline pH 11.6 solutions; scan rate 500 mV/s, t=25°C, under N_2

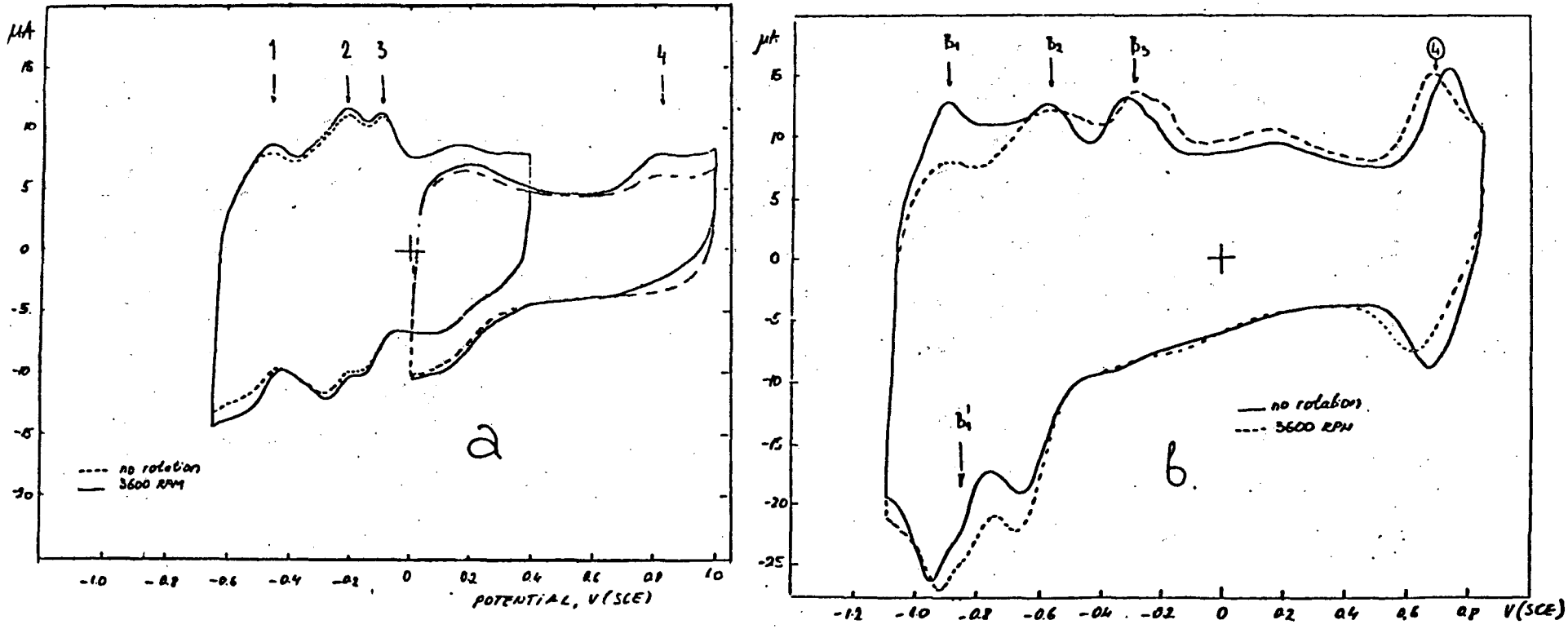
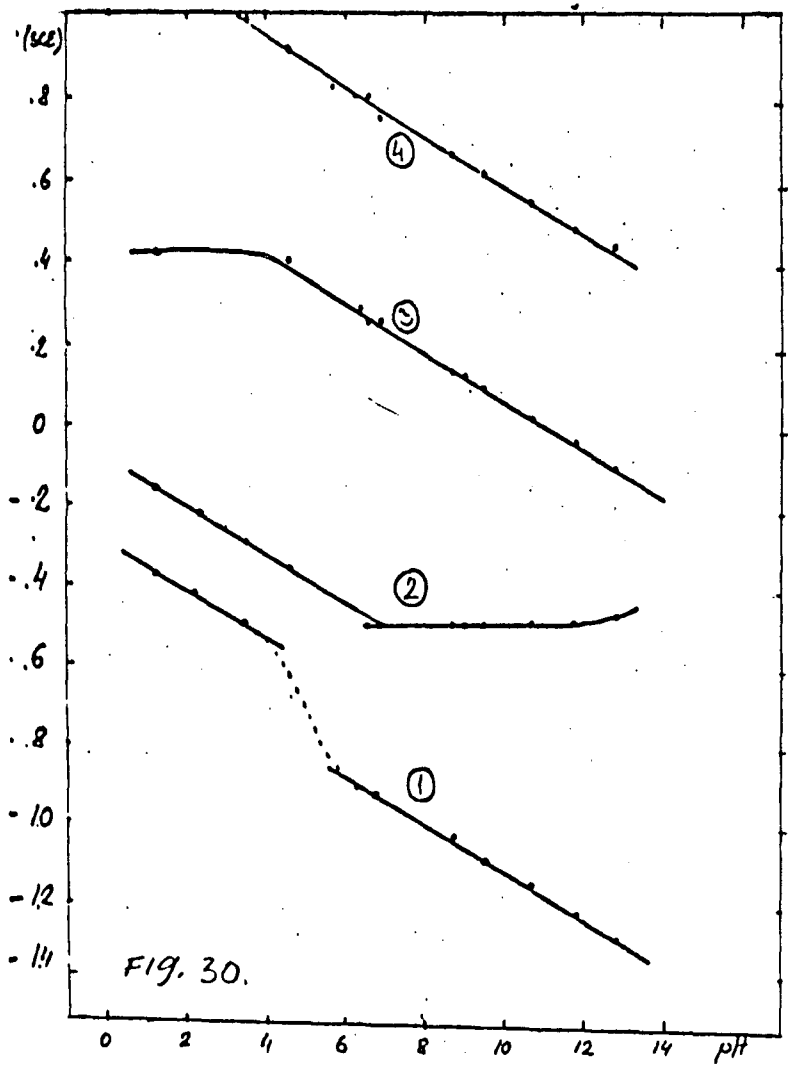
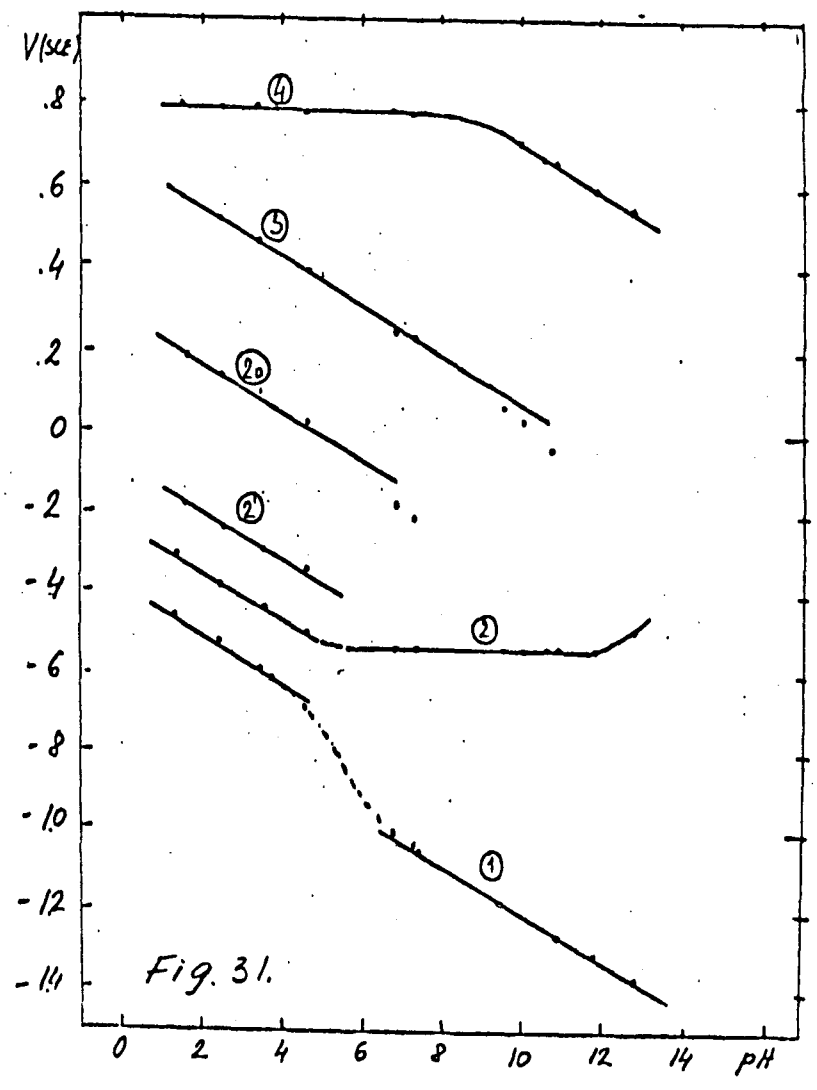
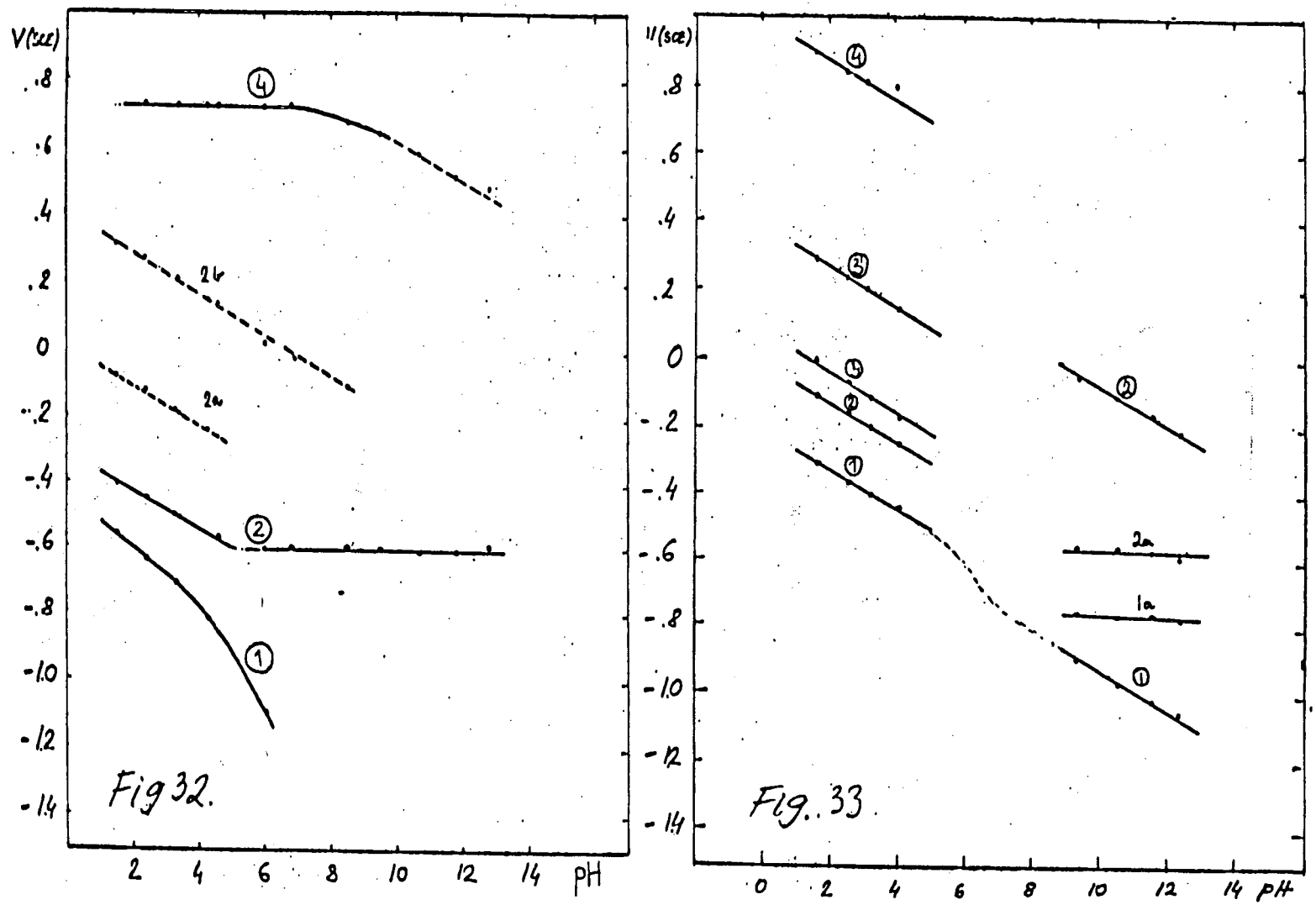


Fig. 5.1.6.29. Voltamograms of 10^{-5}M H_2TSPc on OPG in a) acidic pH 4.5 and b) neutral pH 7.3 solutions; scan rate 500 mV/s, t=25°C, under N_2

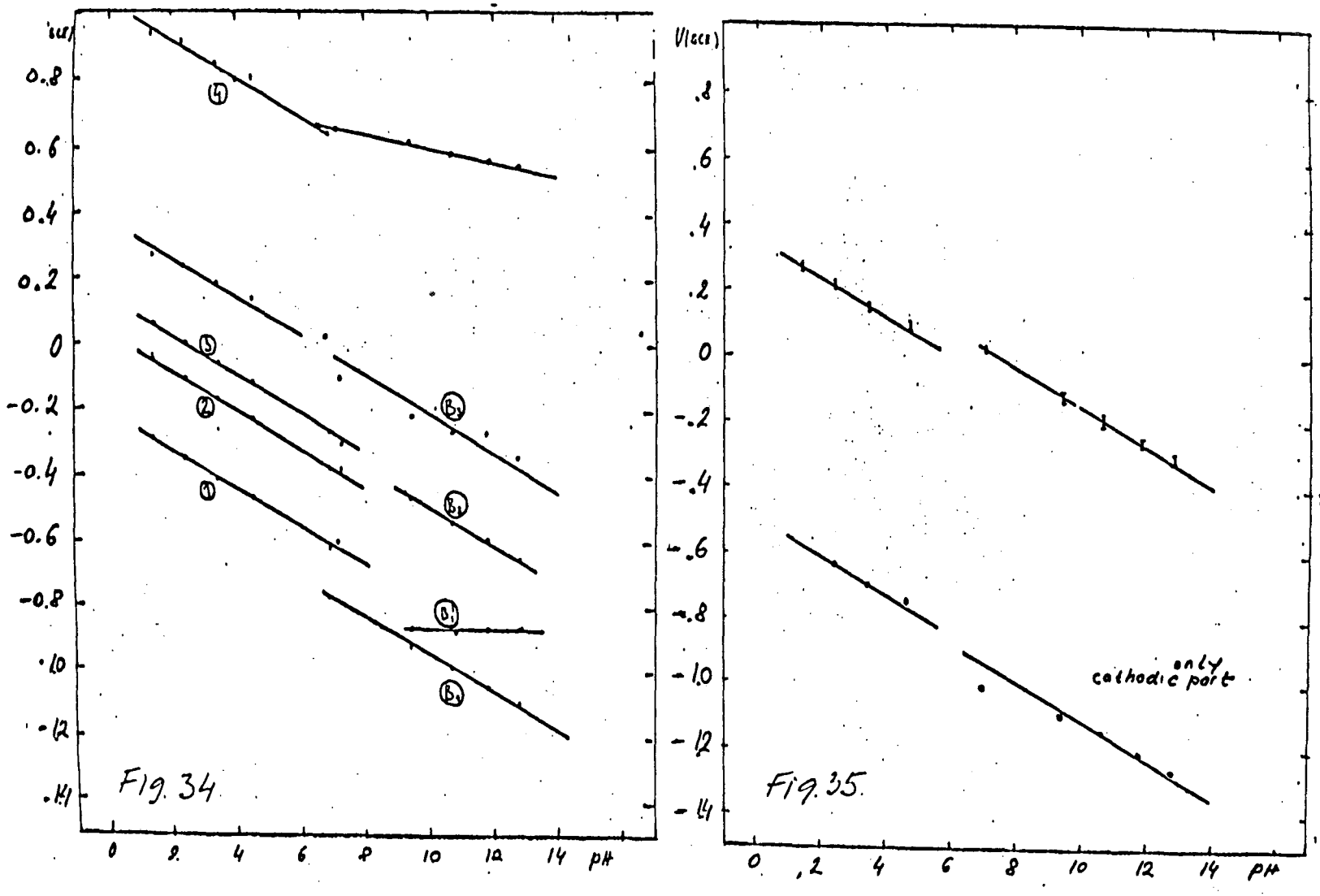




Figs. 5.1.6.30 and 31. Average cathodic-anodic voltammetric peak potential as a function of pH. Fig. 30, 10^{-5}M Fe(III)TSPc; Fig. 31, 10^{-5}M Co(II)TSPc on OPG; t = 25°C, under N_2.



Figs. 5.1.6.32 and 5.1.6.33. Average cathodic-anodic voltammetric peak potential as a function of pH. Fig. 32, pre-adsorbed CoPc. Fig. 33, 10^{-5}M Cu(II)TSPc on OPG. t = 25°C, under N_2.



Figs. 5.1.6.34 and 5.1.6.35. Average cathodic-anodic voltammetric peak potential as a function of pH. Fig. 34, 10^{-5}M H_2TSPc. Fig. 35, blank-OPG only. t - 25°C, under N_2

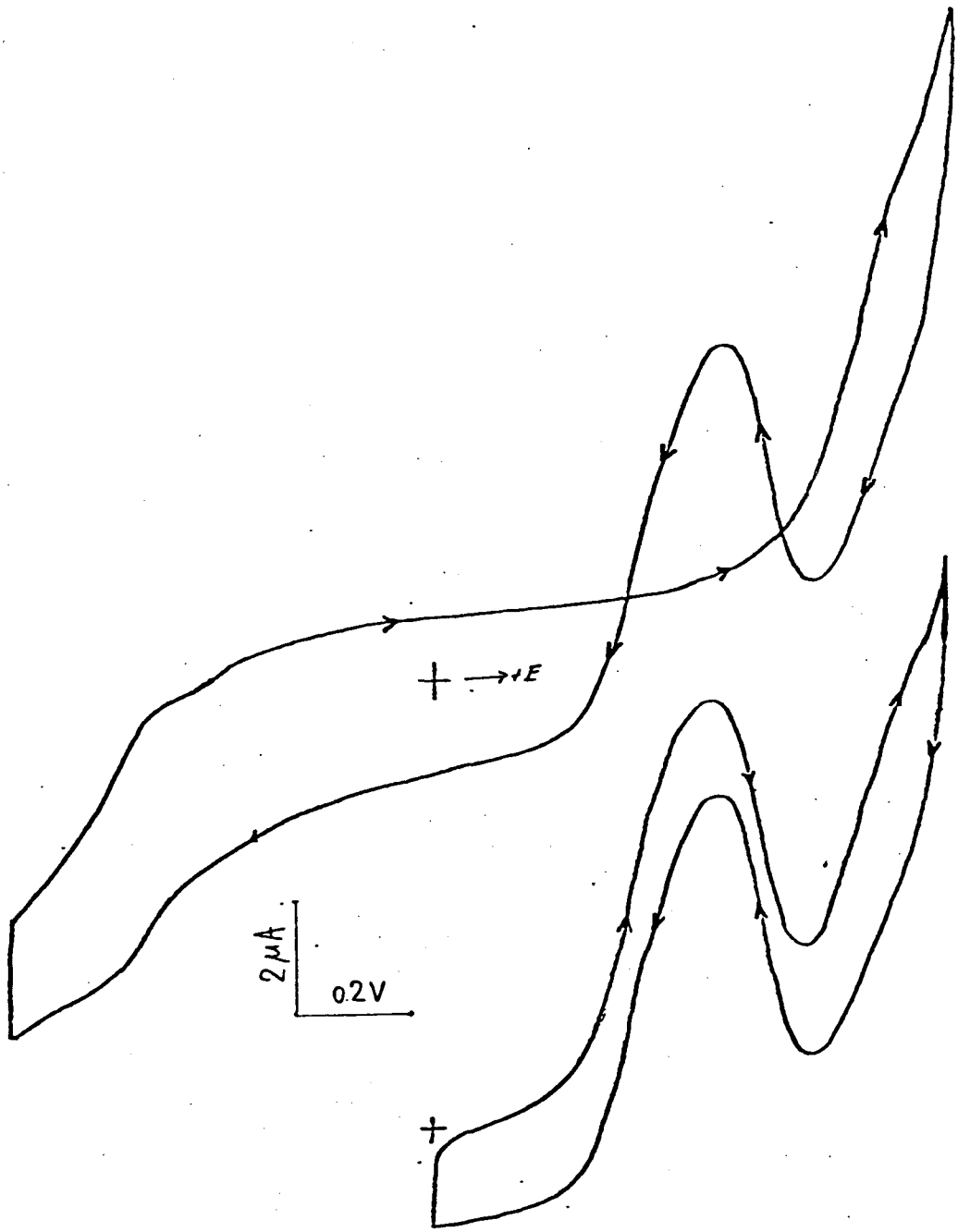


Fig. 5.1.6.36. Voltammograms of 10^{-5}M CoTSPc on OPG in borate buffer solution pH 8.7 in the presence of 10^{-4}M H_2O_2. Scan rate 50 mV/s, 1600 rpm, t = 25°C, under N_2

5.1.7 SPECTROSCOPIC STUDIES OF TRANSITION METAL TETRASULFONATED PHTHALOCYANINES:

I. RESONANT RAMAN SPECTRA OF AQUEOUS SOLUTION OF COBALT AND IRON TETRASULFANATED PHTHALOCYANINES

by

B. Simic-Glavaski and E. B. Yeager

ABSTRACT

Phthalocyanines are of considerable research interest partly as a result of their structure and partly of their multifunctional physicochemical properties ranging from their photo effect to high catalysis through oxygen reduction in electrochemical and similar biological systems.

This study attempts to provide more detailed information concerning physicochemical and electrochemical properties of transition metal phthalocyanines in aqueous media when they are in solution phases and adsorbed on electrode surfaces.

INTRODUCTION

Physicochemical properties of the transition metal phthalocyanines (M-Pc) have been investigated by numerous exprimental methods of which the most notable are UV-visible (1), infra red (2) and Raman (3) spectroscopies. However, M-Pc are not water soluble unless some polar groups are added to their basic molecular structure as in tetrasulfonated Pc(TSPc), hence data on M-TSPc in aqueous media are scarce and sometimes controversial (4), (5).

This paper reports a study of the tetrasulfonated cobalt and iron phthalocyanines (Co-TSPc) and Fe-TSPc) in aqueous solutions at various pH by Raman spectroscopy. Raman spectra were recorded between 200-1700 cm^{-1} by the polarized and the depolarized light scattered from phthalocyanines in acidic, neutral and alkaline solution phases with the objective of providing more definitive data in order to obtain an understanding of molecular behavior of these molecules which are increasingly used and studied as catalyzers in electrochemical aqueous systems (6), (7).

EXPERIMENTAL

Metal tetrasulfonated phthalocyanines (M-TSPc) have been synthesized and purified according to the method of Weber and Busch (8). The electrolytes were prepared from ultrapure grade sulfuric acid and sodium hydroxide (J.T. Baker) and triply distilled water. Aqueous

solutions at pH 1,7 and 13 contained $5x10^{-5}$M M-TSPc. All Raman experiments were performed at room temperature and aerobic atmosphere.

The source of light was the Spectra Physics He-Ne laser model 125 operating at 632.8 nm with an output power of 50 mV. The laser excitation line falls well within the visible absorption spectrum of Co and FeTSPc.

The plane of polarization of the laser incident light was rotated with the Spectra Physics wide band polarization rotator. The Raman polarized and depolarized spectra from aqueous solutions of M-TSPc were obtained using a Spex 1400 double monochromator, FW 130 photomultiplier and photon counting electronics. The monochromator resolution was 5 cm^{-1} in all experiments. The scanning speed was 0.2 cm^{-1}/s and the accuracy of the hand position was $\pm$ 5 cm^{-1}.

RESULTS AND DISCUSSION

The basic molecular structure of phthalocyanine and its schematic molecular orbital energy diagram is shown as the insert of Figure 1, which represents UV-visible absorption spectra of 5.10^{-5}M Co and Fe-TSPc in acidic, neutral and alkaline aqueous solutions.

The absorption bands are interpreted as due to a $_{1u}(\pi)$, a $_{2u}(\pi) \longrightarrow e_g(\pi^*)$ or $\pi - \pi^*$ transitions (9), however possible $n-\pi^*$ transition is not excluded (9). In general, M-TSPc belong to the D_{4h} symmetry point group and that symmetry remains for Co and FeTSPc in aqueous media. The two energy states promote the electronic transisiton $a_{2u}(\pi) \longrightarrow e_g(\pi^*)$ with corresponding Q(0,0)and Q(1,0) absorption bands in the visible region at about 680 and 630 respectively. Often these bands are attributed to a monomeric or a dimeric molecular structure (7). The transition $a_{1u}(\pi) \longrightarrow e_g(\pi^*)$ produces Soret or B(0,0) absorption band at about 340 nm. The additional UV absorption bands may be due to vibrational excitation.

The He-Ne laser excitation at 632.8 nm falls in the region of the Q absorption band and several electronic transitions may occur which may produce a number of symmetry states and thus enhance the Raman bands due to the excitation of overlapped vibronically active modes. Raman spectra of the polarized and depolarized light scattered from aqueous solutions of Co-TSPc and Fe-TSPc at various pH are shown in Figures 2 and 3.

The spectra are similar in appearance and generally are in an agreement with those obtained in prior studies (3) where phthalocyanines were dissolved in organic solvents.

The position of the Raman bands are tabulated in Table I. Shifts of the Raman bands were not observed as a function of pH within the range of the experimental error of $\pm$ 5 cm^{-1}.

The low frequency Raman lines below or around 500 cm^{-1}, according to the previous report (3) could be assigned to the M-N stretching vibrations or to the modified pyrrole skeletal vibrations. The latter possibility appears more plausible since the similar bands are recorded in metal free phthalocyanines (H_2 - TSPc) in a different experimental condition, which will be reported later (10). An aqueous solution of H_2 - TSPc is characterized with intense fluorescence at 690.5 nm which masks Raman spectra and prevents a comparative analysis of the Raman spectra which can be obtained from other metallo phthalocyanines.

The band at 523 cm^{-1} shows an anomalous depolarization ratio $\rho > 3/4$ (in the case of Fe-TSPc) and can be explained as being due to the rise of the asymmetric mode caused by weakening of the pyrrole ring bond which is influenced by the position of the central Fe atom and Fe-N distance. A theoretical study of Fe-Pc (9) was proposed an Fe vibration out of plane as much as 0.49 Å although this high spin state is not favorable energetically.

The strong bands at 616, 699 and 767 cm^{-1} are most probably due to out of plane deformation of the pyrrole rings. A special feature for Co - TSPc is the strong shoulder at 722 cm^{-1} and the much broader linewidth of the band at 699 cm^{-1}. All bands show the normal depolarization ratio $\rho < 3/4$ except the band at 781 cm^{-1} for Co-TSPc in neutral environment, which shows a depolarization ratio close to unity.

The spectral region between 780 - 1300 cm is filled by a number of weaker bands which are due to C-H bending and which are in principle modified by the central metal atom. The two strongest bands at 1352 and 1551 cm^{-1} are due to =C-N and C=C stretching modes, respectively. The intensity of these Raman bands is highly influenced by the laser excitation (9) (3) and by the solvent, since the odd electron in the d_{z^2} orbital is highly sensitive to the presence of a ligand.

The most interesting feature is the behavior of Fe-TSPc in various pH environments. The band at 1352 cm^{-1} shows a frequency shift of about 11 cm^{-1} when the alkaline solvent was used. According to a previous study on porphyrins (11), the frequency shift may be assigned to Fe(II) - Fe(III) transition and may be indicative of an oxidation-reduction mechanism of the iron atom.

In conclusion, the highly complex structure of metallo phthalocyanies may produce very complex Raman spectra which can be described by two possibilities of excitation of the polarizability tensors (12):

(A) Excitation of the diagonal polarizability components which excite totally symmetric modes, and

(B) Excitation of off-diagonal terms which mix the resonant electronic transisiton with another one of higher energy. These modes may have any molecular orbital symmetry.

When the laser excitation falls in the Q band, region the enhancement of B modes appears predominant. Mixing of electronic transitions allows a_{1u}, a_{2u}, b_{1u} and b_{2u} molecular orbital symmetries. In a_{1u} symmetry, no polarized Raman bands are found to be in resonance with a laser excitation within Q bands. Both b_{1u} and b_{2u} give rise to depolarized Raman bands while a_{2u} modes are inactive in normal Raman scattering. The a_{2u} symmetry is associated with the anti-symmetric tensor and produces inverse polarization.

More detailed studies of tetrasulfonated phthalocyanines (i) in aqueous solution phases and (ii) adsorbed on electrode surfaces will be reported in subsequent papers.

The help and interest of Mr. S. Zecevic is gratefully acknowledged, and authors also would like to express their appreciation to the DOE and its financial support.

References

1. L. Edwards and M. Gouterman, J. Mol. Spectrosc. 33, 292, (1970).

2. A.N. Sidorov and I.P. Kotlyar, Opt. i Spectroskopiya, 11, 175 (1961).

3. I.V. Aleksandrov, Ya. S. Babovich, V.G. Maslov and A.M. Sidorox, Opt. Spectrosc., 37, 467 (1974).

4. T. Veprek-Siska, E. Schwertnerova and D.M. Wagerova, Chimia, 26, 75 (1972).

5. L.C. Gruen and R.T. Blagrove, Aust. J. Chem., 26, 319 (1973).

6. A.J. Appleby and M. Savy, Electrochim. Acta, 21, 567 (1976).

7. J. Zagal, R.K. Sen and E. Yeager, J. Electroanal. Chem., 83, 207 (1977).

8. T.H. Weber and D.H. Busch, Inorg. Chem., 4, 469 (1965).

9. A.M. Schaffer, M. Gouterman and E.R. Davidson, Theort. Chim. Acta., 30, 9 (1973).

10. B. Simic-Glavaski, S. Zecevic and E. Yeager, to be published.

11. T.G. Spiro and T.C. Strekas, J. Am. Chem. Soc., 96, 338 (1974).

12. A.G. Albrecht and M.C. Hutley, J. Chem. Phys., 55, 4438 (1971).

TABLE I

Co-TSPc|cm^{-1}|	Fe-TSPc|cm^{-1}|
	327
	394
528	523
621	616
699	699
722	726
781	767
866	870
983	983
1144	1144
1198	1208
1229	1219
1289	1289
1352	1352 (1363 pH 13)
1476	1476
1551	1551

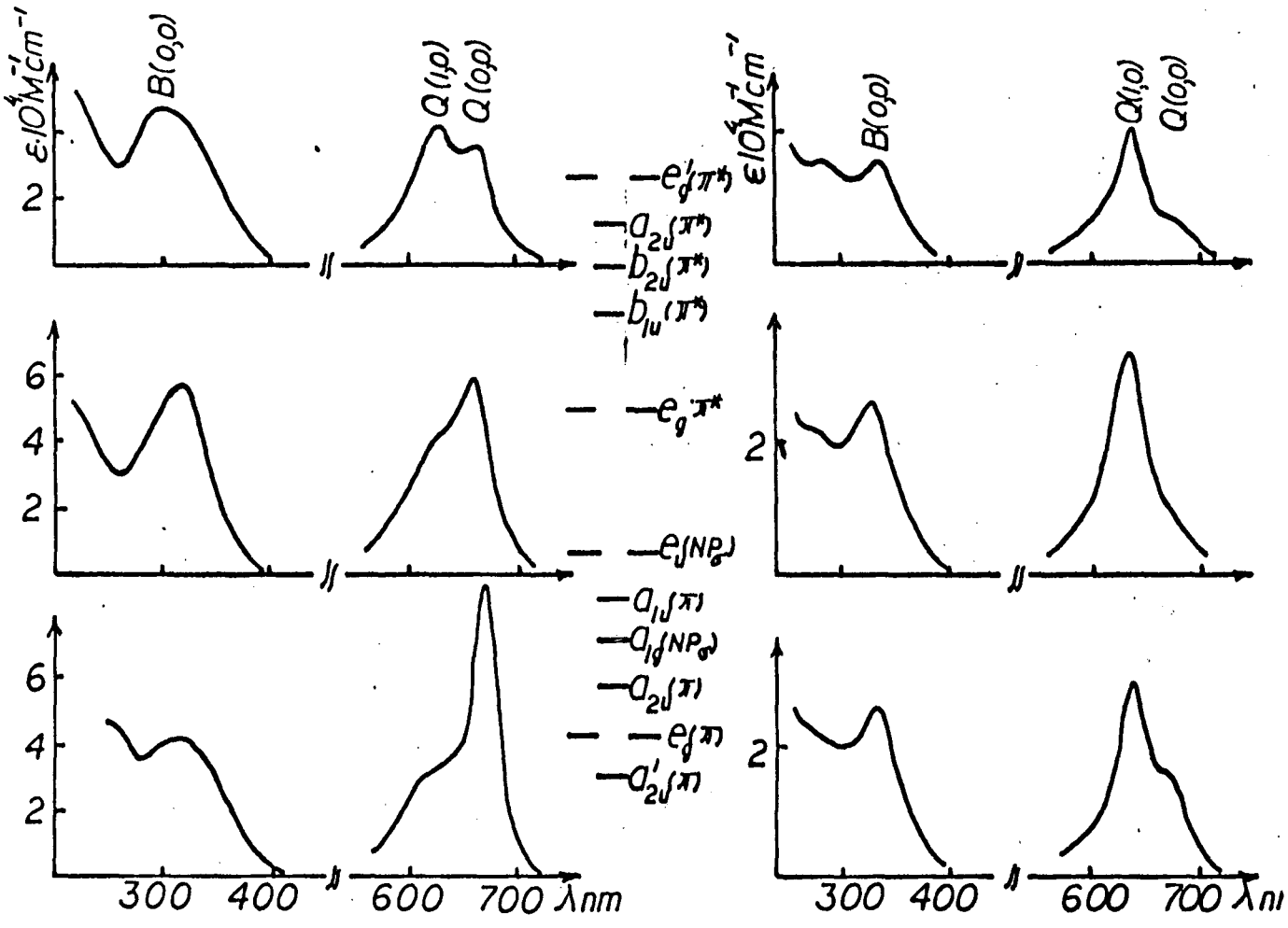


Fig. 5.1.7.1. UV-visible absorption spectra of 5 x 10^{-5}M of cobalt and iron tetrasulfonated phthalocyanines in aqueous media as a function of pH. The insert represents a schematic molecular orbital diagram of metal-free phthalocyanine.

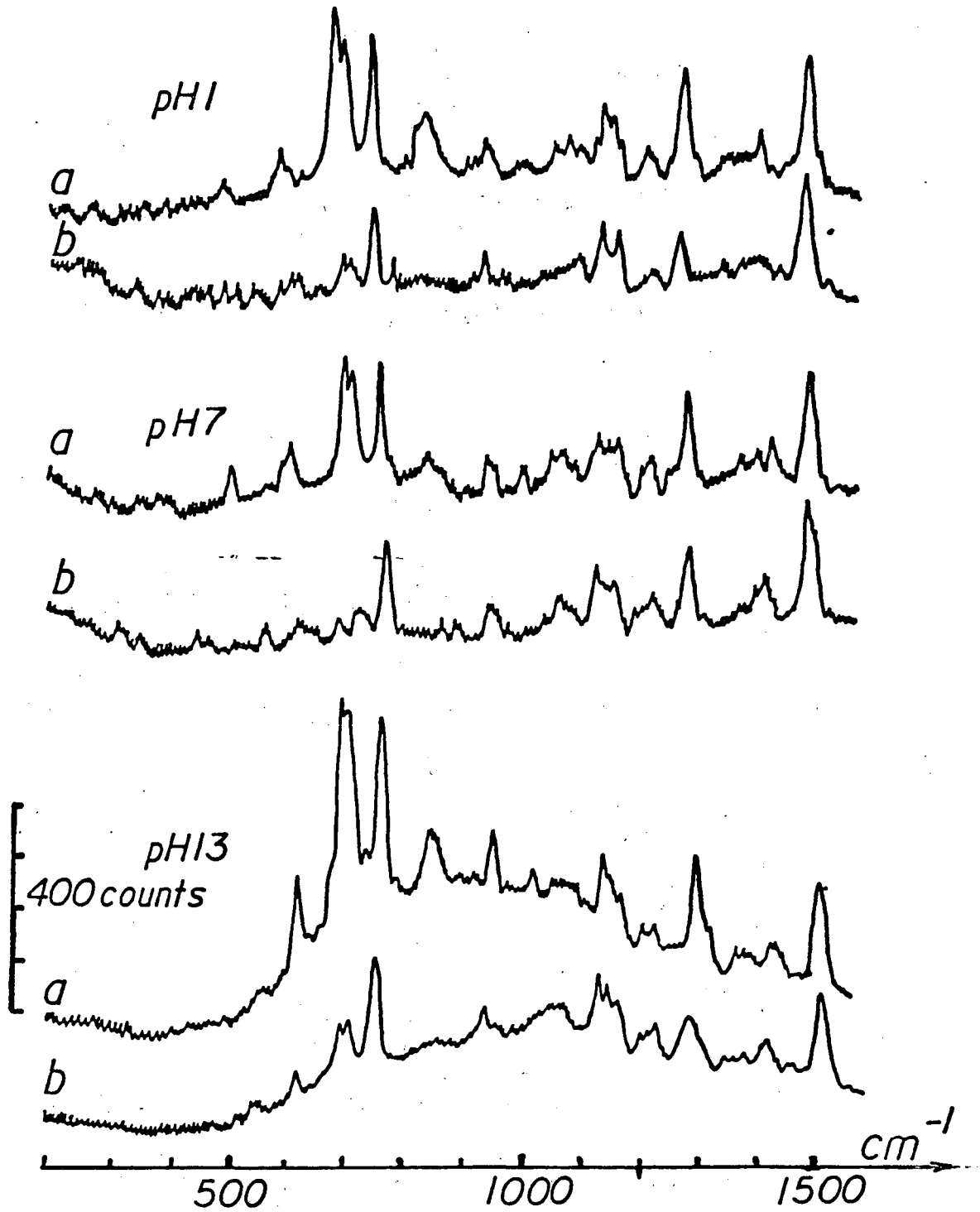


Fig. 5.1.7.2. Raman spectra of a) the polarized and b) the depolarized light scattered from 5 x 10^{-5}M of cobalt tetrasulfonated phthalocyanine in aqueous solutions at pH 1, pH 7 and pH 13. A relative intensity scale is indicated in counts and spectra are twice more intense for alkaline solution, resolution is 2.5 cm^{-1}, laser excitation is at 632.8 nm with 50 mW output power.

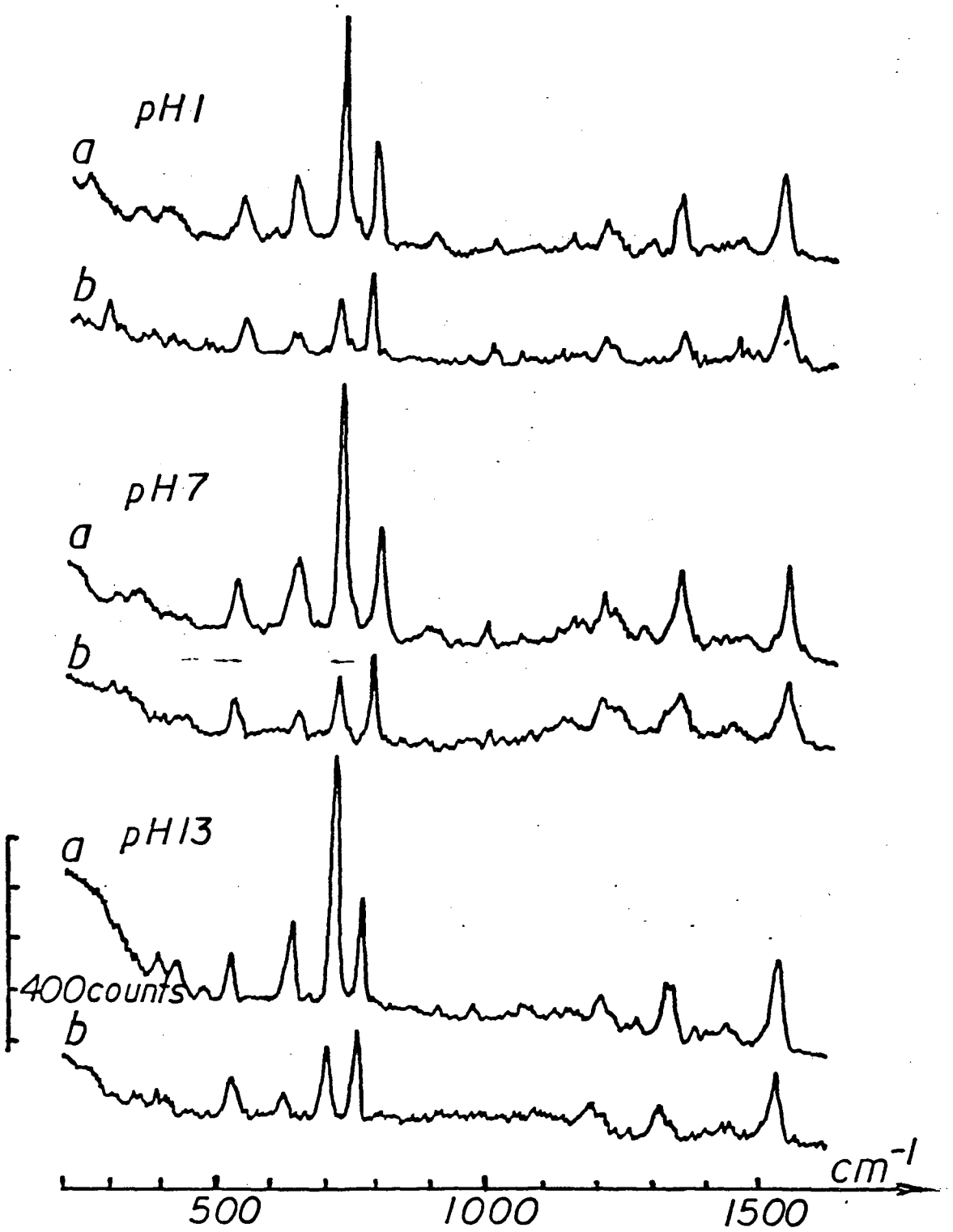


Fig. 5.1.7.3. Raman spectra of a) the polarized and b) the depolarized light scattered from 5 x 10^{-5}M of iron tetrasulfonated phthalocyanine in aqueous media. The legend is the same as in Fig. 5.1.7.2.

5.1.8 THIN LAYER CELL FOR U.V. AND VISIBLE SPECTROELECTROCHEMICAL STUDIES

D. A. Scherson[+], Shantha Sarangapani and F. L. Urbach

ABSTRACT

A new optically transparent thin layer electrochemical cell contained entirely into a standard quartz cell has been designed. The main advantages of this novel configuration are the inertness of its components to most organic and inorganic solvents, the possibility of repeated utilization of the gold minigrid electrode and ease of assembly. Moreover, the use of an appropriate delivery system, such as the one presented in this work in conjunction with the cell, enables the handling and study of oxygen sensitive materials. Path lengths and volume of solution tests have been performed, yielding reproducible results upon repeated assembly. The simple construction allows use of this device as a versatile tool in the analysis of spectral properties of a wide variety of electrochemically generated species.

The use of optically transparent thin layer cells has become a common practice in spectroscopic studies of electrogenerated species. The extremely small volume of solution in direct contact with the electrode allows a rapid equilibration of reactants and products upon changes in potential across the metal-solution interface without appreciable back-diffusion into the bulk of the electrolyte. Several thin layer cell designs have been shown to yield satisfactory results in numerous applications in spectral regions ranging from far U.V. to infrared.[1] One of the most widely utilized systems[2] consists of a gold minigrid placed between two standard microscope slides separated by thin Teflon spacers, allowing the grid to protrude slightly from the edge to make electrical connection. The assembly is sealed by covering the sides with epoxy, leaving a small area exposed. The whole cell is then placed into a separate vessel, normally a Petri dish, containing the solution to be analyzed and suction is applied through the opening until the liquid rises to an appropriate level.

As part of a continuing effort in this laboratory regarding the spectral characterization of transition metal complexes and their redox chemistry, a search for a cell design was initiated, such that it would enable U.V. and visible spectra to be acquired simultaneously, provide strict conditions of anaerobicity and be versatile enough to be used with any organic solvent.

DESCRIPTION OF THE CELL AND ASSEMBLY

A schematic representation of the whole assembly including the delivery system is given in Fig. 1. The cell is built around a standard 20 mm path quartz cuvette and contains all the essential components to

[+]Vittorie deNora Diamond-Shamrock Postdoctoral Fellow

perform most spectroelectrochemical experiments of interest. A precision machined L-shaped Kel-F piece (E) serves the dual purpose of providing feedthroughs for the delivery system and counter and reference electrodes, (B) and (D) respectively. These last two components are placed along the cuvette sides to avoid obstruction of the light beam. The Kel-F piece (E') also mechanically holds in place a quartz plate[≠] (L) which has two vertical strips (∿0.015 cm thick and 0.05 cm wide) which self-adhere to the quartz plate and serve to fix the effective optical path length. This geometry creates a cavity between the plate (L) and the inner cell wall where a minigrid electrode (M) is housed. A rectangular slot in the arm of (E) inside the cell allows a clear light path. A second Teflon piece (although any material would be suitable in most cases) (N) located precisely in front of (E) on the outside with a similar slot through it, serves to affix (E) in the right position by means of a screw (G). A connection to the grid which extends over the cell along its front side is made by a second brass screw (H) which is used to push a small brass piece (F) with a welded thin gold foil at the end, thus allowing electrical contact to the minigrid working electrode. A groove was milled (N) as a guiding channel for (F) in order to avoid rupture of the gruid due to the turning motionof the screw.

The electrolyte delivery system consists of a Teflon container with two drilled-in capillary holes. One of these openings enables either the transfer of solution to the cell through flexible Teflon tubes (A) and (J) or the continuous passage of a solvent-saturated inert gas over the solution in the cell by simply lowering (A) and raising (J). The contact seal provided by the Kel-F piece which sits reasonably tightly onto the quartz cuvette was sufficient to insure an inert atmosphere in the cell as evidenced by the success obtained with known oxygen-sensitive cobalt(II) complexes, [5] while air vent gas was passed through the cell. In a normal experiment (E) is turned ninety degrees counter clockwise, the plate (L) positioned and the minigrid laid on top. The cuvette is then slid in without changing the geometry and (F) is connected by screwing in (G) and (H). Once this step is completed, about 1 to 2 mls of solution are introduced through the delivery system. A slight tipping of the cuvette is sufficient for a thin layer to be spontaneously formed by capillary action.

As a means of examining the reproducibility of the cell geometry upon repeated assembly, two kinds of calibration tests were made, namely the total absorbance of a known standard (chromate, $\varepsilon = 4813$ at $\lambda = 373$ nm) to establish the path length and the total cell volume as measured by the charge passed in the electrolysis of a fast couple (potassium ferro-ferricyanide).

The performance of the cell in spectroelectrochemical experiments was evaluated by using the well characterized oxidation of o-tolidine in acidic solution.

[≠] A piece of quartz of the correct dimension can be made by using the window of a broken cuvette and then grinding off the side walls and excess quartz.

EXPERIMENTAL SECTION

Visible and U.V. spectra were obtained with the cell in Cary 14. A special electrical feedthrough was installed into a circular orifice in the spectrometer body, and the cell positioned onto a specifically designed Lucite holder supported on the cavity rails. Electrochemical experiments were performed using a conventional potentiostat (RDE 3, Pine Instruments, Grove City, Pennsylvania) and an X-Y recorder. The working electrode was a 100 wires/in. gold minigrid, and the counter and reference electrode a gold wire with a piece of discarded gold minigrid at its end, and a miniature standard calomel electrode respectively. Solutions were prepared from Baker analyzed reagents and triply distilled water, and the concentrations similar to those reported in Ref. 2, i.e. 4.0×10^{-3} M $K_4Fe(CN)_6$ in 0.5 M KCl and 1.0×10^{-3} M o-tolidine in 0.5 M acetic acid, 1.0 M $HClO_4$. Standard absorption chromate solutions[4] were made by dissolving $KCrO_4$ in 0.05 N KOH to a concentration of 4×10^{-6} g/liter. Calibration experiments were performed five times and following each run the cell was completely disassembled and the grid and other components thoroughly washed and dried with acetone.

RESULTS

Table I lists the values of the absorbance of chromate and the corresponding calibrated path lengths obtained through five independent experiments as described in the Experimental Section. The average value found was 0.0145 ± 0.005 cm, which is comparable to that of other designs, such as the one referred to in the Introduction.

The results of electrolysis experiments are given in Table II, yielding an average cell volume of 3.2 ± 0.2 ul. The cyclic voltammogram of the $Fe(CN)_6^{-4}/Fe(CN)_6^{-3}$ in the thin layer cell is depicted in Fig. 3 for two different scan rates, i.e. 1 mV/s and 2 mV/s. The shape of the voltammogram shows as expected, some uncompensated resistance (IR drop) due to the restricted ionic path. However, the charge under the cathodic and anodic waves are the same and the value of E_o ∿0.77 vs. NHE is in agreement with the literature.

Figure 4 shows the cyclic voltammogram of an o-tolidine solution prepared as outlined above. The E_o' was similar to that reported by DeAngelis and Heineman[2].

Spectroelectrochemical experiments were conducted at five different potentials (see Fig. 5) and the values of the corresponding absorbances are listed in Table II. The resulting Nernstian plot (see Fig. 6) yielded a slope of 35 mV (n ∿2.21), slightly higher than the potential number of 2.0.

DISCUSSION AND CONCLUSIONS

The advantages of the cell design described above are numerous. The electrolyte comes in contact only with very inert materials,

providing excellent conditions of cleanliness and compatibility with all solvents of interest. Moreover, the thin layer is formed spontaneously, making the use of a suction mechansim unnecessary. The virtual seal between the Teflon spacers, quartz plate and wall cell is such that the liquid layer undergoes no changes during the normal course of an experiment. By proper operation of the delivery system a blanket of solvent saturated inert gas can be continuously passed through the cell, thus avoiding the danger of electrolyte drying which would interrupt the ionic continuity. The fact that the container is a standard quartz cuvette allows convenient mounting of the whole assembly in the cavity of any spectrometer.

Overall, excellent reproducibility characteristics of the cell upon repeated assembly as shown above proves the high versatility of this design in most spectroelectrochemical applications.

ACKNOWLEDGEMENTS

The authors would like to express their appreciation to Professor Ernest Yeager for fruitful discussions and suggestions, and to Keith Schultz of CWRU for his advice and skillful machining during the course of the design and construction. One of us (D.S.) would also like to thank Diamond Shamrock for a fellowship.

References

1. R. Rhodes and K.M. Kadish, Anal. Chem. 53, 1539 (1981), and references therein.

2. T.P. DeAngelis and W.R. Heineman, J. Chem. Ed. 53, 595 (1976).

3. D.F. Rohrbach, W.R. Heineman and E. Deutsh, J. Inorg. Chem. 18, 2537 (1979).

4. G.W. Haupt, J. Research NBS 48, 414 (1952).

5. S. Sarangapani, F.L. Urbach and E. Yeager (manuscript in preparation).

TABLE I

Standard chromate solution absorbances and corresponding calculated path lengths as measured in thin layer cell (T.L.C.) upon repeated assembly

Run #	Absorbance (λ= 373 nm)	Path length (cm)
1	0.15	0.015
2	0.15	0.015
3	0.15	0.015
4	0.135	0.014
5	0.135	0.014

Average: 0.0145 ± 0.005 cm.

TABLE II

Volume of the thin layer cell (T.L.C.) as evaluated from several controlled potential electrolyses of 4 mM $K_4Fe(CN)_6$ in 0.5 M KCl.

Run #	Volume of TLC (µl)
1	32
2	35
3	30
4	32
5	30

Average: 32 ± 0.2 µl

A. GAS INLET

B. COUNTER ELECTRODE/EXTERNAL CONNECTOR

C. AUXILIARY INLET/OUTLET

D. REFERENCE ELECTRODE

E. KEL-F, L-SHAPED, HOLDER-COVER

F. BRASS CONNECTOR WITH WELDED GOLD FOIL IN THE FRONT

G. SUPPORT SCREW

H. SCREW FOR ELECTRICAL CONNECTION TO WORKING ELECTRODE

I,J. INLET GAS/ELECTROLYTE

K. COUNTER ELECTRODE

L. QUARTZ PLATE

M. GOLD MINIGRID

N. TEFLON SUPPORT

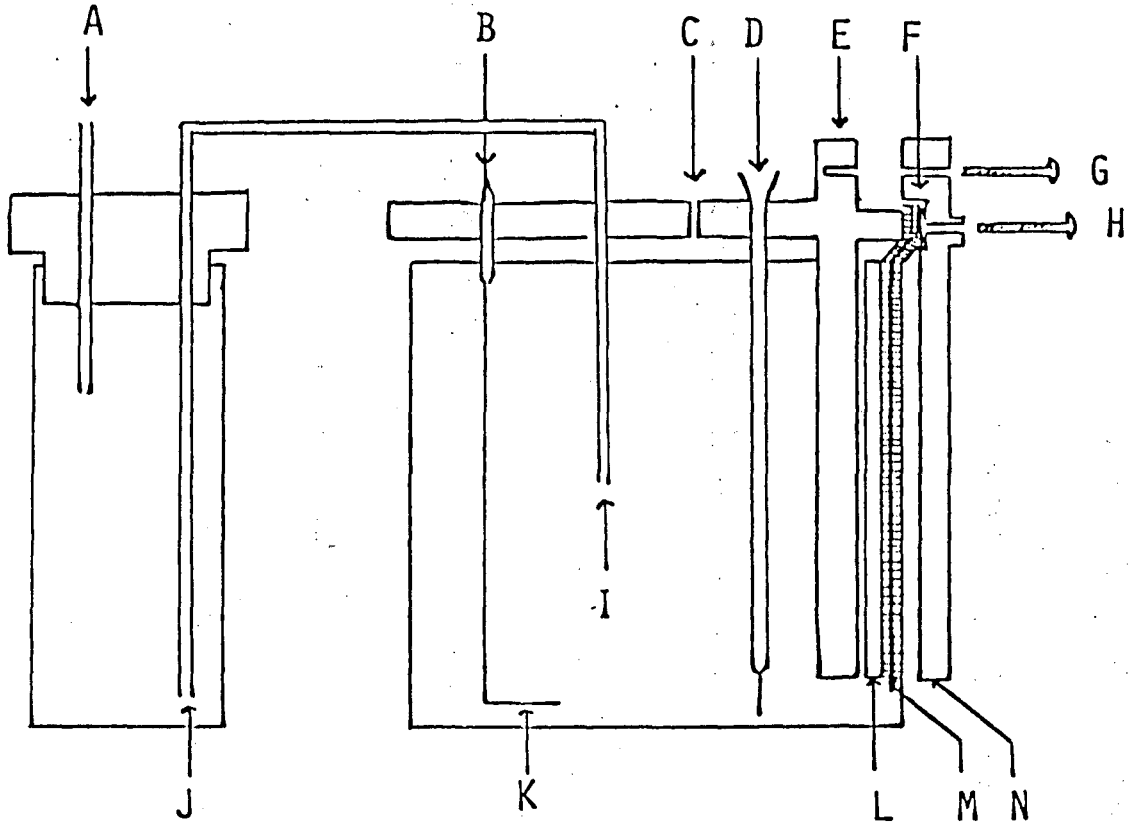


Fig. 5.1.8.1. Schematic diagram of optically transparent thin layer electrochemical cell with associated delivery system for anaerobic manipulation of oxygen-sensitive materials.

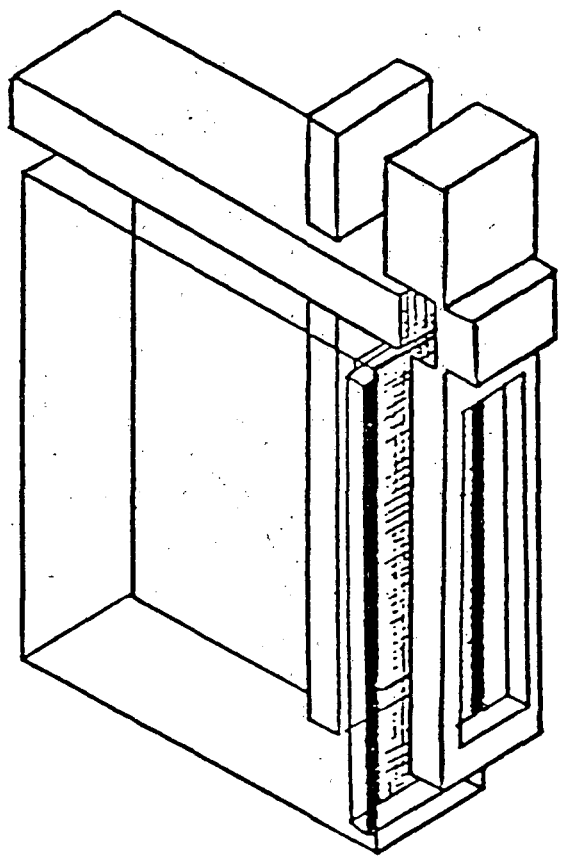


Fig. 5.1.8.2. Three-dimensional view of assembled optically transparent thin layer electrochemical cell. Some details have been omitted for clarity.

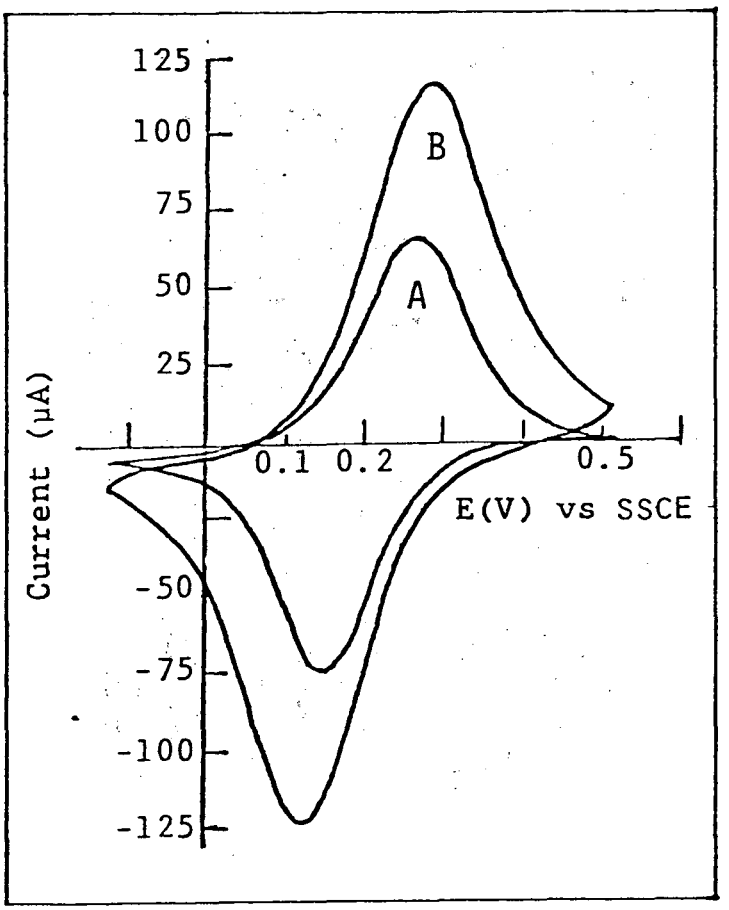


Fig. 5.1.8.3. Cyclic voltammogram of 4 mM $K_3Fe(CN)_6$ obtained in the transparent thin layer electrochemical cell for scan rates of 1 mV s^{-1} (A) and 2 mV s^{-1} (B).

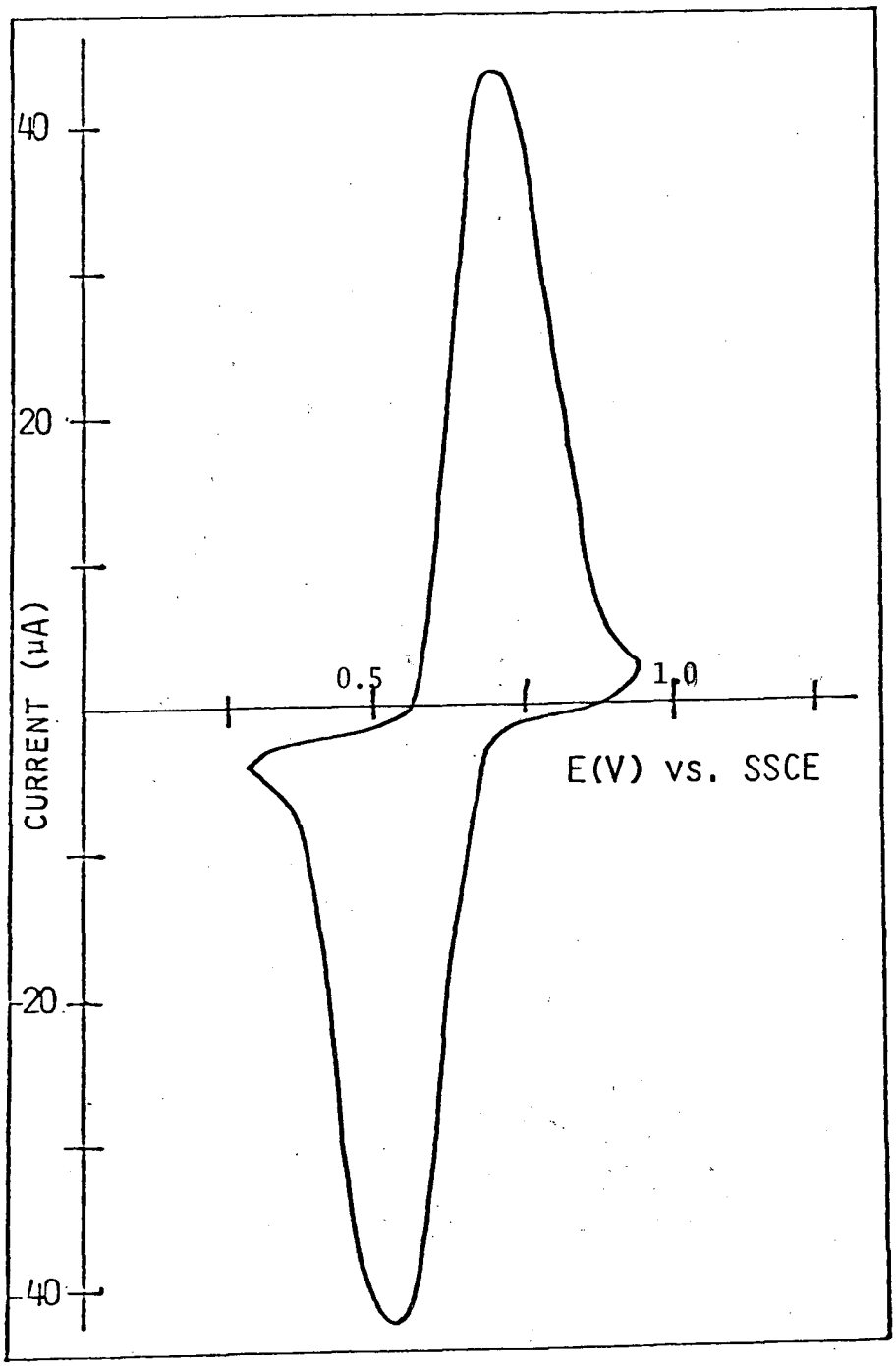


Fig. 5.1.8.4. Cyclic voltammogram of 0.95 mM o-tolidine, 0.5M acetic acid, 1.0 M $HClO_4$. Scan rate 2 mV s^{-1}.

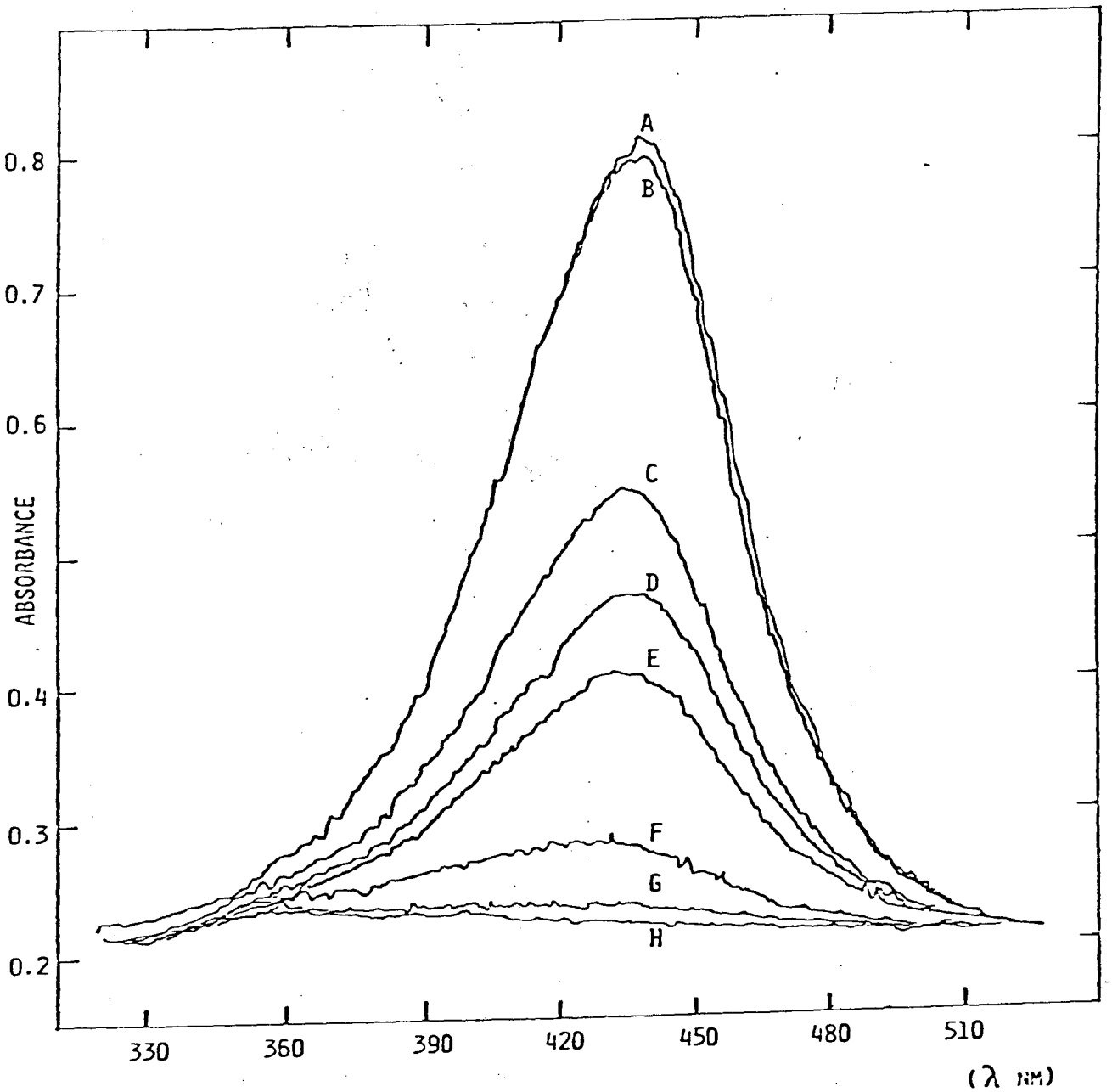


Fig. 5.1.8.5. Thin layer spectra of 0.95 mM o-tolidine, 0.5 M acetic acid, 1.0 M $HClO_4$ obtained at different values of applied potential. Cell thickness 0.014 cm. A = 0.809, B = 0.694, C = 0.630, D = 0.621, E = 0.614, F = 0.595, G = 0.569, H = 0.540 V vs. SSCE.

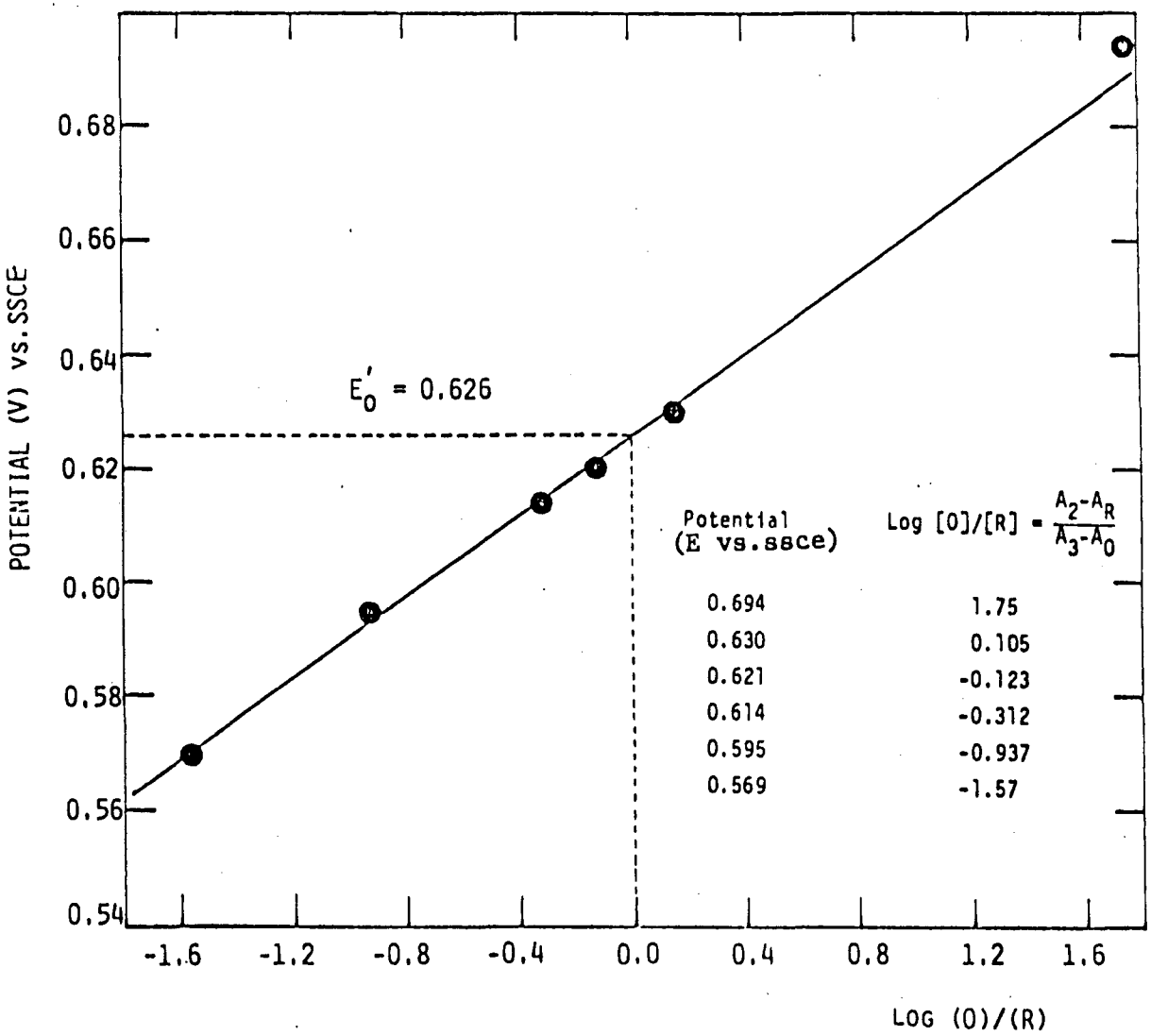


Fig. 5.1.8.6. Nernstian plot for o-tolidine system based on the experimental results given in Fig. 5. Insert: Values of log[O]/[R] = $(A_2-A_R)/(A_3-A_0)$ and E vs. SCE. $A_0 = 0.8$, $A_R = 0.22$.

5.1.8(a) PART II. Thin layer spectro-electrochemistry of binuclear Cobalt(II) and Nickel(II) taph macrocyclic complexes

Shanta Sarangpani and Fred L. Urbach

5.1.8 (a) Part II. THIN LAYER SPECTRO-ELECTROCHEMISTRY OF BINUCLEAR COBALT[II] AND NICKEL[II] TAPH MACROCYCLIC COMPLEXES

Shanta Sarangpani and Fred L. Urbach

ABSTRACT

The redox and spectral properties of a binuclear cobalt macrocycle, $Co_2taph(NO_3)_4 \cdot 4H_2O$ and its nickel analogue were examined using a specially designed thin layer cell.* The results indicate that the anodic processes observed in both cases at 0.5-0.7V vs SCE involve the oxidation of the ligand system. Differences in the cathodic processes observed for the cobalt and nickel complexes are attributed to the presence of a $Co^{[III]}/Co^{[II]}$ couple and to differences in the nature of the ligand reduction in the presence of two metal ions. On the first sweep the cobalt macrocycle undergoes an initial irreversible $4e^-$ reduction at -1.2V. Subsequent sweeps showed the appearance of a couple around -0.5V. The $4e^-$ reduction is attributed to the reduction of the two Schiff base linkages present in the molecule to saturated secondary amine donors. The new redox behavior at -0.5V is attributed to the $Co^{[III]}/Co^{[II]}$ couple of the saturated macrocycle. Negative potentials for the $Co^{[III]}/Co^{[II]}$ couple are known for complexes with an N_4 mcrocyclic environment and axially coordinated OH^- donors.

In the case of the nickel analogue two reduction processes are observed at -0.8V and -1.24V which correspond to a combined total reduction of $4e^-$. In the absence of direct spectroscopic evidence for a Ni[I] species, these cathodic waves are tentatively assigned to stepwise reduction of the two azo methine linkages.

INTRODUCTION

A critical matter in interpreting the electron transfer reactions of metal complexes is the identification of sites that undergo significant change in the oxidation level upon passing from one redox state to another.[1-3] In the present study we are dealing with a new class of macrocycles derived from the ligand 1,4-dihydrazino-phthalazine. The synthesis of the dinickel macrocycle was reported by Rosen[4]. We have synthesized the dicobalt macrocycle and found that it catalyzed the electrochemical reduction of oxygen in alkaline solutions. In order to understand the electronic properties of the macrocyclic structure, the spectral and redox properties of Co_2taph^{4+} and its nickel analogue and that of 1,4-dihydrazinophthalazine (dhph) were compared. A common solvent for these compounds was N,N-dimethyl formamide in which high concentrations of the order of $\sim 10^{-3}$M could be achieved for thin layer work. The sparing solubility of the Co[II] macrocycle in 0.1M NaOH and the fast hydrolysis of the Ni[II] macrocycle in alkaline solution prevented the thin layer spectroelectrochemical study in this medium.

*See Part I

EXPERIMENTAL

The $Co_2taph[NO_3]_4 \cdot 4H_2O$ was prepared according to the procedure given in an earlier report.* The nickel analog was prepared according to the literature except that $Ni[NO_3]_4 \cdot 6H_2O$ was used as the starting material. The IR spectra of the two macrocycles were very similar and the solid samples were always stored in a vacuum desiccator after thorough drying under vacuum. The DMF (ACS certified, Fisher Scientific Company) used for electrochemical purposes was dried over molecular sieves. The supporting electrolyte was 0.5M Et_4NClO_4 (G. Frederick Smith Chemical Company, Columbus, OH). The rest of the procedure for thin layer work is the same as described in Part I. All experiments were carried out under nitrogen. All potentials are reported versus SCE. All spectra were recorded after the currents reached a minimum value (i.e., till there was no change in the magnitude of the current). At very negative potentials beyond -0.9V a residual current was always noted, but at less negative potentials, the current value reached almost zero while the potentials were constant.

The solutions of the macrocycles for spectroelectrochemistry were prepared in the following way. Known volumes of the electrolyte 5 to 10 ml was deaerated for 2 hours in a teflon cell (see part I) and known amounts of the macrocycles were dissolved in the electrolyte to give concentrations typically of the order of 10^{-3} M.

RESULTS

The Electrochemistry of the Macrocycles:

(a) The region between +1.0v and -0.4v:

The Co_2taph^{4+} shows a broad oxidation peak around +0.7v and a reduction peak at -0.3v (Fig. 1). Spectral changes corresponding to the oxidation are shown in Fig. 2. The oxidation corresponds to a $4e^-$ process according to our controlled potential electrolysis data. (See table I). The oxidized species could be reduced by $4e^-$ at -0.4v. The spectral changes observed during this reduction are shown in Figure 3. The end product of the reduction is very similar to that of the starting material. The cyclic voltammogram of the dinickel analog is shown in Figure 1a. The electrochemical response is very similar to that of the cobalt macrocycle. The oxidation of the nickel compound was slow and the electrolysis did not go to completion. Hence quantitative results could not be achieved. However, the spectrum of the partially oxidized species showed the same visible band that was observed in the cobalt case.

(b) The region between 0.5v and -1.4v:

A further excursion into the cathodic region in the case of Co_2taph^{4+} showed a large reduction at -1.2v [n=4]. On reversal new

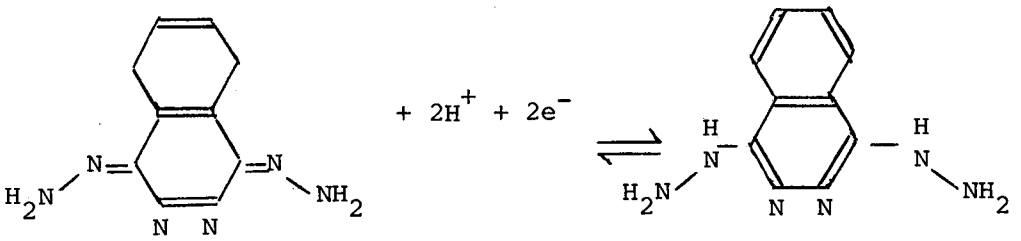
*DOE Report, 1979-80.

peaks appeared between -0.2v and -0.5v (Fig. 4 and 5). The spectral changes observed during this reduction are shown in Figure 6.

In the case of the Ni_2 taph^{4+} the cathodic scan showed two successive reductions, the first of which had a complimentary oxidation peak, independent of the second reduction. (Fig. 7). The spectral changes that occur during this reduction are shown in Figure 8. the n value for the two reductions at -1.3v was found to be 4.

DISCUSSION:

In view of the similarity in the voltammetric behavior as well as spectral changes, the oxidation of the cobalt and nickel macrocycles seems to occur at the ligand. A further evidence is the fact that, dhph when oxidized under the same conditions shows a visible band at 470 nm, even through the extinction coefficient of this band for the oxidized ligand is lower than what is observed for the cobalt macrocycle. The cyclic voltammogram of dhph and the spectral changes observed during its oxidation and reduction are shown in Figures 9 and 10. The oxidation corresponds to an n value of 2 and the oxidized species can be reduced by the same number of electrons. The same compund (dhph) shows a very reversible behavior in alkaline medium. (Fig. 11). The reason for the irreversibility in DMF could be due to the slow loss of protons whereas in alkaline medium the deprotonation of -NH- groups facilitate rapid charge transfer. The following scheme is proposed for the oxidation and reduction of the ligand.



A behavior that could be compared to the electrochemistry of p-phenylene diamine[5]. The same process conceivably occurs in the cobalt and the nickel macrocycles as well. Even though the electrochemistry is irreversible for the oxidation and reduction of the macrocycles, at least in the cobalt case, we have found that the molecule can be cycled between the oxidized and the reduced forms. The cathodic processes remain unaffected by the anodic process. That was our reason for studying the electrochemistry in two parts, which are practically independent of each other.

At -1.2v the 4e reduction observed for the cobalt macrocycle results in the appearance of intense visible bands. After this reduction the molecule does not show its original behavior. The appearance of two new voltammetric peaks indicate the formation of a new species.

The following possibilities exist:

(1) The cobalt [II] centers are reduced to Co[I] followed by a further reduction to Co[O]. But our spectral evidence indicates that the bands at 485 nm grow in intensity as a function of potential in a continuous manner and at the end of complete electrolysis at -1.4v. the intensity ceases to increase, but the bands to not show any further change. Hence, reduction to the Co[O] state can be ruled out.

(2) The Schiff base linkages in the molecule are reduced by four electrons and a more saturated molecule is produced. The intense visible bands may be due to ligand to metal charge transfer. Only very few examples for the electrochemical reduction of double bands of the Schiff base linkages are known. It has been found that the ease of reduction depends on the polarity, and the protic nature of the solvent. Also it is dependent on the nature of the macrocycle. In acetonitrile the trans [14] diene Curtis macrocycle undergoes reduction at -2.7v whereas some nickel macrocycles in CH_3OH show Schiff base reductions around -1.5v.

(3) The elemental analysis of the cobalt macrocycle indicates that 4 to 5 water molecules are associated with each molecule of the macrocycle. At very negative potentials -1.4v where the Schiff base reduction occurs, local changes in pH might occur due to protonation of the reduced macrocycle, resulting in the coordination of OH^- to the cobalt centers. As reported for cobalt trans[14] diene, when coordinated to OH^- shows a redox couple due to Co[III]/Co[II] at negative potentials -0.55v vs SCE.[8]

The behavior of the Ni[II] complex is different from what was observed for the cobalt case. The first reduction has a complimentary oxidation. Then second reduction is irreversible. During the process of reduction intense visible bands appear whose intensities can be diminished by switching to oxidizing potentials (-0.1v). It has been reported that cyclic tetra macrocycles containing Ni[II] either give Ni[I] complexes or metal stabilized ligand radicals, depending on the nature of the ligand. In the absence of epr data it was not possible to distinguish between a ligand radical and Ni[I] species. The high intensity bands could be due to charge transfer from the ligand to metal, if Ni[I] species are not involved. One striking feature about the nickel complex is that the electrochemistry is not complicated by the appearance of any new couples as is observed in the case of the cobalt.

References

1. T.J. Truex and R.H. Holm, J. Am. Chem. Soc., 94, 4529 (1972).

2. Alan L. Balch and R.H. Holm, J. Am. Chem. Soc., 88, 5201 (1966).

3. N. Takvoryan, K. Fermay, D.H. Busch et al J. Am. Chem. Soc., 96, 731 (1977).

4. W. Rosen, Inorganic Chemistry, 10, 1832 (1971).

5. Z. Galus, H.Y. Lee and R.N. Adams, J. Electroanal. Chem. 5, 17 (1963).

6. D.C. Olson and J. Vasilvekis, Inorganic Chemistry, 8, 1610 (1969).

7. E. Kent Barefield, Frank V. Lorecchio, D.H. Busch et al, Inorganic Chemistry, 11, 283 (1972).

8. D.P. Rilemma, J.F. Endicott, and E. Papaconstantinou, Inorganic Chemistry, 10, 1739 (1971).

TABLE I

Thin Layer Spectroelectrochemical Data for Co_2 taph$(NO_3)_4$ .4 H_2O

POTENTIAL	n*	λmax, nm	$\varepsilon m^{-1}cm^{-1}$
		350	16,000
+0.75	4	470, 350	11,700; 16,700
-0.75	4	350	16,00
-1.45	4	485, 335	16,000; 17,000

Thin Layer Spectroelectrochemical Data for Ni_2 taph(NO_3) .4 H_2O

		350	17,000
+0.75	a	470, 350	(?): 17,800
-0.926		575,440,305sh	10,440; 11,000; 22,500
Reoxidized	-0.2	440, 350	5,500; 16,000
Rereduced at -1.48 b		440, 350, 300	15,200; 21,400; 28,000

Thin Layer Spectroelectrochemical Data for dhph

		340	5,500
+0.75	2	540,460,340	1,000; 2,000; 7,500
-1.2v	2	340	6,000

a = an n value could not be obtained due to extremely slow oxidation. The partially oxidized species showed a band at 470 nm, but ε was not obtained.

b = The Ni[II] macrocycle when reduced directly at -1.45v gave an n value of 4.

* = The n values were obtained by controlled potential electrolysis of the thin layer. [The volume of the thin layer cell was calibrated using $K_3Fe(CN)_6$ system.] Typically 3 to 4 electrolyses were carried out at each potential and the n values reported have a maximum deviation of $\pm$ 0.2.

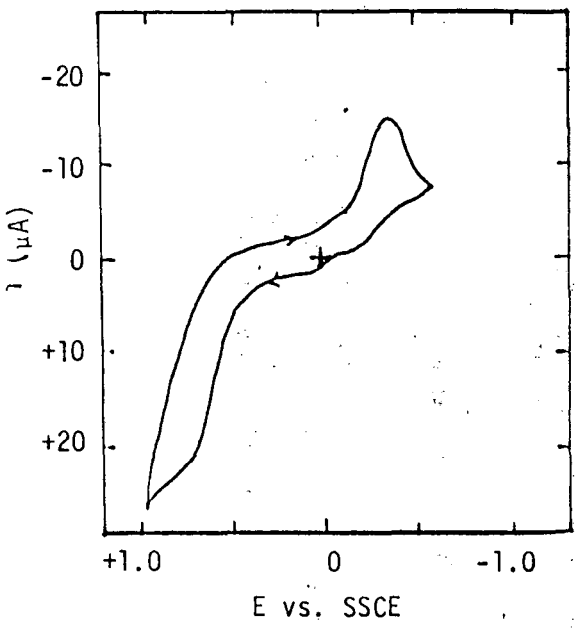


Fig. 5.1.8.1(a). Cyclic voltammogram of $Co_2taph(NO_3)_4 \cdot 4H_2O$ in 0.5M Et_4NClO_4 in DMF Conc. $\simeq 10^{-3}$M. S.R. = 140 mV/s. Au disk. Area = 0.19 cm^2.

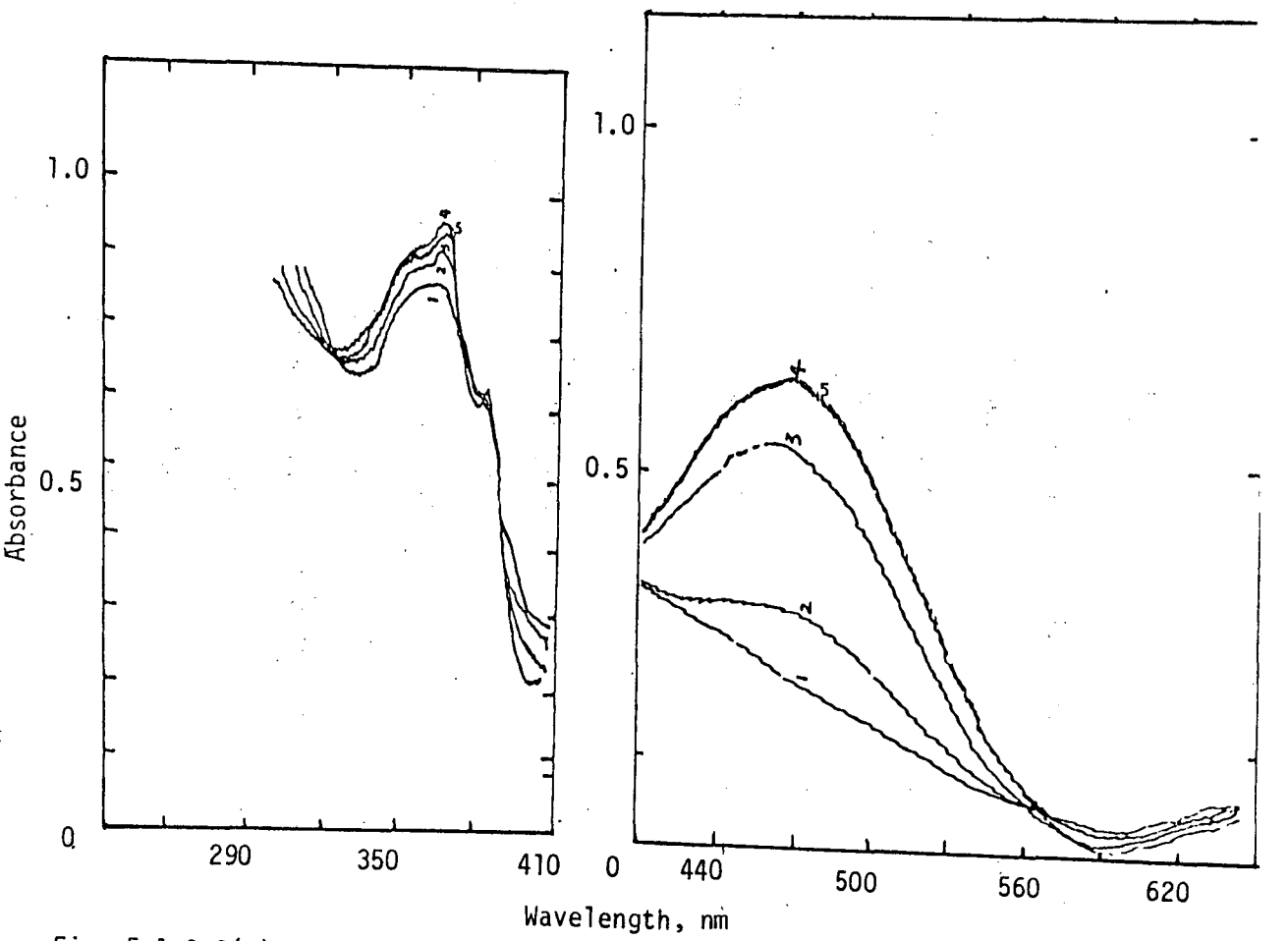


Fig. 5.1.8.2(a). Thin layer spectra obtained during the oxidation of $Co_2taph(NO_3)_4 \cdot 4H_2O$ in 0.5M Et_4NClO_4 in DMF. Conc. 4 x 10^{-3} M. (The spectra that appear in later figures are all parts of the same experiment.)
1 = 0.14V; 2 = 0.24 V; 3 = 0.354 V; 4 = 0.65 V; 5 = 0.75 V.

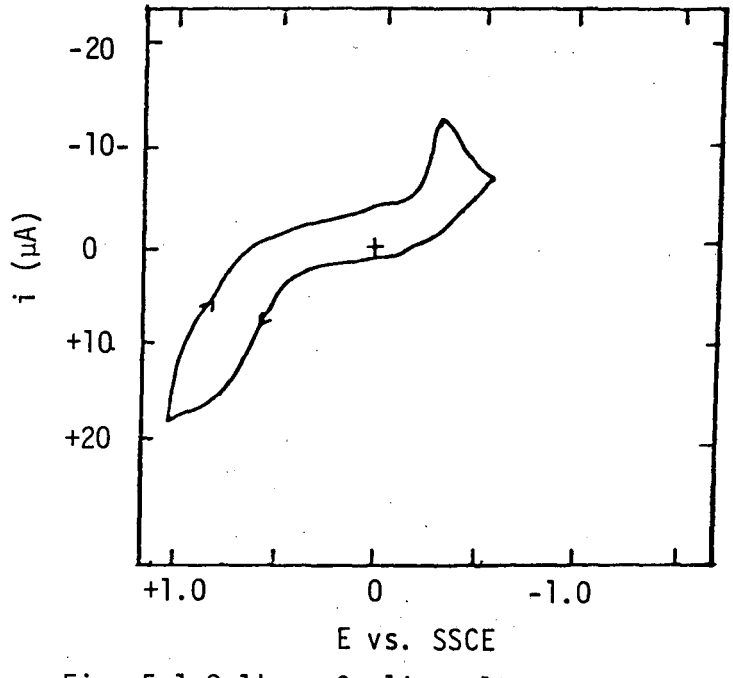


Fig. 5.1.8.1'a. Cyclic voltammogram of Ni_2taph^{4+}. 2 x 10^{-3} M. Au disk: 0.19 cm^2 50 mv/sec.

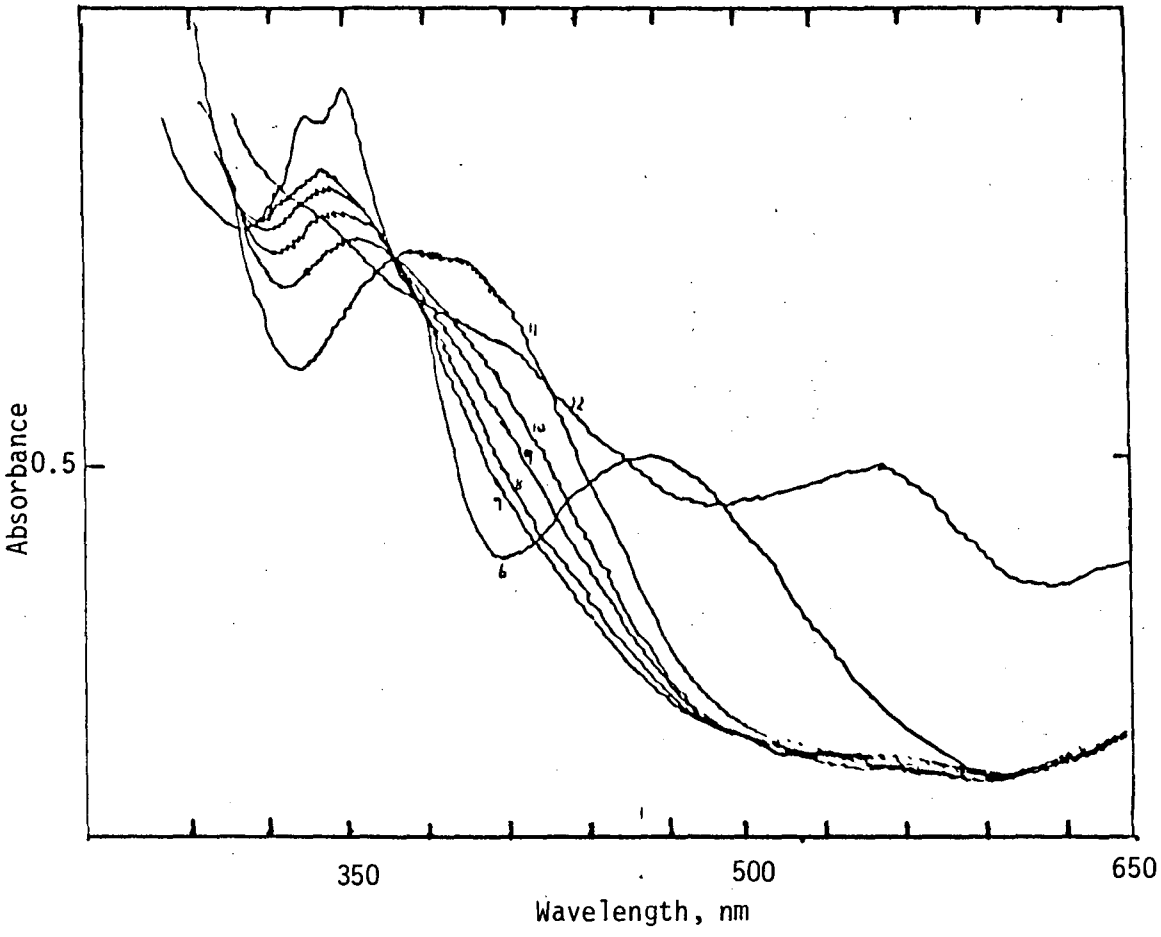


Fig. 5.1.8.3(a). Thin layer spectra obtained during the reduction of Co_2taph^{4+} 6 = -0.05 V; 7 = -0.215 V; 8 = -0.35 V; 9 = -0.51 V; 10 = -0.70 V; 11 = -0.97 V, 12 = -1.06 V.

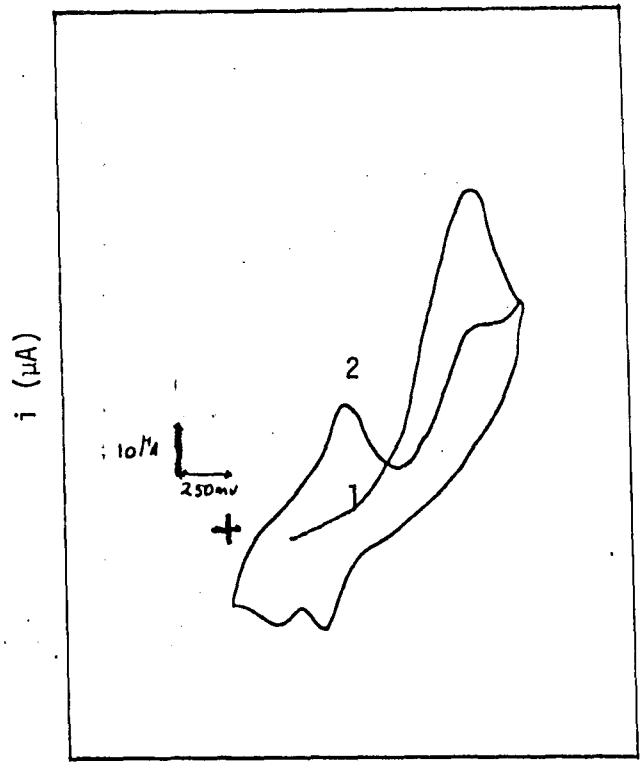


Fig. 5.1.8.4(a). Thin layer cyclic voltammogram of $Co_2taph(NO_3)_4 \cdot 4H_2O$ in 0.5M Et_4NClO_4 in DMF. Concn: 3×10^{-3}M. Scan rate: 1 mV/sec.

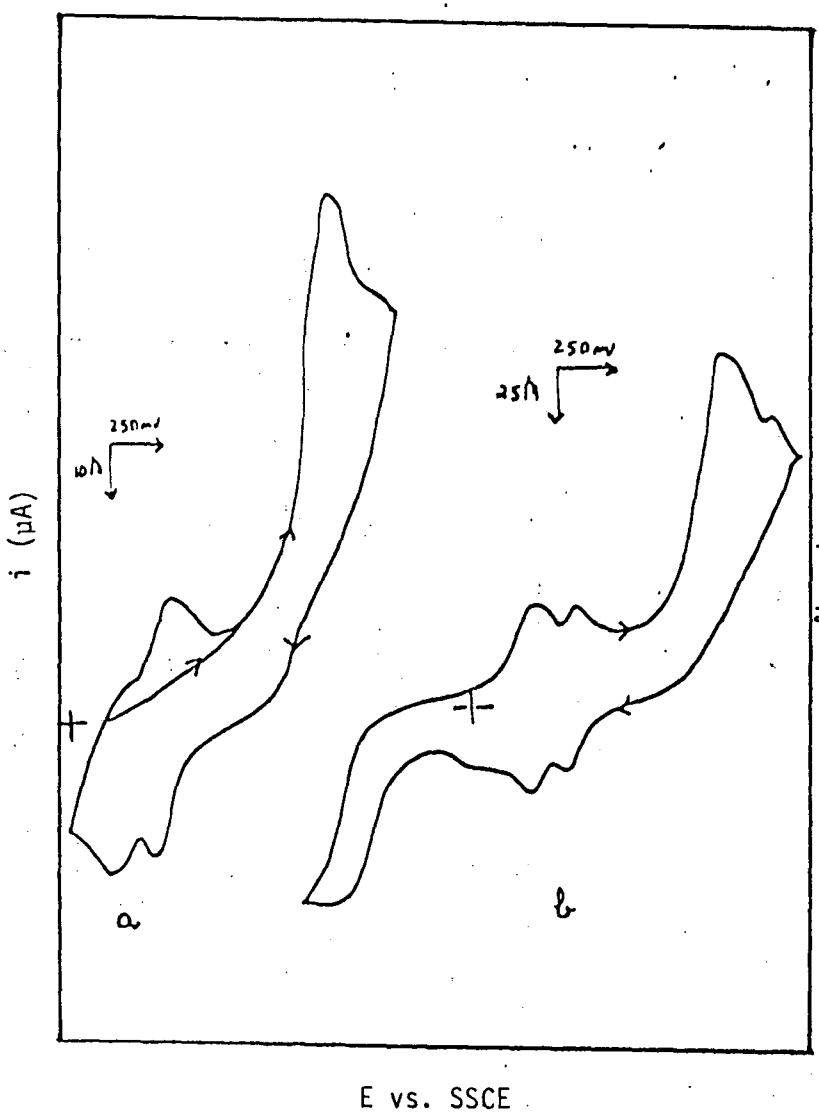


Fig. 5.1.8.5(a). Cyclic voltammogramns of Co_2taph^{4+}: (a) cathodic sweep; (b) anodic sweep. Concn: 1 x 10^{-3} M. Au disk: 0.19 cm^2. Scan rate: a = 50 mV/sec; b = 80 mV/sec.

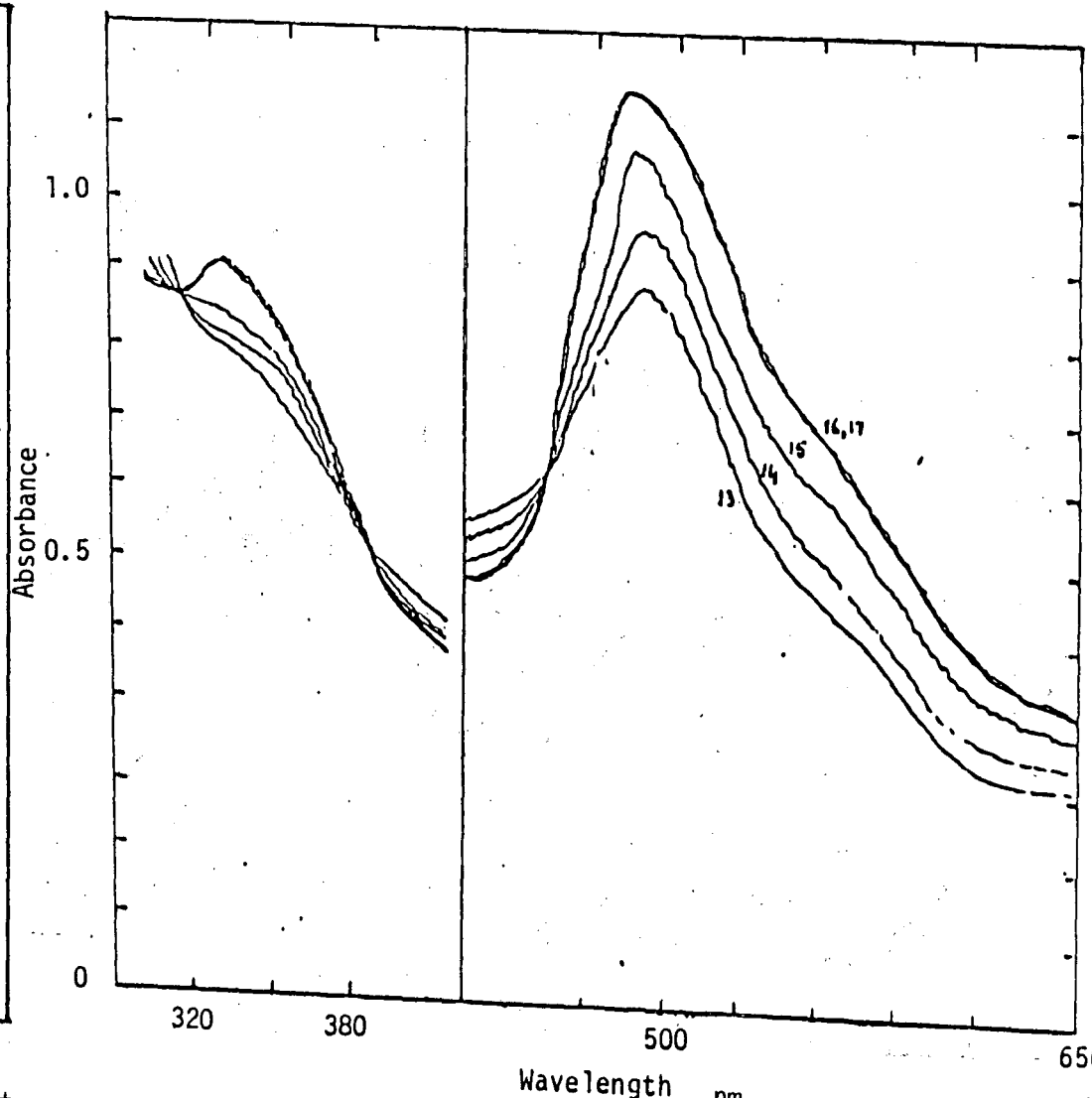


Fig. 5.1.8.6(a). Thin layer spectra obtained on further reduction of Co_2taph^{4+}. 13 = -1.12V; 14 = -1.23 V; 15 = -1.35 V; 16 = -1.44 V; 17 = 1.50 V.

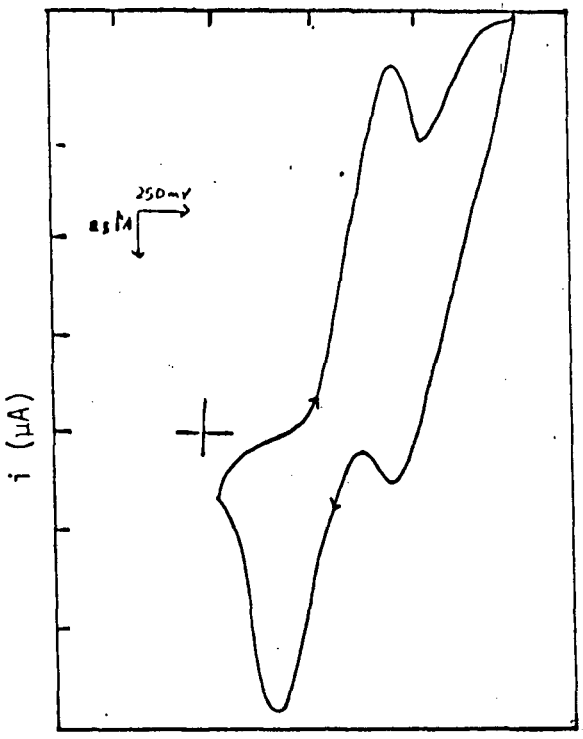


Fig. 5.1.8.7(a). Thin layer cyclic voltammogram of Ni_2taph^{4+}. Scan rate 1 mV/sec. Concn: 6.5×10^{-3} M.

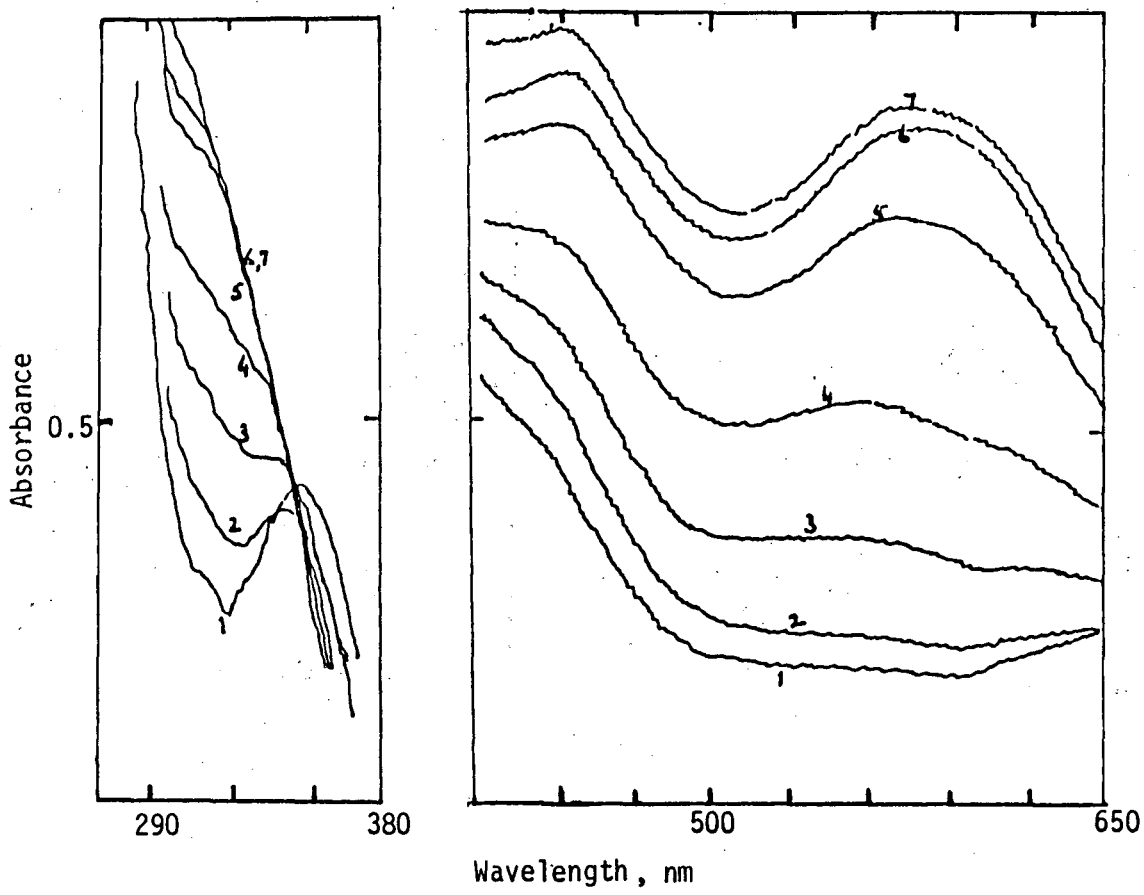


Fig. 5.1.8.8(a). Thin layer spectra obtained during the reduction of Ni_2taph^{4+}. 1 = -0.57 V; 2 = -0.73; 3 = -0.84V; 4 = -0.96 V; 5 = -1.01 V; 6 = -1.10 V; 7 = -1.25 V.

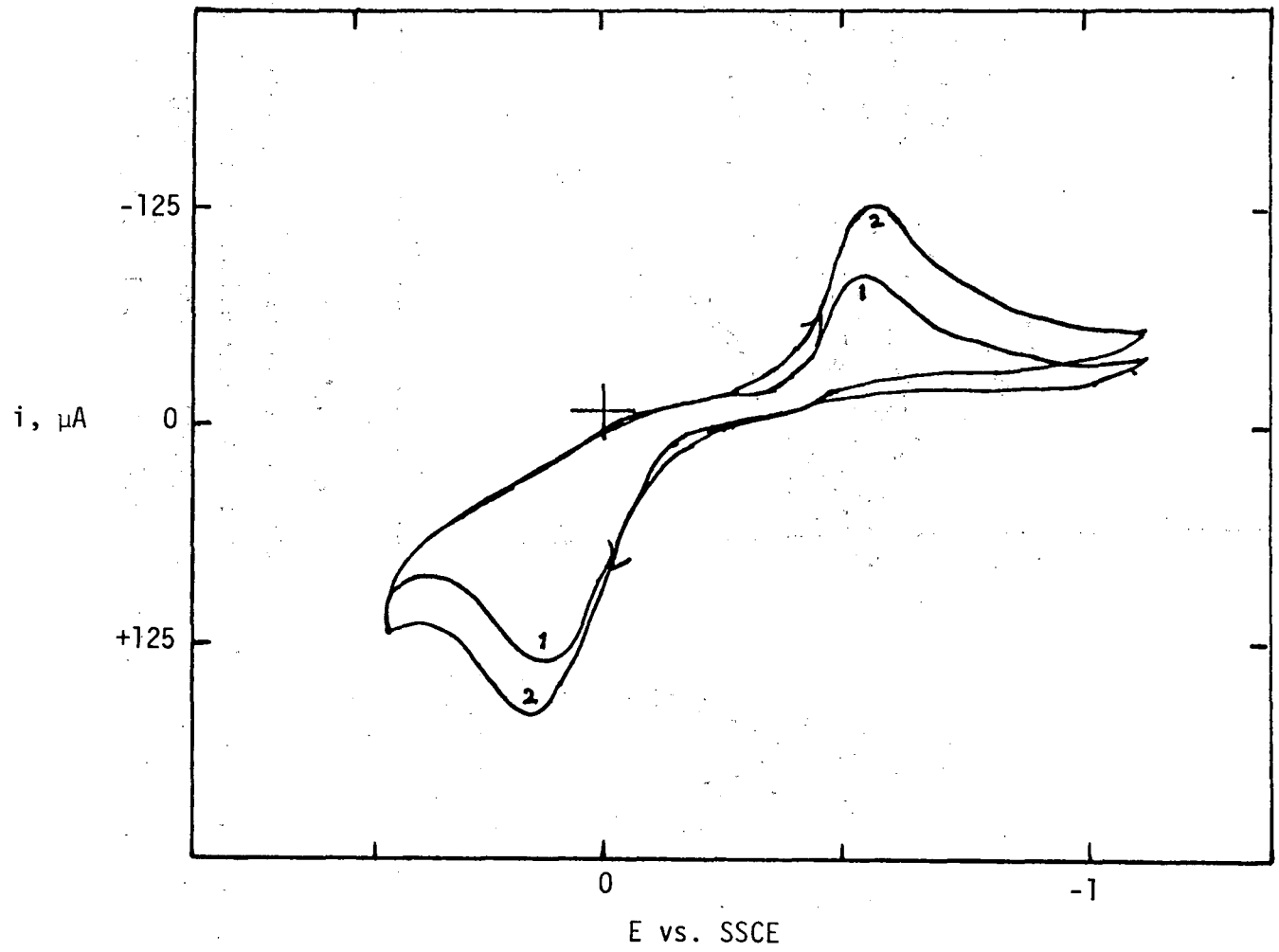


Fig. 5.1.8.9(a). Cyclic voltammogram of "dhph" in DMF. Au disk: 0.19 cm^2. Scan rate: (1) 50 mV/sec; (2) 100 mV/sec. Concn $\simeq$ 1 x 10^{-3} M.

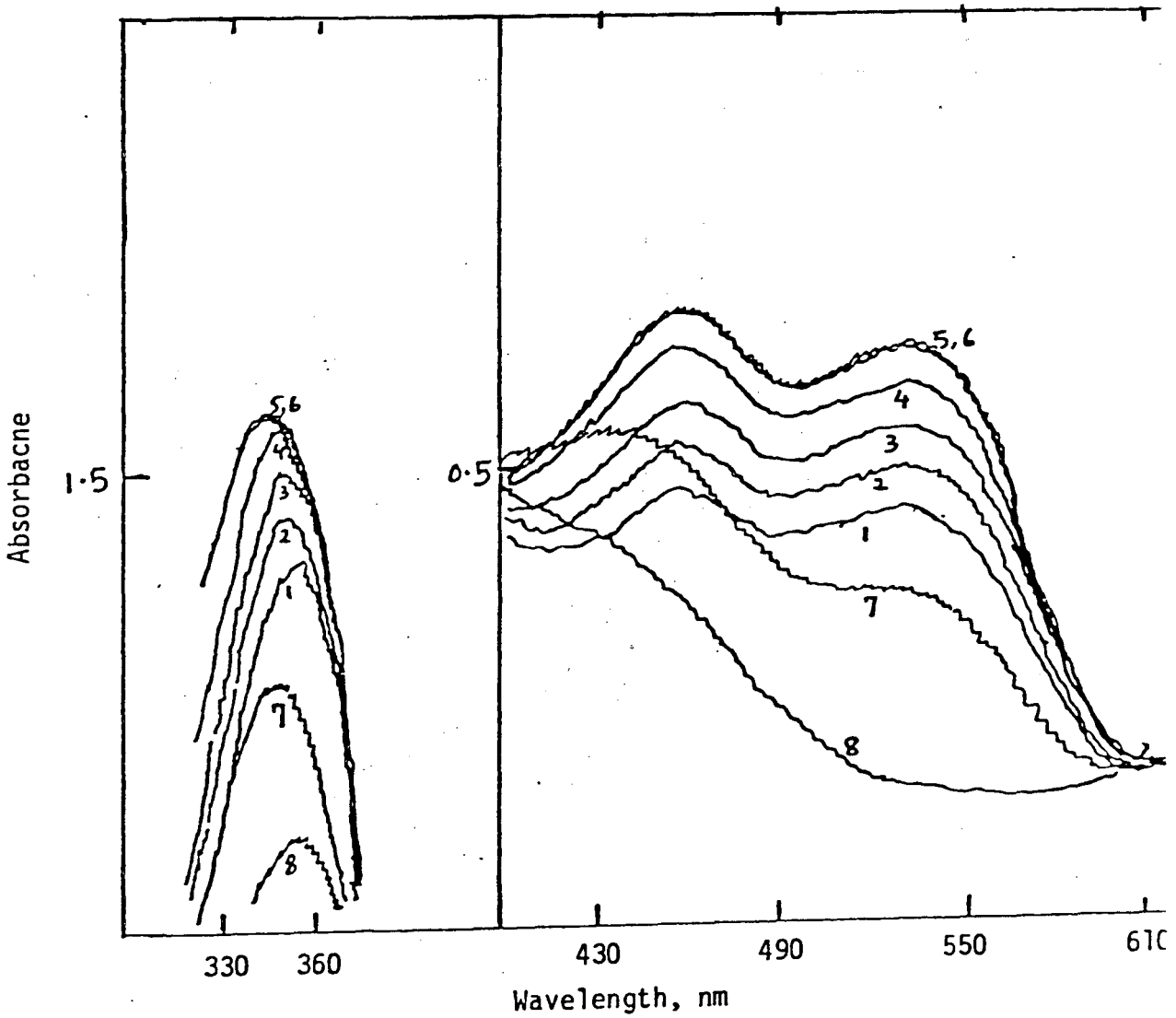


Fig. 5.1.8.10(a). Thin layer spectra obtained during the oxidation of dhph (curves 1 to 6). Reduction of the oxidized species (7,8). Concn: 1.5 x 10^{-2} M. 1 = +0.17 V; 2 = +0.26 V; 3 = +0.37 V; 4 = +0.48 V; 5 = +0.58 V; 6 = +0.68 V; 7 = -0.37 V; 8 = -0.67 V.

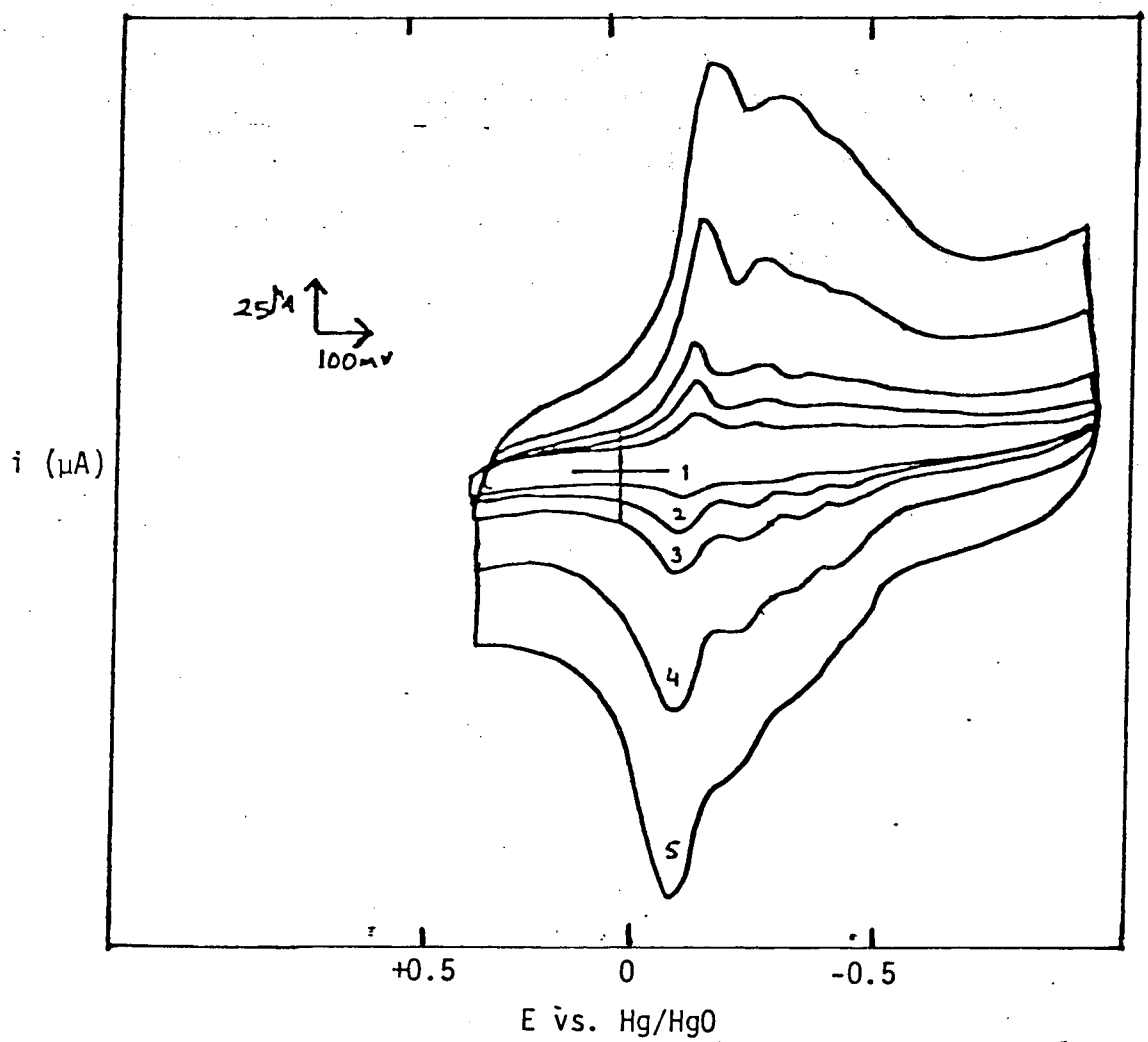


Fig. 5.1.8.11(a). Cyclic voltammogram of "dhph" in 0.1M NaOH, when adsorbed on an ordinary pyrolytic graphite disk. Area: 0.458 cm^2. Scan rates in mV/sec: 1 = 20; 2 = 50; 3 = 100; 4 = 200; 5 = 500.

5.1.8 (b) Part III.ELECTROCATALYTIC PROPERTIES OF THE Fe(II) and Fe(III) COMPLEXES OF 'dhph'. (A PRELIMINARY REPORT)

Shantha Sarangapani, E.B. Yeager and F.L. Urbach

The Fe[II] and Fe[III] complexes of dhph have been found to catalyze the reduction of O_2 to H_2O, by a series mechanism. The complex was prepared by mixing equimolar solutions of dhph and an iron salt, in methanol/water mixture. The complex when adsorbed on ordinary pyrolytic graphite electrode shows activity towards oxygen reduction in alkaline solutions. The disk and the ring currents are shown in Figures 1 and 2. A plot of 1/i (i=disk current) versus $1/\sqrt{f}$ [f=RPM] shows slopes dependent on the potential (Figure 3). A plot of the ratio of the ring to disk currents versus $1/\sqrt{f}$ shows a common intercept and potential dependent slopes, diagnostic of a series mechanism[1].

Further work on the redox and spectral behavior of the iron complexes are underway.

References

1. For example, see Ph.D thesis by Rossano Amadelli, 1982, Case Center for Electrochemical Sciences.

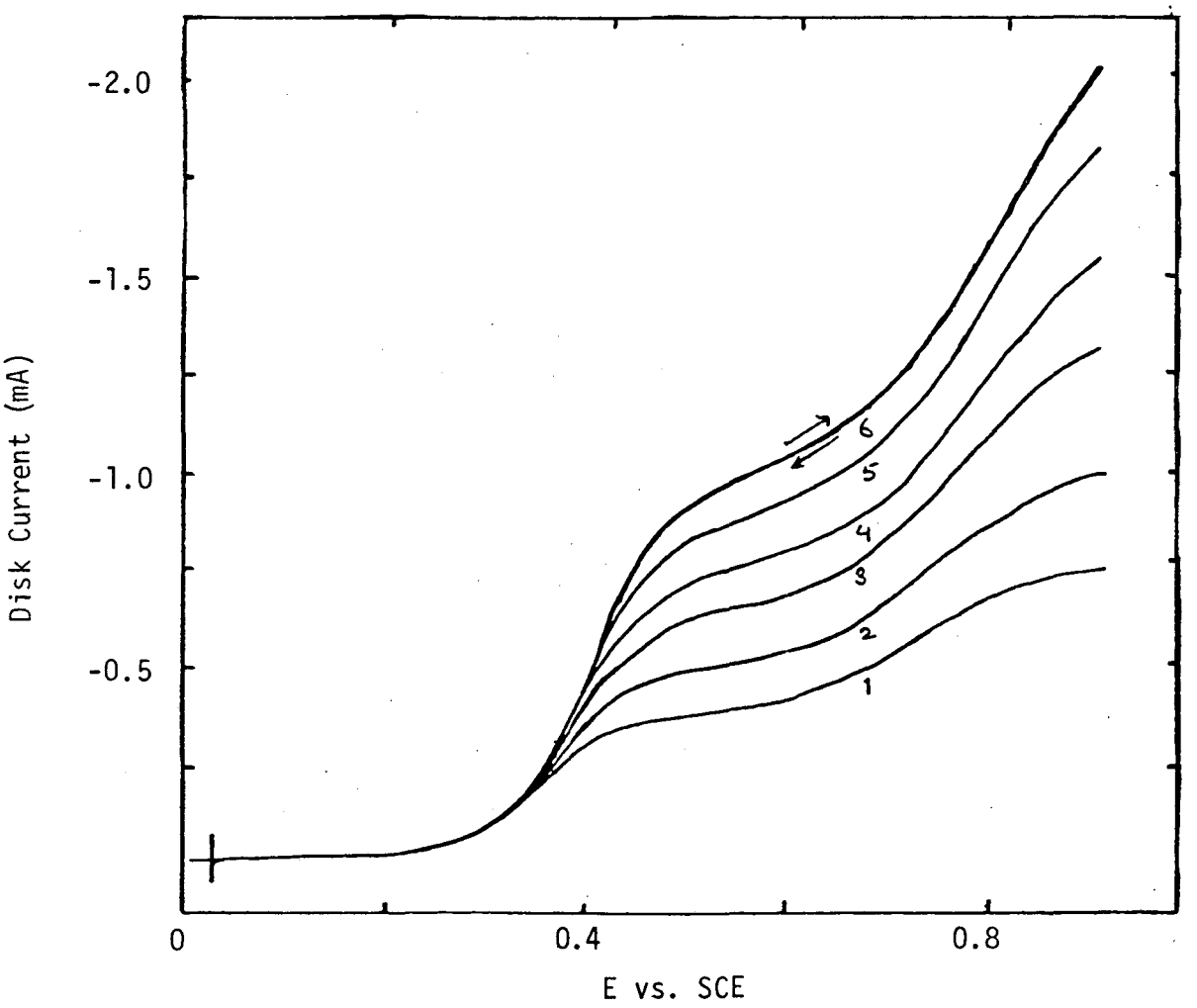


Fig. 5.1.8.1(b). O_2 reduction in the presence of adsorbed $Fe_2(dhph)_2^{4+}$ complex on OPG disk. Area of the disk: 0.458 cm^2. scan rate 5 mV/sec. Electrolyte: 0.1 M NaOH, (O_2satd.). RPM: 1 = 100; 2 = 200; 3 = 400; 4 = 600; 5 = 900; 6 = 1200.

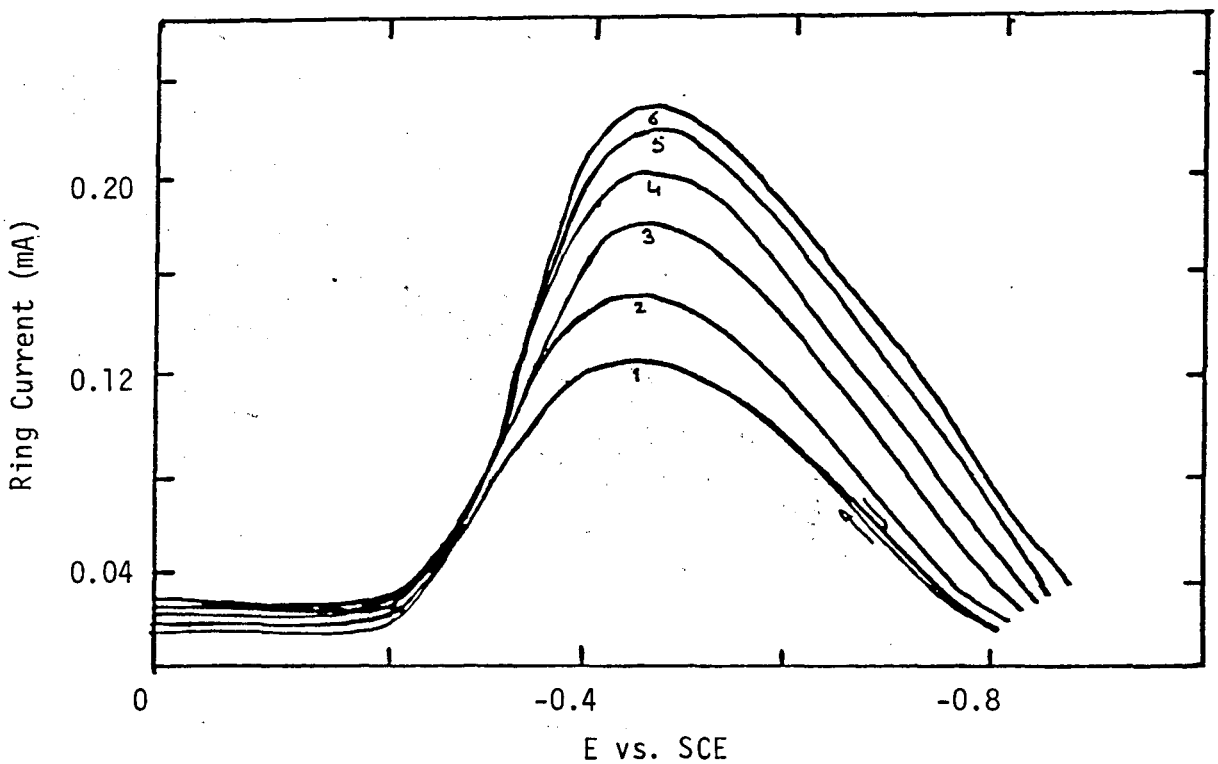


Fig. 5.1.8.2(b). Ring currents recorded during the reduction of oxygen at the OPG disk with pre-adsorbed $Fe_2(dhph)_2^{4+}$. Ring potential : +0.1V vs. SCE. Area: 0.211 cm^2. Collection efficiency 0.4. Ring: Au.

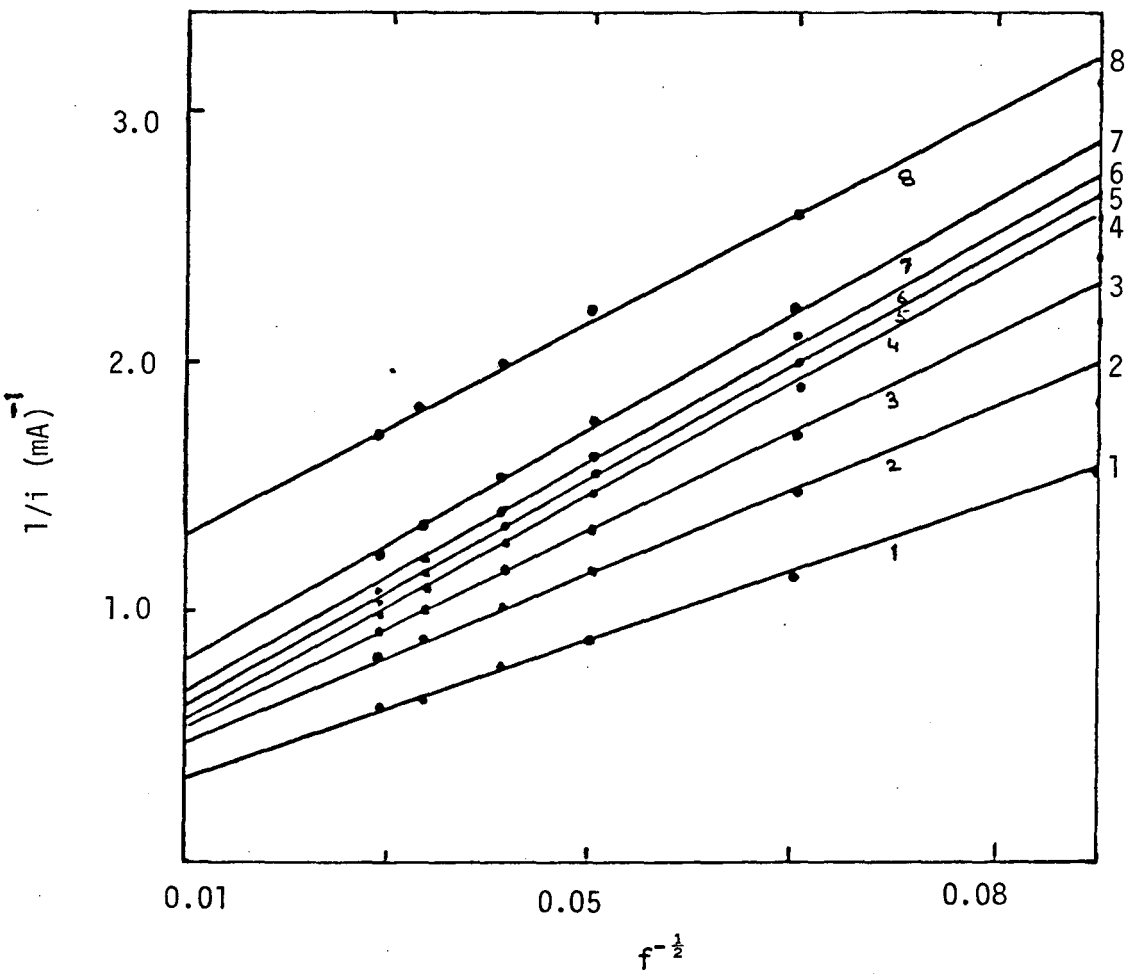


Fig. 5.1.8.3(b). Plot of 1/i vs. $f^{-\frac{1}{2}}$ at various potentials obtained from Fig. 5.1.8.1. Potl. vs. SCE: 1 = -0.40; 2 = -0.45; 3 = -0.50; 4 = -0.55; 5 = -0.6; 6 = -0.65; 7 = -0.7; 8 = -0.8 V.

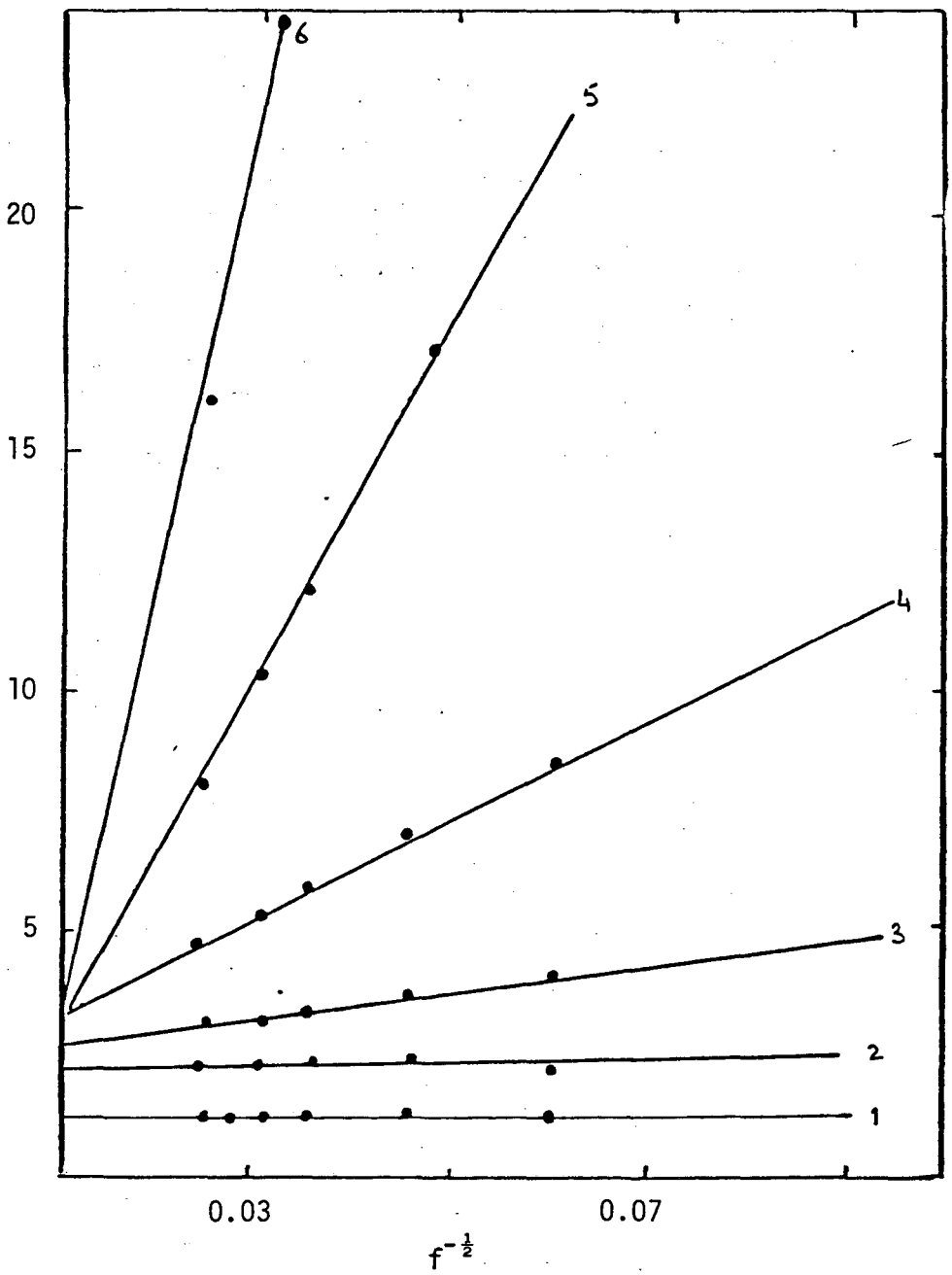


Fig. 5.1.8.4(b). Plot of $\frac{I_D}{I_R}N$ vs. $f^{-\frac{1}{2}}$ obtained from Figs. 5.1.8.1 and 2. Potl vs. SCE: 1 = -0.4V; 2 = -0.65V; 3 = -0.7V; 4 = -0.75V; 5 = -0.8V; 6 = -0.9V.

5.1.9 THE EFFECT OF IMPURITY ON SURFACE RAMAN SPECTRA OF PYRIDINE ON AG ELECTRODE

B. C. Wang and E. Yeager

Recently, the study of the phenomenon of Surface-enhanced Raman has been receiving a considerable amount of attention. Most of the published papers have been concerned with mechanisms of the surface enhancement and have attributed this enhancement to the adsorption of molecules on the solid-solution interface [1]. As is well known, solution phase impurities exert a great influence on adsorption and it has been shown, that even 10^{-9} M of impurities in solution could form a monolayer on surface and change the surface properties appreciably. However, the problem of impurities has been largely ignored in studies of the Raman effect to date. Therefore we have studied the influence of impurities by measuring Raman spectra of pyridine on Ag electrodes in 0.1 M KCI solution with water of varying degrees of purity and KCI from different sources. This communication reports some preliminary results of the investigation.

EXPERIMENTAL

The Raman Spectra of pyridine on the electrode surface were measured using a Spex spectrometer (Ramalog) equipped with holograpruled gratings. The light source was an argon ion laser (coherent radiation CR-8) and the photon counting system contained a GaAs photomultiplier (RCAC 31034) showing flat spectral response in the region of the available lasers lines.

The electrochemical cell had one pyrex optical window for exciting laser beam and for the detection of the Raman scattered light perpendicular to the incident beam. The electrode was fixed to a micrometer gauge shaft, an arrangement that enabled regulation of the distance between electrode and optical window. The angle of incidence of the radiation onto the Ag working electrode was adjusted by means of the cell holder. The angle used in this work is 65°.

The potential of the working electrode was controlled with a potentiostat (P.A.R. 173) and a waveform generator (P.A.R. 175). All potentials are with respect to the saturated calomel electrode (SCE) which was located in external compartment separated by a stopcock from the bulk electrolyte. A ring of platinum wire was used as the counter electrode. A Ag disc ($\sim$0.2 cm^2) embedded in a teflon rod served as the working electrode. It was polished with Al_2O_3 powder (1μm, 0.3μm) to yield a mirror-like finish and carefully rinsed in distilled water, and was finally cleaned in an ultrasonic bath. The 0.1 M KCI elecrolyte was prepared using distilled water or pyrolysed water. The KCI was from two sources: one from Fisher Scientific Company (certified A.C.S.), another from JMC puratronic. The adsorbate was added to the electrolyte in 0.01 M pyridine (Aldrich Chemical). KCI solutions were deaerated by bubbling with nitrogen.

For activation of the Ag electrode a single potential sweep (5 mV/s) from -0.2V to +0.3V vs SCE was performed according to M. Fleischmen and et al [2].

RESULTS AND DISCUSSIONS

Fig. 1 shows Raman spectra of pyridine on Ag in 0.1 M KCI solution with different purity of water and different sources of KCI and their change with potentials in both cathodic and anodic sweeping directions. Fig. 2 displays the hysteresis of intensities for ring breathing mode of pyridine at $\sim$1006 cm^{-1}. The 0.1 KCI solution with JMC puratronic and pyrolyzed water has least hysteresis. The hysteresis is most pronounced in the case of Fischer Scientific Company KCI and distilled water. This can be explained on the fact that, when the solution contains more impurity, expecially heavy metals, and the Ag electrode experiences more negative potentials, upd and bulk deposition of some metal ions can take place, thus changing the properties of the Ag surface appreciably. Thus, pyridine adsorption was decreased, when the potential was returned to initial values. Further evidence in favor of this suggestion is that if the potential was held at -0.8 V for long time in impure 0.1 KCI solution, pyridine intensities were bound to decrease with time. In case of pure solution the adsorbed pyridine was observed to keep its intensities when sweeping the potentials in both cathodic and anodic directions from -0.2V to -0.8V. The hysteresis is shown up more clearly, when sweeping the potentials in both directions was repeated several times, for example three times. In pure 0.1 M KCI solutions the intensities still remain unchanged, but in the case of the Fischer Scientific compound with pyrolized water its intensities reduced almost two times. Therefore we conclude, that hysteresis of Raman intensities can be used as a measure of impurity in a solution.

From Fig. 1 it can be seen, that in the case of pyrolized water no peak at 1025 cm^{-1} was obtained. Fleischman et al. (3) assigned this peak to chemical adsorption of pyridine to Lewis acid site. If one accepts this suggestion, however, it is difficult to explain, why this peak or Lewis acid site dissappears, when potential came back from negative value to initial values. A. Regis et al. (4) have shown that the pyridine adsorbed to AgCl gives peaks at 1025 cm^{-1} and 1052 cm^{-1}, and explain Raman enhancement by electronic resonance by $Cl_2^{\cdot -}$ radical. It seems for us more reasonable to assume, that the peak at 1025 cm^{-1} is due to adsorption of pyridine to $AgCl_2$, which is forming during the oxidation-reduction cycle and is left on the surface. When potential was swept to more negative value, this residual AgCl is reduced to Ag completely, so that this peak disappears. In some cases, whether impurity in solution hinders complete reduction of AgCl at -0.2V or insufficient time is taken for complete reduction of AgCl, the peak at 1025 cm^{-1} can appear. When the electrode potential is shifted to -0.1V or 0.0V small amount of AgCl may be formed and the peak at 1025 cm^{-1} is observed.

Fig. 3 shows pyridine spectra, when Ag was subjected to progressive roughening. With increasing the oxidation-reduction cycles it was found, that more and more AgCl was left on the surface and the peak at 1025 cm^{-1} became more intense with cycling.

REFERENCES

1. For review see: T. E. Furtak and J. Reyes, Surface Science 93, 351-382 (1980).

2. M. Fleischman et al. J. Electroanal. Chem. 117, 243-255 (1981).

3. M. Fleischman et al. Chem. Phys. Lett. 26, 163-166 (1974).

4. A. Regls and J. Corset, Chem. Phys. Lett. 70, No. 2, 305-309 (1980).

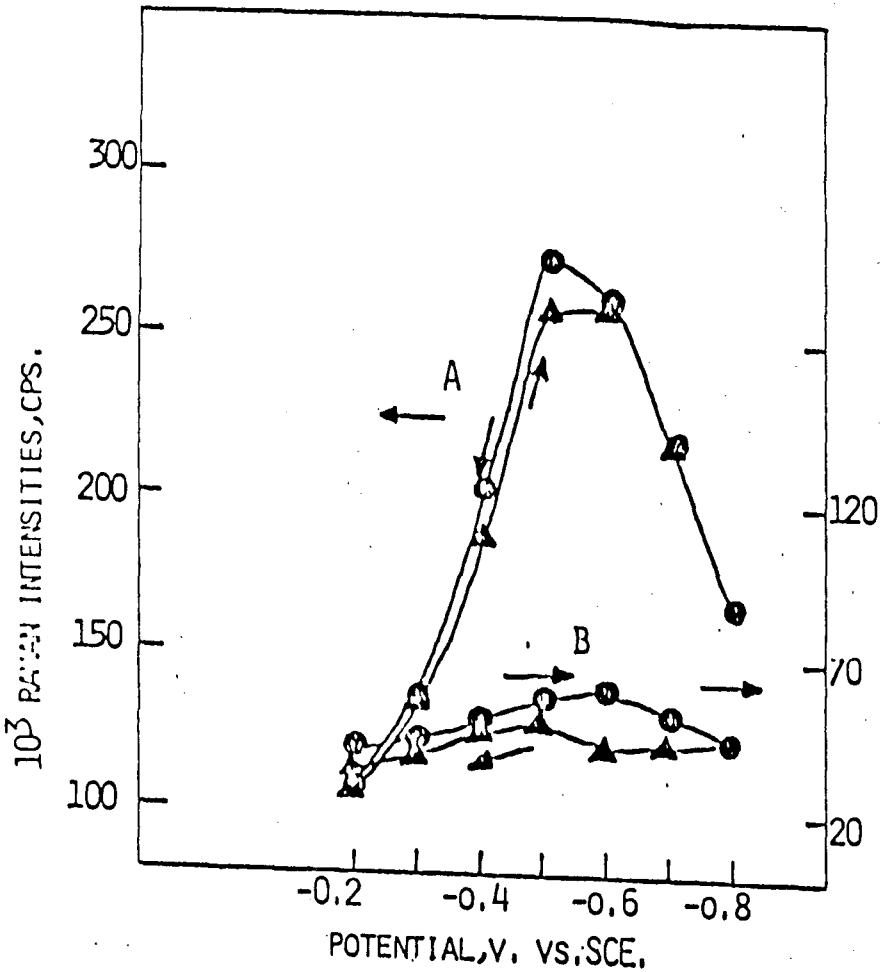


FIG. 5.1.9.1.

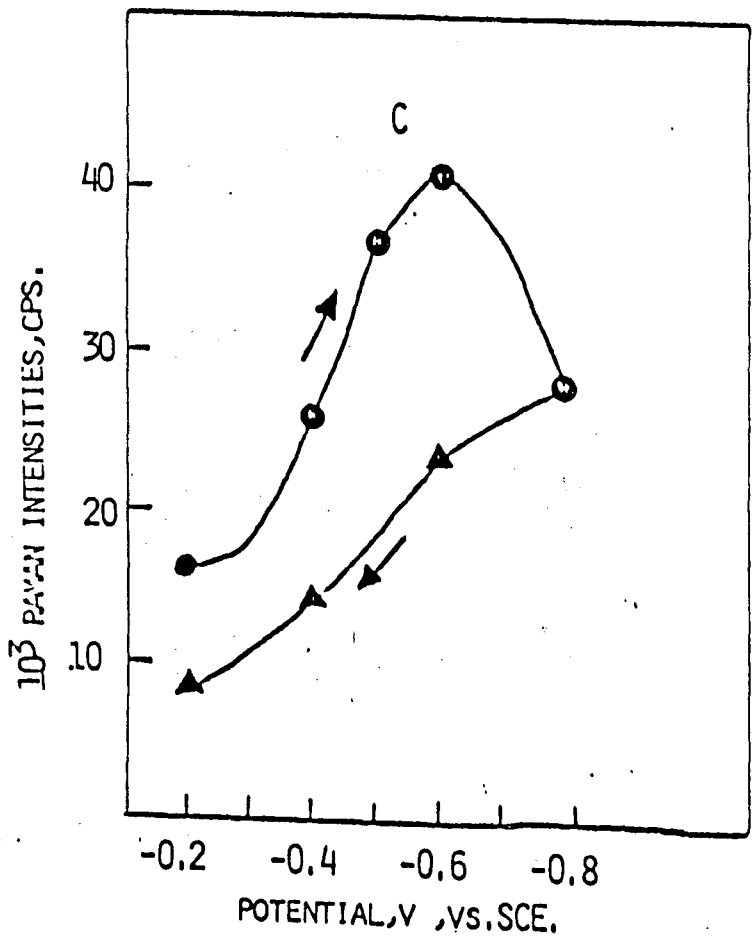


FIG. 5.1.9.2.

DEPENDANCE OF INTENSITIES ON POTENTIAL. (A) J M C PURATRONIC KCL WITH PYROLYZED WATER. (B) FISHER SCINENTIFIC COMPOUND WITH PYROLYZED WATER. (C) FISHER SCIENTIFIC COMPOUND WITH DISTILLATED WATER. λ_0 = 514.5 N M. 80 MW AT THE SAMPLE THE ARROWS INDICATE POTENTIAL SWEEPING DIRECTIONS.

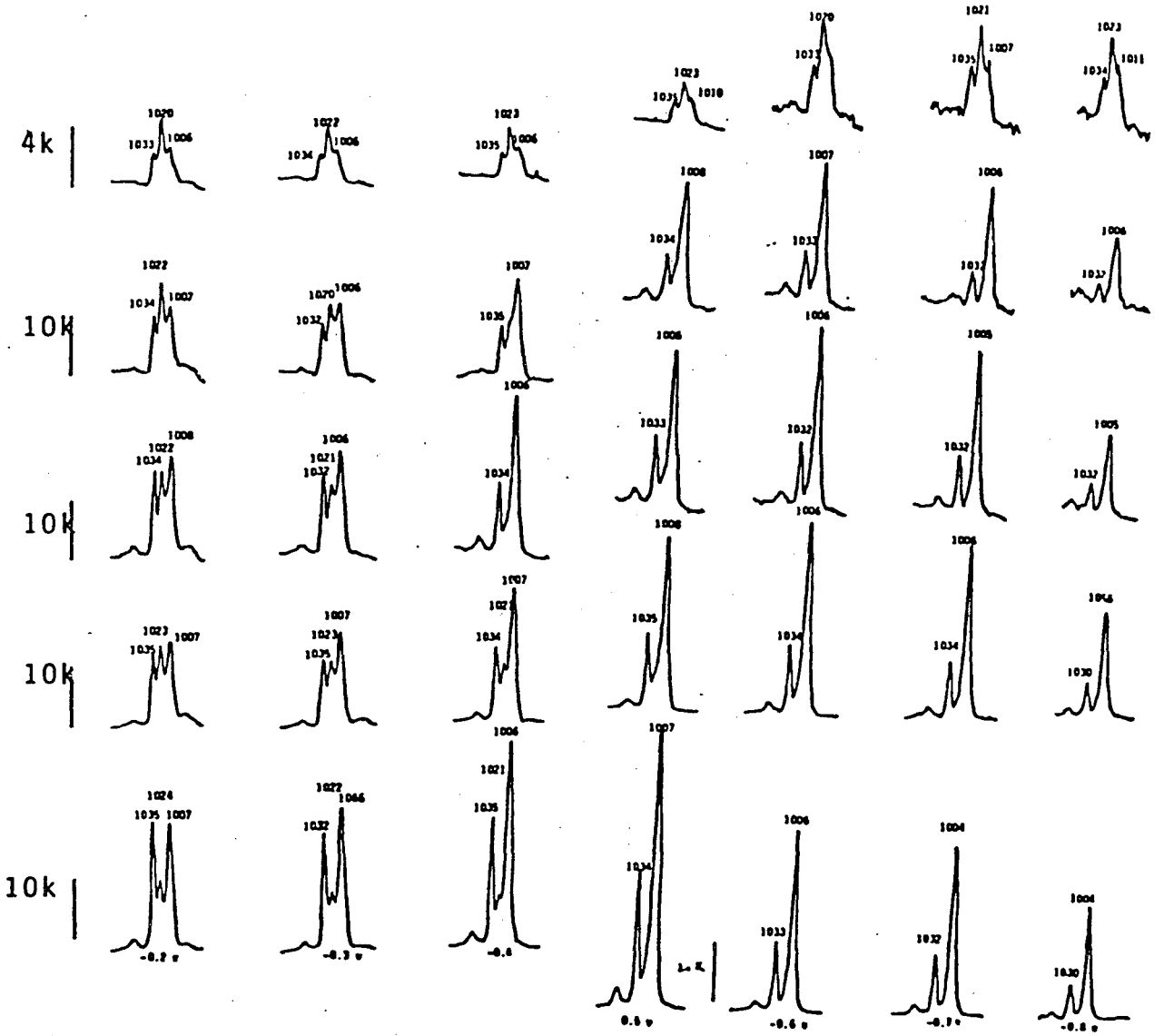


FIG. 5.1.9.3. IN-SITU RAMAN SPECTRA OF PYRIDINE IN 0.1 M KCL FISHER SCIENTIFIC WITH DISTILLED WATER INDEPENDENT OF PROGRESSIVE ROUGHING.

5.1.10 INVESTIGATION OF UPD AND BULK DEPOSITION OF METALS USING SURFACE-ENHANCES RAMAN ON AG ELECTRODE

B. C. Wang and E. Yeager

In-situ surface-enhanced Raman spectroscopy offers intriguing opportunities not only for detection and identification of adsorbed species on the solid-solution interface, but for investigation of many electrochemical processes. Most of the published work to date has been concerned with the surface-enhancement of pyridine on Ag in KCl solution (1,2). It was shown (3), that Raman intensities are dependent on such factors as surface preparation, the concentration of pyridine in solution, the nature and concentration of the supporting electrolyte anion and the electrode potential. On the other hand, nothing is known about the dependence of the vibrational frequencies and intensities of adsorbates on cations in solution. Frequency shifts of vibrational modes during electrode processes like UPD and bulk deposition may give some information about the substrate adsorbate interaction, the nature of the adsorption site, and electronic and optical properties of the Ag electrode surface. UPD and bulk deposition processes which are taking place on a Ag electrode in conjunction with pyridine adsorption affords an interesting opportunity for study of these processes by means of induced change in intensity and frequency of the Raman signals of the adsorbed pyridine. The present paper reports preliminary results of Raman spectral changes of adsorbed pyridine on Ag upon addition of the cations Cd^{++}, Tl^{+}, and Pb^{++} to 0.1M KCl solutions.

EXPERIMENTAL

The Raman spectra were measured with a Spex spectrometer (Ramalog) in combination with an argon ion laser (Coherent Radiation CR-8). The spectral resolution of the monochromator was set to 2.5 cm^{-1} and the integration time of the photocounting system was typically 0.53. The polycrystalline Ag disc, serving as the working electrode, was illuminated by the laser beam at a mean angle of incidence of 65° and typical power at the sample was 80 mw at 514.5 nm. A detailed description of the optical alignment and the electrochemical cell for in situ Raman measurements has been given previously (4). Before each measurement, the silver electrode (0.2 cm^2 surface area) was polished with Al_2O_3 (1 μm, 0.3 μm) and rinsed carefully in distilled water and cleaned in an ultrasonic bath.

The potential of the working electrode was controlled using a PARC 173 potentiostat and a PARC 175 wave form generator. A ring of platinum wire served as a counter electrode. All potentials are quoted with respect to the saturated calomel reference electrode.

The electrolytes 0.1 KCl were prepared from JMC puratronic KCl and pyrolyzed water. The adsorbate was added to the electrolyte in 0.07 M pyridine (Aldrich Chemical). The electrolyte was deaerated by bubbling N_2 through the solutions.

RESULTS AND DISCUSSION

Raman spectra of pyridine adsorbed on an Ag electrode in 0.1 M KCl solution containing Cd^{++} (in form of $CdCl_2$ added) in concentrations ranging from 1.7×10^{-4} M to 7.3×10^{-4} M are shown in Fig. 1. The frequencies of the ring vibration modes of pyridine are not changed in the presence of the Cd^{++} cation. The intensities of peaks at 1007 cm^{-1} or at 1034 cm^{-1} began to decrease at -0.7V and dropped drastically at -0.8 V with addition of Cd^{++} cations.

The voltammogram of the Ag electrode in solution with pyridine and Cd^{++} cations present is plotted in Fig. 2. Curve 1 is the voltammogram of the pure Ag electrode in 0.1 M KCl. Upon addition of pyridine to the 0.1 M KCl solution the double layer capacitance of the smooth electrode decreased a little because of pyridine adsorption. After the oxidation-reduction cycle the surface area of Ag electrode increased about 4-5 times and the adsorbed pyridine exhibits more fine structure.

When Cd++ is added to the 0.1 M KCl solution a peak at -0.6 V was observed. According to the work of E. Schmidt *et al.* (5) on a Ag electrode at a potential more positive than 0.15 V than the reversible Cd/Cd++ potential, the adsorbed layer of Cd was formed. At Er + 0.15 V > E> Er an alloy of Cd with Ag was formed. At -0.7 V it is probable that the adsorption of Cd++ was completed, but the intensity of Raman peaks was reduced only a little bit. One possible explanation for this is that the adsorption of pyridine on the Ag electrode is so strong, that Cd++ ions are unable to displace the pyridine on the Ag surface. It is most likely that in the double layer region, Cd++ ions are positioned outside the layer of adsorbed pyridine and adsorbed Cd++ ions possess ionic character. Therefore, the adsorption of Cd++ doesn't change the frequencies of pyridine ring vibration modes. At -0.8 V Cd deposition takes place and optical and electronic properties of Ag electrode are considerably changed. The surface-enhanced Raman scattering from pyridine adsorbed on cadmium was reported by Loo (6), but the enhancement factor was less than on Ag electrode. Therefore, Raman intensities of pyridine at 0.8 V were reduced but did not disappear.

Fig. 3 and Fig. 4 show Raman spectra for the case where Tl ions were added to 0.1 M KCl, and the voltammograms of a Ag electrode in the presence of pyridine and Tl^{+}. In the case of Tl a 4-5 wave number decrease of symmetric ring vibration made at 1006 cm^{-1} was obtained. This indicated that the Tl cation weakens the bond of pyridine to the Ag surface. This can happen only when the concentration of Tl ions exceeds 5.7×10^{-5} M in 0.1 M KCl. Below this concentration no frequency shifts or intensity change occurs. From Fig. 4, UPD of Tl is seen to occur at -0.6 V and bulk deposition at -0.9 V. From Fig. 3 at -0.7 V and a concentration of 1.3×10^{-4} M Tl, Raman intensities were bound to be decreased drastically, when a monolayer formation of Tl was completed. It is likely that some Tl cations specifically adsorb on the

Ag electrode and displace the adsorbed pyridine, and thus change electrical field across compact double layer and shift the ring vibration mode to less values. It is still not clear how many layers of adsorbed pyridine contribute to surface-enhanced Raman. When the Tl concentration is 1.3×10^{-4} M a large decrease in Raman intensities occurs only at -0.9 V, where the deposition of Tl takes place. At concentrations greater than 1.3×10^{-4} M Raman spectra of pyridine exhibit the normal dependence on potential and it may be assumed that this is the Raman spectral behavior of Tl deposited on silver.

In the case of Pb no frequency shift of the ring vibration mode was obtained in concentratins below 2.4×10^{-5} M Pb^{++}. In contrast to Tl and Cd, a concentration of 8.4×10^{-5} M Pb^{++} depresses the Raman signal of pyridine on Ag. This can be explained by the fact that at 8.4×10^{-5} M Pb^{++} a deposit of Pb is formed on the Ag surface and no surface-enhanced Raman effect is observed on Pb. Thus the ring vibration modes of pyridine disappear completely.

The investigations of UPD and bulk deposition in other electrolytes and using other "probe" molecules are in progress.

REFERENCES

1. M. Fleishman et al., Chem. Phys. Lett. 26, 163-166 (1974).

2. M. G. Albrecht et al., J. Am. Chem. Soc. 99, 5215-5217 (1977).

3. D. L. Jeanmaire and R. P. Van Duyne, J. Electroanal. Chem. 84, 1-20 (1977).

4. B. C. Wang and E. Yeager. DOE Annual Report, CWRU and DSC, 1980-81.

5. E. Schmidt, M. Christen and P. Beyeler, Electroanal. Chem. and Interfacial Electrochemistry 42, 275-289 (1973).

6. B. H. Loo, J. Chem. Phys. 75(12), 5955-5956 (1981).

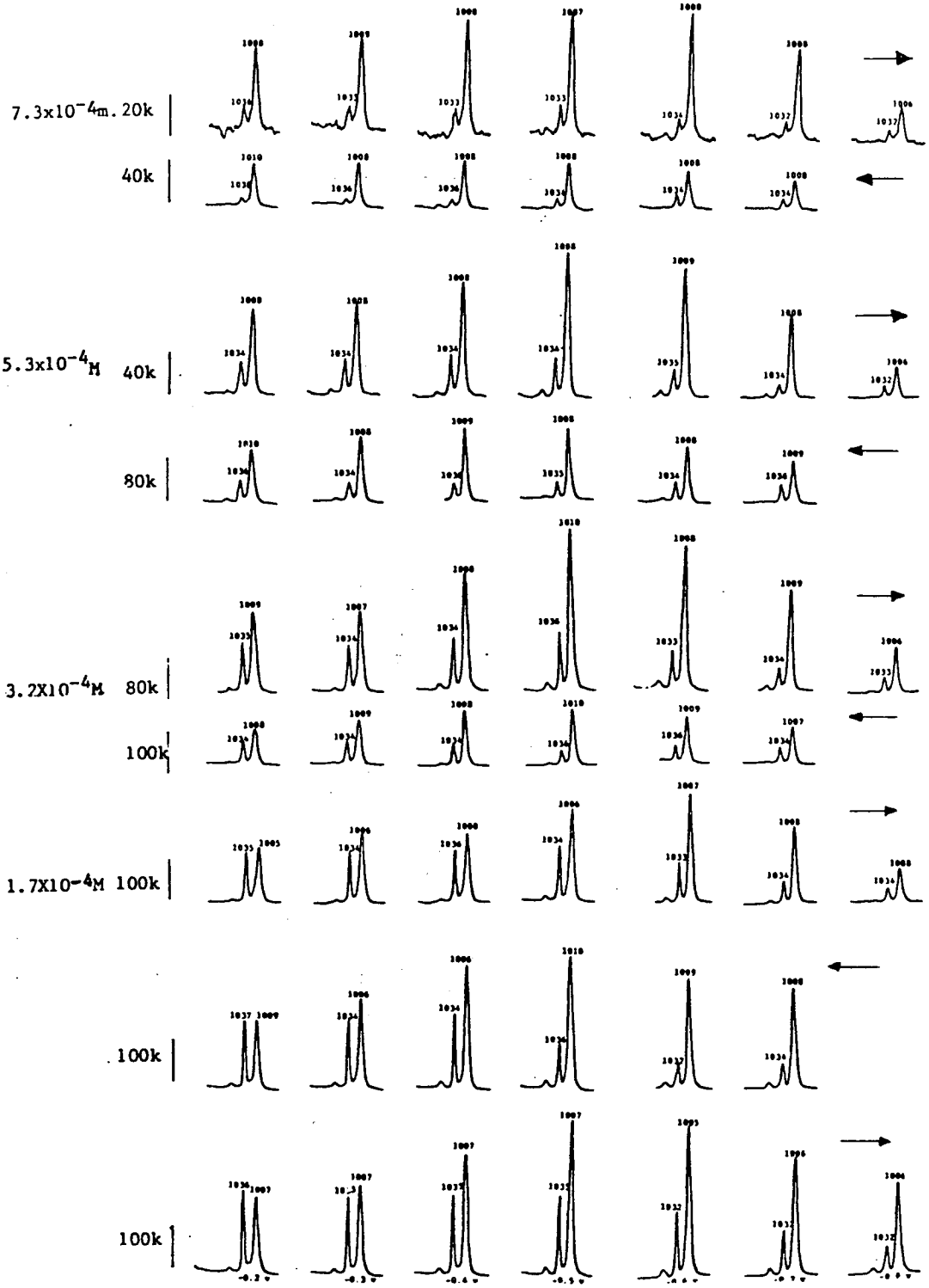


Fig. 5.1.10.1. In-situ Raman spectra of pyridine on a Ag electrode in 0.1 M KCL solution (JMC puratronic KCL with pyrolyzed water) with addition of Cd^{++} ions of different concentrations.

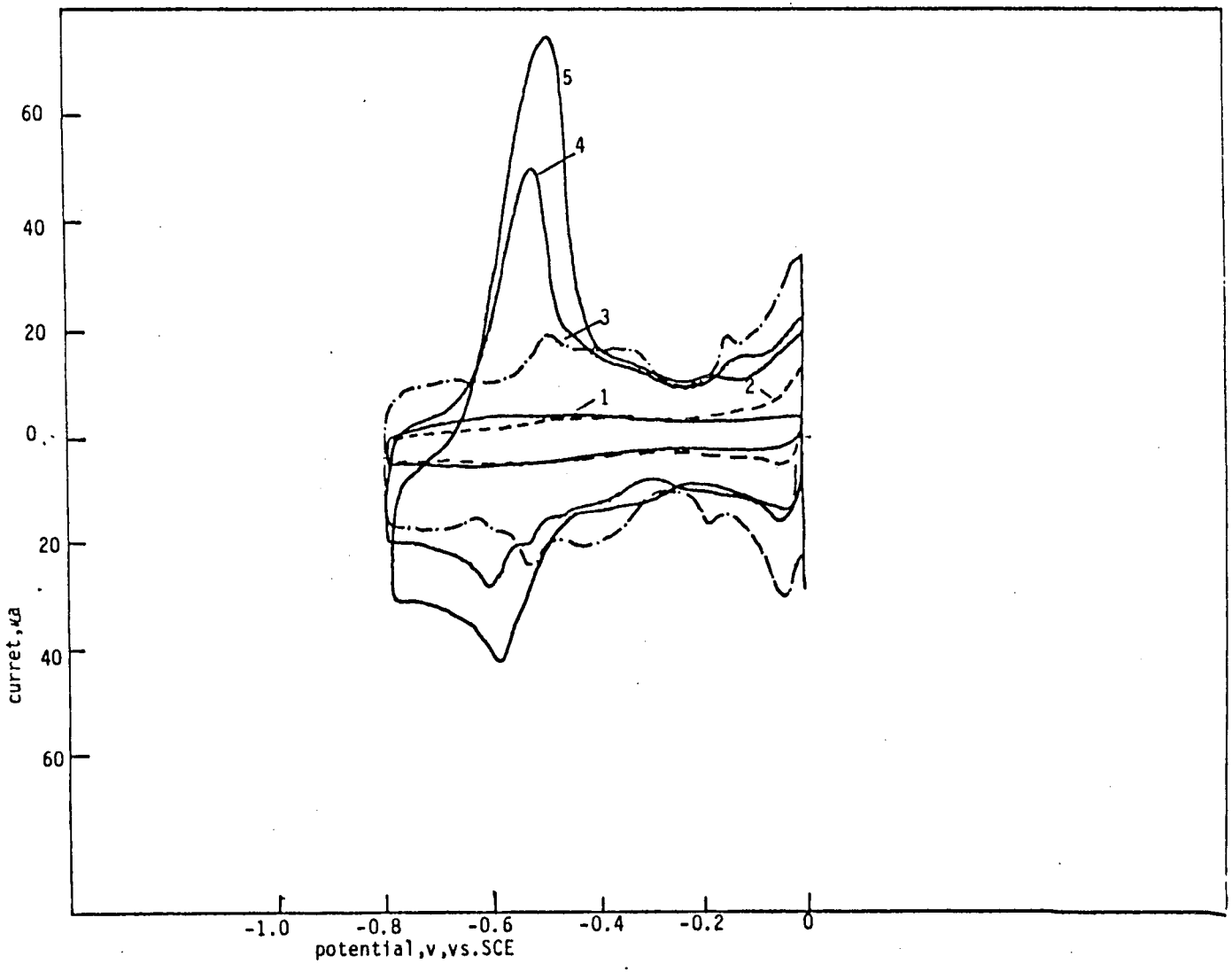


Fig. 5.1.10.2. The voltammogram of Ag electrode in 0.1 M KCL soiution with addition of Cd^{++} ions.1).Ag electrode in 0.1 M KCL solution.2).in 0.1 KCL M solution with 0.01 M pyridine.3).The same as,2)with $1.7X10^{-4}$M Cd^{++}.4)$3.2X10^{-4}$M. Sweeping rate:100 mv/s.

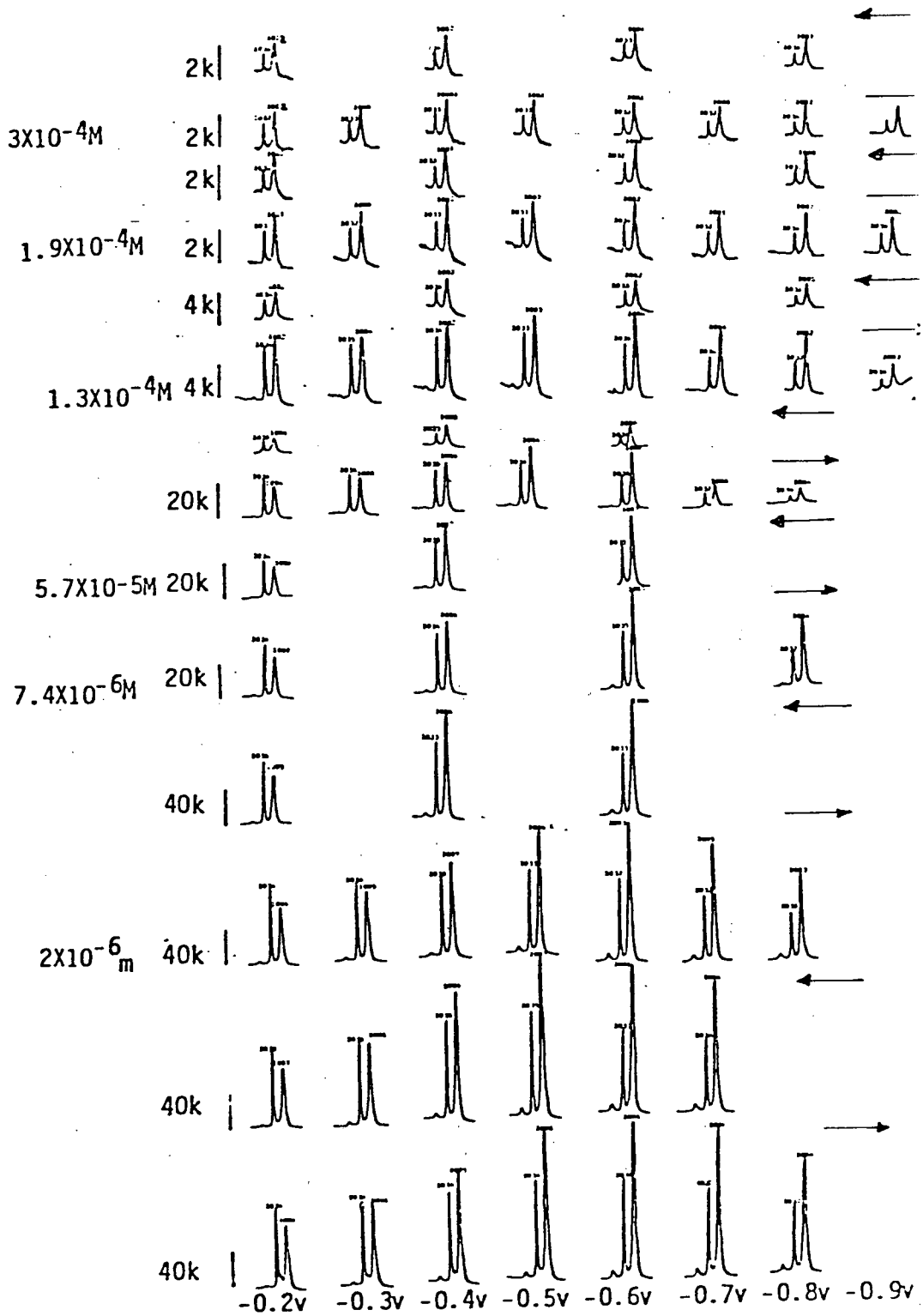


Fig. 5.1.10.3. In-situ Raman spectra of pyridine adsorbed on Ag electrode in 0.1 M KCL solution(JMC puratronic KCL with pyrolyzed water) with addition of Tl^{+} ions of different concentrations.

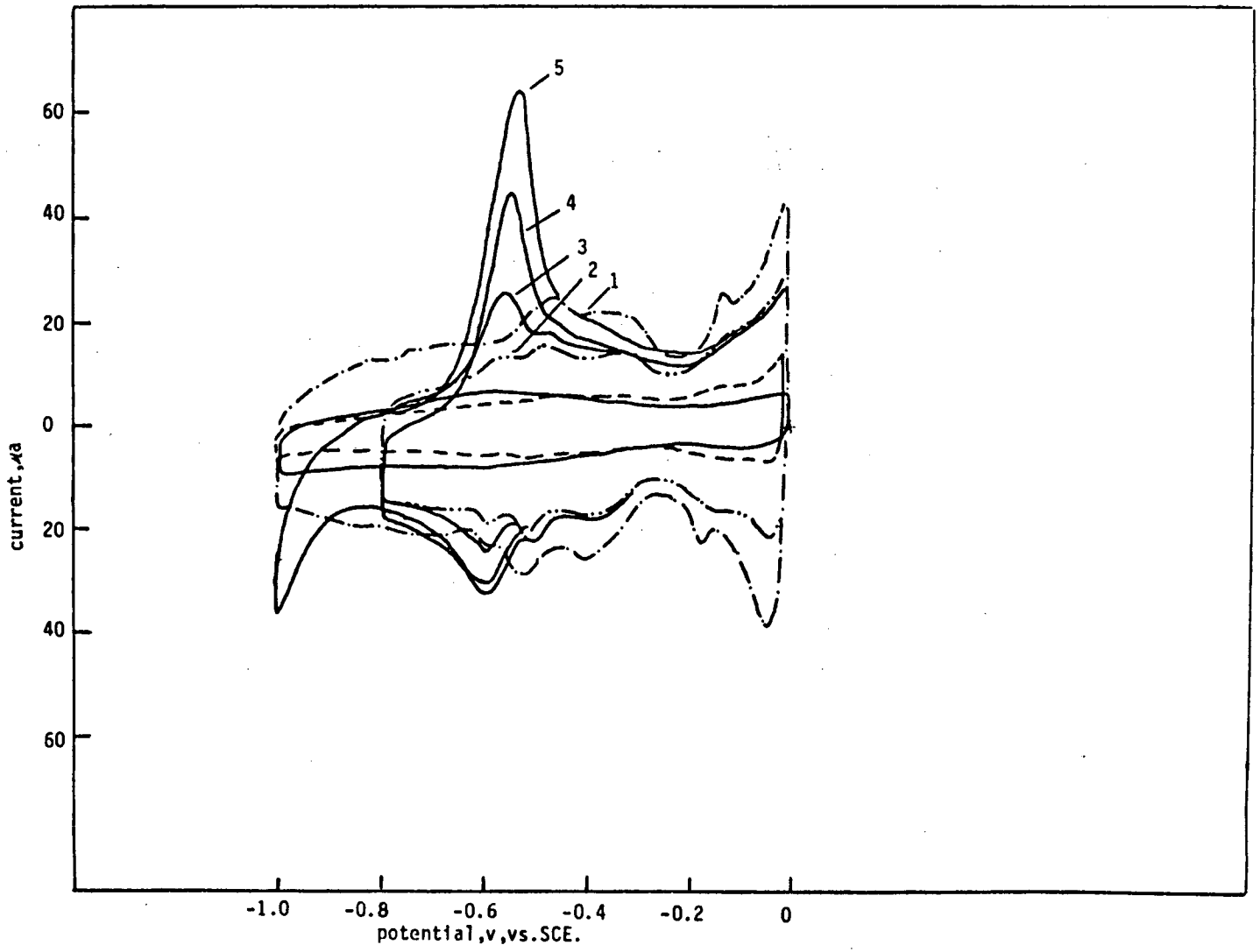


Fig. 5.1.10.4. The voltammogram of Ag electrode in 0.1 M KCL solution with addition of Tl^+ ions: 1) after loughning of Ag electrode in 0.1 M KCL solution (solid line) and with 0,01 M pyridine added(dashed line).2).1.2X10^{-6}M 3)7.4X^{-6}M Tl^+. 4).5.7X^{-5}M Tl^+ 5).1.3X10^{-4}M Tl^+ sweep rate: 100 mv/s.

5.1.11 IN-SITU AND EX-SITU MOSSBAUER SPECTROSCOPY STUDIES OF IRON PHTHALOCYANINE ADSORBED ON HIGH SURFACE AREA CARBON

D. A. Scherson,+ S. B. Yao* and E. B. Yeager

J. Eldridge, M. E. Kordesch° and R. W. Hoffman
Case Center for Electrochemical Sciences and the Department of Physics

ABSTRACT

The physical state of monomeric iron phthalocyanine (FePc) adsorbed on high surface area carbons has been investigated by using ex situ and in situ Mossbauer spectroscopy. Ex situ measurements have indicated that at relatively high loadings (>15% w/w) the spectrum is characterized by two doublets: δ_1 0.39 + 0.01 mm s^{-1} (vs. α-Fe), Δ_1 2.60 + 0.01 mm s^{-1}; Δ_2 0.35 + 0.02 splitting for doublet 1 compare favorably with bulk FePc which is probably present in the form of small crystallites dispersed in the support matrix. At low loadings (3.5%) only doublet 2 attributed to FePc chemically bound to the carbon surface was observed. The relative fraction of these two iron species has also been shown to be sensitive to the specific method of preparation of the sample.

In situ Mossbauer experiments have indicated that the quadrupole splitting decreases about 15-20% upon immersion of the electrode in an alkaline solution, corroborating earlier results obtained by this group. Further evidence concerning the formation of an octahedral complex with OH^- bound in an axial position was obtained by in situ measurements at pH 0. In this case the magnitude of the quadrupole splitting was larger than that obtained in basic operation.

Conventional oxygen reduction polarization curves with fuel cell type electrodes prepared from Mossbauer characterized 15% w/w FePc on XC-72 carbon (Cabot Corp.) haveindicated that the crystalline material plays an important role in the overall electrocatalytic process. A thorough discussion of these results as well as a critical review of earlier work have been included.

INTRODUCTION

Several transition metal macrocyclics have been shown to enhance oxygen electroreduction when adsorbed on a variety of carbon surfaces.[1-15] Attention has been mainly focused on iron and cobalt phthalocyanines and porphyrins since their activity in certain cases has been found to be comparable to that of platinum. In particular, Zagal et al.[13] have investigated the mechanistic aspects of oxygen reduction for water-soluble cobalt and iron tetrasulfonated phthalocyanines adsorbed at monolayer coverages on graphite surfaces in

---

+Vittorio deNora-Diamond Shamrock Postdoctoral Fellow
*On leave from Amoy University, Amoy, Fujian, People's Republic of China
°Weston fellow of The Electrochemical Society.

acid and basic media. Based on their rotating ring disk studies, these authors concluded that CoTsPc promotes O_2 reduction in a two-electron process to yield peroxide, while the iron anaolg was found to catalyze the four-electron reduction to give water. This same behavior was found by Collman et al.[14] for their synthesized cofacial dicobalt porphyrin with 3.5 - 4.0 Å separation of the metal species in acid and basic media when adsorbed on graphite surfaces. The reaction as reported by these workers proceeded at unusually positive potentials. In spite of the high activity exhibited by macrocyclics such as those mentioned above, they usually lack the necessary stability to become viable candidates in actual technological applications.

Essential to the understanding of the mechanism by which these classes of compounds catalyze oxygen reduction is the description of their interactions, not only with the reactant and other species in solution but also with the supporting substrate. Furthermore, a thorough investigation of the chemical properties of these adsorbed molecules can yield valuable insight into the problem of stability during electrochemical operation. In situ techniques can provide much of this needed information and indeed several of these methods are currently being used in the study of these and other systems.

Mossbauer spectroscopy is particularly suited to this specific kind of application. The natural abundance of ^{57}Fe (2.24%) is sufficient in most cases to perform measurements on high area surfaces such as carbon without the need of further enrichment and most important, carbon is highly transparent to the 14.4 keV γ-rays and thus reduces considerably the problem of attenuation of the γ-ray beam. In the case of cobalt the possibility of using ^{57}Co-enriched specimens in emission Mossbauer is especially attractive given that the number of atoms necessary to obtain an acceptable signal-to-noise ratio is several orders of magnitude less than that required for ^{57}Fe in the conventional transmission experiments. Emission experiments, however, can result in spectra difficult to interpret, although studies of the behavior of the parent iron compound can be very useful in the final analysis.

In situ Mossbauer spectroscopy has been successfully utilized in the investigation of passive films on iron.[16,17] The application of these measurements to iron-containing species adsorbed on high surface area electrodes, however, has only recently been reported in a short communication by Scherson et al.[18] In this work, iron phthalocyanine preadsorbed on high surface area carbon was shosen as a model system to assess the feasibility of this in situ spectroscopic technique in the study of electrode materials of electrochemical interest. The ex situ (dry) Mossbauer spectra of 30% w/w FePc on a moderate area carbon, Vulcan XC-72, showed two clearly defined doublets. One of these, denoted as doublet 1 in Ref. 18 (δ_1 0.38, Δ_1 2.59)‡ was assigned to bulk FePc based on a comparison with values obtained in this and other laboratories for the crystalline material. However, no such correlation was found in the case of doublet 2

‡Isomer shifts are referred to α-Fe standard throughout the text, and both δ and Δ are given in $mm.x^{-1}$.

(δ_2 0.36, Δ_2 0.88) and its presence was attributed to a new FePc species chemically bound to the carbon surface. In situ Mossbauer measurements in alkaline solution (1M NaOH) on the same sample indicated a pronounced decrease in the magnitude of the quadrupole splitting of doublet 2 with respect to that obtained for the dry specimen. This phenomenon was attributed to the formation of an octahedral iron phthalocyanine complex bound parallel to the surface with a hydroxyl species in the sixth axial position. These in situ experiments also indicated that the isomer shifts of both doublets as well as the quadrupole splitting and linewidth of doublet 1 were the same as those obtained in ex situ (dry) measurements. Moreover, no further changes in δ or Δ of either doublet were noticed upon polarization of the electrode over a wide region of potentials (-0.65 V to +0.10 V vs. $Hg/HgO,OH^-$).

In an effort to gain insight into the relationship between the physical state of the macrocyclic in the matrix and the electrochemical activity for oxygen reduction, a comprehensive study of the effect of the loading procedure, heat treatment and the nature of the carbon support was initiated. This paper will critically review earlier work in the area, and present new experimental results obtained from ex situ and in situ Mossbauer as well as ex situ electrochemical measurements and discuss the implications of these in the current understanding of the operative catalytic mechanism.

BACKGROUND

Relatively few investigations have been reported on the Mossbauer characterization of iron phthalocyanines adsorbed on high surface area carbons. To the best of our knowledge, such studies were initiated by Larsson et al.[19] in 1972, in an effort to analyze the mode of failure of polymeric FePc/Norit FNX electrodes of the type used for O_2 cathodes in fuel cells. Although no details were given concerning the exact preparation of the specimens, these authors reported Mossbauer parameters for samples of abou 10% loading, in dry form, after contact with moderately concentrated sulfuric acid, with and without exposure to O_2, and also of a similar electrode after electrochemical operation in the O_2 reduction mode. All four specimens yielded the same two well-defined doublets (δ_1 1.14, Δ_1 2.99 $\pm$ 0.01; δ_2 0.04-0.11, Δ_2 0.62 $\pm$ 0.02) and were tentatively assigned to a high spin and a low spin form.

In 1977, Meier et al.[8] re-examined this same system in order to gain insight into the interactions between poly-FePc and the carbon support. The Mossbauer spectra of this material adsorbed on Norit BRX also yielded two doublets. One of these (δ = 0.49, Δ = 2.6 mm/sec) compared favorably with those of the same macrocyclic without support, although different values have been found for the latter by Appleby et al.[5] (see Table I). The second doublet, according to Meier et al., had the same isomer shift as the pure material (see above) and a quadrupole splitting of 0.58 mm/sec. However, a close examination of

the spectra depicted in Fig. 6, Ref. 8, shows a value of $\Delta \sim 1$ mm/sec for 40% poly-FePc on Norit BRX and of about 0.35 mm/sec in the case of 20% loading. This discrepancy is difficult to explain, and the observed change in Δ as the loading fraction is varied is not accounted for. Based on the fact that this second doublet appeared only in the presence of carbon and had also a rather small Δ, these authors attributed it to poly-FePc interacting strongly with the support through surface alkaline groups.

In 1980, Melendres[20] investigated the effect of the fraction and method of loading on the Mossbauer spectra of monomeric FePc adsorbed on Vulcan XC-72 and Norit BRX. The values for the relevant parameters have been collected in Table II. Three doublets were found to give the best statistical fit of samples pre-adsorbed from concentrated sulfuric acid. The author concluded that the evidence was insufficient to unambiguously assign any of the features to adsorbate/substrate interactions. This is not due to the presence of multiple peaks, as Melendres states, however, but simply because the values obtained for pure monomeric FePc in contact with 100% H_2SO_4 without carbon do not differ appreciably from those when the catalyst is supported on carbon (see Table II). Melendres assigned doublet 1 to bulk FePc and doublet 3 to an oxidized form of the macrocyclic based on his results obtained by heating samples in a sealed O_2-containing tube. Although no explanation was offered by this author concerning the nature of the species responsible for doublet 2, the isomer shift and quadrupole splitting compare reasonably with those observed by Grenoble and Drickamer[21] upon heating crystalline FePc in air at 150°C (see Table I). Further work will be required to establish on a firm basis the origin of this spectral feature.

Recently, Blomquist et al[22,23] have reported a thorough study of the Mossbauer characteristics of monomeric and polymeric FePc in both crystalline form and adsorbed onto high surface area Norit FNX carbon under a variety of heat treatments. In particular, these authors compared the spectral features of purified poly-FePc with those obtained after chromatographic separation of the high molecular weight fraction of the mixture resulting from the synthesis. The parameters for both samples as well as those of the difference spectrum are listed in Table I.

One of the doublets present in both specimens (δ_3 0.48-0.54, Δ_3 0.83-0.85), was assigned to an oxidized form of FePc based on the fact that this species disappeared upon heat treatment in vacuum at elevated temperatures ($\sim$570°C), while the other two doublets (δ_2 0.46-0.52, Δ_2 2.66-2.53; δ_1 0.25-0.26, Δ_1 1.97-1.99) were attributed to central and peripheral positions of the monomeric sub-units respectively. This assignment was based on the assumption that the two sites are distinguishable only if the polymer is substituted, since high temperature treatment of unsupported poly-FePc, a procedure which in principle would thermally decompose the attached groups, yielded a single doublet (δ0.50, Δ2.73). The extra doublet observed

in non-chromatographed poly-FePc was attributed to monomeric FePc with COOH or $CONH_2$ groups attached to the ring. These groups, according to Blomquist et al., would cause an attenuation of the 3d electron density at the central iron, thus reducing the magnitude of the isomer shift.

Preliminary results obtained in this laboratory,[24] however, have shown that the Mossbauer spectrum of tetrasulfonated iron phthalocyanine yields two doublets (δ_1 0.38, Δ_1 0.84; δ_2 0.13, Δ_2 1.40). The isomer shift of the large amplitude doublet (1) is very similar to that obtained for pure monomeric FePc. This indicates that the substitution of $-SO_3H$ groups (which have an electron withdrawal ability similar to -COOH or $-CONH_2$) in the ring does not perturb appreciably the electronic density around the iron nucleus, in contrast to the claims made by Blomquist et al.

In the case of 25% w/w monomeric FePc preadsorbed on Norit FNX from concentrated sulfuric acid, Blomquist et al. found a prominent doublet ($\delta_1$0.26, Δ_1 1.25) not present in crystalline FePc and attributed it to FePc bound to the carbon support. In addition, two other small amplitude doublets (δ_2 0.45, Δ_2 0.63; δ_3 0.48 Δ_3 2.46) were observed and assigned to an oxidized form of FePc and to the unsupported catalyst, respectively. Moreover, an increase in the relative amplitude of doublet 2 was observed upon heating at 120° in air in accordance with the observations made by Grenoble and Drickamer and Melendres discussed above. A subsequent reduction in H_2 at 200°C, however, showed only a small decrease in the absorption area of this doublet.

As mentioned previously, a doublet with parameters similar to those attributed by Blomquist et al. to adsorbed FePc was found by Melendres in pure FePc precipitated from 100% H_2SO_4 (see Table II). Therefore, it seems possible that this spectral feature corresponds to some form of interaction between species originating from the acid or byproducts of FePc decomposition (see below) and the macrocyclic itself, and not to FePc-carbon as claimed by the former authors.

Samples prepared in the same fashion as for the monomer yielded a Mossbauer spectrum similar to the pure catalyst in the case of polymeric FePc, leading Blomquist et al. to conclude that this material does not bind through the ion but through side groups to the surface in contrast to the behavior claimed for the monomer. Several conclusions were drawn from a series of heat treated specimens. For instance, a linear correlation was found between the isomer shift corresponding to central units and the absorption area for the peripheral sites. Moreover, the intercept of the straight line yielded a value for the isomer shift in agreement with that observed upon thermal treatment of the unsupported material corresponding to no groups present. Finally, a complete thermal decomposition of these groups could not be achieved when the catalyst was supported, providing evidence that the polymeric species are most probably bound to the surface through carboxylic groups either present on the carbon surface or bound to the macrocyclic itself.

In overall perspective the ue of sulfuric acid in the loading procedure generates additional complications besides the difficulties specified above regarding an unambiguous assignment. The role of the acid in the dissolution process is not only poorly understood, but there is evidence that this acid in concentrated form can demetallate the macrocyclic and subsequently destroy the ring structure,[25,26] a process that is further enhanced in the presence of O_2 as established by Meier et al. in their radioisotope studies.[8] The use of concentrated H_2SO_4, although important from a technological point of view in light of the performance of actual fuel cells,[8] is not appropriate for studies of a more fundamental nature.

The use of solvents such as Me_2SO, DMF, or pyridine can overcome most of the difficulties specified above. In fact, Melendres has shown that spectra obtained from air-dried specimens prepared from these solvents can be fitted with only two doublets (see Table II). In the case of DMF and DMSO, one of the doublets corresponded to crystalline FePc, while for pyridine the values obtained compared favorably with $FePc(py)_2$.[20] Based on the same arguments put forward by Meier, Melendres assigned the second doublet to a FePc/carbon support interaction. However, a misinterpretation of Hudson's rule[27] appears to have been made. This correlation states that the quadrupole splitting, and not the isomer shift as claimed by Melendres, decreases as the basicity of the ligand increases. In fact, the values for the isomer shift for a series of FePc adducts are identical within experimental error.[27] The quadrupole splitting for the second doublet was shown to be sensitive to the amount of preadsorbed FePc. Actually, higher values for Δ were consistently found as the loading was decreased independent of the solvent used. Such a phenomenon, as will be shown later, was not observed in this investigation. Moreover, the parameter values for the doublet assigned to FePc bound to the carbon surface (δ 0.23 - 0.34, Δ 0.36 - 0.66) are somewhat similar to those of doublet 2 for pure FePc (δ 0.22, Δ 0.49).

Assour and Harrison[28] have investigated the difficulties associated with the purification of iron phthalocyanine and found that sublimation of the compound in a N_2 atmosphere at low pressure is not sufficient to remove molecular O_2 trapped in the FePc during its preparation and handling. However, these authors have shown that total elimination of O_2 can be achieved by sublimation at low pressure in a hydrogen-containing atmosphere. Therefore it is possible that the inner doublet observed by Melandres and perhaps Meier et al. corresponds to an oxygen-containing species. Further research will be necessary to clarify this issue.

EXPERIMENTAL

Iron phthalocyanine (Eastman Kodak, New York) was used without further purification for most of the measurements. For a few experiments the FePc was vacuum sublimed three times at $\sim$400°C under a pressure of $\sim 10^{-2}$ mm Hg.A white film developed on the surface of the water-cooled collector during the first and second sublimations,

but not during the third. This white mateiral, as well as the residue at the bottom of the vessel, were discarded. The FePc was then dissolved in spectral grade pyridine (Aldrich) to a concentration of $\sim 10^{-3}$ M. RB carbon (Pittsburgh Carbon Co.) as well as XC-72 were used to support the FePc. The former is an active carbon with a surface area of $\sim$1200 m^2/g. while the latter has no internal structure and has an area of 250 m^2/g. An amount of carbon, carefully weighed to obtain a prescribed proportion in the final mixure, was added to the solution in small quantities under continuous ultrasonic agitation. The solvent was removed either by evaporation starting at room temperature under vacuum with a water aspirator, or by boiling off the pyridine at 85-90°C at 1 atm. The latter procedure tends to keep the carbon for a longer time in suspension as the solvent volume becomes less and then results in a more uniform loading of the FePc on the carbon. The dry samples were placed in a ceramic boat and introduced into a horizontal quartz tube with gas feed-in at one end and out the other, allowing the continuous passage of gas during the heat treatment at either 220°C or 420°C. Helium, hydrogen, or a mixture (4:1) of both was normally used for a period of about 3 hours. The temperature of the tube was controlled thermostatically with a thermocouple junction as a probe located in the quartz tube in the neighborhood of the sample. A white film appeared on the walls of the quartz tube with no apparent further film formation at either 220° or 420°C after the first hour in most instances. A red colored coating however was found in the case of hydrogen at 1 atm when the heat treatment at 420°C was extended beyond 3 hours.

The resulting mixtures referred to hereafter as powder samples were transferred into vials with gas-tight caps. In separate experiments some of the powder samples heat treated at either 220° or 420°C were introduced into a U-shaped small diameter tube immersed in an oil bath at 220°C, and pure hydrogen or helium was passed through the well packed material for 24 hr. At the end of this period crystalline white needles were observed on the cool end of the tube even when the starting FePc had been purified by sublimation at 400°C as described above, and there was a considerable loss of total volume of material. This behavior was not exhibited by XC-72 or RB carbon alone as judged from experiments performed under the same conditions. These observations indicate that extreme precautions beyond three consecutive sublimations must be taken to obtain nominally purified crystals.

Powder samples were used in ex situ measurements as well as in the preparation of electrodes for in situ Mossbauer spectroscopy. It should be emphasized that ultrapurified as well as received Kodak FePc yield no significant differences in the Mossbauer spectra.[5,18] Electrodes for in situ measurements were prepared by mixing the powder samples with an aqueous solution of a Teflon suspension (T30B, duPont Co., Wilmington, DE) which contained Triton X-100 as a stabilizer. This mixture was then filtered and the resulting paste thoroughly homogenized. The final paste was then shaped in a circular cross-section die following a procedure described in detail elsewhere.[18] In one instance, the electrode was carefully transferred directly from the quartz tube into

a plastic bag filled with helium without exposure to the atmosphere. The Mossbauer spectrum of this section was compared with that obtained for the same sample in the presence of air and no differences were found. This means that either the sample was insensitive to O_2 or that even with the helium filled plastic bag, there was still sufficient residual O_2 to interact with the phthalocyanine in the porous electrode. Further handling of materials was carried out without special precautions.

The electrochemical cell for in situ Mossbauer spectroscopy (see Fig. 1) as well as the method used in potential controlled measurements have also been described in detail earlier.[18] Studies involving acid and alkaline solutions were performed in simple polyethylene bags sealed at the top and mounted on the same aluminum bracket used to house the cell with the aluminum plates pressing lightly both faces of the electrodes. Electrode specimens prepared from powder samples treated in pure He tended to float during the initial 24 hours of contact with the solution, dropping only slowly to the bottom of the bag afterwards. However, H_2 treated powder samples yielded electrodes which did not show this behavior. This fact can be associated with a higher wetting ability most likely related to the presence of iron particles in the powder, although no metallic iron was apparent in the electrode spectra (see results section). Partially deaerated 1M NaOH solutions were introduced into the bag after the spectrum for the dry specimen had been recorded and the bag was then resealed. Measurements for the same electrode in contact with acid were conducted by emptying the alkaline solution followed by a thorough washing with distilled water. The electrode was subsequently placed in the bag and 0.5M H_2SO_4 was added. This soaking procedure was utilized to neutralize the alkali trapped in the matrix pores. After two hours the liquid was removed and fresh acid solution of the same concentration was introduced and the top resealed.

Electrodes for conventional oxygen reduction were prepared from Mossbauer-characterized powder samples. The procedure used was similar to that described in Ref. 18. The amount of material used was about 60 mg. After the electrode was shaped and part of the excess water removed using hand pressure in a specially designed die, it was introduced into a quartz tube furnace for 3 hours at 220°C with flowing nitrogen. Subsequently the dry disk was placed into the die and pressed for about a minute at about 6000 psi at room temperature. A nickel screen was then laid on top of the electrode and the pressing was resumed for three minutes at 12,000 psi. The specimen was afterwards turned over and a circular piece of Teflon filter paper (Chemplast 75-XF) placed on top of it, continuing the pressing at about 400 psi for three minutes. The finished electrode (see Fig. 2A) was finally positioned into a special Teflon holder with drilled-in gas inlets and outlets shown in Fig. 2A. A schematic diagram of the electrode assembly is given in Figs. 2B and 2C.

The use of a Teflon shield (g) is required to insure reasonably uniform current distribution for measurements at high current.

Electrical contact to the working electrode was made with a wire inserted through the gas supply tube and connected at the other end to the nickel insert (see Fig. 2). When in use, the holder was force-fitted in a Teflon cap which also contained orifices for glass and Teflon tubes for the reference and counter electrodes. The electrochemical cell was assembled by force-fitting the cap to a truncated Teflon beaker which served as the electrolyte reservoir. The solution was heated by means of a resistive tape placed around the beaker and the temperature monitored with a Teflon coated thermometer.

Polarization measurements were made by means of a Stonehart BC 1200 Potentiostat operated in a galvanostatic mode with IR compensation and correction. Oxygen reduction (discharge) measurements were performed in 9M NaOH at 85°C and the data recorded in the galvanostatic mode. The current was interrupted by a pulse generator having a frequency of about 900 Hz with a current duty cycle of 92%. The IR drop (mostly contact and solution resistance) could then be nulled out by observing the potential (on an oscilloscope) during the off period and adjusting the bridge of the instrument. A dual trace oscilloscope was used to allow simultaneous monitoring of the current waveform.

RESULTS AND DISCUSSION

A. Vacuum Evaporated Specimens

The Mossbauer spectrum of an RB electrode with no catalyst is depicted in curve A Fig. 3, which was best fitted by a single line and a doublet indicating the presence of at least two species of iron impurities. Curve B in Fig. 3 shows the spectrum of an electrode 3.5% w/w/ FePc on RB carbon, where in addition to the contributions arising from the support a doublet originating from the catalyst was found. In order to analyze the effect induced by a decrease in the surface area of the support, an electrode was prepared in the same fashion as outlined above with XC-72. As shown in curve C Fig. 3, a single doublet (δ0.37, Δ0.91) was obtained which correlates well with doublet 2 in curve B Fig. 3. A separate experiment was performed on a pure XC-72 electrode and no iron species were detected.

Melendres[20] has observed an asymmetry in the small quadrupole split doublet for air-dried 14% FePc on Norit BRX carbon adsorbed from DMF solutions. Moreover, Van Veen et al.[15] made a similar observation in their studies of the temperature effects on the stability and activity of several transition metal macrocyclics. The Mossbauer spectrum of thermally untreated Fe porphyrin/Norit BRX at 77 K showed a clear asymmetric doublet (δ0.41, Δ0.61) and an extra peak at approximately 2 mm/sec vs. α-Fe, a value close to one of the components of the doublet in curve A Fig. 2. Van Veen and Visser[12] in a separate communication have listed iron as the second major impurity ($\sim$0.25%) in Norit BRX, a value comparable to that obtained by elemental analysis of the deashed RB carbon ($\sim$0.24%) used in this work. It can therefore be concluded that the asymmetries observed, at least in cases where a moderate heat treatment is used, are most likely due to iron

impurities in the carbon support. At higher temperatures, however, the partial decomposition of FePc can result in new iron species generating additional features in the spectrum that could account for even larger asymmetries.

The effect of the gas atmosphere during the heat treatment was analyzed by preparing powder samples 15% on XC-72 at 420°C under a flow of either He or H_2. The spectra corresponded to curves A and B respectively in Fig. 4. Two prominent doublets were found in the case of the He treated speciments (δ_1 0.39, Δ_1 2.60; δ_2 0.35, Δ_2 0.96). The values of the second doublet compare favorably with that observed in curve C Fig. 3, while the first corresponds to crystalline monomeric FePc (see Table I). This provides evidence that the catalyst tends to form crystallites at this high loading with this mode of preparation. For the H_2 treated specimen, essentially the same doublets were found; however, six additional lines (only the outer four can be seen in curve B Fig. 4) indicate the presence of small iron particles. The formation of metallic iron has also been inferred by Van Veen et al.[15] based on measurements at 4.2 K on samples heated at much higher temperatures (>700°C) in an inert atmosphere with an externally applied magnetic field (4.2T).

In order to study the effect of the loading fraction an electrode 30% w/w FePc on XC-72 was prepared in a He/H_2 ($\sim$4:1) mixture at 420°C. As expected, this sample (see Fig. 5) also showed iron particles and two doublets (δ_1 0.39, Δ_1 2.60; δ_2 0.35, Δ_2 0.87) with parameter values in good agreement with those obtained at lower loadings. Therefore, in contrast to the observations made by Meier[8] and Melendres,[20] the increase in the loading fraction simply results in variations in the relative ratios of both forms of FePc, without changes in the magnitudes of either the isomer shifts or quadrupole splittings of the associated doublets.

B. SPECIMENS WITH SOLVENT REMOVED BY BOILING

A general characteristic found in samples prepared by boiling off the solvent at an elevated temperature at 1 atm. was an increase in the amplitude of the inner doublet corresponding to the adsorbed species with a simultaneous reduction in the amplitude of the doublet corresponding to crystalline FePc. This phenomenon can be attributed to a higher solubility of the macrocyclic due to the increase in temperature of the FePc/carbon/pyridine mixture during the removal of the solvent, improvements in spreading of the solution on the carbon surface at the higher temperature may also bve responsible. Curve A Fig. 6 shows the Mossbauer spectrum of a 15% w/w/ FePc on XC-72 powder sample heat-treated at 220°C in a pure He atmosphere. Four doublets were found to give the best fit to the data. Two of these (δ_1 0.39, Δ_1 2.56; δ_3 0.26, Δ_3 2.05) definitely correspond to crystalline FePc and FePc(pyridine)2, while a third (δ_2 0.33, Δ_2 1.11) compares favorably with that obtained in curve C Fig. 3. The assignment of doublet 4 (δ_4 -0.13, Δ_4 1.68) is rather difficult. The quadrupole splitting Δ_4 is intermediate between that of doublet 1 (or 3) and doublet 2 and it

could conceivably be ascribed to a species bound to the carbon surface with a pyridine molecule coordinated in the sixth axial position. The low isomer shift, however, does not seem consistent with this explanation, and further work will be required to determine the precise nature of this species. Based on these results, a complete removal of pyridine from the adduct cannot be achieved at temperatures at least as high as 220°C, with reasonable heating times ($\sim$3 hrs.).

Curves B and C in Figure 6 are Mossbauer spectra of similar samples, this time heated at 420°C in He and H_2 atmosphere, respectively. Although the inner doublet parameters as well as the quadrupole splitting values for the outer doublet are similar to those found for other samples, the isomer shift of doublet 2 for H_2-treated sample is slightly higher than that expected for crystalline FePc. No iron was detected in the hydrogen-treated sample (see Curve C in Fig. 6) suggesting that only bulk crystalline FePc and not the adsorbed species can be reduced to iron metal.

Finally, part of the same original material from which these last two samples were obtained was heated at 420°C in a pure H_2 atmosphere until a red-colored layer began to develop on the quartz tube walls (see Experimental Section). The Mossbauer spectrum of this specimen is given in Fig. 7. Two of the doublets as judged from the parameter values 9see Table II) correspond to those normally found; however, a third doublet (δ_3 1.32, Δ_3 2.74) was observed, the nature of which has not as yet been determined except for its behavior upon contact with an alkaline solution, to be discussed in the following section.

IN-SITU MEASUREMENTS

An electrode for in-situ Mossbauer examination was prepared from a powder sample 29% w/w FePc on RB carbon heat treated at 420°C for three hours in a mixture He/H_2 ($\sim$4:1), and mounted onto the Teflon bracket of the specially designed electrochemical cell.[18] The Mossbauer spectrum of the powder sample and that corresponding to the dry electrode are shown in curves A and B, Fig. 8 respectively. The parameter values including contributions from impurities in the carbon support and also from doublet 3 (see Fig. 7) in the case of curve B Fig. 8 are listed in Table II. The total amplitude of the RB carbon background was allowed to vary in the statistical analysis. However, the relative amplitudes of the singlet and the doublet as well as their positions and linewidths were assumed constant in all cases.

A previously deaerated 1 M NaOH solution was introduced into the collapsible cell and allowed to wet for about one hour before the in situ Mossbauer spectrum was recorded. The open circuit potential was $\sim$0.0 V vs. Hg/HgO, OH^-. Nitrogen was bubbled through the upper part of the solution during all the measurements.

The in-situ Mossbauer spectrum of the electrode at open circuit as well as the same spectrum in curve B Fig. 8, although in a restricted velocity scale for the purpose of comparison, are given in curve C

and B, Fig. 8 respectively. The isomer shift and quadrupole splitting of doublet 1 (bulk FePc) showed no change in both wet and dry states (see Table III). However, the corresponding parameters of doublet 2 as well as the decrease in the value of the quadrupole splitting upon immersion of the electrode into the alkaline elecrolyte compare very favorably with those obtained in a previous communication.[18]

The electrode was polarized at several potentials ranging from -0.65 V up to +0.20 V vs. $Hg/HgO,OH^-$ and the spectrum recorded at each point. These are shown in Fig. 9, where the sequence follows that in which the different potentials were applied. The parameter values including the calculated contributions arising from the carbon impurities are listed in Table III.

Based on the values of A_2/A_1 obtained it becomes clear that a significant increase in the amplitude ratio of the FePc doublets takes place at the most positive potential. This change is to a large extent reversible as judged from the magnitude of this ratio observed at open circuit and -0.40 V after anodic polarization. Based strictly on the relative amplitudes of both species it would appear that there is a reversible exchange between crystalline and adsorbed forms. A potential induced exchange seems very unlikely. An alternative explanation would be a bulk $Fe^{II}Pc/Fe^{III}Pc$ oxidation-reduction reaction, although no new peaks are observed. Two facts seem to support this explanation. First, the E_o for this couple is expected to be located precisely where this behavior is found, and second, the isomer shift and quadrupole splitting of species generated by heating crystalline monomeric FePc in an oxygen containing atmosphere (see Table I) are similar to those corresponding to the adsorbed species. This would induce a net increase in the amplitude of the inner doublet with respect to the outer doublet at +0.20 V as found in this experiment. The ratio of the amplitude of each doublet to the spectral background gives an indication of the total amount of each species present in the sample however, and this does not seem consistent with this suggested oxidation state change. Specifically, the value of A_2/background observed at +0.20 V, although larger than that obtained at the initial cathodic potentials (curves A, B and C) did not decrease when the potential was subsequently made negative (curves E and F). In-situ measurements on bulk FePc electrodes supported on an appropriate substrate are planned and should yield more conclusive information concerning changes in the oxidation state.

The formation of a hydroxyl coordinated FePc species in one or both of the axial positions (probably one) is consistent with the observed decrease in the magnitude of the quadrupole splitting. An attempt to substantiate further this observation was made by examining the in-situ Mossbauer spectra at a different pH. The ex-situ (dry) and in-situ Mossbauer spectra are shown in Fig. 10 for an electrode made with a powder sample 15% w/w FePc on XC-72 prepared by boiling off the pyridine. This electrode was then washed thoroughly with 0.5 M H_2SO_4 and introduced in the plastic bag following the procedure indicated in the Experimental Section for these specimens. The

corresponding spectrum is given in curve C Fig. 1. The quadrupole splitting of doublet 2 is less than that of the dry sample but greater than that of the sample immersed in basic solution. This indicates, based on Hudson's rule, a decrease in the Lewis base character of the ligand. The most likely explanation of this effect is a protonation of the hydroxyl group to form water, a weaker Lewis base than OH^-. The parameters associated with these measurements are included in Table IV.

As a means of gaining insight into the nature of the iron species formed by an extended heat treatment in hydrogen at 420°C atmosphere (see Experimental Section) an electrode was made with this material and placed in contact with a 1 M NaOH solution. The spectrum obtained (see Fig. 11) shows that doublet 3 (see Table II) disappears almost completely, indiating that this species most likely dissolves in the solution. This is a significant observation because ex-situ (dry) measurements on pyrolyzed materials have been used as a basis for the analysis of the chemical structure of species responsible for the enhanced catalytic activity and stability exhibited by these specimens in O_2 reduction fuel cell cathodes. Based on this observation the presence of spectral features in the ex-situ spectra cannot guarantee their presence once the sample comes in contact with the electrolyte. A composite diagram depicting the spectra for ex-situ (dry), in-situ in 1 M NaoH and 0.50 M H_2SO_4 is given in Fig. 11. Based on the parameter values obtained (see Table IV) the behavior of the quadrupole splitting of the inner doublet was in agreement with the results presented above (see Table IV and Fig. 10).

EX-SITU ELECTROCHEMICAL MEASUREMENTS

Polarization curves for oxygen reduction were conducted on two samples prepared differently with precisely the same loading although significantly different Mossbauer spectral characteristics. These measurements were performed at 85°C in 9 M NaOH using pure O_2 as the feeding gas with Teflon bonded fuel cell type electrodes prepared by the procedure described in the Experimental Section. Samples containing 15% w/w FePc on XC-72 which differed in that one involved vacuum evaporation and the other boiling off the solvent were used. Representative polarization curves as well as the corresponding Mossbauer spectra are given in Fig. 12. The activity of the electrode containing a higher proportion of crystalline material is appreciably higher than that in which the adsorbed species predominates, as judged from the high current at given voltages in the region where mass transport of O_2 is not the predominant controlling factor. Moreover, the more active sample showed a much faster voltage recovery upon current interruption from a 300 μA constant polarization. Several runs were made with both specimens and the same trend was obtained in each instance.

Similar measurements were performed with a 15% w/w FePc powder sample evaporated and heated in H_2 at 420°C for three hours. The behavior was essentially identical to that obtained for the He treated specimen referred to above, ruling out the possibility of metallic iron playing a significant role in the catalysis.

The higher performance of the electrode with the small FePc crystallites rather than the adsorbed macrocyclic appears to indicate that the effective catalytic activity is associated with the small crystallites.

Savy et al.[29,30] have reported O_2 reduction catalytic activity on vacuum evaporated films of monomeric FePc on gold in both alkaline and acid media. Faulkner and Tachikawa[31] on the other hand hve found very small levels of O_2 reduction on films prepared in a similar fashion and have concluded that most of the activity is associated with the support while the macrocyclic only assists the overall reaction by heterogeneous processes which may not be potential dependent. These latter experiments, however, were conducted in unbuffered solutions and the results are therefore open to question.

With the moderately high area carbon electrodes used in this work, the O_2 to peroxide step usually proceeds sufficiently fast so that the electrode potential corresponds to the reversible value for the O_2 peroxide couple in terms of the local concentration. The role of the catalyst then can be two-fold:

1. to promote the peroxide elimination reaction

2. to promote a parallel 4-electron overall reduction to OH^- (or water)

Measurements with the FeTsPc adsorbed on the basal plane of stress-annealed pyrolytic graphite have demonstrated tht this complex can catalyze the overall 4e electroreduction to the exclusion of the series process.[7] On the basal plane O_2 reduction is greatly impeded and hence there is negligible competitive reaction on the bare graphite. It is not clear that FePc has similar activity for O_2 reduction in the adsorbed state. In fact, the adsorbed FePc may interfere with the O_2 reduction to peroxide on the carbon by blocking the carbon surface and thus resulting in lower apparent catalytic activity, as seems to be the situation shown in Fig. 12. Since the total loading with FePc is the same for both curves A and B in this figure, the amount adsorbed on the carbon surface is less for Curve A and presumably the uncovered carbon surface greater.

SUMMARY

The results obtained in this investigation have demonstrated the following:

EX-SITU MEASUREMENTS

1. Two doublets associated with two different iron species are present in preadsorbed FePc on high surface area carbons, (δ_1 0.38 + 0.01, Δ_1 2.60 + 0.01; δ_2 0.35 + 0.02, Δ_2 0.91 + 0.04). At low loadings ($\sim$3.5%) only doublet 2 is observed and has been attributed to FePc interacting with the carbon support. The smaller

quadrupole splitting found for the adsorbed species could be explained by assuming tha the macrocyclic is bound parallel to the carbon surface most likely through alkaline groups present in the support. As the loading is increased, a second doublet (1) whose parameters compare favorably with bulk monomeric FePc is also found, and is probably due to small crystallites dispersed in the matrix.

2. Certain asymmetries observed by other workers have been related to the presence of iron impurities in active carbons which cannot be removed even after deashing.

3. Heat treatment of the specimens at moderate temperatures ($\sim$420°C) in a flowing hydrogen atmosphere results in the formation of small metallic particles.

4. A third doublet is present in the ex-situ (dry) Mossbauer spectra after prolonged exposure to hydrogen under the condition specified in 3, which disappears when the specimen is placed in contact with alkaline and presumably acid solution.

5. The relative amplitudes of these doublets is very sensitive to the way in which the solvent is removed during preparation of the specimens. In particular, samples which are evaporated under vacuum at room temperature show a higher crystalline/adsorbed ratio while the reverse is found in the case in which the solvent is removed by distillation at $\sim$85-90°C.

6. A significant amount of bulk FePc $(py)_2$ remains in the matrix even upon heat treatment at 220°C for 3 hr.

IN-SITU MEASUREMENTS

1. The quadrupole splitting corresponding to the adsorbed species was shown to decrease upon contact of the electrode with an alkaline solution. This phenomenon observed earlier has been attributed to the formation of an octahedral complex involving hydroxyl ion(s) bound to the macrocyclic axial position(s).

2. An increase in Δ_2 with respect to that obtained in alkaline solution was found when the electrode was immersed in an acidic solution. Based on Hudson's rule, this corresponds to a decrease in the Lewis base character of the axial ligand(s) suggesting that hydroxyl groups have become protonated.

EX-SITU ELECTROCHEMICAL MEASUREMENTS

Oxygen reduction polarization curves obtained on Mossbauer characterized electrodes (85°C in 9 M NaOH) indicate that small FePc crystallites are responsible for much of the catalytic activity and stability observed. Direct verification of this fact has been obtained by comparing the performance of electrodes with exactly the same loading although significantly different relative amplitudes of both doublets.

References

1. A. Kozawa, V.G. Zilionis, and R.J. Brood, J. Electrochem. Soc., 117, 1470 (1970).

2. H. Alt, H. Binder, G. Sandstrede, J. Catal., 28, 8 (1973).

3. A. J. Appleby and M. Savy, Electrochim. Acta, 21, 567 (1976).

4. H. Jahnke, M. Schönborn and G. Zimmermann, Fortsch. Chem. Forsch., 61, 133 (1976).

5. A.J. Appleby, J. Fleisch and M. Savy, J. Catal., 44, 281 (1976).

6. F. Beck, J. Appl. Electrochem., 7, 239 (1977).

7. J. Zagal, R.K. Sen and E. Yeager, J. Electroanal. Chem. 83, 207 (1977).

8. H. Meier, U. Tschirwitz, E. Zimmerhacki, W. Albrecht, and G. Zeitler, J. Phys. Chem., 81, 712 (1977).

9. Chr. Kretzschmar, K. Wiesener, M. Musilova, J. Mhra and R. Dabrowski, J. Power Sources, 2, 351 (1977/78).

10. V.S. Bagotsky, M.R. Tarasevich, K.A. Radyushina, O.A. Levina and S.J. Andrusyova, J. Power Sources, 2, 233 (1977/78).

11. M.R. Tarasevich, "Proceedings of the Third Japan-USSR Seminar on Electrochemistry", Vol. 2, p. 337 (1978).

12. J.A. Rob van Veen and C. Visser, Electrochim. Acta, 24, 921 (1979).

13. J. Zagal, P. Bindra and E. Yeager, J. Electrochem. Soc., 127, 1506 (1980).

14. J.P. Collman, P. Denisevich, Y. Konai, M. Marrocco, C. Koval and F.C. Anson, J. Am. Chem. Soc., 102, 6027 (1980).

15. J.A. Rob van Veen, J.F. van Baar and K.J. Kroese, J. Chem. Soc., Faraday Trans., I, 77, 2827 (1981).

16. W.E. O'Grady, J. Electrochem. Soc., 127, 55 (1980) and references therein.

17. J. Eldridge, M.E. Kordesch and R.W. Hoffman, J. Vac. Sci. Technol., 20, 934 (1982).

18. D. Scherson, S.B. Yao, E. Yeager, J. Eldridge, M.E. Kordesch and R.W. Hoffman (to be published in Appl. Surface Sci. (1982)).

References

19. R. Larsson, J. Mrha and J. Blomquist, Acta Chem. Scand., 26, 3387 (1972).

20. C. Melendres, J. Phys. Chem., 84, 1936 (1980).

21. D.C. Grenoble and H.G. Drickamer, J. Chem. Phys., 55, 1624 (1971).

22. J. Blomquist, L.C. Moberg, L.Y. Johansson and R. Larsson, Inor. Chim. Acta, 53, L39 (1981).

23. J. Blomquist, L.C. Moberg, L.Y. Johansson and R. Larsson, J. Inor. Nucl. Chem., 43, 2287 (1981).

24. D. Scherson, J. Eldridge, M.E. Kordesch, R.W. Hoffman and E. Yeager (in preparation).

25. B.D. Berezin, Russ. J. Phys. Chem. (English translation), 36, 258 (1962).

26. B.D. Berezin, Zh. Fiz. Khim., 36, 494 (1962).

27. A. Hudson and H.J. Whitfield, Inorg. Chem., 6 1120 (1967).

28. J.M. Assour and S.E. Harrison, J. Phys. Chem., 68, 872 (1964).

29. M. Savy, P. Andro, C. Bernard and G. Magner, Electrochim, Acta, 18, 191 (1973).

30. M. Savy, C. Bernard and G. Magner, Electrochim. Acta, 20, 383 (1975).

31. H. Tachikawa and L.R. Faulkner, 100, 4379 (1978).

TABLE I

MOSSBAUER PARAMETERS OF MONOMERIC AND POLYMERIC IRON PHTHALOCYANINES IN CRYSTALLINE FORM

FePc Monomer	Doublet	Isomer Shift (δ, mm·s^{-1} vs. α-Fe)	Quadrupole Splitting (Δ, mm·s^{-1})	Linewidth (Γ, mm·s^{-1})	Absorption Area (A,%)	Reference
Eastman Kodak	1	0.40	2.63	--	(0.08)*	20
	2	0.22	0.49	--	(0.01)	
	1	0.39	2.61	0.39	92	This work
	2	0.18	1.02	0.54	8	
Synthesis [a]	1	0.36	2.48	--	56	5
	2	0.29	0.50	--	23	
	3	0.32	1.14	--	15	
	4	0.20	3.52	--	5	
	5	0.61	2.18	--	1	
Synthesis [b]	1	0.38	2.58	--	-0-	21
(heated in 2-pic [e])	1	0.29	0.36	--	-0-	
(sheared)	1	0.35	0.71	--	-0-	
(heated in air)	1	0.35	1.13	--	-0-	
--	1	0.4	2.6		-0-	23
FePc Polymer						
Synthesis [c]	1	0.22	1.80	--	80	5
	2	0.12	2.70	--	15	
	3	0.66	1.32	--	5	
Synthesis [d]	1	0.49	2.6	--	--	8
Synthesis [c]	1	0.25	1.97	0.48	34	22
	2	0.46	2.66	0.48	22	
	3	0.48	0.83	0.58	13	
	4	0.19	2.95	0.56	31	
(chromatographed)	1	0.26	1.99	0.51	63	
	2	0.52	2.53	0.51	24	
	3	0.54	0.85	0.48	13	
(difference spectrum) (see text)	1	0.26	2.99	0.50	-0-	
heated in vacuum, 570°K)	1	0.50	2.73	0.42	-0-	

*Values in parenthesis correspond to fraction absorption

[a] See Ref. 5 for details of synthesis

[b] T. H. Moss and A. B. Robinson, Inorg. Chem., 7, 1692 (1968)

[c] See Ref. 5 for details of synthesis

[d] W. C. Drinkard and J. C. Bailar, J. Am. Chem. Soc., 81, 4795 (1959)

[e] 2-Picoline

TABLE II

MOSSBAUER PARAMETERS FOR MONOMERIC IRON PHTHALOCYANINE ADSORBED ON HIGH SURFACE AREA CARBON

Specimen	Doublet	Isomer Shift (δ, mm s^{-1} vs. α-Fe)	Quadrupole Splitting (Δ, mm s^{-1})	Linewidth (Γ, mm s^{-1})	Absorption Area (A,%)	Reference
FePc Monomer[+]						
45% on XC-72 (H_2SO_4)	1	0.36	2.48	--	0.02	20
	2	0.31	1.11	--	0.03	
	3	0.18	0.53	--	0.02	
15% on XC-72 (H_2SO_4)	1	0.38	2.54	--	0.0046	
	2	0.25	1.19	--	0.0091	
	3	0.32	0.54	--	0.008	
100% H_2SO_4	1	0.36	2.46	--	0.01	
	2	0.21	1.12	--	0.016	
	3	0.20	0.45	--	0.014	
25% on Norit FNX (H_2SO_4)	1	0.48	2.46	0.38	8	23
	2	0.26	1.25	0.33	79	
	3	0.45	0.63	0.40	13	
Heated (120°C/ 408h, [air])	1	0.25	1.26	0.30	62	
	2	0.52	0.83	0.62	38	
Heated (120°C/ 408h, [air]; 200°C/4.5h, [H_2])	1	0.29	1.29	0.47	69	
	2	0.46	0.69	0.45	31	
14% on Norit BRX (DMF)	1	0.40	2.61	--	0.005	20
	2	0.30	0.61	--	0.009	
45% on XC-72	1	0.26	2.01	--	0.03	
	2	0.23	0.36	--	0.007	
13% on XC-72	1	0.27	2.03	--	0.019	
	2	0.33	0.64	--	0.008	
3.5% on RB[#]	2	0.38	0.84	0.56	33 (67)[°]	Fig. 3B
3.5% on XC-72[#]	1	0.37	0.91	0.6	-0-	Fig. 3C
15% on XC-72[#] (He)	1	0.39	2.60	0.28	45	Fig. 4A
	2	0.35	0.96	0.67	55	
15% on XC-72[#] (H_2)	1	0.39	2.60	0.28	55 (12)[∞]	Fig. 4B
	2	0.33	0.91	0.90	33	
30% on XC-72[#]	1	0.39	2.60	0.29	75 (9)[∞]	Fig. 5
	2	0.35	0.87	0.68	16	
15% on XC-72 (220°C, He, boiled)	1	0.39	2.56	0.32	41	Fig. 6A
	2	0.33	1.11	0.70	27	
	3	0.26	2.05	0.27	28	
	4	-0.13	1.68	0.17	4	

(continuation of Table II)

15% on XC-72[#] (He, boiled)	1	0.40	2.61	0.37	13	Fig. 6B
	2	0.37	0.97	0.71	87	
15% on XC-72[#] (H_2, boiled)	1	0.46	2.61	0.39	5	Fig. 6C
	2	0.38	1.12	0.69	95	
15% on XC-72[#] (H_2, extended heat treatment, boiled)	1	0.36	2.50	0.33	16	Fig. 7
	2	0.36	0.81	0.62	46	
	3	1.32	2.74	0.32	38	
29% on RB[#] (powder sample)[‡]	1	0.41	2.54	0.52	28	
	2	0.35	0.81	0.83	67(5)[∞]	Fig. 8A
(electrode)	1	0.40	2.49	0.38	6 9	
	2	0.35	0.94	0.63	82(9)[°]	Fig. 8B
	3	1.39	2.68	0.20	3	

[*] See comment in Table I.

[‡] FePc preadsorbed from pyridine unless otherwise stated (solvent used is given in parenthesis)

[‡] Samples dried in air at room temperature unless otherwise indicated.

[#] Powder samples evaporated under vacuum, heat treated at 420°C in a He/H_2 mixture (4:1) for three hours. Changes in any of these conditions or in the nature of the specimen are indicated in parenthesis.

[°] Value corresponds to absorption area due to carbon impurities (see text).

[++] The statistical fit of this spectrum did not include contributions from iron impurities in the carbon support nor doublet 3.

[∞] Absorption area due to metallic iron.

TABLE III

IN-SITU MOSSBAUER PARAMETERS FOR A 29% w/w FePc ON RB CARBON ELECTRODE IN 1M NaOH AQUEOUS SOLUTION

POTENTIAL (V vs. Hg/HgO,OH^-)	DOUBLET	ISOMER SHIFT (δ,mm/s vs. α-Fe)	QUADRUPOLE SPLITTING (Δ, mm/s)	LINEWIDTH (Γ,mm/s)	ABSORPTION AREA (A, %)	A_2/A_1	FIGURE
-0.65	1	0.40	2.61	0.38	13 (23)°	5.0	9A
	2	0.34	0.69	0.51	65		
-0.40	1	0.40	2.48	0.33	15 (19)	4.4	9B
	2	0.35	0.70	0.53	66		
-0.20	1	0.40	2.4	0.35	14 (16)	4.9	9C
	2	0.35	0.70	0.52	69		
+0.20	1	0.38	2.54	0.29	4 (14)	20.5	9D
	2	0.34	0.69	0.53	82		
OPEN CIRCUIT (~0.0 V)	1	0.39	2.52	0.33	7 (15)	11.1	9E
	2	0.35	0.69	0.52	78		
-0.40	1	0.39	2.49	0.31	8 (15)	9.6	9F
	2	0.35	0.69	0.51	77		

°Values in parenthesis correspond to the absorption area due to iron impurities in the carbon support (see text).

TABLE IV

IN SITU MOSSBAUER PARAMETERS FOR A 15% FePc ON XC-72 CARBON ELECTRODE

IN AQUEOUS SOLUTIONS

ELECTRODE[+]	DOUBLET	ISOMER SHIFT (δ, mm/s vs. α-Fe)	QUADRUPOLE SPLITTING (Δ, mm/s)	LINEWIDTH (Γ, mm/s)	ABSORPTION AREA (A, %)	FIGURE
Dry (420°C [3 hr.] in pure He)	1	0.53	2.10	0.86	0.36	10A
	2	0.38	0.90	0.54	0.64	
1M NaOH	1	0.47	2.23	0.76	0.31	10B
	2	0.36	0.79	0.55	0.69	
0.5 M H_2SO_4	1	0.40	2.37	0.63	0.23	10C
	2	0.36	0.84	0.59	0.77	
Dry (420°C extended heat treatment in pure H_2)	1	0.36	2.50	0.33	0.16	11A
	2	0.36	0.80	0.62	0.46	
	3	1.33	2.74	0.32	0.38	
1 M NaOH	1	0.38	2.51	0.35	0.18	11B
	2	0.35	0.69	0.52	0.82	
0.5 M H_2SO_4	1	0.39	2.50	0.36	0.19	11C
	2	0.36	0.74	0.54	0.81	

[+]Conditions in parenthesis refer to those of preparation of powder sample.

FIGURE CAPTIONS

Figure 1. Three dimensional drawing of electrochemical cell for in-situ Mossbauer effect spectroscopy measurements. INSERT: Working electrode assembly.

A. Working electrode (FePc adsorbed on high surface area XC-72 carbon).

B. Counter electrode (high surface area carbon).

C. Collapsible cell (polyethylene).

D. Reference electrode (Hg/HgO, OH^-).

E. Gas bubbler

F. Teflon holder for working electrode.

G. Stopper with press fitted nickel wire connected to counter electrode.

H. Aluminum frame.

I. Viton O-ring.

J. Teflon cell top.

K. Aluminum plates.

L. Brass screws.

M. Nickel screen annulus (current collector).

N. Teflon ring for electrode mounting and mechanical attachment. to F through pin (not shown for clarity).

Figure 2. Schematic diagram of electrode and electrode holder used for ex situ electrochemical measurements.

A. Fuel cell type electrode. a high surface area teflonated carbon with catalyst . b nickel screen current collector. c Teflon backing.

B. Teflon electrode holder with associated components. a Teflon main body. b gas inlet and outlet. c nickel insert. d Viton O-ring. e,f acrylic washers. g Teflon shield.

C. Side view of assembled system. a wire for connection to working electrode (some details have been omitted for clarity).

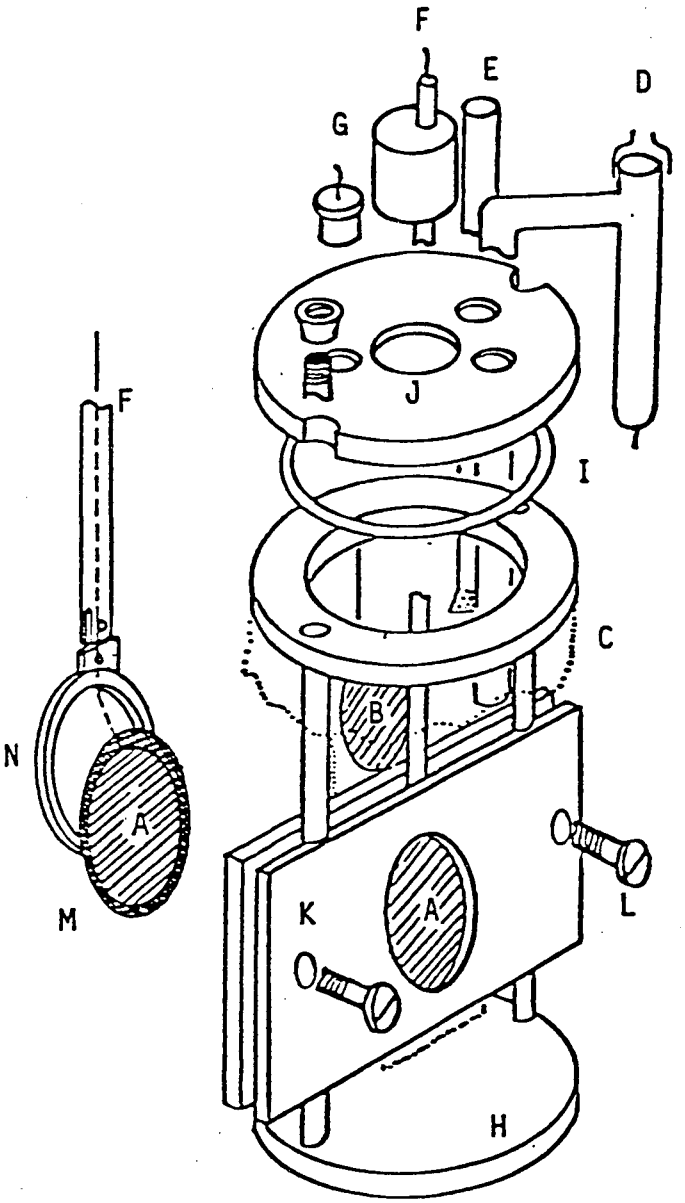


Fig. 5.1.11.1

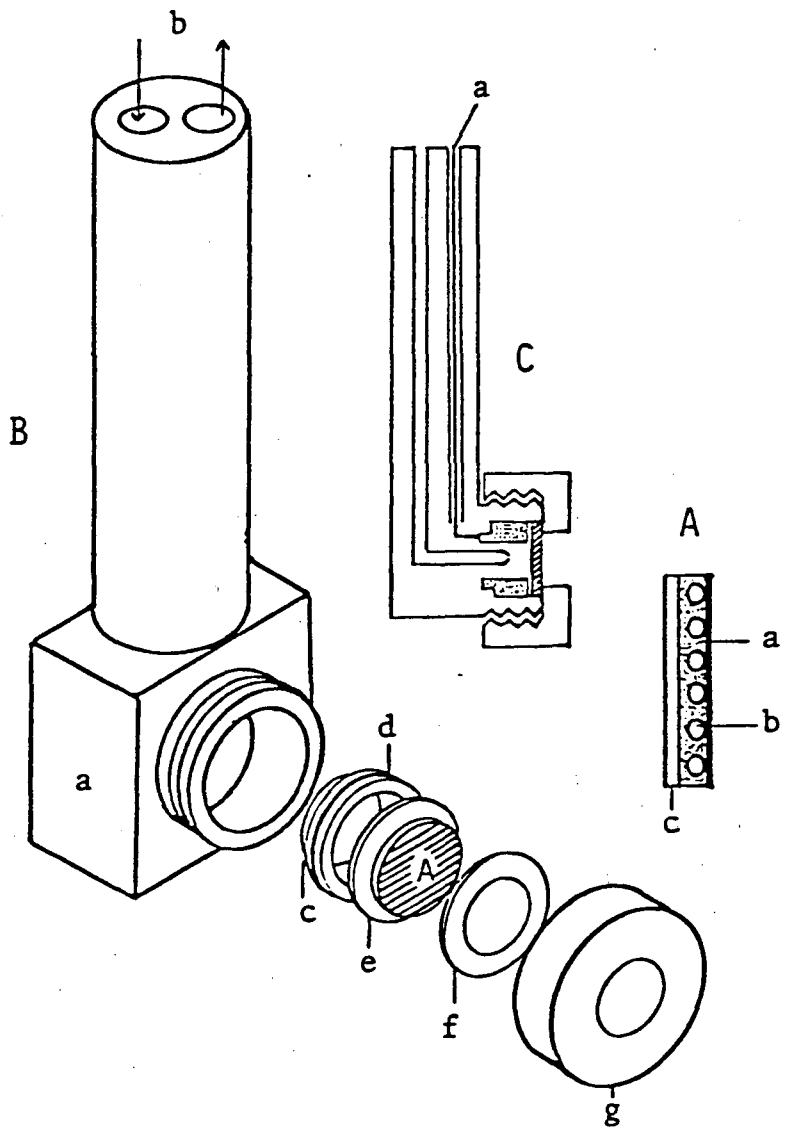


Fig. 5.1.11.2

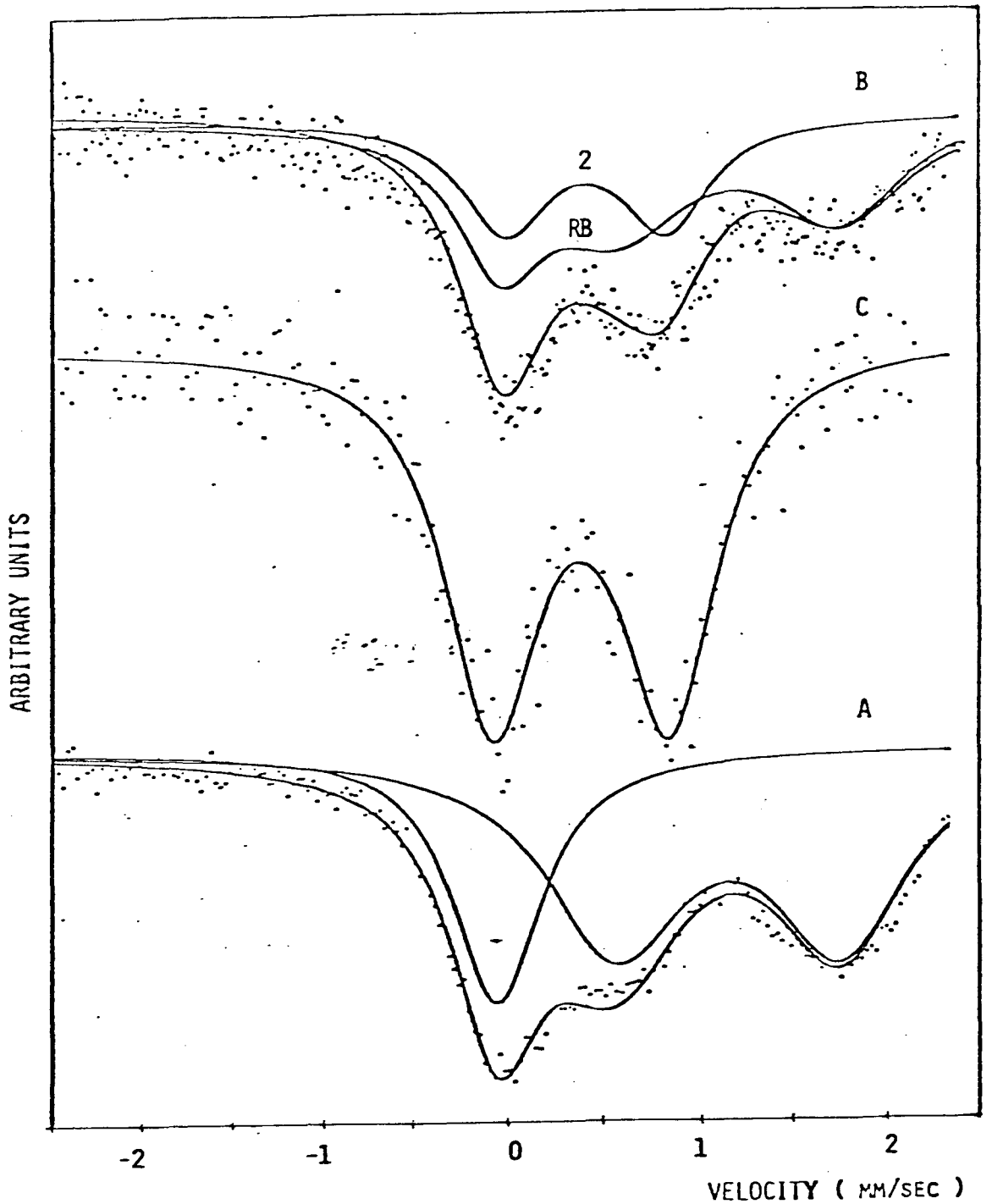


Fig. 5.1.11.3. Mossbauer spectra of carbon electrodes.

A. RB with no catalyst.

B. 3.5% w/w FePc on RB. This spectrum has been decomposed in terms of a doublet, (2) and the contribution from the RB carbon support (RB) based on the spectrum obtained in Curve A.

C. 3.5% w/w FePc on XC-72.

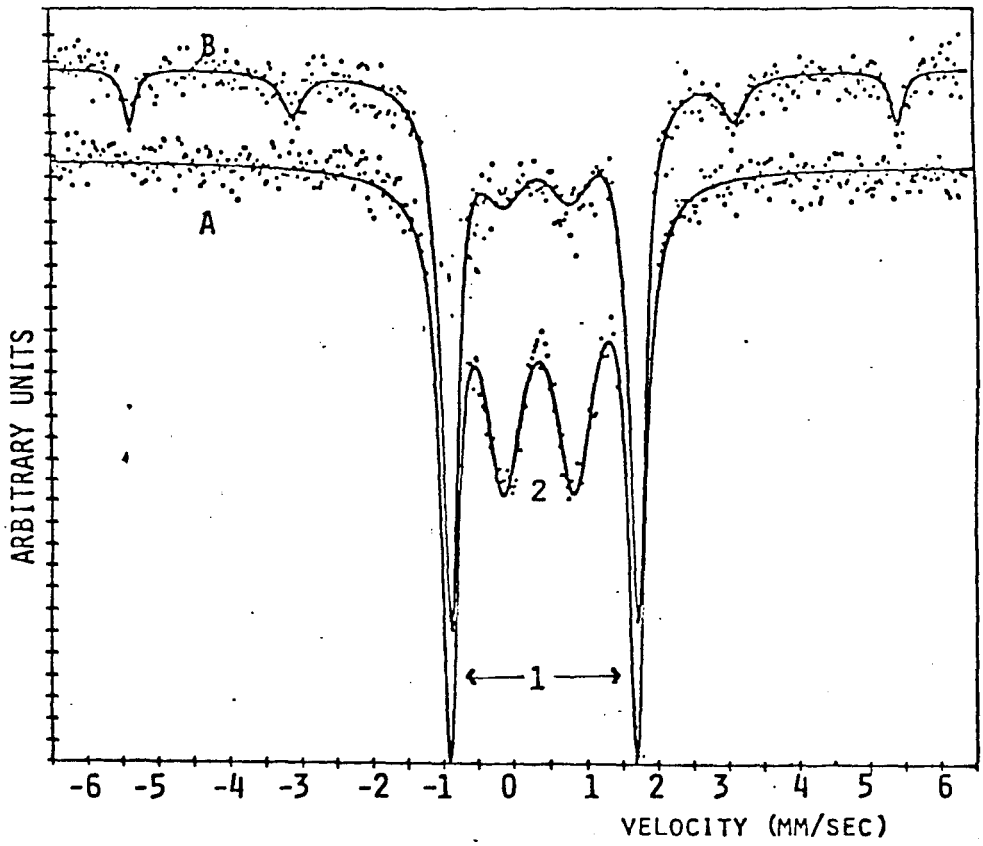


Fig. 5.1.11.4. Ex situ (dry) Mossbauer spectra of powder samples.
A. 15% w/w FePc on XC-72 heated at 420°C in He atmosphere.
B. Same as A but heated in H_2 atmosphere.

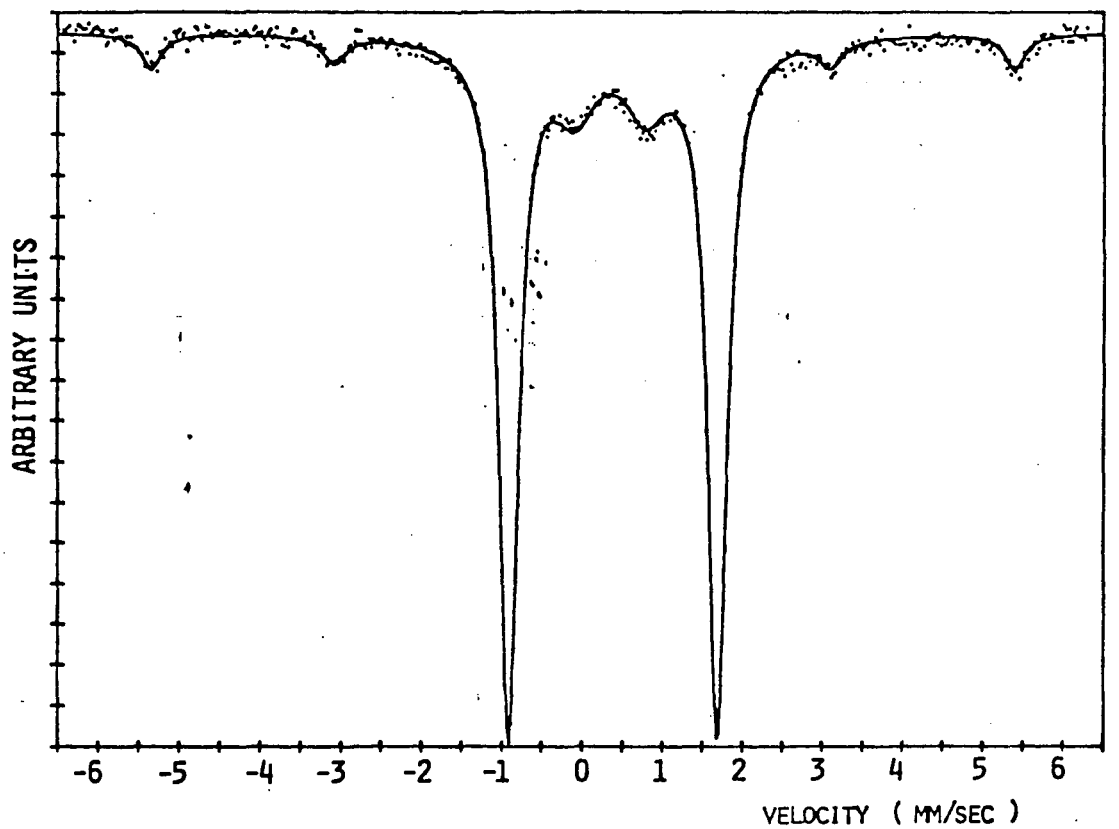


Fig. 5.1.11.5. Ex situ (dry) Mossbauer spectrum of 30% w/w FePc on XC-72 (same as B in Figure 4).

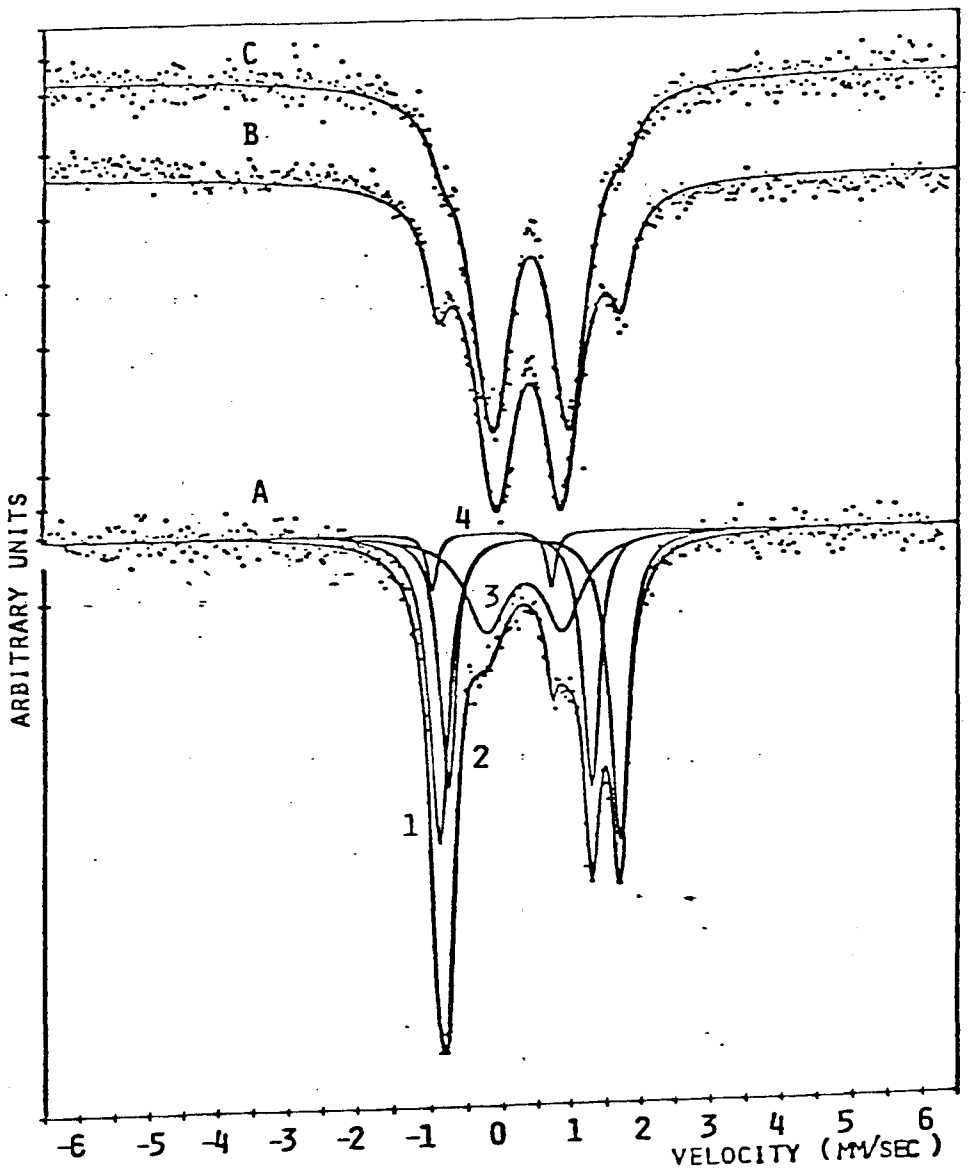


Fig. 5.1.11.6. Ex situ (dry) Mossbauer spectrum of 15% w/w FePc on XC-72 powde samples. Solvent removed by boiling off (see text). Heated at

A. 220°C in He.

B. 420°C in He.

C. 420°C in H_2 atmosphere

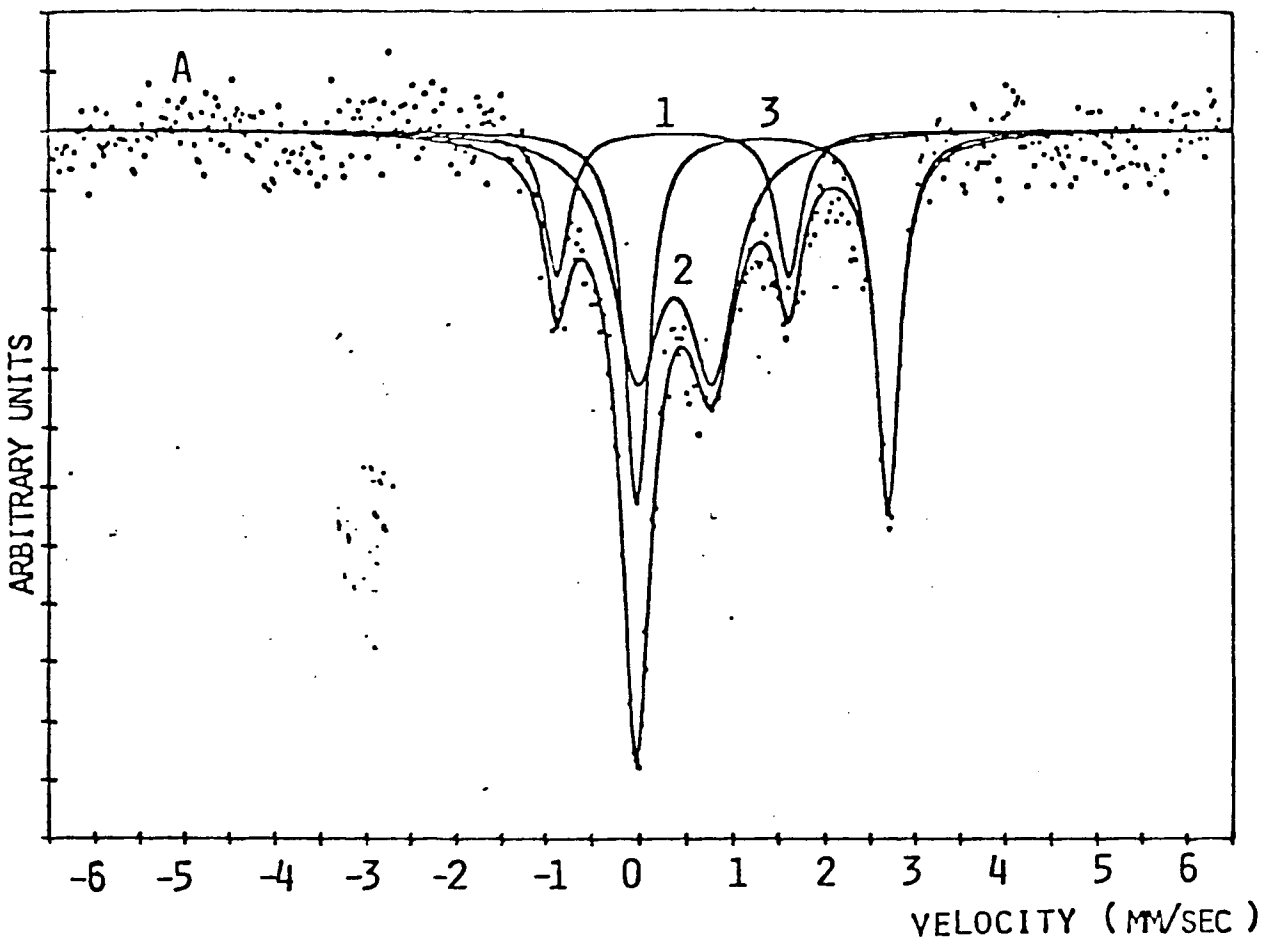


Fig. 5.1.11.7. Ex situ (dry) Mossbauer spectrum of 15% w/w FePc on XC-72 powder sample. Same as curve C in Fig. 6 heat treatment extended until red coating appeared on quartz tube wall.

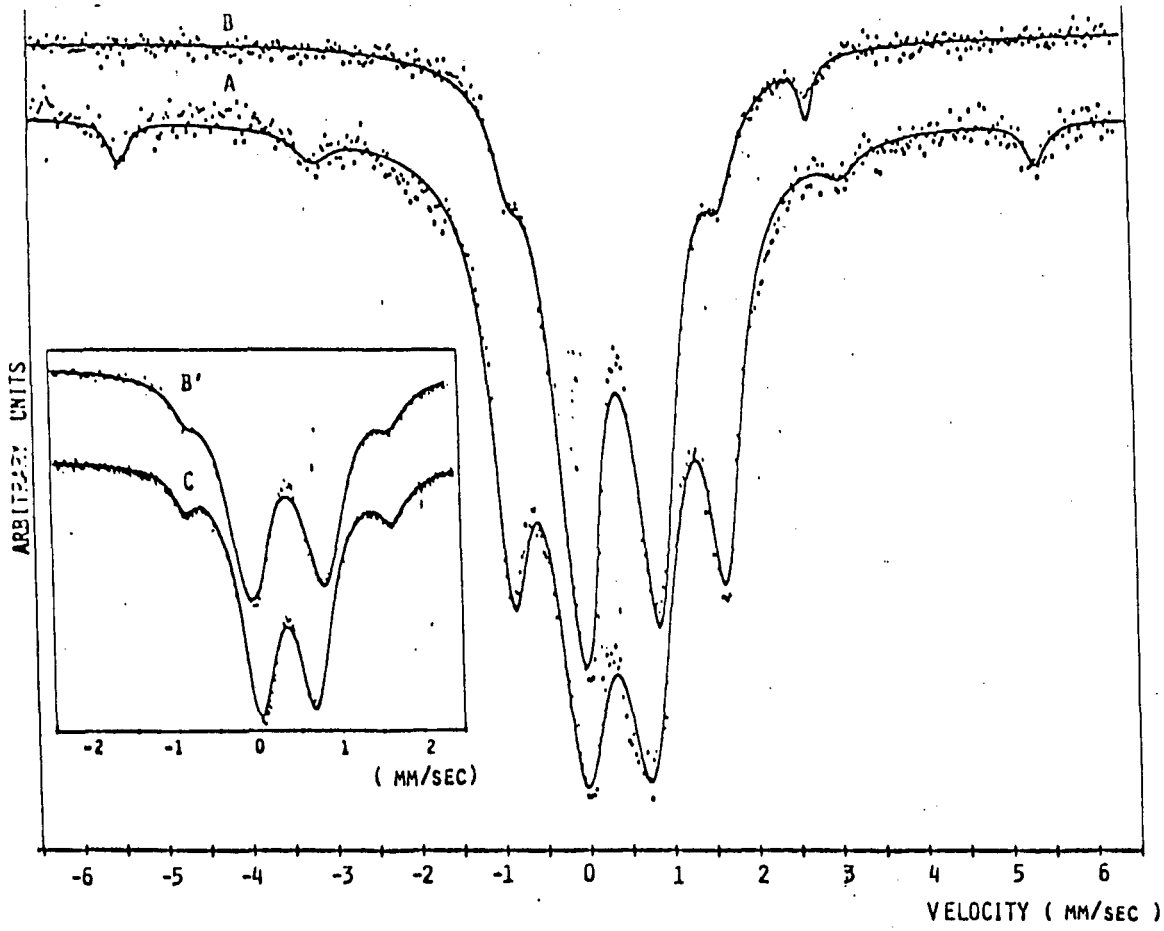


Fig. 5.1.11.8. Ex situ and in situ Mossbauer spectra of 29% w/w FePc on RB carbon.

A. Ex situ powder sample

B. Electrode prepared with sample A

Insert: B'. Same as in curve B Fig. 8 in restricted velocity scale

C. In situ Mossbauer spectrum of 8 B in 1M NaOH.

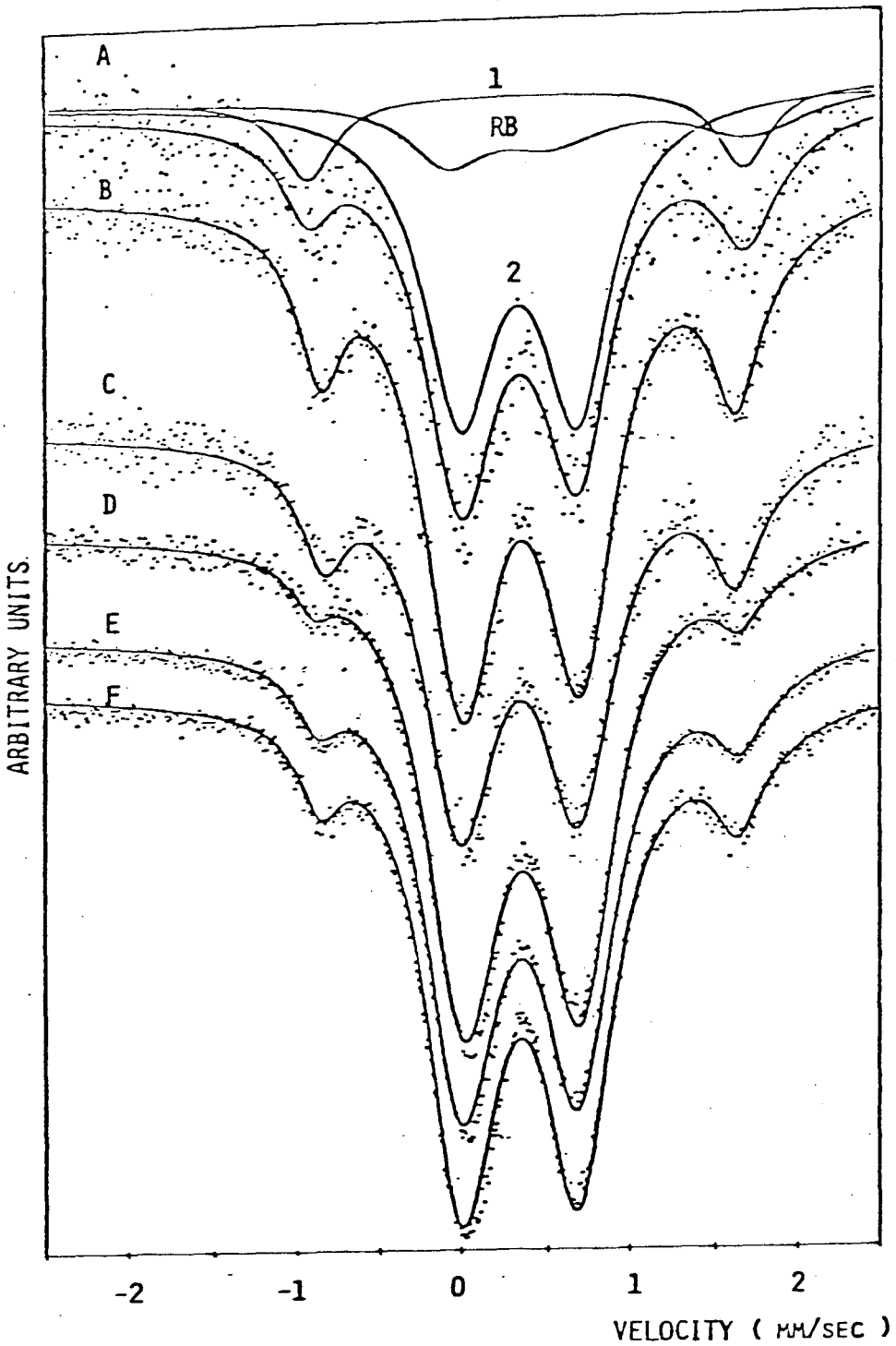


Fig. 5.1.11.9. In situ Mossbauer spectrum of electrode described in caption for Figure 8 polarized at various potentials in $Hg/HgO,OH^-$ in the same sequence as the labelling in the figure.

A. -0.65 V.	D. +0.20 V
B. -0.40 V	E. Open circuit (~0.0 V)
C. -0.20 V	F. -0.40 V

Curve A in this figure gives the decomposition in terms of bulk (1) adsorbed (2) and the impurities in the carbon support (RB) contributions.

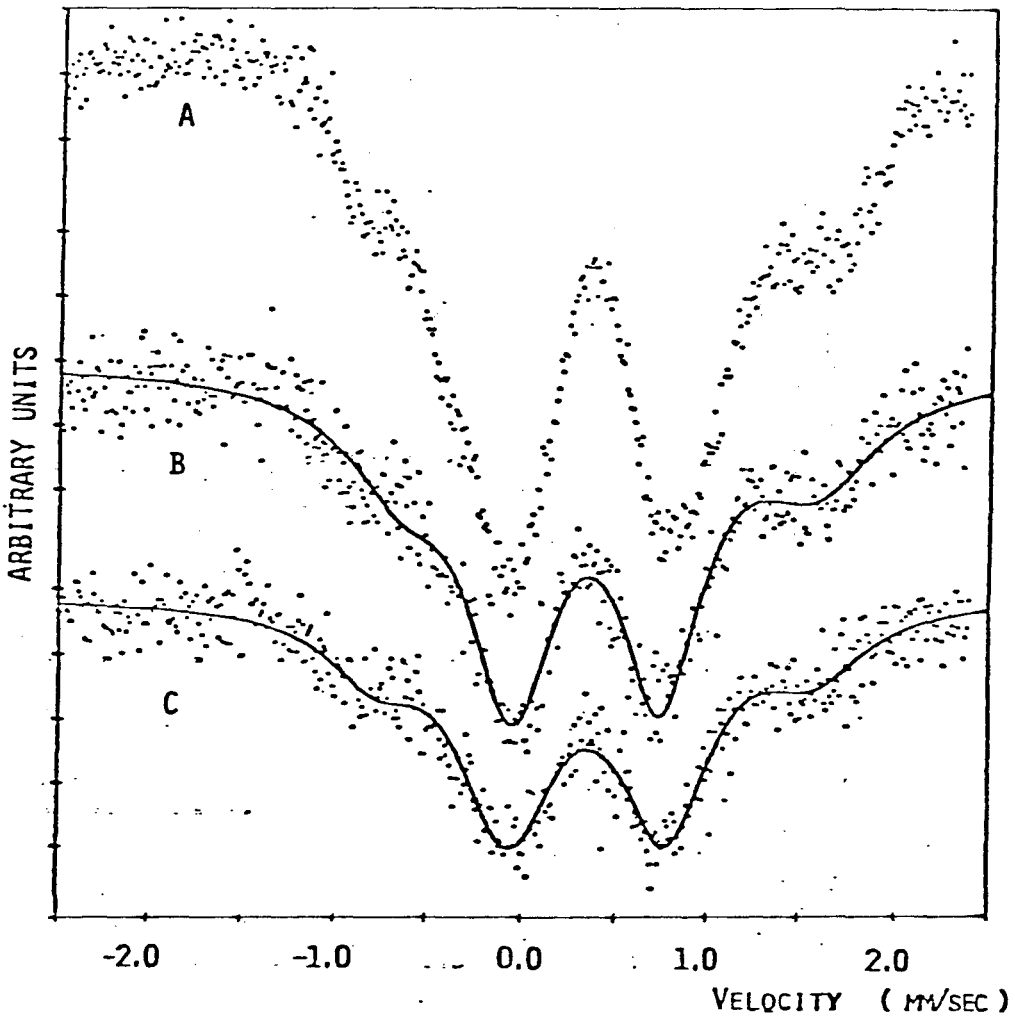


Fig. 5.1.11.10. Mossbauer spectrum of 15% w/w FePc on XC-72 electrode prepared from powder sample heated in He atmosphere at 420°C.

A. Dry

B. 1 M NaOH

C. 0.5 M H_2SO_4

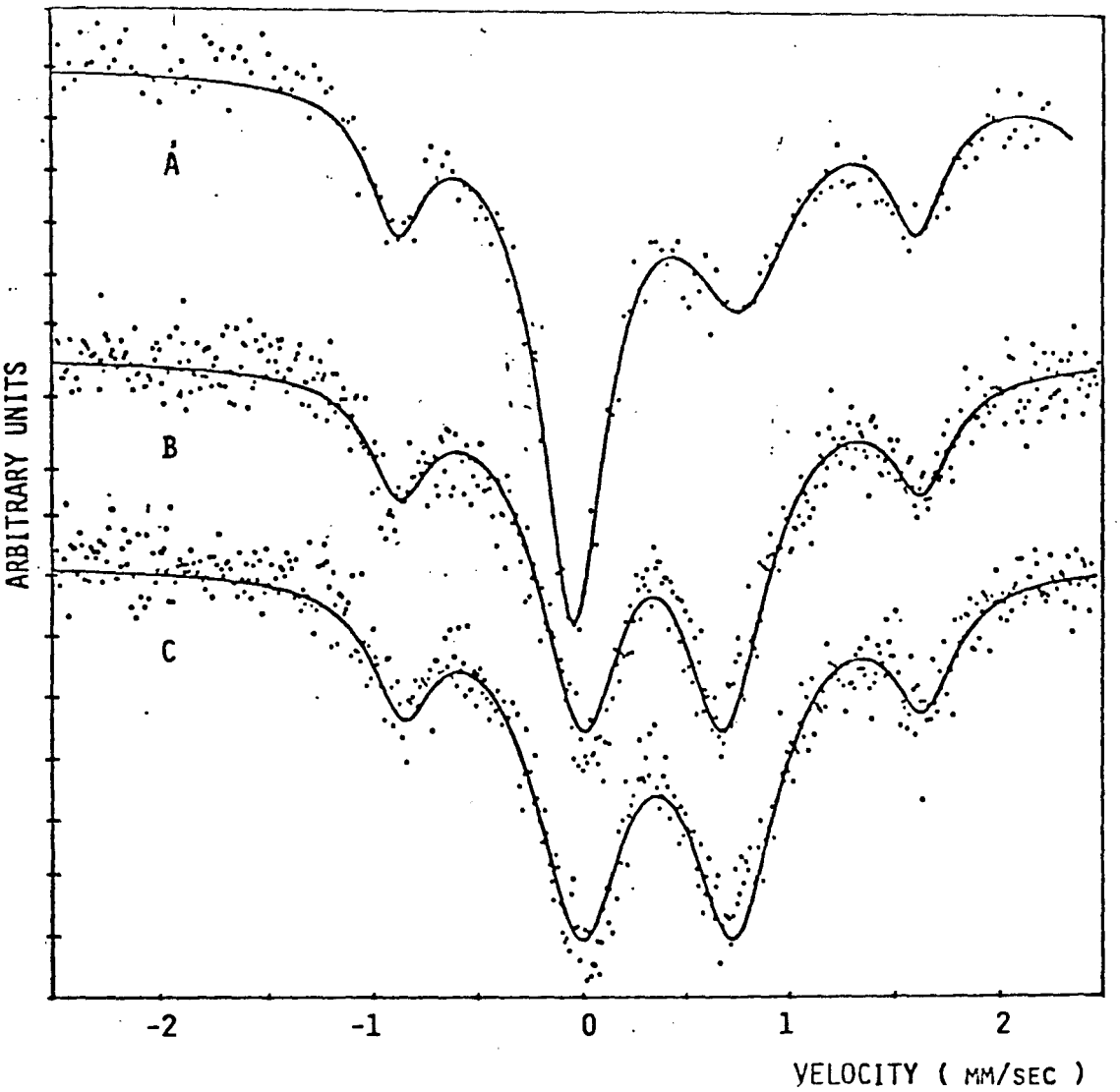


Fig. 5.1.11.11. Mossbauer spectrum of 15% w/w FePc on XC-72 electrode prepared from powder sample described in caption of Figure 7.

A. Dry (the velocity scale has been restricted for the purpose of comparison. See Fig. 7.)

B. 1 M NaOH

C. 0.5 M H_2SO_4

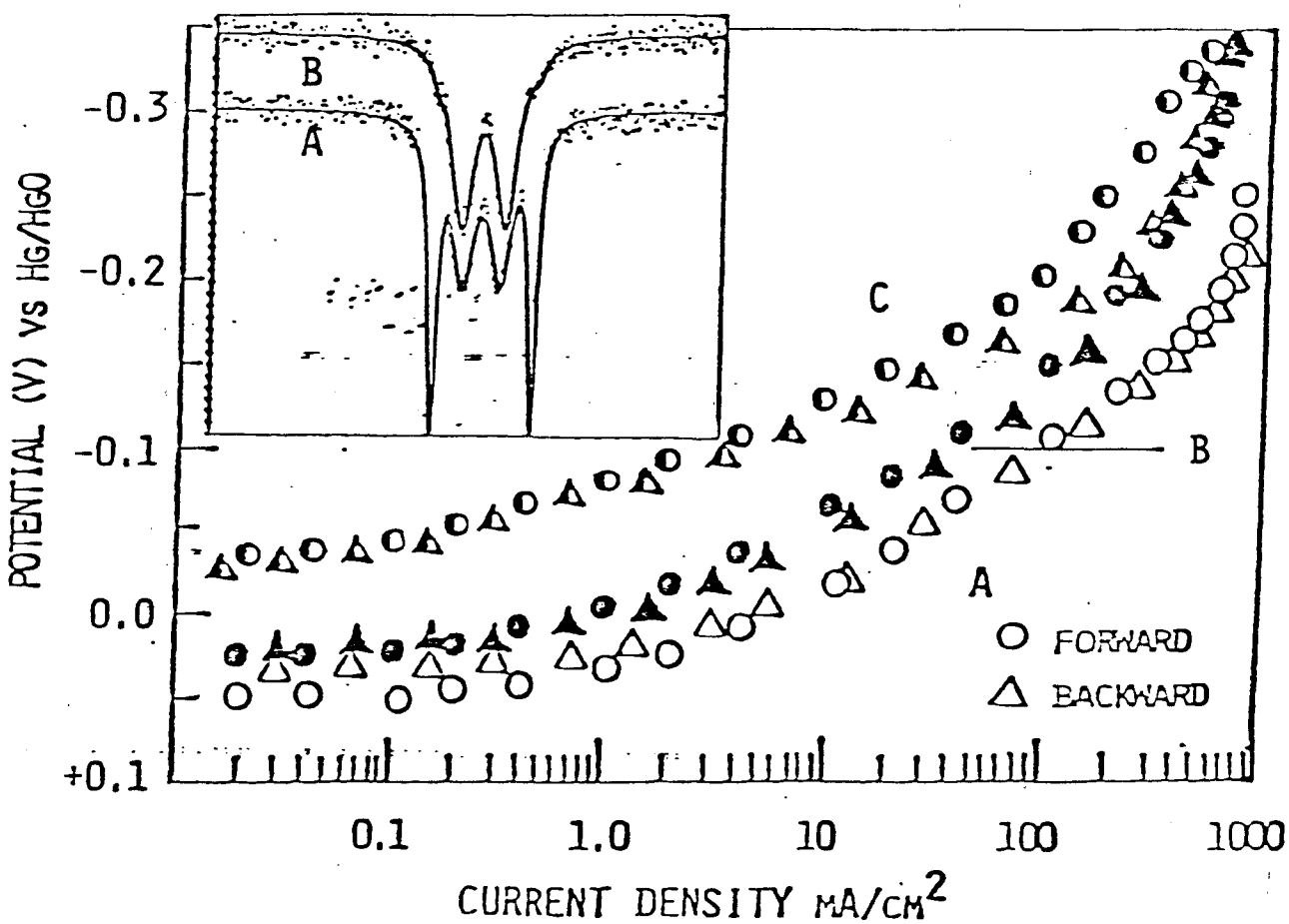


Fig. 5.1.11.12. Oxygen reduction polarization curves in 9 M NaOH at 85°C (pure O_2 fed from the back) of an electrode made with:

A. 15% w/w FePc on XC-72, solvent removed by evaporation. Heat treatment at 420°C in He atmosphere. (curve A Fig. 4).

B. 15% w/w FePc on XC-72, solvent removed by boiling off the solvent Heat treatment at 420°C in H_2 atmosphere. (curve C Fig. 6).

C. XC-72 carbon alone

Insert: Mossbauer spectra of powder samples used in A and B.

5.1.12 DETERMINATION OF THE EQUILIBRIUM CONSTANT FOR SUPEROXIDE DISMUTATION

Juntao Lu, Sandy Tryk and E. Yeager

INTRODUCTION

Dismutation is one of the principal reactions of superoxide in aqueous solutions, but the equilibrium constant of this reaction has not yet been reported in the literature. To evaluate the equilibrium concentrations in the O_2-O_2^--HO_2^- system one has to resort to the standard potential for the O_2/O_2^- couple, E_{O_2/O_2^-}.

Unfortunately, the published values for E_{O_2/O_2^-} are relatively widely scattered. For example, the values listed by Fee (1) are spread over a potential range from -0.33 to -0.27V. This means that the uncertainty in the equilibrium constant for O_2^- dismutation calculated from E_{O_2/O_2^-} might be as large as two orders of magnitude. Conversely, if the equilibrium constant can be determined within an experimental error of $\pm$ 10%, one will be able to evaluate E_{O_2/O_2^-} within an uncertainty of less than $\pm$ 2mV, providing the standard potential for the O_2/HO_2^- couple, E_{O_2/HO_2^-}, has been precisely determined.

METHODS

As is well known, the dismutation of O_2^- in aqueous solution takes place as follows:

$$2O_2^- + H_2O \rightleftharpoons HO_2^- + O_2 + OH^- \qquad (1)$$

The equilibrium constant for the reaction may be determined by measuring the activities of all of the components involved under equilibrium conditions. The activity of H_2O, a_{H_2O}, in alkaline solution was calculated from its vapor pressure listed in the literature (2). Concentrations of O_2 were measured using electron spin resonance spectroscopy (ESR) at liquid nitrogen temperature, while O_2 and HO_2^- concentration were monitored with a dropping mercury electrode.

ESR:

The principle of quantitative ESR analysis is simple. The number of uncompensated electron spins in the sample is directly proportional to the area under the ESR absorption curve. However, to obtain reliable data, certain factors had to be checked or correctd for. The volume of

the ESR sample tube was found to fluctuate within 25%. This variation was corrected for according to the following equation:

$$h_x = h_{rec} \frac{V_s}{V_x}$$

where h_x and h_{rec} are corrected and recorded ESR signals, while V_s and V_x are volumes for standard and sample tubes, respectively. Possible variations in Q factor of the ESR cavity were checked by using a tiny amount of DPPH (1,1-diphenyl-2-picrylhydrazyl) wrapped around the outside wall of the Dewar insert as a marker. The marker signals for the empty cavity, 1 mM CuEDTA and 7NKOH + $O_2^{\cdot-}$ were 46, 48 and 48 respectively, which indicates that no detectable Q factor change was caused by replacing the standard tube (CuEDTA) with the sample tube (KOH + $O_2^{\cdot-}$).

DPPH and its benzene solution are the most commonly used ESR standards. In this work DPPH powder was also used as a g-factor marker, and its g-value was taken to be 2.0037 (3). On the other hand, for quantitative purposes DPPH is not convenient because of its signal decay with time (4). Cu^{++}EDTA and Cu^{++} = 0.01M HCl + 2M $NaClO_4$ have been recommended by some authors (5,6). Fig. 1 shows a comparison of ESR spectra of $O_2^{\cdot-}$ and these standards. The two types of Cu^{++} complex have similar EST spectra. Each cupric ion contains one uncompensated electron spin (7). The second integrals of 1mM Cu^{++} + 10mM EDTA and 1mM Cu^{++} 0.01M HCl + 2M $NaClO_4$ compared favorably (within ± 2%). Fig. 2 illustrates the approximate porportionality between CuEDTA concentrations and ESR signal intensities. Therefore, CuEDTA was used in routine operation. The standard solution of 1mM Cu^{++} + 10mM EDTA was prepared from fresh $CuSO_4 \cdot 5H_2O$ crystal and NaEDTA (Fisher).

The g-values for $O_2^{\cdot-}$ were 2.007 (g_1) and 2.121 (g_{11}), in agreement with those reported in the literature (1,8). Since $O_2^{\cdot-}$ has two narrow peaks in its ESR spectra, a higher modulation amplitude would cause distortion of the spectrum, as shown in Fig. 3. When microwave power exceeded certain limits, saturation took place with both $O_2^{\cdot-}$ and the cupric complexes (Fig. 4). Therefore, to obtain non-distorted spectra the following instrument settings (on the Varian E-3) were adopted throughout the experiment:

microwave power	25 mW
receive gain	2 x 104
modulation amplitude	4 gauss
Scan range	0.5 x 10^3 guass
time constant	0.3 second

scan rate as required, depending on spectral shape.

All ESR measurements were carried out at liquid nitrogen temperature. Since the ESR spectrometer undergoes slight day-to-day variations, standard CuEDTA spectra were measured whenever $O_2^{\cdot-}$ was quantitatively analyzed.

Since the recorded ESR spectrum is approximately the first derivative of the absorption curve, an estimate of the spin concentration must involve evaluation of the second integral of the spectrometer output. The variability in the second integral was often 10% or more, probably due to both the imprecision of the integration procedure and the poor reproducibility of the spectral shape, particularly the base line shift. On the other hand, the reproducibility of the signal height was found to be better than that for the second integral. Thus, instead of the second integral being used directly to evaluate spin concentration, a quantity ($h \cdot r$) was used, where r is the average value of the ratio of the second integral to the signal peak height, h. The spin concentration of the sample was calculated according to the following equation:

$$C_x = \frac{S_s \sqrt{P_s}\, M_s\, r_x\, h_x\, (g_{av}^2)_s}{S_x \sqrt{P_x}\, M_x\, r_s\, h_s\, (g_{av}^2)_x} C_s \qquad (3)$$

where the subscripts s and x designate standard and sample respectively. Receiver gain S, microwave power P and modulation amplitude M actually remain constant for standard and samples and therefore cancel. The parameter (g_{av}^2) is defined to be

$$g_{av}^2 = \frac{1}{9}(g_{11} + 2g_1)^2 \qquad (4)$$

which was introduced by Ausa (9) to correct for the g-factor difference between standards and samples.

POLAROGRAPHY

Polarographic measurements were carried out using a glass polarographic cell of about 20 ml volume and a potentiostat (Pine REDE 3), a mercury pool acting as both the anode and reference electrodes. The dropping time of the DME was 3 to 4 seconds. The instantaneous current just before the drop fall was used for quantitative analysis. Oxygen reduction in alkaline solution was found to give three polarogrpahic waves (Fig. 5-a). The first was assigned to the two-electron reduction of O_2 to HO_2^-. The second and third waves

are not well understood. The ratio of the third wave height i_2 to the first wave height i_1 ranged from 1.9 to 2.3. Fig. 5-b shows a polarogram for H_2O_2 in alkaline solutin. As reportd earlier [10], there are two waves whose potential ranges coincide with these for the second and third waves for O_2 reduction. The first wave for H_2O_2 reduction becomes a wide peak in concentrated alkaline solution and resembles a polarographic maximum. Despite the fact that the double waves for H_2O_2 reduction require further study, there is a good proportionality between i_2 and the H_2O_2 concentration, serving as the basis for quantitative analysis (Fig. 6). The peroxide concentration was calibrated by titration with $KMnO_4$.

In order to estimate the concentration of O_2 and HO_2^- in the presence of $O_2^{\cdot-}$, the contribution of $O_2^{\cdot-}$ to the polarographic current should be corrected for. To do so, it seems reasonable to assume that $O_2^{\cdot-}$ reduction at the DME is diffusion controlled and undergoes one-electron and three-electron transfers over the potential ranges for O_2 reduction to HO_2^- and HO^- respectively and that $O_2^{\cdot-}$ has approximately the same diffusion coefficient as HO_2^-.

SAMPLE PREPARATION

A O_2-$O_2^{\cdot-}$-HO_2^- mixture was prepared in a glass beaker by adding a small piece of KO_2 into approximately 100 ml of alkaline solution. At a certain time interval about 10 ml of the above solution was withdrawn for polarographic measurement, and at the same time a 0.1 ml sample was transferred into an ESR tube and quenched immediately with liquid nitrogen prior to ESR measurement.

RESULTS AND DISCUSSION

HO_2^- dismutation and O_2 supersaturation.

Upon addition of KO_2 solid into alkaline solution most of the superoxide ion dismutates to peroxide and molecular oxygen instantaneously according to Eq. (1), forming a large number of fine bubbles. A few seconds later, however, the solution becomes quiet. On the other hand, peroxide produced from $O_2^{\cdot-}$ dismutation also itself undergoes dismutation which results in a large supersaturation with O_2 in a quiet solution as shown in Fig. 7. The value P_{O_2} here is defined by

$$P_{O_2} = i_{1,corr}/i_1^{\circ} \qquad (5)$$

where $i_{1,corr}$ is the polarographic current i_2 recorded after correction for the $O_2^{\cdot-}$ contribution, and i°_1 is the current observed for the solution saturated with 1 atm O_2. Therefore, P_{O_2} corresponds to the O_2 pressure which would be in equilibrium with the dissolved O_2.

To establish an equilibrium for superoxide dismutation it is obviously necessary to keep P_{O_2} and peroxide concentration constant. These conditions were approximately realized by bubbling the solution with 1 atm O_2 to stimulate the release of excess O_2 and by using high-purity hydroxide in order to depress peroxide dismutation. NaOH (Baker 1-3726) was found more suitable than KOH (Fisher) for ths purpose and was used in the equilibrium constant determination.

In the NaOH solution HO_2^- still decomposes slowly but does not provide a problem because of its high concentration. The decay of HO_2^- did not exceed 2% an hour.

$O_2^{\cdot-}$ Decay

The quilibrium constant K for reaction (1) was calculated according to the equation

$$K = \frac{C_{HO_2} - C_{OH} - P_{O_2}}{C^2_{O_2^{\cdot-}} \; a_{H_2O}} \qquad (7)$$

Here the activity coefficients for all of the ionic components cancel. The product $C_{HO_2}-C_{OH}-P_{O_2}/C^2_{O_2}-a_{H_2O}$ initially after addition of KO_2 to the alkaline solution appeared time dependent (Fig. 8), indicating that the equilibrium had not been reached and that dismutation of $O_2^{\cdot-}$ was slow at this stage.

The mechanism and kinetics of $O_2^{\cdot-}$ dismutation in alkaline solutions have been studied by several authors [11,12,13,14]. They found that $O_2^{\cdot-}$ decayed by both first and second order kinetics and that second order kinetics prevailed only if the solution was very pure. As in the case of HO_2^- dismutation [15,16], the rate constant for second order decay for $O_2^{\cdot-}$ was also found to have widely divergent values in the literature. For example, Behar evaluated the rate constant to be less than 10^2 $M^{-1}S^{-1}$ [12] while Marklund estimated an upper limit of $2M^{-1}S^{-1}$ [13]. Having adopted rigorous precautions to eliminate impurities, Bielski reported probably the most reliable data so far, indicating a rate constant with an upper limit of 0.2 $M^{-1}S^{-1}$ [14]. In our experiments, the $O_2^{\cdot-}$ decay plot shows neither first nor second order kinetics (Fig. 9) in KOH solution which had not been purified. Though the data in Fig. 10 are not accurate enough to carry out kinetic analysis, the slowness of $O_2^{\cdot-}$ decay is evident. As shown in Fig. 9, it took approximately 30 minutes to shift the product

$$\frac{C_{HO_2^-} C_{OH^-} P_{O_2}}{C^2_{O_2^-} a_{H_2O}}$$

one decade toward equilibrium.

Therefore, it was necessary to wait several hours before sampling in order to obtain a valid equilibrium constant.

Estimated value of K and E_{O_2/O_2^-}

After waiting a period of time sufficient for the system to reach equilibrium, the K values obtained were no longer time dependent within experimental error, as shown in Table I and Fig. 10. In these tables t is measured from the time of the initial preparation of the system mixture. Usually sampling started after a period of at least 3 hours. In Fig. 10 also given are two experimental points which were obtained with a system prepared by adding H_2O_2 instead of KO_2 to the alkaline solution. It can clearly be seen that the equilibrium can be approached from either side of reaction (1), as expected. Over a concentration range from 2M to 6M in hydroxide no pH dependence was apparent for the K values. Therefore, the K values obtained in this manner might be considered to be thermodynamic in nature.

Averaging all of the experimental points (Fig. 11 and Table II) yields a value of $3.3(\pm 0.3) \times 10^7$ for the O_2^- dismutation equilibrium constant, $\bar{K}$, or in logarithmic form, $\log K = 7.52 \pm 0.04$.

If the standard potential for the couple O_2/HO_2^- is taken to be -0.064V vs. SHE (17), by using the equilibrium constant for O_2^- dismutation determined above, the standard potential for the O_2/O_2^- couple is calculated to be -0.286 ± 0.001V vs. SHE, in good agreement with Divisek [18].

REFERENCES

1. J. A. Fee and J. S. Valentine, in "Superoxide and Superoxide Dismutations," A. M. Michelson, J. M. McCord, and I. Fridovich, Editors, pp 23-27, Academic Press, London (1977).

2. National Research Council, "International Critical Tables of Numerical Data: Physics, Chemistry and Technology," Vol. 3, p 370, McGraw-Hill, New York (1928).

3. J. R. Bolton, D. C. Borg, and H. M. Swartz, in "Biological Applications of Electron Spin Resonance," H. M. Swartz, J. R. Bolton, and D. C. Borg, Editors, p 101, Wiley-Interscience, New York (1972).

4. L. R. Malcolm, ibid, p 150.

5. L. Broman, J. Mol. Biol., 5, 301 (1962).

6. B. Malmstrom, Biochem. Biophys. Acta 205, 48 (1970).

7. P. F. Knowles, D. Marsh, and H. W. E. Rattle, "Magnetic Resonance of Biomolecules: An Introduction to the Theory and Practice of NMR and ESR," p 199, John Wiley and Sons, London (1976).

8. M. A. Symonyan, Biochem. Biophys. Acta, 583, 279 (1979).

9. R. Aasa, J. Chem. Phys., 52, 1612 (1970).

10. M. Bernard, Compt. Rend., 257, 1282 (1963).

11. G. Czapski, J. Phys. Chem., 68, 1169 (1964).

12. D. Behar, J. Phys. Chem., 74, 3209 (1970).

13. S. Marklund, J. Biol. Chem., 251, 7504 (1976).

14. B. H. J. Bielski, J. Phys. Chem., 81, 1048 (1977).

15. E. Koubek, J. Am. Chem. Soc., 85, 2263 (1963).

16. F. R. Duke, J. Phys. Chem., 65, 304 (1961).

17. J. P. Hoare, in "Encylopedia of Electrochemistry of the Elements," A. J. Bard, Editor, Vol. 2, p 220, Marcel Dekker, New York (1974).

18. J. Divisek and B. Kastening, J. Electroanal. Chem., 65, 605 (1975).

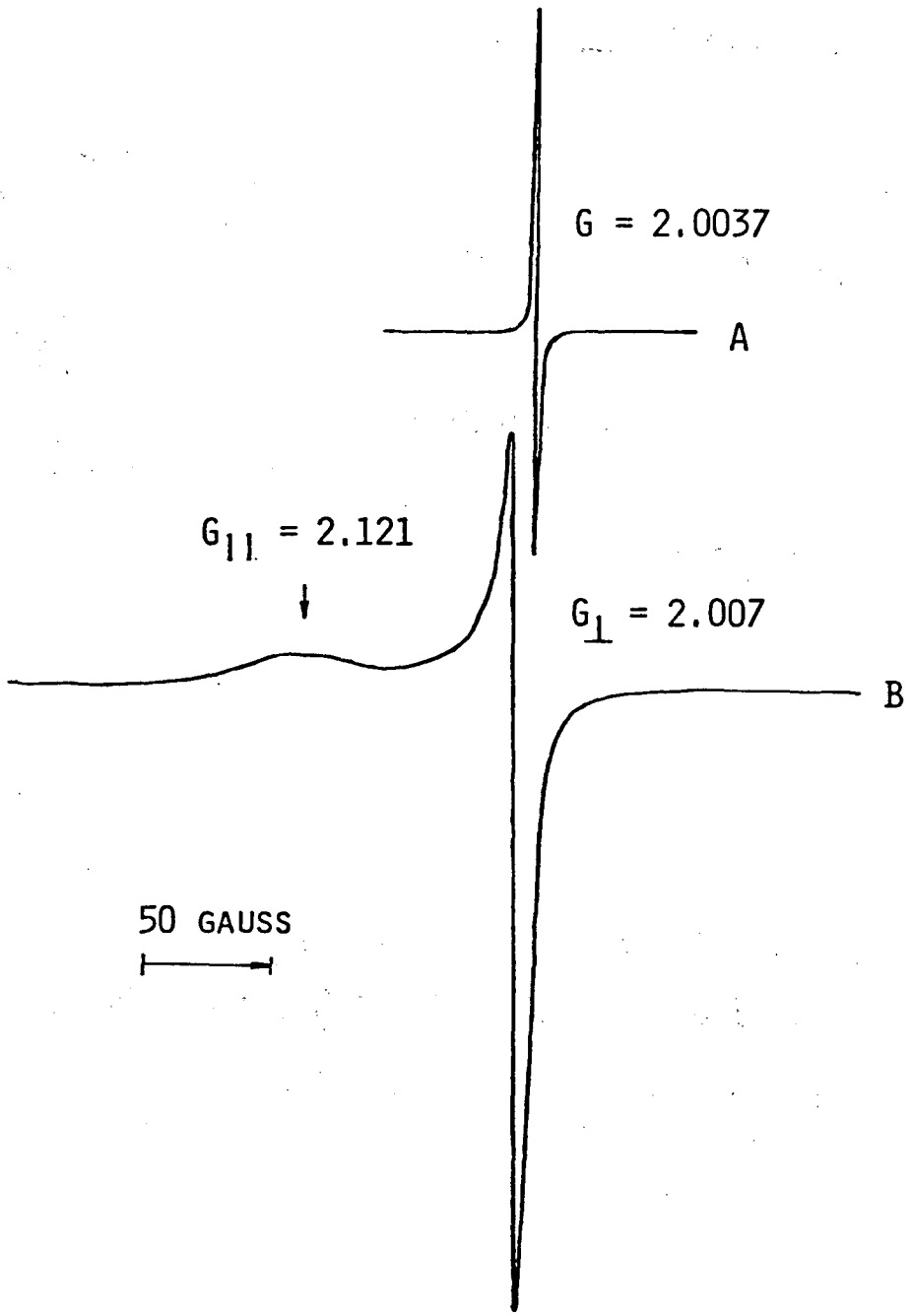


Fig. 5.1.12.1. ESR SPECTRA, AT LIQUID NITROGEN TEMPERATURE ON VARIAN E-3 SPECTROMETER

A. DPPH (1,1-DIPHENYL-2-PICRYLHYDRAZYL) POWDER

B. $O_2^-\cdot$ IN NAOH SOLUTION

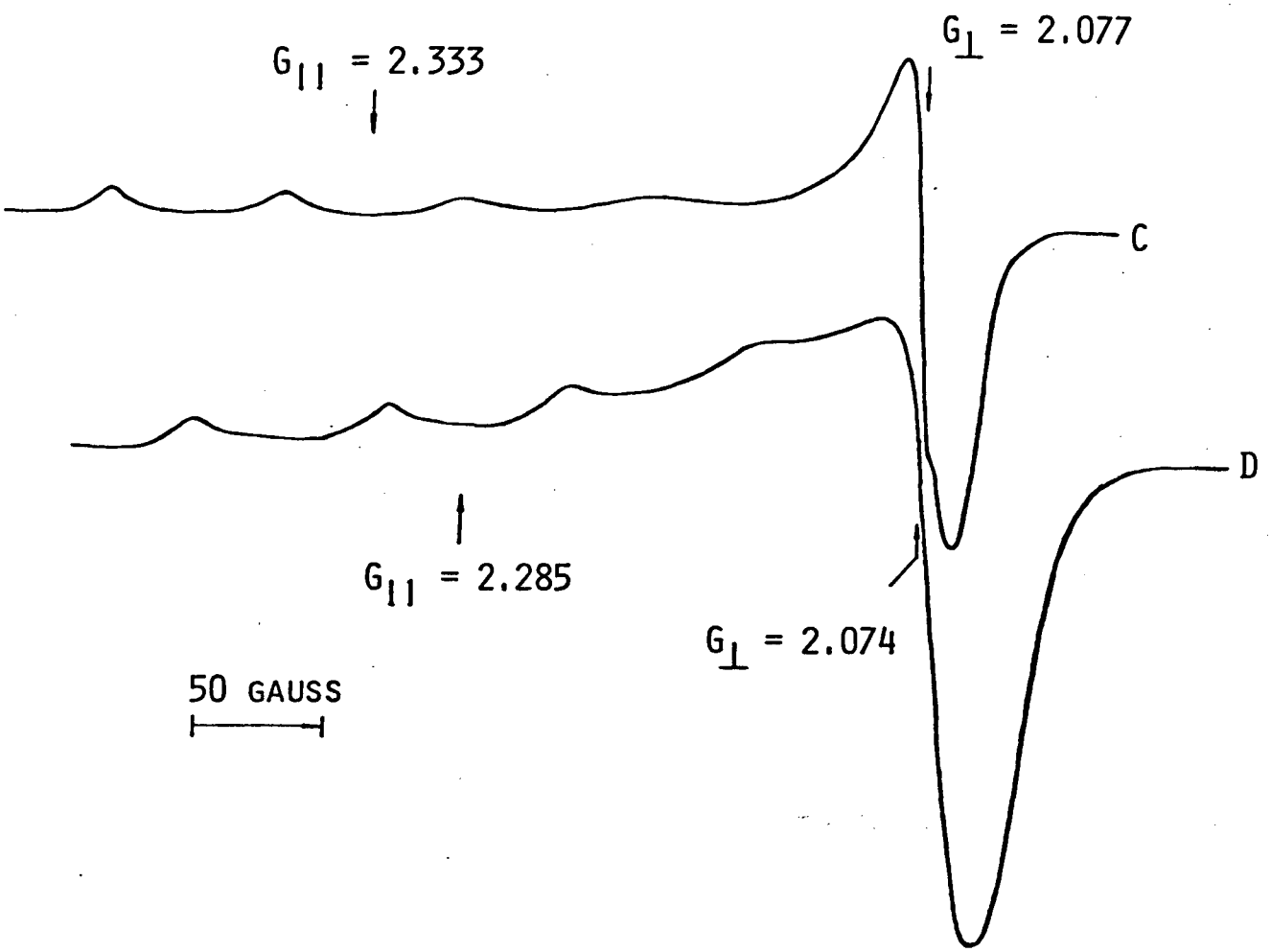


Fig. 5.1.12.1. ESR SPECTRA (CONTINUED)

C. 1 mM Cu(II) + 0.01 M HCL + 2 M $NaClO_4$

D. 1 mM Cu(II) + 10 mM EDTA

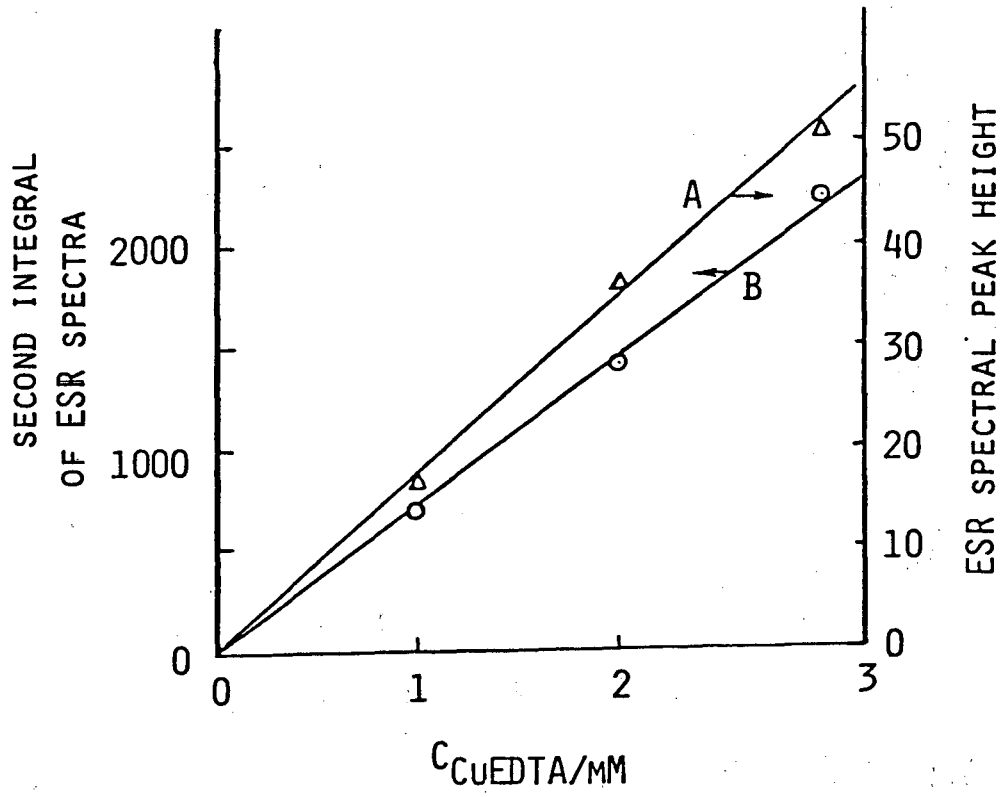


Fig. 5.1.12.2. ESR SIGNAL INTENSITY VS CONCENTRATION FOR Cu(II)EDTA, AT LIQUID NITROGEN TEMPERATURE, ON VARIAN E-3

A. ESR SPECTRAL PEAK HEIGHT

B. THE SECOND INTEGRAL OF ESR SPECTRA

(BOTH ORDINATES IN ARBITRARY UNITS)

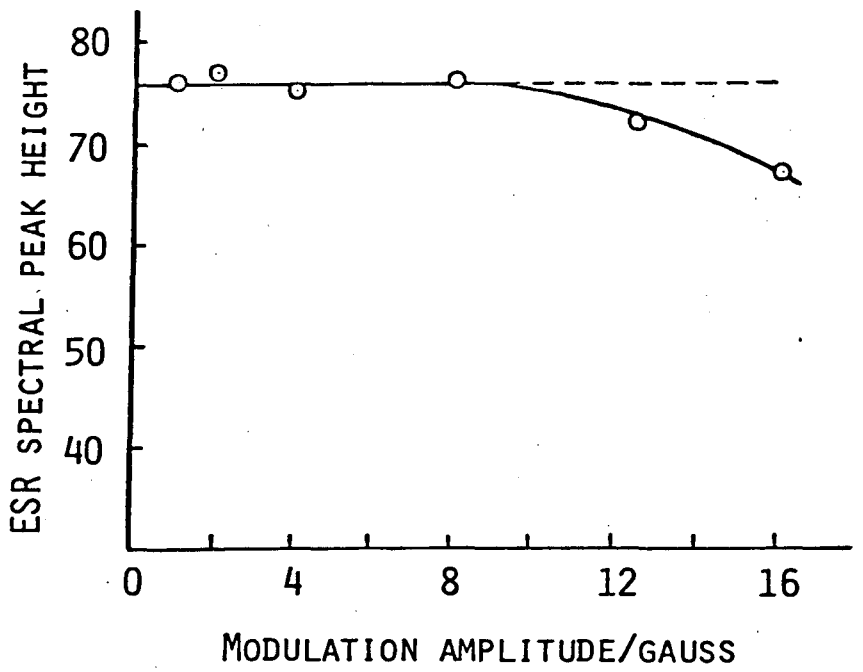


FIG. 5.1.12.3. O_2^-· ESR SPECTRAL DISTORTION TEST IN 8.4 M KOH, AT LIQUID NITROGEN TEMPERATURE ON VARIAN E-3. THE PRODUCT OF MODULATION AMPLITUDE AND RECEIVER GAIN KEPT CONSTANT. (ORDINATE IN ARBITRARY UNITS)

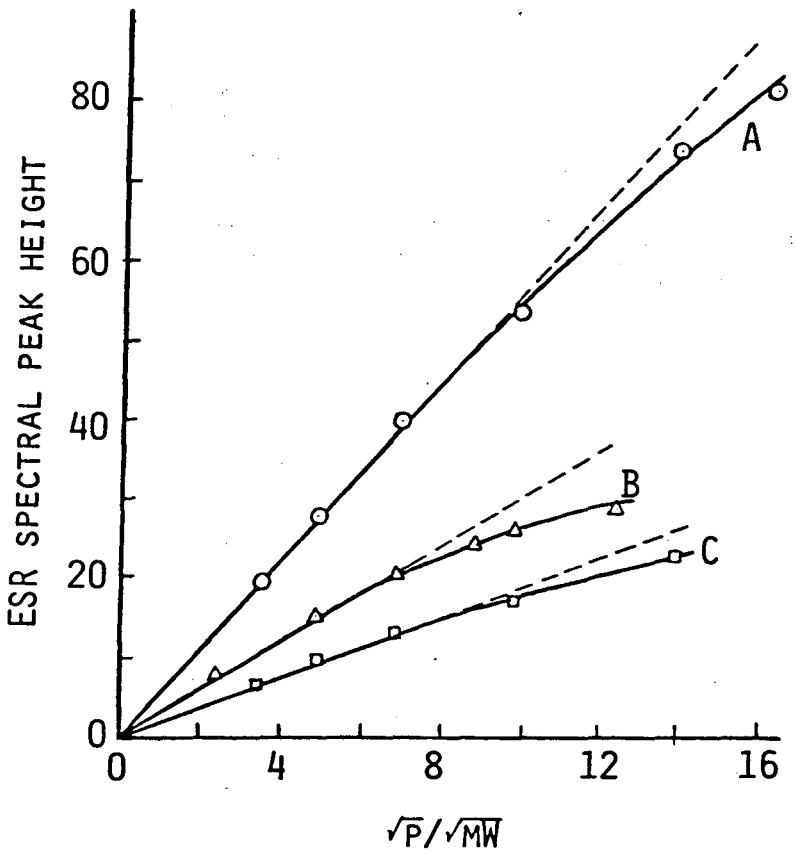


FIG. 5.1.12.4. ESR SATURATION TEST AT LIQUID NITROGEN TEMPERATURE ON VARIAN E-3

A. $O_2^-\cdot$ IN 8.4 M KOH

B. 1 mM Cu(II) + 10 mM EDTA

C. 1 mM Cu(II) + 0.01 M HCL + 2 M $NaClO_4$

(ORDINATE IN ARBITRARY UNITS)

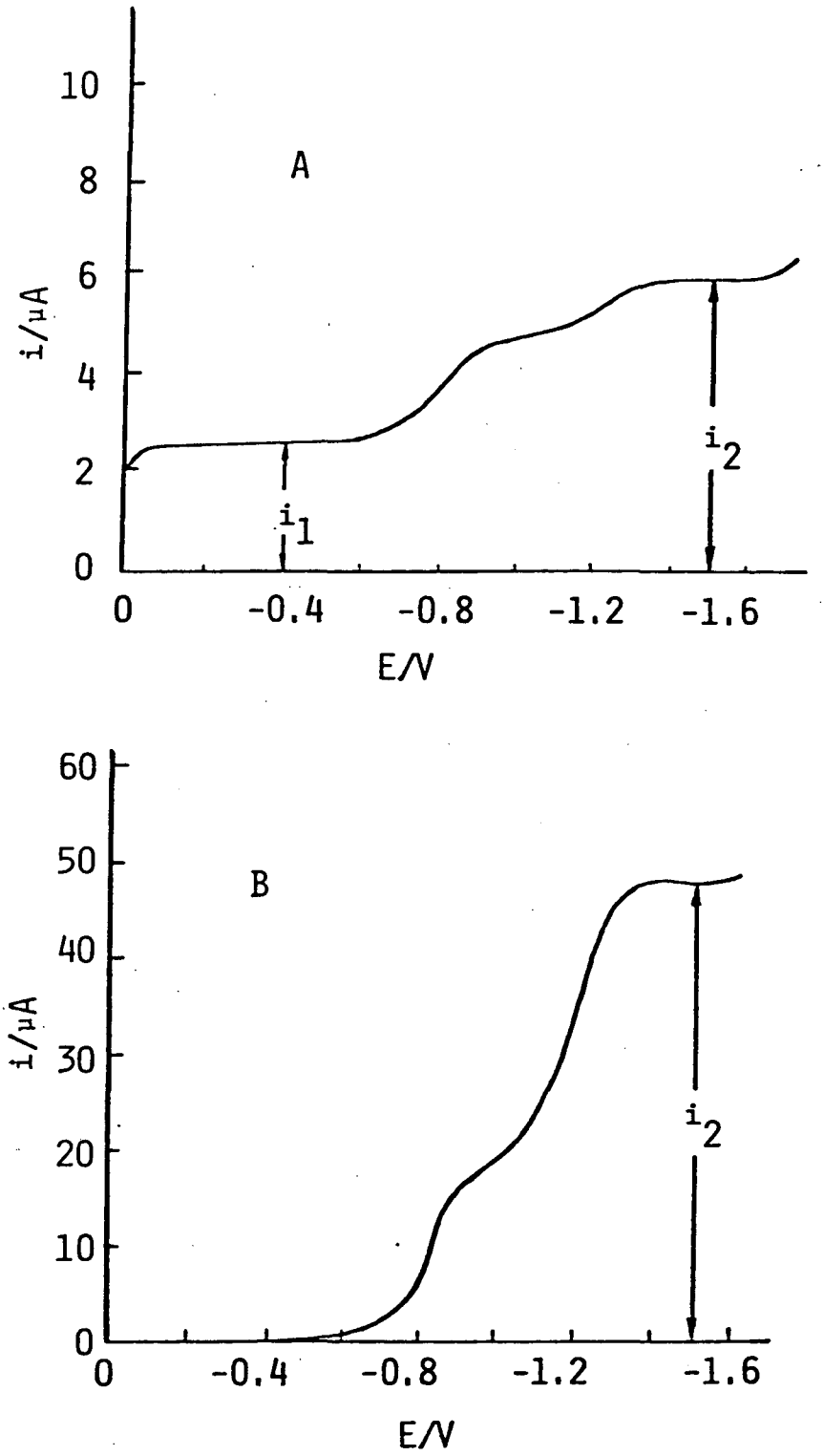


FIG. 5.1.12.5. POLAROGRAMS FOR O_2 AND HO_2^- IN NAOH.

A. 4 M NAOH SATURATED WITH O_2 (1 ATM O_2, 19°C)

B. 6×10^{-3} M HO_2^- IN 4 M NAOH (19°C)

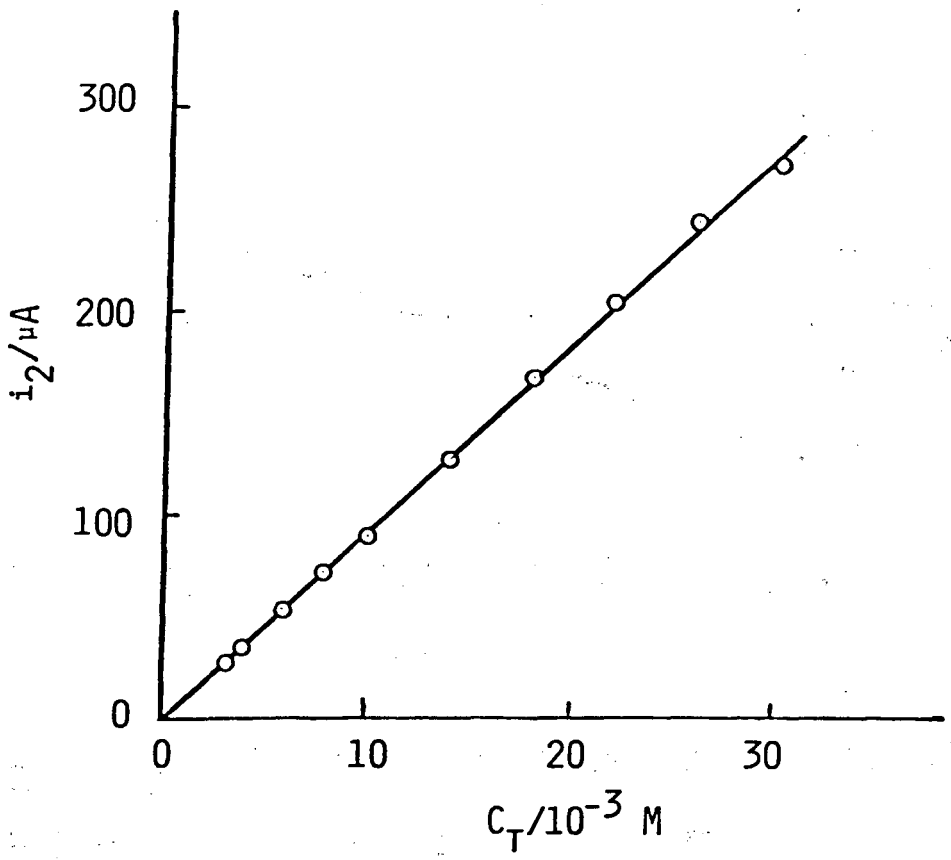


FIG. 5.1.12.6. POLAROGRAPHIC CURRENT i_2 VS. TOTAL CONCENTRATION OF HYDROGEN PEROXIDE, C_T, IN 2 N NaOH (20°C).

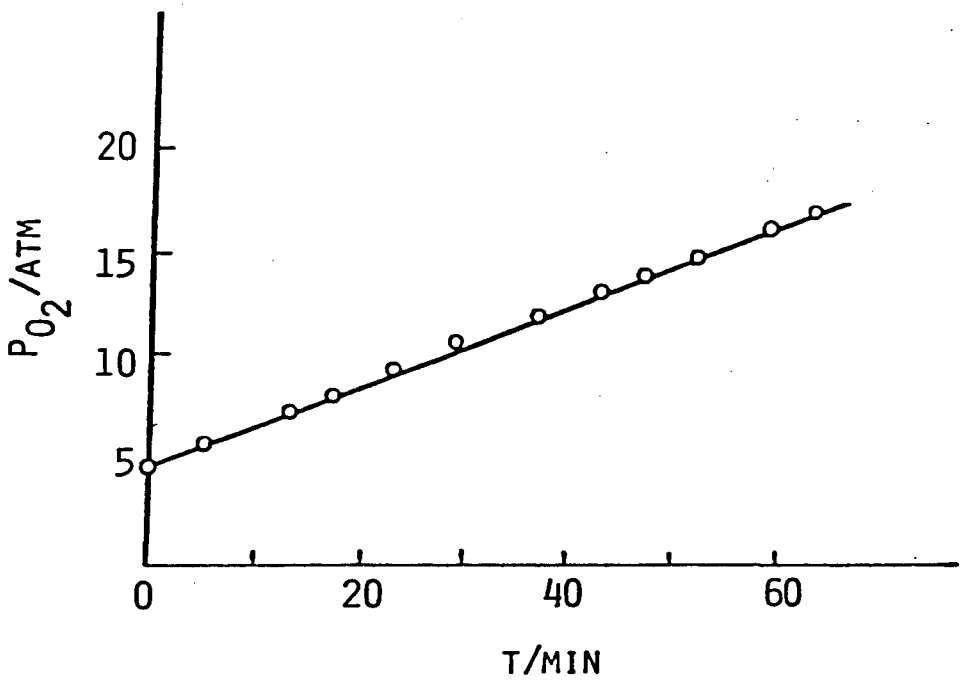


FIG. 5.1.12.7. O_2 SUPERSATURATION IN 6.8 M KOH + KO_2 (~20°C) CAUSED BY $2HO_2^- \rightleftharpoons O_2 + 2OH^-$ AND $2O_2^- \cdot + H_2O \rightleftharpoons O_2 + HO_2^- + OH^-$. SOLUTION NOT STIRRED; NEGLIGIBLE BUBBLE EVOLUTION.

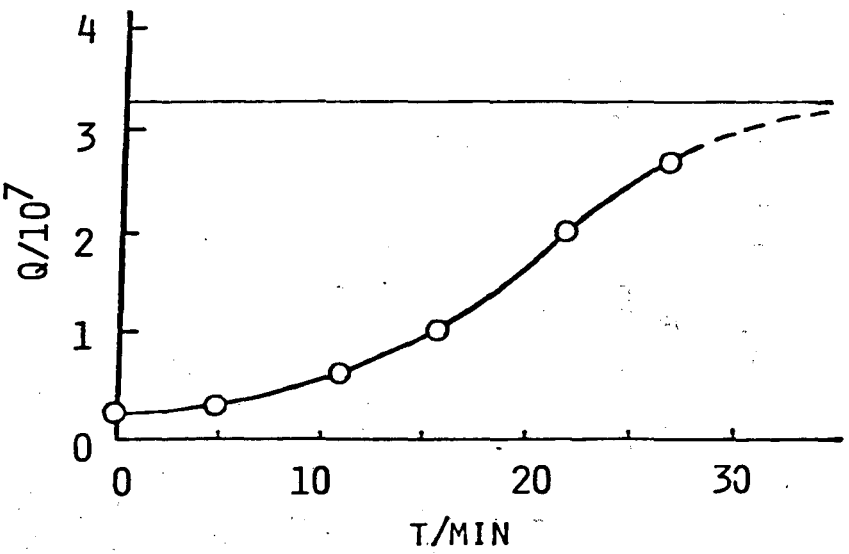


FIG. 5.1.12.8. TIME DEPENDENCE OF

$$Q = (C_{HO_2^-}\ C_{OH^-}\ P_{O_2})/(C^2_{O_2^-}.\ A_{H_2O})$$

IN THE INITIAL STAGE AFTER ADDITION OF KO_2 TO 3.0 M KOH. THE STRAIGHT LINE INDICATING THE EQUILIBRIUM CONSTANT DETERMINED IN THIS WORK.

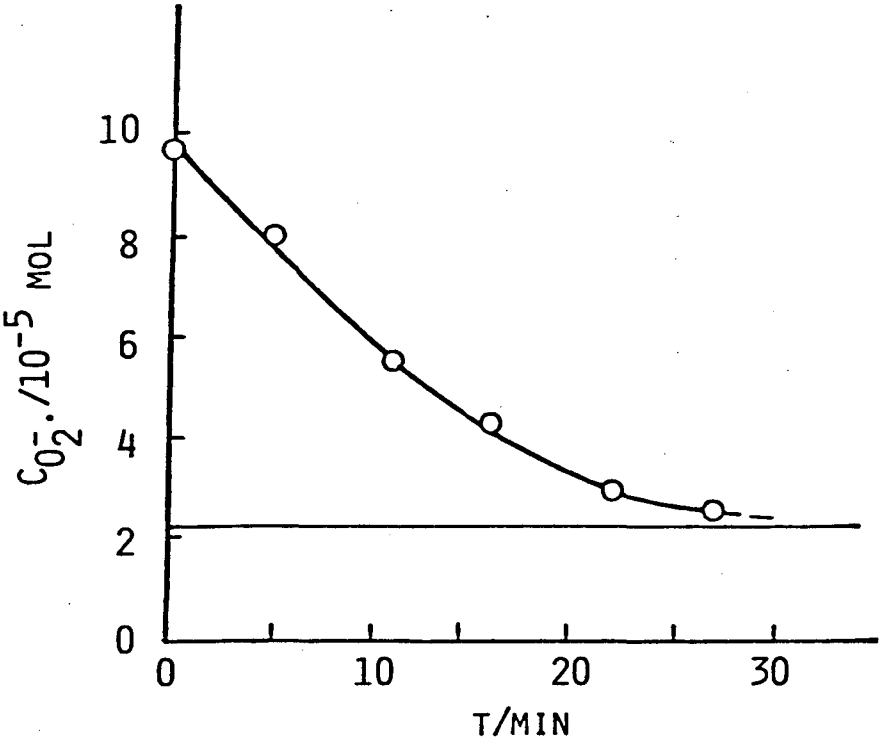


FIG. 5.1.12.9. $O_2^-\cdot$ DECAY IN THE INITIAL STAGE AFTER ADDITION OF KO_2 TO 3.0 M KOH. THE STRAIGHT LINE SHOWS ITS EQUILIBRIUM CONCENTRATION CALCULATED ACCORDING TO THE EQUILIBRIUM CONSTANT K DETERMINED IN THIS WORK.

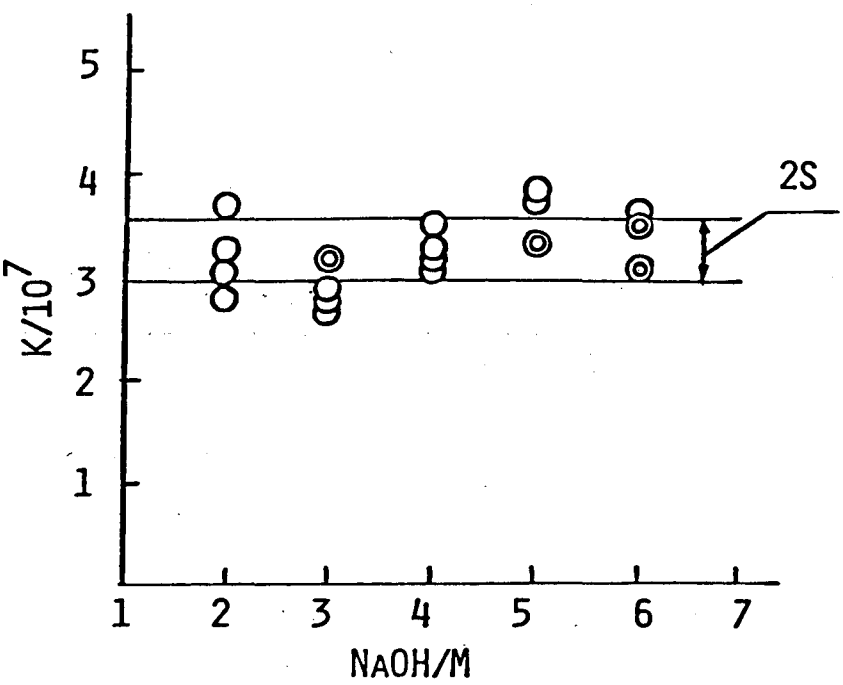


FIG. 5.1.12.10. DISTRIBUTION OF EXPERIMENTALLY DETERMINED K VALUES FOR VARYING ALKALINE CONCENTRATIONS.

S - STANDARD DEVIATION

DEFINITION: $S = [(\Sigma x^2 - n\bar{x}^2)/(n-1)]^{1/2}$

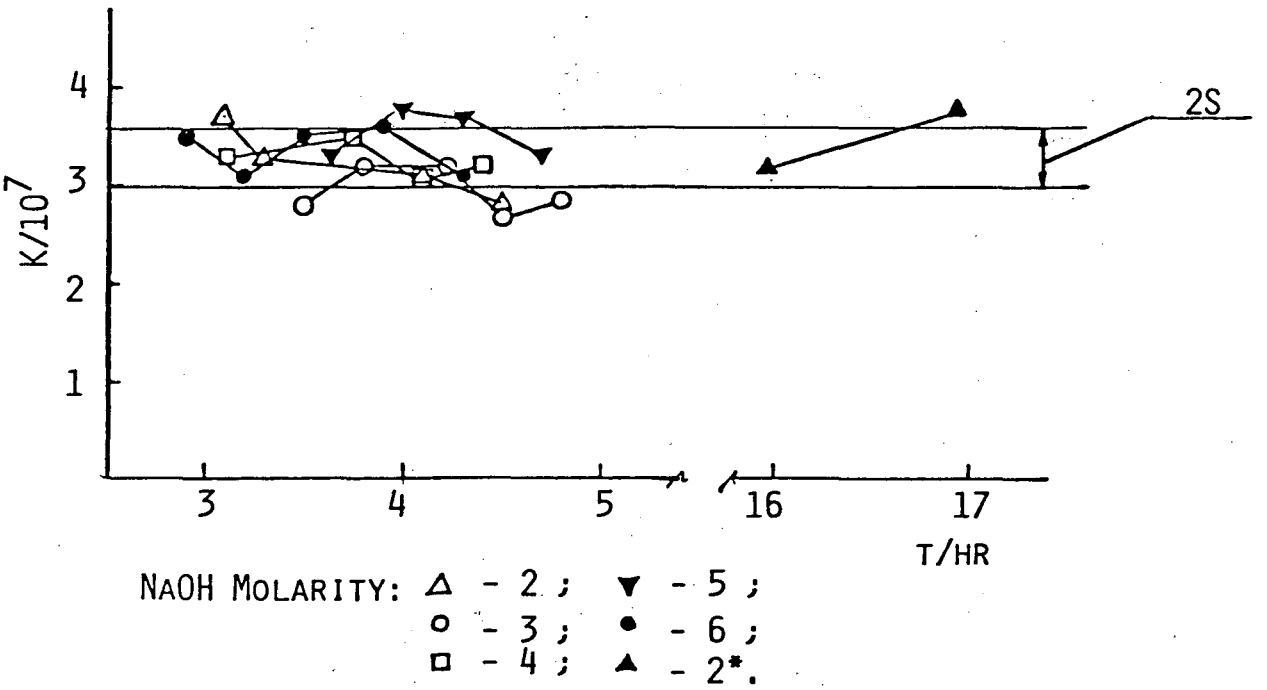


FIG. 5.1.12.11. TIME DEPENDENCE OF Q FOR TIMES > 2.5 HR. Q HAS ESSENTIALLY APPROACHED A STEADY VALUE: Q = K.

* DIFFERENT FROM OTHER CASES, THIS SYSTEM PREPARED BY ADDING 90% H_2O_2 INSTEAD OF KO_2.

5.1.13

COMMENTS ON THE VAN DER BRINK, BARENDRECHT AND VISSCHER METHOD TO EVALUATE RATE CONSTANTS FOR HYDROGEN PEROXIDE DECOMPOSITION AT ROTATING DISK ELECTRODES

D. A. Scherson*, R. Amadelli and E. B. Yeager

Recently, van der Brink *et al.*[1] have proposed a new method to determine the rate constant for hydrogen peroxide decomposition at the surface of a rotating disk electrode. Their analysis was motivated in part by an earlier work by Bagotskii *et al.*[2] and consists in measuring the limiting current at the ring for both anodic and cathodic modes as a function of the rotation rate, maintaining the disk at open circuit. According to these authors a plot of $I_{R,lim}$ vs $\sqrt{\omega}$ should theoretically yield a straight line with negative intercept if peroxide is chemically decomposed, or zero otherwise. As part of an effort in this laboratory directed towards a detailed understanding of oxygen reduction, the use of the diagnostic test referred to above was attempted. Several preliminary experiments were conducted under the conditions prescribed by the theory; however, the plots did not show evidence of a negative intercept even for surfaces known to possess peroxide decomposition abilities. As a result, the mathematical treatment developed by van der Brink *et al.* was thoroughly examined and certain problems found which place their claims in doubt. This short communication will address these issues and present experimental results which are consistent with an appropriate theoretical framework. The assumptions as well as the notation used in this work follow closely those in Ref. 1.

The specific difficulty with the theoretical treatment in Ref. 1 centers on their Eq. (6) for the cathodic limiting ring current in a solution containing H_2O_2 but no O_2 for zero disk current:

$$-\frac{I_{R,lim}^{c}}{N_o AF} = 4\gamma_1\sqrt{\omega}\, c_1^o + \frac{\beta^{2/3}}{N_o AF} I_{D,lim}\, H_2O_2^a - 2k_4 c_2^o \qquad (1)$$

and likewise their Eq. (7) for the anodic limiting ring current:

$$\frac{I_{R,lim}^{a}}{N_o AF} = \frac{\beta^{2/3}}{N_o AF} I_{D,lim}\, H_2O_2^a - 2k_4 c_2^o \qquad (2)$$

---

*Vittorio de Nora-Diamond Shamrock Post-Doctoral Fellow

where the superscript ° refers to the surface solution concentration. The last term on the right-hand side of Eqs. (1) and (2) is questionable. For the cathodic limiting current of H_2O_2 at the ring, shielded by the reactions at the disk, assuming the same mechanism proposed in Fig. 1 (Ref. 1), the following expression is obtained:

$$-\frac{I_{R,lim}^{c}}{N_o AF} = \frac{\beta^{2/3}}{N_o AF} I_{D,lim\ H_2O_2}^{a} - 2[(k_4 + k_3 + k_2^b)c_2^\circ - k_2^f c_1^\circ] \quad (3)$$

$$= \frac{\beta^{2/3}}{N_o AF} I_{D,lim\ H_2O_2}^{a} - 2\gamma_2\sqrt{\omega}(c_2^s - c_2^\circ) \quad (4)$$

[see Eq. (3), ref. (1)]. The corresponding value for the O_2 reduction (4-electron) on the ring is given by

$$-\frac{I_{R,lim}^{c}}{N_o AF} = -4[k_2^f c_1^\circ - k_2^b c_2^\circ + k_1 c_1^\circ - \tfrac{1}{2}k_4 c_2^\circ] \quad (5)$$

$$= 4\gamma_1\sqrt{\omega}c_1^\circ \quad (6)$$

[see Eq. (4), ref. (1)]. Equations (3) and (6) then yield an expression for the total cathodic limiting ring current, namely

$$-\frac{I_{R,lim}^{c}}{N_o AF} = 4\gamma_1\sqrt{\omega}c_1^\circ - 2[(k_4 + k_3 + k_2^b)c_2^\circ - k_2^f c_1^\circ] + \frac{\beta^{2/3}}{N_o AF} I_{D,lim\ H_2O_2}^{a} \quad (7)$$

Even with the condition that $I_D = 0$, that is

$$\frac{I_D}{2FA} = (k_2^b - k_3)c_2^\circ - (2k_1^\circ + k_2^f)c_1 = 0\ , \quad (8)$$

the second term in the right-hand side does not reduce to $-2k_4c_2^o$ as indicated by van der Brink et al. (Eq. (6) in Ref. 1). On the other hand, the combination of Eq. (4) and Eq. (6) yields

$$-\frac{I_{R,lim}^c}{N_o AF} = 4\gamma_1\sqrt{\omega}c_1^o - 2\gamma_2\sqrt{\omega}(c_2^s - c_2^o) + \frac{\beta^{2/3}}{N_o AF} I_{D,lim\ H_2O_2}^a \tag{9}$$

For $I_D = 0$, from Eqs. (3-5), Ref. 1,

$$4\gamma_1\sqrt{\omega}c_1^o = 2\gamma_2\sqrt{\omega}(c_2^s - c_2^o) \tag{10}$$

and

$$-I_{R,lim}^c = \beta^{2/3} I_{D,lim\ H_2O_2}^a \tag{11}$$

Therefore the cathodic ring limiting curent for zero disk current carries no kinetic information in contrast to the conclusion reached in Ref. 1. Likewise for the anodic ring limiting current, regardless of what the disk current is,

$$\frac{I_{R,lim}^a}{N_o AF} = \frac{\beta^{2/3}}{N_o AF} I_{D,lim\ H_2O_2}^a - 2[(k_4 + k_3 + k_2^b)c_2^o - k_2^f c_1^o)] \tag{11}$$

$$= \frac{\beta^{2/3}}{N_o AF} I_{D,lim\ H_2O_2}^a - 2\gamma_2\sqrt{\omega}(c_2^s - c_2^o) \tag{13}$$

Equations (12) and (13) do not match up with the corresponding Eq. (9) in Ref. 1.

Equations (9) and (13) can be derived strictly from the diffusional fluxes in accordance with Levich's theory[3] without explicit reference to the rate constants. These, however, can be introduced in Eq. (4) from the steady state value of c^o_2 as determined from a combination of Eq. (1) and Eq. (2) in Ref. 1, namely,

$$c_2 = \frac{\gamma_2\sqrt{\omega}c_2^s(a_2 + \gamma_1\sqrt{\omega})}{(a_2 + \gamma_1\sqrt{\omega})(a_3 + \gamma_2\sqrt{\omega}) - a_4} \tag{14}$$

where $a_1 = k_2^b + \frac{1}{2}k_4$; $a_2 = k_1 + k_2^f$; $a_3 = k_3 + k_2^b + k_4$; $a_4 = k_2^f (k_2^b + \frac{1}{2}k_4)$ (15)

Therefore,

$$\frac{I_{R,lim}^a}{2N_o FAC_2^s} = \gamma_2\sqrt{\omega}\left(\frac{\beta^{2/3}}{N_o} - 1\right) + \frac{\gamma_2^2\omega(a_2 + \gamma_1\sqrt{\omega})}{(a_3 + \gamma_2\sqrt{\omega})(a_2 + \gamma_1\sqrt{\omega}) - a_4} \tag{16}$$

The dependence of $I_{R,lima}$ on $\sqrt{\omega}$ according to Eq. (16) is non-linear; however, in the limit as $\sqrt{\omega} \rightarrow 0$, $I_{R,lim}{}^{a} \rightarrow 0$. Also, as $\sqrt{\omega} \rightarrow 0$ the following approximation applies:

$$\lim_{\sqrt{\omega}\rightarrow 0} \frac{I_{R,lim}{}^{a}}{2N_o FAc_2^s} = \gamma_2\sqrt{\omega}\left(\frac{\beta^{2/3}}{N_o} - 1\right) \qquad (17)$$

Therefore, in the limit of small rotation rates a straight line with intercept at the origin should be expected if the data are to be plotted as in Fig. 3, Ref. 1. Moreover, the slope should always be positive since $\beta^{2/3} > N_o$.

It is interesting to note that a simple algebraic manipulation of eqs. 3, 4 and 5 in Ref. 1 leads to an expression that relates the rotation rate of the disk to the elementary rate constants, namely

$$\omega = \left[k_{1,r}k^{b}_{2,r} + k_{1,r}k_4 + \tfrac{1}{2}k^{f}_{2r}k_4 + k_{3,r}(k_{1,r} + k^{f}_{2,r})\right]^2 \Big/ \gamma_1^2[k^{b}_{2,r} - k_{3,r}]^2 \qquad (18)$$

This condition can be met only under the premise that the electrochemical rate constants change as a function of an open-circuit potential, which in turn should vary with rotation rate. A similar theoretical observation was also made by Bagotskii et al.[2] Experiments conducted in this laboratory indicate that in a system such as the one studied in this work, the potential increases about 20 mV with rotation rate in a region between $\sim$100 to $\sim$900 rpm, with no further significant increment at higher rotation rates.

The oxidation and reduction limiting currents were examined experimentally under the conditions prescribed by the theory, using a gold disk with a platinum ring in a 2.0 x 10^{-3} M H_2O_2 in 1 M NaOH solution. The area of the disk was 0.196 cm^2, the collection efficiency 0.38 and the calculated value of β, 3.74. The electrolyte was purified utilizing a method developed in this laboratory[4] which includes pre-electrolysis, and is described in detail elsewhere.[4] Hydrogen peroxide solutions were prepared from unstabilized 90% H_2O_2 (FMC Co., Buffalo, New York). Measurements were performed under dynamic polarization conditions sweeping the ring potential at 20 mV s^{-1}, and also at quasi-steady state. The ring was potentiostatted at -800 mV vs. before each scan to obtain a nominally reduced electrode. Results are depicted in Fig. 1. As can be clearly seen, both anodic and cathodic modes yield straight lines with a zero intercept observed only for the anodic mode. The non-zero intercept for the cathodic ring limiting current is beyond the

statistical error and appears quite real.

The limiting ring current in the cathodic case is not completely diffusion controlled as judged from the fact that a plot of $1/I_{R,limc}$ vs. $\omega^{-\frac{1}{2}}$ gives a straight line with a non-zero intercept. Although corrections for kinetic contributions in the case of a disk are straightforward, the analysis in the case of a ring operating below the limiting current, as shown by Rosner,[5] is by no means simple because the concentration profile across the ring surface is indeed not uniform. Nonetheless, we have corrected the apparent cathodic limiting ring currents (I_R) using the equation

$$\frac{1}{I_R} - \frac{1}{I_K} = \frac{1}{I_{R,lim}{}^c} \qquad (19)$$

Complete diffusion control can be experimentally achieved for the reduction of hydrogen peroxide in a system such as the one studied in this work by platinizing the ring. This procedure was successfully utilized by van der Brink et al.[1] as judged from their curve (Fig. 13, Ref. 1). However, traces of platinum can still dissolve in solution, even with an electrode polarized cathodically. In order to reduce the possibility of contaminating the gold disk, a smooth platinum ring was used in this study.

The observed linear behavior in the anodic case (see curves A and B in Fig. 1) and the zero intercept indicate that Eq. (17) is applicable for the observed anodic ring limiting current. Therefore, no information regarding any of the rate constants can be obtained unless sufficiently high rotation rates can be used to gain access to the non-linear region where the second term on the right of eq. (16) becomes significant.

In overall perspective, this method involving $I_D = 0$ is of a rather restricted use.

ACKNOWLEDGMENTS

One of the authors (D.S.) would like to thank Dr. J.D.E. McIntyre for helpful discussions during this work, and the Diamond Shamrock Corporation for a fellowship.

REFERENCES

1. F. van der Brink, E. Barendrecht and W. Visscher, J. Electrochem. Soc., 127, 2003 (1980).

2. V. S. Bagotskii, M. R. Tarasevich and V. Yu. Filinovskii, Sov. J. Electrochem., 5, 1158 (1969).

3. Yu. V. Pleskov and V. Yu. Filinovskii, "The Rotating Disc Electrode", Consultants Bureau, New York, 1976 (Chapter 8).

4. R. Zurilla, R. Sen and E. Yeager, J. Electrochem. Soc., 125, 1103 (1978).

5. D. E. Rosner, J. Electrochem. Soc., 113, 624 (1966).

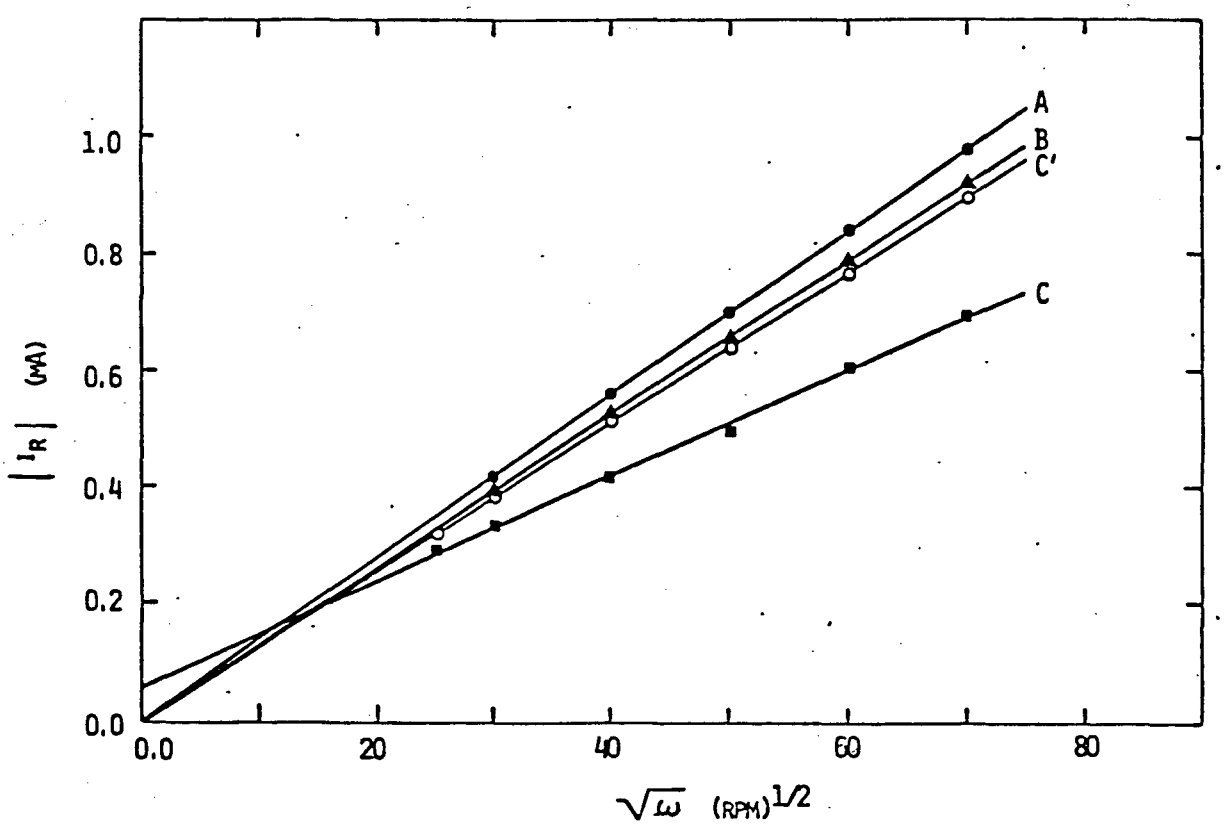


Fig. 5.1.13.1. Plots of the limiting ring currents in a solution 2.0 x 10^{-3} H_2O_2 in 1 M NaOH. The electrode was a gold disk with a concentric platinum ring. Disk area, A = 0.196 cm^2; collection efficiency, N_o = 0.4 and β = 3.79. Measurements were taken with the disk at open circuit and ring currents recorded at +250 mV and -650 mV vs. Hg/HgO for anodic and cathodic modes, respectively.

A. Oxidation with potential scan of 20 mV/s

B. Oxidation at quasi-steady state

C. Reduction with potential scan as in A. (uncorrected)

C'. Same as C but corrected for kinetic effects according to eq. (19) in the text.

5.1.14 GAS FED POROUS ELECTRODES

W. Aldred

OBJECTIVES

Stated simply, the objectives for the porous electrode research are the following:

1. The determination of the relative merits of various catalysts (catalyzed carbons) used in gas fed porous electrodes at 85°C in 9M NaOH.

2. The development and refinement of techniques for fabricating and testing these electrodes.

3. The determination of the relationships of carbon types, fabrication techniques and Teflonation procedures to electrode performance (as measured by polarization data).

BACKGROUND

Porous carbon electrodes were made at Western Reserve University in the 1950's by spraying a solution-suspension of gum rubber, benzene, and active carbon onto the surface of a porous graphite plug. This type of electrode would function satisfactorily for a short time but was found to be fragile and thus impractical for extended use. A mixture of carbon and Teflon emulsion produced a rubbery mixture which could be pressed (hand force) on to a porous plug. This procedure produces an electrode which is reasonably flexible and durable. Variations in technique could lead to a very good porous plug electrode but the time consumption involved in fabrication is prohibitive if extensive catalyst testing is to be done.

Diamond Shamrock researchers developed a 3 layer electrode which proved to be quite successful. A mixture of carbon and Teflon emulsion is worked into a flexible sheet by means of a combination of blending, chopping, and rolling techniques and then a nickel screen is pressed into one side of it and a hydrophobic Teflon layer onto the other. In actual use, gas goes to the hyrophobic side and electrolyte to the screen side.

Attempts were made at CWRU to develop a technique for making Diamond Shamrock style electrodes quickly for short term testing. A relatively simple technique was developed by Gao Liang for mixing carbon with Teflon emulsion and then pressing the mixture into 3 layer electrodes which could be put into a simple holder for polarization measurements in 9M caustic. The technique produced electrodes which had good performance for an hour or two, broke in quickly, and lent themselves to comparitive catalyst testing. Some problems were encountered involving durability and reproducibility but the method proved to be successful. An electrode holder was designed that could be easily assembled and disassembled so that these electrodes (and disks cut from D.S. electrodes) could be run quickly.

EXPERIMENTAL PROCEDURES

The electrode to be tested is mounted in the holder and this is fitted into a circular Teflon piece which sits over the top of a Teflon beaker containing the electrolyte. There are appropriate holes in this Teflon piece for counter electrode, reference electrode and thermometer. A heating tape controlled by a variable transformer (Powerstat) supplies heat for raising the temperature of the electrolyte. Gas is supplied to the electrode holder from tank air or oxygen through a water bubbler. The electrodes are connected to a Galvanostat (Stonehart BC 1200 Potentiostat operating in the Galvanostatic mode). A pulse generator or programmer supplies voltage pulses which control the galvanostat. Current can be set to any value from zero to about 920 mA. The IR bridge feature of the BC 1200 enables the user to balance out IR drop by an adjustment of the bridge "pot" while observing the reference electrode to working electrode voltage on the screen of an oscilloscope. Digital meters built into the BC 1200 (or external meters) read out the reference to working electrode potential and the potential across the series resistor (a measure of the electrode current). The potential and current values are used to plot a polarization curve for the electrode which has been run.

Figure 1 shows a generalized scheme for the interconnection of the measuring devices.

THE ELECTRODE HOLDER

Figure 3 is the drawing of the electrode holder. A nickel insert is press fit into a Teflon body and a Vitron O ring which sits into a groove in the outer wall of the nickel piece seals off the gas compartment. The shoulder in the nickel piece recieves a rubber gasket (PPPE rubber) and the electrode upon that a thin circular nickel ring presses against the screen side of the electrode. Three tiny screws which thread into holes in the nickel insert clamp the electrode against the gasket (to seal off the electrolyte) and enable electrical contact to be made between the ring and insert. A wire attaches to the back of the insert and exits through the gas inlet tube. Gas passes into the gas cavity through this tube and is vented out through a channel in the Teflon which leads to an exit tube.

When operating at high current densities at higher temperatures (85°C), a shielding of the nickel parts is desirable in order to minimize distortion of the IR bridge null. A plexiglass ring fits over the nickel ring. A rubber gasket fits around these rings and a Teflon gasket covers the screw holes. They are held in place by a screw-on Teflon cap. This cap increases the length of the electrode's electrolyte channel and this can cause slow displacement of gas bubbles if O_2 goes through the electrode. Since the reference electrode bridge is outside this channel (in the bulk electrolyte), there is a large increase in solution IR drop when the cap is on.

ELECTRODE FABRICATION

The CWRU electrode fabrication technique has undergone evolution and refinement since it was first conceived. Originally, Teflon emulsion was measured out from a micropipette and diluted about 100:1 with water. The carbon was placed in a small test tube and wetted with water by means of vibration and "swirl" using a "Genie Vortex". While being stirred vigorously, the diluted Teflon was slowly added from a medicine dropper. The mixture was filtered onto filter paper and dried by suction. The semi-dry mixture was placed into a stainless steel die and pressed at a pressure of one to two tons per square inch. The resulting disk was then pressed at higher pressures (5 to 6 tons per square inch), this time with a nickel screen on top of it. The disk (with embedded screen) was then heated in the oven (90°C) for 45 minutes and then returned to the die (screen side down) where a piece of Teflon paper was pressed into the other side at low pressure ($\approx$ 400 lb/in^2).

In the newer technique, the carbon is wetted by agitation using the Genie Vortex and the slurry is transferred to a beaker and placed in the cavity of an ultrasonic cleaner. A diluted suspension ($\approx$ 50 mg/ml) of T30B Teflon emulsion is measured out using a disposable pipette and diluted 10:1 with water. This very dilute suspension is added slowly to the agitated carbon slurry. The slurry is then filtered onto a Nucleopore filter (1 μ pore size). The filtered mixture is placed on a Teflon or aluminum sheet and worked with a spatula for several minutes. If a fine carbon is used and the Teflon content is not high (like 45-50%), the material requires several minutes of kneading at a temperature of 50°C to 70°C (on a steam bath). With working, the mixture becomes quite rubbery and can be pressed into a somewhat flexible electrode. The material is then placed in the pressing die and shaped (using hand pressure) in order to make a reasonably uniform disk and to squeeze out much of the water. The disk is heated in flowing N_2 or He for 2 to 4 hours at a temperature of 250°C to 280°C. This heating thoroughly dries it and also sublimes out much of the triton x-100 surfactant (Teflon stabilizer) which has adsorbed on the carbon. The dried disk is pressed in the die at 1 to 2 tons per square inch pressure. A nickel screen is placed on top of the disk and it is pressed again at 6 tons per square inch pressure. The pressing time is 2 to 3 minutes. The disk is removed from the die and then placed in again screen side down. A circular piece of porous Teflon paper is placed on top of the disk and pressed at about 500 lb/in^2. Figure 2 is the drawing of a finished electrode.

It should be noted here that the use of ultrasonic agitation in the Teflonation and the extensive kneading of the Teflonated carbon generally produces electrodes which press nicely and are more durable but the mass transport properties are usually poorer. Depending upon the type of carbon and the extent of working, the amount of Teflon can also make a significant difference. Larger amounts of Teflon stabilize the electrode for long life but the electrical conductivity, wettability and porosity are affected.

RESULTS

POLARIZATION CURVES FOR EARLY ELECTRODES

Figures 4 through 8 are polarization curves for electrodes (of early 1979) made from RB and XC-72 carbons which had been treated in order to produce deposits of metals (Pt) or macrocyclics (pyrolyzed porphyrins). The Pt (on XC-72) electrode of Fig. 4 and the Pt-Cu combination in Fig. 5 are good electrodes and were considered excellent. The CoTMPP electrodes in Figures 6 through 8 show similar activity to the Pt containing ones. The electrodes of Figures 7 and 8 were fabricated by EMC and show good mass transport. The CWRU electrodes (Figs. 4, 5 and 6) are not so impressive at high current densities.

Figures 9 through 12 are polarization curves for electrodes made in mid 1979 or later by Gao Liang. The CoTPP electrode (Fig. 10) and the CoTMPP electrode of Fig. 9 are very good but the CoOEP electrode of Fig. 11 is even better. The fluorinated macrocyclic in the electrode of Fig. 12 is not as active as similar nonfluorinated ones. All of the porphyrin ctalyzed carbons used to make these electrodes were heated at temperatures from 450°C to 900°C.

Figures 13 through 15 are polarization curves for electrodes fabricated from the Stonehart Pt catalyzed carbons (PC 1000 and PC 2000). In Figs. 13 and 15, the carbon is diluted with uncatalyzed carbon (XC-72) or Shawinigan Black) but the catalytic activity is still as high. The very fine carbons (XC 72 and Shaw Blk.) are difficult to fabricate into electrodes because the Teflonation produces non-flexible structures which generally suffer from gas or electrolyte transport difficulty. Use of high Teflon content or extensive working tend to improve flexibility but the other problems are harder to remedy.

Figures 16 and 17 give polarization curves for electrodes which were made to show the effects of a finer Teflonation and prolonged heating. The electrode of Fig. 16 makes use of a good Liang CoTMPP-RB carbon. Extra triton X100 stabilizer was used so that Teflon precipitation would slow down. In order to eliminate the excess triton X100, the finished electrode ws heated in flowing N_2 (280°C) for several hours. Note the high activity and good O_2 transport. The polarization at 300 and 400 mA/cm2 with air is exceptionally good. The electrode of Fig. 17 contains RB cabon only. It was heated for several hours in N_2 also and it shows relatively low polarization at high current densities.

Figure 18 is the polarization curve for two similar electrodes. One is made from a Pt catalyzed XC-72 carbon and the other has the same amount of Pt plus some Pd. In this case, the extra metal increased the catalytic activity of the platinized carbon. In most cases, the second metals decrease the activity. Figure 19 is the curve for an EMC fabricated version of the Pt-Pd catalyzed XC-72. The activity at low current density is poorer but EMC did produce a better high current density performer. Note that the air curve is quite good. Figure 20 is the polarization curve for an electrode fabricated by EMC from a CWRU Pt-Mo catalyzed XC-72 carbon. This electrode out-performs similar electrodes at high current densities but the open circuit potential is typical of the Pt based bimetallics.

The curve in Fig. 21 is for the best CWRU electrode that was made from CWRU Prototec Pt catalyzed XC-72 carbon. The catalytic activity is almost as good as for electrodes made from the Stonehart Powercat carbons.

Figures 22, 23 and 24 are polarization curves for 3 of the better electrodes made from perovskites which were prepared by Mr. B. C. Wang. The curves of Fig. 22 are fairly typical for an oxide type catalyst (La 0.5 Sr 0.5 CoO_3) matrixed with Shawinigan Black. Figure 23 is the curve for a later perovskite (also La 0.5 Sr 0.5 CoO_3). This batch was ground as fine as possible by hand using a mortar and pestle. The electrode made from it showed greater activity and a flattening out in the lower current density region. The curve of Fig. 24 is for a lead doped perovskite (La 0.5 Sr 0.25 Pb 0.25 CoO_3) which is matrixed with Shawinigan Black at a 50% level. Unlike the other perovskites, this one has high electrical conductivity and so can be used in high concentration. All three of these figures have a Shawinigan Black curve (using O_2) for reference.

Figure 25 is the polarization curve for a lead doped Lead Ruthenate ($Pb_2Ru1.67Pb$ .3306.5), matrixed with Shawinigan Black at a high catalyst level (69% catalyst, 31% S.B.). The catalytic activity with both O_2 and air is very high and the stability at 85°C in 9M NaOH was good for the 2 hour run. (It was also tested on an O_2 evolution electrode but it underwent a decomposition.)

The last two figures are polarization curves for electrodes made from a clamshell phthalocyanine adsorbed on RB carbon (10% catalyst). The macrocyclic (on RB) was heated 3 hours in Argon at 350°C during preparation. Figure 26 shows the O_2 and air curves for the dimer. The dotted line is a typical polarization curbe for RB carbon alone (using O_2). Only about 20 millivolts of activity are gained compared to the plain carbon. It should be noted here that the electrode was polarized (run) a second time (cathodically) and performed even more poorly. Eventually, the open circuit potential could only reach that for RB alone (O_2) and the high current density potentials rose sharply (to values worse than for RB alone).

Figure 27 is the curve(s) for the O_2 and air responses of an electrode made from the clamshell phthalocyanine polymer (adsorbed on RB carbon - 10% polymer). During the preparation, the "macrocylic on RB" was heated 5 hours in He at 550°C. The O_2 curve is reasonably good but it rises too steeply at high current densities. The dot curve is a repeat run made after the air run. This curve shows that there was some activity loss at low current densities and a significant degradation at high current densities. This electrode has been run previously in 5.5M KOH at room temperature and during that run had showed some signs of loss of activity.

TABLES OF POLARIZATION DATA

Tables 1 through 5 are a sort of summation of polarization data taken from many polarization curves which were obtained over a 3 year period. Many of the electrodes included in the tables are not among those described in the previous section but are given here to complete the electrode testing overview.

The first table (Table 1) shows the polarization data for some early Pt containing electrodes made from catalysts prepared by Paul Casson. Note that the first two electrodes are made from PC-Z01 carbon but one is a pressed 3 layer type and the other is a porous plug type. The last two contain a small amount of Cu in addition to the Pt and this seems to decrease the catalytic activity somewhat.

Table 2 is a summation of polarizatin data for electrodes which contain macrocyclics (electrodes and materials prepared by Paul Casson and Gao Liang). The data informs us that certain macrocyclics (specifically CoTMPP and CoOEP) produce very active electrodes when adsorbed on carbon and heated to several hundred degrees centigrade in an inert or hydrogen containing atmosphere. Other macrocyclics show activity too but it is the porphyrins and porphyrin-like structures which are the best.

Table 3 summarizes polarization data for electrodes made from metal oxide and mixed metal oxide catalysts. The 3 types included here are MnO_2, spinels and perovskites. Freeze-dry deposition of oxides on carbon is time consuming and not highly successful. The particles are large and form mixtures, not true deposits. Also, many of these compounds are poor electrical conductors (the perovskites) and require the addition of a fine highly conductive carbon. The physical properties of these oxides are such that the electrodes made from them exhibit poor mass transport. Two interesting electrodes (of Table 3) involve a Pb doped Lead Ruthenate and a Pb doped perovskite. These two have active potentials at low current densities and give some indication of being good catalysts.

Table 4 is a listing of electrodes prepared from Pt or from Pt and another metallic element. The CWRU prepared Prototec Pt (on XC-72 carbon) shows high activity and the PC-1000 and PC-2000 from Stonehart are obviously superior. The electrodes containing Co, Mo, or Pd show fair activity but only the Pd seems to enhance the catalytic activity of the Pt.

Table 5 is a summary of the best electrodes (regardless of catalyst). From this table, we see that (1) RB carbon is a good O_2 electrode by itself. (2) RB carbon with Pt or pyrolyzed porphyrin on it is very good. (3) A fluorinated macrocyclic (CoTTFTP) shows less activity than expected (probably less than one which is not fluorinated).

SCANNING ELECTRON MICROGRAPHS (S.E.M.'s)

During the course of our work with electrodes and electrode materials, every carbon and many electrodes were examined with the scanning electron microscope. What did we learn? We learned that RB carbon looks like a lot of stones, all carbon blacks look pretty much alike (small particles down to 0.01 μm) and charcoals seem to be grooved pieces of wood. Examination of many electrodes shows us that Teflon is hard to distinguish from carbon unless it is present as large clumps or long conspicuous fibers.

The S.E.M.'s of spinels and perovskites show them to be quite coarse. We also see that flexible electrodes are very fibrous whereas brittle electrodes are less fibrous and appear to be full of small cracks. If there has been significant erosion of an electrode, it can be seen in the S.E.M. picture as holes and cracks. General surface conditios can be seen in electrode material and also paricle size distributions of powder samples. To see much more, a higher magnification is required. (Transmission electron microscopy.)

FINAL DISCUSSION

Gas fed porous electrodes for O_2 reduction can be made from several differenct catalyzed carbons but the best ones are: (1) Pyrolyzed porphyrins on RB carbon or (2) very finely divided Pt on RB carbon. RB carbon is specified here because it is easy to handle, easy to Teflonate, easy to press or roll into flexible electrodes and it results in electrodes which work well and generally have good mass transport properties. The long term failure of RB based electrodes operating in 9M NaOH at 85°C is due to oxidation of the carbon but this can be minimized by employing the proper fabrication techniques. Research at E.M.C. indicates that matrixing with Shawinigan Black slows down the RB oxidation.

Electrodes fabricated from fine carbons suffer from physical inflexibility and poorer mass transport compared to those made from RB, especially when air is used for the O_2 source. EMC devleoped techniques for electrode fabrication from the finer carbons but performance with air was not satisfactory.

Some unpyrolyzed macrocyclics (phthalocyanines in particular) have characteristics which make them good catalysts but most of them degenerate and lose activity in hot concentrated caustic in the presence of O_2 and carbon.

Addition of a second metal to a good Pt catalyzed carbon generally decreases the catalytic activity of the Pt. Whether or not some stability is gained has yet to be determined.

Spinels and perovskites are reputed to be good peroxide eliminators but they are generaly coarse and possess low surface area. Deposition of fine particles of either upon a carbon is tricky and time consuming. Also, electrodes containing these compounds yield electrode structures which have poor mass transport. Mixing with carbon(s) and Teflonating was tried and a matrixing with Teflonated Shawinigan Black was also tried. None of the electrodes made in this manner did well at high current densities.

Table 1. Early Platinum Electrodes

Electrode number	Composition	Potential (volt) vs. Hg/HgO at i/A =			
		0.1 mA/cm^2	10 mA/cm^2	100 mA/cm^2	300 mA/cm^2
DPC-Z01	10% Pt on XC-72 1.5 mg Pg/cm^2	+0.047	-0.020	-0.055	-0.137
WAP-PCZ01	10% Pt on XC-72 1.2 mg Pt/cm^2 (porous plug)	+0.068	-0.017	-0.055	-0.105
PC-RB5S	Pt on RB 0.5 mg/cm^2	+0.047	+0.021	-0.044	-0.087
PC-CU006	Pt and Cu on XC-72	+0.042	-0.008	-0.072	-0.117
PC-CU5S	Pt and Cu on RB	+0.037	+0.008	-0.062	-0.156

Table 2. Early Macrocyclic Electrodes

Electrode	Composition	Potential (volts) vs Hg/HgO at i/A =			
		0.1 mA/cm^2	10mA/cm^2	100 mA/cm^2	300 mA/cm
PC-OM00	10% CoOEP[1] on RB	+0.064 (O_2) +0.045 (Air)	+0.036 +0.018	-0.019 -0.055	-0.063 -0.125
GL-OP004	10% CoOEP[1] on RB (500°C, H_2)	+0.072 (O_2) +0.059 (Air)	+0.055 +0.030	-0.010 -0.030	-0.055 -0.170
PC-M470	10% CoTMPP[2] on XC-72 (470°, H_2)	+0.050	+0.023	-0.030	-0.077
PC-MBR480B	EMC fabricated 10% CoTMPP[2] on XC-72 (480°C, H_2)	+0.040 (O_2) +0.022 (Air)	+0.013 -0.008	-0.050 -0.075	-0.090 -0.127
PC-M500B	EMC fabricated 10% CoTMPP on XC-72 (500°C, H_2)	+0.045 (O_2) +0.030 (Air)	-0.013 -0.008	-0.055 -0.075	-0.085 -0.115
26A17158E349 (GL-PC009)	EMC version 5.6% CoPc on RB (500°C, N_2, H_2)	+0.010 (O_2) -0.010 (Air)	-0.030 -0.050	-0.095 -0.025	-0.132 -0.185
PC-NAP00	10% CoNAPC[3] on RB	+0.011	-0.016	-0.075	-0.123
GL-PC040	10% CoNAPC[3] on RB	+0.021	+0.002	-0.058	-0.097
26A17158E350 (GL-P033)	ENC version 9% CoTPP[4] on RB (450°C, H_2)	+0.040	+0.007	-0.055	-
PC-AM00	10% CoTAA[5] on RB	+0.030	+0.008	-0.045	-0.085
GL-TAA005	10% CoTAA on RB (500°C, H_2)	+0.011	-0.015	-0.065	-0.103
GL-TFP002	5% CoTTFTP[6] on RB	+0.040 (O_2) +0.022 (Air)	+0.012 -0.008	-0.040 -0.070	-0.075 -0.145
GL-P018MII	15% CoTMPP[2] on RB (extra stabilizer and heating used in electrode fabrication)	+0.055 (O_2) +0.040 (Air)	+0.018 +0.003	-0.037 -0.060	-0.068 -0.110

[1]CoOEP is cobalt octaethyl porphyrin. [2]CoTMPP is cobalt meso-tetra-p-methoxyphenyl-porphyrin. [3]CoNAPC is cobalt naphthalocyanine. [4]CoTPP is cobalt meso-tetraphenyl-porphyrin. [5]CoTAA is cobalt dibenzotetraazannulene. [6]CoTTFTP is cobalt-meso-tetra-m-trifluorotolylporphyrin.

Table 3. Metal Oxide Electrodes

Electrode number	Composition	Potential (volt) vs Hg/HgO at i/A = 0.1 mA/cm^2	10 mA/cm^2	100 mA/cm^2	300 mA/cm^2
HTRBN1C2-1	3.5% Co,Ni spinel on RB	+0.012	-0.022	-0.085	-0.130
WA-MNRB-2H	35% MnO_2 on RB	+0.060	+0.015	-0.065	-0.135
WA-WPR600	Best $La_{0.5}$, $Sr_{0.5}$ CoO_3 perovskite of B.C. Wang	+0.038	-0.012	-0.085	-0.165
WA-WPRPb-MX2	Pb doped perovskite half $La_{0.5}$, $Sr_{0.25}$, $Pb_{0.25}$, CoO_3 half Shawinigan Black (as T.S.B.)	+0.075	-0.002	-0.115	-0.215
WA-RUPBA-1	Pb doped lead ruthenate ($Pb_2RU^{4}_{1.67}Pb_{0.33}O_{6.5}$) 59% with Shaw. Blk.	+0.115 (O_2) +0.102 (Air)	+0.072 +0.060	+0.008 -0.035	-0.142 -0.230
WA-TSLS-SWMX2	Tseung Sr doped $LaCoO_3$ matrixed with 50% Shaw. Blk. (as T.S.B.)	+0.045	-0.020	-0.112	-0.183

Table 4. Pt and Pt Bimetallic Electrodes

Electrode number	Composition	Potential (volts) vs Hg/HgO at i/A = 0.1 mA/cm^2	10 mA/cm^2	100 mA/cm^2	300 mA/cm^2
WA-EXX5S-1	5% Pt on XC-72	+0.050 (O_2) +0.029 (Air)	-0.005 -0.038	-0.070 -0.140	-0.132
WA-PC1000H	Stonehart PC1000 (10% Pt)	+0.080 (O_2) +0.062 (Air)	+0.045 +0.015	-0.025 -0.072	-0.077 -0.265
WA-RRPT-H1	CWRU 5% Pt on preox. XC-72	+0.046	-0.005	-0.070	-0.120
WA-RPR-400	CWRU 10% prototec Pt on preox XC-72	+0.072 (O_2) +0.052 (Air)	+0.027 -0.004	-0.041 -0.072	-0.077 -0.215
WA-RRCoPT-H3	5% Pt, 1.5% Co on preox. XC-72	+0.040 (O_2) +0.022 (Air)	+0.015 -0.007	-0.048 -0.098	-0.094 -0.275
EMC-F465	5% Pt, 2.4% Mo on preox. XC-72	+0.040 (O_2) +0.015 (Air)	+0.021 -0.009	-0.030 -0.065	-0.067 -0.127
WA-RRPDPT-H1	5% Pt, 2.7% Pd on perox. XC-72	+0.060	+0.010	-0.060	-0.115

Table 5. Comparison of the Best Electrodes

Electrode number	Composition	Potential (volts) vs Hg/HgO at i/A = 0.1 mA/cm^2	10 mA/cm^2	100 mA/cm^2	300 mA/cm^2
GL-P018-MII	15% CoTMPP[1] on RB	+0.055 (O_2) +0.040 (Air)	+0.018 +0.003	-0.037 -0.060	-0.068 -0.110
GA-RBH-1	RB only	-0.010 (O_2) -0.028 (Air)	-0.050 -0.074	-0.120 -0.155	-0.160 -0.220
PC-M650	10% CoTMPP on XC-72	+0.047	+0.004	-0.055	-0.105
PC-M470	10% CoTMPP on XC-72	+0.050	+0.023	-0.030	-0.077
PC-MRB-480A	10% CoTMPP[1] on RB	+0.036 (O_2) +0.021 (Air)	+0.007 -0.011	-0.050 -0.070	-0.092 -0.135
DPC-Z01	10% Pt on XC-72	+0.060	+0.006	-0.063	-0.115
WA-PC1000-H	Stonehart PC1000 (10% Pt)	+0.077 (O_2) +0.060 (Air)	+0.027 +0.007	-0.058 -0.072	-0.090 -0.225
EMC-F412	5% CWRU Pt + 2.7% Pd on Preox. XC-72	+0.030 (O_2) +0.017 (Air)	-0.005 -0.025	-0.065 -0.095	-0.112 -0.160
GL-OP004	10% CoOEP[2] on RB	+0.075 (O_2) +0.060 (Air)	+0.050 +0.027	-0.013 -0.050	-0.060 -0.155
GL-TFP002	5% CoTTFTP[3] on RB	+0.040 (O_2) +0.025 (Air)	+0.010 -0.010	-0.045 -0.078	-0.080 -0.145
EMC-F465	5% Pt 4% Mo on preox. XC-72	+0.042 (O_2) +0.015 (Air)	+0.022 -0.004	-0.030 -0.065	-0.067 -0.127
WA-RPR-400	CWRU prototec Pt on preox. XC-72	+0.072 (O_2) +0.052 (Air)	+0.022 -0.002	-0.042 -0.077	-0.082 -0.205

[1] CoTMPP is cobalt meso-tetra-p-methoxyphenylporphyrin

[2] CoOEP is cobalt octaethylporphyrin

[3] CoTTFTP is cobalt-meso-tetra-m-trifluorotolylporphyrin

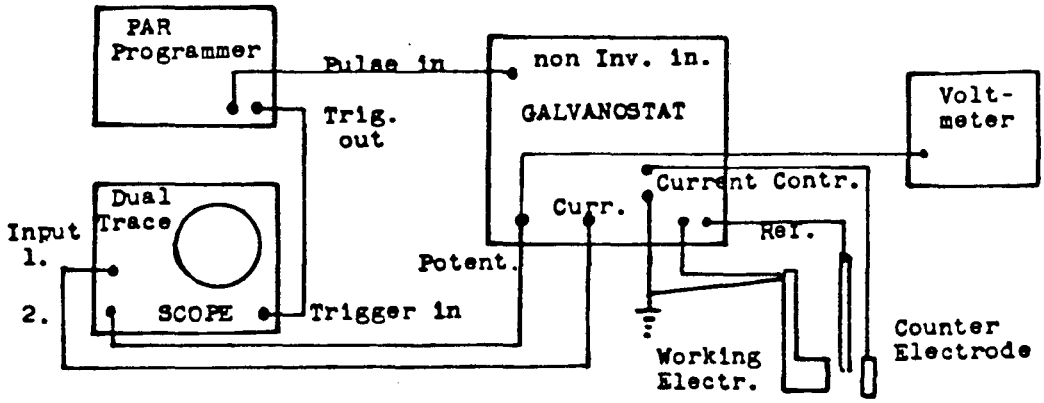


Fig. 5.1.14.1. Electronic apparatus and wiring diagram for making polarization measurements.

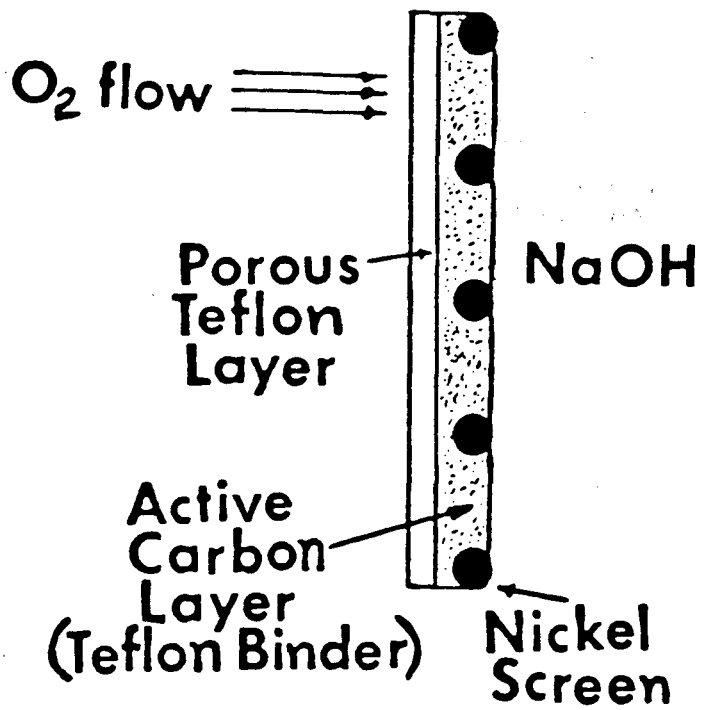


Fig. 5.1.14.2. Three-layer CLES test electrode

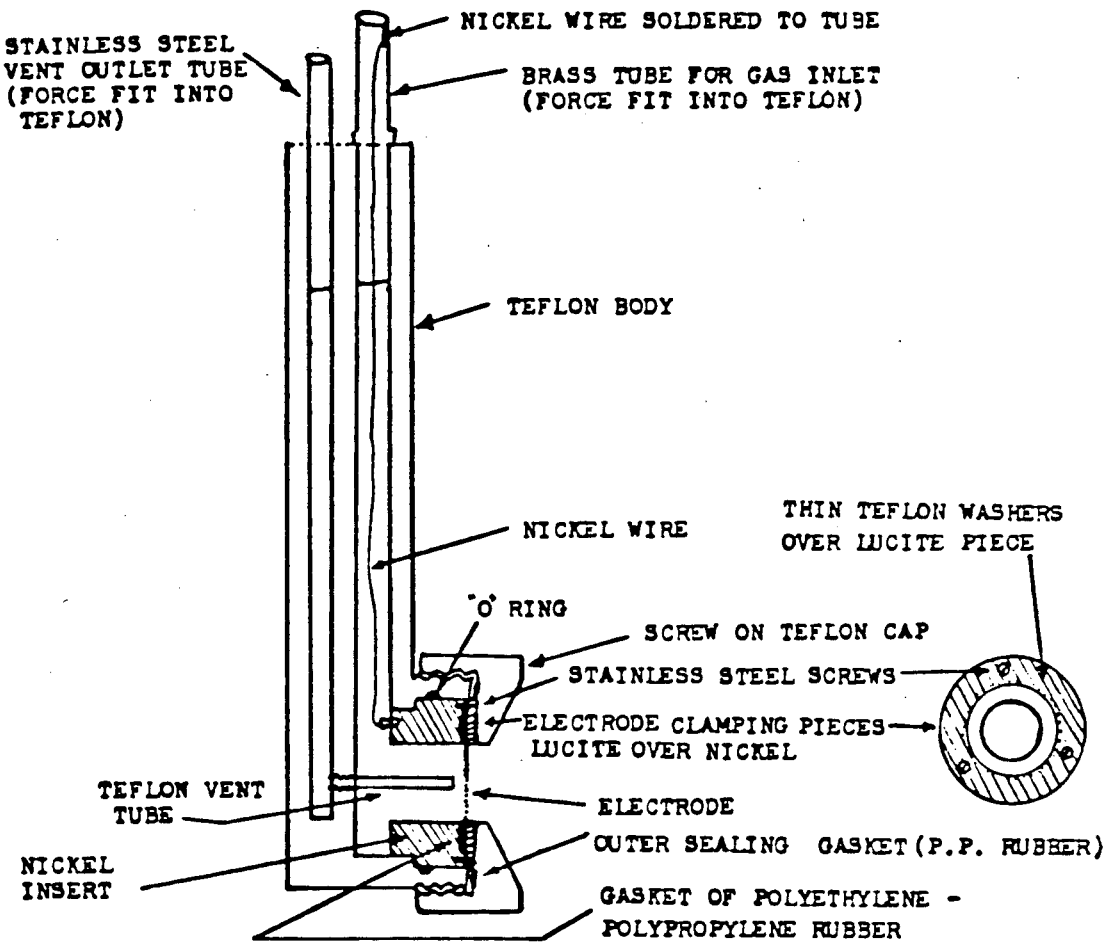


Fig. 5.1.14.3. Nickel and Teflon holder for electrode disks.

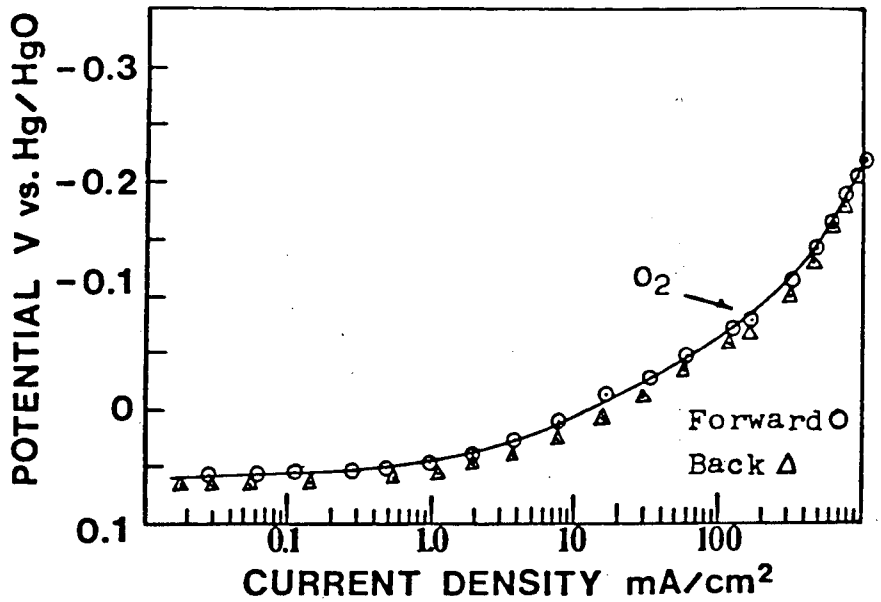


Fig. 5.1.14.4 Polarization Curve for O_2 reduction on a porous plug electrode consisting of a Pt catalyzed XC-72 carbon (10% Pt) with 30% Teflon. Electrode heated 3 Hrs. at 240°C. Polarization temperature: 85°C Electrolyte: 9 M NaOH. 1.2 mg Pt/cm^2 DPC-Z01

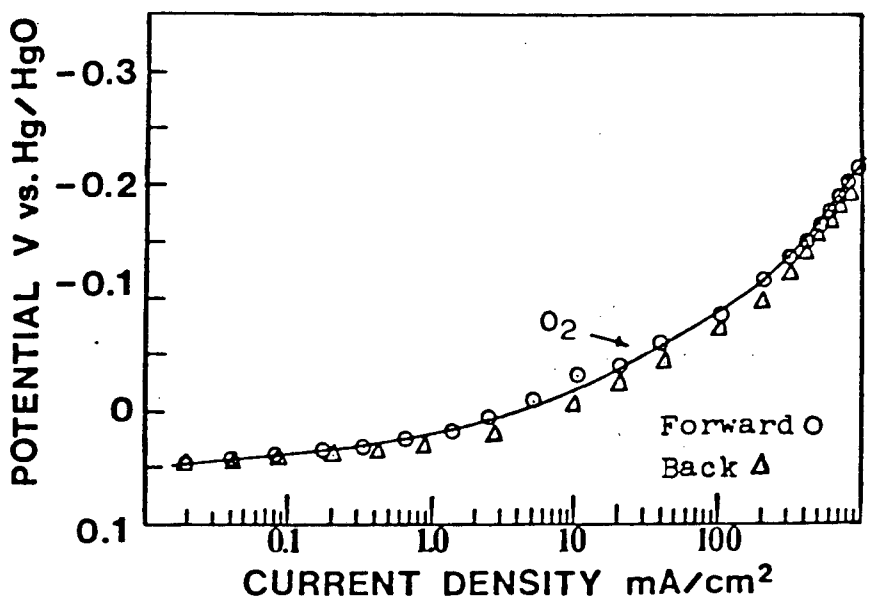


Fig. 5.1.14.5 Polarization Curve for O_2 reduction on an electrode consisting of a Pt and Cu catalyzed XC-72 carbon with 33% Teflon. Electrode heated 1 Hr. at 90°C. Polarization temperature: 85°C , Electrolyte: 9M NaOH PCCU006

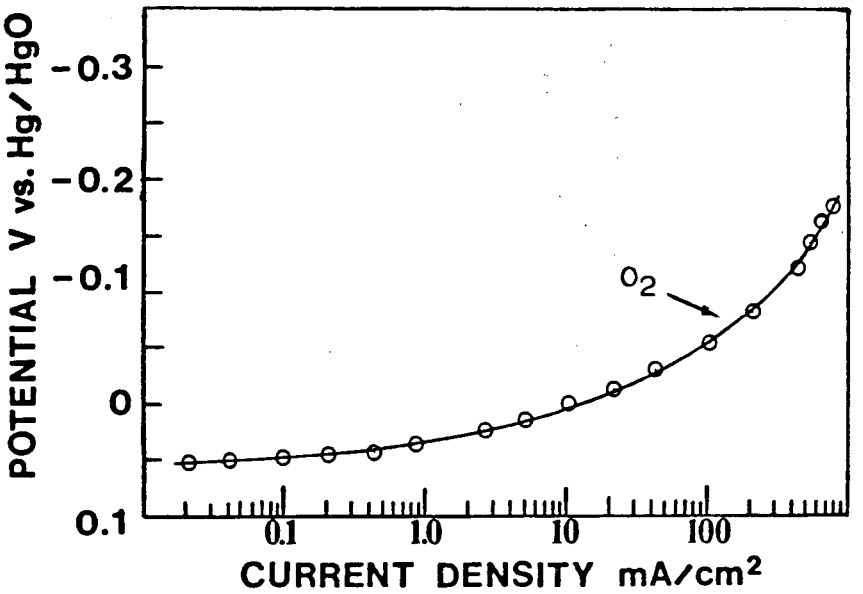


Fig. 5.1.14.6. Polarization Curve for O_2 reduction on an electrode consisting of CoTMPP catalyzed XC-72 carbon (10%) with 33% Teflon. Electrode heated 1 Hr. at 90°C. Polarization temperature: 85°C Electrolyte: 9 M NaOH PC-M650 (catalyzed carbon was H_2 treated at 650°C)

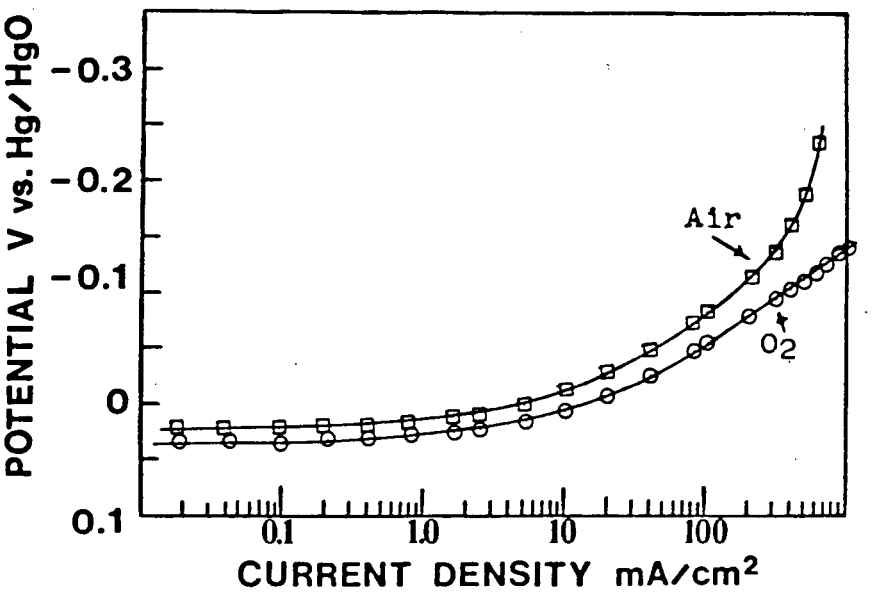


Fig. 5.1.14.7. Polarization Curve for O_2 reduction on an electrode consisting of CoTMPP catalyzed RB carbon (10%) with 33% Teflon. Electrode heated 1 Hr at 90°C. Polarization Temperature: 85°C, Electrolyte: 9 M NaOH. EMC Fabricated PCMRB480A catalyzed carbon was H_2 treated at 480°C)

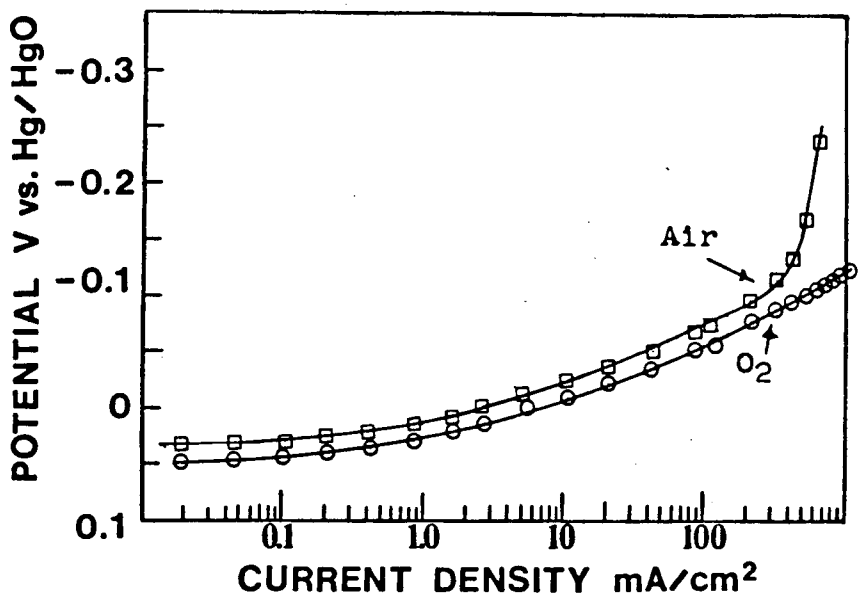


Fig. 5.1.14.8. Polarization Curve for O_2 reduction on an electrode consisting of CoTMPP catalyzed XC-72 carbon (10%) with 33% Teflon. Electrode heated 1 Hr. at 90°C. Polarization temperature: 85°C, Electrolyte: 9 M NaOH. EMC fabricated PCM 500B

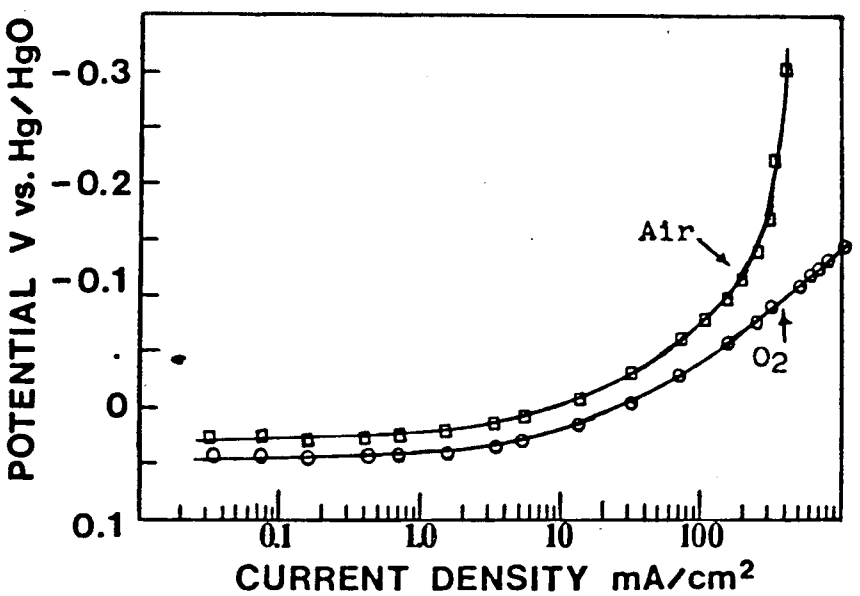


Fig. 5.1.14.9. Polarization Curve for O_2 reduction on an electrode consisting of CoTMPP catalyzed RB carbon (10%) with 33% Teflon. Electrode heated at 1 Hr. at 90°C. Polarization temperature: 85°C, Electrolyte: 9 M NaOH (Catalyzed carbon heated with H_2 at 450°C and N_2 at 9.00°C) GL M025

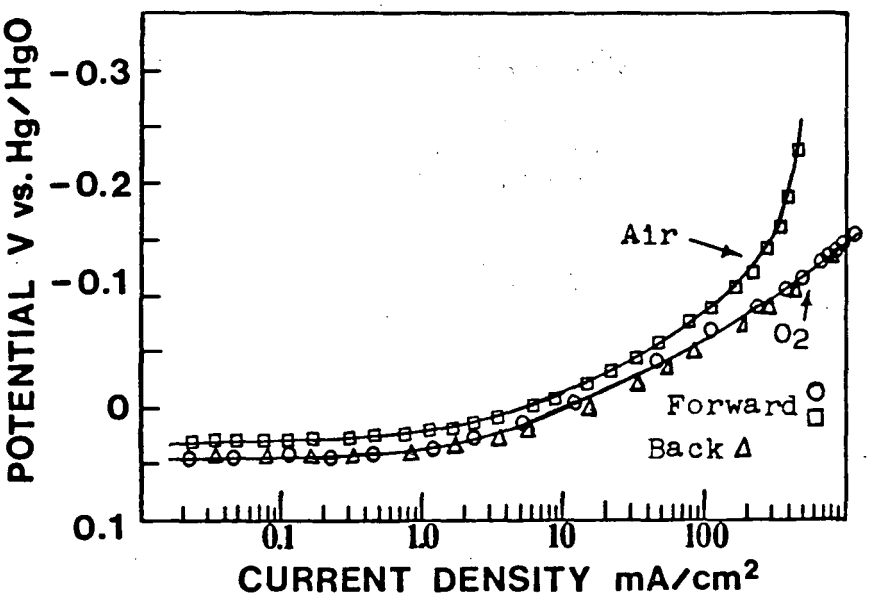


Fig. 5.1.14.10. Polarization Curve for O_2 reduction on an E.M.C. fabricated electrode consisting of CoTMPP catalyzed RB carbon (4%) with Teflon binder. Polarization temperature: 85°C, Electrolyte: 9 M NaOH (catalyzed carbon was heated with H_2 for 2 Hrs. at 450°C) 26A17158E350 (GL P033)

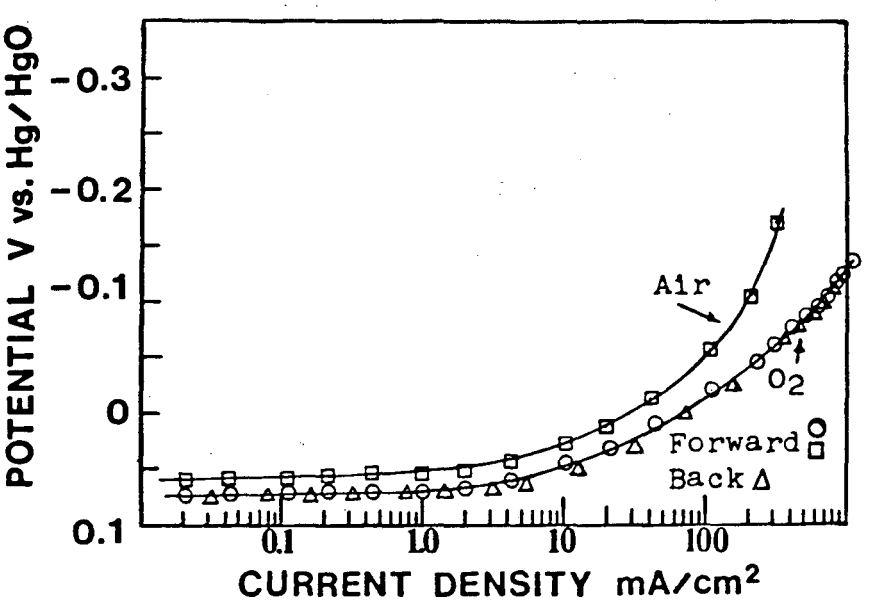


Fig. 5.1.14.11. Polarization Curve for O_2 reduction on an electrode consisting of CoOEP catalyzed RB carbon (10%) with 33% Teflon. Electrode heated 1 Hr. at 90°C. Polarization temperature: 85°C, Electrolyte: 9 M NaOH (catalyzed carbon was heated with H_2 for 2 Hrs. at 500°C) GLOP004 2 mg/cm^2 catalyst density

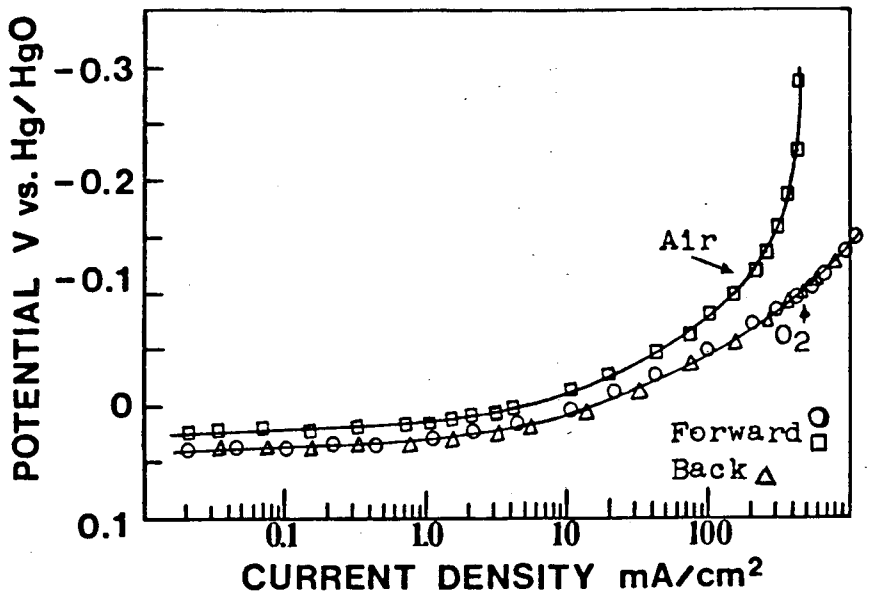


Fig. 5.1.14.12. Polarization Curve for O_2 reduction on an electrode consisting of CoTTFTP catalyzed RB carbon (5%) with 33% Teflon. Electrode heated 1 Hr. at 90°C. Polarization temperature: 85°C, Electrolyte: 9 M NaOH (catalyzed carbon was heated with H_2 for 2 Hrs. at 500°C) GL TFP002 1 mg/cm^2 catalyst density

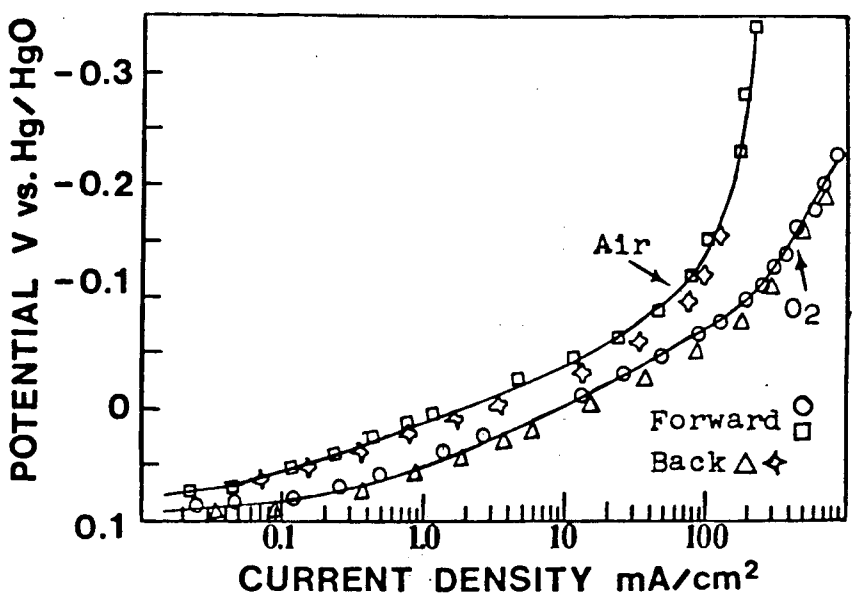


Fig. 5.1.14.13. Polarization Curve for O_2 reduction on a porous plug electrode consisting of half Stonehart PC1000 carbon (10% Pt) and half XC-72 carbon with 45% Teflon. Electrode heated 45 minutes at 270°C. (N_2) Polarization temperature: 85°C, Electrolyte: 9 M NaOH. 0.8 mg/cm^2 Pt density

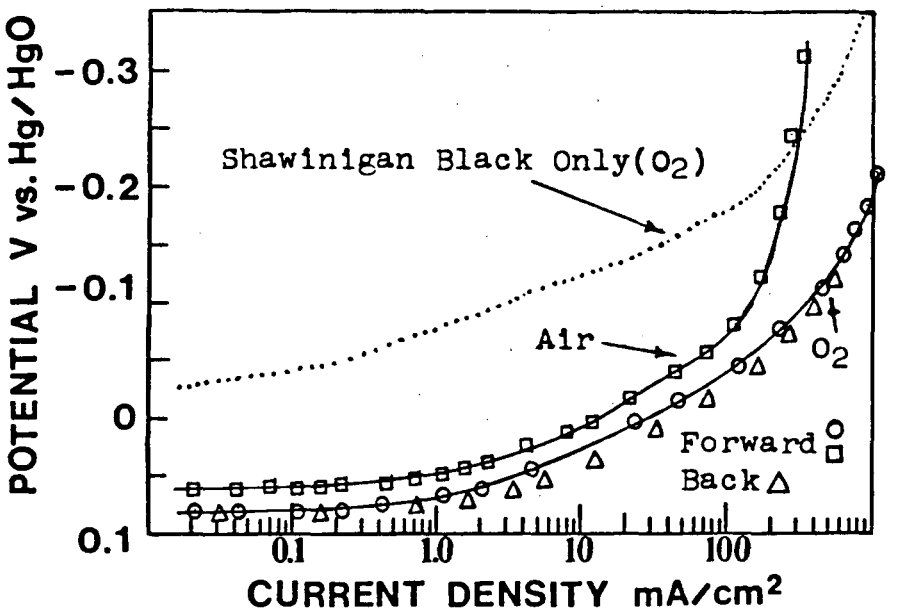


Fig. 5.1.14.14. Polarization Curve for O_2 reduction on an electrode consisting of Stonehart PC1000 carbon (10% Pt) with 40% Teflon. (Electrode was heated 4 Hrs. at 270°C in N_2). Polarization temperature: 85°C, Electrolyte: 9 M NaOH, WAPC1000H, 2.1 mg/cm² Pt density.

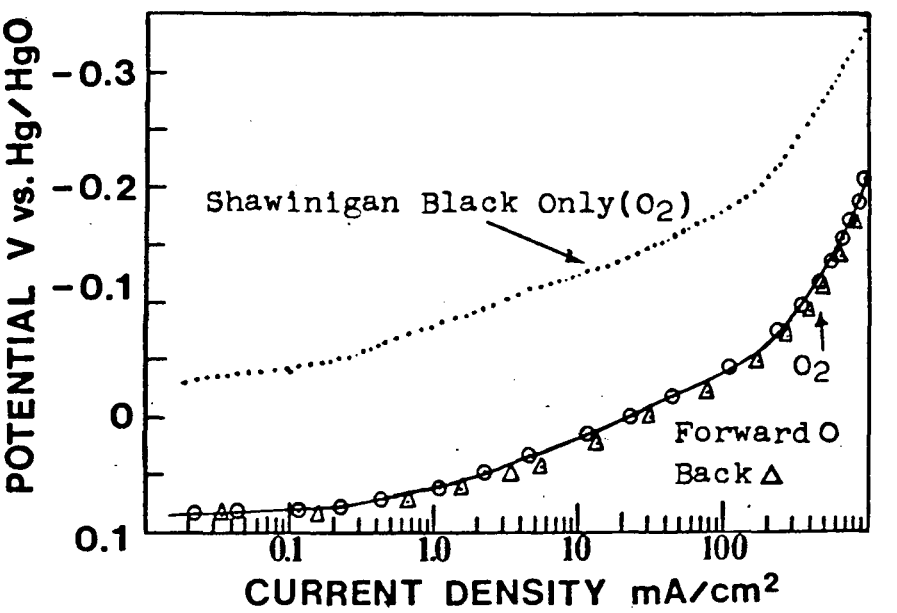


Fig. 5.1.14.15. Polarization Curve for O_2 reduction on an electrode consisting of half Stonehurt PC2000 carbon (10% Pt) and half Shawinigan Black (as Teflonated S.B.) Net Teflon: 15%. (Electrode was heated 3 Hrs. at 270°C in N_2). Polarization temperature: 85°C, Electrolyte: 9 M NaOH, WAPC2000 SWMX-1, 1.0 mg/cm² Pt density

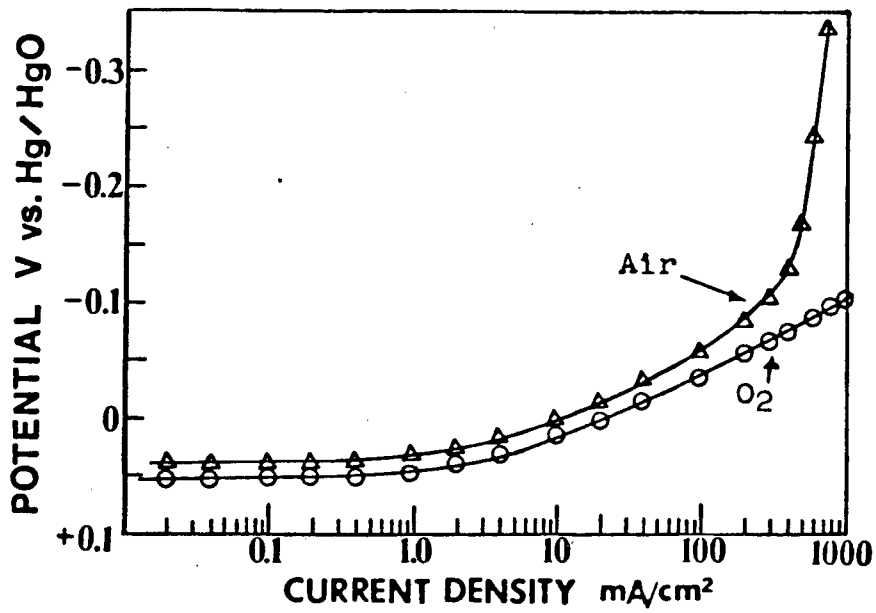


Fig. 5.1.14.16. Polarization Curve for O_2 reduction on an electrode consisting of CoTMPP catalyzed RB carbon (15%) with 30% Teflon. (Electrode was heated 4 Hrs. at 280°C in N_2 after stabilization with extra Triton X-100). Polarization temperature: 85°C, Electrolyte: 9 M NaOH GL-P018-MV 3mg/cm^2 Catalyst density

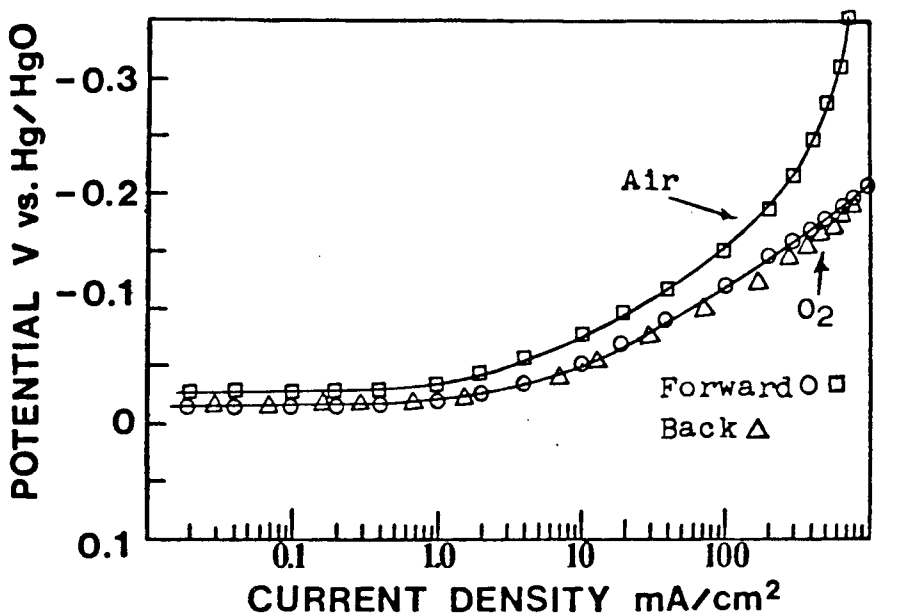


Fig. 5.1.14.17. Polarization Curve for O_2 reduction on an electrode consisting of RB carbon with 33% Teflon. (Electrode was heated 3 Hrs. at 280°C with N_2). Polarization temperature: 85°C, Electrolyte: 9 M NaOH GA-RBH1

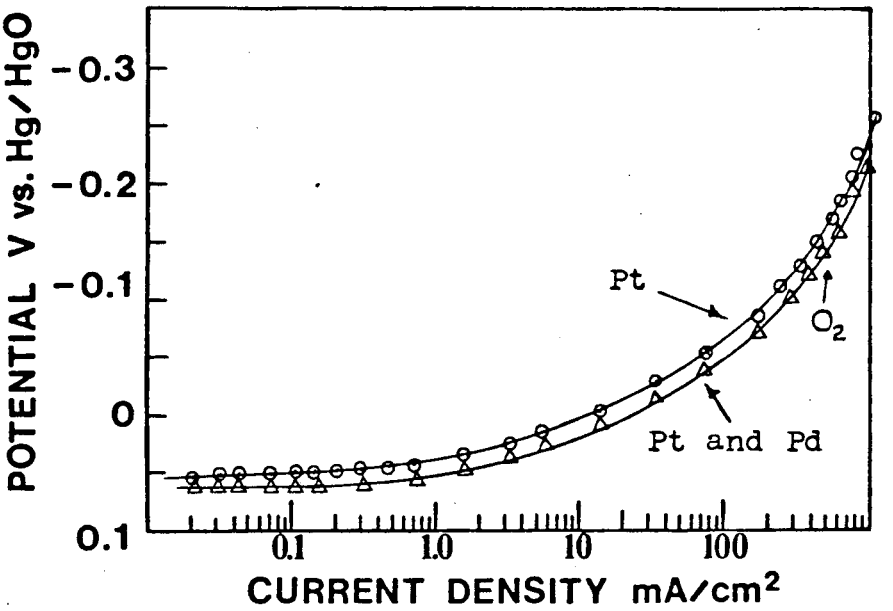


Fig. 5.1.14.18. Polarization Curves for O_2 reduction on electrodes consisting of CWRU (5%) Pt on preoxidized XC-72 carbon and Pt(5%) with Pd(2.7%) on preoxidized XC-72 with 40% Teflon. Electrode heated 5 Hr. at 285°C with N_2. Polarization Temp: 85°C, Electrolyte: 9 M NaOH, WA-RRPT-H1 (RRII-19-23), Pt: 1.1 mg/cm², Pd: 0.50 mg/cm², WARRPDPT-H1(RRII-80-27)

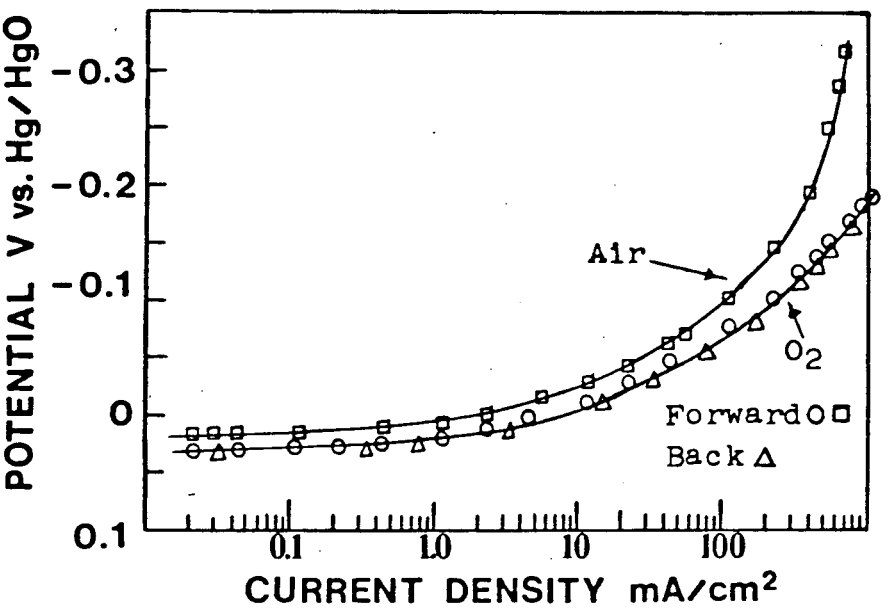


Fig. 5.1.14.19. Polarization Curve for O_2 reduction on an electrode consisting of CWRU Pt (5%) and Pd (2.7%) on preoxidized XC-72 carbon. Electrode fabricated by E.M.C. Polarization temperature: 85°C Electrolyte: 9 M NaOH EMC-F412 (RRII-80-27) Pt: 1.1 mg/cm², Pd: 0.5 mg/cm².

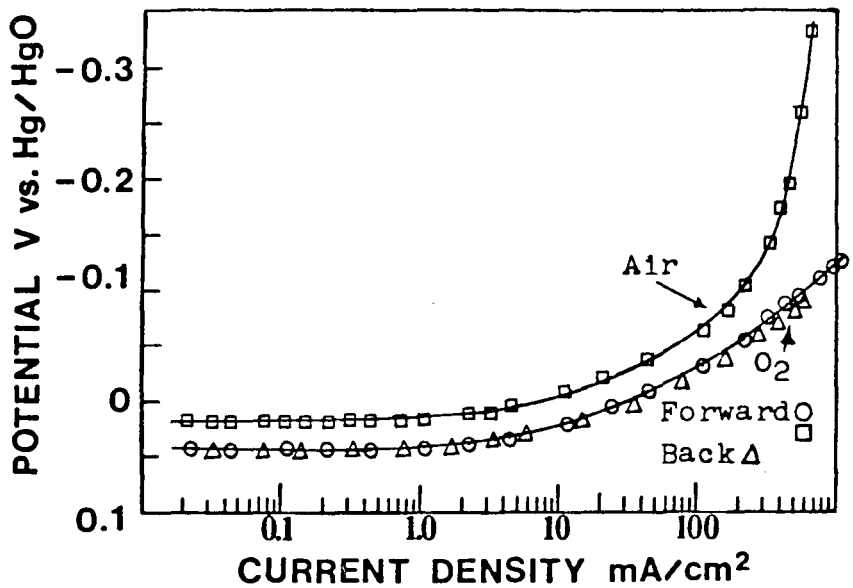


Fig. 5.1.14.20. Polarization Curve for O_2 reduction on an electrode consisting of CWRU Pt(5%) and Mo (2.4%) on preoxidized XC-72 carbon (Electrode fabricated by E.M.C.) Polarization temperature: 85°C Electrolyte: 9 M NaOH EMC-F465 (RRII-80-32) Pt: 0.58 mg/cm^2 Mo: 0.28 mg/cm^2.

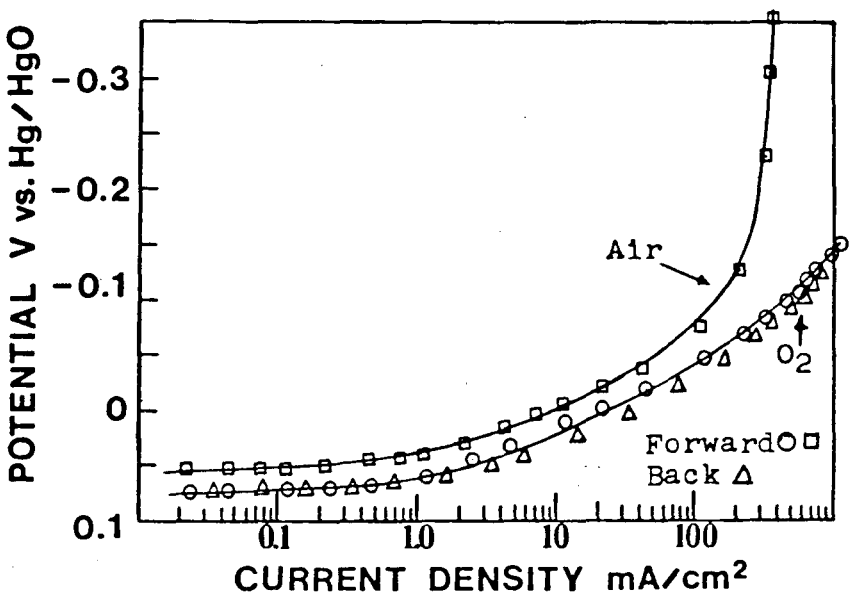


Fig. 5.1.14.21. Polarization Curve for O_2 reduction on an electrode consisting of CWRU Prototac Pt (10%) on preoxidized XC-72 carbon with 40% Teflon. (400°C heat treatment of Platinized carbon), Polarization temperature: 85°C, Electrolyte: 9 M NaOH WA-RPR400 (RRII-80-49) Pt: 2,1 mg/cm^2

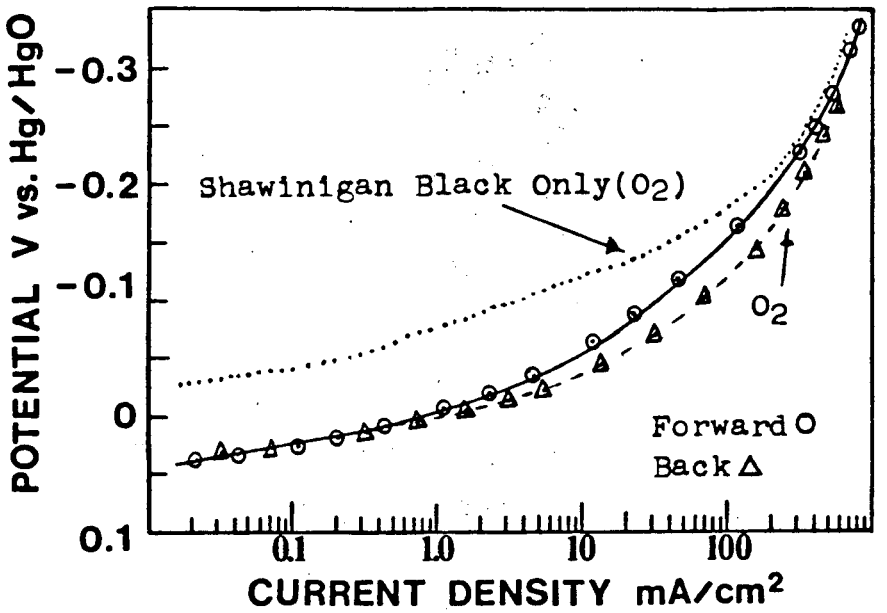


Fig. 5.1.14.22. Polarization Curve for O_2 reduction on an electrode consisting of 20% of $La_{0.5}Sr_{0.5}CoO_3$ and 80% Shawinigan Black (as T.S.B.). Teflon equivalent to 25.6%. Polarization temperature 85°C, electrolyte: 9M NaOH, WA-WLSC-SWMX, 5.5 mg catalyst/cm^2.

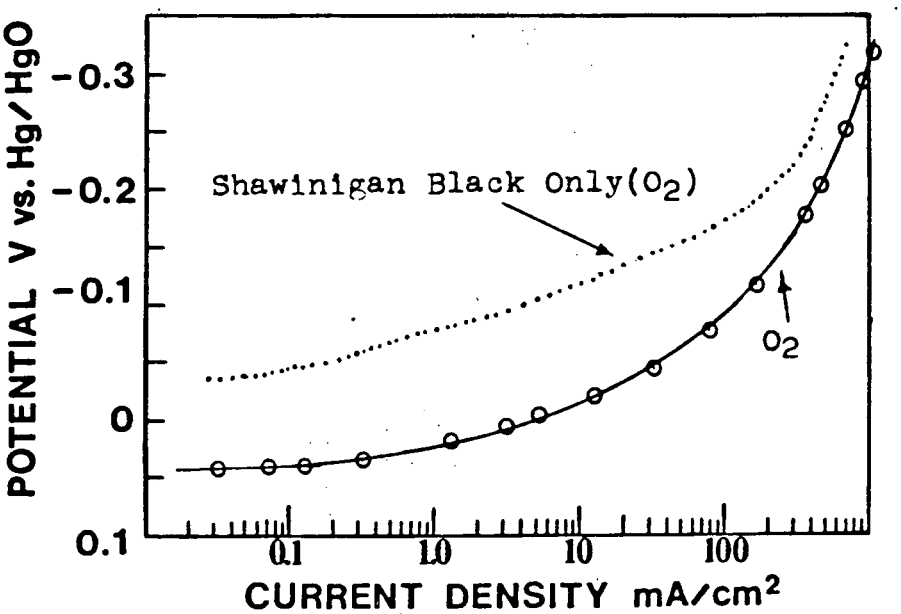


Fig. 5.1.14.23. Polarization Curve for O_2 reduction on an electrode consisting of 20% of a finely mortared $La_{0.5}Sr_{0.5}CoO_3$ and 80% Shawinigan Black (as T.S.B.). Teflon equivalent to 25.6%. Polarization temperature: 85°C; electrolyte: 9M NaOH. WA-WPR600, 5.5 mg/ catalyst/cm^2.

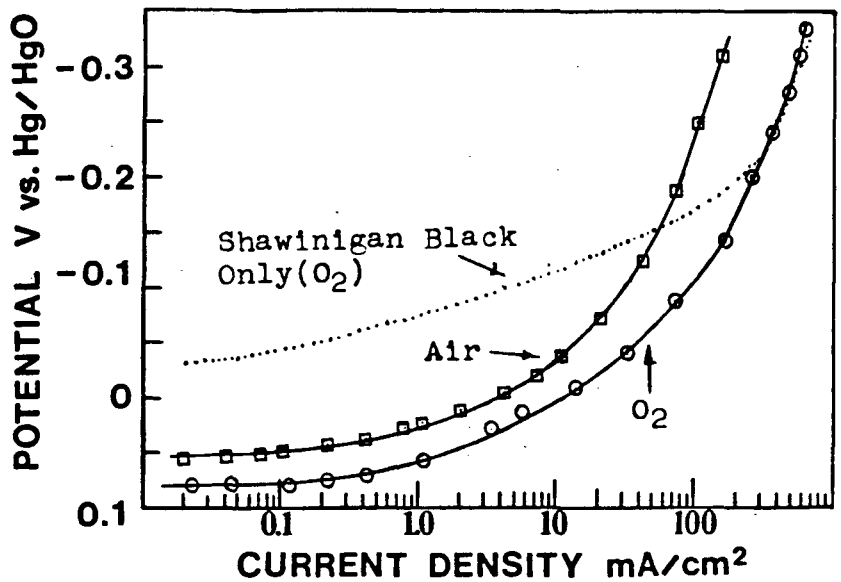


Fig. 5.1.14.24. Polarization Curve for O_2 reduction on an electrode consisting of 50% of a Pb doped perovskite ($La_{0.5}Sr_{0.25}Pb_{0.25}CoO_3$) with 50% Shawinigan Black (as T.S.B.) Teflon equivalent to 15%. Polarization temperature: 85°C, electrolyte: 9M NaOH, WA-WPRPB-MX2. 16 mg catalyst/cm^2.

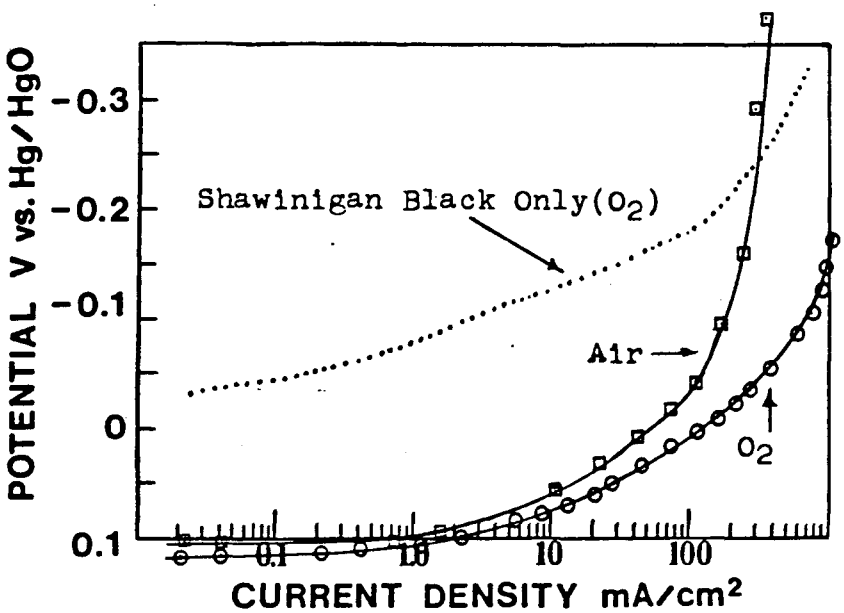


Fig. 5.1.14.25. Polarization Curve for O_2 reduction on an electrode consisting of 60 mg of Pb doped lead ruthenate ($Pb_2[Ru_{1.67}Pb_{0.33}]O_{6.5}$, 29 mg of Shawinigan Black (as T.S.B.) and 13 mg Teflon. Electrode heated 2 hrs at 210°C in N_2. Polarization temperature: 85°C, electrolyte: 9M NaOH, WA-RUPB-1 25 mg catalyst/cm^2.

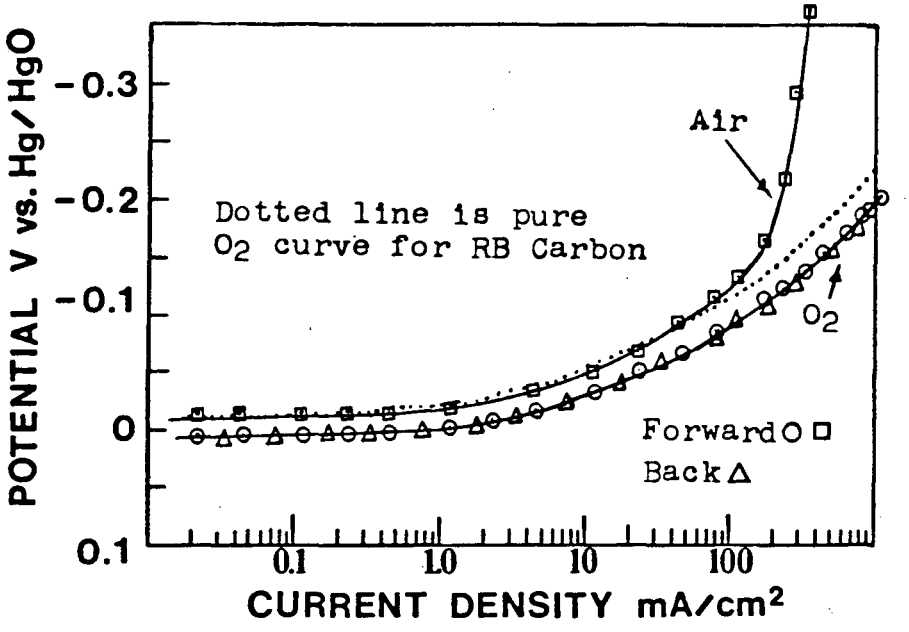


Fig. 5.1.14.26. Polarization Curve for O_2 reduction on an electrode consisting of 10% of a clamshell CoPc (Dimer) on RB carbon with 25% Teflon. Electrode heated 3 Hr. at 260°C in N_2. Polarization temperature: 85°C, Electrolyte: 9 M NaOH 2.5 mg catalyst/cm^2 Catalyzed carbon heated 3 Hr. in N_2 at 350°C.

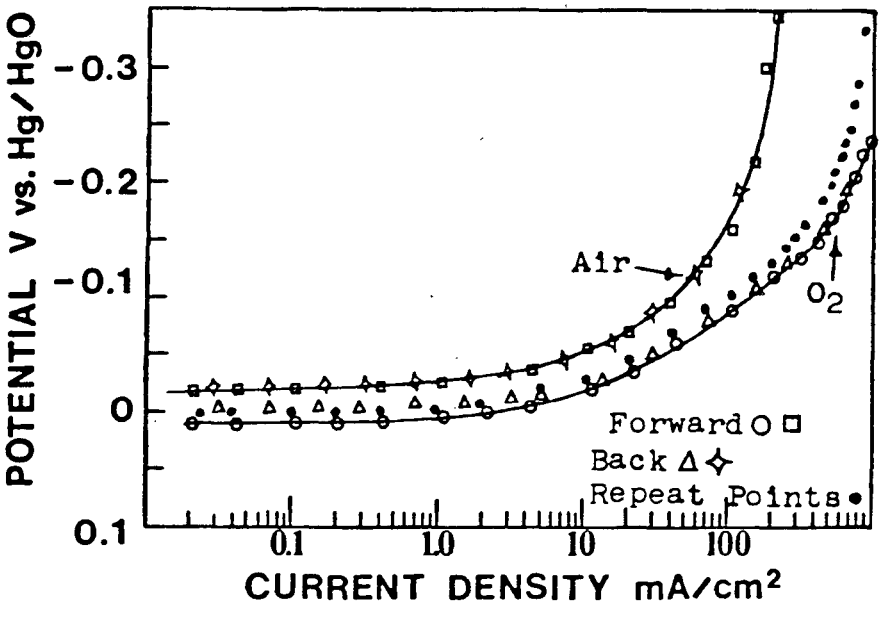


Fig. 5.1.14.27. Polarization Curve for O_2 reduction on an electrode consisting of 10% of a clamshell CoPc(Polymer) on RB carbon with 25% Teflon. Electrode heated 3 Hr at 270°C in N_2. Polarization temperature: 85°C, Electrolyte: 9 M NaOH 2.5 mg catalyst/cm^2 WA-GCOPCP. (Catalyzed carbon heated 5 Hr. in He at 550°C)

THE FABRICATION AND EVALUATION OF HIGH CURRENT DENSITY AIR CATHODES AT DIAMOND SHAMROCK

L.J. Gestaut and J.C. Huang
Diamond Shamrock Corporation
Painesville, Ohio 44077

6.1 INTRODUCTION

In previous reports the performance of air cathodes was linked to both the stability of the carbons and their inherent catalytic activity for oxygen reduction via a peroxide route.(1-3) The instability of these carbons was shown to manifest itself in the simultaneous loss of carbon and platinum surface area in operating electrodes. It was demonstrated that the loss of surface areas was consistent with a mechanism described as electrochemical isolation wherein regions of the electrode were not active for electrochemical processes due to the loss of contact to the bulk of the electrode.

This period we concentrated on the development of new, more chemically stable carbons for use in the electrodes, evaluation of those carbons prior to their fabrication into electrodes, and testing of electrodes from those materials. As a culmination of the air cathode program a description of the scale-up of the air cathode to a full-sized electrolyzer will also be described.

6.2 CARBON MODIFICATIONS

6.2.1 EXPERIMENTAL

Carbons were evaluated utilizing both electrochemical and non-electrochemical techniques. Electrochemical evaluation of the carbon was performed utilizing the rotating ring disc electrode (RRDE) technique. A small sample of the subject carbon powder was mixed with mineral oil to form a paste of thick consistency. The proportions of the materials varied from carbon to carbon due to the different surface and wetting characteristics of the carbons tested. The thick paste was then placed in a recessed gold disc cavity such that the surface of the paste, which now formed the disc electrode, was smooth to the eye. The ring electrode was gold, 0.46 mm wide and 0.5 mm from the edge of the carbon surface. The RRDE experiment was carried out in 1.0M NaOH at room temperature. The measurements were made against a Hg/HgO reference electrode in 1.0M NaOH and converted to

potentials vs. the reversible hydrogen electrode (RHE). The potential ramp was generated by a PAR 175 programmer in association with a Pine Intstruments Bipotentiostat. Peroxide detection was performed by monitoring the peroxide oxidation current at the ring electrode which was potentiostatically held at 1330 mV/RHE.

The heterogeneous decomposition of hydrogen peroxide on the carbon surface was measured by monitoring gas evolution in a sealed system containing a sample of the subject carbon and 100 ml of 2.3M NaOH at 50 deg C. To this sample 400 microliter of 30% hydrogen peroxide was added and the rate of oxygen evolution was measured by collecting the gas in a pneumatic trough. Samples followed psuedo-first order kinetics and the resultant rate constants provided a self-consistant measurement of the rates of peroxide decomposition when the carbon samples were stable. Certain doped samples were found to color the solution indicating their instability. In these cases inordinately high values for the rate constant were obtained, indicating the homogeneous metal-ion catalyzed decomposition of the hydrogen peroxide. Such a carbon, of course, would not be suitable for inclusion in an electrode.

6.2.2 UNTREATED CARBONS

Several carbons were selected as candidates for modification. In order to determine if the treatments were altering the performance of the materials, baseline experiments were performed to determine the activity of the native carbons. These results are summarized in Table 1.

Table 1. Activity of Untreated Carbons

Carbon	Surface Area sq m/g	E(1/2) vs.RHE mV	I(disc) mA @500mV	I(ring) uA	Ir/Id (E-2)	k(H2O2) [min(-1) g(-1)]
RBDA	1000	720	0.75	40	5.3	2.7
XC-72R	265	200	0.8 @-24mV	23 @-24mV	29 @-24mV	<0.1
Ultra-C	1000	675	0.7	30	4.2	2.2
SB	60	635	0.6	5	0.8	0.1
KB	1000	95	0.01	1.5	15	0.1
Kocite UB104	80	680	0.67	30	4.5	--
Degussa Aktiv-Kohl	650	675	0.72	25	3.5	0.7

RBDA = Deashed Pittsburg RB Carbon
XC-72R = Vulcan XC-72R Carbon
Ultra-C = Norit Ultra-C
SB = Shawinigan Black
KB = Ketjenblack

As can be seen from the table, large differences exist between available carbons, even before any modification. Further, no set pattern of activity seems to emerge between carbons. It must be remembered, though, that differences exist between the carbons beyond those given in the table. One major difference, for example, is the method of manufacture of the carbons. RB carbon is considered to be an active carbon while XC-72R is a carbon black. It is certain that these different manufacturing methods result in different surface chemistries and morphologies which, in turn, determine their electrochemical and catalytic properties.

Addition of a platinum catalyst to the carbons, as anticipated, dramatically changes, the materials activity. Several such samples are described in Table 2.

Table 2. Activity of Platinized Untreated Carbons

Carbon	Platinum Loading (w/w)	E(1/2) vs.RHE mV	I(disc) mA @425mV	I(ring) uA	Ir/Id (E-2)	k(H2O2) [min(-1) g(-1)]
RBDA	5%	750	1.09	37	3.4	6.9
RBDA	10%	755	1.12	26	2.3	9.1
RBDA	25%	780	1.90	13	0.66	15
KB	5%	435	0.1	6	6.0	21
KB	5%*	440	0.5	8	1.5	31
KB	5%*	550	0.94	25	2.6	20
XC-72R	5%	700	0.84	31	3.7	<0.1
Ultra-C	5%	740	1.08	36	3.3	4.7

* Reduced in hydrogen atmosphere

It is immediately obvious that the differences that characterized the uncatalyzed material are also relevant to the catalyzed carbons. The data for the RB carbon indicate that the increasing proportions of platinum not only shift the half-wave potentials to more anodic values, but also increase the rate at which peroxide is eliminated from solution. The KB data indicate that these two processes are not directly related, however. Samples with comparitively cathodic oxygen reduction half-wave potentials have peroxide elimination rate constants comparable to those for the platinized RB carbons.

Particle sizes and particle shapes also differ between these materials. These properties have a distinct effect on the characteristics of the electrodes fabricated from the carbons. For all these reasons it is best to compare each individual carbon and its modifications separately. In order to limit the scope of the study to a managable number of samples, only RB, SB, XC-72R, and KB were subjected to further experimentation.

6.2.3 RB CARBON

6.2.3.1 CARBON POWDER STUDIES

RB carbons were subjected to heat treatments of varying duration to determine whether such a treatment could significantly alter the electrocatalytic activity of the active carbon surface. Table 3 gives the electrochemical characteristics for oxygen reduction of the treated carbons.

Table 3. Heat Treatment of RB Carbons
560 deg C, Air Atmosphere

Treatment Time (min.)	E(1/2) vs.RHE mV	I(disc) mA @425mV	I(ring) uA	Ir/Id (E-2)	k(H2O2) [min(-1) g(-1)]
0	720	0.75	40	5.3	2.7
10	740	0.75	44	5.8	2.9
20	725	0.77	41	5.3	3.6
30	700	0.69	39	5.6	3.6

These variations, particularly in the rates of peroxide elimination, were experimentally significant; but were not felt to be large enough to merit a full scale investigation into their utility in actual electrodes. It was previously demonstrated (3) that uncatalyzed, untreated active carbon electrodes are not capable of lifetimes of commercial interest.

6.2.3.2 ELECTRODE STUDIES

By comparison, mixtures of RB carbon in the proprietary Q3-type electrode structure (which contains a second non-active carbon) catalyzed with platinum perform satisfactorily for a longer period (Figures 1 and 2). The cathodes still tend to suffer from performance decline that is consistent with carbon corrosion, however.

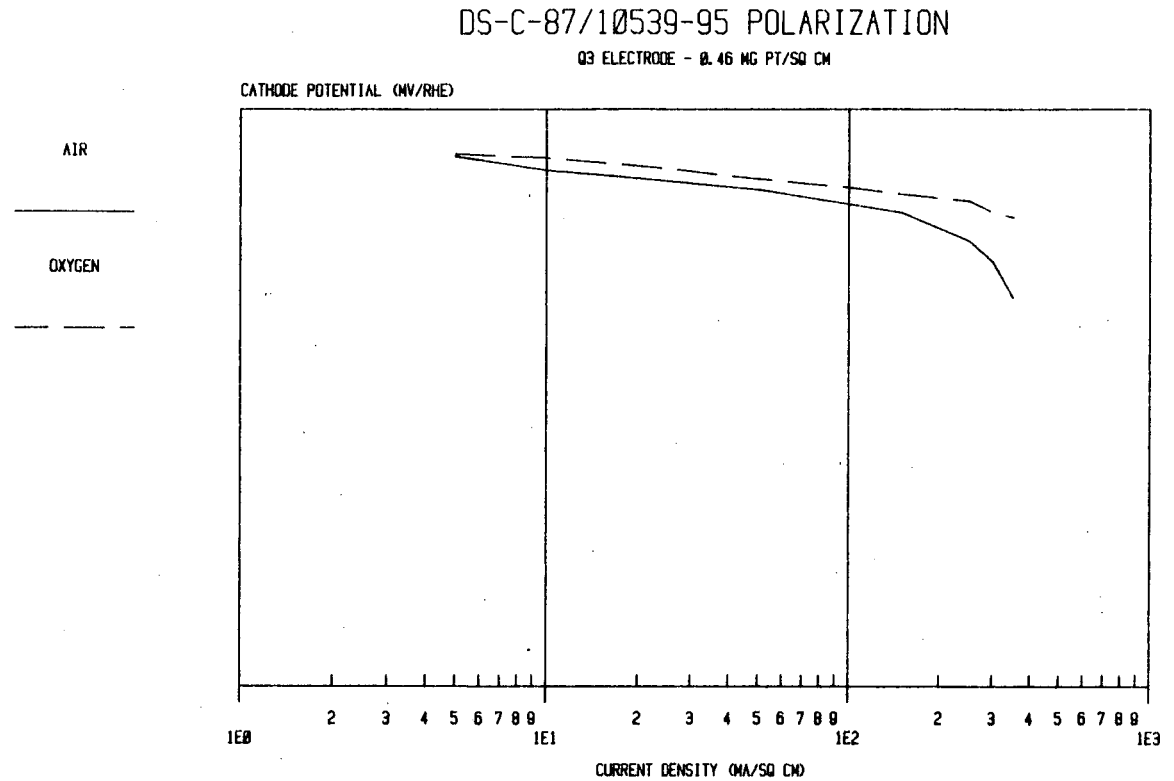


Figure 1.
RB Platinum Catalyzed Q3 Electrode Polarizations

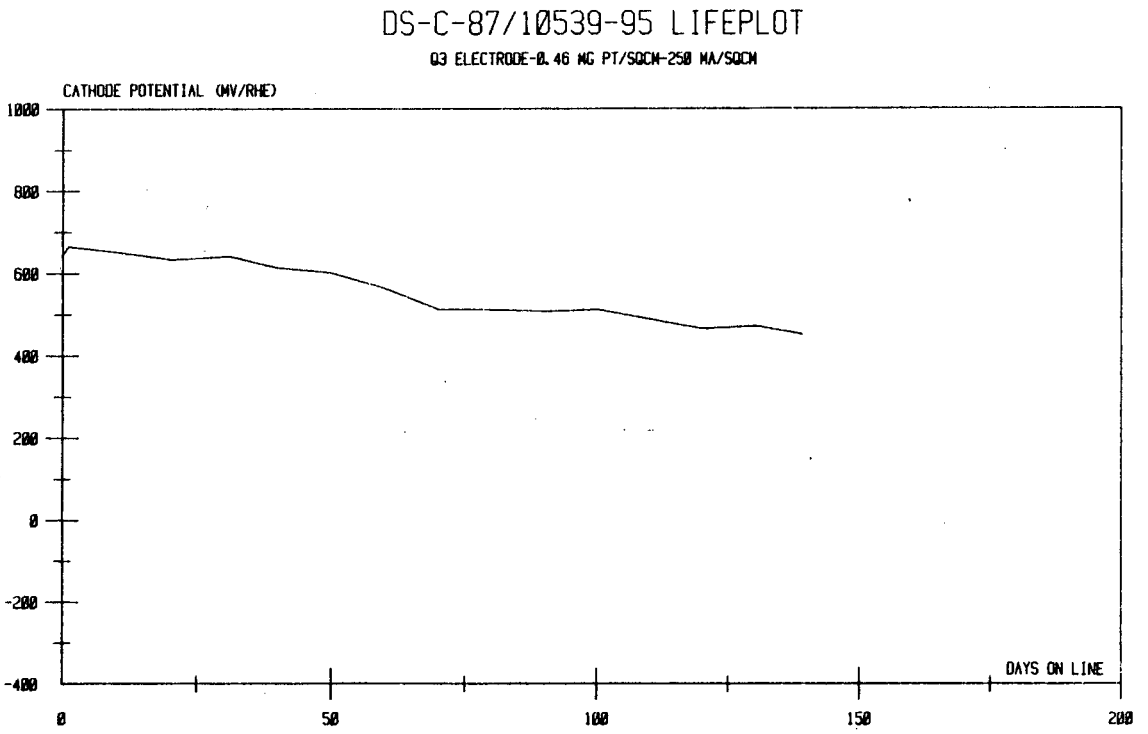


Figure 2.
RB Platinum Catalyzed Q3 Electrode Lifetimes

6.2.4 SHAWINIGAN BLACK CARBON STUDIES

Shawinigan Black (SB) carbon was modified by steam oxidation of the carbon and treatment with salts of nickel, cobalt, aluminum, and ruthenium followed by thermal oxidation at 1000 deg C in steam/nitrogen. The resultant catalyzed material was bound with a sucrose binder and subsequently thermally treated in steam/nitrogen at 1000 deg C. Some materials, noted in the tables, were acid washed with dilute hydrochloric acid prior to testing to remove unreacted metal salts. The materials so prepared were utilized for both the carbon powder studies and the electrode studies described below.

6.2.4.1 CARBON POWDER STUDIES

Table 4 describes the results of RRDE studies on modified SB carbon.

Table 4. Modified Shawinigan Black Powder Studies

Sample 11116-	Ni:Co:Al:Ru umole/g C (X 10)	E(1/2) vs.RHE mV	I(disc) mA @425mV	I(ring) uA	Ir/Id (E-2)	k(H2O2) [min(-1) g(-1)]
88	2:5:6:1	535	0.11	3	2.7	24
88(AW)	2:5:6:1	540	0.4	13	3.3	20
89(AW)	2:5:6:1	720	0.9	9	1.0	16
90	2:5:6:1	610	0.3	10	3.1	32
92(AW)	1:10:10:0.25	500	0.11	6	5.5	18
1	1:2.5:1:0.1	600	0.045	2.5	5.5	7
4	2:5:2:0.2	505	0.22	4.5	2.0	14
100*	0.1:1:1:.025	560	0.26	8.5	3.3	35

AW = Acid Washed
* = Not Sucrose Bound

The data do not present any clear trend, but it is interesting to note that the best performance is obtained from sample 11116-89(AW) which has the most anodic half-wave potential and also the lowest Ir/Id ratio. It also only moderately catalyzed the decomposition of hydrogen peroxide.

A possible explanation is an increased ability of this material to catalyze the four electron reduction of oxygen to hydroxide rather than the two electron reduction to peroxide.

6.2.4.2 ELECTRODE STUDIES

Figures 3 and 4 illustrate polarization curves for two samples of sugar-bonded, steam-activated, metal oxide/platinum catalyzed electrodes.

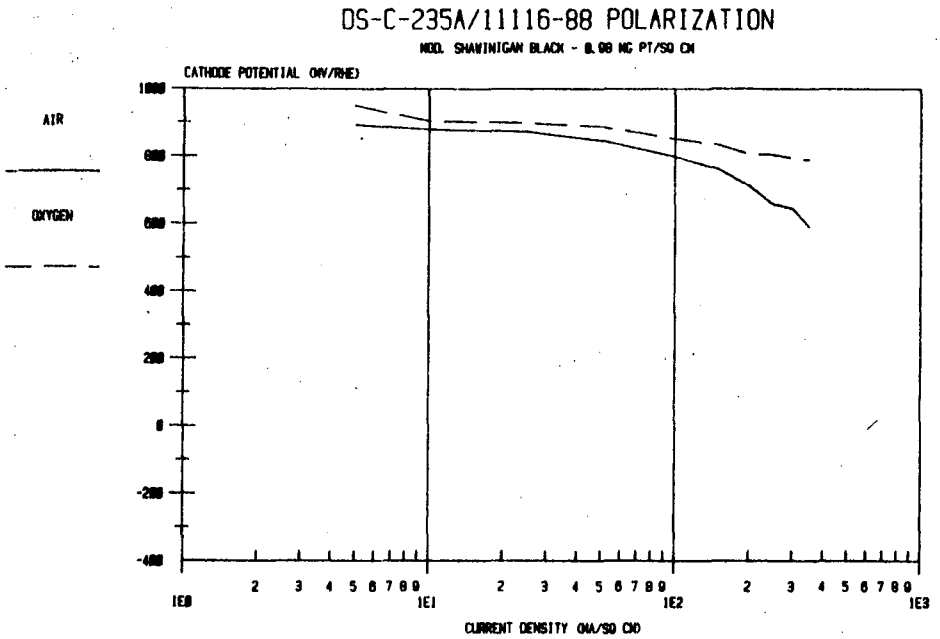


Figure 3.
Polarization of Modified Shawinigan Black Electrode.

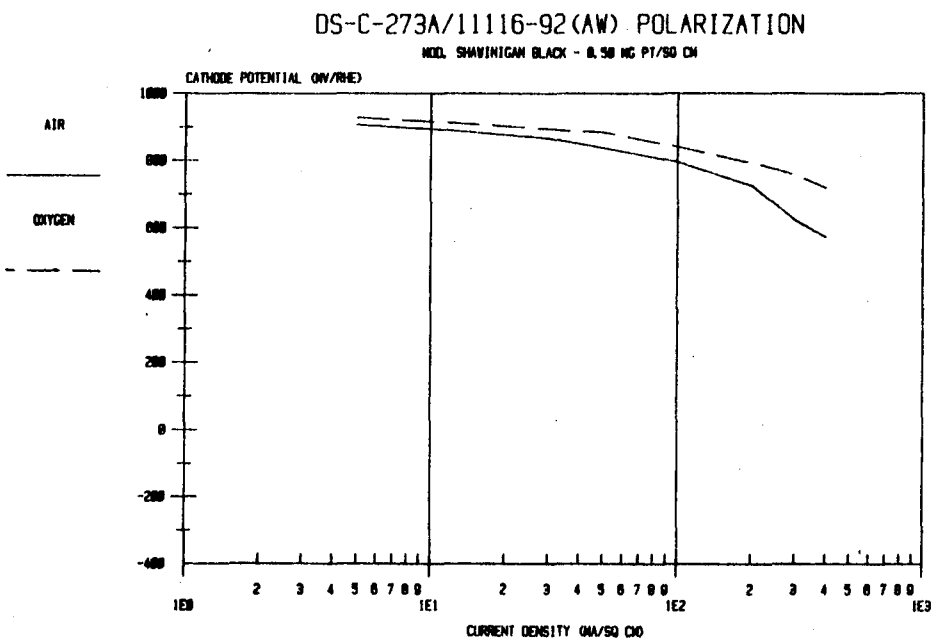


Figure 4.
Polarization of Modified Shawinigan Black Electrode.

Both curves illustrate mass transport limitations in the electrode. While the performance with an oxygen feed is adequate, at higher current densities and air as the depolarizing gas the performance declines rapidly. When used as an oxygen cathode the electrode performs well for extended periods of time (Figure 5) . Further, the polarization of the electrode does not change drastically as the cathode operates (Figure 6). However, when the performance of such an electrode is monitored as a function of time with air as the depolarizing gas a decay rate of approximately 2 mV/day is observed (current density = 2.5 kA/sq m). Such a decay is not adequate for long term operation in a chlor-alkali cell.

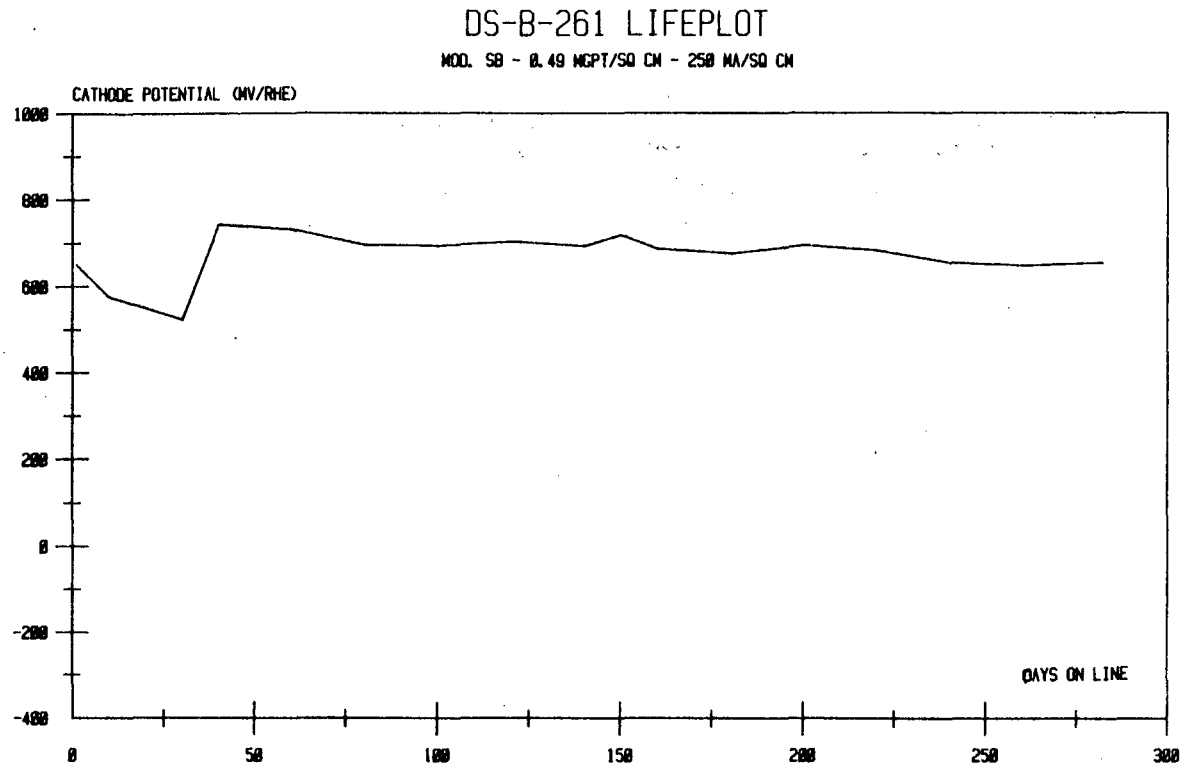


Figure 5.
Lifetest of Modified Shawinigan Black Electrode.

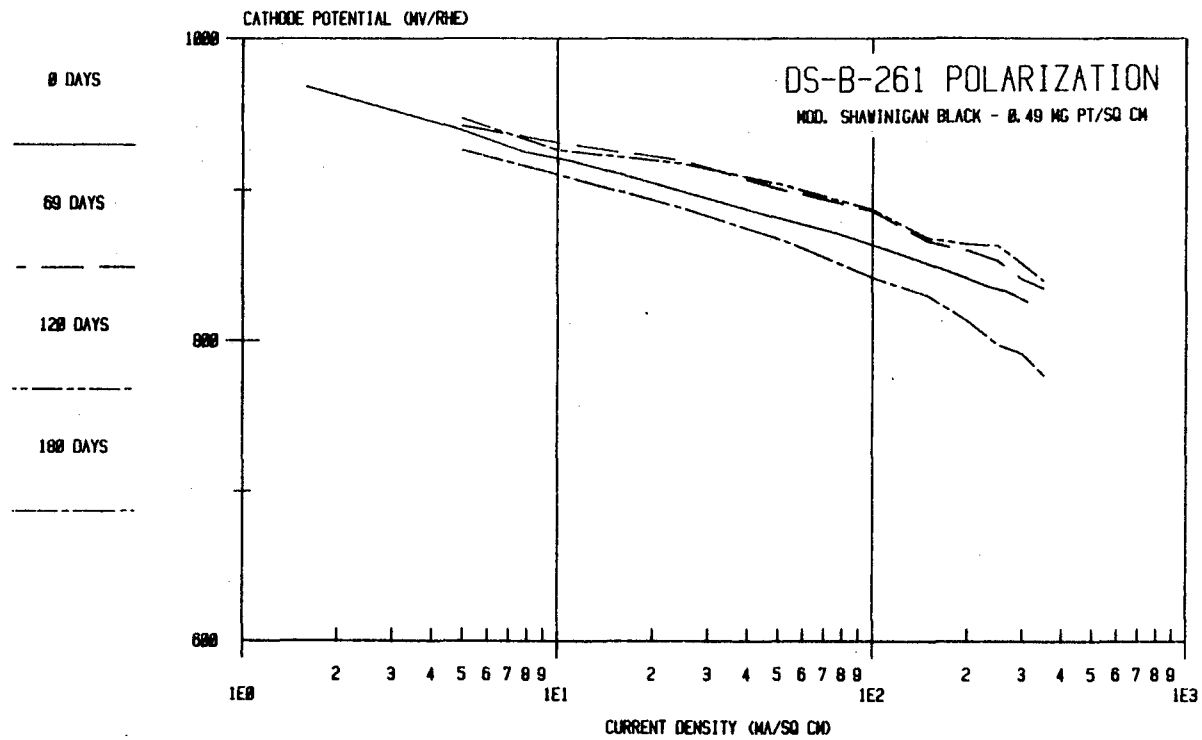


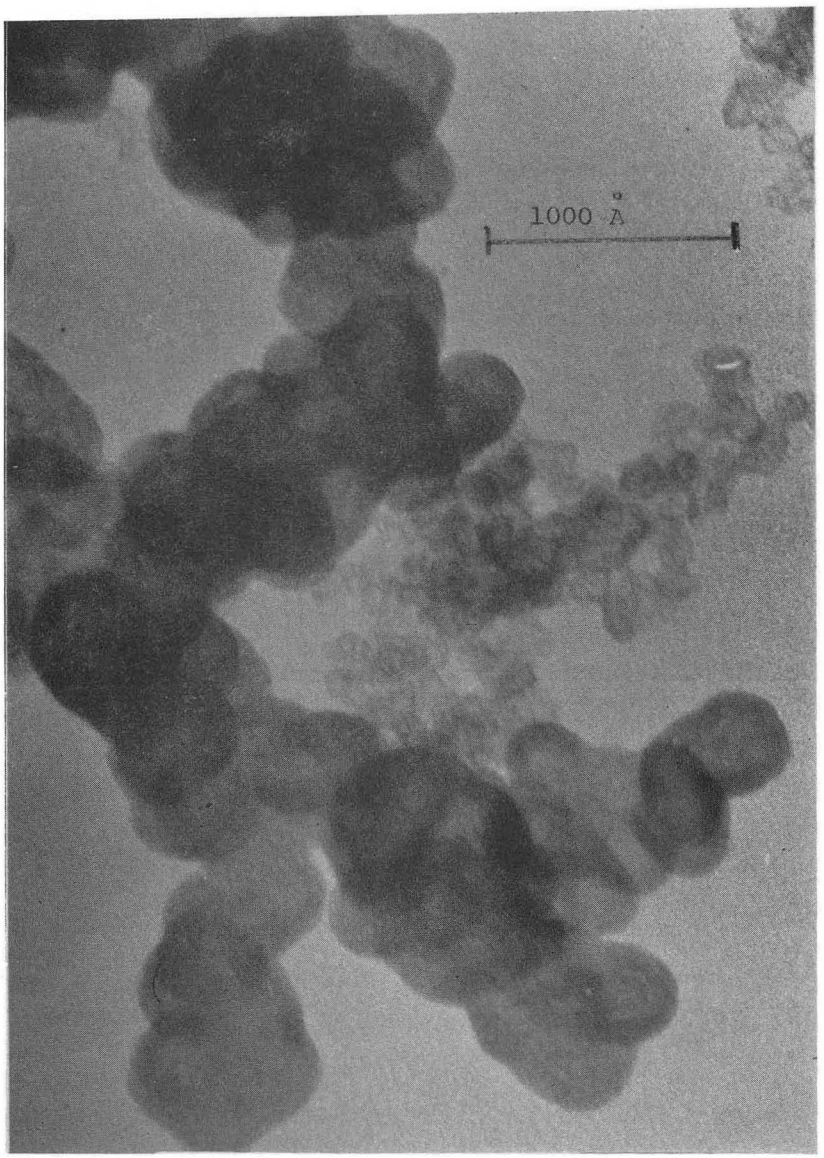
Figure 6.
Life/Polarization Profile of
Modified Shawinigan Black Electrode.

6.2.4.3 EVALUATION

While modification of Shawinigan black produced a material of good activity in an electrochemical sense, the structures formed from that material do not seem capable of extended performance on air at acceptable voltages. No further development was performed on these materials.

6.2.5 XC-72R CARBON

It was previously observed that Vulcan XC-72R, a carbon black manufactured by the Cabot Corporation, exhibited good resistance to corrosion, but was not capable of supporting sufficient mass transport in these electrode structures to allow high current density operation. In an attempt to enhance the mass transport characteristics of the carbon it was subjected to steam/nitrogen activation at 1000 deg C. The micrographs in Figure 7 show the effect of such a steam activation on the carbon. These micrographs suggest the elimination of carbon from the interior of the spherical carbon particles was accomplished, leaving hollow spheres. These spheres were then subjected to carbon and electrode studies.



XBB 8310-8670

Figure 7. Platinized Steam-Activated XC-72R.

6.2.5.1 CARBON POWDER STUDIES

As shown in Table 5, the electrocatalytic properties of the carbon do not appear to have been changed greatly by the steam treatment. Even catalysis by 5% platinum via the Prototech method (USP 4,044,193) did not greatly alter the half-wave potential for oxygen reduction, though the rate of hydrogen peroxide elimination was greatly enhanced.

Table 5. XC-72R Steam Activated Carbon

Carbon Treatment	Surface Area sq m/g	E(1/2) vs.RHE mV	I(disc) mA @425mV	I(ring) uA	Ir/Id (E-2)	k(H2O2) [min(-1) g(-1)]
Untreated	265	200	0.8 @-24mV	23 @-24mV	29 @-24mV	<0.1
Steam Activated 5% Pt (w/w)	422*	270	0.14	5	3.6	11

*BET surface area prior to platinization.

6.2.5.2. ELECTRODE STUDIES

While RRDE experiments would predict a low activity for electrodes fabricated from XC-72R, suprisingly high activity was actually obtained. Figures 8 and 9 illustrate the polarization of two such electrodes. In both cases, the performance on oxygen is adequate, however the performance on air is not as good at high current densities. This reflects mass transport difficulties within the electrode and is also observed in non-steam treated electrodes. Lifetests of these two electrodes were performed (Figure 10). The first electrode was operated under standard operating conditions at 155 mA/sq cm, the second was operated at 250 mA/ sq cm. The low current density electrode operated almost 50 days before a sudden decline in performance was noted. The sample operating at 250 mA/sq cm operated less than ten days before a sudden drop in its performance was noted.

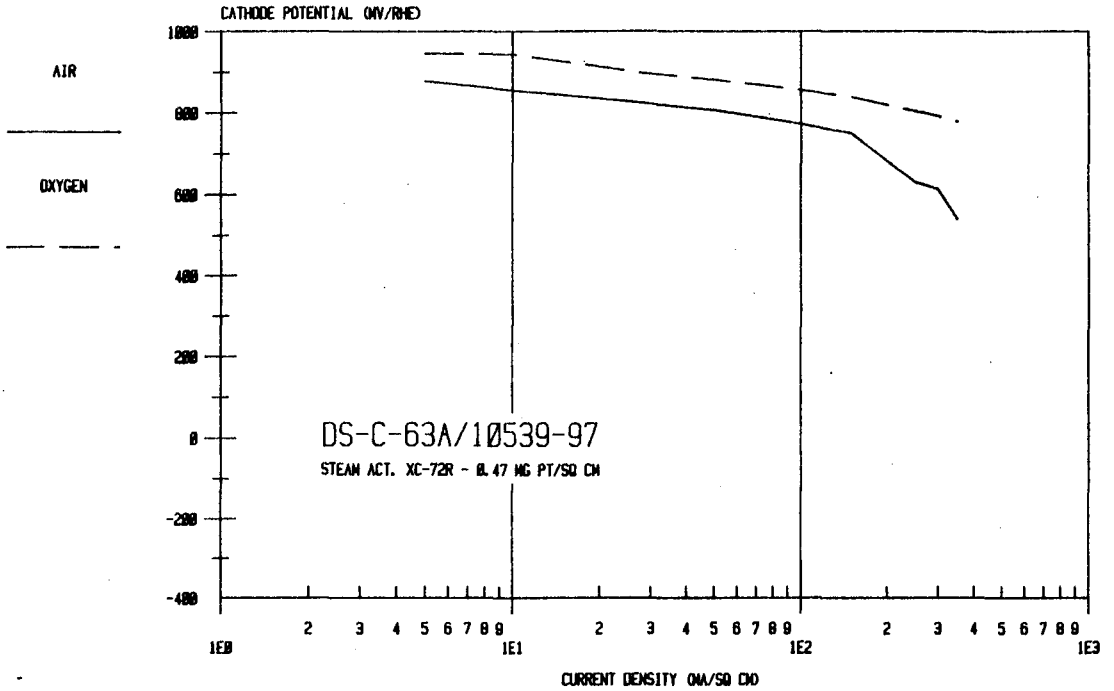


Figure 8. Polarization of Modified XC-72R Electrode.

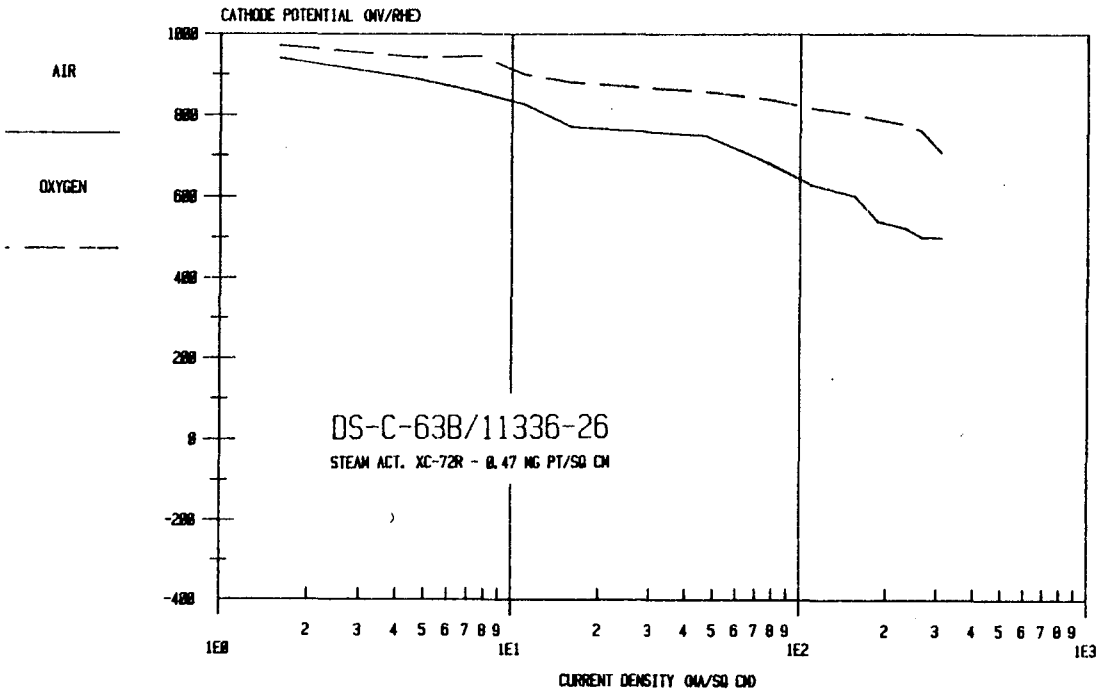


Figure 9. Polarization of Modified XC-72R Electrode.

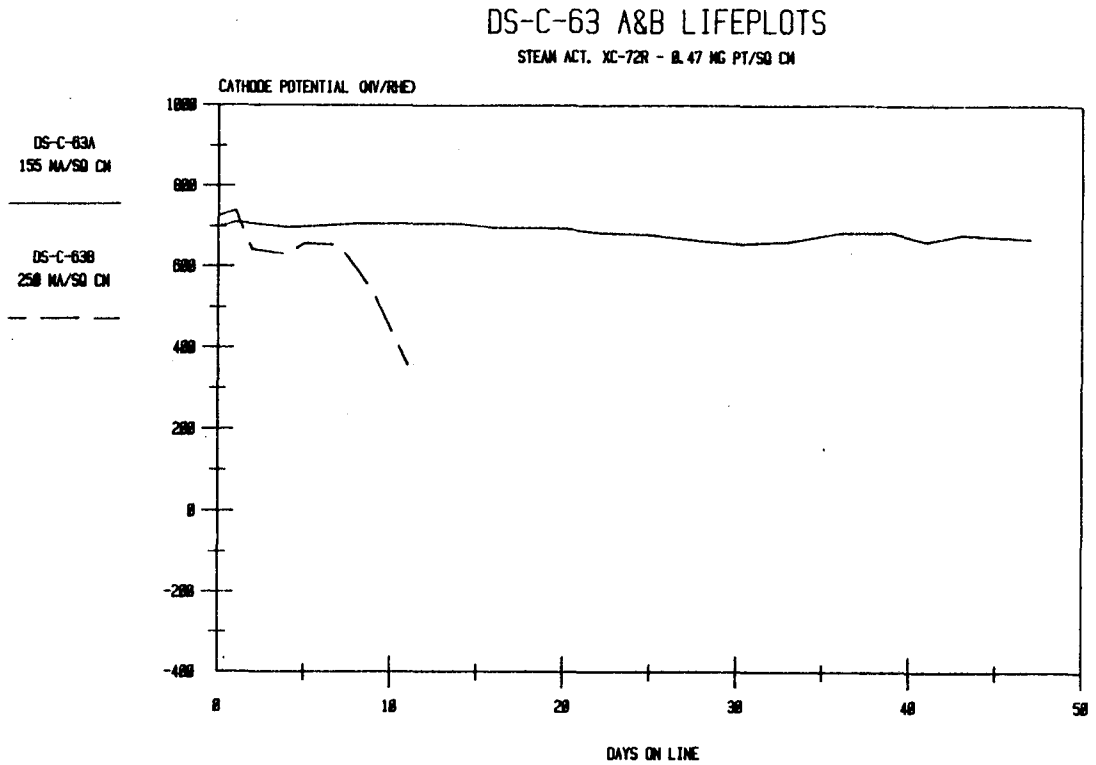


Figure 10. Lifetest of Modified XC-72R Electrode.

In light of the RRDE results it is rather suprising to see the electrodes operating at such anodic potentials. While the underlying reason for this performance is not known, it may relate to the electrodes potential being sufficiently cathodic to reduce surface impurities on the metal thus rendering it more active for oxygen reduction.

While the electrodes performance is enhanced when compared to structures utilizing untreated XC-72R they are still incapable of supporting the current densities necessary for a chlor-alkali cell. Further delevopment of steam activated XC-72R was therefore terminated.

6.2.6 KETJENBLACK CARBON

Ketjenblack Carbon (KB) is purported by the manufacturer to be a carbon black rather than an active carbon, but to have the surface area of an active carbon. BET measurements confirmed the manufacture's claim, to within experimental error, that the surface area was approximately 1000 sq m/g. As was indicated in Table 1, its electrochemical and chemical properties more closely resemble a carbon black such as XC-72R. This similiarity is underscored by their similiar values for the oxygen reduction half-wave potential and their peroxide decomposition rate constants.

Since the KB surface is itself relatively inactive for oxygen reduction reduction it presents a good surface on which to carry out catalyst studies to determine maximum catalyst effectiveness. For this reason KB was studied in both its modified and catalyzed unmodified forms.

6.2.6.1 CATALYZED UNMODIFIED CARBON POWDER STUDIES

Samples of uncatalyzed, platinum catalyzed, and palladium catalyzed KB were prepared to determine the catalytic activities of the respective materials. The platinum was deposited from the Prototech acid using standard techniques (USP 4,044,193). The palladium was deposited via four techniques; Prototech, ion-exchange, colloidal, and simple soaking. The Prototech method is described in the above reference. In the ion-exchange technique the native KB was treated with nitric acid to increase the potential number of exchange sites for palladium deposition. Upon treatment of the resultant carbon with a solution of the palladium salt the material was reduced in 4% hydrogen in argon at 200 deg C for two hours. In the colloidal method a suspension of palladium was prepared by the Prototech method and the carbon added to the suspension. The material was then filtered from the suspension liquor. In the last method the material was merely soaked in a solution of the palladium salt and subsequently reduced by heating in 4% hydrogen in argon at 200 deg C for two hours. The results of the electrochemical characterizations of these materials is summarized in Table 6.

Table 6. Electrochemical Activity of Catalyzed Ketjenblack

Metal and Loading (w/w)	Deposit. Method	E(1/2) vs.RHE mV	I(disc) mA @425mV	I(ring) uA	Ir/Id (E-2)	k(H2O2) [min(-1) g(-1)]
0	---	95	0.01	1.5	15	0.1
5% Pt (H2 Red.)	PR	440	0.5	7.5	1.5	31
5% Pt (No Red.)	PR	435	0.1	6	6.0	21
5% Pd	PR	645	0.83	37	4.5	27
10% Pd	PR	710	0.94	28	3.0	34
5% Pd	IX	755	1.05	21	2.0	25
5% Pd	IX	750	1.27	9	0.7	15
10% Pd	IX	770	1.10	33	3.0	19
10% Pd	IX	755	1.39	10	0.7	22
5% Pd	C	305	0.01	1	1.0	12
10% Pd	C	100	0.02	0.5	5.0	13
5% Pd	S	360	0.27	7.0	2.6	--
10% Pd	S	405	0.19	4.0	2.1	--

PR = Prototech Method
IX = Ion Exchange
C = Colloidal
S = Soaking

It is apparent from the table that large variations can be ascribed to the catalyst loadings as well as their method of application. It is particularly striking that the palladium deposited on ion-exchange enhanced Ketjenblack seems more active for oxygen reduction than any other method of palladium deposition. Since the rates of peroxide decomposition of the samples are not out of line with other samples this may indicate that the enhancement arises from some fraction of the reaction proceeding through a direct oxygen reduction mechanism. The observation that two of the four ion exchange samples have relatively low ring-to-disc current ratios supports the decreased production of peroxide.

While it would be tempting to assume that the ion-exchanged palladium catalyzed KB would make a good material such is not the case for a frequently overlooked reason. While these RRDE data are encouraging they do not indicate the long-term stabilities of the material. As was observed in the last reporting period when testing unpyrolyzed metal macrocyclics, catalysts that have good activity in initial performance can often be life-limited due to other phenemnona not directly related to the oxygen reduction.

6.2.6.2 CATALYZED MODIFIED KETJENBLACK CARBON POWDER STUDIES

A sample of modified KB carbon, prepared in an analagous way to the modified Shawinigan Black carbons (see above), was prepared and subjected to RRDE tests. The results are given in Table 7.

Table 7. Modified Ketjenblack Powder Study

Sample 11116-	E(1/2) vs.RHE mV	I(disc) mA @425mV	I(ring) uA	Ir/Id (E-2)	k(H2O2) [min(-1) g(-1)]
91(AW)	565	0.94	6.0	0.64	11

11116-91(AW) =
(Ni:Co:Al:Ru=0.1:1:1:0.025) umole/g C (X 10)

Since the shift in the half-wave potential and the enhanced peroxide decomposition rates clearly show that the material is quite different than the original KB, it was decided to construct an electrode from a modified material to determine its performance.

6.2.6.3 MODIFIED KETJENBLACK ELECTRODE STUDY

Figure 11 illustrates the polarization of a platinum-catalyzed modified Ketjenblack electrode.

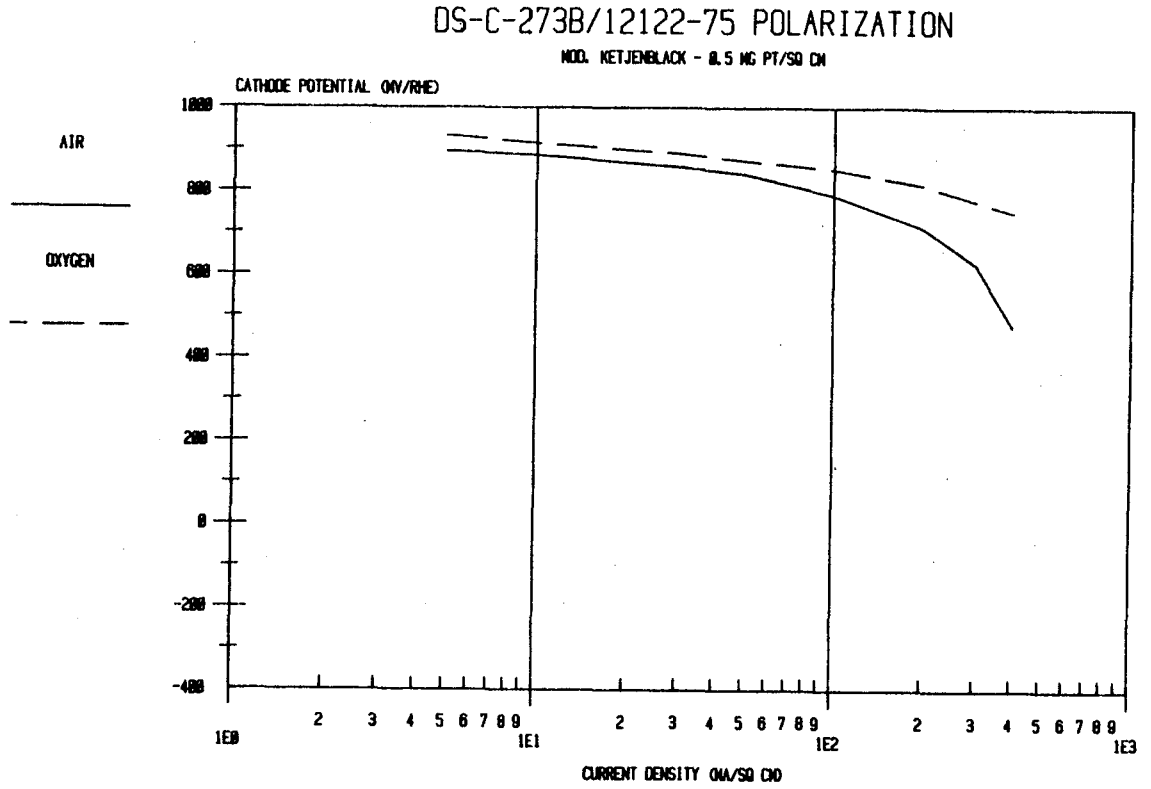


Figure 11.
Polarization of Modified KB Electrode

The polarization curve of this electrode suggest a rather active material, though the diveregence of the curves at higher current densities suggests that mass transport is becoming a limiting factor. The cathode's operating potentials at low current densities, where mass transport is not limiting, is particularly good. This could be due to either very efficient peroxide decomposition or to a significant fraction of the reaction proceeding via a four electron mechanism. The relatively small Ir/Id ratio suggests that a lesser amount of peroxide is liberated from the electrode than with many other materials.

The material also performed well in a lifetest (Figure 12). Through 103 days of operation the performance deteriorated at approximately 0.6 mV/day. At that point a cell upset interupted the test and the electrode began to deteriorate

at a more rapid rate.

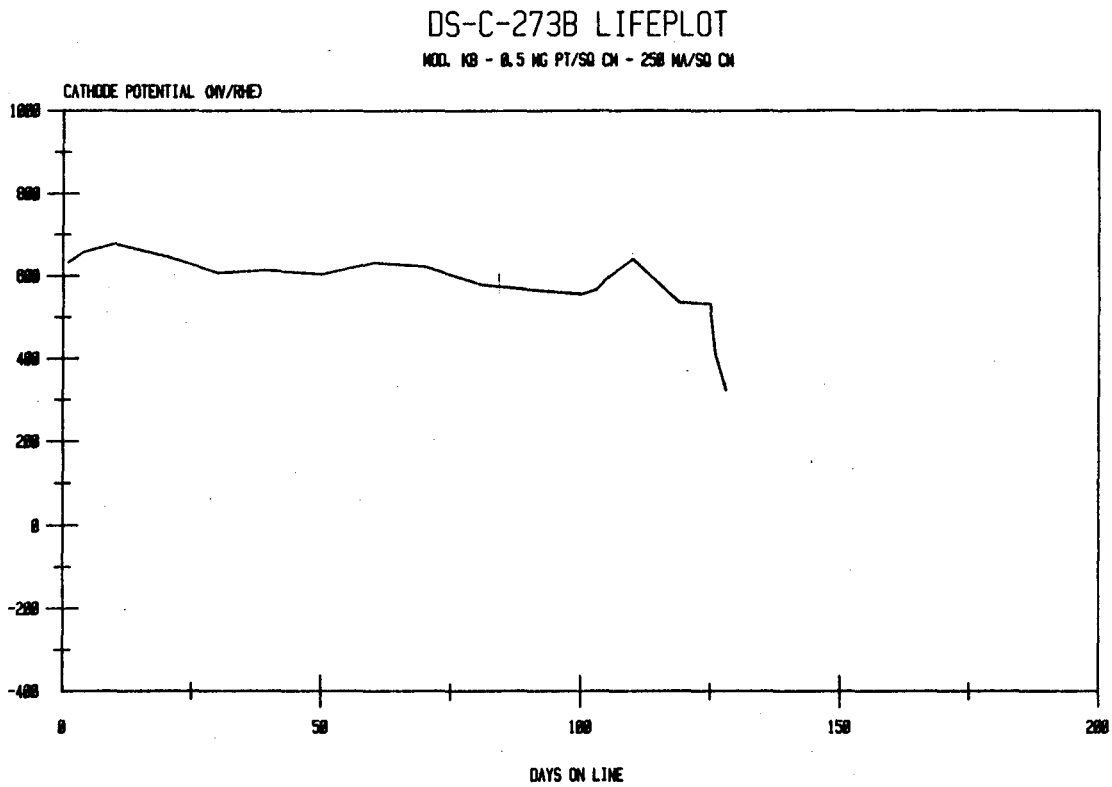


Figure 12.
Lifetest of Modified KB Electrode.

6.2.7 DISCUSSION

Carbon modifications are used to extend the life of the air electrodes. It has been demonstrated (3) that alkaline electrolyte electrodes suffer from catalyst isolation and carbon degradation. This degradation is often accompanied by loss of mass transport due to the corrosion of the carbon and degradation of the gas transport capillary network.

While carbon blacks appear to be more stable than active carbons, they do not exhibit high activity. It was earlier demonstrated that the highly active carbons appeared to suffer from rapid rates of morphological deterioration. It was an effort to combine the desirable characteristics of each that lead to the sucrose bound modified carbons. The thermally modified RB carbons do not appear to be greatly different than the native material. The modified SB and XC-72R carbons, on the other hand, showed some favorable characteristics such as more favorable half-wave potentials and peroxide decomposition rates, but did not appear to be greatly enhanced in lifetime with air operation. (Though some did perform well with oxygen as the depolarizing gas.)

The modified Ketjenblack carbon, on the other hand, exhibited vastly different properties than the parent material. An anodic shift of more than four hundred millivolts in the oxygen reduction half-wave potential and a greater than two orders of magnitude change in the peroxide elimination rate are observed. The lifetest of the platinum-catalyzed structure was also better than any of the other modified carbon elctrodes tested. Other physical changes in the electrode such as the structure formed by the carbon particles, the catalytic activity of the particular metal oxides incorporated into the electrode, and the conductivity of the electrode itself may also be affected.

6.3 COMMERCIAL PROTOTYPE ELECTROLYZER SCALE-UP

The scale-up of air cathode technology to commercial-sized electrolyzer has been the underlying goal of Diamond Shamrock's development of the air cathode. In addition to the contract's goal of developing a high current density alkaline oxygen cathode Diamond Shamrock has pursued an independent effort in developing a commercial cell that could exploit this technology. The substitution of the oxygen reduction reaction for hydrogen evolution has a major effect on the voltage distributions in an operating commercial cell and also point toward likely cell improvements in the future.

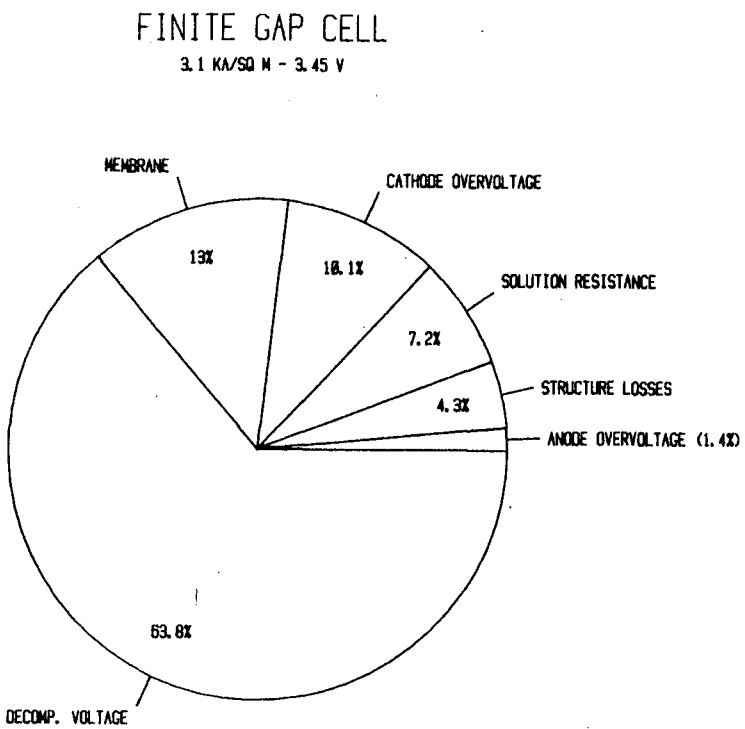


Figure 13.
Finite Gap Cell Voltage Distribution

The distribution of the voltage in a typical operating cell is shown in Figure 13. Somewhat more than 60% of the voltage of a typical cell is required to overcome the decomposition voltage or reversible potential of a hydrogen evolving membrane cell. Of the remaining 40% a significant amount can be saved through cell improvements currently in development stage. Catalytic coatings for the hydrogen evolving cathode could reduce the operating potential by 150-250 mV. Reduction or elimination of the inter-electrode gaps could save another 150-200mV. Improvements in the membrane, some of which will result in decreased gas bubble problems in addition to improved performance could save an additional 150mV. Thus certain cell and membrane improvements will likely be capable of reducing cell voltage by 0.6V at 3.1 kA/sq m. As shown in Figure 14 these improvements will make a substantial improvement in cell performance. Eventually cell operating potentials in the area of 2.9V may be reached.

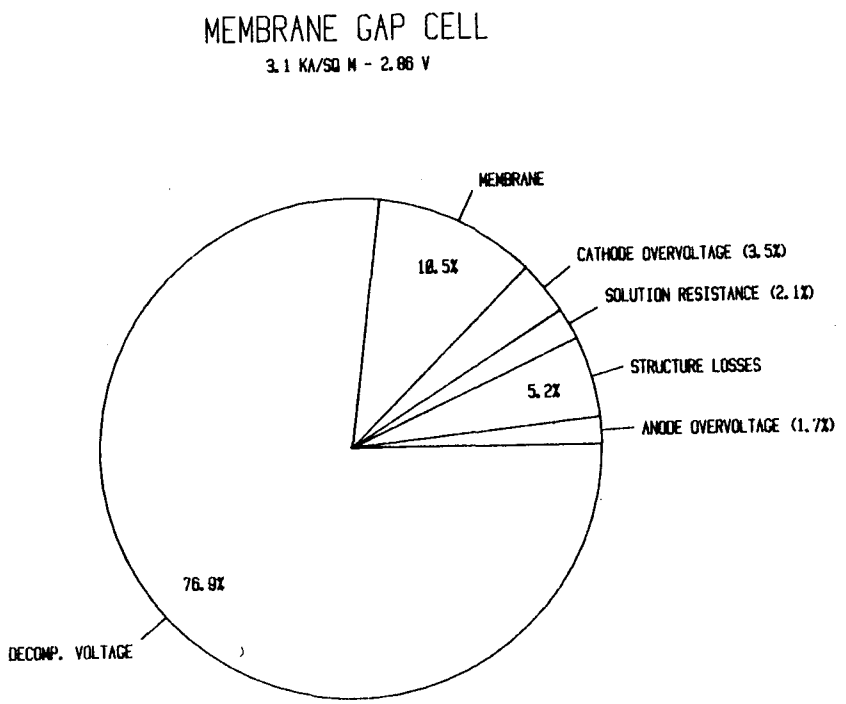


Figure 14.
Membrane Gap Cell Voltage Distribution

The voltage distributions in the resulting cell will be even more striking than in the previous generation cell (Figure 15); over three-fourths of the cells operating voltage will be due to the decomposition (that is, thermodynamically required) voltage. Since this value cannot be altered for any specific reaction it will become increasingly difficult to develop significant further improvements in cell performance in conventional electrolyzers.

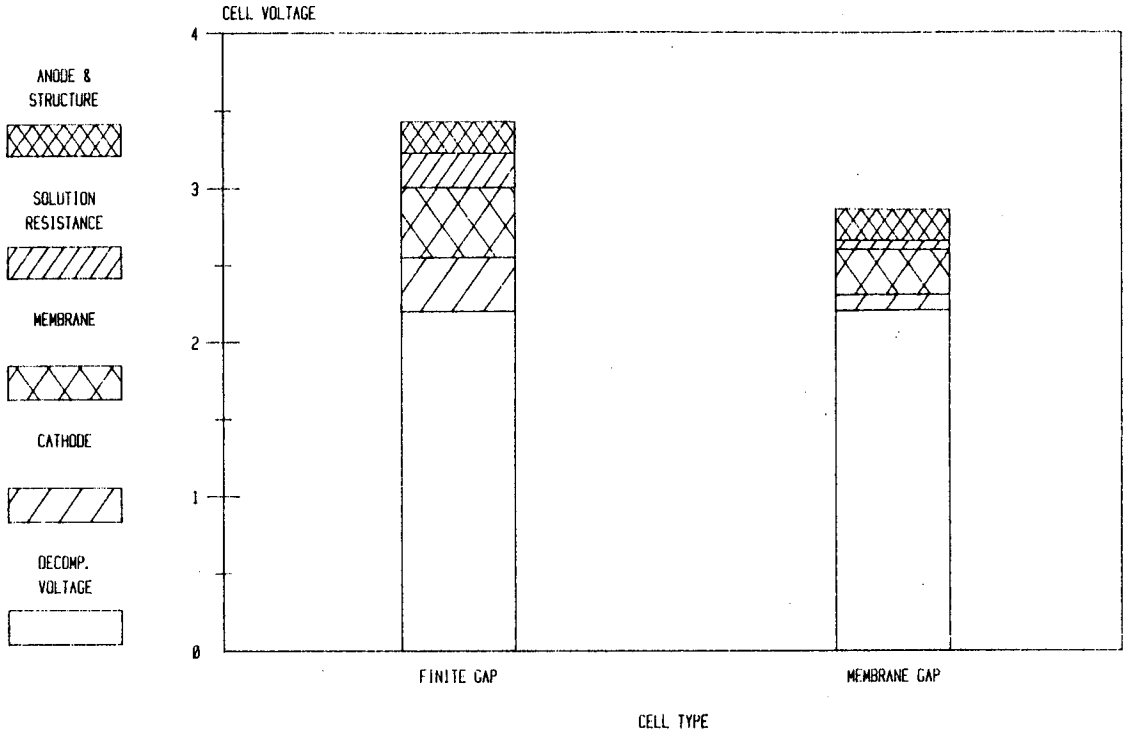


Figure 15.
Cumulative Voltage Distributions

Comparison of the reversible potentials for the oxygen reduction and hydrogen evolution reactions suggests that 1.23 V may be saved by substituting the oxygen reduction reaction. The greater irreversibility of the air cathode, relative to the hydrogen cathode, does not allow that great of a reduction in cell voltage. A substantial fraction of the voltage savings is attainable, however, and it is projected that electrolyzers will be able to operate in the 2.1V region at 3.1 kA/sq m. The accomplishment of such voltages will require a totally new electrode in a new cell configuration.

Figure 16 illustrates the operation of an air cathode in a chlor-alkali cell. The anode processes are unchanged in comparison to a normal membrane cell. Brine entering the

anolyte chamber is oxidized at the dimensionally stable anode to form chlorine gas and sodium ion. The sodium ion migrates through the membrane. The oxygen reduced at the air cathode forms hydroxide ion which combines with the sodium ion and leaves the cell as concentrated caustic. There are three major differences in the air cathode cell.

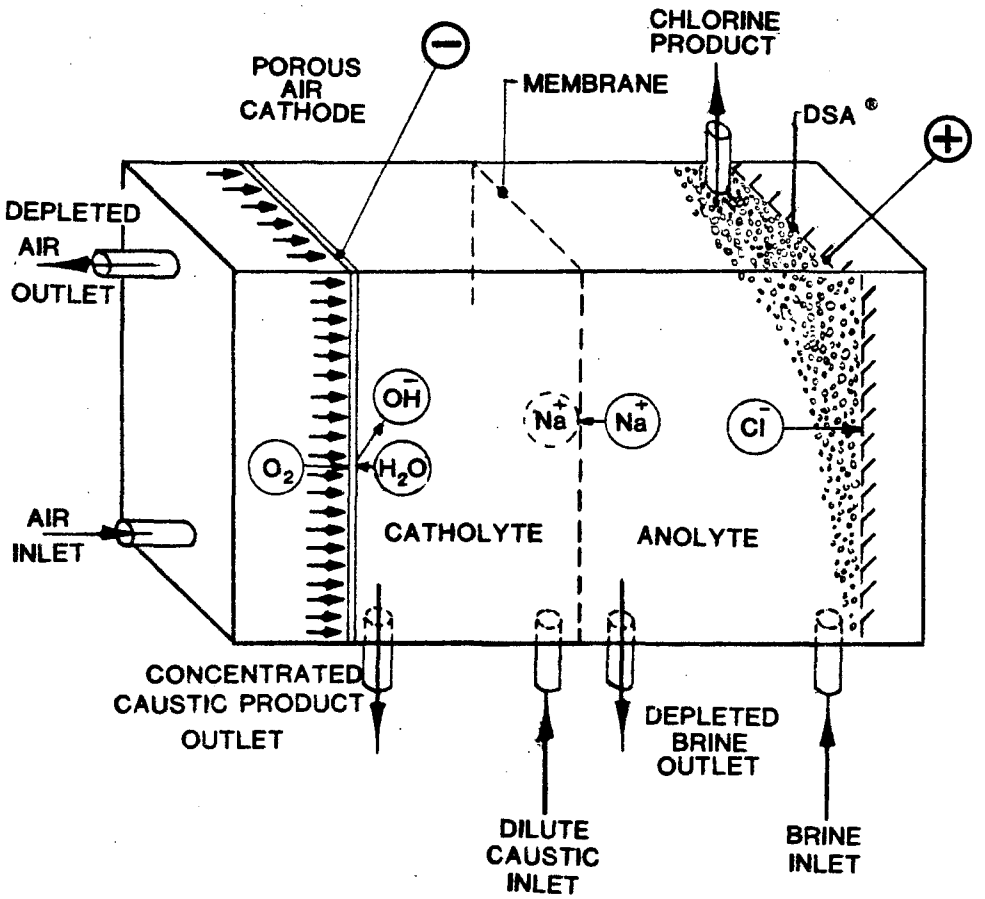


Figure 16.
Air Cathode Chlor-Alkali Cell

The first is the inclusion of an air chamber behind the electrode to provide the air for the cathodic reaction. Second, since no hydrogen is produced by the reduction of oxygen there is no need for porting or hydrogen handling equipment. Most important, of course, is that the cell operates at approximately 1.0V lower potential than a conventional hydrogen evolving cell.

Initial development of the air cathode was pursued in small bench scale cells with cathode areas of only 6 sq cm. It was demonstrated in these tests, however, that air cathodes could perform stably for periods in excess of one year and maintain good performance (Figure 17).

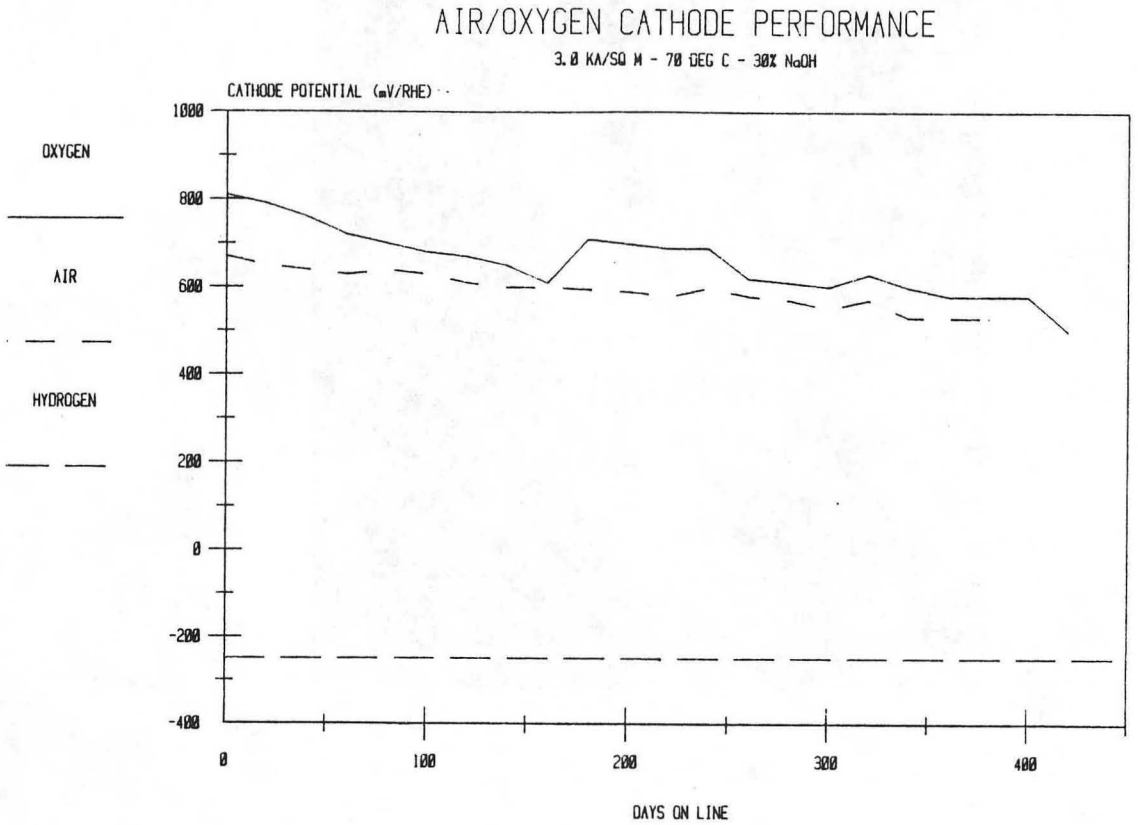
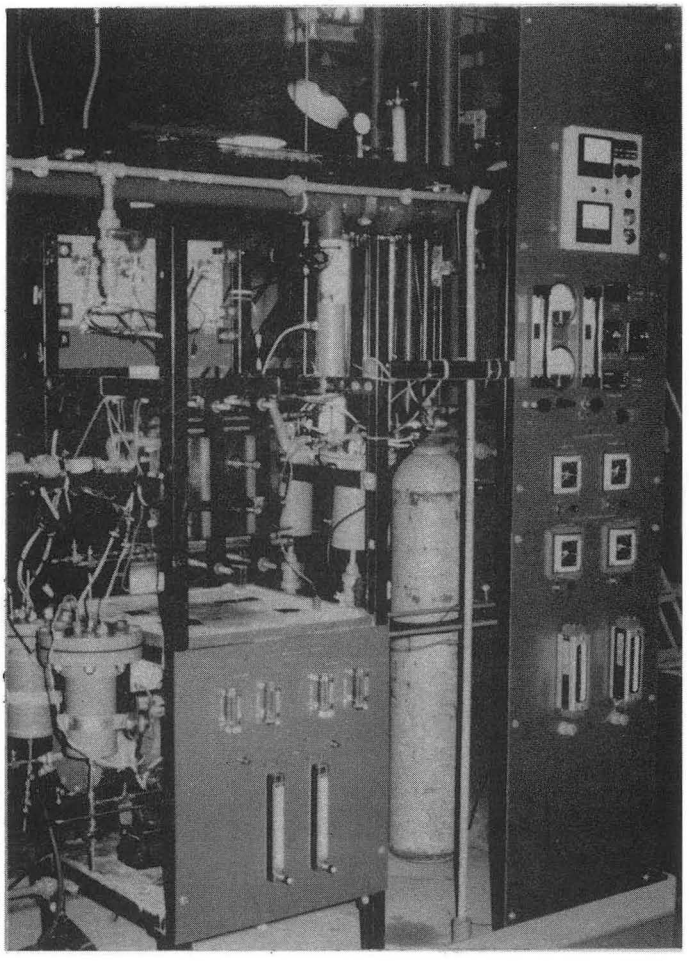


Figure 17.
Bench Scale Cathode Test

Tests in bench scale membrane cells verified that comparable levels of performance were achievable in actual chlor-alkali cells. Tests of larger electrodes in a 0.1 sq m pilot cell demonstrated that performance did not suffer as a result of scaling up cathode size (Figures 18 and 19).

The prototype electrolyzer and support systems have been designed, constructed, and are currently being operated at the Diamond Shamrock's Muscle Shoals test site (Figure 20).



CBB 8310-8671

Figure 18. Pilot Cell

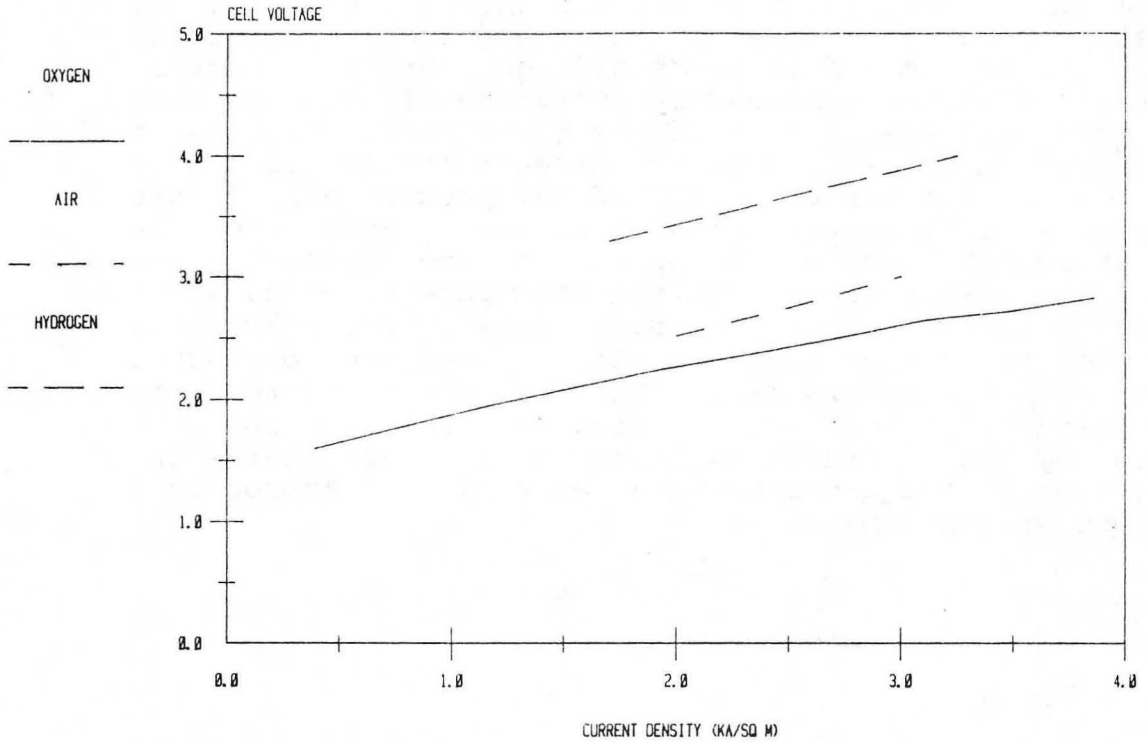
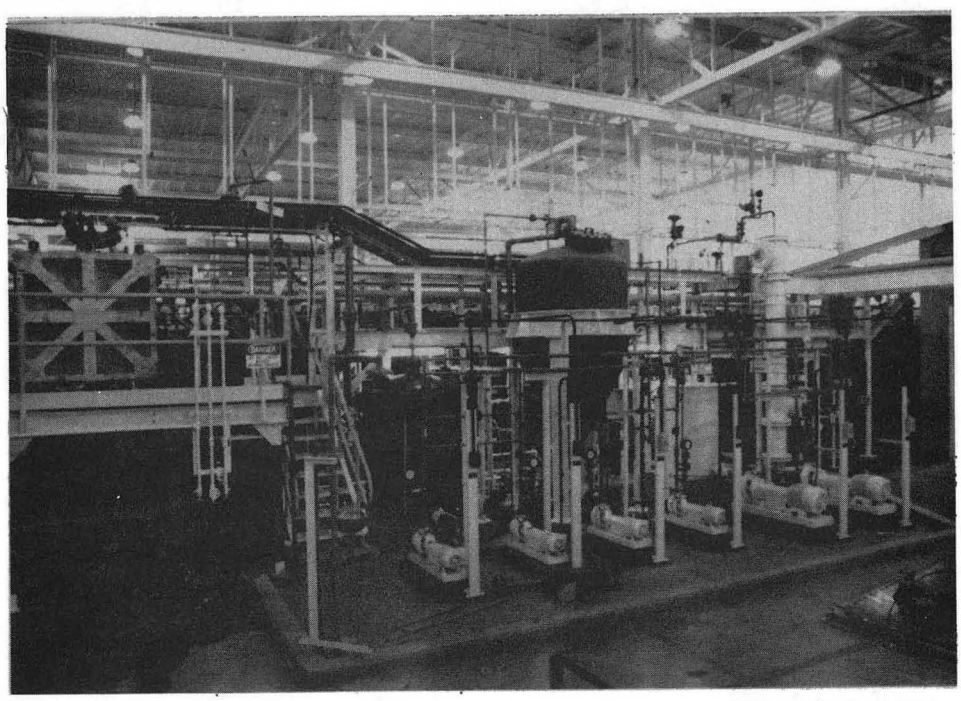


Figure 19. Pilot Cell Performance



CBB 8310-8673

Figure 20. Prototype Installation

The layout of the plant is very similar to a normal membrane cell plant. There are three notable changes, however. As previously noted the absence of hydrogen production eliminates the need for large hydrogen handling systems. The voltage reduction achieved by using the air cathode also allows somewhat smaller rectifiers to be used. Finally, a high performance air scrubbing system must be used to reduce the carbon dioxide concentration of the process air (Figure 21). Failure to adequately scrub the air results in the precipitation of sodium carbonate in the pores of the electrode which in turn affects the transport of oxygen and hydroxide within the electrode. Left unchecked the accumulation of sodium carbonate will cause the premature failure of the cathodes. In the plant system the concentration of the carbon dioxide is continuously monitored by an infrared analyzer and an alarm alerts the cell operator if the level becomes excessive. Appropriate corrections are then made.

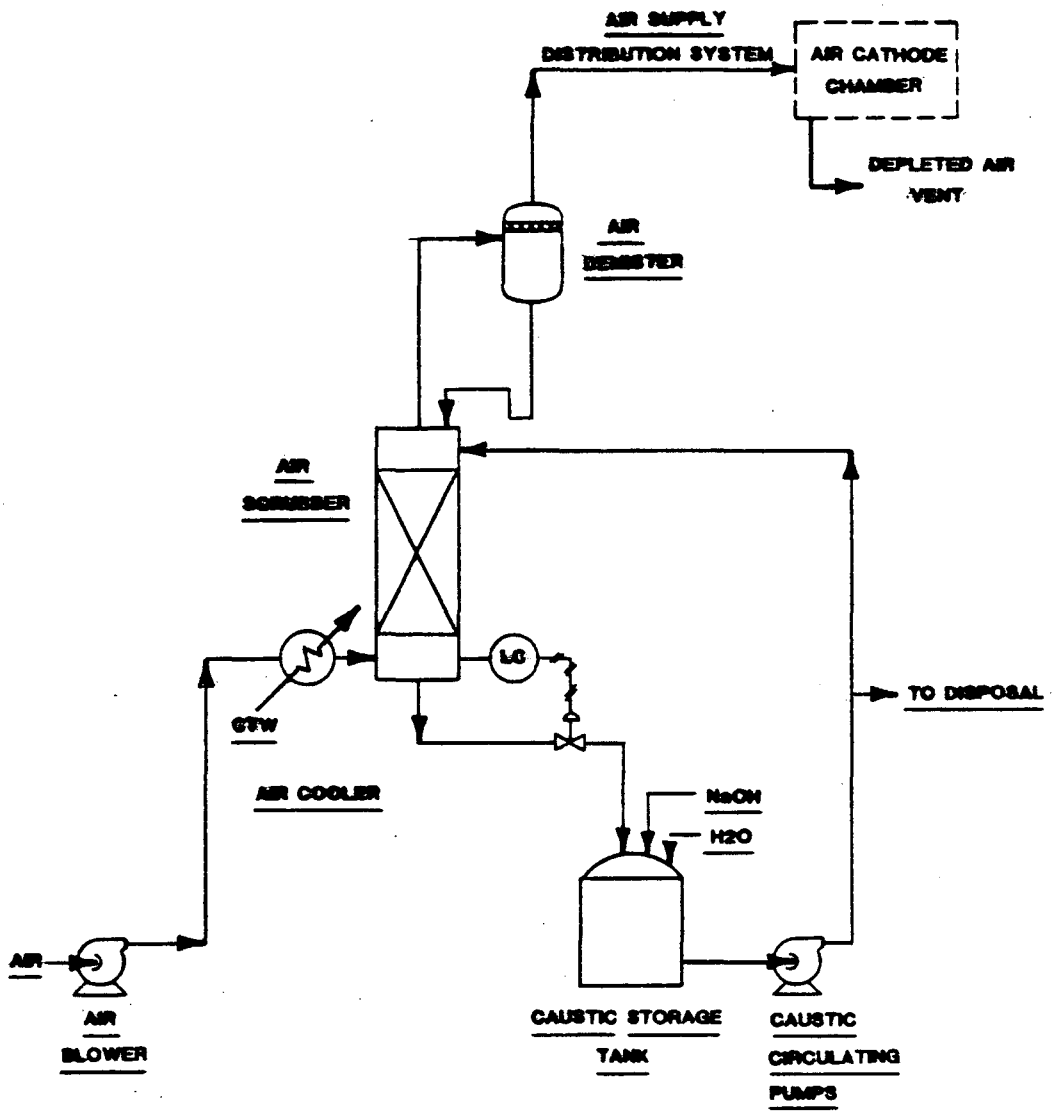


Figure 21. Air Cathode Supplemental Equipment

At the present time test oxygen cathode cells, compared to comparable hydrogen evolving cells, are saving approximately 1.0V over a comparable hydrogen evolving cell (Figure 22).

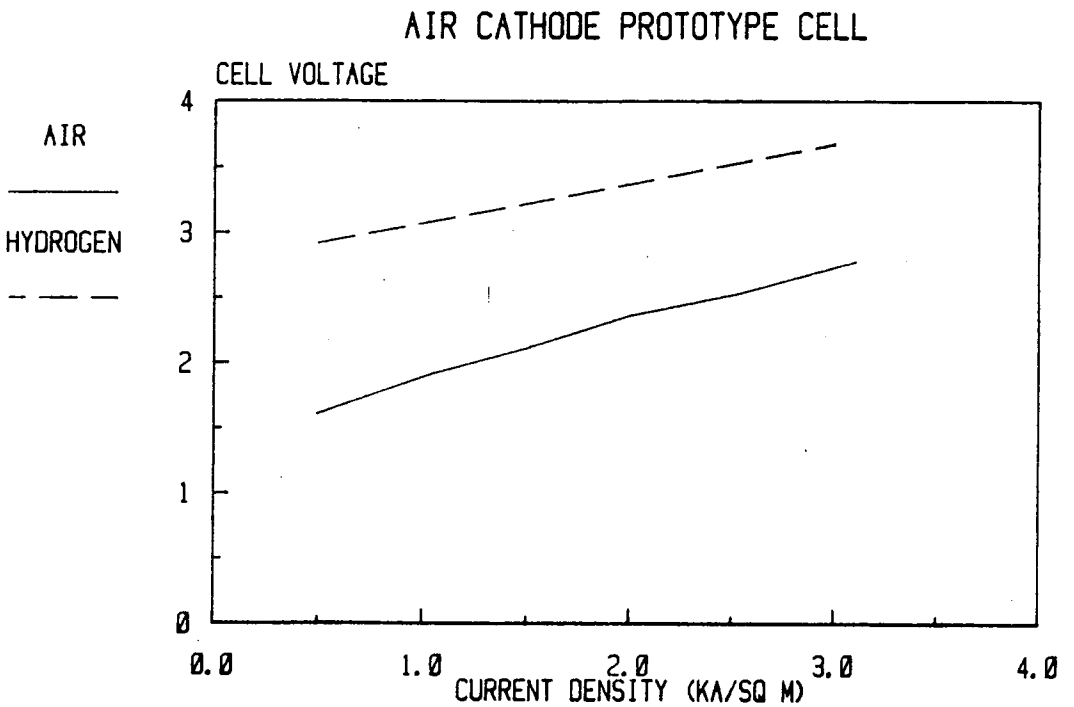


Figure 22. Prototype Cell Polarization.

Most of this improvement arises directly from the substitution of the oxygen reduction reaction for the hydrogen evolution reaction. Part of the voltage reduction arises from absence of the hydrogen bubble-field in the catholyte, thereby raising the effective conductivity of the catholyte. Cell improvements leading to the membrane gap cell may eliminate much of the hydrogen bubble-field effect in hydrogen evolving cells, but the savings of more than 0.8 V will continue to be available with air cathode cells. In comparing the projected cell operating voltages (Figure 23) it can be seen that the air cathode cell, when combined with other cell improvements will operate near 2.1V.

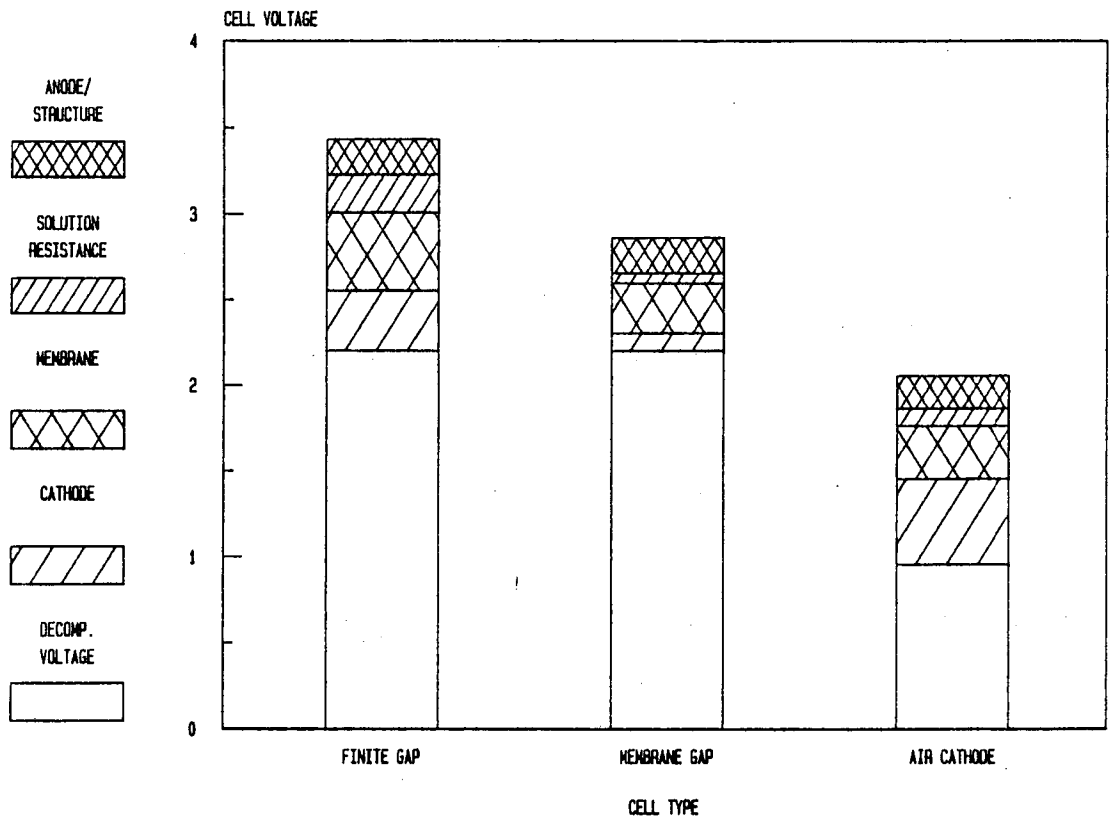


Figure 23. Cell Operating Voltages

This will lead to power consumptions (Figure 24) of approximately 1450 DCkWh/mT NaOH. Such a power savings of 550 DCkWh/mT at 60 mil power corresponds to a power savings of $33/mT.

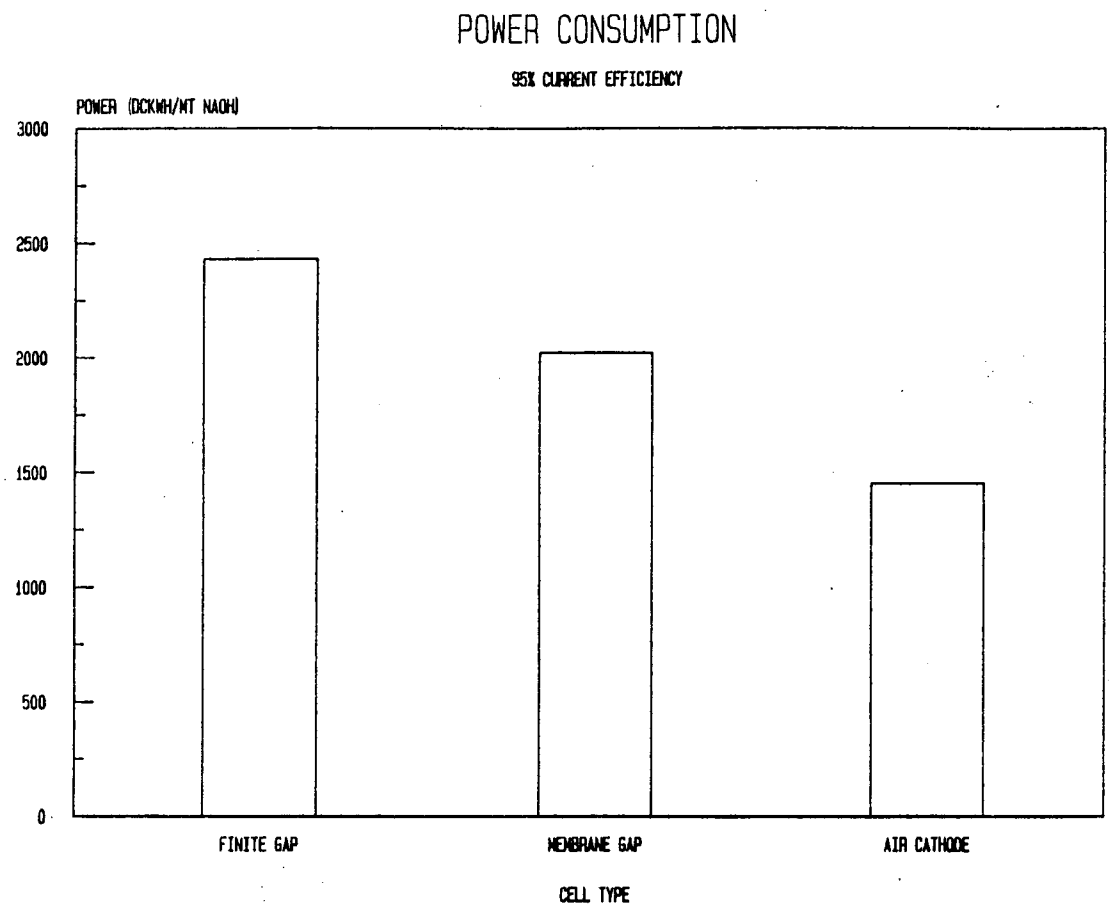


Figure 24. Cell Power Consumption

Figure 25 shows the voltage distributions in such an air cathode cell.

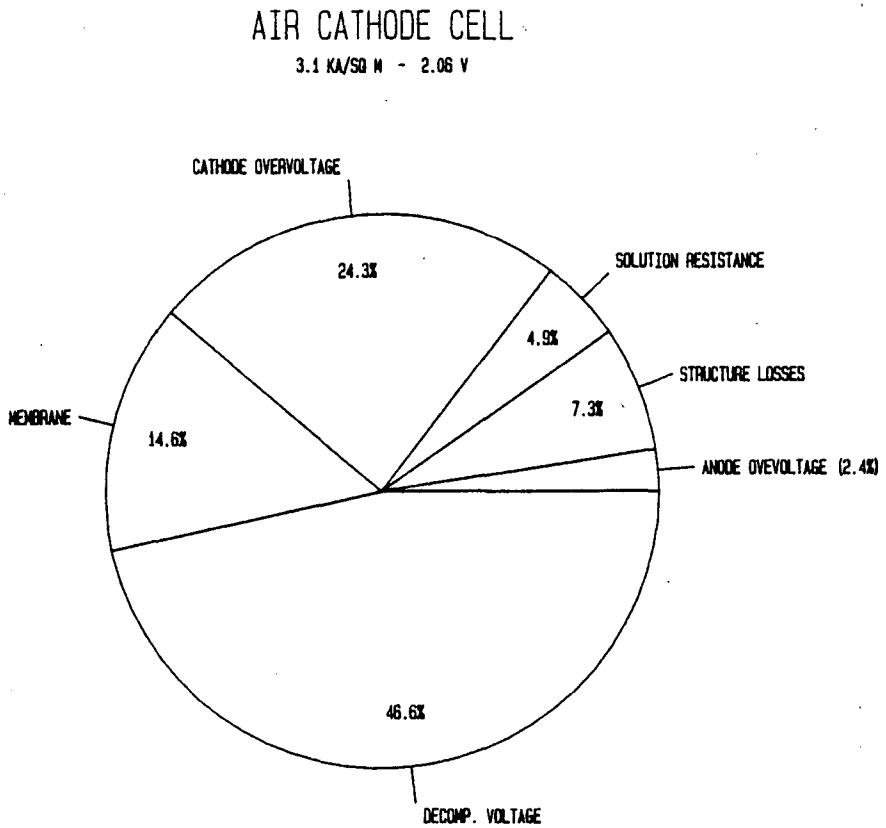


Figure 25.
Air Cathode Cell Voltage Distribution

Looking even further into the future when improved oxygen reduction catalysts become available it is feasible that the large cathode overvoltage will be even further reduced. It is not inconceivable that cell operating voltage less than 2.0V may be achieved.

6.4 CONCLUSIONS

The air cathode has been demonstrated as a feasible technology for the production of chlorine and caustic from chlor-alkali membrane cells. The use of the air cathode in these systems has been demonstrated to reduce cell electrical power consumption by approximately 25%. The electrodes utilized in these systems are satisfactory for initiation of the technology, but suffer from a gradual performance deterioration which eventually requires their replacement. Investigation of a variety of available carbons suggests that material that combines the necessary high activity with resistance to deterioration is not yet available. Such a material would greatly facilitate the further development of low-cost alkaline air cathode technology.

REFERENCES

1. "Oxygen Electrodes for Energy Conversion and Storage", Annual Report Number 1, Department of Energy Contract No. EC-77-C-02-4146, Contractor: Diamond Shamrock Corporation, Painesville, OH, R.K. Sen, Manager, Subcontractor: Case Western Reserve University, Cleveland, OH, Ernst B. Yeager, Manager, January 15, 1980.

2. "Oxygen Electrodes for Energy Conversion and Storage", Annual Report Number 2, Department of Energy Contract No. EC-77-C-02-4146, Contractor: Diamond Shamrock Corporation, Painesville, OH, R.K. Sen, Manager, Subcontractor: Case Western Reserve University, Cleveland, OH, Ernst B. Yeager, Manager.

3. "Oxygen Electrodes for Energy Conversion and Storage", Annual Report Number 3, Department of Energy Contract No. DE-AC02-77ET25502 Contractor: Diamond Shamrock Corporation, Painesville, OH, I. Malkin, Manager, Subcontractor: Case Western Reserve University, Cleveland, OH, Ernst B. Yeager, Manager, November 5, 1981.

7.0 APPENDIX

7.1 PUBLICATIONS UNDER D.O.E. PROJECT

1. "Oxygen Electrodes for Electrochemical Energy Storage Systems," in Energy Storage, J. Silverman, ed., Pergamon Press, New York, 1980, pp. 201-211.

2. "Reflectance Spectra of Monolayers of Tetrasulfonated Transition Metal Phthalocyanines Adsorbed on Electrode Surfaces, "B.Z. Nikolic, R.R. Adzic, and E.B. Yeager, J. Electroanal. Chem., 103, 281-287 (1979).

3. "Optical and Electrochemical Studies of Adsorbed Transisition Metal Complexes and their O_2 Electrocatalytic Properties, "E. Yeager, J. Zagal, B.A. Nikolic and R.R. Adzic, Proceedings of the Third Symposium on Electrode Processes, National Meeting of the Electrochemical Society, Boston, May 1979, S. Bruckenstein, J.D.E. McIntyre, B. Miller and E. Yeager, eds., The Electrochemical Society, Princeton, NJ, 1980, pp. 436-456.

4. "A Mechanistic Study of O_2 Reduction on Water Soluble Phthalocyanines Adsorbed on Graphite Electrodes, "J. Zagal, P. Bindra and E. Yeager, J. Electrochem. Soc., 127, 1506-1517 (1980).

5. "Raman Studies of the Silver-Silver Oxide Electrode," R. Kotz and E. Yeager, J. Electroanal. Chem. 111, 105-110 (1980).

6. "Raman Spectroscopy of Cobalt Phthalocyanine Adsorbed on a Silver Electrode, "R. Kotz and E. Yeager, J. Electroanal. Chem., 113, 113-126 (1980).

7. "Major Electrochemical Developments Related to the Energy Problem," by Ernest Yeager, in Progress in Batteries and Solar Cells, Vol. 3, JEC Press, Inc., Cleveland, 1980, pp. 242-244.

8. "Electrochemistry of Oxygen," by Ernest Yeager, in Progress in Batteries and Solar Cells, Vol. 3, JEC Press Inc., Cleveland, 1980, pp., 238-241.

9. "Mixed Oxides of Manganese as Catalysts for Hydrogen Peroxide Decomposition and Oxygen Cathodes in Alkaline Solutions," by K. Matsuki, H. Takahashi and E. Yeager, Proceedings of the Manganese Dioxide Symposium, Vol. 2, Tokyo, 1980, pp. 74-96.

10. "Recent Advances in the Science of Electrocatalysis," by Ernest Yeager, J. Electrochem. Soc., 128, 160C-171C (1981).

11. "Potential Dependence of Vibrational Frequencies of Adsorbates on a Silver Electrode," by R. Kotz and E. Yeager, J. Electroanal. Chem., 123, 335-344 (1981).

12. "Theory for CN^- and Ag-C Vibrational Frequency Dependence on Potential: Cyanide on a Silver Electrode," by A.B. Anderson, R. Kotz and E. Yeager, Chem. Phys. Letters 82, 139-134 (1981).

13. "Offsetting Impurities in O_2 Electroreduction on Platinum with Adsorbed Metal Ions," by R. Amadelli, J.A. Molla and E. Yeager, J. Electroanal. Chem. 126, 265-271 (1981).

14. "In-situ Mossbauer effect spectroscopy of adsorbed species on high surface area electrodes," by D. Scherson, S.B. Yao, E.B. Yeager, J. Eldridge, M.E. Kordesch and R.W. Hoffman, Applcations of Surface Science, 13 (1982) in press.

7.2. Ph.D. THESES UNDER D.O.E. PROJECT

1. Oxygen Reduction on Water Soluble Phthalocyanines Adsorbed on Graphite Electrodes. Jose H. Zagal-Moya.

2. Influence of Metal Ions on Oxygen Reduction on Gold and Platinum. Rossano Amadelli.

3. Oxygen Reduction on Carbon and Graphite and Carbon-Supported Catalysts. Jaynal Molla. (To be submitted soon)

This report was done with support from the Department of Energy. Any conclusions or opinions expressed in this report represent solely those of the author(s) and not necessarily those of The Regents of the University of California, the Lawrence Berkeley Laboratory or the Department of Energy.

Reference to a company or product name does not imply approval or recommendation of the product by the University of California or the U.S. Department of Energy to the exclusion of others that may be suitable.

TECHNICAL INFORMATION DEPARTMENT
LAWRENCE BERKELEY LABORATORY
UNIVERSITY OF CALIFORNIA
BERKELEY, CALIFORNIA 94720